JUNE 2024

AJNR

VOLUME 45 • PP 673–832

AJNR
AMERICAN JOURNAL OF NEURORADIOLOGY
Official Journal ASNR • ASFNR • ASHNR • ASPNR • ASSR
JUNE 2024 | VOLUME 45 | NUMBER 6 | WWW.AJNR.ORG

THE JOURNAL OF DIAGNOSTIC AND INTERVENTIONAL NEURORADIOLOGY

Radiologic evaluation of dysraphic malformations of the spine and spinal cord
Time-saving 3D MR imaging protocols for face and neck imaging
Outcomes of emergency MR imaging in dizziness and vertigo
Spot sign in multiphase CTA predicts intracerebral hemorrhage growth

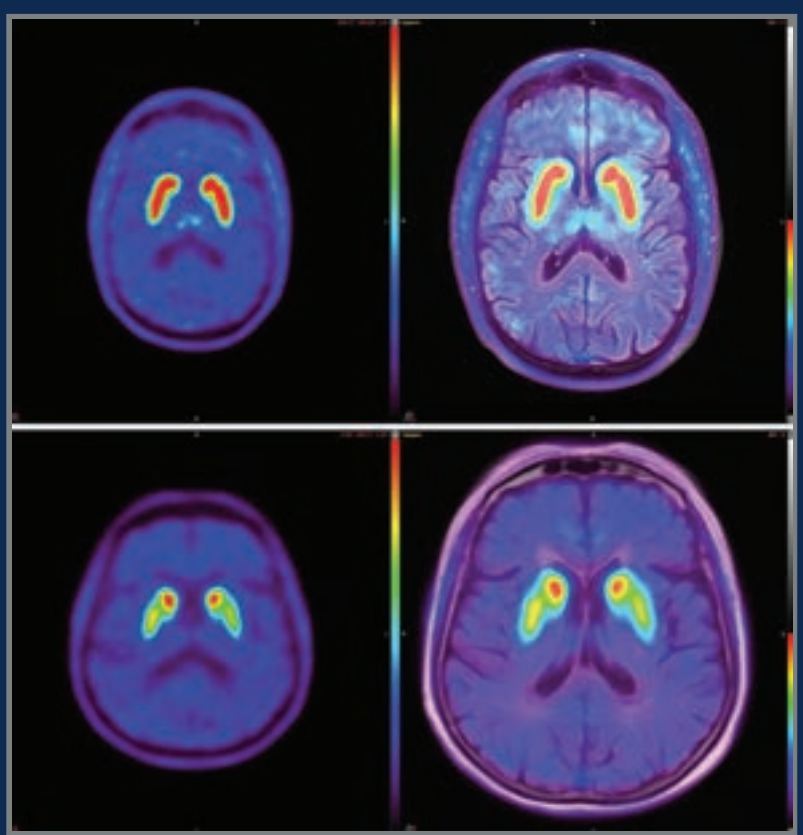

ASNR American Society of Neuroradiology
ASHNR American Society of Head & Neck Radiology
American Society of Pediatric Neuroradiology

Simplify
the MOC Process

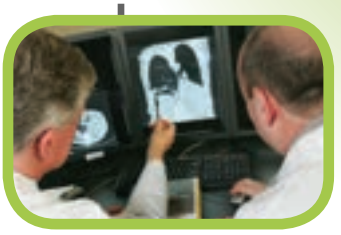

Manage
your CME Credits Online

CMEgateway.org

Available to Members of Participating Societies

- American Board of Radiology (ABR)
- American College of Radiology (ACR)
- American Roentgen Ray Society (ARRS)
- American Society of Neuroradiology (ASNR)
- Commission on Accreditation of Medical Physics Educational Programs, Inc. (CAMPEP)
- Radiological Society of North America (RSNA)
- Society of Interventional Radiology (SIR)
- SNM
- The Society for Pediatric Radiology (SPR)

It's Easy and Free!

Log on to CME Gateway to:

- View or print reports of your CME credits from multiple societies from a single access point.
- Print an aggregated report or certificate from each participating organization.
- Link to SAMs and other tools to help with maintenance of certification.

American Board of Radiology (ABR) participation!

By activating ABR in your organizational profile, your MOC–fulfilling CME and SAM credits can be transferred to your own personalized database on the ABR Web site.

Sign Up Today!

go to CMEgateway.org

AJNR go green

AJNR urges American Society of Neuroradiology members to reduce their environmental footprint by voluntarily suspending their print subscription.

The savings in paper, printing, transportation, and postage directly fund new electronic enhancements and expanded content.

The digital edition of *AJNR* presents the print version in its entirety, along with extra features including:

- **Publication Preview**
- **Case Collection**
- **Podcasts**
- **The *AJNR* News Digest**
- **The *AJNR* Blog**

It also reaches subscribers much faster than print. An electronic table of contents will be sent directly to your mailbox to notify you as soon as it publishes.

Readers can search, reference, and bookmark current and archived content 24 hours a day on www.ajnr.org.

ASNR members who wish to opt out of print can do so by using the AJNR Go Green link on the *AJNR* Website (http://www.ajnr.org/content/subscriber-help-and-services). Just type your name in the email form to stop print and spare our ecosystem.

AJNR

Dear *AJNR* Subscriber:

Towards the end of 2024, *AJNR* is set to undergo a significant change by fully embracing an electronic format, bidding farewell to traditional paper publications. This shift is motivated by the necessity to address rising costs linked to printing, shipping, and storage, and our goal to maintain financial equilibrium.

The transition to an electronic format brings a host of advantages, presenting more personalized content and enriched visual elements. This includes additional images and diverse media types, particularly beneficial in the field of neuroradiology. Supplementary content will enhance your experience, providing easy access to materials, commentaries, and related resources.

Acknowledging the sentimental value attached to physical copies, we are compelled by both practical financial considerations and a commitment to sustainability to embrace technological progress. Our emphasis is on maintaining a positive outlook and adaptability throughout this transition. To actively engage you in this continual journey, the *AJNR* wants to hear your innovative ideas to shape our electronic platform. I have already heard from many of you through email and our online sessions throughout April.

Please reach out directly to me at mw.ajnr.eic@gmail.com with any ideas or suggestions.

Also, please immediately activate your individual subscription account and also consider registering for Publish Ahead of Print (including Preprint) and electronic Table of Contents, Case of the Week, and Keyword/Author Alerts. These links and more information can be found on the *AJNR* website (https://www.ajnr.org/content/ajnr-update) or using the QR code below.

Thank you for your continued engagement.

Sincerely,

Max Wintermark
Editor-in-Chief

AJNR

AMERICAN JOURNAL OF NEURORADIOLOGY

JUNE 2024
VOLUME 45
NUMBER 6
WWW.AJNR.ORG

Publication Preview at www.ajnr.org features articles released in advance of print.
Visit www.ajnrblog.org to comment on AJNR content and chat with colleagues.

REVIEW ARTICLE

STATE OF PRACTICE

GENERAL CONTENTS

AJNR (Am J Neuroradiol ISSN 0195–6108) is a journal published monthly, owned and published by the American Society of Neuroradiology (ASNR), 820 Jorie Boulevard, Oak Brook, IL 60523. Annual dues for the ASNR include approximately 19% for a journal subscription. The journal is printed by Intellicor Communications, 330 Eden Road, Lancaster, PA 17601; Periodicals postage paid at Oak Brook, IL and additional mailing offices. Printed in the U.S.A. POSTMASTER: Please send address changes to American Journal of Neuroradiology, P.O. Box 3000, Denville, NJ 07834, U.S.A. Subscription rates: nonmember $475 ($560 foreign) print and online, $320 online only; institutions $550 ($625 foreign) print and basic online, $1080 ($1160 foreign) print and extended online, $380 online only (basic), $825 online only (extended); single copies are $35 each ($40 foreign). Indexed by PubMed/MEDLINE, BIOSIS Previews, Current Contents (Clinical Medicine and Life Sciences), EMBASE, Google Scholar, HighWire Press, Q-Sensei, RefSeek, Science Citation Index, SCI Expanded, ReadCube, and Semantic Scholar.

ONLINE FEATURES

MEMORIAL

LETTERS

BOOK REVIEWS *R.M. Quencer, Section Editor*

Please visit www.ajnrblog.org to read and comment on Book Reviews.

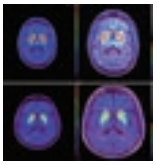

[^{18}F]-FDOPA brain PET can be used to visualize dopaminergic nerve terminals in the striatum for evaluation of parkinsonism. The authors found that image-quality ratings were stable, and that between-subject abnormality detection rates were highly consistent when acquired for at least 10 and up to 20 minutes. [^{18}F]-FDOPA brain PET and fused [^{18}F]-FDOPA brain PET/MR imaging demonstrate the characteristic "comma sign" uptake in the striatum in a healthy subject (*top row*), while the bottom row shows loss of uptake in the bilateral striatum in a patient with clinical deficits.

AJNR

AMERICAN JOURNAL OF NEURORADIOLOGY

Official Journal:
American Society of Neuroradiology
American Society of Functional Neuroradiology
American Society of Head and Neck Radiology
American Society of Pediatric Neuroradiology
American Society of Spine Radiology

JUNE 2024 • VOLUME 45 • NUMBER 6 • WWW.AJNR.ORG

Associate Editors

Nadya Pyatigorskaya, MD, PhD
Neuroradiology Department, Pitié-Salpêtrière Hospital
Researcher, Brain Institute (ICM)
France

Marc Daniel Benayoun, PhD, MD
Assistant Professor of Radiology
Co-Section Head of Nuclear Medicine
Medical Director of Nuclear Medicine and PET
Vice Chair of Radiation Drug Research Committee
Atrium Wake Forest Health
North Carolina

Special Editor

Satoshi Minoshima, MD, PhD
Anne G. Osborn Chair and Professor
Department of Radiology and Imaging Sciences
Spencer Fox Eccles School of Medicine
University of Utah

NEURODEGENERATIVE DISORDER IMAGING

Senior Editor

Gloria Chiang, MD
Associate Professor, Co-Director of the Brain Health Imaging Institute
Department of Radiology
Weill Cornell Medicine/NewYork-Presbyterian Hospital

Associate Editors

Fang Frank Yu, MD
Assistant Professor of Radiology
Division of Neuroradiology, Department of Radiology
Advanced Imaging Research Center
University of Texas Southwestern Medical Center

Priya Rajagopalan, MBBS, MPH
Assistant Professor of Radiology, Division of Neuroradiology
Associate Program Director, Neuroradiology Fellowship
Medical Director, Center for Image Acquisition
Mark and Mary Stevens Neuroimaging and Informatics Institute
Keck School of Medicine, University of Southern California

NEUROIMAGING PHYSICS/FUNCTIONAL NEUROIMAGING/CT AND MRI TECHNOLOGY

Senior Editor

Hongyu An, DSc
Professor, Mallinckrodt Institute of Radiology
Neurology, Biomedical Engineering, Electrical and Systems Engineering, Division of Biology and Biomedical Sciences
Director, Biomedical Magnetic Resonance Center
Associate Director, Center for Clinical Imaging Research
Washington University in St. Louis

Associate Editors

Timothy J. Carroll, PhD
Professor, Department of Radiology
University of Chicago

Hugo de Jong, PhD
Professor of Medical Physics Radiology and Nuclear Medicine
UMC Utrecht
the Netherlands

Special Editor

Roland Bammer, PhD, MEE, MBA, FISMRM
Head/Chair, Department of Radiology and Radiological Sciences
Professor of Radiology and Radiological Sciences, Monash University
Australia

NEUROINTERVENTION

Senior Editor

Steven Hetts, MD, FACR
Co-Chief, NeuroEndovascular Surgery Service Line
Chief of Interventional Neuroradiology, Mission Bay Hospitals
Professor of Radiology, Biomedical Imaging, and Neurological Surgery
University of California, San Francisco

Associate Editors

Kristine Blackham, MD
Associate Professor
Diagnostic and Interventional Neuroradiology
Clinic for Radiology and Nuclear Medicine
University Hospital of Basel

Maksim Shapiro, MD
Clinical Associate Professor
Departments of Radiology, Neurosurgery, and Neurology
Division of Neurointerventional Radiology
NYU Langone Health and Bellevue NYCH + Hospitals
New York

Special Editor

Giuseppe Lanzino, MD
Professor of Neurosurgery
Mayo Clinic, Minnesota

NEUROPSYCHIATRIC IMAGING

Senior Editor

Jody Tanabe, MD
Professor
Chief of Neuroradiology
University of Colorado-Anschutz Medical Campus

Associate Editors

John-Paul J. Yu, MD, PhD
Assistant Professor of Radiology, Psychiatry, and Biomedical Engineering
University of Wisconsin School of Medicine and Public Health

J. Eric Schmitt, MD, PhD
Assistant Professor of Radiology and Psychiatry
Division of Neuroradiology
Perelman School of Medicine, University of Pennsylvania

Special Editor

Leanne Williams, PhD
Vincent V.C. Woo Professor of Psychiatry and Behavioral Sciences
Director of the Stanford Center for Precision Mental Health and Wellness
Stanford University
California

NEUROVASCULAR/STROKE IMAGING

Senior Editor

Ajay Gupta, MD, MS
Professor and Chair, Department of Radiology
Columbia University
New York

Associate Editors

Shalini Amukotuwa, MB BS, PhD, FRANZCR
Head of Neuroradiology and Director of MRI, Monash Health
Associate Professor of Radiology, Monash University
Australia

Mahmud Mossa-Basha, MD
Professor of Radiology, Neurology and Electrical Engineering
Vice Chair of Clinical Research and Clinical Transformation
Co-Director of the Research Vascular Imaging Lab
University of Washington School of Medicine

Special Editors

Bruce Campbell, MBBS (Hons), BMedSc, PhD, FRACP, FAHMS
Consultant Neurologist, Head of Neurology and Stroke
Department of Neurology and Melbourne Brain Centre
Royal Melbourne Hospital
Professor of Neurology, Dame Kate Campbell Fellow
University of Melbourne
Australia

David Liebeskind, MD, FAAN, FAHA, FANA, FSVIN, FWSO
Professor of Neurology
Director, Neurovascular Imaging Research Core
Director, UCLA Comprehensive Stroke Center
University of California, Los Angeles

PEDIATRIC NEUROIMAGING

Senior Editor

Caroline D. Robson, MBChB
Division Chief & Endowed Chair, Neuroradiology
Director, Head & Neck Imaging
Department of Radiology
Department of Otolaryngology
Boston Children's Hospital
Harvard Medical School

Associate Editors

Anna Trofimova, MD, PhD
Assistant Professor, Radiology and Imaging Sciences, Emory University
Pediatric Neuroradiologist, Children's Healthcare of Atlanta

Matthew Whitehead, MD
Department of Radiology, Division of Neuroradiology
Children's Hospital of Philadelphia
Associate Professor of Radiology
Perelman School of Medicine, University of Pennsylvania

Special Editor

Nomazulu Dlamini, MD, MBBS, MRCPCH, MSc (Lon), PhD
Assistant Professor, Director of Children's Stroke Program
The Hospital for Sick Children
Toronto

SPINE IMAGING AND SPINE IMAGE-GUIDED INTERVENTIONS

Senior Editor

J. Levi Chazen, MD
Associate Professor, Neuroradiology
Director, Spine Imaging

International Consensus Statement on the Radiologic Evaluation of Dysraphic Malformations of the Spine and Spinal Cord

Ankit Balani, Jai Sidpra, Sniya Sudhakar, Asthik Biswas, Özgür Öztekin, Valeria Capra, Martin Catala, Andrew J. Copp, Neetu Kumar, Navroop Johal, M. Zubair Tahir, Dominic Thompson, Dachling Pang, David M. Mirsky, Mai-Lan Ho, Thierry A.G.M. Huisman, Andrea Rossi, and Kshitij Mankad

ABSTRACT

SUMMARY: Dysraphic malformations of the spine and spinal cord (DMSSC) represent a spectrum of common congenital anomalies typically (though not exclusively) affecting the lower spinal segments. These may be responsible for varying degrees of neurologic, orthopedic, and urologic morbidity. With advances in neuroimaging, it is now possible to better diagnose and evaluate these disorders both prenatally and postnatally. Neuroimaging, performed at the right time and with technique optimization, is integral in guiding clinical management. However, the terminology used to describe these lesions has become increasingly confusing, and there is a lack of consensus regarding the essential radiologic features and their clinical weighting. This variability in radiologic practice risks unstructured decision making and increases the likelihood of suboptimal, less informed clinical management. In this manuscript, the first of a series of consensus statements, we outline a standardized international consensus statement for the radiologic evaluation of children with suspected DMSSC derived from a critical review of the literature, and the collective clinical experience of a multinational group of experts. We provide recommendations for plain radiography, sonography, CT, and MR imaging in the evaluation of DMSSC with an emphasis on technique of imaging and imaging protocols.

ABBREVIATIONS: DMSSC = dysraphic malformations of the spine and spinal cord; FS = fat suppression; GRE = gradient-echo; SSFSE = single-shot fast spin-echo; US = ultrasound

Dysraphic malformations of the spine and spinal cord (DMSSC) represent a spectrum of congenital malformations presumed to have their origins in defects of early embryogenesis. The clinical consequences of these disorders affect the development of children worldwide and result in significant personal and socioeconomic costs.[1,2] Despite being relatively common (estimated incidence 1–3/1000 live births), their etiology is largely unknown.[3,4] The terms "spinal dysraphism" or "tethered cord" are often used as umbrella terms for these disparate malformations; however, the term "dysraphism" implies a known etiology (anomaly of midline fusion) and "tethered cord" implies a known mechanism of clinical deterioration. Because both of these assertions are incorrect, we use the term DMSSC to encompass these disorders.[1]

Neuroimaging plays a vital role in the diagnosis, classification, and management of DMSSC. With competent image acquisition and interpretation, diagnostic accuracy can be potentially excellent, providing correct anatomic delineation and aid in appropriate management. Despite this, there is currently no consensus as to how children with suspected DMSSC should be radiologically evaluated. In the absence of this guidance, clear differences arise between centers in terms of diagnostic approach, classification schema, clinical management, and, by virtue, prognosis in terms of neurologic and urologic outcomes.[1] This worrying clinical heterogeneity risks unstructured decision making, missed diagnoses, and potentially suboptimal management of the child.

These challenges highlight the need for an expert-driven multidisciplinary effort to better understand the radiologic and clinical classification of these disorders. To this aim, we established an international multidisciplinary DMSSC group with the aims of disseminating knowledge to the broad medical community, improving the diagnosis and management of DMSSC, and accelerating research in the field.

Received May 22, 2023; accepted after revision November 13.

From the Departments of Neuroradiology (A. Balani, J.S., S.S., A. Biswas, K.M.), Urology (N.K., N.J.), and Neurosurgery (M.Z.T., D.T., D.P.), Great Ormond Street Hospital for Children, NHS Foundation Trust, London, UK; Developmental Biology and Cancer Section (J.S., A.J.C., K.M.), University College London, Great Ormond Street Institute of Child Health, London, UK; Department of Neuroradiology (Ö.Ö.), Izmir Bakircay University, Izmir, Turkey; Medical Genetics Unit (V.C.) and Neuroradiology Unit (A.R.), IRCCS Istituto Giannina Gaslini, Genoa, Italy; Laboratoire de Biologie du Développement (M.C.), UMR 7622 de Sorbonne Université et du CNRS, ERL 1156 de l'INSERM et Institut de Biologie Paris Seine, Paris, France; Department of Paediatric Neurosurgery (D.P.), University of California, Davis, Davis, California; Department of Radiology (D.M.M.), Children's Hospital Colorado, University of Colorado School of Medicine, Aurora, Colorado; Department of Radiology (M.-L.H.), Nationwide Children's Hospital, Ohio State University, Columbus, Ohio; Edward B. Singleton Department of Radiology (T.A.G.M.H.), Texas Children's Hospital and Baylor College of Medicine, Houston, Texas; and Department of Health Sciences (A.R.), University of Genoa, Genoa, Italy.

Please address correspondence to Kshitij Mankad, MD, Department of Neuroradiology, Great Ormond St Hospital for Children, NHS Foundation Trust, Great Ormond St, London, United Kingdom WC1N 3JH; e-mail: drmankad@gmail.com; @drmankad

http://dx.doi.org/10.3174/ajnr.A8117

In this manuscript, the first of a series of consensus statements, we outline a standardized international consensus statement for the radiologic evaluation of children with suspected DMSSC derived from a critical review of the literature, and the collective clinical experience of a multinational group of experts.

MATERIALS AND METHODS

Literature Review

PubMed was systematically queried for papers reporting 1) radiologic protocols for the investigation of congenital DMSSC and 2) radiologic findings in congenital DMSSC. The keywords used in the search were as follows: "spinal dysraphism," "spine malformation," "spinal cord malformation," "spina bifida," "myelomeningocele," "lipomyelocele," "lipomyelomeningocele," "terminal myelocystocele," "nonterminal myelocystocele," "abortive myelocystocele," "split cord malformation," "neurenteric cyst," "diastematomyelia," "spinal lipoma," "dorsal lipoma," "transitional lipoma," "caudal lipoma," "filar lipoma," "tethered cord," "thickened filum terminale," "caudal regression syndrome," "dermal sinus tract," and "limited dorsal myeloschisis." The most recent search was performed on April 1, 2022. Following this literature search, the final reference list was generated on the basis of 1) relevance to the scope of our recommendations and 2) relative importance and originality within the field.

The Consensus Process

This article represents an international consensus statement based on 5 meetings of the International DMSSC Consensus Group: a panel of 17 recognized experts invited to participate in this modified Delphi consensus process on the basis of prior scholarship in the field and the need for global representation. Participating experts are pediatric neuroradiologists ($n = 9$), pediatric neurosurgeons ($n = 3$), pediatric urologists ($n = 2$), and developmental neurobiologists ($n = 3$). Delphi rounds were mediated by an independent, nonparticipating author.

Meetings were held on June 26, 2020; July 24, 2020; September 25, 2020; November 17, 2020; and January 8, 2021. Of these meetings, the first 2 contained specific focus discussions on the radiologic evaluation of congenital DMSSC. Before each meeting, consensus statements were prepared by a core team (Asthik Biswas, J.S., S.S., and K.M.) based on evidence from the literature and expert opinion. During meetings, the panel discussed consensus statements and agreed on new or modified recommendations for the radiologic evaluation of congenital DMSSC. Consensus statements were subsequently revised in view of these discussions, and the process iterated until consensus was achieved. Consensus was defined as ≥80% agreement (≥14/17 experts). Unless otherwise stated, all recommendations are reported at this level of consensus. The final manuscript was revised and endorsed by all panel members before submission.

In the first Delphi round, all authors voted on 24 recommendation statements. Agreement was reached for 9 statements, and the remaining 15 revised as per the reasons each author provided for disagreement. In the second round, all authors voted on 16 revised recommendation statements and consensus was achieved in all remaining areas.

Consensus Recommendations

This consensus statement should be applied to the radiologic evaluation of all fetuses, children, and adults with suspected DMSSC.

Plain Film Radiography

Conventional radiography with anteroposterior and lateral views is often the first-line screening investigation to assess abnormalities of the vertebral column in children. Findings seen on plain radiographs may include, but are not limited to, spina bifida, widened spinal canal, lumbosacral soft tissue swelling, segmentation anomalies, and the bony spur of diastematomyelia. Plain film radiographs may also aid the evaluation of associated kyphotic and/or scoliotic deformities in patients with certain malformations, such as segmental spinal dysgenesis.[5] However, plain radiography exposes the child to ionizing radiation and images have poor soft tissue resolution, resulting in low diagnostic sensitivity. In addition, overlying gas and stool shadows can limit the evaluation of the spine. Therefore, in the current era, we recommend that plain radiography should only be used as 1) a preliminary screening investigation when other imaging modalities are not available, 2) an adjunct (with the aid of a marker) to aid vertebral counting if there is uncertainty in determining the lumbosacral junction on ultrasonography, or 3) where there is a need to evaluate/monitor associated spinal deformity.[6,7]

Sonography (Ultrasound)

Ultrasound (US) is the first-line technique for the antenatal diagnosis of DMSSC. Despite this, it has a limited role in the postnatal evaluation of suspected DMSSC.[8] The partially ossified, predominantly cartilaginous, not yet fused posterior vertebral elements in this age group provide a good acoustic window for detailed visualization of the spinal cord and caudal structures. Studies have confirmed good concordance between US and MR imaging. Beyond 3–4 months of age, this acoustic window of opportunity is lost due to ossification and closure/fusion of the posterior arches of the vertebral column. After this time, MR imaging becomes the first-line technique for older children.[2,8] Though individual operator expertise is its main limitation, when performed by an experienced operator, US may be used exclusively for the evaluation of DMSSC in low-risk infants less than 3–4 months of age.[9] The advantages of US are its cost-effectiveness, wide accessibility, bedside acquisition, and rapid image acquisition time, which negates the need for sedation. This said, US has lower resolution than MR imaging, and so we recommend that MR imaging is performed in all children in whom DMSSC is suspected on US. Cranial US performed in the same setting can also expedite the diagnosis of associated intracranial anomalies, such as hydrocephalus and Chiari deformity.[10] US may be of further relevance to exclude other/associated non-neurologic findings, such as urogenital abnormalities.

US Technique. We recommend feeding the infant before the examination as a soothing technique. US should then be performed primarily in the prone position, with the child's head slightly elevated above the feet to permit better filling of the lower CSF spaces.[11,12] The child's neck must be slightly flexed when

evaluating the craniocervical junction; a rolled towel or blanket, placed under the child's abdomen or pelvis, may also help to accentuate the lumbar lordosis and widen the posterior interspinous spaces. Real-time scanning in the lateral decubitus position results in free movement and clustering of the cauda equina nerve roots toward the dependent side, thereby permitting the assessment of cord movement.[13] Positioning the child in a semi-erect fashion, with the head held by the sonographer, may enhance the detection of meningocele.[9] US should not be used to image open DMSSC as this provides limited additional information and increases susceptibility to infection.[14] In open DMSSC, US should be used to image more rostral parts of the vertebral column for the assessment of associated anomalies, such as hydrosyringomyelia and hydrocephalus.

High-frequency linear-array (7–12 MHz) and curved-array (8–10 MHz) transducers should be used to evaluate the spine and spinal cord in the longitudinal and transverse planes with the study limited to the area of interest, usually lumbosacral and lower thoracic region with evaluation and characterization of the filum terminale, cauda equina nerve roots and distal thecal sac, ossified parts of the bony vertebrae (including its posterior elements), and any skin lesions or masses. Sonography aids in assessment of overlying soft tissues for the presence of hemangioma, lipoma, skin covered masses (meningocele), and tracts extending from the skin surface toward the spinal canal. A thick layer of coupling gel or a standoff pad may help in better assessment of superficial soft tissues. Color or power Doppler sonography may also be used as an adjunct to better characterize soft-tissue masses (eg, cutaneous hemangiomas) found on the skin or within the spinal canal.[6,7] The study may be extended to include the entire spinal canal from the craniovertebral junction to the coccyx. If available, a small footprint sector probe may be used for detailed evaluation of the craniocervical junction. Panoramic or extended FOVs can visualize the neonatal spine from T12 to the coccyx in a single image, potentially permitting full visualization of any abnormalities. 3D US is not essential but may be of use in complex cases for visualization in the additional coronal plane.[15]

The position of the conus medullaris should be assessed by identifying the lumbosacral junction and thus the location of the L5 vertebra at the lordotic angle between the lumbar and sacral vertebrae and should be confirmed by counting the vertebral level down from rib 12 or counting cephalad from S5 (rounded or triangular shape of first coccygeal segment when ossified).[6,7,9,12,15] In neonates, wherein the acute angle may not be seen clearly, flexion and extension movements of the pelvis may help to identify the point of motion of the sacrum. Alternatively, comparison with a marked lateral plain radiograph may be used.

Antenatal US. Imaging plays a crucial role in the prenatal diagnosis and classification of DMSSC, as emphasized by recent advances in intrauterine repair.[16] 2D and 3D US is invariably the first-line technique for the morphologic study of the fetus.[17] Second trimester US, in particular, has a high sensitivity for the detection of DMSSC and is employed in routine screening programs across the world, making it possible to suspect and detect neural tube defects early in gestation.[18] Maternal serum alfa-fetoprotein screening can also help to identify high-risk children and define the need for more detailed fetal imaging (US or MR imaging) and/or invasive tests, namely, amniocentesis.[19] As such, the radiologic investigation of suspected DMSSC should always be interpreted in tandem with maternal serum alfa fetoprotein levels.[20]

To screen for suspected DMSSC, the fetal head and entire length of the fetal spine should be studied in the coronal, parasagittal, and transverse planes.[21] US is particularly sensitive in the evaluation of the skin, soft tissues, vertebral body ossification centers, brain for features of Chiari II deformity, in addition to any mass lesions, sacral anomalies, and sac(s), if present. Antenatal US is more sensitive for the diagnosis of open DMSSC than for closed DMSSC.[18]

In cases of myelomeningocele, the anatomic level of the lesion is important both for prognostication and, these days, as an eligibility criterion for possible fetal surgery. Studies have confirmed the comparable accuracy of fetal US and MR imaging in ascertaining level of myelomeningocele defect.[22] Additionally, antenatal sonography also has the advantage of detecting associated anomalies, including cardiac, renal, and bowel anomalies, which are important in determining eligibility for fetal surgery. Antennal US also aids in diagnosis of lower limb abnormalities (eg, equinovarus feet, vertical talus) and assessment of lower limb movements of the fetus, adding a functional perspective to this imaging technique.

MR Imaging

MR imaging is the technique of choice for the evaluation of suspected DMSSC because of its excellent spatial and contrast resolution with multiplanar and multicontrast capabilities in the absence of ionizing radiation.

Sedation. One of the main challenges in pediatric MR imaging acquisition is the varying abilities of children to tolerate the environment of the scanner and the requirements of imaging, namely, the need to remain stationary. In neonates and young infants, imaging during spontaneous sleep following feed with the baby wrapped up in a blanket (feed-and-swaddle or feed-and-wrap) is a viable option and obviates the need for sedation in this age group.[23] Attempts to keep the baby awake, hungry, and due for feed before the scheduled examination help to increase the likelihood of a spontaneous sleep following feeding. Similarly, the availability of dedicated quiet rooms for patient preparation and subsequent awakening greatly improves the chances of success for imaging small infants without sedation. Children aged 4 years and older may be sufficiently cooperative, especially with the support of a child life specialist, including mock-MR training, though this may vary because of acute illness and the developmental stage of the child.[2,24] Younger or severely ill children will typically require sedation, administered according to local guidelines. Cardiorespiratory monitoring with MR imaging–compatible equipment is required in all sedated children. Further techniques to minimize sedation during MR imaging, including fast sequences, motion correction, noise reduction, and reducing scan time, are beyond the scope of this manuscript and are discussed in detail in previously published literature.[25]

Table 1: Recommended MR imaging sequences and parameters for the assessment of children with suspected DMSSC

Sequence	Plane	Imaging Parameters	Notes
Essential sequences			
3 plane scout/localizer	Axial, sagittal, coronal		For subsequent planning
T1-weighted TSE whole spine	Sagittal	3.0 mm thickness (TR, 600 ms, TE, 30 ms)	—
T2-weighted TSE whole spine	Sagittal	3.0 mm thickness (TR, 3000 ms, TE, 120 ms)	—
T2-weighted FS, Dixon, or STIR	Coronal	3.0 mm thickness (TR, 3000 ms, TE, 40 ms)	FS preferred over STIR; whole spine
T1-weighted TSE	Axial	≤3.0 mm thickness	Lumbosacral region (conus and filum terminale) and the suspected area of abnormality (group of axial images through the disc level not applied)
T2-weighted DRIVE, CISS, or FIESTA	Sagittal	0.6 mm thickness	Sagittal acquisition centered on the area of suspected abnormality with 3D reconstructions
Optional sequences			
T2-weighted TSE	Axial	3.0 mm thickness, non-fat-suppressed	Suspected area of abnormality (group of axial images through the disc level not applied)
T1-weighted TSE	Coronal	3.0 mm thickness	Centered onto and along the major axis of the sacrum (for suspected sacral abnormalities)
T1-weighted FS	Sagittal	3.0 mm thickness	Confirmation of lipoma
T1-weighted FS C+	Axial, sagittal, coronal	3.0 mm thickness	Suspected infections/tumors
DWI	Axial or sagittal	3.0–4.0 mm thickness	Suspected dysontogenic abnormalities, epidermoids, dermoids, abscesses
T2-weighted GRE or EPI-GRE	Axial	3.0 mm thickness	Evaluation of bony septum in diastematomyelia
T1-weighted TSE C+	Axial, sagittal, coronal	3.0 mm thickness	Suspected mass lesions, dysontogenic abnormalities, or infections

Note:—DRIVE indicates driven equilibrium; C+ = postcontrast.

Scanner Magnetic Field Strength. Both 1.5T and 3T scanners are suitable for imaging suspected DMSSC. As such, the choice of magnetic field strength depends on local availability and radiologist preference. 1.5T scanners remain the most widely available.[26] Advantages of 3T MR imaging include higher spatial and contrast resolution; the potential for reduced scan times without compromising image quality; and reduced motion artifacts with higher temporal resolution.[27] 3T scanners are, however, more costly, and artifacts caused by field inhomogeneity, magnetic susceptibility, vascular pulsation, and chemical shift are exaggerated. Spinal imaging remains particularly challenging at 3T despite technical advances, such as thin section imaging, parallel imaging, and increasing the receiver bandwidth.[27]

Standardized Spinal MR Imaging Protocol. In cases of myelomeningocele or syndromes associated with dysraphism (eg, VACTERL, cloacal exstrophy), whole spine imaging is required. In isolated, closed dysraphic states, there is limited clinical utility in imaging beyond the lumbosacral region.[28] Optimized MR imaging protocolling is crucial to maximize diagnostic yield and reduce scanning time, thereby limiting the necessity or duration of sedation. We recommend imaging of the whole spine at baseline, including dedicated, high-resolution imaging of the area of the suspected abnormality. Given the inherent challenges of MR imaging in children, essential sequences should be acquired first, with optional sequences acquired subsequently as required.

The standardized spinal MR imaging protocol for DMSSC evaluation is presented in Table 1. Following localizer or scout imaging, high-resolution T1- and T2-weighted TSE images of the whole spine are acquired in the sagittal plane without fat suppression (FS). Advances in MR imaging, the use of multichannel phased array coils, and the combination of multiple images into a single full FOV have enabled visualization of the entire spine, from the craniocervical junction to the coccyx, in a single image, thereby permitting panoramic appraisal and the counting of vertebral levels to identify the exact level of abnormality. In addition, 1 panoramic coronal sequence (T2-weighted TSE [T2-TSE]) with FS (T2-TSE FS, Dixon, or short tau inversion recovery [STIR]) is acquired of the whole spine. T2-weighted FS is preferred because of its inherently high signal-to-noise ratio, good visualization of small anatomic detail, and shorter acquisition time.[29] Axial acquisition on T1-weighted imaging without FS is then used to study specific regions as indicated by clinical findings or by findings on the previously acquired sagittal images (block acquisition and not at the level of intervertebral discs). The section thickness for these sequences should be ≤3.0 mm with submillimeter in-plane resolution and intersection gaps of 0.30–0.50 mm.[2,30] A volumetric acquisition of high-resolution heavily T2-weighted images in the sagittal plane with retrospective multiplanar reconstructions should also be performed, either driven equilibrium (DRIVE), CISS, or FIESTA. These provide exquisite delineation of the cord/root/CSF interfaces and are particularly useful for evaluating subtle structural abnormalities, such as those found in DMSSC.

Routine DWI is not required in children with DMSSC, but it should be performed for the identification and assessment of dysontogenetic mass lesions. The high lesion conspicuity of postoperative inclusion epidermoids/dermoids after repair of a spinal dysraphism on DWI may be advantageous. Similarly, gradient-echo (GRE) or EPI-GRE are useful for the evaluation of the bony septum in children with diastematomyelia.

The intravenous injection of gadolinium-based contrast agents is not routinely indicated and should only be used to evaluate suspected infections and mass lesions inadequately characterized on noncontrast MR imaging. MR angiography may also be used for preoperative identification of the artery of Adamkiewicz (great anterior radiculomedullary artery).

Additional screening of the cranial vault should be considered to exclude associated cerebral and/or cerebellar abnormalities. Other optional sequences may be added to the protocol depending on clinical indication, findings on initial imaging, and national guidance.

With the advances in imaging, it is now possible to decrease examination times while maintaining diagnostic performance which is of paramount importance in radiologic evaluation of DMSSC. These advances include faster sequences, powerful computers for faster image reconstruction, 3D sequences, acceleration techniques, such as parallel imaging, simultaneous multislice imaging, compressed sensing, and deep learning reconstructions. Parallel imaging is the most used technique, available in most modern scanners without the need for specialized software or hardware. In simultaneous multislice imaging, excitation of more than 1 section is done at a time and uses the same coil technology and reconstruction methods as parallel imaging. Both these techniques allow acceleration to a factor up to 2 times without degrading the image quality and when used in combination, can provide an acceleration factor of 4 with similar signal-to-noise ratio and contrast-to-noise ratio. Further, deep learning models can reconstruct the undersampled data to simulate the fully sampled reconstructions.[31]

Follow-up MR Imaging. At follow-up, imaging can be limited to the area of interest with screening T2-weighted images of the whole spine without FS.[2]

Fetal MR Imaging

Fetal MR imaging is the preferred second-line technique (after prenatal sonography) for imaging of the fetus.[32,33] Though not indicated in all children because of availability and technical limitations, it is a powerful adjunct to prenatal US, providing additional information crucial for prenatal counseling, assessing eligibility for prenatal surgery, predicting neurologic outcomes, and guiding perinatal management.[34]

DMSSC become more evident on fetal MR imaging in the second trimester. This fortunately coincides with the optimal age for MR imaging. We recommend waiting until 17–18 gestational weeks (15–16 weeks postfertilization) before performing fetal MR imaging because of the potential risks posed to the developing fetus and the current technical limitations of fetal MR imaging in younger fetuses due to their smaller size and even greater fetal motion. Pregnant women should only undergo MR imaging earlier in their pregnancy if the risk-benefit ratio to the child is favorable and if other nonionizing imaging modalities are inadequate. In all instances, it is important to counsel parents on the likelihood of diagnosing a DMSSC in their child and of the potential effects this may have on their child's development.

Fetal MR imaging aims to identify pertinent anatomic features of DMSSC, such as the level of the spinal defect, by 1) establishing the most caudal hyperintense spinal disc space as L5–S1 and the lowest horizontal vertebral body as L5, and 2) counting the vertebral bodies superior to the highest level of the absence of the posterior elements at the bone/skin defect. Fetal MR imaging can also define and characterize the presence or absence of a spinal cord syrinx; diastematomyelia; and sac; and the continuity of cutaneous soft tissues with the neural tube sac.[35,36] Associated anomalies of the fetal extremities and intracranial anomalies may also be detected on fetal MR imaging, including the severity of the Chiari II deformity according to the degree of posterior fossa hindbrain herniation, lateral ventricular size, and third ventricular size.[36]

Standardized Fetal MR Imaging Protocol. Before undergoing fetal MR imaging, child-bearing women must empty the urinary bladder. A phased array body surface coil is then wrapped around the mother's pelvis and centered over the fetal ROI. Maternal comfort is the priority; both supine and left lateral decubitus positions are acceptable and should be adopted as per maternal preference.[37]

Prenatal imaging of the fetus is a dynamic process that starts with an initial scout or localizer followed by a series of sequences with each sequence acting as a localizer for the next. Images are acquired in all 3 anatomic planes with respect to the fetus. The main challenge of fetal MR imaging is fetal motion artifact. If persistent and severe, it may be necessary to prioritize image acquisition on planes that best visualize the anatomy in maximizing the yield of the study. Due to this, monitoring by the radiologist is essential.

The standardized fetal MR imaging protocol for DMSSC evaluation is presented in Table 2. Fetal MR imaging should be performed at 1.5T or 3T depending on local availability and radiologist preference. 3T is superior to 1.5T for the visualization of cartilage and spine because of the use of single-shot turbo spin-echo and steady-state free precession sequences. The fetal head and entire length of the fetal spine should be studied on all 3 planes (axial, sagittal, and coronal) by using T2-single-shot fast spin-echo (T2-SSFSE) or HASTE and balanced fast-field echo or FIESTA at 3–4 mm section thickness with no intersection gaps and the smallest FOV possible.[38] A minimum of 2 stacks of images in each plane should be obtained (which may be omitted in case of excessive fetal motion). Gradient-echo sequences (ie, EPI and true FISP) have greater ferromagnetic susceptibility and provide greater resolution of bony and vascular structures, especially in fetuses aged less than 27 gestational weeks.

Optional sagittal and coronal T1-weighted spoiled gradient-echo acquisition of the fetus with section thickness 5 mm and with no intersection gaps may also be performed and should have the smallest possible FOV.[35] Prenatal imaging (including T1-weighted images) does not adequately demonstrate fat within the

Table 2: Recommended MR imaging sequences and parameters for the assessment of fetuses with suspected DMSSC

Sequence	Plane	Imaging Parameters	Notes
Essential sequences			
3 plane scout/localizer	Axial, sagittal, coronal	—	For subsequent planning
T2-weighted TSE maternal pelvis	Sagittal	—	To assess the position of the fetus; reposition the coil if the fetal ROI is not in the center of the coil
T2-weighted SSFSE or HASTE	Axial, sagittal, coronal[a]	3-4 mm thickness, no intersection gaps (TR, 2000–3000 ms, TE, 150 ms), FOV 340 mm, flip angle 160°	Provides excellent anatomic detail
T2-weighted EPI-GRE or true FISP	Axial, sagittal, coronal[a]	4 mm thickness, no intersection gap (TR, 4.22 ms, TE, 1.75 ms), FOV 380 mm, flip angle 65°	Evaluation of bony and vascular structures
Optional sequences			
T1-weighted SPGR	Sagittal, coronal	5 mm thickness, no intersection gaps (TR, 600 ms, TE, 30 ms), FOV 340 mm	Improves spatial resolution with increasing gestational age
Cine imaging	Volumetric acquisition	—	Assesses fetal extremity mobility

Note:—SPGR indicates spoiled gradient recalled-echo.

[a] Acquisition of all 3 planes in T2-weighted SSFSE (HASTE) and T2-weighted true FISP may not be feasible if the fetus is moving excessively; and in such a scenario, the protocol can be curtailed with T2-weighted SSFSE in axial and coronal planes (providing anatomic detail) and T2-weighted true FISP in sagittal plane (providing assessment of osseous structures).

defect of closed dysraphism. This is attributable to several factors, including low spatial resolution of T1-weighted images in the fetus, underdevelopment of fetal fat in early gestational age, and relatively increased proportion of brown fat in the fetus and neonate that has slightly different signal characteristics than white fat on MR imaging. Furthermore, optional cine imaging may convey an idea of the motility of fetal extremities, offering an insight into the child's postnatal prognosis.

CT

CT is of limited value for the evaluation of DMSSC because of its poor soft tissue resolution and correspondingly poor sensitivity, exposure of the child to ionizing radiation, and invasiveness in the case of CT myelography.[2,39] This said, we support the use of CT for several specific indications:

1) Vertebral anomalies where there is a need to define bony anatomy, eg, as part of preoperative planning prior to instrumented fixation.
2) Identification of the bony septum in diastematomyelia.
3) Preoperative identification of the artery of Adamkiewicz (great anterior radiculomedullary artery) via CT angiography when MR angiography either fails to identify the vessel or is not feasible.[40]
4) Patients with absolute contraindications to MRI.

Standardized CT Protocol. We recommend that children undergo a low-dose noncontrast CT of the spinal area of interest (section thickness ≤2 mm), acquired continuously in the axial plane with no intersection gaps. Multiplanar 2D- and 3D-reconstructions in bone and soft kernel should also be performed as they have been shown to increase the sensitivity and specificity of the study.[41] As CT is reserved for the elucidation of specific features, it should, therefore, always be performed with the minimum possible FOV and not extended beyond the region of the abnormality to minimize radiation exposure, as per the as low as reasonably achievable principle.[2,42]

CT has limited soft tissue contrast; thus, evaluation of the thecal sac and its contents is limited. Intrathecal injection of iodinated contrast media in CT myelography may facilitate visualization of the thecal sac and its contents. However, the use of CT myelography is not recommended when MR imaging is available as CT myelography is invasive, less sensitive, and exposes the child to ionizing radiation.[2,39]

Imaging Guideline Adaptations and Further Considerations

The challenges of imaging children vary across institutions and countries depending on 1) clinical management and 2) the availability of resources given the expense of additional imaging and the cost and risk of sedation if required. Therefore, the principal adaptation to this consensus statement is for clinical settings without routine access to MR imaging, in which we recommend that children are referred to institutions with MR imaging; however, we do agree that it may not be possible in certain resource-limited care environments. CT should not be performed in lieu of MR imaging given its markedly reduced diagnostic accuracy. US is the first-line technique for the antenatal diagnosis of DMSSC and has a significant but limited role in the evaluation of neonates and infants with suspected DMSSC. US is the first method of screening for infants up to 3–4 months of age before ossification of the vertebral bodies. MR imaging is the technique of choice for the evaluation of suspected DMSSC because of its excellent spatial and contrast resolution.

We recommend imaging patients with combined cutaneous stigmata (combination of 2 or more midline cutaneous lesions) or an atypical skin dimple with MR imaging; however, US may be used in some cases. Atypical dimples are larger than 5 mm and located within 25 mm of the anus. Other criteria include deep dimples, dimples located cranially to the gluteal crease or outside the midline, and multiple dimples. On the other hand, a simple sacral dimple is smaller in size (<5 mm in diameter) with

a midline placement within 25 mm of the gluteal crease from the anus and has no other cutaneous abnormalities (such as asymmetry of the gluteal crease, capillary hemangioma, hypertrichosis, dermal sinus tract, lipoma, subcutaneous dermoid cyst, pseudotail, or true tail).[43,44] In patients with combination of less than 2 cutaneous stigmata, atypical dimple, and deviation of gluteal cleft, we recommend performing an US during the first month of life; if anomalies are detected, MR imaging should be performed. In patients with sacral dimple alone, pigmentary nevus, and little hemangioma, we recommend regular clinical follow-up and to perform MR imaging only in the presence of neurologic or orthopedic alterations.[43]

CONCLUSIONS

Neuroimaging is central to the multidisciplinary evaluation of children with suspected DMSSC. It is our hope that this international consensus statement will provoke the standardization of image acquisition and evaluation, thereby increasing the diagnostic yield of studies and improving care for children worldwide.

Disclosure forms provided by the authors are available with the full text and PDF of this article at www.ajnr.org.

REFERENCES

1. Balani A, Chatur C, Biswas A, et al. **Spinal dysraphisms: highlighting discrepancies in the current literature and emphasizing on the need for a consensus.** *Quant Imaging Med Surg* 2020;10:549–53 CrossRef Medline
2. Rossi A, Biancheri R, Cama A, et al. **Imaging in spine and spinal cord malformations.** *Eur J Radiol* 2004;50:177–200 CrossRef Medline
3. Copp AJ, Stanier P, Greene ND. **Neural tube defects: recent advances, unsolved questions, and controversies.** *Lancet Neurol* 2013;12:799–810 CrossRef Medline
4. Venkataramana NK. **Spinal dysraphism.** *J Pediatr Neurosci* 2011;6: S31–40 CrossRef Medline
5. Tortori-Donati P, Fondelli MP, Rossi A, et al. **Segmental spinal dysgenesis: neuroradiologic findings with clinical and embryologic correlation.** *AJNR Am J Neuroradiol* 1999;20:445–56 Medline
6. Lowe LH, Johanek AJ, Moore CW. **Sonography of the neonatal spine: 1. Normal anatomy, imaging pitfalls, and variations that may simulate disorders.** *AJR Am J Roentgenol* 2007;188:733–38 CrossRef Medline
7. Lowe LH, Johanek AJ, Moore CW. **Sonography of the neonatal spine: 2. Spinal disorders.** *AJR Am J Roentgenol* 2007;188:739–44 CrossRef Medline
8. Orman G, Tijssen MP, Seyfert D, et al. **Ultrasound to evaluate neonatal spinal dysraphism: a first-line alternative to CT and MRI.** *J Neuroimaging* 2019;29:553–64 CrossRef Medline
9. Meyers AB, Chandra T, Epelman M. **Sonographic spinal imaging of normal anatomy, pathology and magnetic growing rods in children.** *Pediatr Radiol* 2017;47:1046–57 CrossRef Medline
10. Richer EJ, Riedesel EL, Linam LE. **Review of neonatal and infant cranial US.** *Radiographics* 2021;41:E206–207 CrossRef Medline
11. Tawfik NA, Ahmed AT, El-Shafei TE, et al. **Diagnostic value of spinal ultrasound compared to MRI for diagnosis of spinal anomalies in pediatrics.** *Egypt J Radiol Nucl Med* 2020;51:18 CrossRef
12. Ladino Torres MF, DiPietro MA. **Spine ultrasound imaging in the newborn.** *Semin Ultrasound CT MR* 2014;35:652–61 CrossRef Medline
13. Unsinn KM, Geley T, Freund MC, et al. **US of the spinal cord in newborns: spectrum of normal findings, variants, congenital anomalies, and acquired diseases.** *Radiographics* 2000;20:923–38 CrossRef Medline
14. Trapp B, de Andrade Lourencao Freddi T, de Oliveira Morais Hans M, et al. **A practical approach to diagnosis of spinal dysraphism.** *Radiographics* 2021;41:559–75 CrossRef Medline
15. Patterson S. **Sonographic assessment of the neonatal spine and the potential for new technologies to aid in diagnoses.** *J Diagn Med Sonogr* 2009;25:4–22 CrossRef
16. Sacco A, Ushakov F, Thompson D, et al. **Fetal surgery for open spina bifida.** *Obstet Gynaecol* 2019;21:271–82 CrossRef Medline
17. Nicolaides KH, Campbell S, Gabbe SG, et al. **Ultrasound screening for spina bifida: cranial and cerebellar signs.** *Lancet* 1986;2:72–74 CrossRef Medline
18. Ben-Sira L, Garel C, Malinger G, et al. **Prenatal diagnosis of spinal dysraphism.** *Childs Nerv Syst* 2013;29:1541–52 CrossRef Medline
19. Leighton PC, Kitau MJ, Chard T, et al. **Levels of alpha-fetoprotein in maternal blood as a screening test for fetal neural-tube defect.** *Lancet* 1975;2:1012–15 CrossRef Medline
20. Ghi T, Pilu G, Falco P, et al. **Prenatal diagnosis of open and closed spina bifida.** *Ultrasound Obstet Gynecol* 2006;28:899–903 CrossRef Medline
21. Budorick NE, Pretorius DH, Nelson TR. **Sonography of the fetal spine: technique, imaging findings, and clinical implications.** *AJR Am J Roentgenol* 1995;164:421–28 CrossRef Medline
22. Sherrod BA, Ho WS, Hedlund A, et al. **A comparison of the accuracy of fetal MRI and prenatal ultrasonography at predicting lesion level and perinatal motor outcome in patients with myelomeningocele.** *Neurosurg Focus* 2019;47:E4 CrossRef Medline
23. Antonov NK, Ruzal-Shapiro CB, Morel KD, et al. **Feed and wrap MRI technique in infants.** *Clin Pediatr (Phila)* 2017;56:1095–103 CrossRef Medline
24. Bharti B, Malhi P, Khandelwal N. **MRI customized play therapy in children reduces the need for sedation: a randomized controlled trial.** *Indian J Pediatr* 2016;83:209–13 CrossRef Medline
25. Barkovich MJ, Xu D, Desikan RS, et al. **Pediatric neuro MRI: tricks to minimize sedation.** *Pediatr Radiol* 2018;48:50–55 CrossRef Medline
26. Tanenbaum LN. **Clinical 3T MR imaging: mastering the challenges.** *Magn Reson Imaging Clin North Am* 2006;14:1–15 CrossRef Medline
27. Phalke VV, Gujar S, Quint DJ. **Comparison of 3.0 T versus 1.5 T MR: imaging of the spine.** *Neuroimaging Clin North Am* 2006;16:241–48 CrossRef Medline
28. Layard Horsfall H, Chari A, Huttunen T, et al. **Whole spine MRI is not required in investigating uncomplicated paediatric lumbosacral lipoma: a retrospective single-institution review.** *Childs Nerv Syst* 2019;35:2163–69 CrossRef Medline
29. Delfaut EM, Beltran J, Johnson G, et al. **Fat suppression in MR imaging: techniques and pitfalls.** *Radiographics* 1999;19:373–82 CrossRef Medline
30. O'Neill BR, Gallegos D, Herron A, et al. **Use of magnetic resonance imaging to detect occult spinal dysraphism in infants**. *J Neurosurg Pediatr* 2017;19:217–26 CrossRef Medline
31. Subhas N. **Establishing a new normal: the 5-minute MRI.** *Radiology* 2021;299:647–48 CrossRef Medline
32. Griffiths PD, Widjaja E, Paley MN, et al. **Imaging the fetal spine using in utero MR: diagnostic accuracy and impact on management.** *Pediatr Radiol* 2006;36:927–33 CrossRef Medline
33. Hayashibe H, Asayama K, Dobashi K, et al. **Prenatal development of antioxidant enzymes in rat lung, kidney, and heart: marked increase in immunoreactive superoxide dismutases, glutathione peroxidase, and catalase in the kidney.** *Pediatr Res* 1990;27:472–75 CrossRef Medline
34. Shekdar K, Feygin T. **Fetal neuroimaging.** *Neuroimaging Clin North Am* 2011;21:677–703 CrossRef Medline
35. Nagaraj UD, Bierbrauer KS, Peiro JL, et al. **Differentiating closed versus open spinal dysraphisms on fetal MRI.** *AJR Am J Roentgenol* 2016;207:1316–23 CrossRef Medline
36. Nagaraj UD, Bierbrauer KS, Stevenson CB, et al. **Spinal imaging findings of open spinal dysraphisms on fetal and postnatal MRI.** *AJNR Am J Neuroradiol* 2018;39:1947–52 CrossRef Medline

37. Huisman TA, Martin E, Kubik-Huch R, et al. **Fetal magnetic resonance imaging of the brain: technical considerations and normal brain development.** *Eur Radiol* 2002;12:1941–51 CrossRef Medline
38. Nagaraj UD, Bierbrauer KS, Stevenson CB, et al. **Prenatal and postnatal MRI findings in open spinal dysraphism following intrauterine repair via open versus fetoscopic surgical techniques.** *Prenat Diagn* 2020;40:49–57 CrossRef Medline
39. Jaspan T, Worthington BS, Holland IM. **A comparative study of magnetic resonance imaging and computed tomography-assisted myelography in spinal dysraphism.** *Br J Radiol* 1988;61:445–53 CrossRef Medline
40. Yoshioka K, Niinuma H, Ehara S, et al. **MR angiography and CT angiography of the artery of Adamkiewicz: state of the art.** *Radiographics* 2006;26 Suppl 1:S63–73 CrossRef Medline
41. Ruiz Santiago F, Lainez Ramos-Bossini AJ, Wang YX, et al. **The value of magnetic resonance imaging and computed tomography in the study of spinal disorders.** *Quant Imaging Med Surg* 2022;12:3947–86 CrossRef Medline
42. Uffmann M, Schaefer-Prokop C. **Digital radiography: the balance between image quality and required radiation dose.** *Eur J Radiol* 2009;72:202–08 CrossRef Medline
43. Ausili E, Maresca G, Massimi L, et al. **Occult spinal dysraphisms in newborns with skin markers: role of ultrasonography and magnetic resonance imaging.** *Childs Nerv Syst* 2018;34:285–91 CrossRef Medline
44. Choi SJ, Yoon HM, Hwang JS, et al. **Incidence of occult spinal dysraphism among infants with cutaneous stigmata and proportion managed with neurosurgery: a systematic review and meta-analysis.** *JAMA Netw Open* 2020;3:e207221 CrossRef Medline

Perspectives on Remote Robotic-Assisted Stroke Treatment: A Commentary Paper

Arturo Consoli, Nicole Mariantonia Cancelliere, Guillaume Charbonnier, Julian Spears, Thomas R. Marotta, and Vitor Mendes Pereira

ABSTRACT

SUMMARY: The proved feasibility of robotic-assisted endovascular treatment of intracranial aneurysms has stimulated the idea of a potential application of remote robotics for the treatment of acute ischemic stroke. The possibility of developing a more advanced remote-controlled robotic system capable of performing a complete mechanical thrombectomy procedure would help bridge the health care gap of lack of technical expertise in isolated areas. This possibility could allow a more equitable access to mechanical thrombectomy to a larger number of patients and be a breakthrough for acute ischemic stroke care worldwide. Many aspects around the technical, human, financial, and regulatory requirements should be discussed to implement remote robotic-assisted procedures. In this State of Practice article, we aimed to outline the major challenges that must be considered, as well as proposed solutions. However, different solutions may be applied in different health care systems on the basis of the availability of human and financial resources.

ABBREVIATIONS: AIS = acute ischemic stroke; GA = general anesthesia; MT = mechanical thrombectomy; RRAP = remote robotic-assisted procedure

The development of endovascular robotics in the past decade may represent a major advance in minimally invasive treatment of vascular diseases. Some advantages have been previously described, such as the reduced radiation exposure and orthopedic strain on the operators,[1-3] as well as enhanced technical accuracy and precision.[4] In 2019, embolization of an intracranial aneurysm using the Corindus CorPath-GRX system (Siemens) marked the first human robotic-assisted procedure in the neuroendovascular field.[5] This soon stimulated thought and discussion of a future application for remote robotic-assisted procedures (RRAPs) for acute ischemic stroke (AIS) treatment.[1,6-8] The aim of this article was to discuss what additional challenges should be considered to build a proper roadmap for new generations of robotic systems and remote procedures. We propose a streamlined discussion on the following topics: geosocial unmet needs, remote site preparation and remote team selection, procedural challenges, training, postprocedural management, and regulatory issues.

Received September 13, 2023; accepted after revision October 26.

From the Diagnostic and Interventional Neuroradiology Department (A.C.), Foch Hospital, Suresnes, France; Division of Neurosurgery (A.C., N.M.C., G.C., J.S., T.R.M., V.M.P.), Department of Surgery, RADIS Lab, Li Ka-shing Knowledge Institute, St. Michael's Hospital, Toronto, Ontario, Canada; Interventional Neuroradiology Department (G.C.), Besançon University Hospital, Besançon, France; and Division of Diagnostic and Therapeutic Neuroradiology (T.R.M.), Department of Medical Imaging, St Michael's Hospital, University of Toronto, Toronto, Ontario, Canada.

Please address correspondence to Arturo Consoli, MD, PhD, Diagnostic and Interventional Neuroradiology Department, Foch Hospital, Suresnes, France, 40 rue Worth, 92150 Suresnes, France; e-mail: onemed21@gmail.com

http://dx.doi.org/10.3174/ajnr.A8085

Geosocial Unmet Needs

One of the main drivers for the development of remote robotic neurointerventional procedures is to address the unequal access in AIS care to mechanical thrombectomy (MT) for patients living in isolated or rural territories. Indeed, most United States[9,10] and European populations do not have timely access to MT treatment, particularly those living in rural areas.[11,12] This geographic problem is exacerbated in larger countries with wider distances between cities. The inhomogeneous geographic distribution of stroke centers,[1] the risk of creating new low-volume centers,[7] the challenges of low-income countries for the needed expertise,[4] and the lack of human resources are the most accredited causes of this inequality. Therefore, the implementation of RRAP could be considered a potential response to this inequality. However, several issues must be addressed before bringing RRAP for stroke to actuality.

Procedural Challenges

Telepresence System. The physical distance between the remote operator and bedside team will demand effective real-time communication between sites. A telecommunication system that can reliably transmit audio and visual information between sites, including the live radiographic imaging, will be required for the remote operation to be performed safely. Minimum telepresence system (Cisco) requirements will need to be defined, such as the number and positions of cameras and microphones to give the operator full confidence and maximum safety during the intervention. We suggest a minimum requirement of a moveable,

side camera above the patient to allow the remote operator to assess the condition of the catheters and devices, to monitor the incision site, and to assess the patient for changes in symptoms. An ideal setup would also include a camera for room view and a second side camera to visualize the robotic arm and supervise loading and unloading maneuvers and perfusions. Also, a private audio feed between the remote operator and bedside technologist will be important to effectively communicate the next steps of the procedure, such as when to exchange devices. A room microphone and speaker may be useful to provide the remote operator additional information on the room environment and the possibility of communicating to the whole team or other team members than the bedside technologist. We strongly believe that these challenges should not be overlooked and should be balanced with the safety limits of defined transmission lag.

Angiographic Imaging Control. During a neuroendovascular procedure, the C-arm can be controlled by the local physician or an x-ray technologist. Fluoroscopy and intermittent DSA runs must be acquired for navigation, and appropriate working projections must be selected to facilitate navigation through tortuous vascular anatomy. Communication of these desired processes may be more challenging in a remote scenario, so the idea of providing remote control of the angiographic system to the remote physician is suggested to make procedures faster, reduce the radiation dose (for both the patient and the bedside technologist), and improve safety. Autonomous control of working projections by an intelligent system may also aid faster navigation, though no specific solutions are currently available.

Robotic System. Finally, the minimum requirements of robotic capabilities should be considered for maximum remote safety and success. The current version of the Corindus CorPath-GRX system allowed simultaneous control of only 1 microcatheter with 1 guidewire or device. This control means that a local physician was required to perform navigation of the aortic arch to place the guide catheter in the internal carotid or vertebral artery at the neck. It also precludes the ability to use a combined approach or contact aspiration for MT.[2,13] Robotic control of a full triaxial system composed of 4 devices should be considered for maximum safety in the next-generation robotic systems. Additional functionality such as control of aspiration or inflation of balloons should also be considered to give the physician full control of the stroke intervention.

The robotic-assisted approach for neurovascular disease treatment has been mostly used for intracranial aneurysm embolization, and for these procedures, all patients were under general anesthesia (GA).[4,5] The choice of GA for future RRAPs, or at least in the early phases, is suggested to ensure patient safety during the procedure, because movement of the patient with a fixed robotic system may carry an increased risk of dissection. A secondary advantage of using GA would be to use the imaging to improve artificial intelligence–based algorithms for automatic correction of the robotic movements, which require minimum motion artifacts. Indeed, engineering and mechatronic implementation are adding a large contribution to the robotic-based approach with encouraging results in terms of automated navigation to reduce the occurrence of unexpected movement of the devices,[3] which may be of great use in a remote setting.

Connectivity. The RRAP will be entirely based on connection systems ensuring a reliable, fast, and stable transmission of data. Although RRAPs have been performed, none of these ever included a remote neuro-endovascular procedure. Five RRAPs of percutaneous coronary interventions were successfully performed in India in 2018,[14] using an optical fiber connection with the CorPath-GRX system, whereas 5G has been successfully used for orthopedic screw placement between Beijing and Zhejiang through the TiRobot system (Tinavi Medical Technologies Co., Beijing, China).[15] Some groups have tested latency requirements for RRAP, and thresholds of non-perceptibility ranged between <400[16] and <250 ms;[17] however, these should be validated in the context of a stroke procedure because neurosurgical procedures carry higher risks. Furthermore, in our opinion, these studies were incomplete because latency is not the only metric that will define safety. Other parameters such as bandwidth, jitter, the use of virtual private networks, and the transmission pathway affect the network performance[1,8] and should be comprehensively studied. We foresee a rigorous testing in each new remote location to find the most reliable and effective connectivity network to link to the operator site with an acceptable latency (<250 ms). A primary network should be used as a default and tested constantly, and a secondary network should be in place in case the first one fails during a procedure.

Nevertheless, several questions should be addressed before accurately assessing latency. These include but are not limited to the telecommunication system requirements, the quality of the angiographic images to be transferred, the transmission pathway, the digital weight of the new-generation robot control, and other potential tools to be added (such as the remote C-arm control). Indeed, these will determine the number of data packages to be transmitted, which will affect overall latency.

Remote Site Preparation and Team Selection

The preliminary in situ development of robotic-assisted procedures helped to define the basic requirements for a novel approach to neuroendovascular procedures, which demanded new workflows and a procedural setup.[4] Although RRAPs could spread the expertise of interventional stroke to remote areas in need,[7] a physical distance would be added between the robotic operator and the remote site. Thus, this would require the presence of a stroke care environment (including a Stroke Unit, Intensive Care Unit, and vascular neurology support) at the remote site to properly manage the acute and subacute phases of patients with AIS. Rehabilitation services should also be available to assist patients who do not make a full recovery after endovascular treatment.[18]

Future versions of endovascular robotic systems should overcome the limitation of current, approved robotic systems that do not support all steps of a MT procedure, thus requiring some steps to be performed manually by an on-site operator, including obtaining vascular access, navigation of the guiding catheter, stent placement, and/or angioplasty maneuvers.[1,2,7] Some authors have suggested that any type of interventionalist, not necessarily on-site but on-call, could be a plausible solution.[7] Some of these tasks, such as obtaining vascular access, could be performed by

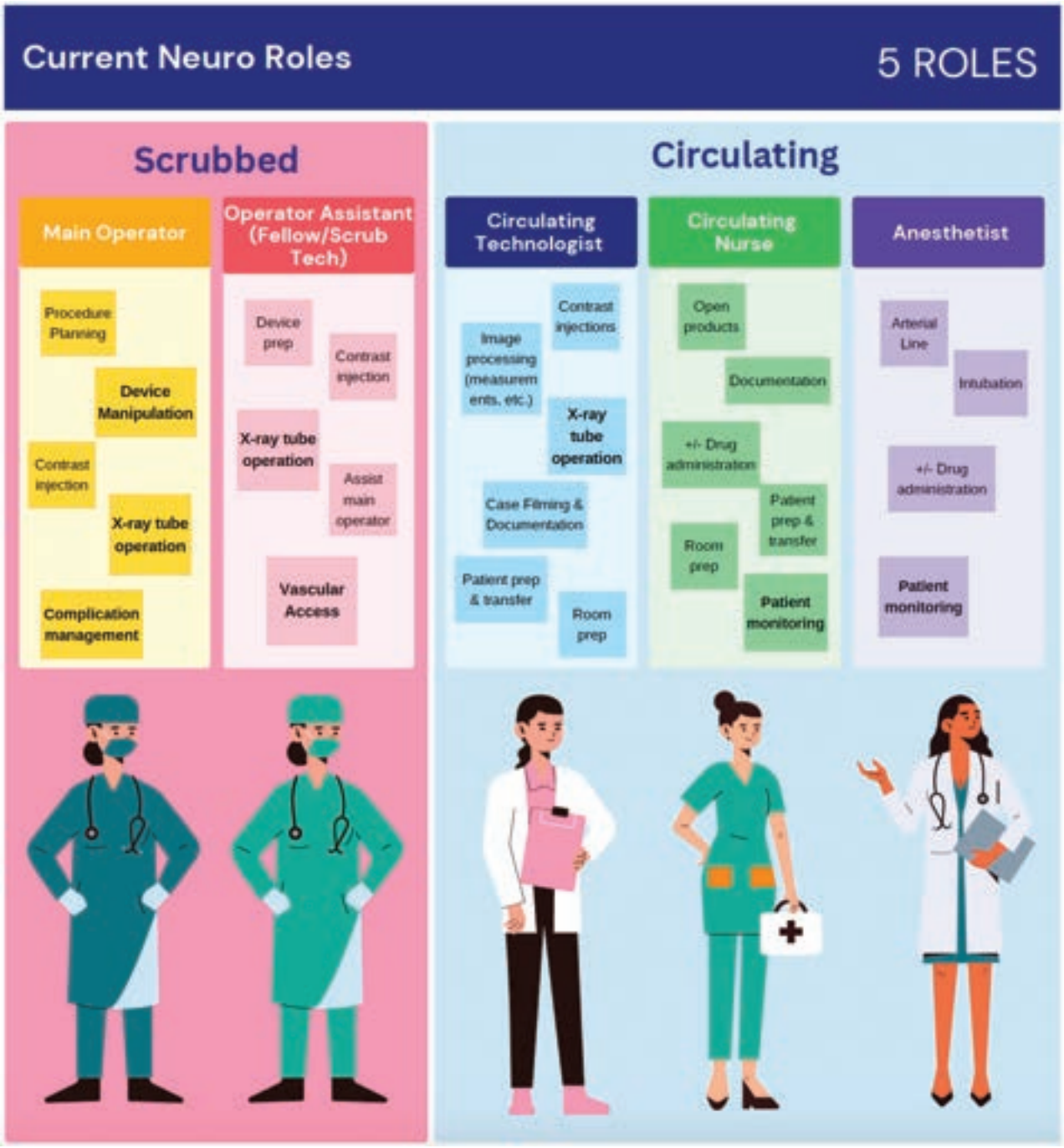

FIG 1. Current scenario and description of the roles of each member involved in neuroendovascular procedures for acute stroke.

another qualified member of the on-site team. In a remote scenario where the operating physician is not in the room, there will need to be a shift in roles for the bedside team. In our opinion, the core team for RRAPs should include the following: a remote, experienced robotic operator, a trained robotic bedside technologist, a supporting physician, an anesthesiologist, and a stroke neurologist locally or on telestroke (https://www.mayoclinic.org/tests-procedures/stroke-and-telemedicine/about/pac-20395081).

In this new scenario, the remote operator would be linked to a local "clinical coordinator" or telestroke for patient selection and to a "technical coordinator" (the bedside technician) to plan the setup for the procedure. Our suggestions for the various team members' roles in a local-versus-remote robotic-assisted scenario are shown in Figs 1 and 2.

Training

RRAP will require more rigorous training for both the remote operator and the on-site team. It is mandatory to create a solid bond of trust[6] and develop effective communication between the 2 teams to ensure proper management during the procedure. We suggest that simulated rehearsals be regularly performed to maintain familiarity with the robotic system and the remote workflow.

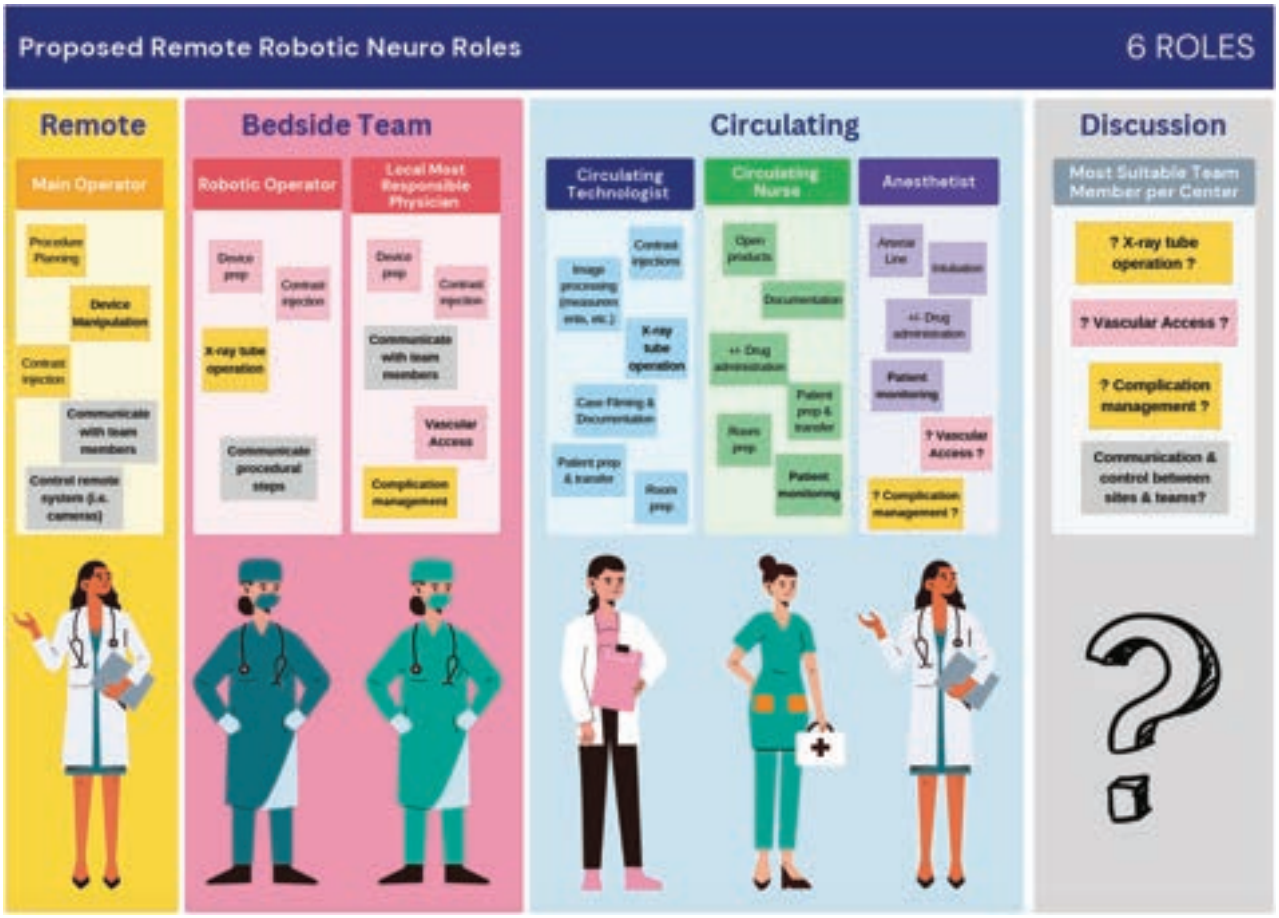

FIG 2. Suggested members and role changes to support remote robotic stroke procedures: a proposal of a new distribution of roles and tasks.

These will also be important to establish communication protocols, verify proper functioning of the robotic system, and practice safety protocols such as the workflow for manual takeover.[5] Simulation-based technology could represent a viable solution for training to flatten the learning curve and reduce technical complications.[19] However, a precise logbook and a definite training protocol[20] will be necessary for future RRAPs.

Regulatory Hurdles

Although the technical feasibility of RRAPs is currently being tested with some encouraging results, several regulatory considerations must be discussed. State licensing and facility credentialing have already represented a limitation for remote imaging in the past and should be considered for remote procedures as well. Although the cost-effectiveness of RRAPs cannot yet be assessed due to lack of data, some simulation-based models have suggested that the introduction of remote stroke care has the potential to improve clinical outcomes and reduce stroke-related costs to the health care system.[21]

Human feasibility studies should be performed after rigorous technical and clinical validation, and clinical trials for stroke RRAP treatment could then be designed with the support from the regulatory bodies to show the noninferiority of remote procedures.[6] Indeed, the management of potential intraprocedural complications would require the presence of an on-site or on-call interventionalist,[7] whereas clear indications about the medical/technical responsibility will need solid and constructive discussions.[1] Furthermore, comprehensive guidelines will necessarily have to be redacted under the guidance of the international scientific societies, to account for all the possible political and regulatory issues.

CONCLUSIONS

We are not yet ready for prime time. There are various considerations in preparation for RRAPs, including telecommunication system and robotic system requirements for increased remote control capabilities, such as triaxial control, and understanding of safety limits. Remote stroke treatment simulations should be performed before a clinical attempt. The potential benefit of remote stroke intervention is real, and it can be transformative. Remote areas in countries with vast geographies or in developing countries with lack of centers and professionals may have a unique opportunity to finally have access to acute stroke care.

Disclosure forms provided by the authors are available with the full text and PDF of this article at www.ajnr.org.

REFERENCES

1. Beaman CB, Kaneko N, Meyers PM, et al. **A review of robotic interventional neuroradiology.** *AJNR Am J Neuroradiol* 2021;42:808–14 CrossRef Medline

2. Crinnion W, Jackson B, Sood A, et al. **Robotics in neurointerventional surgery: a systematic review of the literature.** *J Neurointerv Surg* 2022;14:539–45 CrossRef Medline
3. Britz GW, Panesar SS, Falb P, et al. **Neuroendovascular-specific engineering modifications to the CorPath GRX Robotic System.** *J Neurosurg* 2019;133:1830–36 CrossRef Medline
4. Mendes Pereira V, Nicholson P, Cancelliere NM, et al. **Feasibility of robot-assisted neuroendovascular procedures.** *J Neurosurg* 2021;136:992–1004 CrossRef Medline
5. Mendes Pereira V, Cancelliere NM, Nicholson P, et al. **First-in-human, robotic-assisted neuroendovascular intervention.** *J Neurointerv Surg* 2020;12:338–40 CrossRef Medline
6. Goyal M, Sutherland GR, Lama S, et al. **Neurointerventional robotics: challenges and opportunities.** *Clin Neuroradiol* 2020;30:203–08 CrossRef Medline
7. Panesar SS, Volpi JJ, Lumsden A, et al. **Telerobotic stroke intervention: a novel solution to the care dissemination dilemma.** *J Neurosurg* 2019;132:971–78 CrossRef Medline
8. Miyachi S, Nagano Y, Kawaguchi R, et al. **Remote surgery using a neuroendovascular intervention support robot equipped with a sensing function: experimental verification.** *Asian J Neurosurg* 2021;16:363–66 CrossRef Medline
9. Adeoye O, Albright KC, Carr BG, et al. **Geographic access to acute stroke care in the United States.** *Stroke* 2014;45:3019–24 CrossRef Medline
10. Bulwa Z, Chen M. **Stroke center designations, neurointerventionalist demand, and the finances of stroke thrombectomy in the United States.** *Neurology* 2021;97:S17–24 CrossRef Medline
11. Aguiar de Sousa D, von Martial R, Abilleira S, et al. **Access to and delivery of acute ischaemic stroke treatments: a survey of national scientific societies and stroke experts in 44 European countries.** *Eur Stroke J* 2019;4:13–28 CrossRef Medline
12. Garcia-Tornel A, Millan M, Rubiera M, et al; RACECAT Trial Investigators. **Workflows and outcomes in patients with suspected large vessel occlusion stroke triaged in urban and nonurban areas.** *Stroke* 2022;53:3728–40 CrossRef Medline
13. Cancelliere NM, Lynch J, Nicholson P, et al. **Robotic-assisted intracranial aneurysm treatment: 1 year follow-up imaging and clinical outcomes.** *J Neurointerv Surg* 2022;14:1229–33 CrossRef Medline
14. Patel TM, Shah SC, Pancholy SB. **Long distance tele-robotic-assisted percutaneous coronary intervention: a report of first-in-human experience.** *EClinicalMedicine* 2019;14:53–58 CrossRef Medline
15. Tian W, Fan M, Zeng C, et al. **Telerobotic spinal surgery based on 5G network: the first 12 cases.** *Neurospine* 2020;17:114–20 CrossRef Medline
16. Legeza P, Britz GW, Shah A, et al. **Impact of network performance on remote robotic-assisted endovascular interventions in porcine model.** *J Robot Surg* 2022;16:29–35 CrossRef Medline
17. Madder RD, VanOosterhout S, Mulder A, et al. **Network latency and long-distance robotic telestenting: exploring the potential impact of network delays on telestenting performance.** *Catheter Cardiovasc Interv* 2020;95:914–19 CrossRef Medline
18. Dusenbury W, Mathiesen C, Whaley M, et al; American Heart Association Council on Cardiovascular and Stroke Nursing and the Stroke Council. **Ideal foundational requirements for stroke program development and growth: a scientific statement from the American Heart Association.** *Stroke* 2023;54:e175–87 CrossRef Medline
19. Yamaki VN, Cancelliere NM, Nicholson P, et al. **Biomodex patient-specific brain aneurysm models: the value of simulation for first in-human experiences using new devices and robotics.** *J Neurointerv Surg* 2021;13:272–77 CrossRef Medline
20. Day AL, Siddiqui AH, Meyers PM, et al. **Training standards in neuroendovascular surgery: program accreditation and practitioner certification.** *Stroke* 2017;48:2318–25 CrossRef Medline
21. Sanmartin MX, Katz JM, Eusemann C, et al. **Cost-effectiveness of remote robotic mechanical thrombectomy in acute ischemic stroke.** *J Neurosurg* 2023;139:721–31 CrossRef Medline

Cortical Hyperperfusion on MRI Arterial Spin-Labeling during the Interictal Period of Patients with Migraine Headache

Masami Shimoda, Kaori Hoshikawa, Shinri Oda, Masaaki Imai, Takahiro Osada, Rie Aoki, Azusa Sunaga, and Chiaki Shinohara

ABSTRACT

BACKGROUND AND PURPOSE: Concentrations of calcitonin gene-related peptide, a neuropeptide and potent endogenous vasodilator, are reportedly higher in patients with migraine than in healthy subjects, both during and between migraine attacks, reflecting ongoing activation of the trigeminal nervous system. In this prospective study, we measured CBF during the interictal period of patients with migraine after considering insomnia and depression and examined the effects of ongoing activation of the trigeminal nervous system, including during the interictal period, on CBF.

MATERIALS AND METHODS: In a total of 242 patient with migraine (age range, 18–75 years), CBF was measured by MR imaging arterial spin-labeling during the interictal period and was compared with results from 26 healthy volunteers younger than 45 years of age as control subjects (age range, 22–45 years). Cortical hyperperfusion was defined as identification of ≥2 cerebral cortical regions with regional CBF values at least 2 SDs above the mean regional CBF in control subjects.

RESULTS: The overall frequency of cortical hyperperfusion was significantly higher in patients with migraine (115 of 242, 48%) than in control subjects (1 of 26, 4%). Multivariable analysis revealed the 18- to 40-year age group and patients with migraine without insomnia as significant positive clinical factors associated with cortical hyperperfusion. Among patients with migraine without insomnia, the frequency of cortical hyperperfusion was >92% (89 of 97). One-way ANOVA showed that in all ROIs of the cortex, regional CBF was significantly higher in patients with migraine without insomnia than in patients with migraine with insomnia or control subjects. In patients with migraine without insomnia, cortical hyperperfusion findings showed a sensitivity of 0.918 and a specificity of 0.962 for migraine in the interictal period, representing excellent accuracy. In contrast, among patients with migraine with insomnia, sensitivity was only 0.179 but specificity was 0.962.

CONCLUSIONS: Patients with migraine without insomnia may have cortical hyperperfusion during the interictal period; however, the findings of the present study need to be prospectively validated on a larger scale before clinical applicability can be considered.

ABBREVIATIONS: ACA = anterior cerebral artery; AIS = Athens Insomnia Scale; AI = asymmetry index; ASL = arterial spin-labeling; BDI-II = Beck Depression Inventory, second edition; CGRP = calcitonin gene-related peptide; CHP = cortical hyperperfusion; HIT-6 = Headache Impact Test-6; MHDs = monthly headache days; PCA = posterior cerebral artery; PM = posterior part of the territory of the MCA; PPV = positive predictive value; rCBF = regional CBF

Previous studies have provided suggestive-but-fragmentary knowledge about regional CBF (rCBF) during migraine attacks and auras.[1,2] This issue is because CBF fluctuates dynamically during a migraine attack and significant results are difficult to obtain from sporadic rather than continuous measurements. Furthermore, migraine has been widely shown to be associated with depression and insomnia.[3] Depression and insomnia are interrelated, and both may be independently associated with decreased CBF and impaired CBF autoregulation.[4,5] Moreover, CBF autoregulation in patients with migraine is also impaired.[6] Different results would, therefore, seem likely when studying CBF during attacks in patients with migraine without considering the presence or absence of depression or insomnia.

Calcitonin gene-related peptide (CGRP) is an important neurotransmitter in the migraine headache-generating trigeminovascular system and is believed to play a crucial role in migraine pathophysiology.[7] CGRP, a highly potent microvascular vasodilator, is the most abundant neuropeptide in the trigeminal system, and is found in capsaicin-sensitive C fibers that follow the cerebral and meningeal arteries to innervate tissues.[8] CGRP induces endothelium-independent vasodilation via direct actions on vascular smooth-muscle cells in the cerebral and coronary vascular

Received November 7, 2023; accepted after revision January 25, 2024.

From the Department of Neurosurgery, Tokai University Hachioji Hospital, Tokyo, Japan.

Please address correspondence to: Masami Shimoda, MD, Department of Neurosurgery, Tokai University Hachioji Hospital, 1838 Ishikawa-machi, Hachioji, Tokyo 192-0032, Japan; e-mail: mashimoda-nsu@umin.ac.jp

Indicates open access to non-subscribers at www.ajnr.org

Indicates article with online supplemental data.

http://dx.doi.org/10.3174/ajnr.A8208

SUMMARY

PREVIOUS LITERATURE: Concentrations of calcitonin gene-related peptide (CGRP), a neuropeptide and potent endogenous vasodilator, are reportedly higher in patients with migraine, during both attacks and interictal periods, reflecting ongoing activation of the trigeminal nervous system. This state of high endogenous CGRP levels, including during interictal periods, likely causes cortical hyperperfusion (CHP) on MR imaging arterial spin-labeling (ASL). Migraine is associated with depression and insomnia, both of which are independently associated with decreased CBF. Therefore, studies during migraine attacks, when CBF fluctuations are dramatic or studies that do not take into account the presence or absence of depression and insomnia have not yielded useful results.

KEY FINDINGS: Patients with migraine may have CHP on ASL during the interictal period. Especially in patients with migraine without insomnia, the frequency of CHP (89 of 97, 92%) was significantly higher than in control subjects (1 of 26, 4%). This finding demonstrated excellent diagnostic accuracy for interictal migraine.

KNOWLEDGE ADVANCEMENT: The present study suggests that findings of CHP on ASL during the interictal period as the only characteristic imaging findings of migraine at present may be clinically very useful as an auxiliary diagnostic tool in addition to medical history.

beds. CBF autoregulation is, in part, mediated by CGRP.[9] CGRP concentrations in plasma, tears, and saliva are reportedly higher during migraine attacks as well as in patients with migraine during nonattacks than in healthy subjects.[10,11] In addition to CGRP, molecules such as vasoactive intestinal peptide and nitric oxide, which are intricately related to the pathologic mechanism of migraine, are all involved in vasodilation of the intracranial vasculature.[12] We have previously encountered findings on interictal MR imaging and arterial spin-labeling (ASL) in migraineurs that resemble cortical hyperperfusion (CHP) seen immediately after epileptic seizures.[13,14] These findings may have been due to the effects of vasodilator molecules related to the pathophysiology of migraine described above.

Many image-analysis studies using fMRI have been conducted on patients with migraine but have only aimed to elucidate the pathophysiology of migraine. The advantages of ASL compared with SPECT and PET include absolute quantification, repeatability, avoidance of IV contrast administration and, overall, superior spatial resolution and sensitivity.[2] Additionally, because functional near-infrared spectroscopy is a noninvasive method for measuring cerebrovascular reactivity, it is more suitable for evaluating the vascular effects of migraine drugs rather than for diagnostic imaging.[15]

Studies of ASL performed during the interictal period also reported that patients with migraine showed hyperperfusion of the some gyri, compared with healthy subjects.[2,16] These ASL studies attempted to identify migraine-specific imaging markers that reflect brain tissue perfusion through voxel-based CBF analysis. However, clinically useful image findings have not yet been obtained. Although the main purpose of MR imaging is to exclude secondary headaches, structural changes in the brains of patients with migraine are known to include an increase in cortical thickness, which reflects abnormal neuron hyperexcitability.[17] However, because there are individual differences in baseline cortical thickness depending on factors such as age, structural MR imaging findings are not suitable for diagnosing migraine itself.

In this prospective study, we measured CBF during the interictal period of patients with migraine using minimally invasive MR imaging ASL and compared the findings with those of healthy volunteers as control subjects. Given the results, we considered the factors of depression and insomnia in patients with interictal migraine and examined whether there are cerebral circulation characteristics such as CHP findings due to ongoing activation of the trigeminal nervous system, including during the interictal period.

MATERIALS AND METHODS

Institutional Review Board Approval

All study protocols were approved by the Institutional Review Board for Clinical Research (approval no. 22R-078) and the Conflict of Interest Management Committee (approval No. 22–168) at our university. The study protocol was implemented in accordance with the Declaration of Helsinki, and all patients provided written informed consent before participating in the study. In all patients with migraine, written informed consent for participation was obtained for the prospective study of data acquired during routine medical treatments based on national legislation and institutional requirements. Our report complies with the Strengthening the Reporting of Observational Studies in Epidemiology (STROBE) statement for cohort studies.

Patients

All patients with migraine fulfilled the diagnostic criteria for migraine established in the third edition of the International Classification of Headache Disorders by the International Headache Society.[18] Each patient with migraine showed normal results from neurologic examinations, MR imaging, and MRA. Excluded were patients younger than 18 years of age; smokers; patients with diabetes mellitus, epilepsy, cardiovascular disorders, ongoing treatment with calcium blockers or beta blockers, alcohol abuse, cerebrovascular disease; or those with known systemic diseases such as anemia and hypertension. None of the patients had received Botulinum Toxin injections or CGRP inhibitors.

Of the 266 patients with migraine attending our facility during the study period, 242 patients (age range, 18–75 years; male/female ratio: 27/215) with a clinical diagnosis of migraine who were

outpatients at our institution between October 2022 and May 2023 were included in this prospective cross-sectional study.

Patients with migraine were compared with a control group of 26 healthy volunteers (age range, 22–45 years; male/female ratio: 9/17) selected from our hospital staff with no history of headaches, insomnia, and depression using exclusion criteria identical to those for the groups of patients with migraine.

MR Imaging Perfusion Protocols

CBF studies using MR imaging ASL were performed for all patients with migraine during the interictal period (at least 48 hours after the last attack and migraine treatment such as triptanes). The upper limit from the last migraine attack to the scan was 7 days (168 hours). Consumption of caffeine was forbidden on the day of MR imaging ASL. We performed all MR imaging studies at our hospital on a 1.5T MR imaging scanner (Signa Explorer; GE Healthcare) with an Express head-neck array coil. All MR imaging examinations were completed within 16–18 minutes and included conventional axial T1WI, FLAIR, DWI, MRA, and ASL. The total scanning time of the ASL sequence was approximately 2 minutes 30 seconds. In addition to routine imaging sequences, we acquired 3D pulsed continuous ASL (also known as pseudocontinuous ASL) images with background suppression using the following parameters: TR, 4548 ms; TE, 10.5 ms; FOV, 24 cm; 512 sampling points on 6 spirals (matrix size, 512×6); spatial resolution, 5.0 mm; section thickness, 4 mm; number of sections, 30; excitations, 2; bandwidth, 62.50 Hz; and labeling time, 1.5 seconds. On the basis of a recently published white paper,[19] pseudocontinuous labeling, background suppression, a segmented 3D readout without vascular crushing gradients, and calculation and presentation of both label/control difference images and CBF in absolute units using a simplified model are recommended for optimal default implementation of ASL. The ASL performed in this study used the latest ASL sequence by GE Healthcare, which meets all these recommended conditions. We routinely used 2 postlabeling delays (short ASL, 1525 ms; delayed ASL, 2525 ms). In this study, a postlabeling delay of 1525 ms was used for the CBF analysis because no patients with severe cerebrovascular stenosis were included. Another reason is that longer postlabeling delays reduce the SNR due to relaxation of T1.

For the quantitative ROI analysis of the ASL map, we used the fully-automated ROI-based analysis software 3D stereotaxic ROI template (3DSRT Neuro; FUJIFILM) for the positioning or selection of an ROI offering objectivity and excellent reproducibility.[20] The obtained quantitative CBF images were registered anatomically to the standard brain atlas. The 3D stereotaxic ROI template software has ROIs predefined on the standard brain atlas and provides rCBF values for each of the right and left sides of the following 9 regions: callosomarginal, precentral, central, parietal, angular, temporal, posterior cerebral, pericallosal, and thalamus. We determined rCBF in the territories of major cerebral arteries as previously described (Online Supplemental Data).[21]

We confirmed that there was no significant laterality in rCBF by calculating the asymmetry index (AI) for control subjects and patients with migraine. If there was no significant lateral difference in rCBF, we averaged the left and right regional CBFs and calculated the mean (SD).

AI was calculated for the rCBF as follows:

$$Asymmetry\ index = \frac{(ROIright - ROIleft)}{(ROIright + ROIleft)} \times 100.$$

An absolute AI value of >10 indicated asymmetric perfusion.[14]

In this study, as with the diagnostic criteria for hyperperfusion immediately after an epileptic seizure or postoperative Moyamoya disease, an ROI was defined as exhibiting hyperperfusion if CBF in the ROI was at least 2 SDs higher than the mean reference value for CBF in control subjects.[13] CHP was considered present if ≥2 hyperperfusion cortical ROIs were identified in each cerebral lobe in the unilateral hemisphere.[13]

Variables, Data Extraction, and End Points

The primary end point of this study was to identify the appearance of CHP findings on MR imaging ASL as a feature of the cerebral circulation in patients with migraine during headache-free periods.

One or 2 months before performing MR imaging, we extracted the number of monthly headache days (MHDs) from headache diaries. A headache day was defined as any day on which a patient recorded any type of headache. Moreover, we extracted the following characteristics from the patient medical records: sex; age; age range (in groups of 18–40, 41–60, and 61–75 years of age); episodic migraine; chronic migraine; aura; Headache Impact Test-6 (HIT-6)[22]; morning migraine; Athens Insomnia Scale (AIS);[23] Beck Depression Inventory, second edition (BDI-II);[24] menstrual migraine; weather-related migraine; medication overdose headache; tension-type headache; selective serotonin reuptake inhibitor use; and concomitant prophylactic treatment. We defined "morning migraine" as waking up in the morning with a migraine caused by dehydration, sleep deprivation, or stress. Insomnia was defined as AIS ≥ 4, and depression, as BDI-II ≥ 11.

Statistical Analysis

All statistical analyses were performed using commercially available software (SPSS Statistics for Windows, Version 27.0; IBM).

Distributions of each variable were checked for normality using the Shapiro-Wilk test. The significance of clinical factors potentially associated with a finding of CHP on MR imaging ASL was determined using the Fisher exact test. Continuous variables (age, MHDs, HIT-6, AIS, and BDI-II) were tested using an independent samples Student *t* test. The homogeneity of variance was analyzed using the Levene test. Values of $P < .05$ were considered statistically significant. All data are presented as mean (SD) unless otherwise specified. Sensitivity, specificity, positive predictive value (PPV), and negative predictive value were calculated using standard formulas.

RESULTS

Frequencies and Clinical Features of CHP in Patients with Migraine

No lateral differences in rCBF were identified according to AI in any patient with migraine. We, therefore, averaged left and right local CBF on the basis ROIs in control subjects and patients with

Comparison of CBF using MR imaging of ASL in control subjects and patients with migraine with and without insomnia and/or depression[a]

	Cases	ACA	AM	PM	PCA	Tha
Healthy control	26	48 (SD, 6)[b]	49 (SD, 7)[b]	48 (SD, 6)[b]	47 (SD, 6)[b]	45 (SD, 6)[b]
Baseline for hyperperfusion		60	63	60	59	57
Migraine without insomnia	97	62 (SD, 6)	64 (SD, 5)	63 (SD, 5)	61 (SD, 5)	56 (SD, 6)
Migraine with insomnia	145	51 (SD, 7)[b]	52 (SD, 7)[b]	51 (SD, 7)[b]	50 (SD, 8)[b]	48 (SD, 6)[b]
Migraine without depression	166	57 (SD, 8)	59 (SD, 8)	58 (SD, 8)	56 (SD, 8)	53 (SD, 7)
Migraine with depression	76	51 (SD, 8)[b]	53 (SD, 8)[b]	52 (SD, 8)[b]	51 (SD, 8)[b]	49 (SD, 7)[c]
Migraine without both insomnia and depression	91	62 (SD, 6)	64 (SD, 5)	63 (SD, 5)	60 (SD, 5)	56 (SD, 6)
Migraine with either insomnia or depression	151	51 (SD, 8)[b]	53 (SD, 8)[b]	52 (SD, 8)[b]	50 (SD, 8)[b]	49 (SD, 7)[b]

Note:—Tha indiates thalamus; AM, anterior part of the territory of the MCA; PM, posterior part of the territory of the MCA.
[a]Data are means. Insomnia was defined as a score of ≥4 on the AIS. Depression was defined as a score of ≥11 on the BDI-II. The unit for CBF is mL/100 g/min. rCBF data in migraineurs without insomnia (or depression) were compared with those in healthy controls and migraineurs with insomnia (or depression) and evaluated by ANOVA followed by the Tukey honestly significant difference test.
[b]$P < .001$.
[c]$P = .01$.

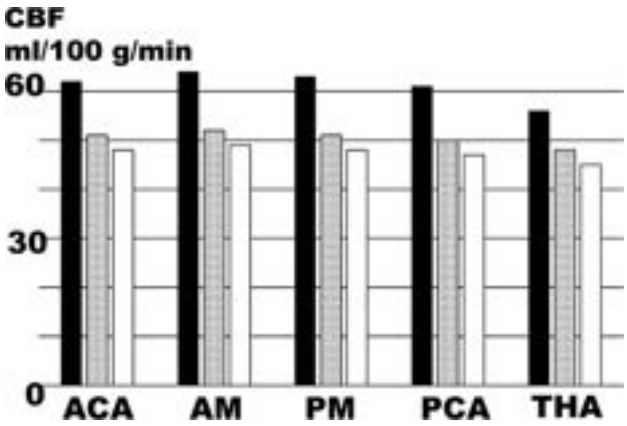

FIG 1. Values of rCBF during the interictal period in patients with migraine with/without insomnia. These plots are graphical representations of the data presented in the Table. In *bar graphs* of mean rCBF, *black bars* indicate migraine without insomnia, *dotted bars* indicate migraine with insomnia, and *white bars* indicate healthy controls. THA indicates rCBF in the territory of the thalamus; AM, anterior part of the territory of the MCA; PM, posterior part of the territory of the MCA.

migraine and then calculated the mean (SD). The baseline CBF values for hyperperfusion obtained from the mean (SD) of rCBF for each cortical region (anterior cerebral artery [ACA], anterior part of the territory of the MCA, posterior part of the territory of the MCA, posterior cerebral artery [PCA]) in control subjects were ≥60 in all regions (Table).

The overall frequency of CHP was significantly higher in patients with migraine (115 of 242, 48%) than in control subjects (1 of 26, 4%) (Online Supplemental Data).

Clinical features associated with CHP in patients with migraine are shown in the Online Supplemental Data. Because data for MHDs and HIT-6 were not normally distributed, nonparametric tests were used for analyses. As a result, the clinical factor significantly associated with CHP in patients with migraine was the age group of 18–40 years as a positive factor. Negative factors for CHP findings were the age group of 41–60 years, morning migraine, AIS, AIS ≥ 4, BDI-II scale, BDI-II ≥ 11, and the use of an oral selective serotonin reuptake inhibitor (Online Supplemental Data). Episodic migraine, chronic migraine, and aura were not significantly associated with CHP findings.

Clinical factors with a significance level of $P < .10$ were subjected to multivariable logistic regression analysis with the presence of CHP as the dependent variable. Multivariable analysis revealed that significant positive clinical factors associated with CHP in patients with migraine were the age group of 18–40 years (OR = 2.985; 95% CI, 1.381–6.452; $P = .005$) and AIS <4 (absence of insomnia) (OR = 53.598; 95% CI, 22.519–127.57; $P < .001$). In multivariable analysis, the association between patients with migraine with depression and CHP was not significant.

Comparison of CBF in Patients with Migraine with/without Insomnia

Among 145 patients with migraine with insomnia, 70 (48%) had depression. Of the 76 patients with migraine with depression, 70 (92%) also had insomnia.

Patients with migraine were subgrouped according to the presence or absence of insomnia and/or depression, and rCBF during headache-free periods in each ROI was compared with that in control subjects (Table and Online Supplemental Data). Because our data for CBF were normally distributed, we used 1-way ANOVA for analysis of multiple comparisons to test for significant differences in CBF data between the clinical groups. Homogeneity of variance was analyzed by using the Levene test. Equal variance of CBF data from each clinical group was confirmed, so the significance of ANOVA was determined by the Tukey honestly significant difference test (Table and Online Supplemental Data). Consequently, in all ROIs, rCBF was significantly higher in patients with migraine without insomnia than in patients with migraine with insomnia or control subjects. However, no significant differences in rCBF were seen between patients with migraine with insomnia and control subjects in any ROIs (Fig 1). Typical CHP findings on ASL in patients with migraine without insomnia, patients with migraine with insomnia, and healthy controls are shown in Fig 2.

Similarly, in all ROIs, rCBF was significantly higher in patients with migraine without depression than in patients with migraine with depression or control subjects. Moreover, in all ROIs, rCBF was significantly higher in patients with migraine without both insomnia and depression than in patients with migraine with either insomnia or depression or control subjects.

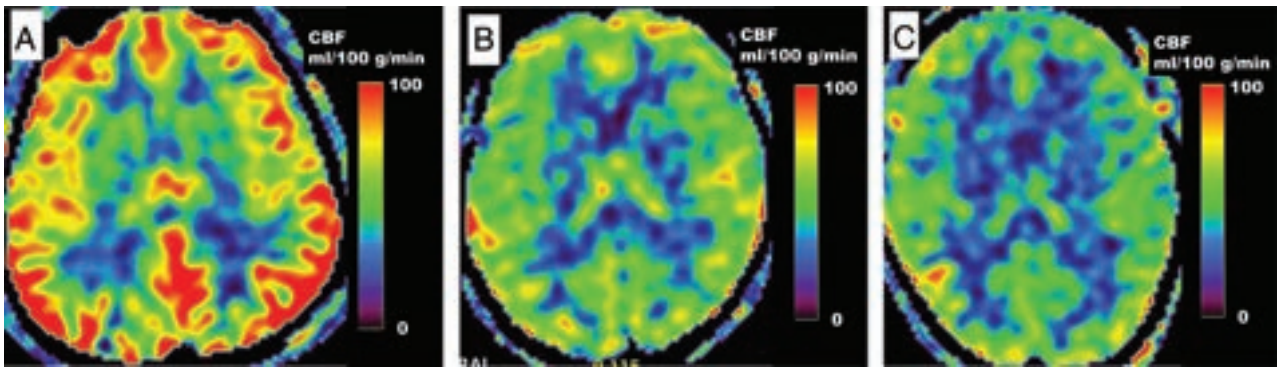

FIG 2. Findings from MR imaging ASL. *A*, Typical CHP findings in a 41-year-old woman with episodic migraine without insomnia. *B* and *C*, Normal findings without CHP in a 48-year-old woman with chronic migraine complicated by insomnia (*B*) and a 30-year-old woman from the healthy control group (*C*).

The statistical significance of pair-wise comparisons against rCBF data in patients with migraine was evaluated with ANOVA followed by the Tukey honestly significant difference test. Comparison of patients with migraine with insomnia, depression, and those with migraine with either insomnia or depression, and healthy controls showed no significant difference in rCBF in any ROI.

Accuracy of Migraine Diagnosis Based on Hyperperfusion on MR Imaging ASL

In patients with migraine without insomnia, regarding the diagnostic accuracy of CHP findings for migraine in the interictal period, sensitivity was 0.918, specificity was 0.962, and PPV was 0.989, showing excellent accuracy. In all cases and patients with migraine with insomnia, the sensitivity was low at 0.475 and 0.179, respectively, but the specificity was 0.962 and 0.962, respectively, and the PPV was good at 0.991 and 0.963, respectively.

DISCUSSION

Mechanisms of CHP in Patients with Migraine

This study showed that patients with migraine, especially those without insomnia, may have interictal CHP. Functional MR imaging is useful for identifying changes in functional connectivity in migraine that are thought to be related to cortical spreading depolarization. However, because blood oxygenation level–dependent signals obtained from fMRI do not directly reflect cerebral perfusion,[16] there are no studies that can be used as a reference for considering the mechanism of CHP in migraine. We speculate that cortical hyperexcitability, which plays an important role in the development of migraine in the trigeminal nerve-thalamocortical pathway, is the cause of CHP. In fact, a previous study of voxel-based CBF analysis of ASL during the interictal period reported high CBF levels in visual, somatosensory, multisensory integration cortices, superior frontal gyri, and postcentral gyri in interictal ASL in patients with migraine with aura.[16]

The mechanism of CHP may also involve vasodilatory neurotransmitters that are associated with migraine development. CGRP mediates CBF autoregulation, in part, by inducing endothelial-independent vasodilation through direct effects on cerebral vascular smooth-muscle cells.[9] Moreover, CGRP released from the trigeminal perivascular nerve is also a potent direct vascular smooth-muscle dilator that counteracts vasoconstriction and hypoperfusion of the cerebral vascular bed as a rescue mechanism in cerebral ischemia.[9,25,26]

Concentrations of CGRP in plasma, tears, and saliva are reportedly higher in patients with migraine both during attacks and during the interictal period compared with healthy subjects.[10,11] Thus, the presence of elevated CGRP levels not only during headache attacks but also during the interictal period indicates that the trigeminal nervous system is continuously activated during headache attacks and during the interictal period.[10] Normally, endogenous CGRP does not change CBF at the steady state. However, migraine,[6] insomnia, and depression are never steady states due to impaired CBF autoregulation. Therefore, a state of high endogenous CGRP levels resulting from ongoing activation of the trigeminal nervous system, including during interictal periods, likely causes CHP on ASL.

ASL Findings in Patients with Migraine Headache with Insomnia and Depression

A common neurophysiologic mechanism underlying both insomnia and depression is hyperactivation of the hypothalamic-pituitary-adrenal axis, which indirectly results in impaired CBF autoregulation.[4,27] There have also been reports of decreased local CBF in the frontal medial, occipital, and parietal cortices and basal ganglia in patients with insomnia.[5,28] Studies of CBF in migraine that do not consider the presence or absence of depression or insomnia would thus seem unlikely to yield results in consensus.

CGRP may be involved in the pathophysiology of depression, and a significant increase in CGRP levels has been reported in patients with migraine with depression.[11] Thus, although CGRP concentration is known to be high in depression, CBF in this study was low among patients with migraine with depression, and the vasodilatory effects of CGRP were not reflected. Previous studies have shown that homocysteine levels in patients with depression were significantly higher.[29] Elevated plasma levels of homocysteine resulted in reduced nitric oxide bioavailability and hypertrophy of vascular smooth-muscle cells, which could decrease the ability of vascular dilation.[4,30] On the basis of these findings, we think that because the vasodilatory ability is reduced in depression and/or insomnia, which is strongly

associated with depression, the vasodilatory effect of CGRP is less likely to occur. As a result, the frequency of CHP may be low in migraine complicated with depression and/or insomnia. In the future, we believe it is important to study how insomnia and depression affect the trigeminovascular system, CGRP levels, and CBF autoregulation in patients with migraine.

Neuroradiologic Diagnosis of Migraine by CHP Findings on ASL

Previous migraine studies using ASL did not emphasize the presence of CHP.[2,16] In contrast, because the strengths of our study compared with previous studies include the large sample size, grouping analysis by presence or absence of insomnia and depression, and strict interictal ASL implementation, we were able to clarify the presence of CHP as a characteristic finding of ASL in patients with migraine.

The CHP findings in this study were more frequent and clinically useful in patients with migraine without insomnia and depression. Moreover, because the CBF value in CHP was ≥10 mL/100 g/min higher than that in healthy controls, the hyperperfusion pattern for the cortex on ASL images is visually impressive. CHP, therefore, seems to allow an easy one-shot diagnosis without checking the CBF value. In addition, if migraine is clearly diagnosed according to the diagnostic criteria, but no CHP findings are evident, insomnia or depression should be suspected, and clinical/psychological medical examinations should be required. These will allow headache specialists to treat migraines more precisely. On the basis of the above, we emphasize that CHP findings on ASL are clinically very useful as one of the supplementary diagnostic tools in addition to interviews, as the only impressive imaging finding for migraine at present.

The differential diagnosis for CHP includes nonconvulsive status epilepticus.[13,14] Additionally, those with typical aura without headache[18] and patients with a family history of migraine may also present with CHP findings, and this possibility is currently under investigation.

Limitations

This study has some limitations. First, it relied on indirect evidence from previous studies, because we were unable to test our hypothesis by simultaneously measuring CGRP levels in both patients with migraine and control subjects and correlating them with ASL findings.

Second, relatively low SNR and low temporal resolution, as the key limitations of ASL, have been overcome due to technical advances in MR imaging.[1] However, ASL remains vulnerable to head-movement artifacts, so the existence of cases that compromised the reliability of CBF values cannot be ruled out. In addition, ASL perfusion findings may be influenced by various factors, such as the MR magnetic field (1.5T versus 3T) and limitation of using single delay, sex, age, and the effect of medications on CBF measures.

Third, the reproducibility of CBF measured with ASL was not assessed. In the future, repeat interval scans will need to be performed to confirm that the results of this study are a consistent phenomenon rather than obtained by chance.

Fourth, because the main purpose of this study was to demonstrate that migraine can be diagnosed on the basis of the finding of CHP on ASL, we did not perform a group-level voxelwise CBF analysis to look for the spatial extent of the abnormalities.

CONCLUSIONS

Patients with migraine without insomnia may have CHP during the interictal period; however, the findings of the present study need to be prospectively validated on a larger scale before clinical applicability can be considered.

ACKNOWLEDGMENTS

The authors are grateful to the radiologic technologists and nursing staff at our institute for their assistance in this work.

Disclosure forms provided by the authors are available with the full text and PDF of this article at www.ajnr.org.

REFERENCES

1. Park S, Lee DA, Lee HJ, et al. **Brain networks in migraine with and without aura: an exploratory arterial spin labeling MRI study.** *Acta Neurol Scand* 2022;145:208–14 CrossRef Medline
2. Russo A, Silvestro M, Tessitore A, et al. **Arterial spin labeling MRI applied to migraine: current insights and future perspectives.** *J Headache Pain* 2023;24:71 CrossRef Medline
3. Saçmacı H, Tanik N, İnan LE. **Current perspectives on the impact of chronic migraine on sleep quality: a literature review**. *Nat Sci Sleep* 2022;14:1783–800 CrossRef Medline
4. Liu M, He E, Fu X, et al. **Cerebral blood flow self-regulation in depression.** *J Affect Disord* 2022;302:324–31 CrossRef Medline
5. Park S, Hong H, Kim RY, et al. **Firefighters have cerebral blood flow reductions in the orbitofrontal and insular cortices that are associated with poor sleep quality.** *Nat Sci Sleep* 2021;13:1507–17 CrossRef Medline
6. Müller M, Marziniak M. **The linear behavior of the system middle cerebral artery flow velocity and blood pressure in patients with migraine: lack of autonomic control?** *Stroke* 2005;36:1886–90 CrossRef Medline
7. Iyengar S, Johnson KW, Ossipov MH, et al. **CGRP and the trigeminal system in migraine.** *Headache* 2019;59:659–81 CrossRef Medline
8. Nisar A, Ahmed Z, Yuan H. **Novel therapeutic targets for migraine.** *Biomedicines* 2023;11:569 CrossRef Medline
9. Hong KW, Pyo KM, Lee WS, et al. **Pharmacological evidence that calcitonin gene-related peptide is implicated in cerebral autoregulation.** *Am J Physiol* 1994;266:H11–16 CrossRef Medline
10. Kamm K. **CGRP and migraine: what have we learned from measuring CGRP in patient with migraine so far?** *Front Neurol* 2022; 13:930383 CrossRef Medline
11. Alpuente A, Gallardo VJ, Asskour L, et al. **Salivary CGRP and erenumab treatment response: towards precision medicine in migraine.** *Ann Neurol* 2022;92:846–59 CrossRef Medline
12. Biscetti L, Cresta E, Cupini LM, et al. **The putative role of neuroinflammation in the complex pathophysiology of migraine: from bench to bedside.** *Neurobiol Dis* 2023;180:106072 CrossRef Medline
13. Ohtomo S, Otsubo H, Arai H, et al. **Hyperperfusion in the thalamus on arterial spin labelling indicates non-convulsive status epilepticus.** *Brain Commun* 2021;3:fcaa223 CrossRef Medline
14. Hauf M, Slotboom J, Nirkko A, et al. **Cortical regional hyperperfusion in nonconvulsive status epilepticus measured by dynamic brain perfusion CT.** *AJNR Am J Neuroradiol* 2009;30:693–98 CrossRef Medline

15. Pourshoghi A, Danesh A, Tabby DS, et al. **Cerebral reactivity in patient with migraine measured with functional near-infrared spectroscopy.** *Eur J Med Res* 2015;20:96 CrossRef Medline
16. Fu T, Liu L, Huang X, et al. **Cerebral blood flow alterations in patient with migraine with and without aura: an arterial spin labeling study.** *J Headache Pain* 2022;23:131 CrossRef Medline
17. Szabo E, Ashina S, Melo-Carrillo A, et al. **Peripherally acting anti-CGRP monoclonal antibodies alter cortical gray matter thickness in patient with migraine: a prospective cohort study.** *Neuroimage Clin* 2023;40:103531 CrossRef Medline
18. **Headache Classification Committee of the International Headache Society (IHS) The International Classification of Headache Disorders, 3rd edition.** *Cephalalgia* 2018;38:1–211 CrossRef Medline
19. Alsop DC, Detre JA, Golay X, et al. **Recommended implementation of arterial spin-labeled perfusion MRI for clinical applications: a consensus of the ISMRM perfusion study group and the European Consortium for ASL in Dementia.** *Magn Reson Med* 2015;73:102–16 CrossRef Medline
20. Iwanaga T, Harada M, Kubo H, et al. **Operator-bias-free comparison of quantitative perfusion maps acquired with pulsed-continuous arterial spin labeling and single-photon-emission computed tomography.** *Magn Reson Med Sci* 2014;13:239–49 CrossRef Medline
21. Inoue Y, Tanaka Y, Hata H, et al. **Arterial spin-labeling evaluation of cerebrovascular reactivity to acetazolamide in healthy subjects.** *AJNR Am J Neuroradiol* 2014;35:1111–16 CrossRef Medline
22. Shin HE, Park JW, Kim YI, et al. **Headache Impact Test-6 (HIT-6) scores for patient with migraine: their relation to disability as measured from a headache diary.** *J Clin Neurol* 2008;4:158–63 CrossRef Medline
23. Soldatos CR, Dikeos DG, Paparrigopoulos TJ. **Athens Insomnia Scale: validation of an instrument based on ICD-10 criteria.** *J Psychosom Res* 2000;48:555–60 CrossRef Medline
24. Arnarson TO, Olason DT, Smári J, et al. **The Beck Depression Inventory Second Edition (BDI-II): psychometric properties in Icelandic student and patient populations**. *Nord J Psychiatry* 2008; 62:360–65 CrossRef Medline
25. McCulloch J, Uddman R, Kingman TA, et al. **Calcitonin gene-related peptide: functional role in cerebrovascular regulation.** *Proc Natl Acad Sci U S A* 1986;83:5731–35 CrossRef Medline
26. Mulder IA, Li M, de Vries T, et al. **Anti-migraine calcitonin gene-related peptide receptor antagonists worsen cerebral ischemic outcome in mice.** *Ann Neurol* 2020;88:771–84 CrossRef Medline
27. Roth T, Roehrs T, Pies R. **Insomnia: pathophysiology and implications for treatment.** *Sleep Med Rev* 2007;11:71–79 CrossRef Medline
28. Smith MT, Perlis ML, Chengazi VU, et al. **Neuroimaging of NREM sleep in primary insomnia: a Tc-99-HMPAO single photon emission computed tomography study.** *Sleep* 2002;25:325–35
29. Karakuła H, Opolska A, Kowal A, et al. **Does diet affect our mood? The significance of folic acid and homocysteine** [in Polish]. *Pol Merkur Lekarski* 2009;26:136–41 Medline
30. Lai WK, Kan MY. **Homocysteine-induced endothelial dysfunction.** *Ann Nutr Metab* 2015;67:1–12 CrossRef Medline

Timing of Spot Sign Appearance, Spot Sign Volume, and Leakage Rate among Phases of Multiphase CTA Predict Intracerebral Hemorrhage Growth

MacKenzie Horn, Ericka Teleg, Koji Tanaka, Abdulaziz Al Sultan, Linda Kasickova, Tomoyuki Ohara, Piyush Ojha, Sanchea Wasyliw, Sina Marzoughi, Ankur Banerjee, Girish Kulkarni, Kennedy Horn, Amy Bobyn, Anneliese Neweduk, Nishita Singh, Wu Qiu, David Rodriguez-Luna, Dar Dowlatshahi, Mayank Goyal, Bijoy K. Menon, and Andrew M. Demchuk

ABSTRACT

BACKGROUND AND PURPOSE: The presence of spot sign is associated with a high risk of hematoma growth. Our aim was to investigate the timing of the appearance, volume, and leakage rate of the spot sign for predicting hematoma growth in acute intracerebral hemorrhage using multiphase CTA.

MATERIALS AND METHODS: In this single-center retrospective study, multiphase CTA in 3 phases was performed in acute intracerebral hemorrhage (defined as intraparenchymal ± intraventricular hemorrhages). Phases of the spot sign first appearance, spot sign volumes (microliter), and leakage rates among phases (microliter/second) were measured. Associations between baseline clinical and imaging variables including spot sign volume parameters (volume and leakage rate divided by median) and hematoma growth (>6 mL) were investigated using regression models. Receiver operating characteristic analysis was used as appropriate.

RESULTS: Two hundred seventeen patients (131 men; median age, 70 years) were included. The spot sign was detected in 21.7%, 30.0%, and 29.0% in the first, second, and third phases, respectively, with median volumes of 19.7, 31.4, and 34.8 μl in these phases. Hematoma growth was seen in 44 patients (20.3%). By means of modeling, the following variables, namely the spot sign appearing in the first phase, first phase spot sign volume, spot sign appearing in the second or third phase, and spot sign positive and negative leakage rates, were associated with hematoma growth. Among patients with a spot sign, the absolute leakage rate accounting for both positive and negative leakage rates was also associated with hematoma growth (per 1-μl/s increase; OR, 1.26; 95% CI, 1.04–1.52). Other hematoma growth predictors were stroke history, baseline NIHSS score, onset-to-imaging time, and baseline hematoma volume (all P values $< .05$).

CONCLUSIONS: The timing of the appearance of the spot sign, volume, and leakage rate were all associated with hematoma growth. Development of automated software to generate these spot sign volumetric parameters would be an important next step to maximize the potential of temporal intracerebral hemorrhage imaging such as multiphase CTA for identifying those most at risk of hematoma growth.

ABBREVIATIONS: ICH = intracerebral hemorrhage; mCTA = multiphase CTA

Stroke is one of the leading causes of morbidity and mortality worldwide. Spontaneous, nontraumatic intracerebral hemorrhage (ICH) is the most severe form of stroke, with a mortality rate of 40% at 1 month from onset.[1,2] The growth in hematoma volume occurs in approximately one-third of patients with acute ICH within 6 hours and is associated with early neurologic deterioration and functional outcome.[3,4] Therefore, identifying patients with the highest risk of hematoma growth would be beneficial in clinical practice by further refining the ideal target population for intensive antihypertensive or promising hemostatic treatment. The spot sign is ≥1 foci of enhancement within the hemorrhage in contrast-enhanced CT, which is predictive of hematoma growth and poor prognosis in patients with acute ICH.[5,6] Biologic underpinnings of the spot sign generally are

Received November 27, 2023; accepted after revision January 23, 2024.

From the Foothills Medical Centre, Departments of Clinical Neurosciences (M.H., E.T., K.T., A.A.S., P.O., K.H., A. Bobyn, A.N., N.S., B.K.M., A.M.D.), Radiology (B.K.M., M.G., A.M.D.), and Community Health Sciences (B.K.M.), and Hotchikiss Brain Institute (M.G., B.K.M., A.M.D.), Cumming School of Medicine, University of Calgary, Calgary, Canada; Department of Neurology (L.K.), University Ostrava, Ostrava, Czech Republic; Department of Neurology (T.O.), Kyoto Prefectural University of Medicine, Kyoto, Japan; Department of Medicine (S.W.), Division of Neurology, University of Saskatchewan, Saskatoon, Canada; Department of Medicine (S.M.), Division of Neurology, University of British Columbia, Vancouver, Canada; Department of Medicine (A. Banerjee), Division of Neurology, University of Alberta, Edmonton, Canada; Department of Neurology (G.K.), National Institute of Mental Health and Neurosciences, Bengaluru, India; Department of Neurology (D.R.-L.), Vall d'Hebron University Hospital, Barcelona, Spain; Department of Biomedical Engineering (W.Q.), Huazhong University of Science and Technology, Wuhan, China and Department of Medicine (D.D.), Division of Neurology, University of Ottawa, Ottawa, Canada.

M. Horn, E. Teleg, and K. Tanaka contributed equally to this work.

Please address correspondence to Andrew M. Demchuk, MD, Departments of Clinical Neurosciences and Radiology, and Hotchikiss Brain Institute, Cumming school of Medicine, University of Calgary, Calgary, Canada, 1403 29 St N.W., Calgary, AB, T2N 2T9 Canada; e-mail: ademchuk@ucalgary.ca

Indicates article with online supplemental data.

http://dx.doi.org/10.3174/ajnr.A8254

contrast leakage from the source bleeding arteriole or peripheral small vessels surrounding the hematoma that bleed due to mechanical effect/tearing.[7,8]

Imaging studies such as dynamic CT have revealed temporal characteristics of the spot sign, in which contrast appeared in the arterial phase and dispersed into the hematoma in later phases.[7,9] Multiphase CTA (mCTA) is another form of dynamic/temporal imaging that uses 3 phases and has been adopted by many centers primarily for ischemic stroke, evaluating collateral blood flow, and occlusion detection (region of delayed washout).[10] Some of these centers have also used mCTA for ICH to detect the first appearance of the spot sign by phase, improving the prediction ability for hematoma growth.[11,12] Recent studies using mCTA demonstrated that hematoma growth was greater in cases with the spot sign detected in the arterial phase than those detected in the venous phase.[13,14] Given that spot signs represent ongoing bleeding, volumetric analysis of the spot sign across time may improve the predictive performance for hematoma growth; however, associations between the spot sign volume parameters and hematoma growth remain unclear. In this study, we aimed to investigate volumetric characteristics of the spot sign for predicting hematoma growth and outcome in patients with acute ICH who underwent mCTA.

MATERIALS AND METHODS

Study Design

This was a single-center retrospective study comprising consecutive patients with acute ICH who underwent mCTA between February 2012 and May 2020 at the Foothills Medical Centre in Calgary, Alberta, Canada. Confirmed cases with acute ICH by NCCT immediately underwent mCTA unless they had contraindications (no baseline MRIs were performed). Patients underwent follow-up imaging by NCCT or MR imaging between 12 and 72 hours. Patients younger than 18 years of age, who underwent surgery without imaging before surgery, those having only intraventricular hemorrhage, or with a secondary cause of ICH (eg, tumor, trauma, or AVM-related) were excluded. This study was approved by the ethics committee at the University of Calgary beginning in 2017. Radiologic data assessment was completed by study members blinded to the clinical information. Any disagreements among reviewers were resolved by consensus.

Study Participants

Patients' clinical characteristics were collected from the medical charts. These included age, sex, history of stroke, prior antithrombotic medication (antiplatelets and/or anticoagulants including warfarin, direct oral anticoagulants, or low-molecular weight heparin), and vascular risk factors including hypertension, diabetes mellitus, current smoking, and alcohol consumption. Blood pressure measurement and routine blood chemistry examinations were performed on admission. The severity of neurologic symptoms was assessed by the NIHSS score. Onset-to-imaging time was defined as the time from symptom onset or last known well to the first CT scan. Anticoagulation reversal treatment was performed if indicated. Functional outcome was assessed at 90 days by mRS. Unfavorable outcome was defined as mRS $\geq$3.

mCTA Protocol

The center for the research uses 2 distinct mCTA imaging protocols for acute stroke using Revolution or Discovery 750 HD (GE Healthcare). The ischemic stroke protocol scans the neck first and then the brain 3 times, 8 seconds apart.[10] The mCTA ICH protocol scans the brain only (no neck imaging) in 3 phases after contrast material injection. In the mCTA ICH protocol, from the beginning of the first phase to the start of the second phase is 10–11 seconds; and from start of second phase to the start of the third phase, 16–18 seconds. This protocol represents peak arterial, peak venous, and late venous phases. Seventy milliliters of contrast material (68% ioversol, Optiray 320; Mallinckrodt) was injected at a rate of 6 mL/s for both protocols. The axial images were acquired with a 0.625-mm section thickness and reconstructed at 1-mm overlapping sections. Scanning parameters were a tube voltage of 120 kV and the tube current set to automatically modulated, with a minimum of 200 mA and a maximum of 625 mA. The total radiation dose per our mCTA ischemic stroke protocol was 1450 and 770 mGy for the mCTA ICH stroke protocol.

Imaging Analysis and Definition of Hematoma Growth

Imaging analysis was performed using semiautomatic segmentation software, Quantomo, Version 1 (Cybertrial, Calgary, Canada).[15] Quantomo allows seeding the volume by selecting a single pixel and then correcting the spot sign volume manually. Semiautomation of Quantomo is the seeding feature. Manual-correction tools include a pencil for additions, an eraser for subtraction, and a blocking tool to reject incorrect seeding. Quantomo-generated volume measures up to 2 decimal places. Quantomo files were converted and input into ITK-SNAP software Version 3 (www.itksnap.org) to determine volume in microliters. The time between the phases differed in the 2 mCTA protocols and was considered when calculating the interval between phases. The leakage rate was calculated by the volume difference between phases (microliter)/interval between the phases (seconds). Because the leakage rate can be negative if the spot sign disperses or disappears, we calculated the absolute leakage rate, accounting for both positive and negative leakage rates. The absolute leakage rate was calculated by (|leakage rate between first and second phases| + |leakage rate between second and third phases|)/2. Hematoma volume was measured on baseline NCCT and follow-up NCCT.

ICH included both intraparenchymal hemorrhage and intraventricular hemorrhage. For patients who underwent only MR imaging, hematoma volume was measured in either FLAIR (TR/TE range, 8421–10,934/85–126 ms) or T2 sequences (TR/TE range, 4030–10,162/94–120 ms). SWI or gradient-echo was not used given concerns for blooming artifacts.[16] In patients who underwent both T2 and FLAIR, we chose either one. The location of the hematoma was classified as deep cerebral (globus pallidus, putamen, thalamus, caudate, or combined), lobar, or infratentorial (brainstem or cerebellum). Hematoma growth was defined as an increase in ICH volume of $>$6 mL.[17] The spot sign was defined according to the following criteria: 1) serpiginous or spotlike appearance within the margin of a parenchymal hematoma without connection to an outside vessel; 2) contrast density of $>$1.5 mm in diameter in at least 1 dimension; 3) contrast density (Hounsfield units at least double

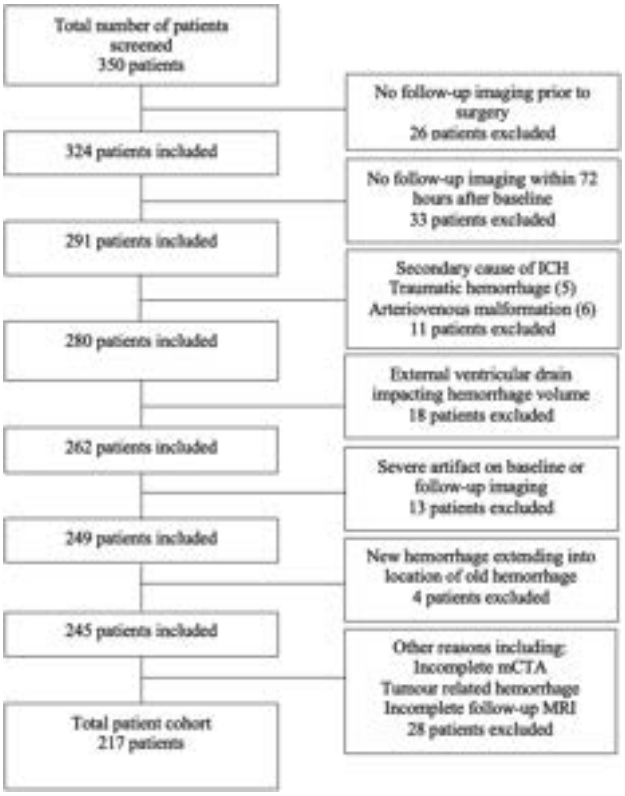

FIG 1. Patient inclusion/exclusion flow chart. Patients were screened according to the inclusion/exclusion criteria of the study. Of the 350 patients screened, 217 patients were included in the study.

those of the background hematoma); and 4) no hyperdensity at the corresponding location on NCCT.[18]

Statistical Analysis

Statistical analysis was performed using STATA software, Version 18.0 (StataCorp). Data were expressed as medians and interquartile ranges for continuous variables and counts and percentages for categoric variables. Intraclass correlations coefficients (1-way and 2-way random effects models) were calculated for the reliability of measurement of the spot sign volume among 3 readers (A.A.S. and K.T., experienced researcher and neurologist with >6 and 11 years of neuroimaging experience; and M.H., medical student/research assistant with >5 years' experience in spot sign detection and volumetric software measurements) using a sample of 20 cases and 60 images (20 images for each phase). A value of zero was assigned for spot sign volume if it disappeared in later phases. Univariable (χ^2 test, Fisher exact test, Wilcoxon rank-sum test as appropriate) and multivariable analyses (logistic regression) were performed to identify variables associated with hematoma growth. All clinical characteristics (see Study Participants section) and imaging parameters were included in univariable analysis. Five different multivariable models were built, each including a different prespecified spot sign parameter as an independent variable: 1) spot sign presence in first phase (single-phase CTA equivalent, model one); 2) the phase of first appearance of spot sign (mCTA, model two); 3) spot sign volume in first phase (divided by median, model three); 4) spot sign positive/negative leakage rate between phases (model four); and 5) spot sign absolute leakage rate (patients with a spot sign, model five). These models are conceptually different by focusing on individual elements of spot sign imaging characterization such as timing, volume, and leakage rate. Collinearity among the various spot sign parameters means that they cannot all be included in the same models.

The model performance was evaluated by the area under the receiver operating characteristic curve (C-statistic), the Akaike information criterion, or the Bayesian information criterion. The Delong test was performed to compare C-statistics in each model. Sensitivity analyses were performed defining hematoma growth as >12.5 mL and as >33% from baseline to follow-up imaging[4] and unfavorable outcome. Finally, a mixed-effects regression model was used to model the relationship between spot sign growth across time assessed using mCTA and ICH growth, with the spot sign volume in each phase as a repeated measures independent variable, phase acquisition time in seconds with phase 1 acquisition time as time = 0 seconds as a fixed effects variable, "patient" as a random effects variable, and ICH growth between baseline to follow-up imaging in 3 categories: no hematoma growth, hematoma growth of ≤6 mL, and >6 mL as the dependent variable. A 2-sided P value < .05 was considered statistically significant.

RESULTS

Characteristics of Patients with and without Hematoma Growth

A total of 350 patients were screened during the study period with 217 patients included in the analysis (flow chart in Fig 1). One hundred thirty-one of the included patients were men, with a median age of 70 years and a median NIHSS score on admission of 10. The median onset-to-CT imaging time was 225 minutes (interquartile range, 109–392 minutes), and the median baseline ICH volume was 18.9 mL (interquartile range, 5.4–34.4 mL). Additional baseline characteristics are shown in the Table 1.

The primary outcome of hematoma growth (defined as >6 mL) was seen in 44 patients (20.3%). Hematoma growth, when defined as >12.5 mL, was seen in 33 (15.2%) patients and, when defined as >33% hematoma growth, was seen in 39 (18.0%) patients. Thirty-seven patients received anticoagulants including 24 on warfarin, 12 on direct oral anticoagulants, and 1 on low-molecular-weight heparin. Anticoagulation reversal treatment was initiated in 27 patients, including prothrombin complex concentrate ($n = 23$), coagulation factor VIIa ($n = 4$), and/or protamine ($n = 1$). Follow-up imaging was performed at a median of 21.9 hours from baseline imaging, and hematoma volume was evaluated by CT in 154 patients; FLAIR, in 57 patients; and T2, in 6 patients.

A history of stroke (20.5% versus 6.9%, $P = .018$), NIHSS on admission (median, 18.5 versus 8, $P < .001$), onset-to-imaging time (median, 151 versus 243 minutes, $P = .008$), and baseline hematoma volume (median 28.7 versus 12.8 mL, $P < .001$) were associated with hematoma growth on univariable analysis. All these variables were also associated with hematoma growth in multivariable analysis (Online Supplemental Data).

Spot Sign Parameters in Association with Hematoma Growth

One hundred seventy-seven patients were scanned at baseline using the ICH mCTA protocol, and 40 patients were scanned using the ischemic mCTA stroke protocol. A median 11-second

Table 1: Baseline characteristics stratified by presence or absence of hematoma growth[a]

Variable	Total (n = 217)	Hematoma Growth		P Value
		Yes (n = 44)	No (n = 173)	
Age (yr)	70 (59.5–80)	75 (61–83)	69 (59–79)	.209
Sex (male)	131 (60.4)	27 (61.4)	104 (60.1)	.880
History of stroke	21 (9.7)	9 (20.5)	12 (6.9)	.018
Ischemic	16 (7.4)	8 (18.2)	8 (4.6)	
Hemorrhagic	5 (2.3)	1 (2.3)	4 (2.3)	
Hypertension	182 (83.9)	39 (88.6)	143 (82.7)	.491
Diabetes mellitus	41 (18.9)	10 (22.7)	31 (17.9)	.467
Current smoking	23 (10.6)	3 (6.8)	20 (11.6)	.583
Alcohol consumption	9 (4.2)	1 (2.3)	8 (4.6)	.690
Prior antithrombotic medication	59 (27.2)	17 (38.6)	42 (24.3)	.056
Antiplatelets	26 (12.0)	8 (18.2)	18 (10.4)	.192
Anticoagulants	37 (17.1)	11 (25.0)	26 (15.0)	.116
SBP (mm Hg)	190 (171–205)	200 (174–210)	190 (168–200)	.160
Hemoglobin (g/L)	141 (131–153)	141 (132–148)	142 (131–154)	.432
Serum glucose (mmol/L)	6.9 (5.7–8.2)	6.9 (5.7–8.2)	6.7 (4.9–8.1)	.751
International normalized ratio	1 (1.0–1.1)	1 (1.0–2.4)	1 (1.0–1.1)	.146
NIHSS score on admission	10 (5–20)	18.5 (9–23)	8 (3.25–17)	<.001
Onset-to-imaging time (min)	225 (109–392)	151 (102–248)	243 (134–422)	.008
Baseline ICH volume (mL)	18.9 (5.4–34.4)	28.7 (13.7–58.8)	12.8 (4.2–30.9)	<.001
Hematoma location				.150
Deep cerebral	115 (53.0)	26 (59.1)	89 (51.5)	
Lobar	80 (36.9)	17 (38.6)	63 (36.4)	
Infratentorial	22 (10.1)	1 (2.3)	21 (12.1)	
Timing of spot sign appearance				<.001
No spot sign	148 (68.2)	10 (22.7)	138 (79.8)	
First appearing in the first phase	47 (21.7)	26 (59.1)	21 (12.1)	
First appearing in the second phase	20 (9.2)	8 (18.2)	12 (6.9)	
First appearing in the third phase	2 (0.9)	0 (0)	2 (1.2)	

Note:—SBP indicates systolic blood pressure.

[a] Hematoma growth is defined as a >6-mL increase in volume of the hematoma from baseline. Data are presented as No. (%) or median (interquartile range).

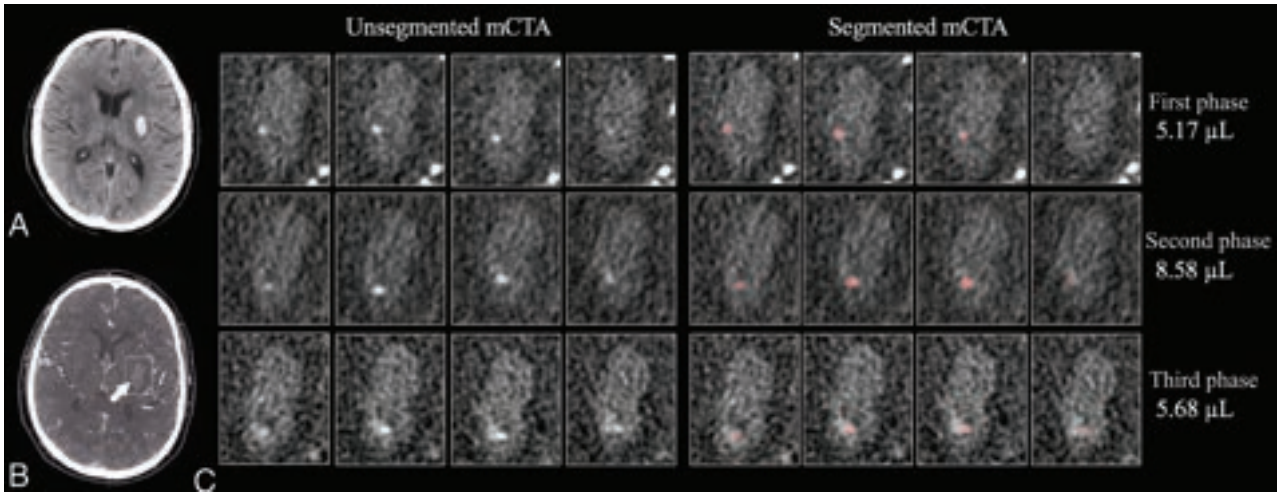

FIG 2. Representative slices of the spot sign in each phase of mCTA. *A*, Noncontrast CT shows a hematoma in the left putamen. *B*, mCTA shows a spot sign in the hematoma in the first phase (*arrow*). *C*, Segmentation of the spot sign in each phase. The volume of the spot sign in the first phase increases in the second phase. In the third phase, the contrast seems to partially disperse into the hematoma, and the volume of the spot sign decreases.

interval was noted between the first and second phases, and 18 seconds, between the second and third phases. Sixty-nine patients (31.8%) had a spot sign in any phase of mCTA. The spot sign was seen in 47 patients in the first phase (21.7%), 65 (30.0%) in the second phase, and 63 (29.0%) in the third phase. Two patients had a spot sign only in the first phase, and another 2 patients had a spot sign only in the third phase. Figure 2 shows representative slices of the spot sign in each phase. Contrast dispersal was seen in some spot signs at the third phase, which may affect the spot sign volume and leakage rate in later phases. In the sample of 20 cases, inter- and intrarater reliability assessed using the intraclass correlation coefficient for the spot sign volume in the first phase was 0.84 and 0.62; in the second phase, it was 0.77 and 0.92; and in the third phase, it was 0.76 and 0.86, respectively.

Table 2: Spot sign parameters when compared with hematoma growth

Spot Sign Volume Parameter	Total[a]	Spot Sign First Appearing in the First Phase			Spot Sign First Appearing in the Second Phase		
		Hematoma Growth		*P*	Hematoma Growth		*P*
		Yes (n = 26)	No (n = 21)	Value	Yes (n = 8)	No (n = 12)	Value
Volume in the first phase (μL)	19.7 (5.7–64.3)	32.7 (12.9–74.3)	6.7 (4.4–59.0)	.033			
Leakage rate between first and second phases (μL/sec)	2.6 (0.6–7.7)	3.8 (1.1–9.7)	1.2 (0.4–6.5)	.034			
Volume in the second phase (μL)	31.4 (7.4–108.8)	95.9 (44.1–172.0)	19.7 (8.2–133.0)	.017	17.0 (5.8–40.3)	6.3 (4.8–14.4)	.216
Leakage rate between second and third phases (μL/sec)	0.1 (−0.2–1.3)	0.4 (−0.1–2.5)	0.0 (−2.1–2.1)	.153	0.6 (−0.1–2.1)	0.1 (0.1–0.5)	.396
Volume in the third phase (μL)	34.8 (10.0–129.0)	58.0 (32.9–172.6)	34.8 (7.3–156.7)	.121	31.5 (1.9–79.1)	10.8 (6.2–18.5)	.440
Absolute leakage rate (μL/sec)	1.02 (0.5–4.7)	3.5 (1.0–8.1)	0.9 (0.5–3.8)	.017			

[a] The number of patients was 47 for volume in the first phase and leakage rate between the first and second phases, 67 for volume in the second phase and leakage rate between second and third phases, and 69 for volume in the third phase. Data are presented as median (interquartile range).

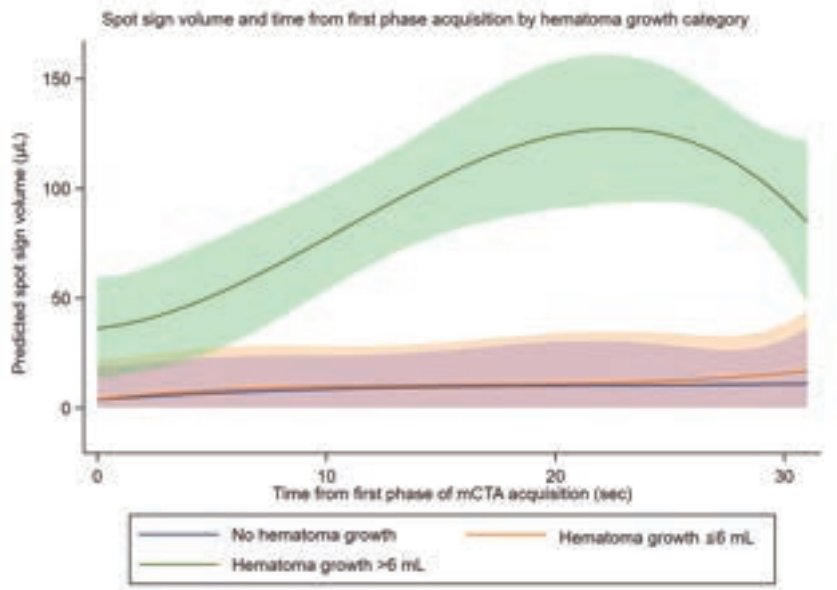

FIG 3. Predicted spot sign volume by mCTA phase time stratified by hematoma growth category. A mixed-effects regression model estimated a change in spot sign volume across time stratified by different ICH growth category. The x-axis measures time in seconds under the assumption that phase 1 of the mCTA is acquired at time = 0 seconds, and the relationship between the predicted spot sign volume change and time are shown in patients without hematoma growth and hematoma growth of ≤6 mL and >6 mL. The area shows 95% CIs.

An association between spot sign volume parameters and hematoma growth is shown in the Table 2. The median volume of the spot sign in each phase was 19.7, 31.4, and 34.8 μl, respectively. Among patients with the spot sign in the first phase, the leakage rate was a median of 2.6 μl/s between the first and second phases and a median of 0.2 μl/s between second and third phases. Among patients with the spot sign first appearing in the first phase, those with hematoma growth had larger volumes of the spot sign in the first phase (32.7 versus 6.7 μl, $P = .033$) and a larger leakage rate between the first and second phases (3.8 versus 1.2 μl/s, $P = .034$) compared with those without it. The absolute leakage rate was a median of 1.02 μl/s, which was larger in patients with hematoma growth than those without it (2.4 versus 0.7 μl/s, $P = .002$). The frequencies of hematoma growth by the spot sign parameter were separated by more than or equal to the median and are shown in the Online Supplemental Data.

Hematoma growth was seen in 8 (36.4%) of 22 patients with the spot sign first appearing in the second or third phase. Among patients with the spot sign first appearing in the first phase, hematoma growth was seen in 16 (66.7%) of 24 patients with a volume of ≥19.7 μl, and 23 (65.7%) of 35 patients with absolute leakage rate of ≥1.02 μl/s. The relationship between the spot sign volume across time/phase and hematoma growth is shown in Fig 3. The spot sign volume increased more in patients with hematoma growth than in those without it. The spot sign volume increased significantly after the first phase acquisition in patients with hematoma growth, while it did not increase or was absent throughout the entire acquisition in those without hematoma growth.

Multivariable Analysis of Spot Sign Parameters for Hematoma Growth

Evaluation of variables associated with hematoma growth (Table 3) included the prespecified spot sign imaging variables of interest in separate statistical models, given the collinearity among the phase of appearance, volume, and leakage rate. In model 1, the spot sign in the first phase (OR, 10.5; 95% CI, 5.0–22.7) was associated with hematoma growth. In model 2, the spot sign first appearing in the first phase (OR, 17.1; 95% CI, 7.2–40.4) and the spot sign first appearing in the second or third phase (OR, 7.9; 95% CI, 2.7–23.2) were associated with hematoma growth. In model 3, the spot sign first appearing in the first phase with volume <19.7 μl (OR, 10.6; 95% CI, 3.7–30.9) and ≥19.7 μl (OR, 27.6; 95% CI, 9.9–84.6), and the spot sign first appearing in the second or third phase were associated with hematoma growth. In model 4, both positive (OR, 10.1; 95% CI, 4.2–24.1) and negative (OR, 23.0; 95% CI, 8.1–65.5) leakage rates were associated with hematoma growth. In model 5, the absolute leakage rate was associated with hematoma growth among patients with the spot sign (per 1-μl/s increase; OR, 1.26; 95% CI, 1.04–1.52) (Fig 4). The C-statistic in model 2 was

Table 3: Logistic regression analysis for hematoma growth

	OR (95% CI)	*P* value	C-Statistic	BIC	AIC
Model 1			0.735	190.2	183.5
No spot sign in the first phase (reference)	1.0				
Spot sign in the first phase	10.5 (5.0–22.7)	<.001			
Model 2			0.798	182.8	172.7
No spot sign (reference)	1.0				
Spot sign first appearing in the first phase	17.1 (7.2–40.4)	<.001			
Spot sign first appearing in the second or third phase	7.9 (2.7–23.2)	<.001			
Model 3			0.807	185.6	172.3
No spot sign (reference)	1.0				
Spot sign first appearing in the first phase with volume <19.7 μL	10.6 (3.7–30.9)	<.001			
Spot sign first appearing in the first phase with volume ≥19.7 μL	27.6 (9.9–84.6)	<.001			
Spot sign first appearing in the second or third phase	7.9 (2.7–23.2)	<.001			
Model 4			0.800	182.4	172.2
No spot sign (reference)	1.0				
Spot sign with positive leakage rate between phases	10.1 (4.2–24.1)	<.001			
Spot sign with negative leakage rate between any phases	23.0 (8.1–65.5)	<.001			
Model 5[a]			0.713	95.4	99.9
Absolute leakage rate (per 1-μL/sec increase)	1.26 (1.04–1.52)	.019			

Note:—AIC indicates Akaike information criterion; BIC, Bayesian information criterion.
[a] Model 5 includes only patients with the spot sign ($n = 69$).

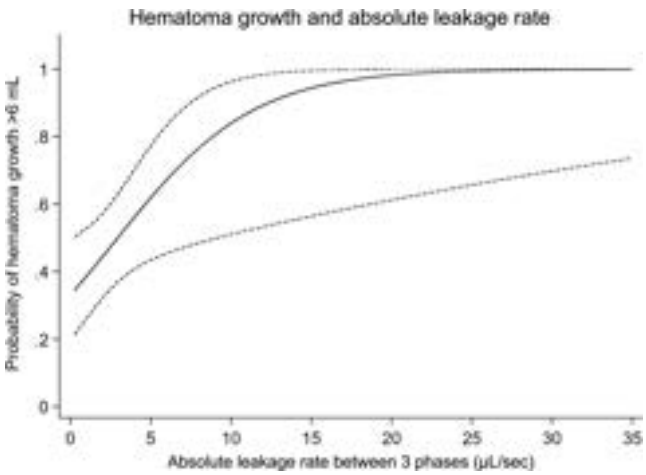

FIG 4. Hematoma growth probability as predicted by absolute spot sign leakage rate. The probability of hematoma growth of >6 mL is predicted by the absolute spot sign leakage rate ([|leakage rate between first and second phases| + |leakage rate between second and third phases|]/2). The area shows 95% CIs.

superior to that in model 1 (single-phase CTA versus mCTA spot sign, $P = .010$). C-statistics were not statistically different among models 2, 3, and 4 (mCTA spot sign parameters, $P = .312$).

Analysis by Hematoma Growth Definition, mCTA Protocol, and Follow-up CT Only

Sensitivity analyses using other definitions of hematoma growth are reported in the Online Supplemental Data and show similar results. We performed the same analysis including only patients who underwent mCTA using the ICH mCTA protocol ($n = 177$) and only patients who underwent follow-up imaging by CT ($n = 154$), but the results were unchanged (Online Supplemental Data).

Spot Sign Parameters and Functional Outcomes

Functional outcomes at 90 days were available in 155 patients, and unfavorable outcomes were seen in 94 patients (60.6%). The frequency of unfavorable outcomes was 52.8% (57 of 108 patients) in patients without the spot sign and 93.8% (15 of 16 patients) in those with the spot sign first appearing in the first phase with a volume of ≥19.7 μl and an absolute leakage rate of ≥1.02 μl/s. The associations between spot sign parameters and functional outcomes are shown in the Online Supplemental Data.

DISCUSSION

This study has shown that the timing of the spot sign appearance, spot sign volume, and spot sign leakage rate using temporal imaging of mCTA predict hematoma growth. This study is the first to both measure the spot sign volumes and investigate changes in volume (leakage rate) of the spot sign by mCTA. The volume of the spot sign generally increased early and then plateaued thereafter.

Our study revealed that the spot sign volume in the first phase and absolute leakage rate were the key imaging parameters strongly associated with hematoma growth regardless of the definition of that growth. Our findings indicate that earlier and larger spot signs represent more active bleeding. With 2-phase CTA, Kim et al[19] showed an increase in size and Brouwers et al[20] showed enlargement in the volume of spot sign–predicted hematoma growth. Significant associations of both positive and negative leakage rates with hematoma growth in this study indicate that the dispersion of the spot sign can be another predictor of hematoma growth. Some previous studies suggest that the pathophysiology of the spot sign differs according to phase patterns: active bleeding without homeostasis in earlier phases and process of pooling of blood accumulation, with better hemostasis in later phases.[7,20] Therefore, spot signs appearing in later phases may represent a slower and smaller leak, resulting in a marginal utility of spot sign parameters in the third phase.

The negative results from the spot sign in positive hemostatic trials[21] and the modest accuracy of the spot sign for predicting hematoma growth in large spot sign collaborations may be explained by the limitations of using the spot sign with single phase CTA. mCTA can provide dynamic information of the spot

sign with fixed timing for image acquisitions and a faster and easier manner. C-statistics were not statistically different among spot sign parameters (models 2, 3, and 4), which may be because of the correlations among these parameters. Despite no statistical significance, models including a volume or leakage rate had higher C-statistics than the model including phase-only information, suggesting that volumetric analysis of the spot sign is a promising method for identifying patients with a high risk of hematoma growth in acute ICH. We may not have been able to show statistical significance because these comparisons may have been underpowered. The consistency of the results in different thresholds of hematoma growth of >6 mL, >12.5 mL, or >33%, supports the utility that can help better stratify patients at risk of hematoma growth in different decision-making scenarios, including clinical trials for hemostatic treatment. We also found a higher frequency (93.8%) of unfavorable outcomes in patients with the spot sign first appearing in the first phase, volume of ≥19.7 μl, and absolute leakage rate of ≥1.02 μl/s, suggesting that the volumetrics of the spot sign are promising in predicting functional outcomes, though the sample size was underpowered for multivariable analysis.

This study has several limitations. First, it was a retrospective design from a single center with multiple years of experience performing mCTA. Differences by sex may have confounded our analysis, though biologic plausibility for such confounding is considered low.[22,23] Twenty-six patients with active bleeding were excluded from the analysis because surgery was performed before follow-up imaging could be obtained. Second, we used last-known-well time, which may have resulted in a long onset-to-imaging time in this study (median, 225 minutes) and therefore a reduced proportion of positive CTA spot signs and overall predictive ability for hematoma growth, which was higher in the earlier time strata.[24] Third, due to the small volume of the spot sign with the unit of microliters, it may be difficult to eliminate measurement error, though interrater reliability was very good.

Moreover, other spot sign characteristics (number, shape, location, or density) were not studied. Establishing automated measurement methods using artificial intelligence algorithms could eliminate such measurement errors, advance spot sign parameter evaluation, and improve hematoma growth prediction. Fourth, follow-up timing and imaging technique (CT versus MR imaging) were not uniform, which might impact comparisons with baseline volumes. Fifth, the mCTA ischemic stroke/ICH protocol adds radiation exposure,[25] albeit minimal. A comparative study between mCTA and dynamic CTA derived from CTP could be performed, but this would need to be justified ethically, given the additional 3.5-mSv radiation dose of CTP in acute ICH. Finally, 90-day clinical outcome was not available in all patients. Our results need to be validated in a multicenter cohort for generalizability.

CONCLUSIONS

Timing of the spot sign appearance, spot sign volume, and spot sign leakage rate are each important predictors of hematoma growth. Volumetric analysis of the spot sign may provide additional predictive performance for hematoma growth in acute ICH. However, automated software would be needed to allow fast determination of these parameters in a clinical setting. These parameters could also be incorporated into mCTA spot sign grading by more simplified approaches for clinicians. These strategies are important next steps before we can practically apply mCTA to better predict hematoma growth and direct ICH treatment decision-making.

Disclosure forms provided by the authors are available with the full text and PDF of this article at www.ajnr.org.

REFERENCES

1. Qureshi AI, Mendelow AD, Hanley DF. **Intracerebral haemorrhage.** *Lancet* 2009;373:1632–44 CrossRef Medline
2. Van Asch CJ, Luitse MJ, Rinkel GJ, et al. **Incidence, case fatality, and functional outcome of intracerebral hemorrhage over time, according to age, sex, and ethnic origin: a systematic review and meta-analysis.** *Lancet Neurol* 2010;9:167–76 CrossRef Medline
3. Davis SM, Broderick J, Hennerici M, et al; Recombinant Activated Factor VII Intracerebral Hemorrhage Trial Investigators. **Hematoma growth is a determinant of mortality and poor outcome after intracerebral hemorrhage.** *Neurology* 2006;66:1175–81 CrossRef Medline
4. Dowlatshahi D, Demchuk AM, Flaherty ML, et al; VISTA Collaboration. **Defining hematoma expansion in intracerebral hemorrhage: relationship with patient outcomes.** *Neurology* 2011;76:1238–44 CrossRef Medline
5. Phan TG, Krishnadas N, Lai VW, et al. **Meta-analysis of accuracy of the spot sign for predicting hematoma growth and clinical outcomes.** *Stroke* 2019;50:2030–36 CrossRef Medline
6. Demchuk AM, Dowlatshahi D, Rodriguez-Luna D, et al; PREDICT/Sunnybrook ICH CTA study group. **Prediction of haematoma growth and outcome in patients with intracerebral haemorrhage using the CT-angiography spot sign (PREDICT): a prospective observational study.** *Lancet Neurol* 2012;11:307–14 CrossRef Medline
7. Dowlatshahi D, Wasserman JK, Momoli F, et al; Ottawa Stroke Research Group. **Evolution of computed tomography angiography spot sign is consistent with a site of active hemorrhage in acute intracerebral hemorrhage.** *Stroke* 2014;45:277–80 CrossRef Medline
8. Dowlatshahi D, Hogan MJ, Sharma M, et al. **Ongoing bleeding in acute intracerebral haemorrhage.** *Lancet* 2013;381:152 CrossRef Medline
9. Chakraborty S, Alhazzaa M, Wasserman JK, et al. **Dynamic characterization of the CT angiographic 'spot sign.'** *PLoS One* 2014;9:e90431 CrossRef Medline
10. Menon BK, d'Esterre CD, Qazi EM, et al. **Multiphase CT angiography: a new tool for the imaging triage of patients with acute ischemic stroke**. *Radiology* 2015;275:510–20 CrossRef Medline
11. Rodriguez-Luna D, Dowlatshahi D, Aviv RI et al; PREDICT/Sunnybrook ICH CTA Study Group. **Venous phase of computed tomography angiography increases spot sign detection, but intracerebral hemorrhage expansion is greater in spot signs detected in arterial phase.** *Stroke* 2014;45:734–39 CrossRef Medline
12. Wada R, Aviv RI, Fox AJ, et al. **CT angiography "spot sign" predicts hematoma expansion in acute intracerebral hemorrhage**. *Stroke* 2007;38:1257–62 CrossRef Medline
13. Rodriguez-Luna D, Coscojuela P, Rodriguez-Villatoro N, et al. **Multiphase CT angiography improves prediction of intracerebral hemorrhage expansion.** *Radiology* 2017;285:932–40 CrossRef Medline
14. Rodriguez-Luna D, Pancorbo O, Coscojuela P, et al. **Derivation and validation of three intracerebral hemorrhage expansion scores using different CT modalities.** *Eur Radiol* 2023;33:6045–53 CrossRef Medline
15. Kosior JC, Idris S, Dowlatshahi D, et al; PREDICT/Sunnybrook CTA ICH study investigators. **Quantomo: validation of a computer-assisted methodology for the volumetric analysis of intracerebral haemorrhage.** *Int J Stroke* 2011;6:302–05 CrossRef Medline
16. Rindler RS, Allen JW, Barrow JW, et al. **Neuroimaging of intracerebral hemorrhage.** *Neurosurgery* 2020;86:E414–23 CrossRef Medline
17. Rodriguez-Luna D, Boyko M, Subramaniam S, et al; PREDICT/Sunnybrook ICH CTA study group. **Magnitude of hematoma volume**

measurement error in intracerebral hemorrhage. *Stroke* 2016;47:1124–26 CrossRef Medline

18. Thompson AL, Kosior JC, Gladstone DJ, et al; PREDICTS/Sunnybrook ICH CTA Study Group. **Defining the CT angiography 'spot sign' in primary intracerebral hemorrhage**. *Can J Neurol Sci* 2009;36:456–61 CrossRef Medline
19. Kim H, Goo JH, Kwak HS, et al. **Correlation between spot sign and intracranial hemorrhage expansion on dual-phase CT angiography.** *Diagnostics (Basel)* 2019;9:215 CrossRef Medline
20. Brouwers HB, Battey TW, Musial HH, et al. **Rate of contrast extravasation on computed tomographic angiography predicts hematoma expansion and mortality in primary intracerebral hemorrhage.** *Stroke* 2015;46:2498–503 CrossRef Medline
21. Gladstone DJ, Aviv RI, Demchuk AM, et al; SPOTLIGHT and STOP-IT Investigators and Coordinators. **Effect of recombinant activated coagulation factor VII on hemorrhage expansion among patients with spot sign-positive acute intracerebral hemorrhage: the SPOTLIGHT and STOP-IT randomized clinical trials.** *JAMA Neurol* 2019;76:1493–501 CrossRef Medline
22. An SJ, Kim TJ, Yoon BW. **Epidemiology, risk factors, and clinical features of intracerebral hemorrhage: an update.** *J Stroke* 2017;19:3–10 CrossRef Medline
23. Wang S, Zou XL, Wu LX, et al. **Epidemiology of intracerebral hemorrhage: a systematic review and meta-analysis.** *Front Neurol* 2022;13:915813 CrossRef Medline
24. Dowlatshahi D, Brouwers HB, Demchuk AM, al. **Predicting intracerebral hemorrhage growth with the spot sign: the effect of onset-to-scan time.** *Stroke* 2016;47:695–700 CrossRef Medline
25. Demchuk AM, Menon BK, Goyal M. **Comparing vessel imaging: noncontrast computed tomography/computed tomographic angiography should be the new minimum standard in acute disabling stroke.** *Stroke* 2016;47:273–81 CrossRef Medline

Contrast Staining in Noninfarcted Tissue after Endovascular Treatment of Acute Ischemic Stroke

Mohamad Abdalkader, Thanh N. Nguyen, Anurag Sahoo, Muhammad M. Qureshi, Charlene J. Ong, Piers Klein, Matthew I. Miller, Asim Z. Mian, Johannes Kaesmacher, Adnan Mujanovic, Wei Hu, Hui Sheng Chen, and Bindu N. Setty

ABSTRACT

BACKGROUND AND PURPOSE: Contrast staining is a common finding after endovascular treatment of acute ischemic stroke. It typically occurs in infarcted tissue and is considered an indicator of irreversible brain damage. Contrast staining in noninfarcted tissue has not been systematically investigated. We sought to assess the incidence, risk factors, and clinical significance of contrast staining in noninfarcted tissue after endovascular treatment.

MATERIALS AND METHODS: We conducted a retrospective review of consecutive patients who underwent endovascular treatment for anterior circulation large-vessel occlusion acute ischemic stroke. Contrast staining, defined as new hyperdensity on CT after endovascular treatment, was categorized as either contrast staining in infarcted tissue if the stained region demonstrated restricted diffusion on follow-up MR imaging or contrast staining in noninfarcted tissue if the stained region demonstrated no restricted diffusion. Baseline differences between patients with and without contrast staining in noninfarcted tissue were compared. Logistic regression was used to identify independent associations for contrast staining in noninfarcted tissue after endovascular treatment.

RESULTS: Among 194 patients who underwent endovascular treatment for large-vessel occlusion acute ischemic stroke and met the inclusion criteria, contrast staining in infarcted tissue was noted in 52/194 (26.8%) patients; contrast staining in noninfarcted tissue, in 26 (13.4%) patients. Both contrast staining in infarcted tissue and contrast staining in noninfarcted tissue were noted in 5.6% (11/194). Patients with contrast staining in noninfarcted tissue were found to have a higher likelihood of having an ASPECTS of 8–10, to be associated with contrast staining in infarcted tissue, and to achieve successful reperfusion compared with those without contrast staining in noninfarcted tissue. In contrast staining in noninfarcted tissue regions, the average attenuation was 40 HU, significantly lower than the contrast staining in infarcted tissue regions (53 HU). None of the patients with contrast staining in noninfarcted tissue had clinical worsening during their hospital stay. The median discharge mRS was significantly lower in patients with contrast staining in noninfarcted tissue than in those without (3 versus 4; $P = .018$). No independent predictors of contrast staining in noninfarcted tissue were found.

CONCLUSIONS: Contrast staining can be seen outside the infarcted tissue after endovascular treatment of acute ischemic stroke, likely attributable to the reversible disruption of the BBB in ischemic but not infarcted tissue. While generally benign, understanding its characteristics is important because it may mimic pathologic conditions such as infarcted tissue and cerebral edema.

ABBREVIATIONS: AIS = acute ischemic stroke; CS = contrast staining; CS-I = contrast staining in infarcted tissue; CS-NI = contrast staining in noninfarcted tissue; EVT = endovascular treatment; HU = Hounsfield unit; IQR = interquartile range; LVO = large-vessel occlusion

Accurate interpretation of the imaging findings after endovascular therapy (EVT) for acute ischemic stroke (AIS) is important for appropriate management and prognostication. Hyperdensities on NCCT head scans are common findings after EVT, having been described in up to 84% of patients.[1-5] Although these hyperdensities may represent extravasated blood products or other hemorrhagic complications, most are due to retained iodinated contrast material from intra-arterial iodine contrast injection, a phenomenon termed contrast staining (CS).

Received November 5, 2023; accepted after revision February 3, 2024.

From the Departments of Radiology (M.A., T.N.N., A.S., M.M.Q., P.K., A.Z.M., B.N.S.) and Neurology (T.N.N., C.J.O.), Boston Medical Center, Boston University Chobanian & Avedisian School of Medicine, Boston, Massachusetts; Department of Neurology (C.J.O.), Brigham & Women's Hospital, Harvard Medical School, Boston, Massachusetts; Department of Medicine (M.I.M.), Cambridge Health Alliance, Cambridge, Massachusetts; Institute of Diagnostic and Interventional Neuroradiology, Institute of Diagnostic, Interventional and Pediatric Radiology and Department of Neurology (J.K., A.M.), Bern University Hospital, and University of Bern, Bern, Switzerland; Department of Neurology and Stroke Center (W.H.), Division of Life Sciences and Medicine, The First Affiliated Hospital of the University of Science and Technology of China, Hefei, Anhui, China; and Department of Neurology (H.S.C.), General Hospital of Northern Theater Command, Shenyang, China.

Please address correspondence to Mohamad Abdalkader, MD, Department of Radiology, Boston Medical Center, 840 Harrison Ave, Boston, MA 02118; e-mail: Mohamad.abdalkader@bmc.org; @AbdalkaderMD; @NguyenThanhMD

Indicates article with online supplemental data.

http://dx.doi.org/10.3174/ajnr.A8222

Brain ischemia is known to induce gradual and time-dependent changes in the integrity of the BBB. which is impermeable to contrast molecules in a physiologic state.[6-8] Varying degrees of increased permeability permit the fluid and plasma protein leakage seen in cerebral edema, contrast material leakage causing CS, and the blood product extravasation seen in hemorrhagic transformation.[6,7,9] The increased duration and severity of the ischemic insult are associated with a higher degree of microvascular injury and BBB disruption, while collateral circulation in the involved region may protect the microvasculature.[6,10,11]

The presence of CS has been considered an indicator of irreversible brain injury and has been associated with the development of symptomatic intracranial hemorrhage and poor clinical outcome.[12-15] However, CS may also occur in noninfarcted territories and may resolve without sequelae. This phenomenon of transient CS in noninfarcted tissue poses radiologic and management challenges because it may mimic pathologic conditions such as infarcted tissue, extravasated blood products, intracranial hemorrhage, and cerebral edema. Prior studies that demonstrated the association of CS with irreversible injury focused on staining in areas of core infarct, and, to our knowledge, CS in the noninfarcted tissue has not been systematically investigated. This study aimed to characterize the incidence of CS in noninfarted tissue (CS-NI), its radiologic characteristics, potential risk factors, and its clinical and imaging outcomes.

MATERIALS AND METHODS

Ethics approval was obtained from Boston University institutional review board. According to institutional protocol, written informed consent for EVT was obtained from patients and/or their legal representatives. Anonymized data are available from the corresponding author on reasonable request. This article followed the Strengthening the Reporting of Observational Studies in Epidemiology (STROBE) guidelines.

Study Design and Patient Selection

We performed a retrospective review of a prospectively maintained neuroendovascular database of consecutive patients who presented with anterior circulation large-vessel occlusion AIS (LVO-AIS) and underwent EVT between January 2016 and January 2022. Patients were included in the analysis under the following conditions: 1) an NCCT was obtained within 24 hours after EVT, 2) a follow-up MR imaging of the brain was obtained within 72 hours after EVT, and 3) clinical follow-up was available 3 months after EVT. Patients were excluded if they had posterior circulation stroke, complete infarction of the affected vascular territory, and subarachnoid or parenchymal hemorrhage, as determined by SWI.

Clinical, Radiologic, and Endovascular Data Collection

Patient demographics (age, sex), vascular risk factors (diabetes mellitus, hypertension, atrial fibrillation, coronary artery disease, kidney disease, heart failure, smoking), preprocedural stroke and imaging characteristics, procedural details, follow-up imaging data, and outcome data are presented as detailed in the Online Supplemental Data and Tables 1 and 2. In addition, blood pressure measurements at presentation and intraprocedurally, NIHSS shift at 24 hours after the procedure, NIHSS at 1 week or discharge if earlier, and the mRS at 90 days after EVT were recorded. Clinical worsening postprocedure was defined as neurologic deterioration of $\geq$ 4points on the NIHSS from baseline.

Imaging Analysis

All NCCTs within 24 hours after EVT and follow-up MR imaging within 72 hours after EVT were independently evaluated by 2 board-certified neuroradiologists with 5 (M.A,) and 15 (B.N.S.) years of experience who were blinded to treatment details. CS was defined as new parenchymal hyperdensities on early CT imaging performed within 24 hours after EVT without evidence of blood products on SWI. CS was categorized as contrast staining in infarcted tissue (CS-I) if the stained region demonstrated restricted diffusion on follow-up DWI. CS was categorized as CS-NI if the stained region demonstrated no corresponding signal abnormality on T2, FLAIR, or DWI.

For patients with CS, the Hounsfield unit (HU) of the attenuation of the stained tissue was measured using the free-form ROI and compared with the contralateral symmetric normal region. CT and MR imaging were also analyzed for associated signs of infarction (loss of the gray-white matter, gyral swelling, and sulcal effacement) and signs of intracranial hemorrhage.

Statistical Analysis

The descriptive analysis compared demographics, medical comorbidities, radiographic details, and procedural details between patients with and without CS-NI. Continuous variables were expressed as mean (SD) and median (interquartile range [IQR]) and were compared using the Student t test or Mann-Whitney U test, as appropriate. Differences in categoric variables were examined with the χ^2 test or Fisher exact test. Variables achieving $P \leq .1$ in univariable analyses and a priori selected variables based on prior literature (eg, hypertension and diabetes mellitus) were carried forward into a multivariable logistic regression to evaluate potential independent factors associated with CS-NI. To account for sparse data, all logistic regression models used the Firth adjustment.[16] All statistical analyses were performed on SAS, Version 9.4 (SAS Institute). All tests were 2-sided, and a P value $< .05$ was considered significant.

RESULTS

Among 254 patients who underwent EVT for LVO-AIS during the study period, 194 patients were included after the exclusion of 60 patients due to complete territorial infarct ($n = 10$), parenchymal or subarachnoid hemorrhage ($n = 30$), posterior circulation stroke ($n = 17$), or lack of imaging follow-up ($n = 3$) (Fig 1).

Among the 194 included patients, CS-I was noted in 52 (26.8%) patients, and CS-NI was noted in 26 (13.4%) patients. Both CS-I and CS-NI were noted in 5.6% (11/194) of patients who underwent EVT in our study. Examples of CS-NI are depicted in Figs 2 and 3. In the overall cohort, the median age was 72 (IQR, 59–82) years, 48.5% were men, and the median baseline NIHSS was 18 (IQR, 13–21), with no difference between groups. Other baseline demographic and clinical characteristics of patients with or without CS-NI are shown in the Online Supplemental Data.

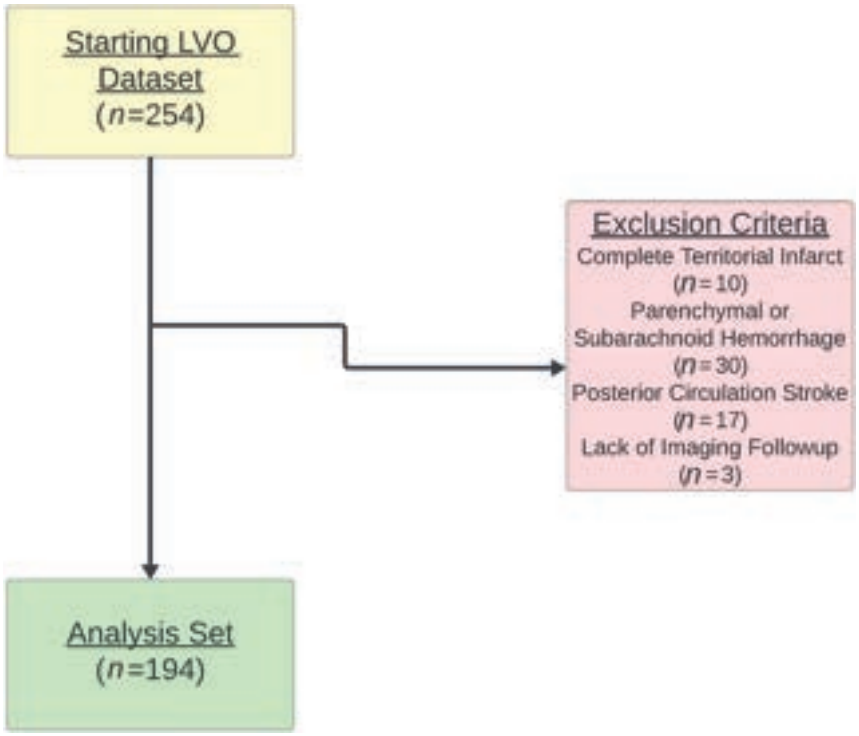

FIG 1. Eligibility criteria for study inclusion are demonstrated.

Imaging and Procedural Characteristics

The most common occlusion site was the M1 segment of the MCA (45.9%, 89/194). There was no difference in lesion location between those with and without CS-NI ($P = .21$). The most common first-line technique of EVT was a stent retriever (74.7%, 145/194), and a balloon guide catheter was used in 78.9% (153/194) of cases. In 84.5% (164/194) of cases, ≤3 passes were completed. Patients with successful reperfusion, defined as an expanded TICI of ≥2b, were more likely to develop CS-NI than those without successful reperfusion (16.2% versus 0, $P = .01$). Patients with ASPECTS of 8–10 on preprocedural CT were also more likely to have CS-NI than those with ASPECTS of 5–7 (16.2% versus 5.8%, $P = .059$); however, this difference did not reach statistical significance. There was no difference between the median volume of contrast used during the

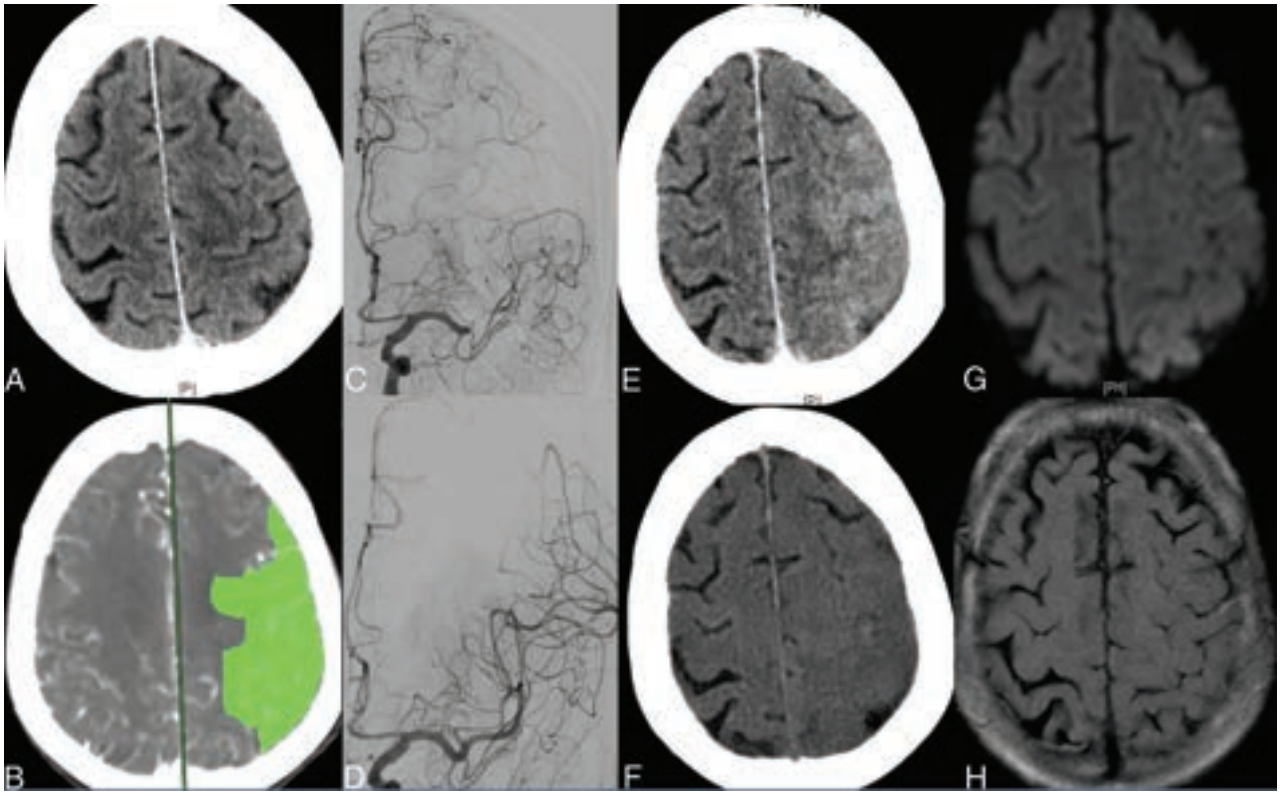

FIG 2. Noncontrast head CT (*A*) and perfusion imaging map (*B*) of a patient who presented with an acute left M1 occlusion stroke, showing preserved brain parenchyma and a large area of penumbra (in green, *B*). Angiogram before (*C*) and after (*D*) mechanical thrombectomy shows complete recanalization of the left MCA territory. Note good leptomeningeal collaterals in the contrast-stained region. NCCT performed after the procedure (*E*) shows contrast staining with increased attenuation and sulcal effacement in the left cerebral convexity, which was completely effaced on the virtual noncontrast dual-energy CT (*F*). MR imaging follow-up shows normal findings on MR images with no corresponding signal abnormality on DWI (*G*) and FLAIR (*H*) images.

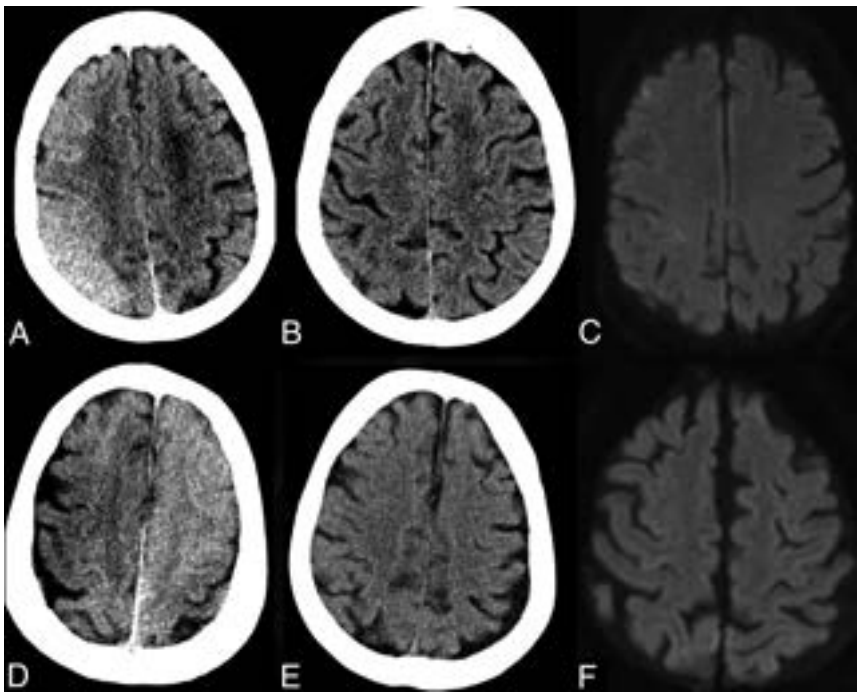

FIG 3. Transient contrast staining of noninfarcted regions in the right cerebral convexity after endovascular treatment of a right M1 MCA occlusion (*A–C*) and left M1 MCA occlusion (*D–F*), manifesting as increased parenchymal attenuation and effacement of the cortical sulci (*A* and *D*) on the early posttreatment CT imaging. Repeat CT imaging 48–72 hours later (*B* and *E*) shows normalization of the brain parenchyma and cortical sulci. DWI (*C* and *F*) shows normal brain parenchyma with no restricted diffusion in the previously stained region.

Table 1: Clinical outcomes by contrast staining status

	All	With CS-NI	Without CS-NI	*P* Value
NIHSS (24 hr) No. (median, IQR)	94 (12.5, 3–19)	15 (12, 5–17)	79 (13, 2–20)	.77
NIHSS (discharge) No. (median, IQR)	170 (9, 3–19)	22 (6, 2–9)	148 (9.5, 3–20.5)	.08
mRS (discharge) No. (median, IQR)	194 (4, 3–5)	26 (3, 2–4)	168 (4, 3–5)	.02
mRS (3 mo) No. (median, IQR)	183 (3, 2–5)	25 (3, 1–3)	158 (3, 2–5)	.06
Worsening postprocedure, No. (column %)				.08
No	173 (89.2)	26 (100.0)	147 (87.5)	
Yes	21 (10.8)	0 (0.0)	21 (12.5)	

procedure, the mean systolic blood pressure, or blood pressure variability between those with and without CS-NI. There was no statistical significance in the duration of the procedure between patients with or without CS-NI. There was a higher incidence of CS-NI observed in patients with kidney disease; however, the increase did not reach statistical significance.

NCCT was performed at a median interval of 517 (IQR, 400–767) minutes after EVT, with no difference between those with and without CS-NI. In CS-NI regions, the average mean attenuation was 40 HU, and the average maximum attenuation was 53 HU, which was greater than the average mean (32 HU) and average maximum attenuation (43 HU) in the contralateral normal hemisphere ($P < .001$). For patients with both CS-NI and CS-I (11 patients), HU values were higher in CS-I regions than in CS-NI regions for both the average mean (53 versus 40; $P = .027$) and the average maximum (70 versus 52; $P = .014$). In Hounsfield unit measurements in areas considered normal, CS-I or CS-NI were calculated and are shown in Table 3. While there was a trend suggesting a higher incidence of CS-NI in patients with CS-I, CS-NI was identified in 22.2% (11/52) of patients with CS-I compared with 10.6% (15/142) in patients without CS-I; this difference did not reach statistical significance. In our cohort, only 8 of the 194 patients underwent CT perfusion, and 2 of them exhibited CS-NI.

Outcomes

None of the patients with CS-NI had clinical worsening after EVT compared with 12.5% of patients with CS-I (0% versus 12.5%; $P = .08$). There was no difference in the median NIHSS at 24 hours post-EVT (12 versus 13; $P = .77$) or median NIHSS at discharge (6 versus 9.5; $P = .08$) between patients with and without CS-NI. The median discharge mRS was significantly lower in patients with CS-NI compared with those without (3 versus 4; $P = .018$), and there was no difference in median 3-month mRS between the 2 groups (3 versus 3; $P = .06$) (Table 1).

Univariable and Multivariable Analysis

In univariable analysis, no significant differences between patients with and without CS-NI were observed by sex, comorbidities, NIHSS, administration of IV thrombolysis, occlusion site, laterality, time of postprocedural CT, endovascular technique, contrast volume, or blood pressure measurements. In multivariable analysis, there was a trend toward a higher incidence of CS-NI with higher ASPECTS (8–10) and higher reperfusion (TICI 2b–3), but it did not achieve statistical significance. Otherwise, no independent association for CS-NI was found (Table 2).

DISCUSSION

In this retrospective analysis of 194 patients who underwent EVT for anterior circulation LVO stroke, we describe a phenomenon of CS-NI that consists of a benign and transient parenchymal enhancement on early NCCT after EVT, without evidence of infarct on follow-up imaging. CS-NI was identified in 13.4% (26/194); CS-I was observed in 26.8% (52/194); and both, in 5.6% (11/194) of patients who underwent EVT in our study. In contrast to CS-I, indicating permanent brain injury and poor outcomes, patients with CS-NI in our series showed a favorable clinical course with no post-EVT worsening.[12,17-20]

Table 2: Crude and adjusted odds of contrast staining outside the infarcted tissue[a]

	Univariable			Multivariable		*P* Value
Hypertension						
No		Ref			Ref	
Yes	1.76	(0.69–4.41)	0.24	1.81	(0.68–4.85)	.23
Diabetes mellitus						
No		Ref			Ref	
Yes	1.78	(0.74–4.26)	0.19	1.71	(0.60–4.87)	.23
Kidney disease						
No		Ref			Ref	
Yes	2.50	(0.95–6.57)	0.06	1.66	(0.54–5.12)	.37
Time to CT scan (min)	0.999	(0.998–1.0)	0.21	0.999	(0.997–1.0)	.16
ASPECTS						
5–7		Ref			Ref	
8–10	2.78	(0.85–9.06)	0.09	3.46	(0.96–12.53)	.06
Core infarct staining						
No		Ref			Ref	
Yes	2.28	(0.98–5.31)	0.06	1.74	(0.70–4.34)	.23
Contrast volume	1.01	(0.999–1.02)	0.09	1.01	(0.999–1.02)	.01
Recanalization score						
TICI 0–2a		Ref			Ref	
TICI 2b–3	13.10	(0.75–229.98)	0.08	12.10	(0.77–190.21)	.08

[a] Data are OR (95% CI).

Table 3: Hounsfield units in healthy controls, penumbra, and core tissue[a]

	No.	HU Value CSP	*P* Value
Hounsfield units (mean)			<.0001
Control	26	32.35	
Penumbra	26	40.12	
Hounsfield units (max)			<.0001
Control	26	42.42	
Penumbra	26	52.96	
Hounsfield units (mean)			
Penumbra	11	39.73	.027
Core	11	53.09	
Hounsfield units (max)			
Penumbra	11	52.45	.014
Core	11	69.73	

Note:—Max indicates maximum; CSP, contrast staining in penumbra.

CS-NI is likely linked to a reversible, milder BBB disruption, differing from the more severe, potentially irreversible BBB disruption seen in CS-I. In addition to the BBB breakdown, the no-reflow phenomenon could contribute to contrast staining outside of the infarcted tissue. The no-reflow phenomenon describes a lack of blood flow at the capillary level despite established flow on the macrovascular level, preventing blood washout in the microcirculation and resulting in contrast retention and staining.[21] The potential contribution of the glymphatic system to this phenomenon cannot be excluded.[22] Existing evidence indicates that the functionality of the glymphatic system might be significantly compromised following AIS, resulting in reduced glymphatic perfusion and inadequate molecular clearance.[23] We believe that CS is distinct from contrast-induced neurotoxicity/encephalopathy, which results from hyperosmolarity and direct neurotoxic effects caused by extravasated contrast and is marked by more pronounced and diffuse contrast enhancement, accompanied by abnormal MR imaging findings in the affected regions.[24]

No existing literature demonstrates the association between BBB integrity and the degree or type of contrast staining on conventional cross-sectional imaging. However, several studies, including perfusion imaging and electron microscopic examinations, have explored the regional heterogeneity of BBB disruption in AIS.[25-27] Krueger et al[27-29] found, through electron microscopic and immunofluorescence studies, that BBB injury extends to the penumbral areas, which showed less structural BBB damage than core infarct regions. Other studies revealed regional variations in BBB disruption between the core infarct and the penumbra on perfusion imaging, with the penumbra regions showing reduced BBB disruption.[30]

In the current study, CS-NI is characterized by mild parenchymal enhancement on noncontrast CT, with an average HU of 40, which was significantly lower than the CS-I (53 HU) and lower than what is typically described in the literature for contrast staining after EVT (mean, 63.4 [SD, 17.0] HU; range, 39–140 HU).[9] Furthermore, CS-I is typically seen in the basal ganglia, whereas CS-NI was exclusively located in the cerebral convexities, which typically represent ischemic but not infarcted regions due to leptomeningeal collaterals (ie, penumbra).[6,31] Parenchymal enhancement in CS-NI in our series was typically accompanied by increased attenuation in the CSF spaces, which could be related to the progressive clearance of the extravasated contrast molecules to the CSF spaces and/or the glymphatic system.[23] Staining of the parenchyma and sulci in a given region can mimic cerebral edema and may be mistaken for irreversible tissue damage/infarction (Figs 2 and 3). CS-NI on CT may represent a phenomenon similar to that of the hyperintense acute reperfusion marker, which is a delayed enhancement of the subarachnoid or subpial space observed on postcontrast FLAIR MR imaging.[32]

Despite the statistical nonsignificance, the increased incidence of contrast staining in patients with kidney disease might also result from the direct effects of kidney disease on the integrity of the BBB or due to impaired renal function with a significantly prolonged half-life of the contrast medium (exceeding 16 hours compared with around 2 hours in patients with normal kidney function).[33,34] Additionally, sustained exposure to microvascular risk factors, including kidney disease, hypertension, diabetes mellitus, amyloid angiopathy, and inflammatory conditions, may potentiate the effects of ischemia on the cerebral microvasculature and increase the risk of staining.[6,21,35] Most interesting, no association was found between the occurrence of CS-NI and the use of IV thrombolysis, the duration of the procedure, or the volume of contrast injected, which have been described to potentially compromise the integrity of the BBB.[6,36-38]

There are several limitations to our study. First, the retrospective and single-center study design introduces selection bias. Despite using the Firth regression adjustment, the small sample size may not have the statistical power to expose potential small effects. Additionally, preprocedural perfusion imaging was not obtained for most of the included patients, preventing us from assessing the perfusion status of brain regions that developed CS-

NI. Moreover, we could not evaluate collateral circulation because we performed only single-phase CTA in our patients. Furthermore, we relied on restricted diffusion on MR imaging as a surrogate for irreversible infarction (core infarct) without considering the possibility of restricted diffusion reversibility after EVT. Finally, systematic recording of microcatheter contrast injection distal to the occluded side was not performed.

CONCLUSIONS

CS can be seen outside the infarcted tissue after EVT of AIS and is likely due to a reversible milder degree of BBB disruption. Although potentially benign, knowing its characteristics is important because it may mimic pathologic conditions such as infarcted tissue and cerebral edema. Further studies are required to comprehend the role of the BBB after ischemic stroke and its potential role as a target for neuroprotection after stroke therapy.

Disclosure forms provided by the authors are available with the full text and PDF of this article at www.ajnr.org.

REFERENCES

1. Parrilla G, García-Villalba B, Espinosa de Rueda M, et al. **Hemorrhage/contrast staining areas after mechanical intra-arterial thrombectomy in acute ischemic stroke: imaging findings and clinical significance**. *AJNR Am J Neuroradiol* 2012;33:1791–96 CrossRef Medline
2. Lummel N, Schulte-Altedorneburg G, Bernau C, et al. **Hyperattenuated intracerebral lesions after mechanical recanalization in acute stroke.** *AJNR Am J Neuroradiol* 2014;35:345–51 CrossRef Medline
3. Chang GC, Ma DC, Li W, et al. **Contrast enhancement by location and volume is associated with long-term outcome after thrombectomy in acute ischemic stroke.** *Sci Rep* 2022;12:16998 CrossRef Medline
4. Abdalkader M, Siegler JE, Lee JS, et al. **Neuroimaging of acute ischemic stroke: multimodal imaging approach for acute endovascular therapy.** *J Stroke* 2023;25:55–71 CrossRef Medline
5. Shulman JG, Abdalkader M. **Imaging of central nervous system ischemia.** *Continuum (Minneap Minn)* 2023;29:54–72 CrossRef Medline
6. Del Zoppo GJ, Von Kummer R, Hamann GF. **Ischaemic damage of brain microvessels: inherent risks for thrombolytic treatment in stroke.** *J Neurol Neurosurg Psychiatry* 1998;65:1–9 CrossRef Medline
7. Hamann GF, Okada Y, Del Zoppo GJ. **Hemorrhagic transformation and microvascular integrity during focal cerebral ischemia/reperfusion.** *J Cereb Blood Flow Metab* 1996;16:1373–78 CrossRef Medline
8. Pardridge WM. **Drug transport across the blood–brain barrier**. *J Cereb Blood Flow Metab* 2012;32:1959–72 CrossRef Medline
9. Dekeyzer S, Nikoubashman O, Lutin B, et al. **Distinction between contrast staining and hemorrhage after endovascular stroke treatment: one CT is not enough.** *J Neurointerv Surg* 2017;9:394–98 CrossRef Medline
10. Suzuki R, Yamaguchi T, Kirino T, et al. **The effects of 5-minute ischemia in Mongolian gerbils: I. Blood-brain barrier, cerebral blood flow, and local cerebral glucose utilization changes.** *Acta Neuropathol* 1983;60:207–16 CrossRef Medline
11. Montaner J, Molina CA, Monasterio J, et al. **Matrix metalloproteinase-9 pretreatment level predicts intracranial hemorrhagic complications after thrombolysis in human stroke.** *Circulation* 2003;107:598–603 CrossRef Medline
12. Chang GC, Nguyen TN, Qiu J, et al. **Predicting symptomatic intracranial hemorrhage in anterior circulation stroke patients with contrast enhancement after thrombectomy: the CAGA score.** *J Neurointerv Surg* 2023;15:e356–362 CrossRef Medline
13. Costalat V, Lobotesis K, Machi P, et al. **Prognostic factors related to clinical outcome following thrombectomy in ischemic stroke (RECOST Study): 50 patients prospective study.** *Eur J Radiol* 2012;81:4075–82 CrossRef Medline
14. Cabral FB, Castro-Afonso LH, Nakiri GS, et al. **Hyper-attenuating brain lesions on CT after ischemic stroke and thrombectomy are associated with final brain infarction.** *Interv Neuroradiol* 2017;23:594–600 CrossRef Medline
15. Amans MR, Cooke DL, Vella M, et al. **Contrast staining on CT after DSA in ischemic stroke patients progresses to infarction and rarely hemorrhages.** *Interv Neuroradiol* 2014;20:106–15 CrossRef Medline
16. Firth D. **Bias reduction of maximum likelihood estimates.** *Biometrika* 1993;80:27–38 CrossRef
17. Renú A, Amaro S, Laredo C, et al. **Relevance of blood–brain barrier disruption after endovascular treatment of ischemic stroke: dual-energy computed tomographic study**. *Stroke* 2015;46:673–79 CrossRef Medline
18. Leigh R, Jen SS, Hillis AE, et al; STIR and VISTA Imaging Investigators. **Pretreatment blood–brain barrier damage and post-treatment intracranial hemorrhage in patients receiving intravenous tissue-type plasminogen activator**. *Stroke* 2014;45:2030–35 CrossRef Medline
19. Obach V, Oleaga L, Urra X, et al. **Multimodal CT-assisted thrombolysis in patients with acute stroke: a cohort study.** *Stroke* 2011;42:1129–31 CrossRef Medline
20. Kassner A, Mandell DM, Mikulis DJ. **Measuring permeability in acute ischemic stroke.** *Neuroimaging Clin N Am* 2011;21:315–25 CrossRef Medline
21. Mujanovic A, Ng F, Meinel TR, et al. **No-reflow phenomenon in stroke patients: a systematic literature review and meta-analysis of clinical data.** *Int J Stroke* 2023;19:58–67 CrossRef Medline
22. Iliff JJ, Wang M, Liao Y, et al. **A paravascular pathway facilitates CSF flow through the brain parenchyma and the clearance of interstitial solutes, including amyloid β.** *Sci Transl Med* 2012;4:147ra111 CrossRef Medline
23. Gaberel T, Gakuba C, Goulay R, et al. **Impaired glymphatic perfusion after strokes revealed by contrast-enhanced MRI: a new target for fibrinolysis?** *Stroke* 2014;45:3092–96 CrossRef Medline
24. Chu YT, Lee KP, Chen CH, et al. **Contrast-induced encephalopathy after endovascular thrombectomy for acute ischemic stroke.** *Stroke* 2020;51:3756–59 CrossRef Medline
25. Arba F, Rinaldi C, Caimano D, et al. **Blood–brain barrier disruption and hemorrhagic transformation in acute ischemic stroke: systematic review and meta-analysis**. *Front Neurol* 2020;11:594613 CrossRef Medline
26. Nagaraja TN, Karki K, Ewing JR, et al. **Identification of variations in blood-brain barrier opening after cerebral ischemia by dual contrast-enhanced magnetic resonance imaging and T 1sat measurements.** *Stroke* 2008;39:427–32 CrossRef Medline
27. Krueger M, Mages B, Hobusch C, et al. **Endothelial edema precedes blood-brain barrier breakdown in early time points after experimental focal cerebral ischemia.** *Acta Neuropathol Commun* 2019;7:17 CrossRef Medline
28. Krueger M, Bechmann I, Immig K, et al. **Blood-brain barrier breakdown involves four distinct stages of vascular damage in various models of experimental focal cerebral ischemia.** *J Cereb Blood Flow Metab* 2015;35:292–303 CrossRef Medline
29. Krueger M, Härtig W, Frydrychowicz C, et al. **Stroke-induced blood–brain barrier breakdown along the vascular tree: no preferential affection of arteries in different animal models and in humans**. *J Cereb Blood Flow Metab* 2017;37:2539–54 CrossRef Medline
30. Heidari P, Blayney S, Butler J, et al. **The relationship between penumbral tissue and blood-brain barrier disruption in acute stroke patients presenting in an extended time window.** *Front Neurol* 2020;11:582994 CrossRef Medline
31. Romero JR, Pikula A, Nguyen TN, et al. **Cerebral collateral circulation in carotid artery disease.** *Curr Cardiol Rev* 2009;5:279–88 CrossRef Medline

32. Althaus K, Kasel M, Ludolph AC, et al. **HARM revisited: etiology of subarachnoid hyperintensities in brain FLAIR MRI.** *Int J Stroke* 2022;17:1121–28 CrossRef Medline
33. Hernandez L, Ward LJ, Arefin S, et al; GOING-FWD Collaborators. **Blood–brain barrier and gut barrier dysfunction in chronic kidney disease with a focus on circulating biomarkers and tight junction proteins**. *Sci Rep* 2022;12:4414 CrossRef Medline
34. Gupta A, Bansal A, Young K, et al. **Blood-brain barrier permeability in ESKD: a proof-of-concept study.** *J Am Soc Nephrol* 2023;34:1508–11 CrossRef Medline
35. Seker F, Qureshi MM, Möhlenbruch MA, et al. **Reperfusion without functional independence in late presentation of stroke with large vessel occlusion**. *Stroke* 2022;53:3594–604 CrossRef Medline
36. Lukic-Panin V, Deguchi K, Yamashita T, et al. **Free radical scavenger edaravone administration protects against tissue plasminogen activator induced oxidative stress and blood brain barrier damage.** *Curr Neurovasc Res* 2010;7:319–29 CrossRef Medline
37. Kurosawa Y, Lu A, Khatri P, et al. **Intra-arterial iodinated radiographic contrast material injection administration in a rat middle cerebral artery occlusion and reperfusion model: possible effects on intracerebral hemorrhage.** *Stroke* 2010;41:1013–17 CrossRef Medline
38. Khatri P, Broderick JP, Khoury JC, et al; IMS I and II Investigators. **Microcatheter contrast injections during intra-arterial thrombolysis may increase intracranial hemorrhage risk.** *Stroke* 2008;39:3283–87 CrossRef Medline

Concurrent Moyamoya-like Intracranial Steno-Occlusive Disease and Dural Arteriovenous Fistulas

Vaishnavi L. Rao, Jee Won Shin, James P. Klaas, and Giuseppe Lanzino

ABSTRACT

SUMMARY: The simultaneous presentation of intracranial steno-occlusive disease, Moyamoya disease, or Moyamoya-like vasculopathy and dural arteriovenous fistulas (DAVFs) has been documented in very few case reports worldwide. We aimed to better characterize this association by reviewing the clinical and radiologic findings of 4 patients with concurrent intracranial steno-occlusive disease or Moyamoya-like vasculopathy and DAVFs evaluated in our institution. All 4 patients were of Asian descent. One patient presented with ischemic stroke secondary to intracranial stenosis, 2 presented with symptoms related to the DAVF, and the diagnosis was incidental in the fourth patient. Three patients underwent embolization of the DAVF, which was followed by surgical ligation in 2. One patient underwent extracranial-intracranial bypass for Moyamoya-like intracranial steno-occlusive disease. One patient is being managed conservatively with close follow-up. Our case series details findings in 4 patients with associated intracranial steno-occlusive disease and DAVFs. Further studies and reporting of similar cases are necessary to establish whether this is pure coincidence or if there is indeed a relationship between these 2 conditions, especially in certain ethnic groups.

ABBREVIATIONS: DAVF = dural arteriovenous fistula; MMD = Moyamoya disease

Moyamoya disease (MMD), Moyamoya-like vasculopathy, and intracranial steno-occlusive disease are cerebrovascular conditions with a higher incidence in East Asian countries than in the Western Hemisphere.[1] Dural arteriovenous fistulas (DAVFs) are relatively uncommon cerebrovascular entities characterized by abnormal shunting between the meningeal arteries and the dural venous sinuses or subarachnoid veins,[2] accounting for 10%–15% of intracranial vascular malformations,[3] with an incidence as high as 0.29 per 100,000 person-years in Japan.[4] There have been very few case reports worldwide documenting the co-occurrence of these 2 disease entities before surgical intervention or head trauma. Here, we describe an institutional series of 4 patients presenting with concurrent Moyamoya-like vascular changes or intracranial steno-occlusive disease and DAVFs.

CASE SERIES

We identified all patients with intracranial steno-occlusive disease, Moyamoya, Moyamoya-like vasculopathy, and DAVFs from a prospectively maintained database of cases evaluated and/or treated by the senior author (G.L.) at our institution between January 2008 and 2023. The diagnosis of idiopathic Moyamoya or Moyamoya-like vasculopathy was made on the basis of the presence of both stenosis or occlusion of the terminal ICA or the proximal middle and/or anterior cerebral artery and an abnormal network of blood vessels on cerebral angiography, according to the 2021 diagnostic criteria for MMD published by the Ministry of Health, Labor and Welfare in Japan.[5] More recently, patients underwent high-resolution MR imaging with vessel wall enhancement to distinguish eccentric (more consistent with intracranial atherosclerosis) from concentric (more consistent with idiopathic vasculopathy) enhancing patterns.[6,7] The Cognard system was used to classify the type of DAVF, because it is useful for predicting the associated risk and guiding management decisions.[8]

This retrospective study was reviewed and approved by our institutional review board (19–001663), and all protocols were followed in accordance with institutional review board guidelines. A common denominator of these patients was their Asian ethnicity. Demographics, clinical presentation, and treatment are summarized in the Online Supplemental Data. Angiographic findings are presented in Figs 1–4. MR vessel wall imaging was available for cases 2 and 4, which presented more recently after vessel wall imaging was incorporated into practice at our institution. For these patients, vessel wall imaging demonstrated circumferential

Received November 15, 2023; accepted after revision January 15, 2024.

From the Departments of Neurosurgery (V.L.R., G.L.), and Neurology (J.P.K.), Mayo Clinic, Rochester, Minnesota; and Mayo Clinic Alix School of Medicine (J.W.S.), Rochester, Minnesota.

Please address correspondence to Giuseppe Lanzino, MD, Department of Neurosurgery, Mayo Clinic, 200 First St, SW, Rochester, MN 55905; e-mail: Lanzino.giuseppe@mayo.edu; @GLanzinoNSGY

Indicates article with online supplemental data.

http://dx.doi.org/10.3174/ajnr.A8197

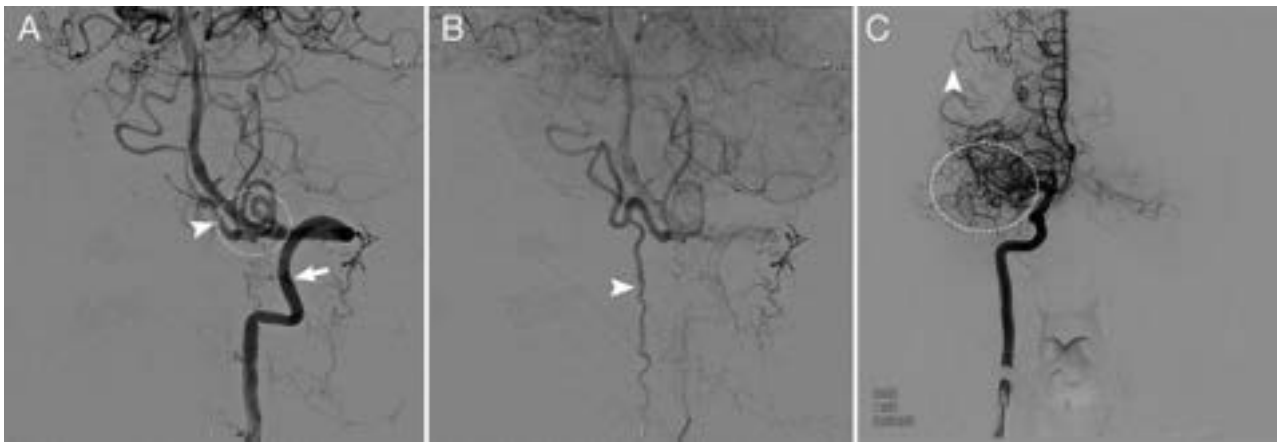

FIG 1. Case 1. A 57-year-old Asian man who presented with several weeks of progressive myelopathy. *A*, Conventional angiography shows a craniocervical junction AVF (*white circle*) with a large arterialized draining vein (*arrowhead*) arising from the dura adjacent to the point where the vertebral artery pierces the dura, supplied by branches of the left vertebral artery (*arrow*). *B*, The same injection demonstrates the venous drainage of the fistula down the anterior and posterior spinal veins, which are filled early (*arrowhead*). *C*, A right ICA injection, anterior-posterior view shows incidental occlusion of the M1 segment with Moyamoya-like collaterals (*white circle*) reconstituting the distal MCA territory in addition to leptomeningeal collaterals (*arrowhead*) from the distal anterior cerebral artery. He underwent surgical ligation of the fistula after failed embolization. The asymptomatic MCA occlusion was treated medically.

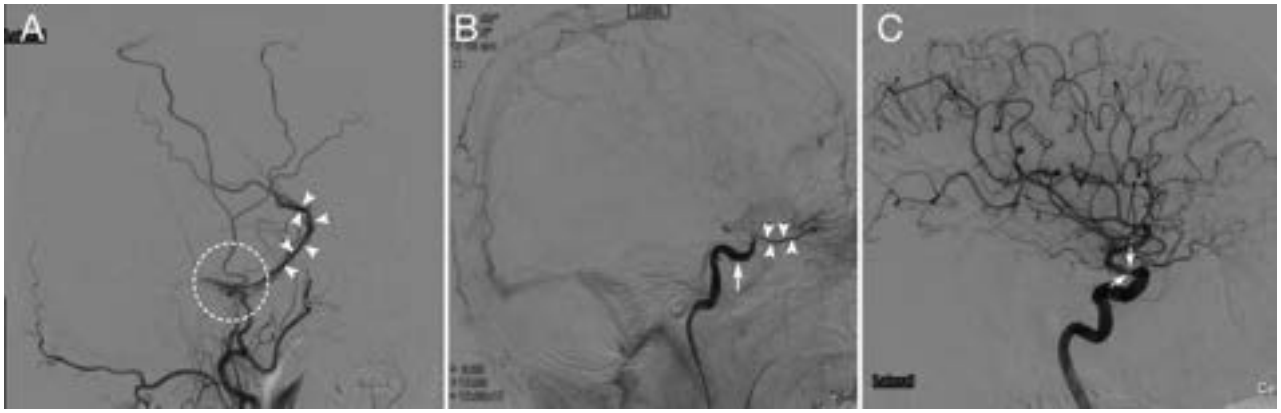

FIG 2. Case 2. A 63-year-old Asian man who presented with multiple left-hemisphere infarcts during 1 year. *A*, A left common carotid artery injection shows a left sphenoparietal DAVF (*circle*) supplied by the left middle meningeal artery with exclusive retrograde cortical venous drainage *(arrowheads*). *B*, There is delayed filling of the left ICA (*arrow*), which is occluded distal to the origin of the ophthalmic artery (*arrowheads*). *C*, Selective right ICA injection, lateral view, shows severe stenosis of the right supraclinoid ICA (*arrows*). The patient underwent partial embolization of the DAVF followed by surgical ligation and left superficial temporal artery–to-MCA bypass.

vessel wall enhancement involving the distal left ICA in case 2 and lack of any vessel wall enhancement whatsoever in case 4, suggesting a steno-occlusive picture outside intracranial atherosclerosis. For cases 1 and 3, we elected to treat the DAVFs because they were symptomatic, while in case 2, we attempted treatment of the DAVF because of the retrograde cortical venous drainage/venous hypertension and its potential role in aggravating perfusion issues related to the steno-occlusive disease. For case 4, we elected for observation of the DAVF because of its asymptomatic status/incidental finding and potential risks associated with embolization (ie, compromise of retinal blood flow supply) or surgical therapy (brain manipulation in the setting of steno-occlusive disease and marginal perfusion). The steno-occlusive disease in each patient was medically managed with aspirin monotherapy, while patient 2 underwent surgical revascularization for recurrent left-hemispheric infarcts.

DISCUSSION

We describe 4 patients of Asian ethnicity with concomitant idiopathic Moyamoya disease, Moyamoya-like vasculopathy, or steno-occlusive disease and intracranial DAVFs. The rare concurrent appearance of intracranial steno-occlusive disease and DAVFs as seen in our 4 cases has been previously documented in only a few single case reports and usually after surgical therapy or trauma. De novo formation of DAVFs in patients with Moyamoya-like vasculopathy has been observed in a delayed fashion following direct bypass,[9,10] indirect bypass,[11] and head trauma;[12] however, there have been a very few cases of simultaneous presentation in the absence of prior surgery or trauma. These include a patient with unilateral MMD who presented with intraventricular hemorrhage and was found to have an ipsilateral transverse-sigmoid DAVF, which was ultimately treated with endovascular embolization,[13] similar to case 3 in our series, as

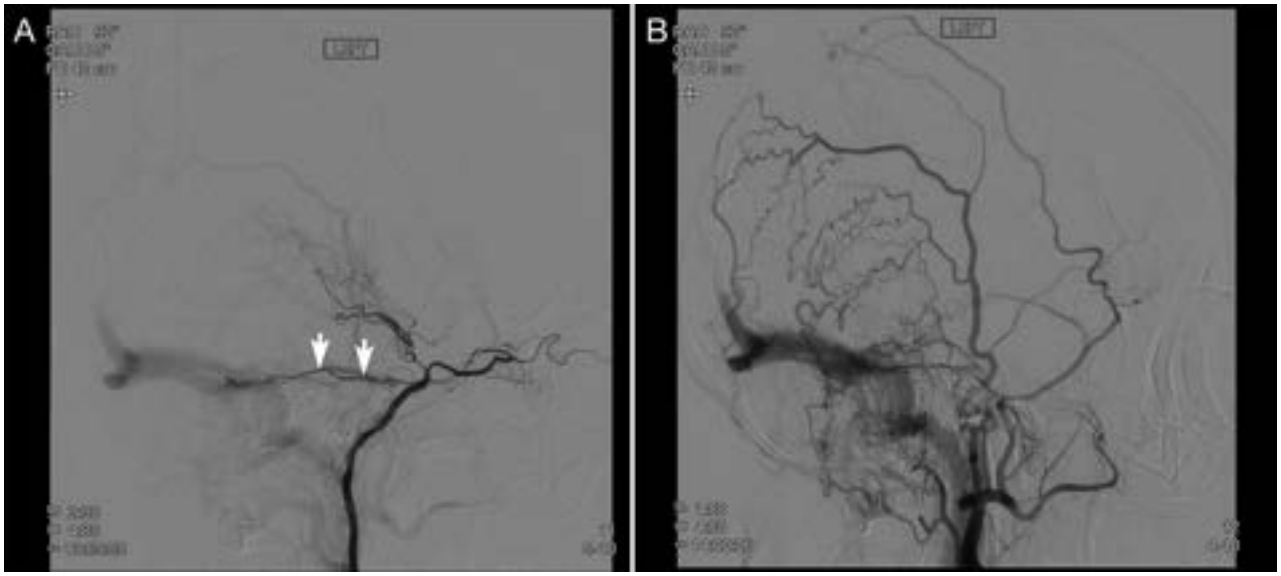

FIG 3. Case 3, A 74-year-old Asian woman who presented with episodic vision loss, papilledema, and cognitive decline. *A*, Conventional angiography, selective left ICA injection, shows an incidental left supraclinoid ICA occlusion as well as a left transverse-sigmoid junction DAVF with arterial feeders from the left meningohypophyseal artery (*arrows*). *B*, External carotid artery injection, lateral view, shows a high-flow transverse-sigmoid sinus DAVF. The DAVF was occluded via a transvenous approach with resolution of symptoms at follow up. Low-dose aspirin was prescribed for the incidental carotid occlusion.

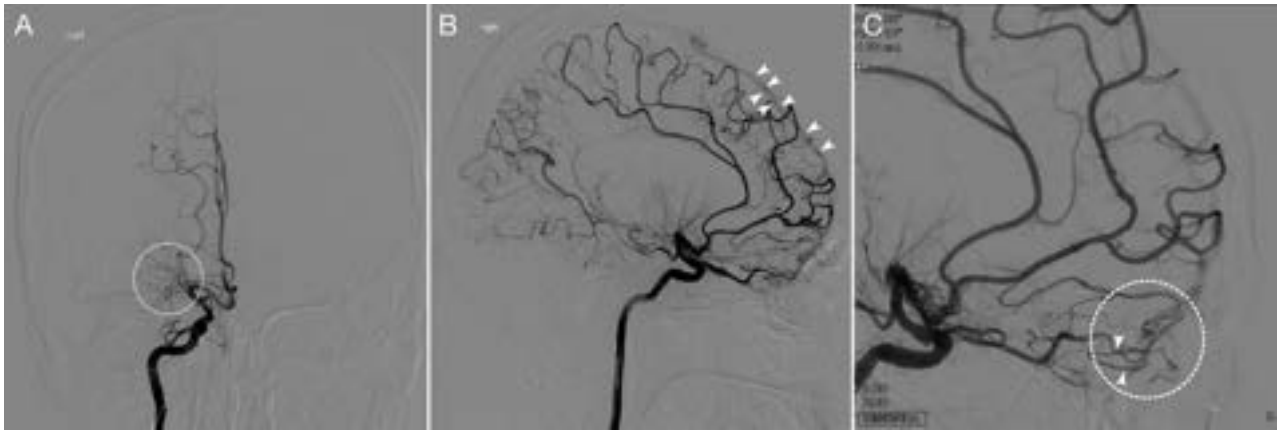

FIG 4. Case 4. A 42-year-old Asian man with right-sided headache. *A*, Selective right ICA injection, anterior-posterior view, early arterial phase, shows occlusion of the MCA with a Moyamoya network (*white circle*). *B*, Selective right ICA injection, lateral view, early arterial phase, shows a lack of opacification in the MCA territory and early filling of the superior sagittal sinus (*arrowheads*). *C*, Right ICA selective injection, magnified oblique view, shows enlarged and tortuous distal ophthalmic artery branches (*arrowheads*) feeding a dural/pial AVF (*white circle*), with early opacification of a cortical vein draining into the superior sagittal sinus.

well as ipsilateral cavernous and tentorial DAVFs observed in patients with MMD in China[14] and Spain,[15] respectively.

A proposed mechanism for the formation of DAVFs in these patients is that aberrant flow dynamics in intracranial steno-occlusive disease leads to an increased demand and decreased perfusion, with the subsequent ischemia triggering an angiogenic response in the dural vasculature, resulting in arteriovenous shunting.[16] Indeed, increased expression of proangiogenic factors has been reported in the dura of patients with MMD, including vascular endothelial growth factor[17] and fibroblast growth factor.[18] These factors are also involved in the formation of DAVFs.[19]

Of note, all 4 patients in our series are of East Asian ethnicity, suggesting that a genetic association may potentially exist in cases of concurrent intracranial steno-occlusive disease and DAVF. None of the previous case reports we came across specified the patients' ethnicity, so we could not confirm such an association on the basis of prior literature. Nevertheless, variants of the *HLA* genes and the *RNF213* susceptibility gene have been found to be associated with East Asian patients with MMD.[20,21] Unfortunately, the patients included in our study did not undergo genetic testing to evaluate these pathogenic variants; however, this association would be an interesting area of future study. Overall, intracranial stenosis is more prevalent in Asians,[22] often with a younger mean age of onset and independent of vascular risk factors compared with Caucasians.[23]

In our small institutional case series, we describe the simultaneous presentation of the two entities of Moyamoya pattern/steno-

occlusive intracranial disease and DAVF in 4 patients of East Asian descent. While our series does not establish causality, future reporting and study of similar cases may further determine whether a potential relationship exists between ethnicity and the concurrence of these cerebrovascular phenomena. As more patients like these are identified, the pathophysiology of these two conditions can be more clearly elucidated and the presence of an underlying genetic association can be investigated.

ACKNOWLEDGMENTS

We acknowledge Peggy Chihak and Arielle Davis for their help in formatting the figures and manuscript.

Disclosure forms provided by the authors are available with the full text and PDF of this article at www.ajnr.org.

REFERENCES

1. Zhang H, Zheng L, Feng L. **Epidemiology, diagnosis, and treatment of moyamoya disease.** *Exp Ther Med* 2019;17:1977–84 CrossRef Medline
2. Reynolds MR, Lanzino G, Zipfel GJ. **Intracranial dural arteriovenous fistulae.** *Stroke* 2017;48:1424–31 CrossRef Medline
3. Newton TH, Cronqvist S. **Involvement of dural arteries in intracranial arteriovenous malformations.** *Radiology* 1969;93:1071–78 CrossRef Medline
4. Satomi J, Satoh K. **Epidemiology and etiology of dural arteriovenous fistula.** *Brain Nerve* 2008;60:883–86 Medline
5. Kuroda S, Fujimura M, Takahashi J, et al; Research Committee on Moyamoya Disease (Spontaneous Occlusion of Circle of Willis) of the Ministry of Health, Labor, and Welfare, Japan. **Diagnostic criteria for moyamoya disease: 2021 revised version.** *Neurol Med Chir (Tokyo)* 2022;62:307–12 CrossRef Medline
6. Mossa-Basha M, de Havenon A, Becker KJ, et al. **Added value of vessel wall magnetic resonance imaging in the differentiation of moyamoya vasculopathies in a non-Asian cohort.** *Stroke* 2016;47:1782–88 CrossRef Medline
7. Liu S, Lu M, Gao X, et al. **The diagnostic performance of high-resolution magnetic resonance-vessel wall imaging in differentiating atherosclerosis-associated moyamoya vasculopathy from moyamoya disease.** *Eur Radiol* 2023;33:6918–26 CrossRef Medline
8. Cognard C, Gobin YP, Pierot L, et al. **Cerebral dural arteriovenous fistulas: clinical and angiographic correlation with a revised classification of venous drainage.** *Radiology* 1995;194:671–80 CrossRef Medline
9. Feroze AH, Kushkuley J, Choudhri O, et al. **Development of arteriovenous fistula after revascularization bypass for Moyamoya disease: case report.** *Operative Neurosurgery* 2015;11(Suppl 2):E202–06 CrossRef Medline
10. Hanaoka M, Matsubara S, Satoh K, et al. **Dural arteriovenous fistulae after cerebral infarction: report of two cases.** *Neurosurgery* 2011;68:E575–79; discussion E580 CrossRef Medline
11. Koduri S, Wilkinson DA, Griauzde JM, et al. **Development of bilateral dural arteriovenous fistulae following pial synangiosis for moyamoya syndrome: case report.** *J Neurosurg Pediatr* 2019;24:9–13 CrossRef Medline
12. Zaletel M, Surlan-Popović K, Pretnar-Oblak J, et al. **Moyamoya syndrome with arteriovenous dural fistula after head trauma**. *Acta Clini Croat* 2011;50:115–19 Medline
13. Killory BD, Gonzalez LF, Wait SD, et al. **Simultaneous unilateral moyamoya disease and ipsilateral dural arteriovenous fistula: case report.** *Neurosurgery* 2008;62:E1375–76; discussion E1376 CrossRef Medline
14. Liu P, Xu Y, Lv X, et al. **Progression of unilateral moyamoya disease resulted in spontaneous occlusion of ipsilateral cavernous dural arteriovenous fistula: case report.** *Interv Neuroradiol* 2016;22:362–64 CrossRef Medline
15. Cajal Campo B, Delgado Acosta F. **Enfermedad moyamoya y fístula arteriovenosa dural simultánea**. *Revista de Neurologia* 2010;50:317–18 CrossRef Medline
16. Lawton MT, Jacobowitz R, Spetzler RF. **Redefined role of angiogenesis in the pathogenesis of dural arteriovenous malformations.** *J Neurosurg* 1997;87:267–74 CrossRef Medline
17. Sakamoto S, Kiura Y, Yamasaki F, et al. **Expression of vascular endothelial growth factor in dura mater of patients with moyamoya disease.** *Neurosurg Rev* 2008;31:77–81; discussion 81 CrossRef Medline
18. Hoshimaru M, Takahashi JA, Kikuchi H, et al. **Possible roles of basic fibroblast growth factor in the pathogenesis of moyamoya disease: an immunohistochemical study.** *J Neurosurg* 1991;75:267–70 CrossRef Medline
19. Uranishi R, Nakase H, Sakaki T. **Expression of angiogenic growth factors in dural arteriovenous fistula.** *J Neurosurg* 1999;91:781–86 CrossRef Medline
20. Mertens R, Graupera M, Gerhardt H, et al. **The genetic basis of moyamoya disease.** *Transl Stroke Res* 2021;13:25–45 CrossRef Medline
21. Hiraide T, Suzuki H, Momoi M, et al. **RNF213-associated vascular disease: a concept unifying various vasculopathies.** *Life (Basel)* 2022;12:555 CrossRef Medline
22. Suri MF, Johnston SC. **Epidemiology of intracranial stenosis.** *J Neuroimaging* 2009;19(Suppl 1)11S–6S CrossRef Medline
23. Leng X, Hurford R, Feng X, et al. **Intracranial arterial stenosis in Caucasian versus Chinese patients with TIA and minor stroke: two contemporaneous cohorts and a systematic review.** *J Neurol Neurosurg Psychiatry* 2021 Mar 30 [Epub ahead of print] CrossRef Medline

Lesion-Filling Index from Quantitative DSA Correlates with Hemorrhage of Cerebral AVM

Ruinan Li, Yu Chen, Pingting Chen, Li Ma, Heze Han, Zhipeng Li, Wanting Zhou, Xiaolin Chen, and Yuanli Zhao

ABSTRACT

BACKGROUND AND PURPOSE: Rupture is the most life-threatening manifestation of cerebral AVMs. This study aimed to explore the hemodynamic mechanism of AVM rupture. We introduced a new quantitative DSA parameter that can reflect the degree of intranidal blood stasis, called the lesion-filling index.

MATERIALS AND METHODS: This study examined patients with AVMs who had undergone both DSA and MR imaging between 2013 and 2014. Clinical presentations, angioarchitecture, and hemodynamic parameters generated from quantitative DSA were analyzed using univariate and multivariable logistic regression. The lesion-filling index was defined as the arterial diagnostic window divided by the volume of the AVM. To assess the correlation between the lesion-filling index and rupture, we incorporated the lesion-filling index into 2 published prediction models widely recognized for predicting AVM rupture risk, R_2eD and VALE. The DeLong test was used to examine whether the addition of the lesion-filling index improved predictive efficacy.

RESULTS: A total of 180 patients with AVMs were included. The mean lesion-filling index values in the ruptured group were higher compared with the unruptured group (390.27 [SD, 919.81] versus 49.40 [SD, 98.25]), $P < .001$). A higher lesion-filling index was significantly correlated with AVM rupture in 3 different multivariable logistic models, adjusting for angioarchitecture factors (OR = 1.004, $P = .02$); hemodynamic factors (OR = 1.005, $P = .009$); and combined factors (OR = 1.004, $P = .03$). Both R_2eD (area under the curve, 0.601 versus 0.624; $P = .15$) and VALE (area under the curve, 0.603 versus 0.706; $P < .001$) predictive models showed improved predictive performance after incorporating the lesion-filling index and conducting 10-fold cross-validation.

CONCLUSIONS: The lesion-filling index showed a strong correlation with AVM rupture, suggesting that overperfusion is the hemodynamic mechanism leading to AVM rupture.

ABBREVIATIONS: ADW = arterial diagnostic window; AUC = area under the curve; FWHM = full width at half maximum; LFI = lesion-filling index; QDSA = quantitative DSA; TRV = transnidal relative velocity

Cerebral AVMs involve abnormal tangles of brain arteries and veins, posing a risk of intracranial bleeding and neurologic issues. Among these symptoms, hemorrhage stands out as the most life-threatening manifestation, remarkably affecting patients' quality of life.[1,2] A comprehensive understanding of the mechanism of AVM rupture is crucial. Previous research has revealed that hemodynamics could play a pivotal role as a risk factor for rupture.[3-5] The most influential early research was conducted by Spetzler et al,[3] in 1992, in which they used micropipette direct puncture pressure measurement techniques to substantiate the impact of perfusion pressure on AVM rupture. Nevertheless, the intraprocedural puncture of feeding arteries, being an invasive procedure, entails certain risks and operational complexities. Consequently, contemporary research in hemodynamics now places greater emphasis on noninvasive investigative approaches.

Noninvasive hemodynamic measurement techniques such as quantitative DSA (QDSA) have been proved to assist in assessing rupture risk and planning treatments.[5-10] QDSA is a medical imaging technique used to assess the structure and function of blood vessels. It builds on conventional DSA by providing

Received November 27, 2023; accepted after revision February 2, 2024.

From the Department of Neurosurgery (R.L., Y.C., L.M., H.H., Z.L., X.C., Y.Z.) and Beijing Neurosurgical Institute (Y.C., X.C., Y.Z.), Beijing Tiantan Hospital, Capital Medical University, Beijing, China; China National Clinical Research Center for Neurological Diseases (Y.C., X.C., Y.Z.), Beijing, China; College of Energy and Power Engineering (P.C.), Nanjing University of Aeronautics and Astronautics, Nanjing, China; Department of Neurological Surgery (L.M.), University of Pittsburgh Medical Center, Pittsburgh, Pennsylvania; and Department of Artificial Intelligence (W.Z.), Beijing University of Posts and Telecommunications, Beijing, China.

This study was supported by the Natural Science Foundation of China (82202244 to Yu Chen; 81771234 and 82071302 to Yuanli Zhao; 62376037 to Wanting Zhou) and the National Key R&D Program (2021YFC2501101, 2020YFC2004701 to Xiaolin Chen).

Ruinan Li and Yu Chen are co-first authors.

Please address correspondence to Yuanli Zhao, MD, Department of Neurosurgery, Beijing Tiantan Hospital, Beijing, 100070, P. R. China; e-mail: zhaoyuanli@126.com

Indicates article with online supplemental data.

http://dx.doi.org/10.3174/ajnr.A8218

SUMMARY

PREVIOUS LITERATURE: Using quantitative digital subtraction angiography (QDSA) for the study of ruptured brain arteriovenous malformations, early recognition was associated with the mean transit time as published by Chen et al, correlating with silent intralesional microhemorrhages. Subsequent studies by Lin et al and Chen et al utilized QDSA-derived ROI curves, introducing a series of hemodynamic parameters strongly linked to rupture. These parameters were successfully employed in predicting AVM occlusion post-Gamma Knife treatment. While investigating the correlation between AVM rupture and hemodynamics, these studies concurrently demonstrated the valuable utility of QDSA parameters in the diagnosis and treatment of AVM.

KEY FINDINGS: We have found a novel QDSA hemodynamic parameter, Lesion-Filling Index (LFI), strongly correlated with AVM rupture.

KNOWLEDGE ADVANCEMENT: We discovered a novel QDSA hemodynamic parameter, designated as LFI, exhibiting a strong correlation with AVM rupture.

quantitative measurements of blood-flow dynamics. Previous studies had proposed several hemodynamic parameters associated with AVM rupture, such as MTT, the Stasis Index, and transnidal relative velocity (TRV), demonstrating the correlation of QDSA with AVM rupture[6,9,11] However, regrettably, these parameters did not consider the supply arteries, draining veins, and the nidus as a unified entity in their hemodynamic analysis, somewhat compromising the reliability of these parameters.

Therefore, in this study, we propose the lesion-filling index (LFI), a new QDSA parameter that integrates the difference in filling between supply arteries and draining veins along with the nidus volume, embarking on a more holistic interpretation of hemodynamic-related hemorrhage.

MATERIALS AND METHODS

Study Design and Participants

This retrospective study was approved by Beijing Tiantan hospital institutional review board (KY 2020–003-01), adhering to Helsinki Declaration guidelines and STrengthening the Reporting of OBservational studies in Epidemiology (STROBE) reporting for observational case-control studies.

Patient Selection

To explore the connection between AVM hemodynamics and hemorrhagic presentation, we examined 384 consecutive brain AVMs between January 2013 and January 2014 from a single-center database registered in a nationwide multicenter registry. The MATCH registry (https://clinicaltrials.gov/study/NCT04572568), registered on ClinicalTrials.gov as NCT04572568, aimed to study the natural history and optimal individualized management strategy of AVMs in China. In this study, the inclusion criteria encompassed AVM diagnosis through DSA and/or MR imaging, with available preoperative DSA DICOM data. Exclusions were hereditary hemorrhagic telangiectasia, lack of preoperative DSA, and insufficient baseline information.

Study Parameters

We collected baseline characteristics, conventional DSA angioarchitecture, and QDSA parameters from all enrolled patients. All clinical parameters were assessed by 2 neurosurgeons with at least 5 years of clinical practice experience. All radiologic characteristics were independently evaluated by 2 credentialed senior neurointerventional radiologists. If inconsistency existed, the final determination would be made by a professor of senior neurointerventional radiology with >30 years of clinical experience. Researchers who performed angioarchitecture and hemodynamic assessments were blinded to the clinical data.

Clinical baseline characteristics encompassed age on admission, sex, onset symptoms (hemorrhage, seizure, neurofunctional deficits, and others), and the mRS score on admission.

Angioarchitecture characteristics comprised the localization of AVMs, involvement of eloquent regions, and an array of features that had been analyzed in prior QDSA studies.[7,12-15] Building on the angioarchitecture characteristics documented in prior literature, we investigated the following features in our study: dilation of feeding arteries, presence of single or multiple feeding arteries, categorization of venous drainage as either superficial or deep, identification of single or multiple venous drainage, assessment of draining venous stenosis, evaluation of nidus diffuseness, and identification of flow-related aneurysms. The definitions for these angioarchitecture features were aligned with the guidelines established by the American Society of Interventional and Therapeutic Neuroradiology.[14] The definition of architecture characteristics is listed in the Online Supplemental Data.

QDSA parameters mainly refer to the hemodynamic parameters involved in previous QDSA-related studies and the quantitative hemodynamic parameters that can be calculated according to the fitted time-density curve, including the following: 1) TTP, 2) MTT, 3) full width at half maximum (FWHM), 4) arterial diagnostic window (ADW), 5) TRV, 6) the Stasis Index, and 7) LFI, and so forth.[11]

DSA Acquisition and Quantitative Hemodynamics

All cases underwent the same DSA procedures with the same Axiom Artis angiosuite (Artis zee; Siemens) in our institution. The DSA standardized acquisition protocol is described in the Online Supplemental Data. For postprocessing of all QDSA data, syngo iFlow software (Siemens) was used.

In this study, certain hemodynamic parameters were defined with reference to previously published research.[6,9,16] We chose the lateral view of common carotid angiography images to draw ROIs. For each patient, we investigated the following ROIs: 1) cavernous sinus segment of the ICA; 2) distal segment of the feeding artery; 3) AVM nidus; 4) proximal segment of the main

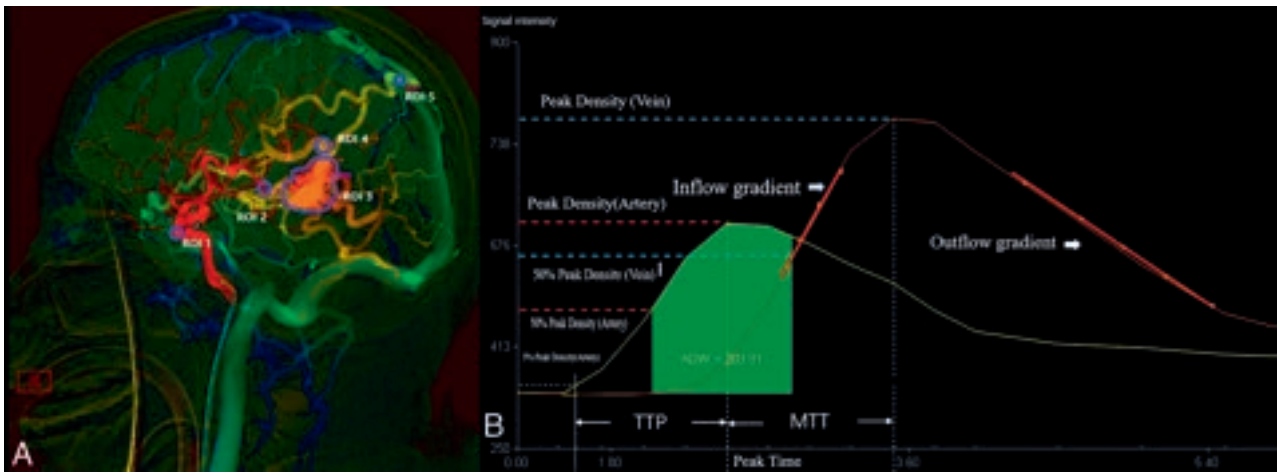

FIG 1. The time-density curve and color-coded QDSA. *A*, Lateral view of the color-coded QDSA. Selected ROIs are the following: 1) cavernous sinus segment of the ICA; 2) distal segment of the feeding artery; 3) AVM nidus; 4) proximal segment of the main draining vein; and 5) junction area of the draining vein and the venous sinus. *B*, Quantitative parameters in the time-density curve from QDSA. TTP indicates the time required for the bolus to reach peak attenuation, $\mathrm{ADW} = \int_{T50\%A}^{T50\%v} A(t)dt$.

draining vein; and 5) junction area of the draining vein and venous sinus (Fig 1*A*).[17] We used a standard circular ROI to delineate the supplying artery and draining vein characterized by the earliest contrast enhancement. For the AVM lesion, a polygonal tool was used to outline the ROI. The coordinates of time-density curves were measured by GetData Graph Digitizer (Version 2.24; S. Fedorov), and a customized program (Matlab; MathWorks) was used to fit the measured coordinate value (with the γ variable function, based on the least squares method) to get the standardized time-density curve.[17]

$$\text{Gamma variable function}: C(t) = K(t - AT)^{\wedge}\alpha \times \exp[-(t - AT)/\beta].$$

C(t) is the attenuation increment, t is the time after the start of contrast medium injection, K is a constant scale factor, α and β are fit coefficients, and AT (arrival time) is the time of arrival of the contrast medium.

The calculation formulas involving the parameters above were as follows (Fig 1*B*): TTP indicates the time required for the bolus to reach peak attenuation; MTT, the duration between peak attenuation of different ROIs; FWHM, the duration of the time-density curve rising to 50% peak attenuation and falling to 50% peak attenuation; $\mathrm{ADW} = \int_{T50\%A}^{T50\%v} A(t)dt$, calculated from the area under the curve (AUC) of the feeding arterial signal from Time (50% maximal arterial signal) to Time (50% maximal venous signal); TRV, maximum diameter (nidus)/FWHM; Stasis Index, inflow gradient/outflow gradient; LFI, ADW/volume (nidus).

Measurements of the Nidus

All enrolled patients underwent 1.5T or 3T MR imaging in our center. The maximum diameter was the greatest distance between 2 points within the AVM nidus, using MR imaging in the plane that most accurately depicted the largest cross-sectional area of the AVM. To calculate the volume of nidus, we used the ellipsoid volume formula, which assumes that the AVM shape is approximately ellipsoidal in nature. The formula is

$$V = 4/3\ \pi abc.$$

V is the volume of the nidus, and a, b, and c are the lengths of 3 perpendicular axes (measurements) of the nidus.

Statistical Analysis

Statistical analysis was performed using SPSS software (Version 26.0; IBM) and MedCalc for Windows (Version 22.013; MedCalc Software). For categoric variables, we presented frequencies and percentages, using the Pearson χ^2 test, Fisher exact test, and the Kruskal-Wallis ANOVA test for comparisons. Continuous variables were evaluated on the basis of normality assessment, using the independent Student *t* test or Mann-Whitney *U* rank-sum test as appropriate.

Univariate and multivariable logistic regression analyses were performed to calculate ORs and 95% CIs to identify predictors of hemorrhage in baseline characteristics, angioarchitecture, and hemodynamic features. The DeLong test was used to assess the statistically significant difference in the area under the receiver operating characteristic curve among the compared models. We selected 2 models, R_2eD (https://www.ahajournals.org/doi/10.1161/STROKEAHA.119.025054) and VALE (https://jamanetwork.com/journals/jamanetworkopen/fullarticle/2801834), from previously published studies known for their high correlation with AVM rupture.[18,19] The R_2eD system incorporates factors such as AVM size, deep venous drainage, nidus location, race, and monoarterial feeding. Meanwhile, the VALE system considers ventricular system involvement, venous aneurysm, deep location, and exclusively deep drainage. We further supplemented these 2 models by adding LFI to investigate its additive value associated with rupture. Performance of these models was evaluated using 10-fold cross-validation.

All P values were 2-sided, and statistical significance was considered at $P < .05$.

RESULTS

Baseline Characteristics

A total of 180 patients met the inclusion criteria and were included in this study (Fig 2). No significant differences in age, sex, and Spetzler-Martin grade distribution were observed between the ruptured ($n = 103$) and the unruptured ($n = 77$) groups. In comparison, ruptured AVMs often had higher mean mRS scores on admission (1.2 [SD,1.3] versus 0.8 [SD, 0.6], $P = .002$) and were less prone to patients experiencing concurrent seizure symptoms (16.5% versus 41.6%, $P < .001$) (Table 1).

Differences in Hemodynamic and Angioarchitecture Characteristics

To identify the risk factors associated with hemorrhage, we performed a comparative analysis of angioarchitecture and hemodynamic characteristics between cases of unruptured and ruptured AVMs (Table 2). The mean nidus volume, a key indicator of AVM size, was significantly larger in unruptured cases compared with ruptured cases (40.2 [SD, 46.4] mL versus 13.6 [SD, 21.0] mL, $P < .001$).

In terms of angioarchitecture, several notable differences were observed. The unruptured group had a higher prevalence of feeding artery dilation (74.0% versus 49.5%, $P = .001$), while the ruptured group had a higher incidence of a single feeding artery (34.0% versus 15.6%, $P = .003$). Other characteristics such as deep venous drainage, single draining vein, drainage vein stenosis, diffuse nidus, and flow-related aneurysms were also compared; however, no significant differences were found between the 2 groups.

Regarding hemodynamics, we examined various parameters for feeding arteries and drainage veins. While some differences were observed, including the FWHM, these did not reach statistical significance. Additionally, the study evaluated MTT ($P = .017$) and TRV ($P < .001$), both of which were significantly different between the two groups. LFI also showed a substantial difference ($P < .001$).

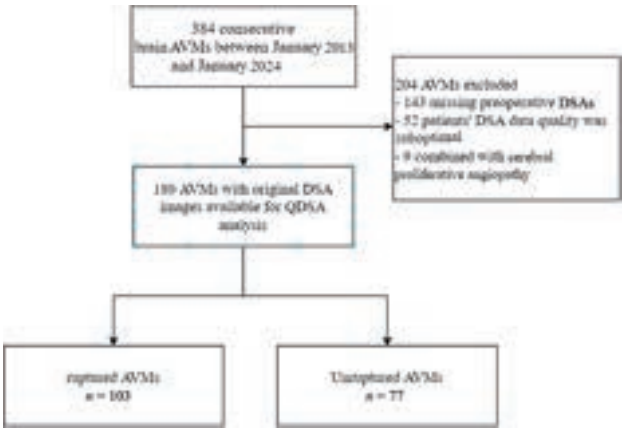

FIG 2. Flow diagram of the enrolled patients.

Association of LFI and Risk of AVM Rupture at Presentation in Hemodynamic, Angioarchitecture, and Combined AVM Models

To assess the statistical power and stability of the association between LFI and AVM rupture, we conducted several logistic regression analyses with LFI incorporated separately into the 3 models: hemodynamics, angioarchitecture, and a combined model. In the univariable analysis, LFI exhibited a significant association with AVM rupture risk (OR, 1.007; 95% CI, 1.003–1.010; $P = .001$). Similarly, in the angioarchitecture model, LFI remained significantly associated with rupture risk (OR, 1.004; 95% CI, 1.001–1.008; $P = .02$). The hemodynamic model also showed a significant association between AVM rupture and LFI (OR, 1.005; 95% CI, 1.001–1.009; $P = .009$). The combined model, which incorporates both angioarchitecture and hemodynamic factors, demonstrated a statistically significant association between AVM rupture and LFI as well (OR, 1.004; 95% CI, 1.000–1.007; $P = .03$) (Table 3). Notably, deep venous drainage, diffuse nidus, and flow-related aneurysms had significant associations with AVM rupture risk in the angioarchitecture model. All variables in the logistic regression had variance inflation factor values below the threshold of 10, demonstrating the absence of significant multicollinearity concerns.

Overall, these findings underscore the importance of LFI as a risk factor of AVM rupture, with consistent significance across various models.

Table 1: Baseline characteristics

Characteristics	All Cases	Unruptured	Ruptured	*P* Value
No. of patients	180	77	103	
Age (mean) (yr)	24.6 (SD, 12.7)	25.2 (SD, 11.9)	24.2 (SD, 13.3)	.60
Sex (male)	110 (61.1%)	50 (64.9%)	60 (58.3%)	.22
Admission mRs score (mean)	1.0 (SD, 1.1)	0.8 (SD, 0.6)	1.2 (SD, 1.3)	.002[a]
Clinical presentation				
Seizure	49 (27.2%)	32 (41.6%)	17 (16.5%)	<.001[a]
Headache (nonruptured)	25 (13.9%)	24 (31.2%)	1 (1.0%)	<.001[a]
Focal neurologic deficit	20 (11.1%)	12 (15.6%)	8 (7.8%)	.08
Spetzler-Martin grade				.07
I	30 (16.7%)	8 (10.4%)	22 (21.4%)	
II	61 (33.9%)	26 (33.8%)	35 (34.0%)	
III	53 (29.4%)	25 (32.5%)	28 (27.2%)	
IV	28 (15.6%)	15 (19.5%)	13 (12.6%)	
V	8 (4.4%)	3 (3.9%)	5 (4.9%)	

[a] Statistical significance ($P < .05$).

Additive Value Assessment of LFI in the Previous Models

LFI has been established as a stable and robust risk factor of rupture in multivariate logistic regression analyses. To further assess its effectiveness, we incorporated LFI as a parameter into the previously published AVM rupture-risk scoring systems, such as the R_2eD and VALE score systems, and observed whether LFI enhances the predictive performance of the model.[18,19]

We adjusted variables with statistically significant differences identified in the univariate analysis presented in

Table 2. We aimed to explore the stable relationship between LFI and rupture. Thus, 3 multivariable logistic regressions were performed to adjust for angioarchitectural, hemodynamic, and both factors. The selection of confounders was based on exploratory analysis using logistic regression (Table 2). Due to the cross-sectional nature of this study, there were inherent population differences, and some parameters in our study may differ from those in models such as R_2eD and VALE.

Table 2: Comparison of angioarchitecture and hemodynamics between the unruptured and ruptured AVMs

Characteristics	Unruptured	Ruptured	*P* Value
No. of patients	77	103	
Mean nidus volume (mean) (mL)	40.2 (SD, 46.4)	13.6 (SD, 21.0)	<.001[a]
Angioarchitecture			
Feeding artery dilation	57 (74.0%)	51 (49.5%)	.001[a]
Single feeding artery	12 (15.6%)	35 (34.0%)	.003[a]
Deep venous drainage	17 (22.1%)	38 (36.9%)	.035[a]
Single draining vein	33 (42.9%)	65 (63.1%)	.07
Drainage vein stenosis	11 (14.3%)	27 (26.2%)	.07
Diffuse nidus	15 (19.5%)	38 (36.9%)	.01[a]
Flow-related aneurysm	14 (18.2%)	43 (41.7%)	.001[a]
Hemodynamics			
Feeding artery			
TTP (mean) (sec)	2.88 (SD, 0.80)	3.14 (SD, 1.01)	.07
FWHM (mean) (sec)	2.83 (SD, 1.02)	3.33 (SD, 1.29)	.006[a]
Inflow gradient (mean)	1265.61 (SD, 912.53)	1317.85 (SD, 1018.43)	.72
Outflow gradient (mean)	636.89 (SD, 505.72)	600.35 (SD, 511.84)	.63
Stasis index (mean)	2.42 (SD, 0.99)	2.63 (SD, 1.04)	.16
Drainage vein			
TTP (mean) (sec)	3.62 (SD, 1.07)	3.76 (SD, 1.30)	.42
FWHM (mean) (sec)	3.00 (SD, 0.75)	3.56 (SD, 1.29)	<.001[a]
Inflow gradient (mean)	1854.28 (SD, 2794.89)	1289.84 (SD, 975.82)	.06
Outflow gradient (mean)	741.99 (SD, 568.85)	610.58 (SD, 522.51)	.11
Stasis index (mean)	2.38 (SD, 0.65)	2.52 (SD, 0.97)	.28
MTT (ICA-sinus) (mean) (sec)	1.48 (SD, 1.03)	1.97 (SD, 1.70)	.02[a]
MTT (feeding-draining) (mean) (sec)	0.73 (SD, 0.97)	0.62 (SD, 1.04)	.47
ADW (mean)	695.02 (SD, 607.38)	742.75 (SD, 720.42)	.64
TRV (mean)	225.35 (SD, 211.26)	115.93 (SD, 157.39)	<.001[a]
LFI (mean)	49.40 (SD, 98.25)	390.27 (SD, 919.81)	<.001[a]

[a] Statistical significance ($P < .05$).

In the initial analysis, the R_2eD model exhibited an AUC of 0.755 (95% CI, 0.684–0.826), serving as the reference model. After the inclusion of LFI, the AUC for the R_2eD + LFI model increased to 0.791 (95% CI, 0.725–0.857), indicating a statistically significant improvement ($P = .03$) (Fig 3*A*). Additionally, LFI itself demonstrated significance as an independent risk factor (OR, 1.004; 95% CI, 1.000–1.008; $P = .04$).

Similarly, the VALE model, with an initial AUC of 0.760 (95% CI, 0.689–0.831) served as another reference model. After the inclusion of LFI, the VALE + LFI model showed a significant enhancement in discriminatory power, with an AUC of 0.823 (95% CI, 0.762–0.884) and a *P* value of .005 (Fig 3*B*). LFI, when added to the VALE model, was also found to be a significant risk factor (OR, 1.005; 95% CI, 1.002–1.009; $P = .004$) (Table 4).

We conducted a 10-fold cross-validation to prove the statistical power of adding LFI to the R_2eD and VALE models. Both models showed improvement in terms of AUC, accuracy, specificity, and other aspects (Table 5).

These results suggest that the addition of LFI to the previous models substantially enhances their predictive performance in assessing outcomes related to AVMs.

DISCUSSION

In this QDSA-based investigation, we undertook a comprehensive examination of hemodynamic characteristics associated with AVM rupture. Our study unearthed a robust association

Table 3: Univariate and multivariate logistic regression analyses of LFI and 3 LFI-combined models of factors associated with rupture in AVMs

	Univariable Analysis		Angioarchitecture Model		Hemodynamic Model		Combined Model	
	OR (95% CI)	*P* Value	OR (95% CI)	*P* Value	OR (95% CI)	*P* Value	OR (95% CI)	*P* Value
LFI	1.007 (1.003–1.010)	.001[a]	1.004 (1.001–1.008)	.02[a]	1.005 (1.001–1.009)	.009[a]	1.004 (1.000–1.007)	.03[a]
Mean nidus volume			0.979 (0.964–0.994)	.007[a]			0.959 (0.931–0.988)	.005[a]
Angioarchitecture								
Feeding artery dilation			1.047 (0.443–2.472)	.92			1.028 (0.429–2.461)	.95
Single feeding artery			0.783 (0.299–2.049)	.62			1.112 (0.768–1.608)	.57
Deep venous drainage			2.315 (1.018–6.947)	.05[a]			2.684 (1.132–6.361)	.03[a]
Diffuse nidus			2.863 (1.180–6.947)	.02[a]			2.990 (1.114–8.022)	.03[a]
Flow-related aneurysm			3.417 (1.521–7.678)	.003[a]			3.617 (1.544–8.474)	.003[a]
Hemodynamic								
Feeding artery								
FWHM (sec)					1.067 (0.703–1.619)	.76	0.949 (0.590–1.524)	.83
Drainage vein								
FWHM (sec)					1.218 (0.750–1.978)	.43	1.17 1 (0.695–1.974)	.55
MTT (ICA-sinus)					1.084 (0.811–1.448)	.59	1.297 (0.933–1.803)	.12
TRV					0.999 (0.997–1.001)	.26	1.004 (0.999–1.009)	.14

[a] Statistical significance ($P < .05$).

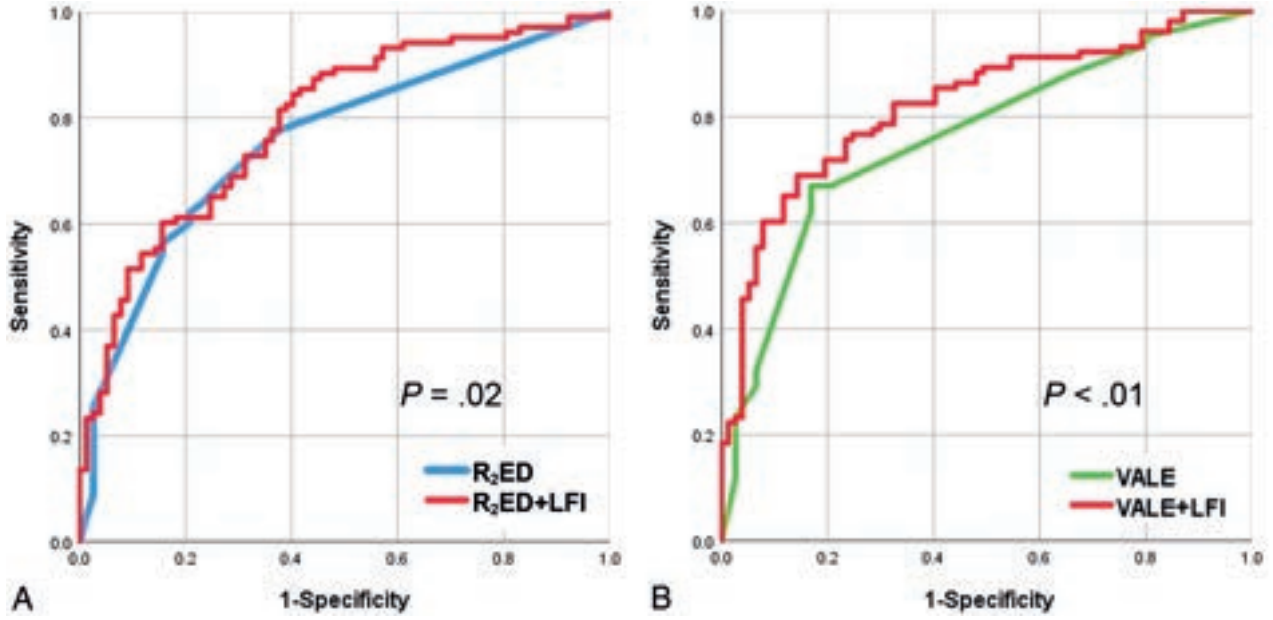

FIG 3. Comparison of 2 AVM rupture-prediction models before and after the inclusion of the LFI. *A*. Comparing R_2ED and R_2ED+LFI reveals that the original R_2ED AUC value is 0.755. After the inclusion of LFI, the AUC value increases to 0.791. Based on the DeLong' test, the significance level is $P = .03$. *B*, Comparing VALE and VALE+LFI reveals that the original VALE AUC value is 0.760. After the inclusion of LFI, the AUC value increases to 0.823. Based on DeLong test, the significance level is $P = .005$.

Table 4: Performance of previous models after the addition of LFI

Model	AUC (95% CI)	*P* Value	LFI (95% CI)	*P* Value
R_2eD	0.755 (0.684–0.826)	Reference	Reference	Reference
R_2eD + LFI	0.791 (0.725–0.857)	.03[a]	1.004 (1.000–1.008)	.04[a]
VALE	0.760 (0.689–0.831)	Reference	Reference	Reference
VALE + LFI	0.823 (0.762–0.884)	.005[a]	1.005 (1.002–1.009)	.004[a]

[a] Statistical significance ($P < .05$).

Table 5: 10-fold cross-validation of performance with 2 previous models after incorporating LFI

Model	AUC (95%CI)	*P* Value	Accuracy	Precision	Sensitivity	Specificity
R_2eD	0.601 (0.515–0.687)	Reference	0.611	0.674	0.621	0.597
R_2eD + LFI	0.624 (0.541–0.707)	.15	0.639	0.702	0.641	0.636
VALE	0.603 (0.518–0.688)	Reference	0.556	0.610	0.621	0.468
VALE + LFI	0.706 (0.629–0.783)	<.001[a]	0.683	0.717	0.738	0.610

[a] Statistical significance ($P < .05$).

between the hemodynamic parameter LFI and the occurrence of AVM rupture, signifying the extent of vascular filling within the lesion. Furthermore, we integrated the LFI into existing AVM rupture-prediction models, and this integration notably bolstered the predictive performance of these models. This outcome reconfirms the significant role of intravascular stasis and obstructive congestion as potential mechanisms contributing to AVM rupture. It also underscores the potential utility of incorporating hemodynamic parameters in the construction of multimodal prediction models, offering the prospect of improved accuracy in forecasting future AVM ruptures.

Owing to the intricate architecture of AVM lesions, prior investigations have often overlooked hemodynamic analysis of AVM niduses, primarily focusing on the feeding arteries or draining veins. For example, Lin et al[9], established a correlation between the Stasis Index of the principal draining vein and AVM rupture, Spetzler et al[3] associated elevated intravascular pressure in feeding arteries with AVM rupture, and Chen et al[11] identified a significant relationship between the TTP ratio of feeding arteries and draining veins and AVM microbleeds.' Nevertheless, the primary and most immediate site of AVM rupture is the AVM lesion itself, the anomalous niduslike structure. This lesion stands as the pivotal and direct site for understanding the hemodynamic mechanisms of AVM rupture. Regrettably, due to the intricate vascular architecture inherent in AVM lesions, techniques such as hemodynamic simulation, intravascular pressure measurement, and transcranial Doppler ultrasound are often not applicable for lesion analysis.

In a preceding study, Chen et al[6] pioneered an innovative method rooted in QDSA to directly assess the hemodynamic attributes of AVM lesions, proposing that TRV could signify the degree of intravascular stasis within the lesion. However, this study encountered several limitations, including measurement errors attributable to the complex 3D structure of the lesion and an ambiguous interpretation of the meaning of FWHM. In this study, we introduce a novel parameter, the LFI, also founded on QDSA. LFI is derived from the ADW, a metric that reflects blood filling within the ROI and is subsequently normalized by volume. The LFI constitutes the second hemodynamic parameter

developed for the explicit characterization of intravascular stasis within AVM lesions.

The LFI takes inspiration from pervious hemodynamic research conducted in DSA and MR imaging.[16,20,21] At present, hemodynamic indices derived from QDSA focus more on the analysis of ROI curves, because certain mathematic characteristics within these curves could reflect the blood-flow condition.[13,22,23] In contrast, there are notable gaps in research pertaining to the AUC of ROIs. In QDSA, the AUC is typically regarded as the volume of contrast agent passing through the ROIs, serving as an indirect measure of blood-flow volume. In our exploration of the AUC, we drew inspiration from the concept of the ADW, as defined by Raoult et al[24] and Kramer et al.[25] In their research, ADW is defined as a specified time window that theoretically represented good arterial filling with no significant venous contamination. We hypothesize that during the time window represented by ADW, the AVM nidus undergoes maximal blood inflow throughout the entire "inflow-outflow" process. This hypothesis suggests that during this specific period, the perfusion pressure within the nidus exceeds that of other time intervals. The numeric value of the ADW, corresponding to the difference in AUC between arterial and venous phases, is presumed to reflect the discrepancy in blood flow between arteries and veins. A larger ADW indicates a more substantial difference in blood flow between these 2 vascular components. However, as shown in Table 2, there is no statistically significant difference in the ADW between the ruptured and nonruptured groups. By examining the ROI as well as relevant factors affecting AUC, we found that it is necessary to combine this hemodynamic with some fundamental characteristics of AVM to enhance its specificity in discriminating ruptured cases. In fact, nidus volume is the most significant factor affecting the AUC, and ADW represents the maximum filling in the ROI. Therefore, the maximum filling degree per unit volume of the lesion can be calculated by dividing the ADW by the nidus volume—that is, the LFI (ADW/volume [nidus]). In this context, we contend that LFI represents the maximum prefusion pressure endured by the lesion within a unit volume. A higher LFI suggests an elevated risk of rupture.

Volume is a key parameter in the LFI calculation process. However, the question of whether AVM volume contributes to the risk of rupture remains debated within the academic community.[18,26–29] In this study, data revealed an association between smaller lesions and rupture. To mitigate the impact of lesion volume on the results, we attempted to normalize the results obtained from the ADW by dividing them by the lesion volume, yielding a unit volume blood-filling index amenable to cross-case comparison. This concept is reminiscent of the TRV, in which lower TRV values were correlated with higher Stasis Indices, indicating sluggish blood flow within AVM lesions. TRV is derived by dividing the FWHM by the maximum diameter of the AVM. Similar to our study, a trend of smaller lesion sizes in the ruptured group was observed, thereby leading us to postulate that the LFI and TRV both reflect, to some extent, blood volume filling and stasis within the lesion.

Stasis of blood within AVM lesions may potentially lead to rupture, with underlying mechanisms likely involving chronic mechanical stress exerted on the vessel walls, triggering inflammatory responses and subsequent endothelial damage, diminished deformability, and causing eventual rupture.[11,30,31] Studies by Fry[32] demonstrated the impact of shear stress on flow-related changes in venous endothelial cells, while Frösen et al[31] established that high wall shear stress conditions activate proinflammatory signaling pathways within vascular endothelial cells, driving remodeling in unruptured intracranial aneurysms.' Within our study, this mechanism of rupture is reflected by an elevated LFI, signifying greater unit volume of blood filling.

Univariate analysis indicated that the arterial Stasis Index, TRV, and LFI all demonstrated statistical differences between the 2 groups; however, in multivariate analysis, only LFI remained statistically significant. Consequently, we posit that all 3 parameters mentioned above exert some influence on rupture, yet LFI is the most sensitive indicator with the greatest discriminatory capacity. We attribute this phenomenon to 2 parameters used in the calculation of LFI. We have incorporated volume and the ADW, both of which have been established in multiple studies as having distinct differentiating significance for filling and rupture. The synergy of these 2 parameters amplifies the credibility and discriminative capability of LFI. In further research, our goal is to substantiate the reliability and precision of LFI using more direct measurement techniques, including computational fluid dynamics modeling of the lesion or direct prefusion pressure measurement.

According to the definition of ADW, we believe it reflects the degree of blood-flow filling within the AVM nidus during a specified time window. However, it lacks quantifiability and comparability across cases. Therefore, we attempted to normalize the ADW by dividing it by the volume of the AVM lesion, resulting in a quantitative metric to assess the degree of blood filling within the lesion. Due to the cross-sectional nature of this study, long-term follow-up results for patients with nonruptured AVMs with high LFI levels are unavailable. However, the results demonstrate statistically significant differences in LFI levels among patients with ruptured AVMs, aligning with our hypothesis of a correlation between high perfusion within the lesion volume and rupture. Therefore, we aim to conduct future prospective cohort studies to confirm the predictive ability of LFI for rupture occurrence.

In this study, a comprehensive evaluation of baseline characteristics, angioarchitecture, and hemodynamic features revealed several key insights. Angioarchitecture characteristics differed between the ruptured and unruptured groups, with factors such as feeding artery dilation, single feeding artery, deep venous drainage, single draining vein, drainage vein stenosis, diffuse nidus, and flow-related aneurysms demonstrating significant associations with rupture risk. Hemodynamic parameters, including TTP, MTT, FWHM, ADW, TRV, Stasis Index, and LFI, were also evaluated. While some differences in these parameters were observed, LFI stood out as a robust risk factor of AVM rupture.

Study Limitations

This study has certain limitations. First, the analysis for all enrolled patients was conducted postadmission, and ruptured AVMs may exhibit temporal variations in vascular architecture and hemodynamics. These changes could impact the reliability of the conclusions. Therefore, future research will require a larger sample of patients with prerupture imaging and long-term follow-up observations. Second, QDSA is based on 2D imaging,

which may have limitations such as overlapping structures. Further research using 3D and 4D imaging for hemodynamic analysis may provide a more accurate reflection of pressure within the lesion. Third, this study relied on cross-sectional data, introducing the potential for selection bias to impact the findings. Moreover, the emphasis of the study is on revealing the correlation between LFI and AVM rupture, rather than establishing predictive capabilities or causal relationships. This limitation restricts the direct clinical applicability of the study's results. To bolster the reliability and robustness of the findings, further validation with a larger prospective cohort is imperative.

CONCLUSIONS

In this cross-sectional study, we discovered that a high-filling state of AVM lesions, indicated by elevated LFI levels, is associated with rupture. This association could be a result of excessive arterial perfusion, and it is necessary to evaluate QDSA hemodynamic parameters in the assessment of AVM rupture risk.

ACKNOWLEDGMENTS

We would like to express our gratitude to Beijing Tiantan Hospital for their technical support in this research.

Disclosure forms provided by the authors are available with the full text and PDF of this article at www.ajnr.org.

REFERENCES

1. Abecassis IJ, Xu DS, Batjer HH, et al. **Natural history of brain arteriovenous malformations: a systematic review.** *Neurosurg Focus* 2014;37:E7 CrossRef Medline
2. Rutledge C, Cooke DL, Hetts SW, et al. **Brain arteriovenous malformations.** *Handb Clin Neurol* 2021;176:171–78 CrossRef Medline
3. Spetzler RF, Hargraves RW, McCormick PW, et al. **Relationship of perfusion pressure and size to risk of hemorrhage from arteriovenous malformations.** *J Neurosurg* 1992;76:918–23 CrossRef Medline
4. Stapf C, Mast H, Sciacca RR, et al. **Predictors of hemorrhage in patients with untreated brain arteriovenous malformation.** *Neurology* 2006;66:1350–55 CrossRef Medline
5. Burkhardt JK, Chen X, Winkler EA, et al. **Delayed venous drainage in ruptured arteriovenous malformations based on quantitative color-coded digital subtraction angiography.** *World Neurosurg* 2017;104:619–27 CrossRef Medline
6. Chen Y, Chen P, Li R, et al. **Rupture-related quantitative hemodynamics of the supratentorial arteriovenous malformation nidus.** *J Neurosurg* 2023;138:740–49 CrossRef Medline
7. Li Z, Chen Y, Chen P, et al. **Quantitative evaluation of hemodynamics after partial embolization of brain arteriovenous malformations.** *J Neurointerv Surg* 2021;14:1112–17 CrossRef Medline
8. Hu YS, Lee CC, Wu HM, et al. **Stagnant venous outflow predicts brain arteriovenous malformation obliteration after gamma knife radiosurgery without prior intervention.** *Neurosurgery* 2020;87:338–47 CrossRef Medline
9. Lin TM, Yang HC, Lee CC, et al. **Stasis index from hemodynamic analysis using quantitative DSA correlates with hemorrhage of supratentorial arteriovenous malformation: a cross-sectional study.** *J Neurosurg* 2019;132:1574–82 CrossRef Medline
10. Lin CJ, Chen KK, Hu YS, et al. **Quantified flow and angioarchitecture show similar associations with hemorrhagic presentation of brain arteriovenous malformations.** *J Neuroradiol* 2023;50:79–85 CrossRef Medline
11. Chen X, Cooke DL, Saloner D, et al. **Higher flow is present in unruptured arteriovenous malformations with silent intralesional microhemorrhages.** *Stroke* 2017;48:2881–84 CrossRef Medline
12. Li R, Chen P, Han H, et al. **Association of nidus size and rupture in brain arteriovenous malformations: Insight from angioarchitecture and hemodynamics.** *Neurosurg Rev* 2023;46:216 CrossRef Medline
13. Wang J, Cheng JJ, Huang KY, et al. **Quantitative assessment of angiographic perfusion reduction using color-coded digital subtraction angiography during transarterial chemoembolization.** *Abdom Radiology (NY)* 2016;41:545–52 CrossRef Medline
14. Atkinson RP, Awad IA, Batjer HH, et al; Joint Writing Group of the Technology Assessment Committee American Society of Interventional and Therapeutic Neuroradiology; Joint Section on Cerebrovascular Neurosurgery a Section of the American Association of Neurological Surgeons and Congress of Neurological Surgeons; Section of Stroke and the Section of Interventional Neurology of the American Academy of Neurology. **Reporting terminology for brain arteriovenous malformation clinical and radiographic features for use in clinical trials.** *Stroke* 2001;32:1430–42 CrossRef Medline
15. Lv X, Wu Z, Jiang C, et al. **Angioarchitectural characteristics of brain arteriovenous malformations with and without hemorrhage.** *World Neurosurg* 2011;76:95–99 CrossRef Medline
16. Dautry R, Edjlali M, Roca P, et al. **Interest of HYPR flow dynamic MRA for characterization of cerebral arteriovenous malformations: comparison with TRICKS MRA and catheter DSA.** *Eur Radiol* 2015;25:3230–37 CrossRef Medline
17. Todaka T, Hamada J, Kai Y, et al. **Analysis of mean transit time of contrast medium in ruptured and unruptured arteriovenous malformations: a digital subtraction angiographic study.** *Stroke* 2003;34:2410–14 CrossRef Medline
18. Feghali J, Yang W, Xu R, et al. **R_2eD AVM score.** *Stroke* 2019;50:1703–10 CrossRef Medline
19. Chen Y, Han H, Meng X, et al. **Development and validation of a scoring system for hemorrhage risk in brain arteriovenous malformations.** *JAMA Netw Open* 2023;6:e231070 CrossRef Medline
20. Benson JC, Chiu S, Flemming K, et al. **MR characteristics of unruptured intracranial arteriovenous malformations associated with seizure as initial clinical presentation.** *J Neurointerv Surg* 2020;12:186–91 CrossRef Medline
21. Scharf J, Brauherr E, Forsting M, et al. **Significance of haemorrhagic lacunes on MRI in patients with hypertensive cerebrovascular disease and intracerebral haemorrhage.** *Neuroradiology* 1994;36:504–08 CrossRef Medline
22. Chen CW, Wong HF, Ye YL, et al. **Quantitative flow measurement after placing a flow diverter for a distal internal carotid artery aneurysm.** *J Neurointerv Surg* 2017;9:1238–42 CrossRef Medline
23. Chen Y, Ma L, Yang S, et al. **Quantitative angiographic hemodynamic evaluation after revascularization surgery for moyamoya disease.** *Transl Stroke Res* 2020;11:871–81 CrossRef Medline
24. Raoult H, Bannier E, Maurel P, et al. **Hemodynamic quantification in brain arteriovenous malformations with time-resolved spin-labeled magnetic resonance angiography.** *Stroke* 2014;45:2461–64 CrossRef Medline
25. Kramer H, Michaely HJ, Requardt M, et al. **Effects of injection rate and dose on image quality in time-resolved magnetic resonance angiography (MRA) by using 1.0M contrast agents.** *Eur Radiol* 2007;17:1394–402 CrossRef Medline
26. Kim H, Salman RA, McCulloch CE, et al; MARS Coinvestigators. **Untreated brain arteriovenous malformation.** *Neurology* 2014;83:590–97 CrossRef Medline
27. Hernesniemi JA, Dashti R, Juvela S, et al. **Natural history of brain arteriovenous malformations: a long-term follow-up study of risk of hemorrhage in 238 patients.** *Neurosurgery* 2008;63:823 CrossRef Medline
28. Ai X, Ye Z, Xu J, et al. **The factors associated with hemorrhagic presentation in children with untreated brain arteriovenous malformation: a meta-analysis.** *J Neurosurg Pediatr* 2018;23:343–54 CrossRef Medline

29. Chen Y, Meng X, Ma L, et al. **Contemporary management of brain arteriovenous malformations in mainland China: a Web-based nationwide questionnaire survey.** *Chin Neurosurg J* 2020;6:26 CrossRef Medline
30. Kim H, Su H, Weinsheimer S, et al. **Brain arteriovenous malformation pathogenesis: a response-to-injury paradigm.** *Acta Neurochir Suppl* 2011;111:83–92 CrossRef Medline
31. Frösen J, Cebral J, Robertson AM, et al. **Flow-induced, inflammation-mediated arterial wall remodeling in the formation and progression of intracranial aneurysms**. *Neurosurg Focus* 2019;47:E21 CrossRef Medline
32. Fry DL. **Acute vascular endothelial changes associated with increased blood velocity gradients.** *Circ Res* 1968;22:165–97 CrossRef Medline

Modeling Robotic-Assisted Mechanical Thrombectomy Procedures with the CorPath GRX Robot: The Core-Flow Study

Alejandro Tomasello, David Hernández, Jiahui Li, Riccardo Tiberi, Eila Rivera, Joan Daniel Vargas, Cristina Losada, Magda Jablonska, Marielle Esteves, Maria Lourdes Diaz, Judith Cendrero, Manuel Requena, Francesco Diana, Marta De Dios, Trisha Singh, Laura Ludovica Gramegna, and Marc Ribo

ABSTRACT

BACKGROUND AND PURPOSE: Endovascular robotic devices may enable experienced neurointerventionalists to remotely perform endovascular thrombectomy. This study aimed to assess the feasibility, safety, and efficacy of robot-assisted endovascular thrombectomy compared with manual procedures by operators with varying levels of experience, using a 3D printed neurovascular model.

MATERIALS AND METHODS: M1 MCA occlusions were simulated in a 3D printed neurovascular model, linked to a CorPath GRX robot in a biplane angiography suite. Four interventionalists performed manual endovascular thrombectomy ($n = 45$) and robot-assisted endovascular thrombectomy ($n = 37$) procedures. The outcomes included first-pass recanalization (TICI 2c–3), the number and size of generated distal emboli, and procedural length.

RESULTS: A total of 82 experimental endovascular thrombectomies were conducted. A nonsignificant trend favoring the robot-assisted endovascular thrombectomy was observed in terms of final recanalization (89.2% versus manual endovascular thrombectomy, 71.1%; $P = .083$). There were no differences in total mean emboli count (16.54 [SD, 15.15] versus 15.16 [SD, 16.43]; $P = .303$). However, a higher mean count of emboli of >1 mm was observed in the robot-assisted endovascular thrombectomy group (1.08 [SD, 1.00] versus 0.49 [SD, 0.84]; $P = .001$) compared with manual endovascular thrombectomy. The mean procedural length was longer in robot-assisted endovascular thrombectomy (6.43 [SD, 1.71] minutes versus 3.98 [SD, 1.84] minutes; $P < .001$). Among established neurointerventionalists, previous experience with robotic procedures did not influence recanalization (95.8% were considered experienced; 76.9% were considered novices; $P = .225$).

CONCLUSIONS: In a 3D printed neurovascular model, robot-assisted endovascular thrombectomy has the potential to achieve recanalization rates comparable with those of manual endovascular thrombectomy within competitive procedural times. Optimization of the procedural setup is still required before implementation in clinical practice.

ABBREVIATIONS: BGC = balloon guide catheter; EVT = endovascular thrombectomy; MA = manual; MT = mechanical thrombectomy; RA = robot-assisted; SR = stent retriever

Mechanical thrombectomy (MT) is the most effective treatment for acute ischemic stroke due to large-vessel occlusion when combined with IV-tPA, unless contraindicated, and is currently strongly recommended by all therapeutic guidelines.[1,2] However, logistic and geographic limitations in the availability of rapid performance of the thrombectomy procedure create geographic inequities among territories due to the procedure being more accessible in urban areas than in remote rural locations distant from major cities.[2-4] Appropriate MT programs require not only modern angiography suites but also certified physicians who are well-trained in neurointerventional procedures and remain in continual contact with the neuroscientific society; this scenario ensures the highest-quality standards. In recent years, endovascular robotic devices have emerged as a revolutionary technology that may transform the field of neurointerventional treatment.

The CorPath GRX System (Corindus) is the first FDA-cleared and CE Marked medical device for percutaneous coronary and vascular procedures. It uses articulated robotic arms with multiple degrees of freedom to handle microguidewires and microcatheters, enabling submillimeter movements of both devices to

Received August 29, 2023; accepted after revision January 12, 2024.

From the Interventional Neuroradiology Section (A.T., D.H., J.D.V., C.L., M. Requena, F.D., M.D.D., T.S.), Stroke Research (J.L., RT., M.J., J.C., M. Requena, M. Ribo) Vall d'Hebron Institut de Recerca (E.R., F.D., L.L.G.), Stroke Unit (M. Requena, M. Ribo), Neurology Department Experimental Surgery Unit (M.E.), Vall d'Hebron Barcelona Hospital Campus, Barcelona, Spain; Departamento de Medicina (A.T.), Universitat Autònoma de Barcelona, Barcelona, Spain; 2nd Department of Radiology (M.J.), Medical University of Gdańsk, Gdańsk, Poland; and Departament De Radiologia Vascular Interventista (M.L.D.), Hospital General Universitario Arnau de Villanova, Lleida, Spain.

Please address correspondence to Alejandro Tomasello, MD, Interventional Neuroradiology Section, Vall d'Hebron University Campus Hospital, Pg. Vall d'Hebron, 119-129 08035 Barcelona, Spain; e-mail: alejandrotomasello@gmail.com

Indicates article with online supplemental data.

http://dx.doi.org/10.3174/ajnr.A8205

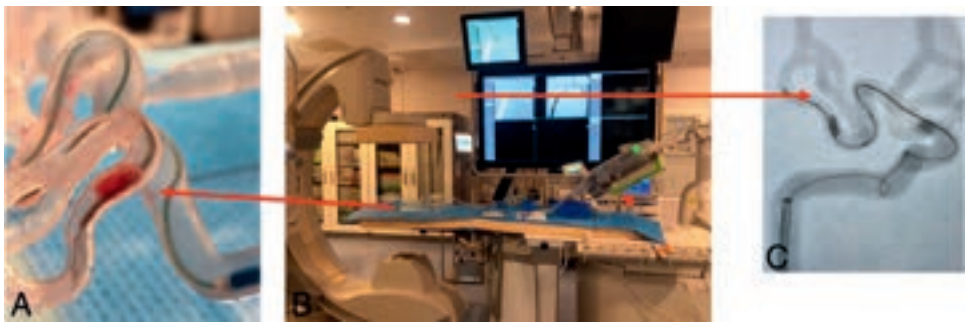

FIG 1. A benchtop 3D printed vascular model with a thrombus inside (*A*) was connected to a Corindus CorPath GRX robot (*B*, *arrowhead*), and MT was performed using SRs (*C*).

perform precise neurovascular interventions. Physicians can control it remotely, reducing radiation exposure and providing a comfortable and more precise working distance.[5-7]

Studies focusing on the embolization of intracranial aneurysms have been published dating back to the first-in-human experience reported in 2018, in which a transradial diagnostic coronary angiography was performed.[6,7]

The potential use of robotic treatment in stroke thrombectomy procedures could represent a substantial advancement in stroke treatment, providing an alternative solution for patients in nonurban areas. Robot-assisted endovascular thrombectomy (RA-EVT) could save time by avoiding long transfers; it also offers patients the possibility of being treated remotely by highly-skilled neurointerventionalists, ultimately improving patient outcomes and quality of life. Although the CorPath GRX, which is capable of performing biaxial procedures, is not fully optimized for thrombectomy procedures, it allows multiple catheter maneuvers and yields an accuracy comparable—or superior—to manual procedures.

The present study aims to describe a potential setup and explore the feasibility (reaching the occlusion), safety (distal embolization), and efficacy (recanalization) of RA-EVT compared with manual procedures performed by operators with varying levels of experience in robotics, using a 3D printed neurovascular model.

MATERIALS AND METHODS

Study Design

Two neurointerventionalists with >3 years of clinical experience in robotic-assisted neuroendovascular embolizations (ie, robot-experienced) performed both manual EVT (MA-EVT, $n = 18$) and RA-EVT ($n = 24$). One experienced neurointerventionalist in training for the robotic procedure (ie, robot-novice) performed both MA-EVT ($n = 6$) and RA-EVT ($n = 13$) procedures. Due to the exploratory nature of this pilot feasibility study, the total number of experiments performed by each interventionalist was not predefined on the basis of efficacy assumption; a total number between 19 and 21 experiments per operator was decided.

Neurovascular Flow Loop Model

The neurovascular model was based on the vascular anatomies extracted from anonymized CTA images. The manufacturing procedure comprises the following steps: medical image segmentation to generate the preliminary 3D geometry of the vascular anatomy; mesh modeling to simplify the anatomy and prepare a printable model; 3D printing setting; postprinting processing; and assembly.

Data in the DICOM format was imported and loaded in 3D Slicer (http://www.slicer.org),[8,9] where opacity threshold segmentation was performed to obtain the preliminary 3D geometry of the model. The preliminary 3D geometry was exported to Autodesk Meshmixer (https://meshmixer.com/)[10] for the modeling stage and exported to PreForm (Formlabs) to configure the printing material, resolution, optimal geometry orientation, and support structure for 3D printing. The model was printed with commercially available photopolymer resin Elastic 50A at a resolution of 100 μm with a Form 3 SLA printer (Formlabs). The postprinting process consisted of removing support structures from the model, a 10-minute dip in isopropyl alcohol, and exposure to 305-nm ultraviolet light at a temperature of 60°C for 10 minutes. After the postprocessing, the model parts were assembled to constitute the final version of the neurovascular model, which includes the aortic arch, bilateral carotid arteries, MCAs (up to 2 distal M2 MCA branches), anterior cerebral arteries (up to the proximal A2), anterior communicating artery, posterior communicating arteries, and posterior cerebral arteries (up to the proximal P2 posterior cerebral artery segments).

The neurovascular model was connected in a flow-loop setup to mimic blood circulation. The experimental setup comprised a hydraulic pump recirculating saline solution at 800 mL/min, a 3D printed model, and a 100-μm filter at the outflow of the model to collect the periprocedural emboli. All elements were connected through a silicone tubing system. To simulate the transfemoral access, we connected an 8F sheath attached to a silicone tube to the descending aorta. An inflow filter was added between the hydraulic pump and the neurovascular model to filter out the undesired particles introduced into the system by reused devices.

Experimental Thrombectomy Setup

The study was performed using biplane angiography (Clarity, Philips Healthcare): As previously described,[11] 2 × 4 mm (radiopaque) clot analogs were made from porcine blood and used to create arterial occlusions in a benchtop 3D printed model (Fig 1*A*).[12]

The CorPath CRX robot, consisting of a control console and a robotic unit equipped with an extension arm that can hold a single-use cassette, was installed in the interventional neuroradiology section. The control console, enabling the operator to perform procedures comfortably while seated, was placed in the RX control

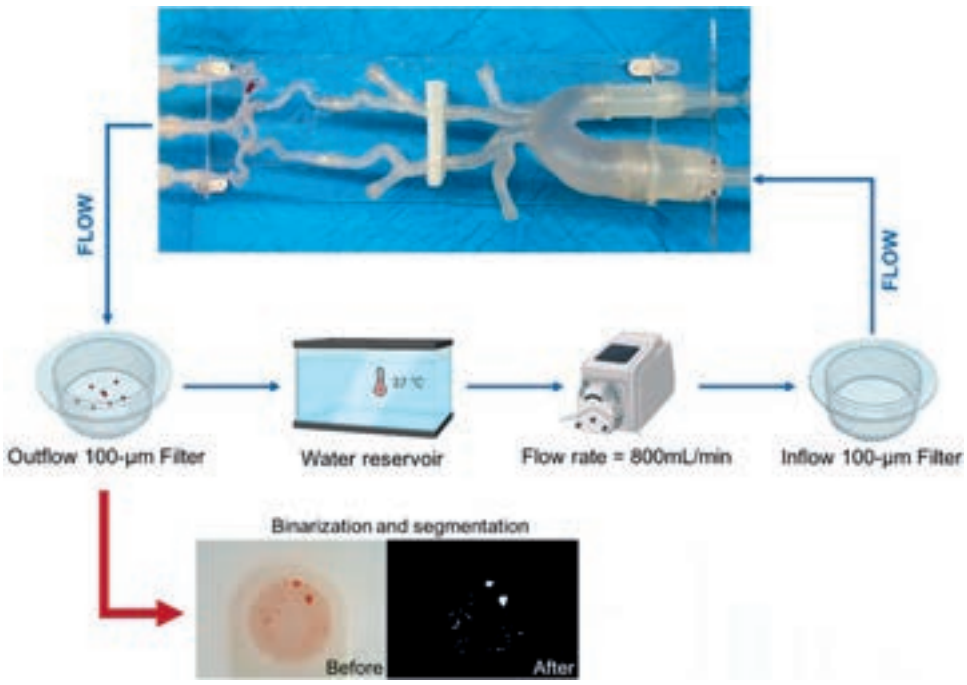

FIG 2. Experimental setup for robot-assisted and manual EVTs.

room. The extension arm and robotic unit were positioned on the lateral side of the table in the angiosuite. A single-use cassette was loaded with a microcatheter and a balloon guide catheter (BGC) (Gateway; Stryker), both of which were connected to the neurovascular model.

The robotic system is currently unable to perform catheterization of the aortic arch because it is limited to an advancement movement of 20 cm. An initial assessment of the optimal positioning of the different devices was performed. Due to the abovementioned limited range of movement of the microcatheter when using the robot, the limiting factor to reach and cross the clot with the microcatheter is the initial position of the BGC in the ICA. We identified the lowest point in the ICA in which the tip of the BGC should be manually positioned before initiating the RA-EVT for different occlusion locations (Fig 2) and decided to place it in the vertical part of the petrous segment of the ICA. Given this limitation, RA-EVT was considered optimal for occlusions located in the ICA and in the M1 segment of the MCA and in any case beyond the proximal M2 branches.

After clot embolization, experiments were allocated into one of the following treatment arms: 1) robot-experienced/MA-EVT; 2) robot-experienced/RA-EVT; 3) robot-novice/MA-EVT; 4) robot-novice/RA-EVT. A 6F BGC was manually advanced by an experienced specialist nurse to the level of the distal ICA, then a 0.021-inch microcatheter (Phenom 21; Medtronic) was manually advanced to the level of the tip of the BGC. For RA-EVT procedures, the microcatheter and a 0.014-inch microguidewire (Synchro 2; Stryker) were then connected to the CorPath GRX robot by a trained assistant nurse; the neurointerventionalist could take control of the system from the console located in the control room outside the angiosuite (Fig 1).

The thrombectomy technique, manual and robot-assisted, consisted of navigating the microcatheter under fluoroscopy to the MCA to cross the clot and then deploy a 4 × 40 mm stent retriever (SR: Solitaire X; Medtronic) from the M2 to the M1 segment of the MCA. After an embedding time of 1–2 minutes, the BGC was inflated and the SR was retrieved into the BGC under proximal flow arrest and continuous pump aspiration (Penumbra) (Fig 1*C*). For RA-EVT device exchanges in the robotic system, balloon inflation/deflation and aspiration were performed at the neurointerventionalist's indication, executed by an assistant nurse.

Each experiment consisted of a single pass per embolized clot. The primary outcome was first-pass recanalization (TICI 2c–3); the secondary outcome was the characterization of the collected distal emboli after each experiment.[13] The duration of the MT procedure was defined as the moment when the neurointerventionalist first initiated control of the console and began maneuvering the microcatheter, until completion of the first pass.

Characterization of Distal Emboli

Characterization of generated distal emboli has been performed as previously described.[12] The distal segments of the neurovascular model have vessels as narrow as 1 mm. Thus, most embolized particles would end up in the filter located at the outflow of the model. An RBG image of the particles in the filter was captured with a high-resolution digital camera (IPEVO, Inc., Sunnyvale, California) to analyze the emboli generated after each pass. Then, the RBG images were processed by an image-processing algorithm developed on Matlab R2020a (MathWorks). The algorithm comprises 2 primary stages: 1) RGB image binarization, which involves highlighting the emboli ("1") and removing the background ("0") (Fig 2); and 2) quantification of the major-axis length of each particle, using a circle of known dimensions as a reference. Additionally, the algorithm provides output such as the overall particle count as well as the number of emboli of >1 mm.

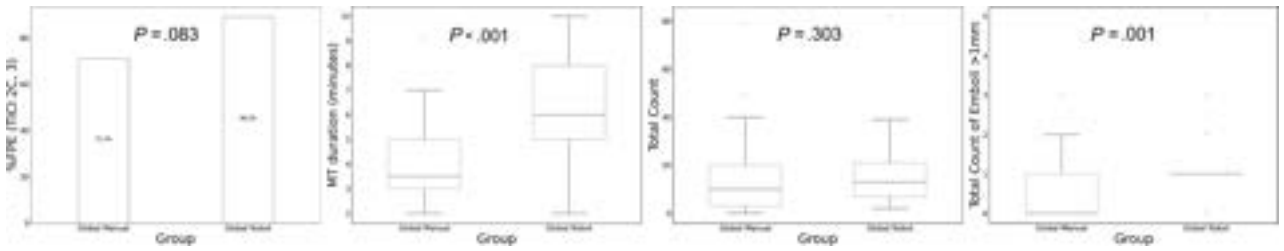

FIG 3. Boxplot analysis shows the difference in median values of various outcomes of thrombectomy (such as recanalization rate, procedural length, and distal emboli generation) when comparing all RA-EVTs and all MA-EVTs. FPE indicates first-pass effect.

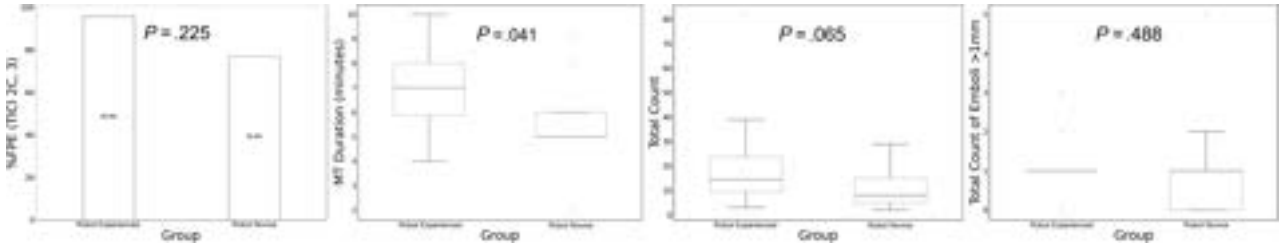

FIG 4. Boxplot analysis shows the difference in median values of various outcomes of thrombectomy (such as recanalization rate, procedural length, and distal emboli generation) when comparing robotic-EVT performed by a robotic-experienced interventional neuroradiologist and robotic-EVT performed by a robot-novice interventional neuroradiologist. FPE indicates first-pass effect.

Statistical Analysis

Results were expressed as mean (SD). Data were analyzed using the SciPy library from Python (https://scipy.org/). Normality was tested with Shapiro-Wilk test, and the Mann-Whitney *U* test was used to evaluate differences between RA-EVTs and MA-EVTs. Multiple subgroup analyses were performed to assess the safety and efficacy of the procedure among the 4 treatment arms using a χ^2 test.

As a subgroup analysis, differences in different outcomes (ie, final recanalization rate, number and dimension of emboli, and duration of the MT procedure) were compared between RA-EVT performed by a robot-experienced interventionalist and RA-EVT performed by a robot-novice neurointerventionalist who all had the same levels of experience in MT procedures (>10 years).

Statistical significance was $P < .05$.

RESULTS

We conducted a total of 82 experimental EVTs: 37 RA-EVTs and 45 MA-EVTs. Each interventionalist performed between 19 and 21 experiments. There were no robotic system failures or incidences that required the technician to step in during the thrombectomy attempts.

Robot-Assisted EVT versus Manual EVT

Overall, when comparing all RA-EVTs ($n = 37$) versus all MA-EVTs ($n = 45$), nonsignificant trends were observed in terms of the final recanalization rate in favor of RA-EVT: 89.2% versus MA-EVT: 71.1%; $P = .083$. The distal emboli analysis revealed a similar mean total count of particles (RA-EVT: 16.54 [SD, 15.15] versus MA-EVT: 15.16 [SD, 16.43]; $P = .303$); however, a significantly mean higher number of emboli of >1 mm in diameter were observed in the RA-EVT (1.08 [SD, 1] versus 0.49 [SD, 0.84]; $P = .001$). In addition, the mean RA-EVT procedural length was significantly longer (RA-EVT: 6.43 [SD, 1.71] minutes versus MA-EVT: 3.98 [SD, 1.84] minutes; $P < .001$) (Fig 3).

Robot-Experienced versus Robot-Novice Interventionalists

To assess the impact of the operator's prior experience in the use of the robot, we compared outcomes in experiments performed by robot-experienced ($n = 24$) and robot-novice ($n = 13$) interventionalists (Online Supplemental Data). The observed recanalization rates were 95.8% among the robot-experienced interventionalist and 76.9% among the robot-novice interventionalist ($P = .225$). No significant differences were observed in terms of total emboli count ($P = .065$) or number of emboli of >1 mm ($P = .488$). However, the mean procedural length was found to be slightly-but-significantly longer for robot-experienced (6.85 [SD, 1.54] minutes) compared with robot-novice neurointerventionalists (5.65 [SD, 1.80] minutes; $P = .041$) (Fig 4).

DISCUSSION

In this pilot study, we aimed to characterize the procedural setup and feasibility of performing MT with a robotic-assisted device using a 3D vascular model. We determined that the current robotic features allow an adequate setup to perform RA-EVT in intracranial occlusions located up to the proximal segments on the M2 MCA branches using BGCs and an SR. Thus, patient anatomy should allow navigation of the BGC up to the C2–C3 segments of the ICA. In these conditions, intracranial RA-EVTs performed by physicians with different levels of expertise in the use of the robot were able to achieve similar recanalization rates compared with MA-EVT. RA-EVT may not appear to provide a substantial advantage on its own; however, the current results present opportunities for future scenarios in which skilled neurointerventionalists could potentially perform the intracranial part

of a MT remotely on patients located in distant centers without specialized interventionalists.

In our study, the mean procedural time was slightly higher in the robotic arm compared with the manual procedure, particularly among physicians with experience in robotic procedures. However, in a potential scenario of remote RA-EVT, the absolute increase in the RA procedural time could be neglected if compared with the delays associated with transferring a patient to a comprehensive stroke center to receive EVT.

Furthermore, we aimed to test the safety of the procedure in terms of generation of distal emboli. Overall, our study showed that the total count of generated distal emboli is similar between RA-EVT and MA-EVT. However, we observed a significantly higher number of emboli of >1 mm in the RA-EVT group, which deserves special attention. These results may have been influenced by the use of a 3D plastic model because the friction coefficients between the clot/devices and the vessels are higher than those in human arteries. However, we cannot exclude the possibility that this high rate of clots of >1 cm may be due to the operator's lack of experience with the robot, including performing a procedure in the absence of haptic feedback. Nevertheless, we believe that in the preliminary phases of developing a device, it is important to collect data on the physician's performance with the device, because the data may provide insight into characteristics of the device and help identify areas for improvement. We anticipate that both operator experience and device performance can be improved in the future.

A possible explanation may lie in the relative absence of compliance with the current version of the robotic system when pushing the microcatheters across the thrombus. During manual procedures, the interventionalist can modulate the applied force to gradually advance the microcatheter, avoiding sudden tension releases of the system; however, this step may be more challenging with RA-EVT. Sudden tension releases of the system may also be exacerbated by the increased vessel wall friction of the 3D models compared to a patient's arteries. However, robotic systems have the potential to include automatic compensation and adjustment systems with the ability to optimize microcatheter navigation through the occluding clots.

Most interesting, expert physicians in robot handling achieved results similar to those of physicians with limited robotic exposure (Fig 4), suggesting that spreading this new technology with short learning curves among neurointerventionalists may be relatively straightforward.

Future developments of regional networks will likely consider performing a local MT by an interventionalist not dedicated to neuroendovascular procedures or opting for a remote RA-EVT performed by skilled neurointerventionalists to ensure universal and timely endovascular treatment of patients with stroke with large-vessel occlusions,.

To our knowledge, this is the first study that explores the feasibility of robotic assistance in the intracranial part of the MT. Our results suggest that further adjustments will make implementation of this technology possible in assisting acute ischemic procedures in rural areas, thus massively reducing workflow times.

The current CorPath GRX technology still presents limitations that prevent the immediate application of the studied model in clinical practice: It is currently unable to perform the catheterization of the supra-aortic trunks and deliver the microcatheter up to the clot occlusion. Moreover, the main limitation is the limited range of motion and the impossibility of controlling triaxial catheter systems, preventing the use of intermediate distal-access catheters that provide support during microcatheter navigation and allow distal aspiration.

Our pilot study aimed to provide a preliminary assessment of the feasibility of technology to assist in performing intracranial MT and to generate initial efficacy data. Our results are promising and represent a necessary step toward the implementation of robotics in MT procedures. In the future, integration of acquired vessel imaging, such as CTA or angiography, with the robotic system may enable the robot to recognize the anatomy and offer an assisted navigation in cases of challenging anatomy. Such development allowing a faster, more precise, and safer procedure may facilitate the expansion of an adoption of robotic procedures among less experienced operators or for remote assistance in rural regions.

Limitations

Our study has several limitations. A limited number of operators participated in the study, which may have affected the comparability of the observed outcomes among the various study groups. However, the operators—each having a varying level of experience—conducted multiple experiments to simulate multiple scenarios. Another important limitation is the use of a single 3D printed model, which is a significant constraint due to its limited comparability with real patients. Despite the neurovascular model being internally coated with hydrophilic agents, the friction coefficients between the clot/devices and the vessels are generally higher than those observed in human arteries. This difference may partially explain the increased number and size of distal emboli observed in the RA-EVT arm. Additionally, the model exhibits higher resistance to perforation than in vivo conditions, which hinders the assessment of such complications. Furthermore, a single 3D model was used precluding the wider evaluation according to anatomic variations. We concur with the importance of further exploring the use of robotics to support the catheterization of challenging anatomies in future studies with new iterations of the robotic devices.

CONCLUSIONS

In a 3D printed neurovascular model, RA-EVT has the potential to achieve recanalization rates comparable with MA-EVT within competitive procedural times. Optimization of the procedural setup is still required before implementation in clinical practice.

Disclosure forms provided by the authors are available with the full text and PDF of this article at www.ajnr.org.

REFERENCES

1. Majoie CB, Cavalcante F, Gralla J, et al; IRIS Collaborators. **Value of intravenous thrombolysis in endovascular treatment for large-vessel anterior circulation stroke: individual participant data meta-analysis of six randomised trials.** *Lancet* 2023;402:965–74 CrossRef Medline
2. Kamel H, Parikh NS, Chatterjee A, et al. **Access to mechanical thrombectomy for ischemic stroke in the United States.** *Stroke* 2021; 52:2554–61 CrossRef Medline
3. Perez de la Ossa N, Abilleira S, Dorado L, et al; Catalan Stroke Code and Reperfusion Consortium. **Access to endovascular treatment in**

remote areas: analysis of the Reperfusion Treatment Registry of Catalonia. *Stroke* 2016;47:1381–84 CrossRef Medline
4. El Nawar R, Lapergue B, Piotin M, et al; ETIS Investigators. **Higher annual operator volume is associated with better reperfusion rates in stroke patients treated by mechanical thrombectomy: the ETIS Registry.** *JACC Cardiovasc Interv* 2019;12:385–91 CrossRef Medline
5. Mahmud E, Schmid F, Kalmar P, et al. **Feasibility and safety of robotic peripheral vascular interventions: results of the RAPID Trial.** *JACC Cardiovasc Interv* 2016;9:2058–64 CrossRef Medline
6. Mendes Pereira V, Rice H, De Villiers L, et al. **Evaluation of effectiveness and safety of the CorPath GRX robotic system in endovascular embolization procedures of cerebral aneurysms.** *J Neurointerv Surg* 2023 Oct 4. [Epub ahead of print] CrossRef Medline
7. Karas PJ, Lee JE, Frank TS, et al. **Robotic-guided direct transtemporal embolization of an indirect carotid cavernous fistula.** *J Neurointerv Surg* 2023;15:1122–23 CrossRef Medline
8. Kikinis R, Piper S, Vosburgh, K. **3D Slicer: A Platform for Subject-Specific Image Analysis, Visualization, and Clinical Support**. In: Jolesz FA. *Introperative Imaging and Imaging-Guided Therapy*. Springerlink; 2014:277–89
9. Fedorov A, Beichel R, Kalpathy-Cramer J, et al. **3D Slicer as an image computing platform for the Quantitative Imaging Network.** *Magn Reson Imaging* 2012 Nov;30(9):1323–41 CrossRef Medline
10. Autodesk MeshMixer. https://meshmixer.com/download.html.
11. Kan I, Yuki I, Murayama Y, et al. **A novel method of thrombus preparation for use in a swine model for evaluation of thrombectomy devices.** *AJNR Am J Neuroradiol* 2010;31:1741–43 CrossRef Medline
12. Li J, Tiberi R, Canals P, et al. **Double stent-retriever as the first-line approach in mechanical thrombectomy: a randomized in vitro evaluation.** *J Neurointerv Surg* 2023;15:1224–28 CrossRef Medline
13. Li J, Tiberi R, Bhogal P, et al. **Impact of stent-retriever tip design on distal embolization during mechanical thrombectomy: a randomized in vitro evaluation.** *J Neurointerv Surg* 2023;16:285–89 CrossRef Medline

Impact of Target Artery Size on the Performance of Aspiration Thrombectomy: Insights from a Swine Model with Real-Time Visualization

Ichiro Yuki, Timothy Shimizu, Hemdeep Kaur, Zachary W. Hsu, Earl Steward, and Shuichi Suzuki

ABSTRACT

SUMMARY: A novel swine model was developed to investigate the underlying reasons for the failure of aspiration thrombectomy. The model allows direct visualization of the target artery during thrombectomy in vessels of different sizes. The behavior of the target artery undergoing aspiration thrombectomy was recorded with high-resolution digital microscopy and fluoroscopic visualization, providing valuable insight into how the different sizes of treated arteries affect the effectiveness of mechanical thrombectomy.

ABBREVIATIONS: CCA = common carotid artery; LVO = large-vessel occlusion; SCA = superficial cervical artery; TIMI = Thrombolysis in Myocardial Infarction

Aspiration thrombectomy is a widely used technique for treating acute ischemic stroke with large-vessel occlusion (LVO).[1-3] Recent advances in catheter technology have improved the effectiveness of the procedure, though the success rate of the first pass remains limited, ranging from 25.1% to 53.7% of cases.[4-6]

The primary reasons hindering successful outcomes were often explained as inadequate aspiration force, insufficient contact between the catheter tip and the clot surface, or clot fragmentation during the procedure.[7,8] Although a consensus exists with interventionalists that a larger-lumen aspiration catheter may enhance recanalization rates, this consensus remains a topic of ongoing debate with limited supporting evidence. To enhance our understanding of how aspiration thrombectomy works, studies using animal models such as swine, canines, and rabbits as well as human cadaver–based models have been conducted.[9-12] However, many aspects remain unknown, including how the size of the target vessel with different flow volumes affects the effectiveness of aspiration thrombectomy.

For bridging this knowledge gap, a novel swine LVO model was developed, enabling real-time visualization of target arteries undergoing mechanical thrombectomy. Two distinct vessel sizes were chosen as targets: the common carotid artery (CCA) and the superficial cervical artery (SCA), simulating the human ICA and M1 segment of the MCA, respectively. The study examined the behaviors of the target vessels during aspiration thrombectomy, encompassing vessel collapse, vessel traction, and local reverse blood flow, to investigate how the size of the target artery impacts the performance of the procedure.

By investigating the underlying causes of the failure of aspiration thrombectomy, this model has the potential to inform about the development of improved aspiration devices and enhance the refinement of endovascular techniques in clinical settings.

TECHNIQUE

All procedures were performed in accordance with the policies of the University of California, Irvine Chancellor's Institutional Animal Care and Use Committee. The SCA, also known as the omocervical artery, originates from the thyrocervical trunk in swine.[13] This straight branch, typically 2–3 mm in diameter with a bifurcation, simulates the human MCA,[14] and it was used to represent a small-diameter artery in this study. On the other hand, the CCA, typically 4–5 mm in diameter, was used to represent a large-diameter artery.

Under general anesthesia, a female swine was intubated and placed on the surgical table. In the supine position, a 20-cm straight skin incision was made along the sternocleidomastoid muscle. The connective tissue of the lateral and dorsal aspect of the muscle was surgically dissected to expose the SCA. Technical details are available elsewhere.[14] Subsequently, the medial connective tissue of the same muscle was dissected to expose the CCA. After carefully dissecting and removing the adventitial layer of the artery to optimize visibility during the procedure, approximately 15 cm of the arterial segment was exposed. A 4–0 Prolene suture (Ethicon) was meticulously placed around the artery. The degree of stenosis was assessed and adjusted to maintain it at <50% stenosis. In cases in which

Received October 21, 2023; accepted after revision January 15, 2024.

From the Departments of Neurosurgery (I.Y., T.S., H.K., Z.W.H., S.S.) and Surgery (E.S.), University of California, Irvine, Irvine, California.

Please address correspondence to Ichiro Yuki, MD, Department of Neurological Surgery, University of California Irvine Medical Center, 200 S. Manchester, Suite 210, Orange, CA 92868; e-mail: iyuki@hs.uci.edu

http://dx.doi.org/10.3174/ajnr.A8198

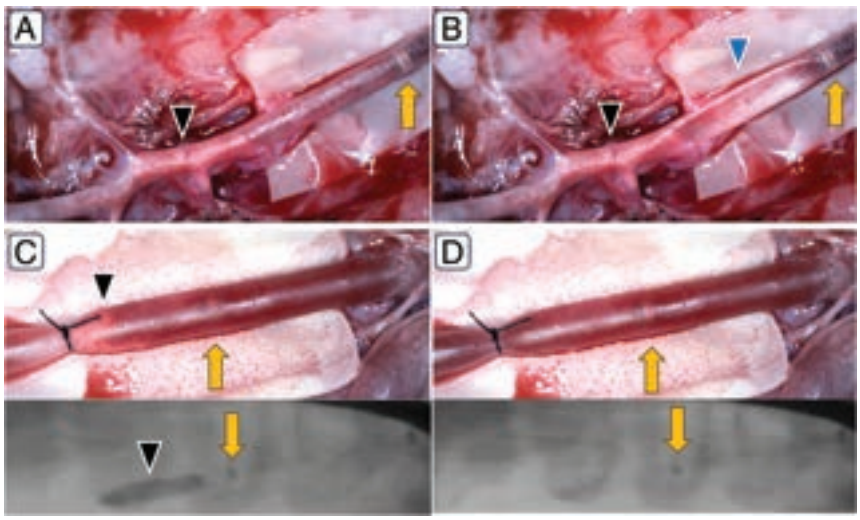

FIG 1. Direct visualization of the vessels undergoing aspiration thrombectomy. *A*, The SCA before remote aspiration. The surgically exposed SCA is occluded with a clot analog (*black arrowhead*). Note that the distal end of the aspiration catheter is visible through the translucent vessel wall (*yellow arrow*). *B*, The SCA after remote aspiration. Vessel collapse (*blue arrowhead*) is observed immediately after the application of the aspiration force. The position of the clot remains unchanged (*black arrowhead*), indicating an unsuccessful recanalization. *C*, The CCA before remote aspiration. A 5-0 Prolene suture is placed on the surgically exposed CCA to replicate mild stenosis and stabilize the clot analog (*black arrowhead*). The radiograph below shows that the tip of the catheter is remote from the clot analog (*black arrowhead*). *D*, The CCA after remote aspiration. A local reverse flow was induced near the tip of the aspiration catheter (*yellow arrowhead*), and the clot was aspirated into the catheter, resulting in successful recanalization. Note that there was no observed vessel collapse during the maneuver. The radiograph below shows that the clot analog is no longer visible because it was aspirated into the catheter.

vasospasm resulting from surgical maneuvers was observed in the target vessels, a topical application of papaverine (3 mg/mL) was administered to alleviate the vasospasm.

Intraprocedural, continuous observation of the target vessels was performed using a high-resolution digital microscope camera (Dino-Lite Edge 3.0 AM73115MTF; AnMo Electronics) (11.9 × 3.3 cm). The microscope camera has an extralong working distance, allowing the farthest available working distance of 70 cm with a magnification of 10×–70× at 45 frames per second. Real-time video images were displayed on a dedicated monitor, and the captured images were processed using the DinoCapture 2.0 software (Dino-Lite). Additionally, vessel size was verified in the angiographic images using ImageJ software (https://imagej.net/ij/download.html).

An angiographic system (OEC 9800; GE Healthcare) was used for selective DSA followed by endovascular procedures. An 8F femoral sheath was placed in the right femoral artery, and a 6F guiding sheath, 0.088-inch Ballast catheter (Balt), was navigated to the origin of the right subclavian artery followed by the SCA. Next, under roadmap image guidance, a clot analog was injected into the SCA. The fibrin-rich clot analogs used in this model were reproduced following the established methodology described in multiple publications in the past.[8,14,15] They were produced from allogeneic whole blood characterized by its fibrin-rich component using a modified chandler loop technique. A control angiogram was performed to confirm the complete occlusion of the target vessel. The same procedure was repeated for the CCA.

By means of the 2 different types of vessels described above, performance of aspiration thrombectomy was evaluated and recorded. We used different sizes of aspiration catheters: 0.058-inch ID (Catalyst 5; Stryker Neurovascular), 0.068-inch ID (React 68; Medtronic) and an 0.088-inch ID. The procedure was always initiated with remote aspiration with the tip of the catheter placed 20 mm away from the clot, and continuous aspiration of 4 minutes was applied using a 60-mL syringe. If no recanalization was seen, the aspiration catheter was advanced with 5-mm increments and the same maneuver was repeated. If remote aspiration failed, contact aspiration was performed with the aspiration catheter in direct contact with the clot analog under direct visualization.

Vessel behaviors under direct visualization during the procedure, such as vessel collapse, vessel traction, vasospasm, clot fragmentation, and cavitation in the target vessels, were recorded. After each procedure, the degree of reperfusion was described using the Thrombolysis in Myocardial Infarction (TIMI) scale. The typical behaviors of 2 different-sized vessels, the CCA group versus SCA group, undergoing aspiration thrombectomy were compared, and the mechanism of successful/unsuccessful reperfusion on each target artery was described.

RESULTS

A total of 3 CCAs and 4 SCAs in 3 animals with a mean weight of 68.3 kg (range, 56–87 kg) were surgically exposed, and concurrent fluoroscopic and transmural direct visualization were successfully performed in all vessels. All target vessels were successfully occluded (TIMI 0) immediately after the injection of the clot. In all cases, injected clot analogs, the tip of aspiration catheter, and the vessel behaviors during the thrombectomy procedure were observed and allowed us to assess the mechanism of successful/unsuccessful reperfusion.

The mean diameter was 5.2 mm (range, 5.0–5.5 mm) for the CCA group and 2.3 mm (2.0–3.0 mm) for the SCA group. Figure 1 shows the typical behavior of the vessels undergoing aspiration thrombectomy. In the SCA group (4 vessels) with remote aspiration, we observed the following findings: 1) vessel collapse (all 4 vessels): the immediate collapse of the vessel segment between the tip of catheter and the proximal end of the clot (no movement of the clot was seen during the aspiration regardless of the catheter size [058, 068, and 088 mm]); 2) vessel traction (1 case): vessel collapse followed by substantial traction of target vessel (approximately 20 mm) in 1 SCA sample, while the aspiration catheter (058 mm) was retracted with continuous aspiration. In the SCA group with contact aspiration, successful recovery of the clot was

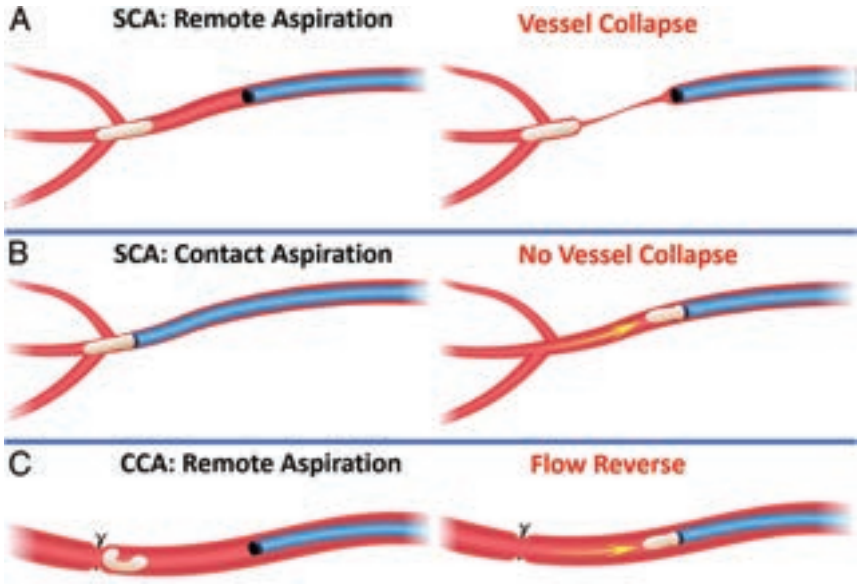

FIG 2. Schematic view showing the impact of vessel size on target vessel behavior during aspiration thrombectomy. *A*, SCA remote aspiration. The target vessel remains occluded with a clot analog after remote aspiration, and vessel collapse it seen. *B*, SCA contact aspiration. The tip of the catheter is placed against the proximal end of the clot. The clot is engulfed in the tip of the catheter, and successful recanalization is seen. *C*, CCA remote aspiration. A focal reverse flow is induced near the tip of the catheter, and the clot is aspirated into the catheter, achieving successful recanalization.

observed in 3 vessels (058 and 068 mm) (TIMI 3), and 1 vessel showed partial recanalization (TIMI 2) due to clot fragmentation during the retrieval (058 mm). In the CCA group with remote aspiration, successful recanalization was achieved in all 3 vessels (TIMI 3) and did not require contact aspiration. The aspiration catheters used were 068, 088, and 088 mm, respectively. Local reverse flow was generated during the aspiration, and none of the vessels showed vessel collapse except 1 in which a temporal reduction of the vessel diameter was seen at the beginning of the aspiration (088 mm). No vessel pulling and elongation during aspiration catheter pullback were observed in the CCA group. Figure 2 depicts a schematic view showing the impact of vessel size on target vessel behavior during aspiration thrombectomy.

DISCUSSION

The procedure, mechanical thrombectomy, incorporates a semiblinded maneuver, given that the operator lacks direct visibility of the clot or vessel being manipulated. Therefore, it remains uncertain whether the clot has been effectively engaged and captured during the aspiration thrombectomy until the devices are retrieved, followed by another control angiogram.

Flow arrest within the aspiration tube is often used as an indicator of successful clot capture during aspiration thrombectomy.[16] If no backflow is observed in the aspiration tube, which is under continuous negative pressure while withdrawing, it is often inferred that the clot has been captured inside the catheter or at its tip. However, flow arrest can also result from the catheter tip merely being in the collapsed vessel without engaging the clot. The animal model described in this report clearly demonstrated that vessel collapse can occur immediately after the application of aspiration in relatively small-sized vessels.

Previously reported various LVO models have described a similar phenomenon.[11,12] What remained unknown, however, was whether vessels of varying sizes have distinct responses to the same thrombectomy maneuver. The model presented in this report indicates that the performance of aspiration thrombectomy may indeed vary significantly depending on the vessel size, suggesting a need for potential adjustments in treatment strategies accordingly.

While this model sheds light on catheter-vessel interactions during thrombectomy, some limitations exist. For instance, human intracranial arteries are known to have different histologic features compared with peripheral arteries or arterioles. These arteries are less elastic, contain fewer elastic fibers, and have thinner layers of smooth muscle. The arteries used in our study were from swine; thus, variations stemming from different species should also be considered. Additionally, clot-related factors can impact aspiration thrombectomy outcomes, such as clot components, length, and fragility. Hence, further research with a larger sample size, diverse clot types, and systematic catheter variations, as well as stent retrievers, is warranted.

CONCLUSIONS

A new swine LVO model was created to study artery behavior undergoing aspiration thrombectomy. The model simulated vessel collapse, vessel traction, and reverse blood flow in vessels of different sizes, revealing how the size of the target vessel impacts the performance of the thrombectomy procedure. Further investigation with an increased number of sample sizes with different types of clot analogs and aspiration catheters is warranted to better understand the mechanism of aspiration thrombectomy.

Disclosure forms provided by the authors are available with the full text and PDF of this article at www.ajnr.org.

REFERENCES

1. Vargas J, Spiotta A, Fargen K, et al. **Long-term experience using the ADAPT technique for the treatment of acute ischemic stroke.** *J Neurointerv Surg* 2017;9:437–41 CrossRef
2. Turk AS, Frei D, Fiorelle D, et al. **ADAPT FAST study; a direct aspiration first pass technique for acute stroke thrombectomy.** *J Neurointerv Surg* 2014;6:260–64 CrossRef Medline
3. Lapergue B, Blanc R, Gory B, et al; ASTER Trial Investigators. **Effect of endovascular contact aspiration vs stent retriever on revascularization in patients with acute ischemic stroke and large vessel occlusion: the ASTER randomized clinical trial.** *JAMA* 2017;318:443–52 CrossRef Medline

4. Ducroux C, Piotin M, Gory B, et al; ASTER Trial Investigators. **First pass effect with contact aspiration and stent retrievers in the aspiration versus stent retriever (ASTER) trial.** *J Neurointerv Surg* 2020;12:386–91 CrossRef Medline
5. Zaidat OO, Castonguay AC, Linfante I, et al. **First pass effect: a new measure for stroke thrombectomy devices.** *Stroke* 2018;49:660–66 CrossRef Medline
6. Lapergue B, Blanc R, Costalat V, et al; ASTER Trial Investigators. **Effect of thrombectomy with combined contact aspiration and stent retriever vs stent retriever alone on revascularization in patients with acute ischemic stroke and large vessel occlusion: the ASTER2 randomized clinical trial.** *JAMA* 2021;326:1158–69 CrossRef Medline
7. Bernava G, Rosi A, Boto J, et al. **Direct thromboaspiration efficacy for mechanical thrombectomy is related to the angle of interaction between the aspiration catheter and the clot.** *J Neurointerv Surg* 2020;12:396–400 CrossRef Medline
8. Chueh JY, Wakhloo AK, Hendricks GH, et al. **Mechanical characterization of thromboemboli in acute ischemic stroke and laboratory embolus analogs.** *AJNR Am J Neuroradiol* 2011;32:1237–44 CrossRef Medline
9. Gory B, Bresson D, Rouchaud A, et al. **A novel swine model to evaluate arterial vessel injury after mechanical endovascular thrombectomy.** *Interv Neuroradiol* 2013;19:147–52 CrossRef Medline
10. Kan I, Yuki I, Murayama Y, et al. **A novel method of thrombus preparation for use in a swine model for evaluation of thrombectomy devices.** *AJNR Am J Neuroradiol* 2010;31:1741–43 CrossRef Medline
11. Liu Y, Abbasi M, Arturo Larco JL, et al. **Preclinical testing platforms for mechanical thrombectomy in stroke: a review on phantoms, in-vivo animal, and cadaveric models.** *J Neurointerv Surg* 2021;13:816–22 CrossRef Medline
12. Anagnostakou V, Epshtein M, Kühn AL, et al. **Preclinical modeling of mechanical thrombectomy**. *J Biomech* 2021;130:110894 CrossRef Medline
13. Damian A, Chirilean L, Tuns F, et al. **Features of the subclavian arteries and their branching in the domestic pig.** *Scientific Works Series C Veterinary Medicine* 2015;LXI(1):25–30
14. Yuki I, Kan I, Golshan A, et al. **A swine model to analyze arterial structural changes induced by mechanical thrombectomy.** *AJNR Am J Neuroradiol* 2013;34:E87–90 CrossRef Medline
15. Duffy S, Farrell M, McArdle K, et al. **Novel methodology to replicate clot analogs with diverse composition in acute ischemic stroke.** *J Neurointerv Surg* 2017;9:486–91 CrossRef Medline
16. Boisseau W, Escalard S, Fahed R, et al. **Direct aspiration stroke thrombectomy: a comprehensive review.** *J Neurointerv Surg* 2020;12:1099–106 CrossRef Medline

Lateral Compression Manipulation: A Simple Approach for Sizing Taller-Than-Wide Intracranial Aneurysms with the Woven EndoBridge Device

Han Seng Chew, Ming Yao Chong, Waleed Butt, Samer Al-Ali, Benjamin Butler, Mohammad Al-Tibi, Swarupsinh Chavda, and Saleh Lamin

ABSTRACT

BACKGROUND AND PURPOSE: The Woven EndoBridge (WEB) system has established itself as a safe and effective option for managing wide-neck bifurcation aneurysms. Addressing aneurysms with a greater height than width using conventional WEB-sizing methods has proved ineffective due to the inherent configuration of the devices. To overcome this limitation, we propose an intuitive approach that involves swapping the width and height dimensions of the aneurysm to determine the appropriate WEB size.

MATERIALS AND METHODS: A retrospective analysis was conducted on patients undergoing WEB embolization at a single neuroscience center from March 2013 to February 2023.

RESULTS: Twenty-five eligible aneurysms were identified, with the height dimension exceeding the width by an average of 2.33 mm (ranging from 1.4 to 4.5 mm). Of these, 20 cases adhered to the recommended sizing technique, resulting in a 100% success rate of adequate occlusion (14/20 complete occlusion, 6/20 proximal recess filling). In contrast, the outcomes for the remaining 5 cases that did not follow the proposed sizing method were less favorable ($P < .05$). Among these, 4 cases treated with undersized WEBs showed neck remnants during follow-up, and 1 patient who received an oversized WEB required device replacement during the same procedure.

CONCLUSIONS: The simple sizing method we proposed for treating taller-than-wide aneurysms has demonstrated promising results, allowing the WEB system to address twice the original size range of treatable aneurysms. Further research with a larger sample size is recommended.

ABBREVIATIONS: SL = single-layer; SLS = single-layer sphere; WEB = Woven EndoBridge; WOS = WEB Occlusion Scale

The Woven EndoBridge (WEB; MicroVention) device has emerged as a reliable and effective solution for the treatment of wide-neck intracranial bifurcation aneurysms.[1] Accurate device sizing is crucial for achieving favorable angiographic outcomes.[2] However, traditional sizing methods like the +1/−1 rule or referencing the manufacturer's sizing chart may not be able to deliver the necessary height extension to achieve an optimal fit for aneurysms characterized by a high height-to-dome ratio (Fig 1). To address this issue, we introduce an intuitive approach that prompts the device to undergo considerable lateral compression, leading to a substantial increase in its vertical extension. The main purpose of this article was to provide an in-depth exploration of the proposed sizing strategy and highlight its potential in enhancing the clinical utility of the WEB system.

MATERIALS AND METHODS

We conducted a retrospective review of patients who underwent WEB embolization at our institution from March 2013 to February 2023. We define an aneurysm as taller-than-wide when its height-to-dome ratio surpasses 1, enabling it to qualify for inclusion in the analysis.

Data collection included patient demographics, aneurysm characteristics, device parameters, and angiographic outcomes. Surveillance imaging protocols for individuals who undergo WEB embolization include DSA and MRA at 6-month and 2-year intervals. However, starting from 2020, due to the coronavirus 2019 pandemic and in adherence to local infection-control policies, all cases are exclusively followed up using MRA alone to minimize the risk of viral transmission.

Received November 21, 2023; accepted after revision January 16, 2024.

From the Department of Neuroradiology Queen Elizabeth Hospital Birmingham, Birmingham, UK.

Please address correspondence to Han Seng Chew, MD, Neuroradiology, Queen Elizabeth Hospital Birmingham, Mindelsohn Way, Birmingham, B15 2GW, United Kingdom of Great Britain and Northern Ireland, e-mail; hanseng.chew@uhb.nhs.uk; @hanseng78

Indicates open access to non-subscribers at www.ajnr.org

Indicates article with online supplemental data.

http://dx.doi.org/10.3174/ajnr.A8172

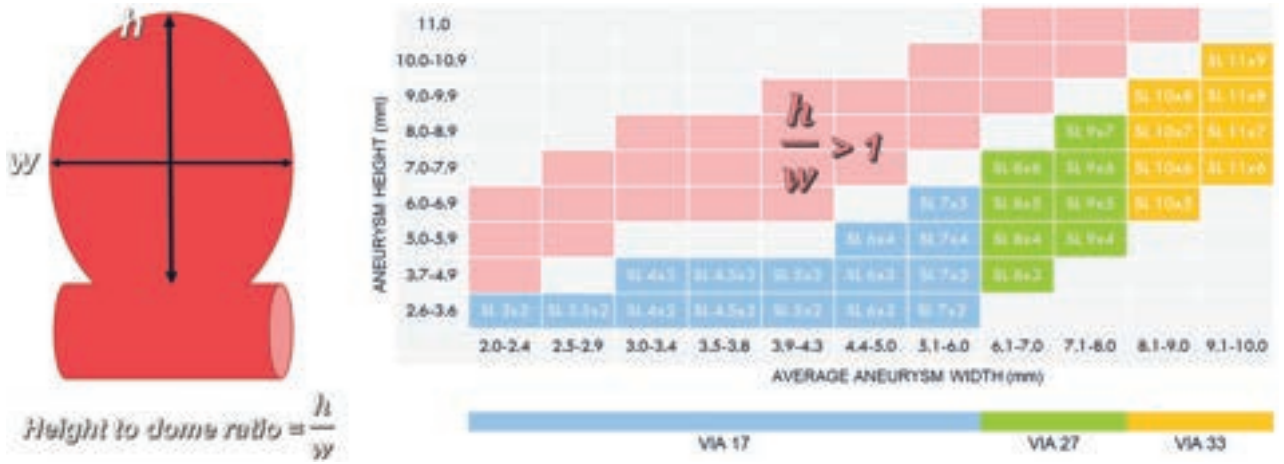

FIG 1. The manufacturer's sizing chart for the WEB device does not cover aneurysms with a height-to-dome ratio of >1. Our proposed approach expands the original range of treatable aneurysms to include those shown in the *red zone*, effectively doubling the spectrum of aneurysms without the need for additional fixed-sized WEB devices.

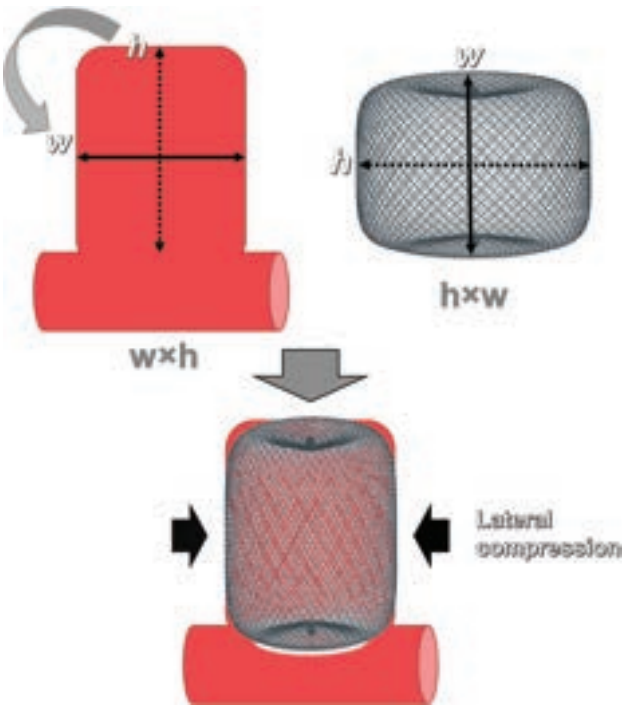

FIG 2. Diagram depicting the proposed sizing strategy for aneurysms with a high height-to-dome ratio. The appropriate WEB size is determined by strategically swapping the height and width dimensions of the aneurysm. For an aneurysm measuring $w \times h$, it is advisable to use a $h \times w$ WEB. When fully deployed, the device undergoes significant lateral compression, leading to a substantial increase in its vertical extension, which helps to achieve an optimal fit for the aneurysm.

Technical Details

After acquiring both 2D and 3D angiographic images, the target aneurysm is evaluated from 2 orthogonal projections, with one of them typically being the "down-the-barrel" view. After excluding redundant spaces such as daughter sacs and side blebs, the appropriate WEB size can be determined by strategically swapping the height and width dimensions of the aneurysm (Fig 2). For an aneurysm that measures w millimeters in width and h millimeters in height, the recommended WEB size would be $h \times w$ mm.

Figure 3 demonstrates a practical application of the suggested sizing technique. A highly elongated cylindrical aneurysm on the right MCA, measuring 3.82 mm in width and 8 mm in height, was under consideration for WEB embolization to safeguard the adjacent temporal branch. On the basis of the size measurements, an 8 × 4 mm WEB single-layer (SL) was selected for the procedure. The device underwent substantial lateral compression, resulting in a reduction of its width from 8 to 4 mm and a similar increase in its height from 4 to approximately 8 mm. This dynamic transformation led to effective occlusion of the aneurysm, which remained stable during subsequent follow-ups.

Sizing of Noncylindrical Aneurysms

The process of choosing the appropriate WEB size for standard cylindrical aneurysms is often straightforward because their shape closely matches that of the recommended device. When dealing with noncylindrical aneurysms, interobserver disparity in image interpretation and aneurysm measurement can result in inconsistent results. To improve sizing consistency, we recommend adding a minor adjustment that involves targeting the maximum height and width of the aneurysm.

Because the actual volume of a noncylindrical aneurysm is inherently smaller in comparison with its cylindrical counterpart with equivalent maximum height and width, it becomes necessary to downsize the selected WEB device by reducing the device height while keeping its width constant. In most cases, a 1-mm reduction in height is adequate to prevent oversizing the WEB implant. However, aneurysms that significantly deviate from the standard cylindrical model may require a 2-mm reduction. In cases in which lowering the device height is not feasible, the width of the device can be reduced as a last resort to decrease the overall volume of the WEB.

Figure 4 provides an example to demonstrate the downsizing procedure. In this visual representation, all 3 aneurysms share the same maximum width and height dimensions of 5 × 8 mm, suggesting that they should be treated with an 8 × 5 mm WEB device according to the recommended sizing method. However, it

becomes apparent that the volumes of the 2 noncylindrical aneurysms are, in fact, smaller and would not provide sufficient room for an 8 × 5 mm device. The WEB device can be downsized by reducing the height by 1 mm, making an 8 × 4 mm device a more appropriate choice for these aneurysms to address this issue.

With the predetermined range of commercially available WEBs, size adjustments for the device are typically limited to 1-mm increments. Given the general ease of reaching a consensus on the maximum width and height of the aneurysm, the downsizing approach effectively minimizes interobserver variation in size selection to just 1 or 2 options (Fig 5).

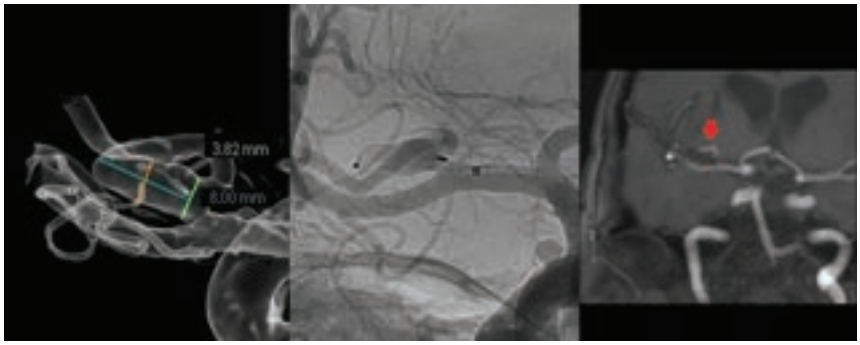

FIG 3. An elective embolization was performed on a right cylindrical MCA aneurysm, with measurements indicating a maximum width of 3.82 mm and a height of 8 mm. An 8 × 4 mm WEB SL device was successfully deployed without impeding the adjacent temporal branch. As a result of intense lateral compression, the base of the SL device assumed a cup-shaped configuration, leaving a small "dog ear" at the neck of the aneurysm. At the 6-month follow-up, the aneurysm continued to show satisfactory results (*red arrow*).

RESULTS

A total of 25 cases were identified of 315 WEB embolization procedures during a 10-year period. The average age of the patients was 61.8 (SD, 13) years, with 68% being women. Among the cases, 76% presented with acute SAH, while the remaining cases were elective procedures.

The heights of treated aneurysms surpassed their widths by a range of 1.4 to 4.5 mm, with an average difference of 2.33 mm. Approximately 44% of the aneurysms were located at the anterior communicating artery; 40% were found at the MCA bifurcation or M1 segment; 8%, at the ophthalmic segment of the ICA; 4%, at the pericallosal artery; and 4%, at the anterior choroidal artery. The average aneurysm width was 5.04 mm (range, 3.32–8.20 mm), and the average aneurysm height was 7.38 mm (range, 5.24–11.39 mm). The WEB devices underwent an average lateral compression of 2.03 mm (range, 0.03–4.00 mm) following full deployment. All patients underwent surveillance studies at 6 months, and imaging follow-up at the 2-year interval was available for 60% of the cases.

Angiographic Occlusion Rates

To evaluate the effectiveness of the proposed sizing method, we divided the patient cohort into 2 categories:

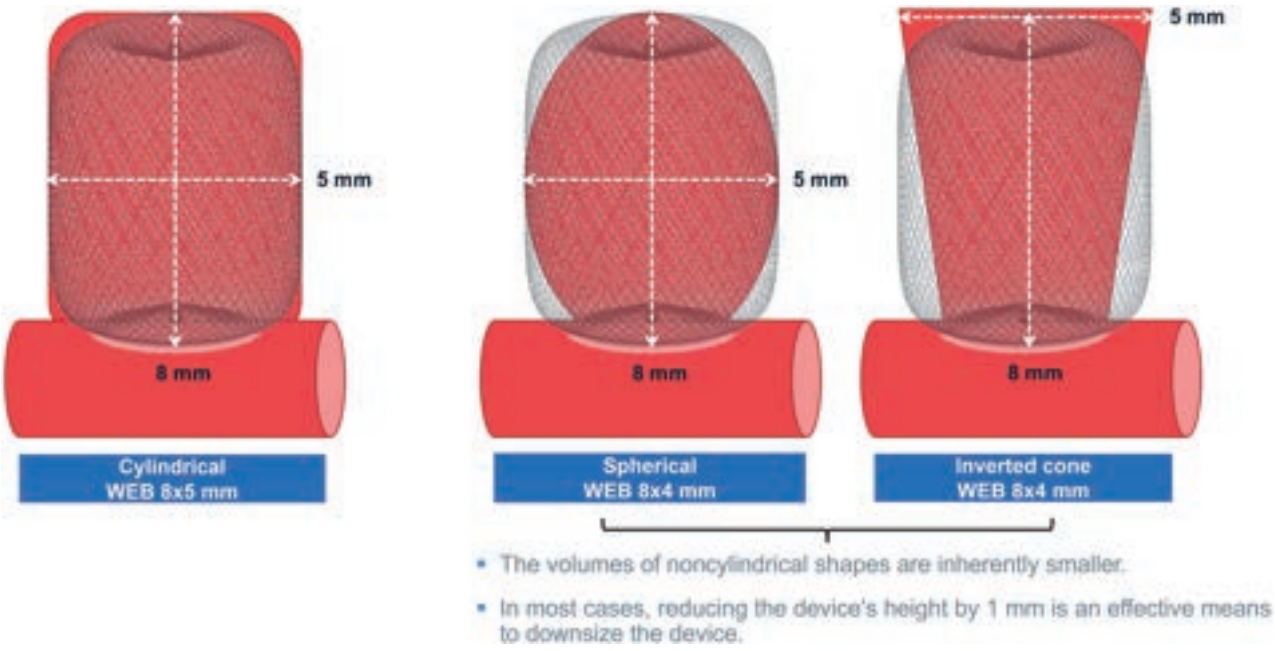

FIG 4. When one deals with aneurysms of noncylindrical shapes, interobserver discrepancies in image interpretation and aneurysm measurement can result in inconsistent results. Aneurysms with noncylindrical shapes generally have smaller actual volumes than their cylindrical counterparts with the same maximum width and height. To ensure an adequate fit within the aneurysms, one must downsize the WEB device by reducing the device height. In this visual representation, all 3 aneurysms share the same maximum width and height dimensions of 5 × 8 mm, suggesting that they should be treated with an 8 × 5 mm WEB device according to the recommended sizing method. However, the actual volumes of the 2 noncylindrical aneurysms are smaller and would not provide sufficient room for an 8 × 5 mm device. The WEB device can be downsized by reducing the height by 1 mm, making an 8 × 4 mm device a more appropriate choice for these aneurysms to address this issue.

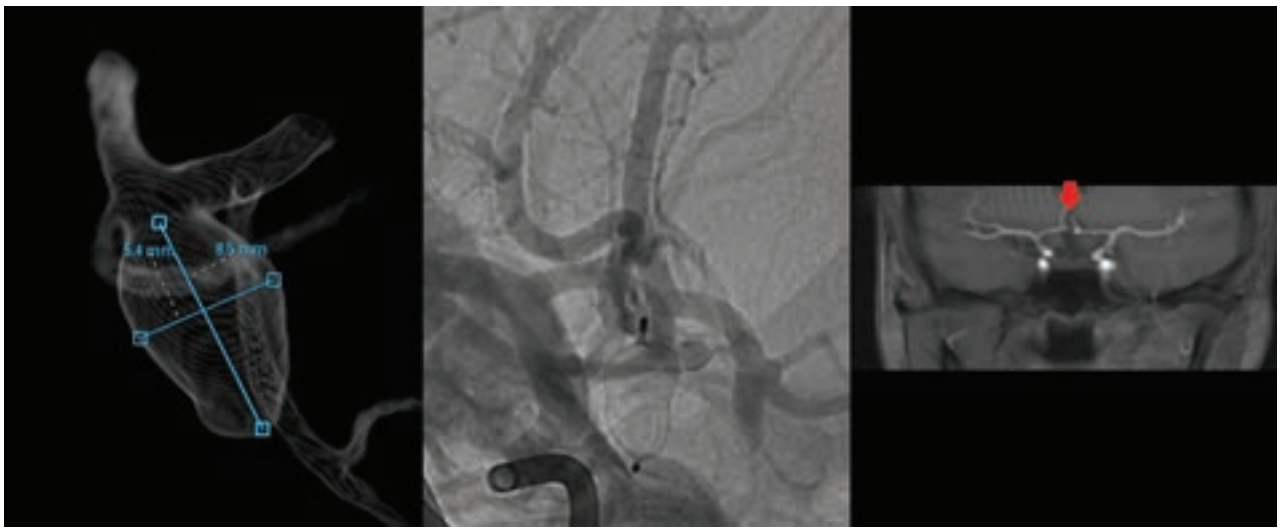

FIG 5. WEB embolization of an acute anterior communicating artery aneurysm, characterized by a maximum width of 5.4 mm and a height of 8.5 mm. A strategic downsizing was performed due to the noncylindrical shape of the aneurysm. Instead of using an 8 × 5 mm device, an 8 × 4 mm WEB SL was selected for the procedure. A follow-up at 6 months showed that the aneurysm remained fully occluded (*red arrow*).

group A consisted of individuals whose devices adhered to the recommended sizing technique, whereas group B included those whose devices deviated from it (Table and Online Supplemental Data).

In all 20 cases within group A, a single WEB device was effectively deployed without the need for subsequent replacement arising from sizing errors. Angiographic surveillance shows that 70% (14/20) of the aneurysms exhibited complete occlusion (WEB Occlusion Scale [WOS], grade A), while the remaining 30% (6/20) had proximal recess filling (grade B). No incidence of persistent neck remnant (grade C) or aneurysm remnant (grade D) was observed.

The remaining 5 patients in group B underwent treatment with WEB devices that were selected without adhering to the recommended sizing strategy. These cases predominantly occurred during the initial phase of introducing the WEB system, preceding widespread acceptance of the recommended sizing strategy in our department. Among these patients, 4 were treated with WEB devices that were smaller than what was advised, resulting in aneurysm neck recurrence (grade C) in all 4 cases and 1 patient undergoing additional treatment with a flow-diverting stent. The last patient in this group received a WEB device larger than necessary, which was replaced with a smaller device during the same procedure, and subsequent follow-up examinations demonstrated complete aneurysm occlusion at the 2-year interval.

DISCUSSION

A recently published meta-analysis revealed that an aspect ratio of ≥1.5 increased the risk of rupture, independent of the aneurysm size.[3] While these aneurysms can often be treated with coil embolization alone, a subset of cases with a neck size exceeding 4 mm may still pose significant challenges.[4] Designed to function as a stand-alone device, the WEB system provides a safe and effective treatment option without the need for additional assistance devices. The WEB is typically oversized by 1–2 mm from the average diameter of the aneurysm in 2 perpendicular planes. To accommodate the vertical extension resulting from lateral compression, its height is reduced by 1–2 mm in comparison with the aneurysm height.[5] However, due to the inherent wider-than-tall design of WEB devices, this sizing approach often proves ineffective for addressing elongated aneurysms. For example, adjusting the width and height of the device by 1–2 mm for a 5 × 8 mm aneurysm would result in the choice of a 6 × 7 or 7 × 6 mm SL device, both of which are commercially unavailable.

The strategy we put forward offers a simple approach that can be readily implemented in everyday practice. Through the interchange of width and height dimensions, all patients in the compliant group achieved adequate aneurysm occlusion during subsequent surveillance. In contrast, those who deviated from the proposed sizing method experienced significantly less favorable angiographic outcomes ($P < .05$). Furthermore, a substantial degree of lateral compression greatly enhances the resistance of the device to delayed compaction in the compliant group, possibly contributing to the high occlusion rate observed in surveillance imaging.[6]

The Clinical Assessment of WEB device in Ruptured Aneurysms (CLARYS) trial demonstrates promising outcomes in the application of the WEB for treating ruptured aneurysms, with protection against early and mid-late rebleeds.[7] Seventy-six percent of patients in our small series presented with ruptured aneurysms. On the basis of our limited experience, there appears to be no significant increase in the risk of aneurysmal wall injury attributed to elevated wall tension, potentially underscoring the high compliance of the WEB system.

Clinical Applications

Conventional sizing methods such as the +1/−1 rule and the official sizing chart restrict each individual device to a narrow range of treatable aneurysms. As a result, expanding the use of the WEB to treat a broader spectrum of aneurysms will require adding new device sizes, which may increase the complexity in inventory

Comparison of patient demographics and details of operative procedures between group A, which adhered to the proposed sizing method, and group B, which did not

	Group A	Group B	*P* Value
Patient demographics			
No. (total =25)	20	5	
Age (mean) (yr)	63.8 (SD, 11.2)	58.6 (SD, 14.5)	
Sex (female/male)	13:7 (65.0%)	4:1 (80.0%)	.642
Rupture status			.289
Acute SAH	14 (70%)	5 (100%)	
Elective	6 (30%)		
Location of aneurysm			
MCA	7 (35%)	3 (60%)	
AcomA	11 (55%)		
Ophthalmic ICA	1 (5%)	1 (20%)	
Pericallosal		1 (20%)	
Anterior choroidal	1 (5%)		
Morphology of aneurysm			
Cylindrical	6 (30%)		
Teardrop	1 (5%)	1 (20%)	
Spindle	2 (10%)		
Irregular	11 (55%)	4 (80%)	
Aneurysm dimensions (mean, range)			
Width	4.95 mm (3.32–8.40 mm)	5.40 mm (3.55–7.73 mm)	
Height	7.11 mm (5.24–10.60 mm)	8.44 mm (6.60–11.39 mm)	
Neck	3.70 mm (2.36–6.00 mm)	3.81 mm (2.36–4.70 mm)	
Degree of lateral compression	2.05 mm (1.4–4.0 mm)	2.00 mm (0.03–3.27 mm)	
2-Year imaging follow-up	10 (50%)	5 (100%)	.061
Occlusion rate			.001 (<.05)
WOS grade A	14 (70%)	1 (20%)[a]	
WOS grade B	6 (30%)		
WOS grade C		4 (80%)	
Operative procedure			
WEB sizes (width)			.822
3–7 mm	14 (70%)	3 (60%)	
8–9 mm	4 (20%)	1 (20%)	
10–11 mm	2 (10%)	1 (20%)	
WEB models			.012 (<.05)
SL/SLS	18 (90%)	2 (40%)	
SL/SLS 17	2 (10%)	3 (60%)	

Note:—AcomA indicates anterior communicating artery.

[a] Successful replacement of an oversized WEB device conducted during the same procedure resulted in complete angiographic occlusion on subsequent follow-up.

management. The sizing method we proposed has the potential to double the original range of treatable aneurysms, all without the need for additional fixed-sized WEB implants (Fig 1). The concept of enhancing the clinical versatility of the WEB device through lateral-compression manipulation is relatively underexplored and merits further investigation.

Impacts of Extreme Lateral Compression

In instances in which the height of an aneurysm markedly surpasses its width, an extreme level of lateral compression is unavoidable on the full deployment. This can cause a significant morphologic transformation of the WEB device, which may impact its intended deployment.

In the case of the WEB SL, the corners of the device typically generate the greatest radial forces, while the waist is more susceptible to external compression. When subjected to extreme lateral compression, the WEB SL device tends to assume a characteristic "hourglass" shape. In contrast, the WEB single-layer sphere (SLS) with its initially broader waist diameter is more likely to take on a cylindrical configuration (Fig 6).

Consequently, the base of the WEB SL device, which covers the aneurysm neck, frequently adopts a concave, cup-shaped appearance, while the proximal recess of the WEB SLS device tends to form a flat surface. Under extreme lateral compression, the 2 models essentially switch roles to accommodate aneurysm configurations that deviate from their originally intended targets. This role reversal can potentially affect the neck coverage during the treatment of the aneurysm (Fig 3). It is, therefore, important to anticipate the impact of role reversal on the performance of the device.

Study Limitations

There are several limitations to our study. Due to the limited sample size, inherent variations (such as ruptured status, WEB models, and larger device/aneurysms) between the 2 groups could influence the statistical difference in treatment outcomes.[8] Its retrospective design may introduce inherent biases associated with the use of historical data. Additionally, being conducted at a single neuroscience center may limit the applicability of the results to wider populations.

Despite recent progress in neurovascular device manufacturing, MR imaging of a WEB device remains difficult due to a combination of magnetic susceptibility artifacts and the Faraday cage effect. The low sensitivity of 3D TOF-MRA for the detection of aneurysm remnants suggests that DSA remains the criterion standard for follow-up.[9] The use of site interpretation rather than core laboratory assessment of angiographic outcomes may render the result susceptible to observer bias.

Further illustrative cases are available in the Online Supplemental Data, including an irregularly-shaped aneurysm a noncompliant case, and an atypical location.

CONCLUSIONS

Our proposed approach for sizing WEB devices to address taller-than-wide aneurysms has shown promising results. The intuitive strategy, which involves the interchange of width and height dimensions of the aneurysm, presents a simple and practical solution to the limitations of conventional sizing methods. Further investigation with a larger sample size is recommended to evaluate the applicability of this sizing approach across diverse aneurysm configurations.

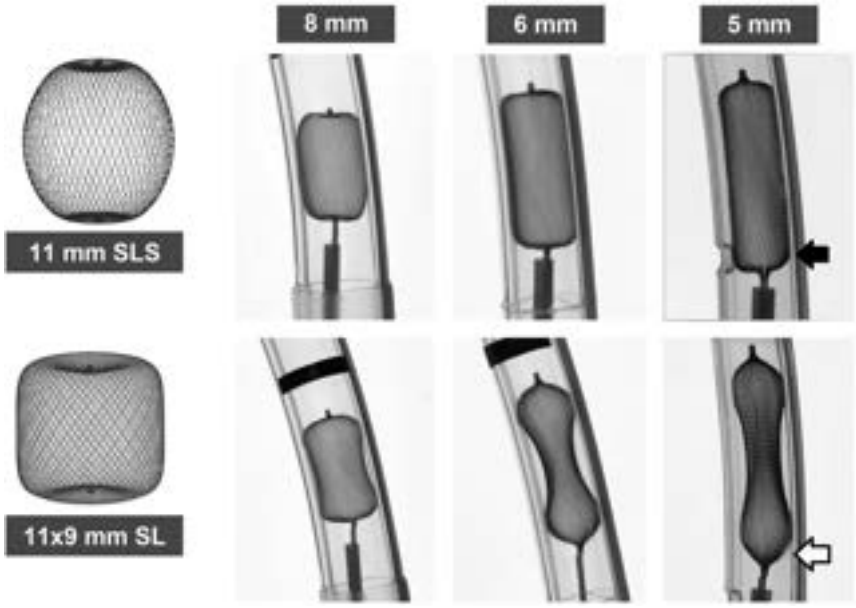

FIG 6. When subjected to extreme, lateral compression, the WEB SL device tends to assume a characteristic hourglass shape, while the WEB SLS is more likely to take on a cylindrical configuration. As a result, the base of the WEB SL device frequently adopts a concave, cup-shaped appearance (*open arrow*), whereas the WEB SLS device tends to create a flat base (*solid arrow*). This inversion of configurations can potentially affect the neck coverage during the treatment of the aneurysm.

Disclosure forms provided by the authors are available with the full text and PDF of this article at www.ajnr.org.

REFERENCES

1. Lv X, Zhang Y, Jiang W. **Systematic review of woven EndoBridge for wide-necked bifurcation aneurysms: complications, adequate occlusion rate, morbidity, and mortality.** *World Neurosurg* 2018;110:20–25 CrossRef Medline
2. Behme D, Berlis A, Weber W. **Woven EndoBridge intrasaccular flow disrupter for the treatment of ruptured and unruptured wide-neck cerebral aneurysms: report of 55 cases.** *AJNR Am J Neuroradiol* 2015;36:1501–06 CrossRef Medline
3. Sanchez S, Hickerson M, Patel RR, et al. **Morphological characteristics of ruptured brain aneurysms: a systematic literature review and meta-analysis.** *Stroke: Vascular and Interventional Neurolog* 2023;3:e000707 CrossRef
4. Brinjikji W, Cloft HJ, Kallmes DF. **Difficult aneurysms for endovascular treatment: overwide or undertall?** *AJNR Am J Neuroradiol* 2009;30:1513–17 CrossRef Medline
5. van Rooij WJ, van Rooij SB, Kortman HG, et al. **The Woven EndoBridge finally coming home across the Atlantic: what to expect?** *AJNR Am J Neuroradiol* 2018;39:1964–66 CrossRef Medline
6. Delgado Almandoz JE, Kayan Y, Copelan AZ, et al. **Lateral compression is the strongest independent predictor of aneurysm occlusion after endovascular treatment of intracranial aneurysms with the Woven EndoBridge device.** *Neurosurgery Practice* 2023;4:e00054 CrossRef
7. Spelle L, Herbreteau D, Caroff J, et al. **CLinical assessment of WEB device in Ruptured aneurYSms (CLARYS): results of 1-month and 1-year assessment of rebleeding protection and clinical safety in a multicenter study.** *J Neurointerv Surg* 2022;14:807–14 CrossRef Medline
8. Fortunel A, Javed K, Holland R, et al. **Impact of aneurysm diameter, angulation, and device sizing on complete occlusion rates using the Woven Endobridge (WEB) device: single center United States experience.** *Interv Neuroradiol* 2023;29:260–67 CrossRef Medline
9. Timsit C, Soize S, Benaissa A, et al. **Contrast-enhanced and time-of-flight MRA at 3T compared with DSA for the follow-up of intracranial aneurysms treated with the WEB device.** *AJNR Am J Neuroradiol* 2016;37:1684–89 CrossRef Medline

Time-Saving 3D MR Imaging Protocols with Millimeter and Submillimeter Isotropic Spatial Resolution for Face and Neck Imaging as Implemented at a Single-Site Major Referral Center

Jeffrey P. Guenette and Lei Qin

ABSTRACT

SUMMARY: MR imaging has become the routine technique for staging nasopharyngeal carcinoma, evaluating perineural tumor spread, and detecting cartilage invasion in laryngeal carcinoma. However, these protocols traditionally require in the range of 25 to 35 minutes of acquisition time. 3D sequences offer the potential advantage of time savings through the acquisition of 1-mm or submillimeter resolution isotropic data followed by multiplanar reformats that require no further imaging time. We have iteratively optimized vendor product 3D T1-weighted MR imaging sequences for morphologic face and neck imaging, reducing the average acquisition time of our 3T protocols by 9 minutes 57 seconds (40.9%) and of our 1.5T protocols by 9 minutes 5 seconds (37.0%), while simultaneously maintaining or improving spatial resolution. This clinical report describes our experience optimizing and implementing commercially available 3D T1-weighted MR imaging pulse sequence protocols for clinical face and neck MR imaging examinations using illustrative cases. We provide protocol details to allow others to replicate our implementations, and we report challenges we faced along with our solutions.

ABBREVIATIONS: ETL = echo-train length; SPACE = sampling perfection with application optimized contrasts by using different flip angle evolution; VIBE = volumetric interpolated breath-hold examination

Development of MR imaging pulse sequences has largely focused on the brain (small body part that can remain motionless), heart (dynamic imaging techniques), and other organ-specific indications. Pulse sequences have not been specifically designed for imaging the intricate structures of the face and neck, where there are also challenges associated with swallowing and breathing motion and acquiring data through the relatively large head to the thin neck to the wide shoulders. Many radiology groups, thus, use pulse sequences designed for the brain, shifting the scan range to the face and adding slices for the neck. These vendor product 2D T1-weighted and 2D T2-weighted sequences typically have 5-mm section thickness and 1-mm section gaps. Cranial nerves, neural foramina, extrinsic tongue muscles, and other small structures are difficult to visualize on these images, restricting the extent to which imaging can impact decisions on clinical management. In centers with subspecialized head and neck radiologists and sufficient MR imaging physicist and/or technologist resources, vendor product protocols are often adapted to generate higher-resolution images, typically along the lines of 3-mm section thickness with no section gap and with in-plane resolution of 0.5–0.7 mm (often in the range of 0.75-mm^3 rectangular voxels). With these improvements, MR imaging has become the routine technique for staging nasopharyngeal carcinoma,[1,2] evaluating perineural tumor spread,[3] and detecting cartilage invasion in laryngeal carcinoma.[4] However, these protocols require in the range of 25 to 35 minutes of acquisition time. Since May 2021, we have intermittently modified, tested, and implemented more rapid face and neck MR imaging protocols while aiming to maintain or improve overall spatial resolution and soft-tissue contrasts.

Given previous successful optimization of 3D steady-state, 3D T2-weighted TSE, and 3D ultrashort echo time sequences for visualization of the cranial nerves,[5-8] we iteratively optimized vendor product 3D T1-weighted MR imaging sequences for morphologic face and neck imaging. To date, we have modified the T1-weighted acquisitions in our general/trans-spatial, nasopharynx/nasal cavity, oropharynx/oral cavity, and sinus MR imaging protocols. Our optimization process was as follows: 1) The MR imaging physicist coauthor adapted a vendor product pulse sequence protocol for 1-mm or submillimeter resolution imaging of the face and neck ROI by adjusting the FOV, matrix, scan volume, TR, TE, flip

Received September 9, 2023; accepted after revision January 26, 2024.

From the Division of Neuroradiology (J.P.G.), Brigham and Women's Hospital, Dana-Farber Cancer Institute, Harvard Medical School, Boston, Massachusetts; and Department of Imaging (L.Q.), Dana-Farber Cancer Institute, Harvard Medical School, Boston, Massachusetts.

This study was funded in part by the Association of University Radiologists GE Radiology Research Academic Fellowship.

Please address correspondence to Jeffrey P. Guenette MD, MPH, Division of Neuroradiology, Brigham and Women's Hospital, 75 Francis St, Boston, MA 02115; e-mail: jpguenette@bwh.harvard.edu

Indicates article with online supplemental data.

http://dx.doi.org/10.3174/ajnr.A8184

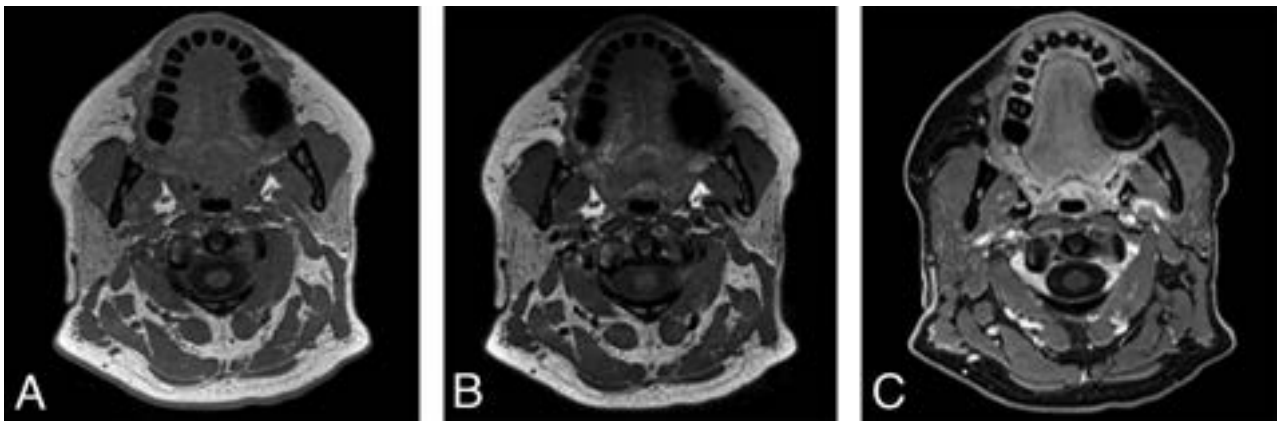

FIG 1. Sample 3D T1 VIBE (*A*), 3D T1 SPACE (*B*), and postcontrast 3D T1 VIBE Dixon fat-suppression (*C*) images acquired in the same session on a 3T Magnetom Vida system (Siemens) at the level of the oral cavity, retromolar trigone, and parotid glands in a 44-year-old woman with neck pain show excellent discrimination of soft-tissue structure boundaries with subjectively better soft-tissue contrasts on the SPACE than on VIBE and robust fat suppression on the VIBE Dixon.

angle, bandwidth, and acceleration factors based on past experience. 2) The new sequence protocol was run on a patient in addition to the standard routine protocol at the time. 3) The neuroradiologist coauthor reviewed the images and provided the physicist with constructive criticisms on the subjective quality and the process was repeated,[1] or the neuroradiologist was satisfied with the quality and the sequence protocol was adopted. Using this process, we have reduced the average acquisition time for 1) the 3T general/trans-spatial, nasopharynx/nasal cavity, oropharynx/oral cavity, and sinus MR imaging protocols from 24 minutes 21 seconds to 14 minutes 24 seconds, yielding a 9 minute 57 second (40.9%) time savings on average (range, 6 minutes 23 seconds to 13 minutes 18 seconds, 27.7% to 55.4% time savings) and for 2) the same 1.5T protocols from 24 minutes 33 seconds to 15 minutes 29 seconds, yielding a 9 minute 5 second (37.0%) time savings on average (range, 5 minutes 3 seconds to 13 minutes 46 seconds; 21.7% to 59.3% time savings). The total acquisition time for our face and neck MR imaging protocols is now routinely in the 10- to 17-minute range on 3T systems (Table). We have simultaneously maintained or improved the spatial resolution. For example, we have improved the overall spatial resolution in our oropharynx protocol by 35%, decreasing voxel volume from 0.75 to 0.65 mm^3.

This clinical report describes our experience optimizing and implementing commercially available 3D T1-weighted MR imaging pulse sequence protocols for clinical face and neck MR imaging examinations. We provide protocol details to allow others to replicate our implementations, and we outline challenges we faced along with our solutions.

Case Series

Case 1: 3D T1-Weighted Gradient-Echo, TSE, and Fat-Suppression Techniques. We began by optimizing T1-weighted gradient-recalled echo images, called the volumetric interpolated breath-hold examination (VIBE; Siemens) before T1-weighted TSE sequences were available across our scanners. The soft-tissue contrast on the VIBE images was subjectively considered poor by our neuroradiology faculty relative to the 2D and 3D TSE images, providing less contrast between fat and muscle, while blood vessels also had roughly similar intermediate signal intensity. We, therefore, turned to 3D T1-weighted TSE sequences as they became available across our fleet of scanners. We used the Sampling Perfection with Application-optimized Contrasts by using different flip angle Evolution (SPACE sequence; Siemens) and the Cube sequence (GE Healthcare). Our optimization work has been performed with the SPACE sequence on 3T systems, then applied to the Cube sequence, and then adapted for 1.5T systems. Direct comparisons of T1-weighted VIBE and SPACE images are provided for a 44-year-old woman with neck pain in Fig 1.

For postcontrast imaging, the opportunity to acquire both T1-weighted in-phase images and fat-suppressed images in the same acquisition is highly appealing. The fat-suppression technique described by Dixon,[9] in 1984, includes a single-sequence acquisition of both in-phase and opposed-phase data, allowing mathematic processing into 4 contrasts: T1-weighted in-phase, T1-weighted opposed-phase, T1-weighted water, and T1-weighted fat. The implementation of Dixon with a 3D spoiled gradient-echo sequence on Siemens systems is called VIBE Dixon, and on GE Healthcare systems, it is called liver acquisition with volume acceleration flex (LAVA Flex). Anecdotally, we have found the Dixon technique to be more robust than the spectral fat-suppression techniques we use in 2D imaging. Direct comparison of the T1-weighted VIBE Dixon fat-suppressed images is provided in Fig 1 in conjunction with the T1-weighted precontrast images from the same patient.

All our optimized 3D T1-weighted protocol parameters are provided in the Online Supplemental Data to allow replication at other institutions. Information on our optimized 2D T1-weighted protocols and detailed protocol parameters is provided in the Online Supplemental Data.

Case 2: Whole-Neck Protocol and Early Protocol Iteration Showing an Invasive Cutaneous Lesion. For the nonfocal whole-neck protocol, we acquired data in the sagittal plane, which minimizes the scan range and eliminates the potential for wrap artifacts from the body and vertex scalp. Given that this protocol is used

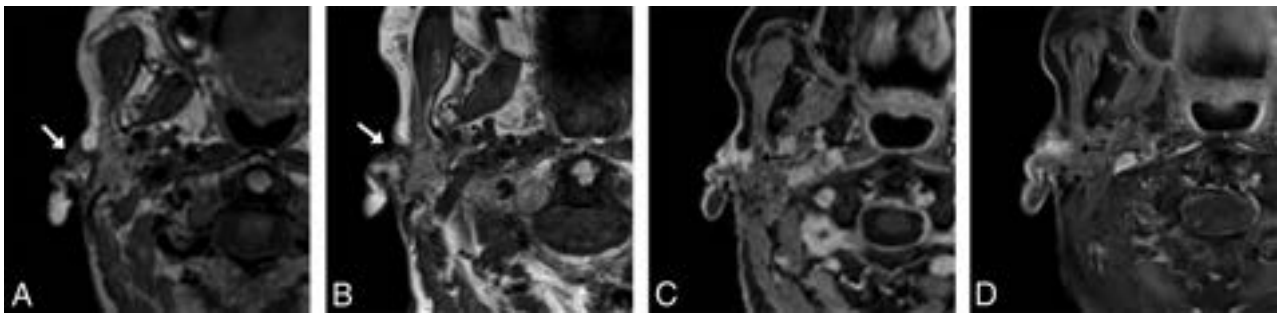

FIG 2. A 92-year-old woman with squamous cell carcinoma. *A*, T1 SPACE sequence performed in the full-neck MR imaging protocol with 2.7-mm^3 (1.4 mm isotropic) voxels during early optimization iterations reformatted into the axial plane clearly shows a cutaneous preauricular lesion (*arrow*) that is not visible due to volume averaging on the 2D T1-weighted image (*B*) with 1-mm^3 (4 × 0.5× 0.5 mm) voxels. The T1 VIBE Dixon (*C*) reformatted image in the axial plane shows the associated infiltrating tumor into the parotid gland (*arrow*) to advantage compared with the 2D T1-weighted image (*D*) with spectral fat suppression. The case convinced us that the SPACE sequence was a reasonable alternative to the 2D standard-of-care and led us to improve the spatial resolution of the SPACE sequence. These images were obtained contemporaneously on a 3T Magnetom Vida system.

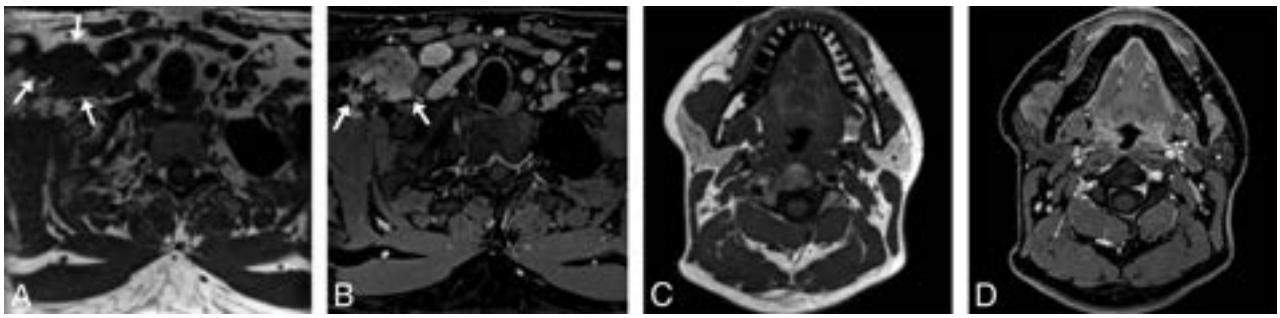

FIG 3. A 27-year-old man with right supraclavicular and chest wall desmoid tumor images on a 1.5T Magnetom Aera system (Siemens). The tumor (*arrows*) is shown on a general neck protocol, 1.0-mm isotropic sagittal acquisition T1 SPACE axial reformat (*A*) and T1 VIBE Dixon (*B*) postcontrast axial reformatted images. Image quality and fat suppression remain good at the level of the thoracic inlet. In addition, T1 SPACE axial reformat (*C*) and T1 VIBE Dixon (*D*) postcontrast axial reformat images through the face are provided to show image quality in that region.

Gradient time savings from MR imaging protocols on 3T Magnetom Prisma and 1.5T Magnetom Aera systems for reference

Protocol	2D T1 Version	3D T1 Version	Time Savings	Savings
3T general	23:05	16:42	6:23	27.7%
3T nasopharynx	23:42	13:38	10:04	42.5%
3T oropharynx	26:37	16:33	10:04	37.8%
3T sinus	24:00	10:42	13:18	55.4%
Mean	24:21	14:24	9:57	40.9%
1.5T general	23:15	18:12	5:03	21.7%
1.5T nasopharynx	24:11	15:26	8:45	36.2%
1.5T oropharynx	27:33	18:48	8:45	31.8%
1.5T sinus	23:14	9:28	13:46	59.3%
Mean	24:33	15:29	9:05	37.0%

Note:—Times listed as minutes:seconds.

for identification of gross soft-tissue abnormalities without the necessity for finer spatial detail, we acquired it at 1-mm isotropic resolution. However, even with 1-mm^3 voxels, this sequence can often more clearly show smaller lesions than in what we traditionally called high-resolution 2D acquisition images, which were submillimeter in-plane but with 3-mm or thicker section thickness. An example is provided in Fig 2 of images from a 92-year-old woman with a small focal preauricular metastasis of cutaneous squamous cell carcinoma invading the parotid gland.

Case 3: One-Millimeter Sagittal Isotropic Whole-Neck Protocol with 1.5T Adaptation. Our 1.5T protocol was adapted from the 3T protocol to provide the same resolution; 1.5T protocol parameters are provided in the Online Supplemental Data alongside the 3T protocol parameters. An example is provided in Fig 3, images from a 27-year-old man with a right supraclavicular and chest wall desmoid tumor.

Case 4: Submillimeter Axial Isotropic Focused Face Protocol. For the higher-resolution targeted 3D T1-weighted protocols, we acquired data in the axial plane to minimize the scan range and allow higher-resolution imaging (0.9 × 0.9 × 0.8 mm) in shorter scan times. This approach requires oversampling to avoid wrap artifacts. However, even with oversampling and the somewhat longer acquisition time compared with the axial 2D protocol, we achieved considerable time savings due to submillimeter near-isotropic voxels, allowing multiplanar reconstructions and eliminating multiple-plane acquisitions (Table). We minimized axial-acquisition time- and phase-encoding steps using a left-right phase-encoding direction and a rectangular FOV. Reformatting images into the coronal and sagittal planes provided us with 3 planes of T1-weighted imaging through the ROI. Furthermore, individual radiologists can adjust the isotropic image planes in our PACS viewer to optimize viewing. To give a rough

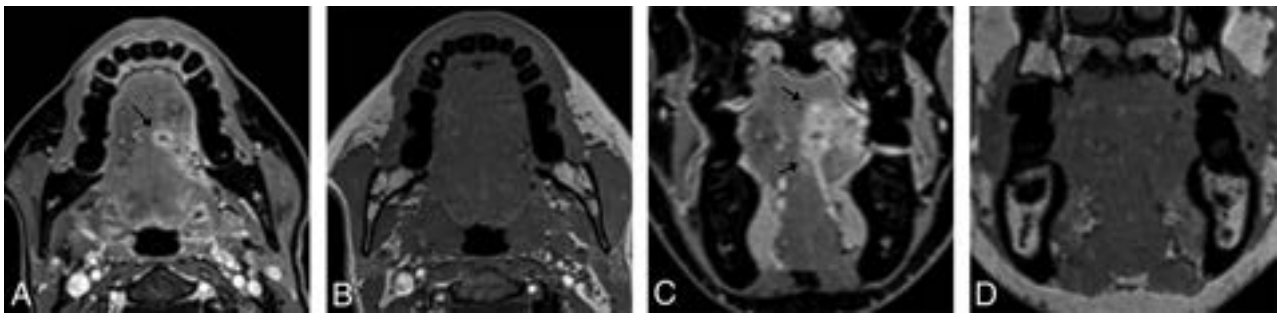

FIG 4. A 44-year-old woman with newly diagnosed oral cavity squamous cell carcinoma (*arrows*) shown on oropharynx protocol T1 VIBE Dixon 0.8 × 0.9 × 0.9 mm resolution axial acquisition (*A*) and coronal reformat images (*B*) and a corresponding precontrast T1 SPACE axial acquisition (*C*) and coronal reformat images (*D*) obtained on a 3T Magnetom Vida system.

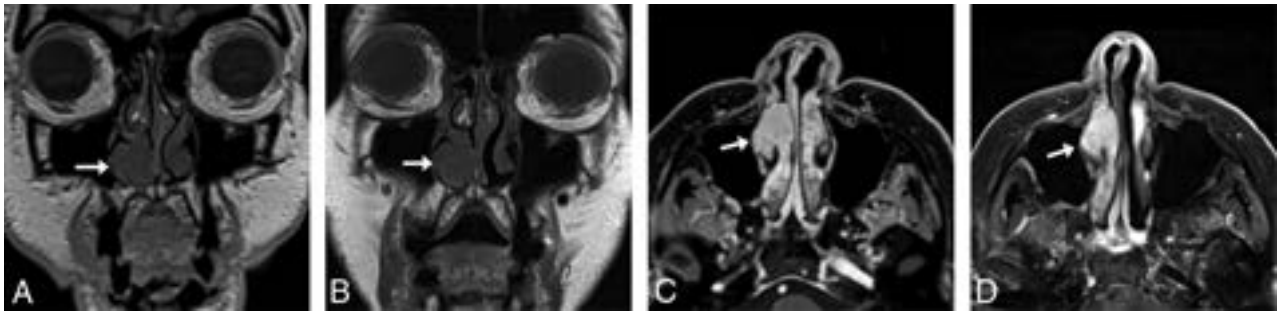

FIG 5. An 83-year-old woman with melanoma and a stable untreated nasal cavity mass of unknown pathology with sinus protocol MR imaging. T1 SPACE coronal acquisition (*A*) performed with 1-mm^3 (1.0 mm isotropic) voxels shows a mass (*arrow*) along the anterior aspect of the right inferior turbinate, seen similarly on the 2D T1-weighted image (*B*) with 0.8-mm^3 (3 × 0.5 × 0.52 mm) voxels. The T1 VIBE Dixon axial reformat (*C*) shows the mass (*arrow*) to advantage compared with the 2D T1-weighted image (*D*) with spectral fat suppression; the former shows the extent of the mass relative to the more heterogeneously enhancing turbinate. The 3D images were acquired on a 3T Magnetom Vida system 6 months following the acquisition of the 2D images on a 3T Magnetom Skyra system (Siemens).

comparison of visual contrast of the 3D images relative to the 2D images of our prior protocol, we measured the signal intensity ratio in 3 consecutive patients who had imaging with the 3D protocol in mid-July of 2023 and who had prior imaging with the 2D protocol also on a 3T MR imaging scanner. In this sample, the lateral pterygoid muscle to retroantral fat mean signal intensity ratio (visual contrast) is similar at 0.41 (SD, 0.05) for this 3D protocol compared with 0.35 (SD, 0.06) for the 2D protocol.

For postcontrast T1-weighted images, we also acquired data in the axial plane at 0.9-mm isotropic resolution with a left-right phase-encoding direction and a rectangular FOV to minimize acquisition time. We have compared anterior-posterior and left-right phase-encoding directions and observed no substantial flow artifacts on images using either encoding direction. In the same sample of 3 consecutive patients, the mean retroantral fat-to-lateral pterygoid muscle signal intensity ratio (visual contrast) was 0.83 (SD, 0.07) for this 3D protocol versus 0.38 (SD, 0.13) for the 2D protocol for examinations performed at different timepoints; there is greater muscle-fat contrast for the 3D than for 2D images.

We show images for this protocol from a 44-year-old woman with newly diagnosed oral cavity squamous cell carcinoma in Fig 4.

Case 5: One-Millimeter Coronal Isotropic Sinus Protocol Showing a Nasal Cavity Mass. For sinus imaging, we acquired data in the coronal plane, from the tip of the nose to the vertebral bodies, to minimize the scan range and scan times. We show sample images of this protocol compared with 2D images for an 83-year-old woman with a stable untreated nasal cavity mass of unknown pathology in Fig 5.

Case 6: Submillimeter Coronal Isotropic Sinus Protocol Showing Perineural Tumor. During our optimization phase, we tested submillimeter coronal acquisitions in our sinus protocol, similar to our high-resolution axial protocol for the nasopharynx and oropharynx. We show an example of perineural tumor from one of these examinations in an 85-year-old man with a spindle cell sarcoma in Fig 6.

DISCUSSION

In this clinical report, we show that it is feasible to leverage commercially available 3D T1-weighted MR imaging pulse sequence protocols to substantially reduce the scan time for clinical face and neck MR imaging examinations while preserving overall spatial resolution and perhaps improving diagnostic quality. We also describe our experience optimizing these sequences and provide protocol parameter details so that others can replicate our implementations.

For quality assurance, our neuroradiologists were asked by group e-mail and in division staff meetings to send negative, positive, and constructive feedback on the diagnostic quality of these images throughout and following the protocol-optimization

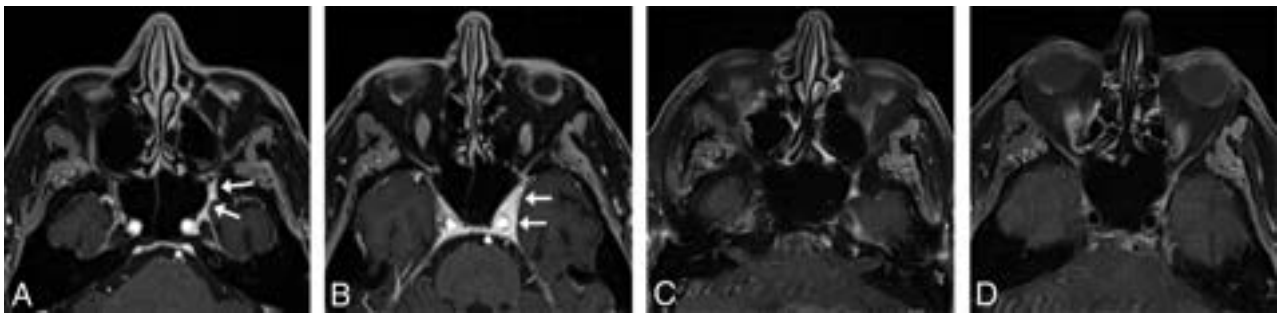

FIG 6. An 85-year-old man with spindle cell sarcoma with sinus protocol MR imaging. T1 VIBE Dixon axial acquisition performed with 0.9-mm^3 (0.74 mm isotropic) voxels clearly shows tumor (*arrows*) along the left V2 (*A*) and in the left lateral cavernous sinus wall (*B*), neither of which is clearly seen on the 2D T1-weighted images (*C* and *D*) with spectral fat suppression with 2-mm^3 (4 × 0.7 × 0.7 mm) voxels. The 3D examination shown was performed on a 3T Magnetom Prisma Fit system (Siemens) 3 weeks before the 2D examination, which was performed on a Siemens 3T Vida system, with no intervening treatment.

process via our department's critical results, peer review, and quality-assurance closed-loop communication tool.[10] We also welcomed and encouraged informal feedback. All feedback requests were open-ended. The group initially provided primarily informal mixed feedback on the quality and appropriateness of the 3D acquisition images. The feedback was always preference-based; we identified no cases in which diagnostic information was obtained on the 2D images but not the 3D images (though we did identify the converse, as shown in Figs 3, 4, and 6). In addition, we initially ran the 3D protocols alongside the 2D protocols. At that time, we were working with the 3D gradient-recalled echo T1-weighted sequence. We gradually phased out the 2D-acquisition images on one of our scanners and then on several additional scanners. We did not introduce the 3D TSE T1-weighted protocol until after the 2D protocols were phased out; thus, we do not have any same-patient same-examination comparisons of 3D TSE T1-weighted images and 2D TSE T1-weighted images for quantitative SNR and contrast-to-noise ratio comparisons. Because our neuroradiologists have become accustomed to the qualitative appearance of the 3D protocol images, we have had no further negative feedback.

The primary technical frustration we have encountered is that while 3D protocols can be set to automatically generate multiplanar reformats on the scanner on Siemens systems, this reformatting mechanism reformats only the in-phase VIBE Dixon images and cannot be modified to select the fat-suppression images for automatic reformatting. We, therefore, rely on a combination of manual reformatting by the technologists at the scanner and on-the-fly reformatting by the radiologists when reviewing images in our PACS system, which has an excellent 3D multiplanar reformatting tool.

On the positive side, not only can shortening acquisition times help reduce motion artifacts, lessen concern for claustrophobia, and increase throughput, it can also provide time to add other useful sequences. In our case, given increasing evidence for DWI utility in head and neck imaging,[11,12] we have been able to add DWI back to our face and neck MR imaging protocols. Time constraints, a focus on high-resolution morphologic imaging, and poor-quality DWI led to removal of DWI from our protocols several years ago. We are also excited to test quantitative arterial spin-labeling and dynamic contrast-enhancement perfusion imaging,[13-16] both of which show considerable promise for diagnostic utility but add acquisition time. Also exciting but currently investigative is the potential for 3D synthetic MR imaging techniques, such as multiplanar multiecho imaging,[17,18] that allow acquisition of all contrasts simultaneously and that could allow mathematic derivation and generation of novel contrasts tailored to face and neck applications.

We report only on T1-weighted imaging protocols because we have not successfully implemented 3D T2 techniques with fat suppression. We have attempted to image with 3D T2 STIR techniques, but the fat suppression consistently fails in the region of the nape of the neck. We hypothesize that this failure is related to the section thickness we tried to achieve and the signal decrease due to the much longer echo-train length (ETL) for 3D (attempted ETL = 150 to keep the scan time within 6 minutes) than 2D STIR (ETL = 31), despite our efforts to set a similar effective TE for both 3D and 2D STIR. Furthermore, due to the extended ETL in 3D, the acquired echoes can contain signals from recovered fat, resulting in inadequate fat suppression. Vendor product 3D T2-weighted protocols with Dixon-type fat suppression are not currently available.

We may be able to further reduce acquisition times as we explore deep learning reconstruction capabilities on commercially available vendor upgrades. Optimization of 3D T2-weighted imaging with some form of fat suppression would help further reduce scan times and provide 3-plane T2-weighted images for easy cross-referencing. It may also be worth exploring T1-weighted ultrashort echo time sequences, given the ability to visualize bone and cranial nerves on these images.[6,19] For now, the optimized commercially available 3D T1-weighted protocols have substantially improved our clinical face and neck MR imaging examination workflows and also anecdotally appear to have had a positive impact on our diagnostic capabilities.

In summary, our experience shows that it is feasible to leverage commercially available 3D T1-weighted MR imaging pulse sequence protocols to substantially reduce the scan time for clinical face and neck MR imaging examinations while preserving overall spatial resolution and perhaps improving diagnostic quality.

Disclosure forms provided by the authors are available with the full text and PDF of this article at www.ajnr.org.

REFERENCES

1. Razek AA, King A. **MRI and CT of nasopharyngeal carcinoma.** *AJR Am J Roentgenol* 2012;198:11–18 CrossRef Medline
2. Chong VF, Fan YF. **Skull base erosion in nasopharyngeal carcinoma: detection by CT and MRI.** *Clin Radiol* 1996;51:625–31 CrossRef Medline
3. Moonis G, Cunnane MB, Emerick K, et al. **Patterns of perineural tumor spread in head and neck cancer.** *Magn Reson Imaging Clin N Am* 2012;20:435–46 CrossRef Medline
4. Cho SJ, Lee JH, Suh CH, et al. **Comparison of diagnostic performance between CT and MRI for detection of cartilage invasion for primary tumor staging in patients with laryngo-hypopharyngeal cancer: a systematic review and meta-analysis.** *Eur Radiol* 2020;30:3803–12 CrossRef Medline
5. Guenette JP, Ben-Shlomo N, Jayender J, et al. **MR imaging of the extracranial facial nerve with the CISS sequence.** *AJNR Am J Neuroradiol* 2019;40:1954–59 CrossRef Medline
6. Guenette JP, Seethamraju RT, Jayender J, et al. **MR imaging of the facial nerve through the temporal bone at 3T with a noncontrast ultrashort echo time sequence.** *AJNR Am J Neuroradiol* 2018;39:1903–06 CrossRef Medline
7. Casselman JW, Kuhweide R, Deimling M, et al. **Constructive interference in steady state-3DFT MR imaging of the inner ear and cerebellopontine angle.** *AJNR Am J Neuroradiol* 1993;14:47–57 Medline
8. Alkan A, Sigirci A, Ozveren MF, et al. **The cisternal segment of the abducens nerve in man: three-dimensional MR imaging.** *Eur J Radiol* 2004;51:218–22 CrossRef Medline
9. Dixon WT. **Simple proton spectroscopic imaging.** *Radiology* 1984;153:189–94 CrossRef Medline
10. Glazer DI, Zhao AH, Lacson R, et al. **Use of a PACS embedded system for communicating radiologist to technologist learning opportunities and patient callbacks.** *Curr Probl Diagn Radiol* 2022;51:511–16 CrossRef Medline
11. Miracle AC, El-Sayed IH, Glastonbury CM. **Diffusion weighted imaging of esthesioneuroblastoma: differentiation from other sinonasal masses.** *Head Neck* 2019;41:1161–64 CrossRef Medline
12. Yeom KW, Lober RM, Mobley BC, et al. **Diffusion-weighted MRI: distinction of skull base chordoma from chondrosarcoma.** *AJNR Am J Neuroradiol* 2013;34:1056–61, S1 CrossRef Medline
13. Amukotuwa SA, Marks MP, Zaharchuk G, et al. **Arterial spin-labeling improves detection of intracranial dural arteriovenous fistulas with MRI.** *AJNR Am J Neuroradiol* 2018;39:669–77 CrossRef Medline
14. Sun Z, Hu S, Ge Y, et al. **Can arterial spin labeling perfusion imaging be used to differentiate nasopharyngeal carcinoma from nasopharyngeal lymphoma?** *J Magn Reson Imaging* 2021;53:1140–48 CrossRef Medline
15. Baba A, Kurokawa R, Rawie E, et al. **Normalized parameters of dynamic contrast-enhanced perfusion MRI and DWI-ADC for differentiation between posttreatment changes and recurrence in head and neck cancer.** *AJNR Am J Neuroradiol* 2022;43:1184–89 CrossRef Medline
16. Ota Y, Liao E, Capizzano AA, et al. **Diagnostic role of diffusion-weighted and dynamic contrast-enhanced perfusion MR imaging in paragangliomas and schwannomas in the head and neck.** *AJNR Am J Neuroradiol* 2021;42:1839–46 Medline
17. Cheng CC, Preiswerk F, Hoge WS, et al. **Multipathway multi-echo (MPME) imaging: all main MR parameters mapped based on a single 3D scan.** *Magn Reson Med* 2019;81:1699–713 CrossRef Medline
18. Cheng CC, Preiswerk F, Madore B. **Multi-pathway multi-echo acquisition and neural contrast translation to generate a variety of quantitative and qualitative image contrasts.** *Magn Reson Med* 2020;83:2310–21 CrossRef Medline
19. Bracher AK, Hofmann C, Bornstedt A, et al. **Ultrashort echo time (UTE) MRI for the assessment of caries lesions.** *Dentomaxillofac Radiol* 2013;42:20120321 CrossRef Medline

Back to the Future: Dynamic Contrast-Enhanced Photon-Counting Detector CT for the Detection of Pituitary Adenoma in Cushing Disease

Ian T. Mark, Jamie Van Gompel, Irina Bancos, Alex A. Nagelschneider, Derek R. Johnson, Girish Bathla, Ajay A. Madhavan, Nikkole M. Weber, and Lifeng Yu

ABSTRACT

SUMMARY: Historically, MR imaging has been unable to detect a pituitary adenoma in up to one-half of patients with Cushing disease. This issue is problematic because the standard-of-care treatment is surgical resection, and its success is correlated with finding the tumor on imaging. Photon-counting detector CT is a recent advancement that has multiple benefits over conventional energy-integrating detector CT. We present the use of dynamic contrast-enhanced imaging using photon-counting detector CT for the detection of pituitary adenomas in patients with Cushing disease.

ABBREVIATIONS: EID = energy-integrating detector; PCD-CT = photon-counting detector CT

MR imaging is the primary technique to evaluate pituitary lesions.[1] Postcontrast dynamic imaging of the pituitary gland has been shown to be helpful for the identification of pituitary lesions, especially small lesions.[1,2] MR imaging of the sella remains extremely challenging, predominantly due to the small size of the pituitary gland and artifacts related to the skull base and sphenoid sinus aeration patterns. Historically, MR imaging has been unable to detect a pituitary adenoma in up to one-half of patients with Cushing disease.[3] This is problematic because the identification of the adenoma is an imperative step in successful surgical resection. Photon-counting detector CT (PCD-CT) is a new technique with increased spatial and contrast resolution relative to conventional energy-integrating detector (EID) CT.[4] The purpose of this report was to describe our dynamic contrast-enhanced PCD-CT technique for the identification of pituitary microadenomas in Cushing disease.

PCD-CT Technique

A dynamic contrast-enhanced CT protocol was developed on a PCD-CT scanner (Naeotom Alpha; Siemens) for imaging patients with Cushing disease. Our institutional practice is to obtain a preoperative skull base CTA to assist surgeons with operative planning. The protocol consists of a skull base CTA scan (120-kV, CAREkeV image-quality level of 230) followed by 4 delayed scans of the sella (effective mAs of 260) spaced 20 seconds apart. All scans used a high-resolution mode with a detector collimation of 120 × 0.2 mm. The CTA scan is triggered by using contrast bolus tracking with an ROI over the ascending aorta and a trigger threshold of 175 HU at 90 kV. For the 4 scans over the sella, images were reconstructed at both 0.2- and 0.6-mm section thickness using a smooth kernel of Hr40 (with quantum iterative reconstruction strength setting of 3). Virtual monochromatic imaging at 70 keV and a low-energy threshold (T3D) were used for the 0.6- and 0.2-mm reconstructions, respectively. We performed a preliminary evaluation on multiple virtual monochromatic imaging energies, 40, 50, 60, and 70 keV, and found that the 70-keV images had the optimal balance between contrast enhancement and noise. A lower keV did increase the contrast between a microadenoma and pituitary tissue, but the increased noise degraded the image quality; 70 keV had the best visual image quality. Per our CTA protocol, the contrast dose for patients weighing <136 kg included Iohexol 350 (Omnipaque-350; GE Healthcare), 100 mL at 4 mL/s, followed by 35 mL of 0.9% NaCL at 4 mL/s. The CT dose index volume was 44.6 mGy for each delayed scan of the sella.

Cases

We present 3 patients who were diagnosed with Cushing disease after a work-up by endocrinology. These patients were defined endocrinologically as having pituitary tumors. Each patient was scheduled to undergo a preoperative skull base CTA to help guide our surgical team. The clinically indicated CTA was then augmented with 4 delayed imaging passes of the sella as described above. In all 3 patients, we identified discrete hypoenhancing lesions, compatible with a pituitary adenoma. These adenomas

Received December 11, 2023; accepted after revision January 15, 2024.

From the Departments of Radiology (I.T.M., A.A.N., D.R.J., G.B., A.A.M., N.M.W., L.Y.), Neurosurgery (J.V.G.), and Endocrinology (I.B.), Mayo Clinic, Rochester, Minnesota.

Please address correspondence to Ian Mark, MD, Department of Radiology, Mayo Building, 3-72W, Rochester, MN 55905; e-mail: Mark.Ian@mayo.edu; @iantmark

http://dx.doi.org/10.3174/ajnr.A8171

were most conspicuous on different delayed sequences in each patient. In 2 cases, the CT-identified lesions were not seen with certainty on the comparison MR imaging.

Patient 1. A 67-year-old woman with osteoporosis, muscle weakness, and progressive weight gain was diagnosed with Cushing disease. Preoperative 1.5T MR imaging including dynamic contrast-enhanced images showed heterogeneous enhancement in the right pituitary gland without a clear lesion. PCD-CT (Fig 1) found 2 clear hypoenhancing lesions (measuring 7 and 4 mm) in the right aspect of the pituitary gland on the third dynamic series. The patient underwent transsphenoidal resection of these lesions, and pathologic examination confirmed corticotroph adenomas.

Patient 2. A 57-year-old woman who presented with uncontrolled diabetes mellitus type 2 and hypertension was diagnosed with Cushing disease. Preoperative 1.5T MR imaging demonstrated a 2- to 3-mm area of T2-hyperintense signal (Fig 2) in the left superior aspect of the pituitary gland with heterogeneous enhancement on the dynamic contrast-enhanced series. PCD-CT demonstrated a hypoenhancing lesion in the same location, best seen on the first PCD-CT series of the pituitary gland. Intraoperatively, a whitish fluid-filled lesion was seen and thought by the neurosurgical team to be consistent with a tumor, but given its liquidus consistency, it did not generate sufficient material to yield a pathologic diagnosis of corticotroph adenoma. However, biochemical remission was documented postoperatively as the patient developed postoperative adrenal insufficiency.

Patient 3. A 68-year-old man presented with osteoporotic vertebral body compression fractures, with subsequent work-up demonstrating Cushing disease. His preoperative 3T MR imaging with dynamic postcontrast imaging was severely motion-degraded and nondiagnostic. PCD-CT identified a 4-mm hypoenhancing lesion in the right aspect of the pituitary gland that involved the cavernous sinus, best seen on the fourth series (Fig 3). Intraoperatively, this imaging finding corresponded with a firm lesion that contained a pseudocapsule. Pathologic examination of the resected lesion confirmed a corticotroph adenoma.

DISCUSSION

In this report, we describe an imaging protocol for dynamic postcontrast imaging of the pituitary gland on PCD-CT. Pituitary lesions were identified on PCD-CT in 3 patients with Cushing disease.

Traditional EID-CT converts x-ray photons to visible light and subsequently converts the light to electrical signals. PCD-CT, on the other hand, simplifies this process by directly converting each photon to an electrical signal and recording its energy information. PCD-CT has shown an advantage for increased spatial resolution compared with typical clinical protocols on MR imaging and EID-CT.[5] In addition to improved spatial resolution and the potential to lower the radiation dose, PCD-CT has a higher iodine signal

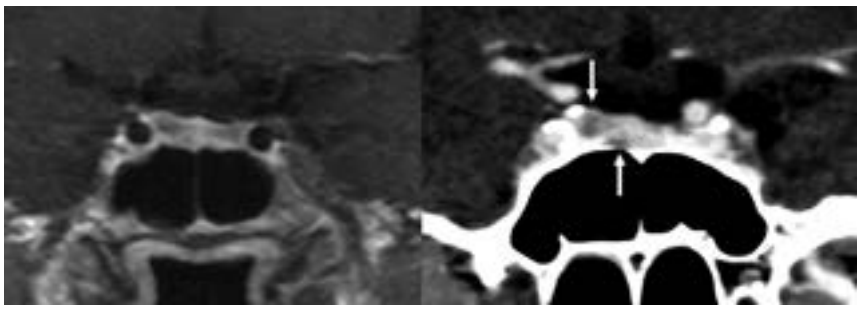

FIG 1. Patient 1, a 67-year-old woman with Cushing disease. Her preoperative dynamic postcontrast T1-weighted image (*left*) shows heterogeneous enhancement in the right pituitary gland without a definite lesion. Dynamic contrast-enhanced PCD-CT (*right*) depicting the third imaging series of the sella with 0.6-mm section thickness shows 2 distinct hypoenhancing lesions (*arrows*) in the right pituitary gland, found to be pathology-proved adenomas.

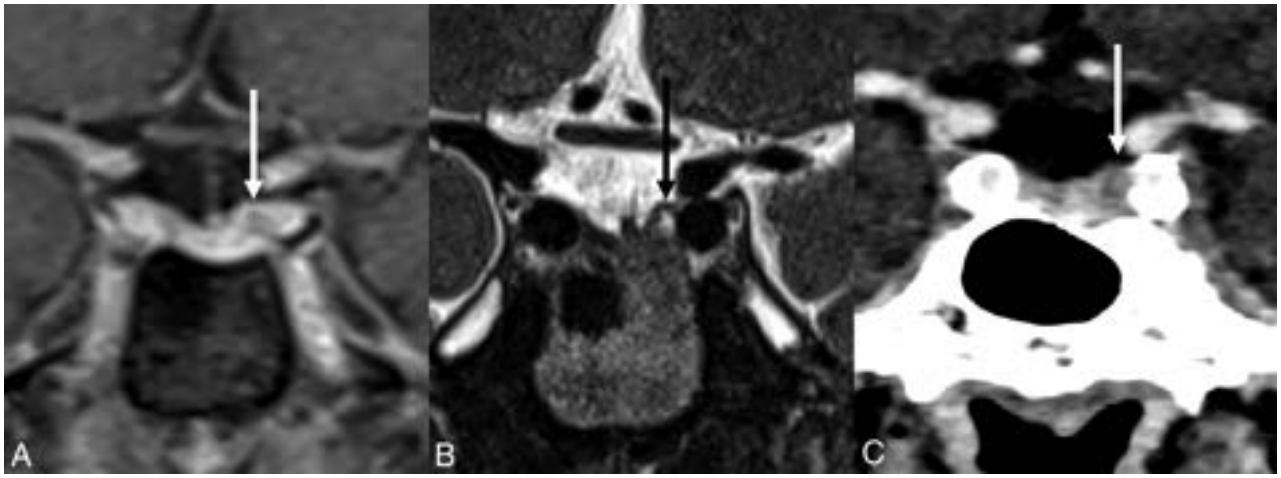

FIG 2. Patient 2, a 57-year-old woman with Cushing disease. Coronal dynamic contrast-enhanced MR imaging (*A*, *white arrow*) shows a small, hypoenhancing lesion in the left superior aspect of the pituitary gland with a corresponding T2-hyperintense signal (*B, black arrow*). PCD-CT (*C*, *white arrow*) shows corresponding hypoenhancement on the first series of the sella, seen as a coronal reconstruction at 0.6-mm section thickness.

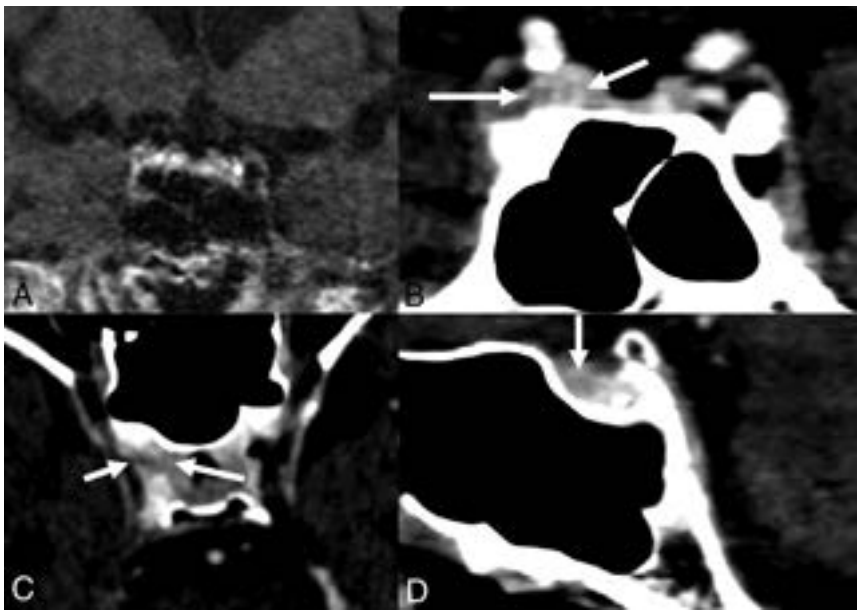

FIG 3. Patient 3, a 68-year-old man with Cushing disease. His preoperative MR imaging (*A*) was nondiagnostic secondary to motion. Coronal (*B*), axial (*C*), and sagittal (*D*) images from the fourth sequence of a dynamic contrast-enhanced PCD-CT show a hypoenhancing lesion (*arrows*) in the right aspect of the pituitary gland, which involves the cavernous sinus. This was a pathology-proved adenoma.

than EID-CT due to higher weighting of low-energy photons during photon detection, which increases the conspicuity of iodine-enhanced soft-tissue structures.[6] While it is a new application only receiving FDA approval in 2021, PCD-CT has already been shown to have multiple useful applications, including evaluation of multiple myeloma involving the spine,[7] CSF-venous fistula,[8] and temporal bone[9] among many other applications. None of these, however, have been applied to pituitary imaging.

Dynamic contrast-enhanced EID-CT imaging of the sella was previously described in the 1980s[10] and 1990s[10,11] A study published in 2015, including patients imaged beginning in 2004, found that dynamic EID-CT was more effective than MR imaging without dynamic contrast-enhanced imaging.[12] Modern imaging, however, has abandoned CT in favor of MR imaging.[1] Neuroimaging of the pituitary gland in patients with Cushing disease continues to serve an imperative function in its diagnosis and management. Cushing disease is caused by a pituitary adenoma that secretes corticotropin, subsequently leading to an increase in the production of cortisol from the adrenal cortex. Hypercortisolism leads to the development of features of overt Cushing syndrome on examination (skin fragility, bruising, striae, supraclavicular and dorsocervical pads, facial rounding, proximal myopathy); comorbidities such as hypertension, diabetes, obesity, fractures, infections, and pulmonary embolism; and an increase in mortality.[13] While inferior petrosal sinus sampling can help to distinguish Cushing disease from ectopic Cushing syndrome, it has not been shown to reliably localize a lesion within the pituitary gland.[14] This finding is particularly important because surgical resection is the standard-of-care treatment for Cushing disease. If MR imaging is unable to locate an adenoma, surgical resection is associated with a higher rate of complications and decreased cure rates.[13]

Our experience is too limited to advocate for PCD-CT as a replacement for MR imaging; however, there are several situations in which CT has advantages over MR imaging. CT tables generally have higher weight limits than MR imaging tables to accommodate larger patients, and the larger bore size of CT could help patients who cannot tolerate MR imaging due to claustrophobia. As shown in patient 3, the faster acquisition time of CT can be helpful in patients who are unable to lie still long enough for diagnostic-quality MR images to be acquired. Additionally, PCD-CT could help in patients who are unable to undergo MR imaging secondary to metal safety concerns, nonconditional implants, or gadolinium-based contrast reactions. Finally, in cases in which patients have overpneumatized sphenoid sinuses that produce problematic artifacts over the sella on MR imaging, CT image quality is not confounded by this problem. Specific to PCD-CT, the imaging technique allows thin, submillimeter section thickness. In our experience, the primary benefit of this technique is outlining the peripheral margin of the adenoma relative to the normal pituitary gland, allowing greater confidence in identifying a hypoenhancing lesion as an adenoma.

At our institution, patients scheduled for pituitary surgery undergo a preoperative skull base CTA to help with surgical planning. Thus, as is the case with all CT scans, this technique increases the radiation dose to the patient. Further work studying a larger number of patients could further refine the imaging technique to decrease the number of imaging passes of the sella and help decrease the radiation dose. Given the clear advantages of PCD-CT over EID-CT and the importance of preoperative adenoma identification in patients with Cushing disease, we believe that this technique should be thoroughly studied, and we will continue to use it as our institutional preference.

CONCLUSIONS

We provide the first description of dynamic contrast-enhanced imaging on PCD-CT for the evaluation of pituitary adenomas in Cushing disease. Given the importance of preoperative tumor localization of pituitary microadenomas to patient outcomes, this technique may potentially serve as an adjunct to cases negative on MR imaging.

ACKNOWLEDGMENTS

The authors acknowledge the support of the Mayo Clinic CT Clinical Innovation Center and Siemens Healthineers, who own the photon-counting CT used for a portion of this study under the terms of a sponsored research agreement with the Mayo Clinic.

Disclosure forms provided by the authors are available with the full text and PDF of this article at www.ajnr.org.

REFERENCES

1. Bonneville JF, Potorac I, Petrossians P, et al. **Pituitary MRI in Cushing's disease: an update**. *J Neuroendocrinol* 2022;34:e13123 CrossRef Medline
2. Friedman TC, Zuckerbraun E, Lee ML, et al. **Dynamic pituitary MRI has high sensitivity and specificity for the diagnosis of mild Cushing's syndrome and should be part of the initial workup**. *Horm Metab Res* 2007;39:451–56 CrossRef Medline
3. Bashari WA, Gillett D, MacFarlane J, et al. **Modern imaging in Cushing's disease**. *Pituitary* 2022;25:709–12 CrossRef Medline
4. Nehra AK, Rajendran K, Baffour FI, et al. **Seeing more with less: clinical benefits of photon-counting detector CT.** *Radiographics* 2023;43:e220158 CrossRef Medline
5. Rajendran K, Petersilka M, Henning A, et al. **First clinical photon-counting detector CT system: technical evaluation.** *Radiology* 2022;303:130–38 CrossRef Medline
6. Dane B, Qian K, Soni R, et al. **Crohn's disease inflammation severity assessment with iodine density from photon counting CT enterography: comparison with endoscopic histopathology**. *Abdom Radiology (NY)* 2023;49:271–78 CrossRef Medline
7. Baffour FI, Glazebrook KN, Ferrero A, et al. **Photon-counting detector CT for musculoskeletal imaging: a clinical perspective.** *AJR Am J Roentgenol* 2023;220:551–60 CrossRef Medline
8. Madhavan AA, Yu L, Brinjikji W, et al. **Utility of photon-counting detector CT myelography for the detection of CSF-venous fistulas.** *AJNR Am J Neuroradiol* 2023;44:740–44 CrossRef Medline
9. Benson JC, Rajendran K, Lane JI, et al. **A new frontier in temporal bone imaging: photon-counting detector CT demonstrates superior visualization of critical anatomic structures at reduced radiation dose.** *AJNR Am J Neuroradiol* 2022;43:579–84 CrossRef Medline
10. Bonneville JF, Cattin F, Portha C, et al. **Computed tomographic demonstration of the posterior pituitary.** *AJR Am J Roentgenol* 1986;146:263–66 CrossRef Medline
11. Stadnik T, Spruyt D, van Binst A, et al. **Pituitary microadenomas: diagnosis with dynamic serial CT, conventional CT, and T1-weighted MR imaging before and after injection of gadolinium.** *Eur J Radiol* 1994;18:191–98 CrossRef Medline
12. Kinoshita M, Tanaka H, Arita H, et al. **Pituitary-targeted dynamic contrast-enhanced multisection CT for detecting MR imaging-occult functional pituitary microadenoma.** *AJNR Am J Neuroradiol* 2015;36:904–08 CrossRef Medline
13. Ntali G, Asimakopoulou A, Siamatras T, et al. **Mortality in Cushing's syndrome: systematic analysis of a large series with prolonged follow-up**. *Eur J Endocrinol* 2013;169:715–23 CrossRef Medline
14. Lonser RR, Wind JJ, Nieman LK, et al. **Outcome of surgical treatment of 200 children with Cushing's disease**. *J Clin Endocrinol Metab* 2013;98:892–901 CrossRef Medline

T2-FLAIR Mismatch: An Imaging Biomarker for Children's *MYB/MYBL1*–Altered Diffuse Astrocytoma or Angiocentric Glioma

E.A. van Maren, J.W. Dankbaar, P. Wesseling, S. Plasschaert, A. Muhlebner, E.W. Hoving, P.A. Robe, T.J. Snijders, R. Hoogendijk, M.E.G. Kranendonk, and M.H. Lequin

ABSTRACT

BACKGROUND AND PURPOSE: T2-FLAIR mismatch is a highly specific imaging biomarker of *IDH*-mutant diffuse astrocytoma in adults. It has however also been described in *MYB/MYBL1*–altered low grade tumors. Our aim was to assess the diagnostic power of the T2-FLAIR mismatch in *IDH*-mutant astrocytoma and *MYB/MYBL1*–altered low-grade tumors in children and correlate this mismatch with histology.

MATERIALS AND METHODS: We evaluated MR imaging examinations of all pediatric patients, performed at the Princess Máxima Center for Pediatric Oncology and the University Medical Center Utrecht between January 2012 and January 2023, with the histomolecular diagnosis of *IDH*-mutant astrocytoma, diffuse astrocytoma *MYB/MYBL1*–altered, or angiocentric glioma, and the presence of T2-FLAIR mismatch was assessed. Histologically, the presence of microcysts in the tumor (a phenomenon suggested to be correlated with T2-FLAIR mismatch in *IDH*-mutant astrocytomas in adults) was evaluated.

RESULTS: Nineteen pediatric patients were diagnosed with either *IDH*-mutant astrocytoma ($n = 8$) or *MYB/MYBL1*–altered tumor ($n = 11$: diffuse astrocytoma, *MYB*- or *MYBL1*-altered $n = 8$; or angiocentric glioma $n = 3$). T2-FLAIR mismatch was present in 11 patients, 3 (38%) in the *IDH*-mutant group and 8 (73%) in the *MYB/MYBL1* group. No correlation was found between T2-FLAIR mismatch and the presence of microcysts or an enlarged intercellular space in either *IDH*-mutant astrocytoma ($P = .38$ and $P = .56$, respectively) or *MYB/MYBL1*–altered tumors ($P = .36$ and $P = .90$, respectively).

CONCLUSIONS: In our pediatric population, T2-FLAIR mismatch was more often found in *MYB/MYBL1*–altered tumors than in *IDH*-mutant astrocytomas. In contrast to what has been reported for *IDH*-mutant astrocytomas in adults, no correlation was found with microcystic changes in the tumor tissue. This finding challenges the hypothesis that such microcystic changes and/or enlarged intercellular spaces in the tissue of these tumors are an important part of explaining the occurrence of the T2-FLAIR mismatch.

ABBREVIATIONS: NGS = next-generation sequencing; WHO = World Health Organization

Pediatric-type low-grade astrocytoma with *MYB* or *MYBL1* alteration is a newly defined CNS tumor type listed in the 5th edition of the World Health Organization (WHO) CNS tumor classification.[1] It is considered a CNS WHO grade 1 tumor, despite the infiltrative growth into the CNS parenchyma, which is the defining feature of grade 2 gliomas.[2,3] The WHO CNS tumor classification describes 2 types of grade 2 tumors with a *MYB* or *MYBL1* alteration: 1) diffuse astrocytoma, *MYB* or *MYBL1*–altered,[1,4] and 2) angiocentric glioma with a *MYB-QKI* fusion.[5] These types of tumors show radiologic and histologic differences but have molecular overlap with *MYB* or *MYBL1* alterations as tumor drivers and close clustering in DNA methylation profiling studies.[2,6]

A few years ago, Kalelioglu et al[7] published 2 cases of pediatric-type low-grade astrocytomas with *MYB/MYBL1* alteration with their MR imaging characteristics. They also mentioned T2-FLAIR mismatch as a possible imaging marker. This mismatch was defined as a tumor with a homogeneous high T2-weighted MR signal intensity that showed a decreased signal in the central part and a hyperintense rim on FLAIR. In adults, T2-FLAIR mismatch has emerged as a highly specific imaging biomarker for *IDH*-mutant astrocytoma, with a reported specificity of 100%.[8] How often T2-FLAIR mismatch is seen in *MYB/MYBL1*–altered low-grade tumors and in *IDH*-mutant astrocytomas in children has yet to be elucidated. This information is highly relevant because the *MYB/MYBL1*–altered tumors are designated CNS WHO grade 1 and have a better prognosis than *IDH*-mutant

Received June 23, 2023; accepted after revision January 23, 2024.

From the Departments of Radiology and Nuclear Medicine (E.A.v.M., J.W.D., M.H.L.), Pathology (A.M.), Neurosurgery (E.W.H., P.A.R.), and Neurology (T.J.S.), UMC Utrecht Brain Center, University Medical Center Utrecht, Utrecht, the Netherlands; Princess Máxima Center for Pediatric Oncology (P.W., S.P., E.W.H., R.H., M.E.G.K., M.H.L), Utrecht, the Netherlands; and Department of Pathology (P.W.), Amsterdam University Medical Centers/VU Medical Center, Amsterdam, the Netherlands.

Please address correspondence to Jan W. Dankbaar, MD, 3508 GA Utrecht, the Netherlands Mailbox 85500; e-mail: j.w.dankbaar@umcutrecht.nl

Indicates article with online supplemental data.

http://dx.doi.org/10.3174/ajnr.A8203

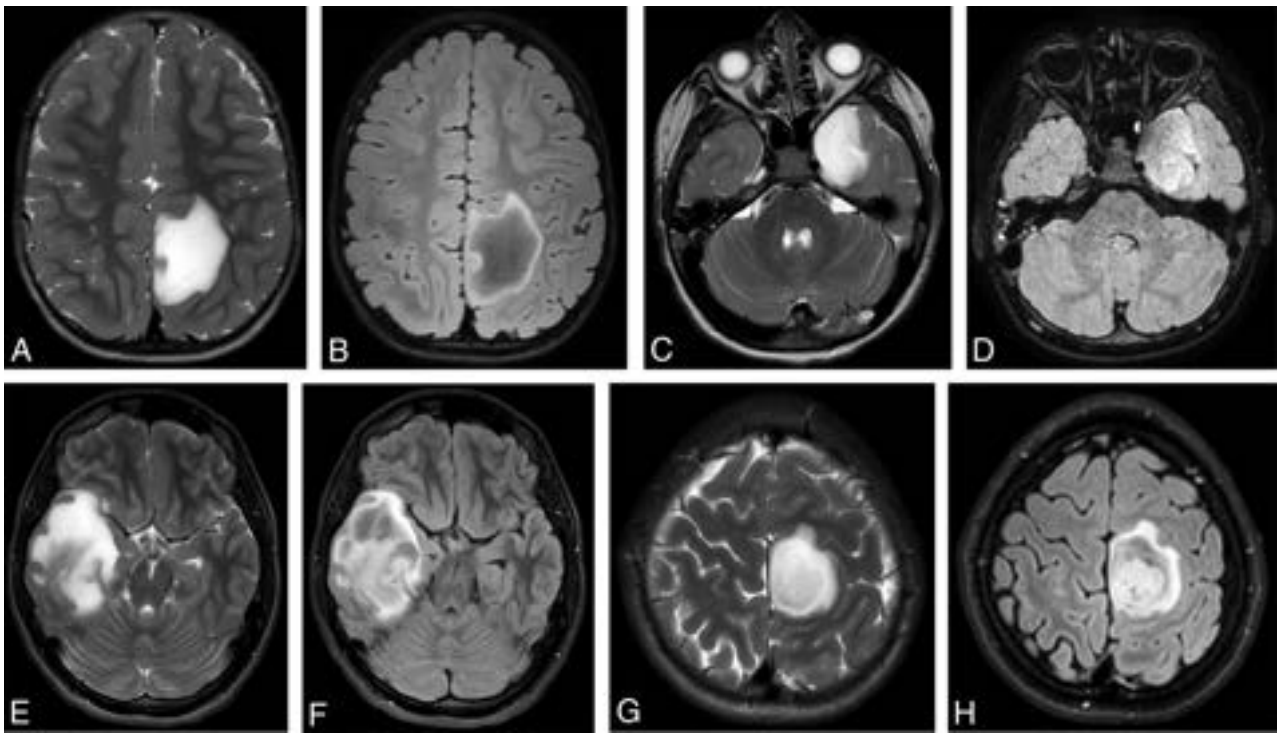

FIG 1. T2-FLAIR mismatch sign and area in *MYB/MYBL1*–altered diffuse astrocytoma and *IDH*-mutant glioma, T2- and T2-FLAIR-weighted sequences. *A* and *B*, *MYB/MYBL1*–altered diffuse astrocytoma left parietal lobe, mismatch sign. *C* and *D*, *MYB/MYBL*–altered diffuse astrocytoma left temporal lobe, mismatch area. *E* and *F*, *IDH*-mutant astrocytoma right temporal lobe, mismatch sign. *G* and *H*, *IDH*-mutant astrocytoma left frontoparietal lobe, mismatch area.

diffuse astrocytomas, which can progress to a CNS WHO grade 4 tumor.[6]

Therefore, we performed a retrospective study to assess the presence of T2-FLAIR mismatch in pediatric patients with a *MYB/MYBL1*–altered tumor or *IDH*-mutant astrocytoma. A second aim was to test the hypothesis that microcystic change and/or an enlarged intercellular space as seen by histopathologic analysis in adult-type *IDH*-mutant astrocytomas with T2-FLAIR mismatch underlies the mismatch in these pediatric tumors as well.[9]

MATERIALS AND METHODS

Relevant clinical, histopathologic, molecular, and imaging data of all consecutive pediatric patients from the Princess Máxima Center for Pediatric Oncology and the University Medical Center Utrecht with the histomolecular diagnosis of diffuse astrocytoma, *MYB/MYBL1*–altered, angiocentric glioma, or *IDH*-mutant astrocytoma were collected from January 2012 until January 2023.

Imaging

All patients underwent a dedicated brain tumor imaging protocol, including T2-FLAIR, T2 TSE, and T1-weighted imaging before and after contrast administration and DWI. MR imaging studies were performed at field strengths of 1.5T and 3T. The imaging protocol slightly changed during the period of inclusion. However, T2-FLAIR and T2 TSE were always available. Good interrater agreement ($\kappa = 0.75$) for the T2-FLAIR mismatch was found using a cohort with different field strengths and acquisition protocols.[10]

The imaging features assessed were T1 and T2 signal intensity of the tumor, location, existence of only solid or also cystic parts, diffuse infiltrative versus more expansile with sharp borders (on T2 FLAIR and T2), diffusion restriction (visual assessment of the ADC map with restriction being areas of low signal compared with normal brain tissue), contrast enhancement of the solid part of the tumor, and T2-FLAIR mismatch.

Because not all our cases showed the T2-FLAIR mismatch in the whole tumor, we distinguished between the T2-FLAIR mismatch sign (Fig 1*A*, -*B*, -*E*, and -*F*) and T2-FLAIR mismatch area (Fig 1*C*, -*D*, -*G*, and -*H*) using the following definitions:

T2-FLAIR Mismatch Sign.

- T2-FLAIR mismatch in the central solid part of the whole tumor shows a high signal on T2 and a lower signal on FLAIR with a thin hyperintense rim on the FLAIR image.
- No necrotic or cystic parts in the tumor are visible on the MR images.

T2-FLAIR Mismatch Area.

- Homogeneous hyperintense T2-weighted signal only in the solid part of the tumor
- FLAIR hypointense signal, with a surrounding hyperintense rim around the same (solid) area but without a hyperintense rim around the nonsolid parts of the tumor.

Two neuroradiologists (with 2 and 8 years of experience in pediatric neuro-oncology) evaluated these features independently, blinded to the molecular diagnosis.

Pathobiology

All patients underwent surgery for biopsy or (partial) resection. Three board-certified neuropathologists evaluated all patients'

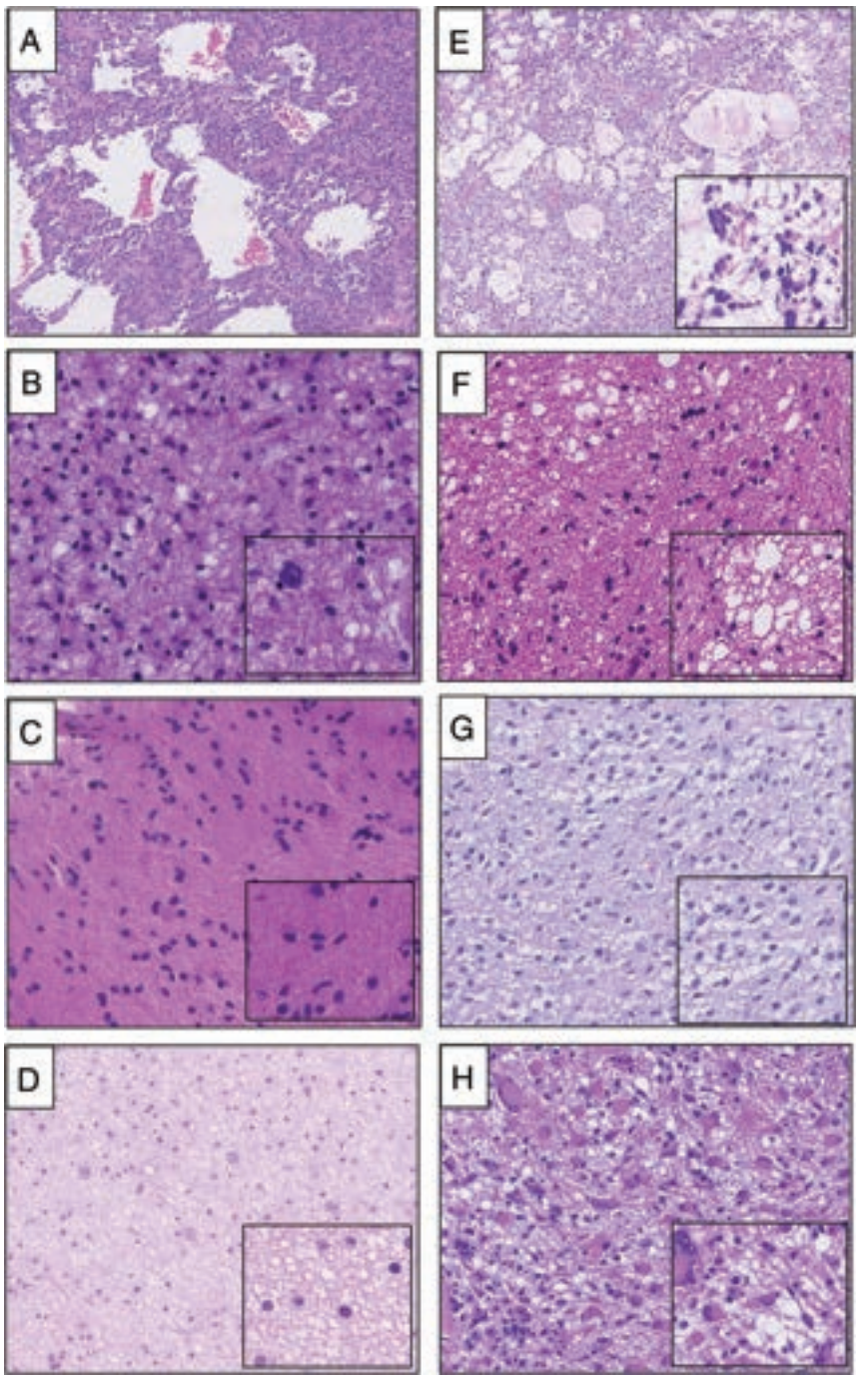

FIG 2. *A–D*, Low-grade tumors, *MYB/MYBL1*–altered. *A*, T2-FLAIR mismatch and microcysts in an angiocentric glioma. *B*, T2-FLAIR mismatch and an enlarged intercellular space (EIS). *C*, T2-FLAIR mismatch without microcyst or EIS. *D*, No T2-FLAIR mismatch with EIS. *B–D*, All from diffuse astrocytomas, *MYB/MYBL1*–altered. *E–H*, Diffuse astrocytoma, *IDH*-mutant. *E*, T2-FLAIR mismatch and microcysts in grade 3 astrocytoma. *F*, No T2-FLAIR mismatch with microcysts in grade 2 astrocytoma. *G*, No T2-FLAIR mismatch and no microcyst or EIS in grade 2 astrocytoma. *H*, No T2-FLAIR mismatch with EIS in grade 2 astrocytoma. Magnification, 50–100×; inset, 200–400×.

tumors histologically, immunohistochemically, and molecularly, and all tumors on review were diagnosed according to the CNS WHO 2021 classification.

The molecular analysis included DNA methylation profiling, next-generation sequencing (NGS) panel mutation analysis, and/or whole transcriptome sequencing. Histologic re-evaluation included assessment of the presence/absence of atypia, mitotic activity, and necrosis, with special attention to the presence/absence of microcysts and enlarged intercellular spaces described by Yamashita et al.[9] The presence of microcystic change was determined to be positive if true microcysts could be detected at overview (with the 0.5× objective), and the presence of an enlarged intercellular space was determined to be positive if true microcysts could be detected with the 10× objective (Fig 2*B, -D*).

Statistical Analyses

The interrater reliability for the T2-FLAIR mismatch was determined using the Cohen κ coefficient. The presence of the T2-FLAIR mismatch (sign and area) between the *MYB/MYBL1* group and the *IDH*-mutant group was statistically analyzed using the Fisher exact test for independent proportions.

For further analyses, consensus on the presence of T2-FLAIR mismatch was reached in all cases, again blinded to the molecular diagnosis.

The differences in T2-FLAIR mismatch between the *IDH*-mutant and the *MYB/MYBL1*–altered group were statistically analyzed using the Fisher exact test for independent proportions. Correlations between T2-FLAIR mismatch on the one hand and the presence of histologic microcysts or an enlarged intercellular space on the other were tested using the Kendall rank correlation coefficient.

RESULTS

Nineteen pediatric patients were identified with either an *IDH*-mutant astrocytoma (2 grade 2, five grade 3, and 1 grade 4) or a *MYB/MYBL1*–altered tumor (8 diffuse astrocytomas, *MYB/MYBL1*–altered, and 3 angiocentric gliomas, all grade 1). One of our patients in the *IDH*-mutant astrocytoma group underwent surgery shortly after 18 years of age. Characteristics and the imaging/pathobiologic results of the 2 groups are outlined in Tables 1 and 2. Additional imaging characteristics are outlined in the Online Supplemental Data.

Imaging

In 15/19 cases, the 2 neuroradiologic reviews were concordant (κ = 0.58). Consensus was reached for discrepant findings in these 4 cases.

Table 1: Characteristics and results of the cases with diffuse astrocytoma *MYB/MYBL1*–altered or angiocentric glioma, CNS WHO grade 1

Case	Age (yr)	Subgroup	Fusion/Methylation Analysis	T2-FLAIR Mismatch Sign (S) or Area (A)	Histology	
					Microcysts	Enlarged Intercellular Spaces
1	1.1	Diffuse Astro.	*MYBL1::MMP16*	+ (A)	–	–
2	3.2	Diffuse Astro.	*MYBL1::STAU2-AS1*	+ (S)	–	–
3	9.7	Diffuse Astro.	*MYBL1::PACRG*	+ (S)	+	+
4	9.0	Angio-centric glioma	No fusion analysis[a]	+ (A)	–	+
5	3.9	Diffuse Astro.	*MYBL1::TOX*	+ (S)	+	+
6	11.4	Diffuse Astro.	No fusion analysis, diagnosis based on methylome profile	+ (A)	–	+
7	4.4	Diffuse Astro.	No fusion analysis[a]	+ (A)	–	+
8	15.9	Angio-centric glioma	*MYB::QKI*	–	–	–
9	5.7	Diffuse Astro.	No fusion analysis[a]	–	–	+
10	9.6	Diffuse Astro.	No fusion analysis[a]	–	–	+
11	8.2	Angio-centric glioma	*MYB::QKI*	+ (A)	–	–

Note:—The + indicates presence; –, absence of the characteristic; Astro. astrocytoma.
[a] In case no fusion analysis was available, the diagnosis of diffuse astrocytoma, *MYB*- or *MYBL1*–altered or angiocentric glioma was based on results of histology in combination with methylome profiling using the Infinium MethylationEPIC (850k) BeadChip (Illumina, San Diego, CA) methylation array.

Table 2: Characteristics and results of the cases with astrocytoma, *IDH*-mutant, CNS WHO grades 2–4

Case	Age (yr)	Subgroup	Fusion/Methylation Analysis	T2-FLAIR Mismatch Sign (S) or Area (A)	Histology	
					Microcysts	Enlarged Intercellular Spaces
12	17.7	*IDH* +, WHO 2	*IDH (R132H), ATRX, TP53*	+ (A)	+	+
13	9.2	*IDH* +, WHO 2	*IDH (R132H), TP53*	–	+	+
14	18.7	*IDH* +, WHO 2	*IDH (R132H), ATRX, TP53*	+ (S)	–	+
15	14.0	*IDH* +, WHO 2	*IDH (R132H), ATRX, TP53*	–	+	+
16	10.6	*IDH* +, WHO 2	*IDH (R132H), TP53*	–	–	+
17	4.0	*IDH* +, WHO 2	*IDH (R132H), PIK3CA, NF1*	–	+	–
18	17.1	*IDH* +, WHO 3	*IDH (R132H), PTEN, TP53*	–	+	+
19	15.6	*IDH* +, WHO 4	*IDH (R132H), TP53, MSH6, ATRX, CDKN2A, CIC.*	–		

Note:—The + indicates presence; –, absence of the characteristic.

T2-FLAIR mismatch was present in 10 patients (Fig 1), 8 in the *MYB/MYBL1* group (73%), and 2 in the *IDH*-mutant group (25%) ($P = .07$). Of the 8 cases in the *MYB/MYBL1* group with T2-FLAIR mismatch (sign and area), 6 were diffuse astrocytomas, *MYB* or *MYBL1*–altered, and 2 were angiocentric gliomas. The angiocentric gliomas showed a T2-FLAIR mismatch area in the solid parts; additional cystic parts were also visible on MR imaging. None of the angiocentric gliomas had a T2-FLAIR mismatch sign. No *MYB/MYBL1*–altered diffuse astrocytoma or angiocentric glioma showed restricted diffusion or enhancement after gadolinium. In the *IDH*-mutant diffuse astrocytomas, there was restricted diffusion in 2 (25%) cases, both in WHO grade 2 tumors. Sharp borders have been noted in 9 of 11 diffuse astrocytomas, *MYB/MYBL1*–altered, and only 3 of 8 in the *IDH*-mutant cases.

Correlation of Pathology and Imaging

Histopathologically, all *MYB- or MYBL1*–altered tumors showed diffuse growth of relatively monomorphic glial cells with ovoid or spindled nuclei within a fibrillar matrix. There was no frank atypia, mitotic activity, florid microvascular proliferation, or necrosis; all were CNS WHO grade 1. Only 2 cases showed histologically clear-cut microcystic changes, and both were found to have T2-FLAIR mismatch (18%). Three cases with T2-FLAIR mismatch showed an enlarged intercellular space of limited size (27%), while 3 other cases with T2-FLAIR mismatch did not show either microcystic changes or an enlarged intercellular space in the tissue that was available for histopathologic analysis (27%). Of the 3 cases without T2-FLAIR mismatch, 2 cases had enlarged intercellular spaces (Fig 2*A*–*D*).

The *IDH*-mutant astrocytomas showed more variable histology. Most cases were in line with CNS WHO grade 2 (moderate atypia, low mitotic activity, and no necrosis), but 1 case was regarded as grade 4 because of increased mitotic activity, pronounced nuclear pleomorphism, palisading tumor necrosis, and extensive florid microvascular proliferation. Two cases showed T2-FLAIR mismatch, both with microcystic changes (25%). Of the 6 cases that were negative for T2-FLAIR mismatch, 4 cases also had microcysts, and 3 cases showed enlarged intercellular spaces comparable with, or even more pronounced than those in the *MYB/MYBL1*–altered tumors (Fig 2*E*–*H*).

Microcysts were significantly more often observed in *IDH*-mutant astrocytomas than in *MYB/MYBL*–altered tumors ($P = .02$). However, there was no correlation of a T2-FLAIR mismatch and the presence of microcysts in the *IDH*-mutant astrocytoma group ($\tau = 0.33$, $P = .38$). Furthermore, no significant correlation was found between T2-FLAIR mismatch and the presence of an enlarged intercellular space in *IDH*-mutant astrocytoma ($\tau = 0.22$, $P = .56$). Also, in *MYB/MYBL1*–altered tumors, no significant correlation was found between T2-FLAIR mismatch and the

presence of microcysts or an enlarged intercellular space (τ = 0.29, P = .36 and τ = –0.04, P = .90, respectively).

DISCUSSION

T2-FLAIR mismatch is a noninvasive biomarker that can identify patients with *IDH*-mutant lower-grade astrocytomas with a positive predictive value up to 100% in the adult population.[10,11] This biomarker has not been not tested thoroughly in the pediatric population, in which the occurrence and specificity for *IDH*-mutant astrocytoma is still being determined. Kalelioglu et al,[7] for example, reported a T2-FLAIR mismatch in 1 of their 2 patients with a *MYB/MYBL1*–altered diffuse astrocytoma.

In this study, we have shown both the presence and histologic correlation of T2-FLAIR mismatch in children, not only in *IDH*-mutant astrocytomas but also in *MYB/MYBL1*–altered tumors (either diffuse astrocytoma, *MYB/MYBL1*–altered, or angiocentric glioma). The T2-FLAIR mismatch was present in 25% of the *IDH*-mutant astrocytomas and in 73% of *MYB/MYBL1* tumors. Acknowledging the possibility of a *MYB/MYBL1*–altered tumor is essential because there is an important difference in prognosis and treatment compared with *IDH*-mutant diffuse astrocytoma. Chiang et al[2] showed that 10-year progression-free survival and overall survival rates were 90% and 95% in patients (median age, 5 years; range, 0–26 years) with *MYB/MYBL1*–altered tumors. In contrast, adults with lower-grade *IDH*-mutant astrocytoma, 1p/19q-noncodeleted, show worse outcomes with a median survival period of 6.3 years.[12] In children, the clinical impact of *IDH1* mutation is less clear. These tumors may have the same biology as in the adult malignancy but are identified earlier in life. At least, they probably behave less indolently than other pediatric low-grade diffuse astrocytomas, and patients should be more closely followed.[13]

In our cohort, only 25% showed a T2-FLAIR mismatch in the *IDH*-mutant, 1p/19q-noncodeleted cases, which is lower than that in the adult population, which ranges around ≥50% in the *IDH*-mutant, 1p/19q-noncodeleted cases. Furthermore, 73% of *MYB/MYBL1* tumors showed a T2-FLAIR mismatch. Therefore, in the case of a pediatric CNS tumor with a T2-FLAIR mismatch with additional MR imaging characteristics compatible with a more low-grade appearance (no enhancement, no diffusion restriction), neuroradiologists should also consider a *MYB/MYBL1*–altered tumor in their differential diagnosis. This suggestion especially holds true for pediatric cases with the T2-FLAIR mismatch sign, which we almost exclusively observed in our *MYB/MYBL1*–altered diffuse astrocytoma cases. In contrast, in our (small) case series, the T2-FLAIR mismatch area was relatively frequently observed in angiocentric glioma. When a T2-FLAIR mismatch is observed, clinicians may be more hesitant to follow a watch-and-wait strategy because of the *IDH*-mutant astrocytoma in the differential diagnosis. The clinical consequence would be to obtain tissue to be confident of the histopathologic diagnosis. The finding of the T2-FLAIR mismatch in the more indolent *MYB/MYBL1*–altered tumors might change the radiologic differential diagnosis.

Additionally, the location of the tumor can be influential. We had only 1 *MYB/MYBL1*–altered infratentorial diffuse astrocytoma; all other cases were supratentorial, like all our *IDH*-mutant tumor cases. Therefore, in case of an infratentorial T2-FLAIR mismatch area, the presence of a *MYB/MYBL1*–altered angiocentric glioma should be especially considered.

Diffusion restriction or enhancement, commonly seen in high-grade brain tumors, was also not noted in our *MYB/MYBL1*–altered tumors cases.

There is still debate on the tissue characteristics that may underlie the T2-FLAIR mismatch phenomenon (sign or area). The newest insights are that T2-FLAIR mismatch in *IDH*-mutant astrocytoma is due to microcystic changes and/or enlarged intercellular spaces within the tumor that contain enough fluid volume to cause suppression on FLAIR images.[9] A histopathologic review of our cases showed microcystic changes and/or an enlarged intercellular space in 64% of *MYB/MYBL1*–altered tumors and 88% of *IDH*-mutant astrocytomas. However, the T2-FLAIR mismatch sign was observed just as often in *MYB/MYBL1*–altered tumors and *IDH*-mutant astrocytomas without microcystic changes or enlarged intercellular spaces. In our case series, a clear-cut correlation was absent. One explanation might be the sampling effect, because in some of our cases, only needle biopsy material was available for histologic analysis. Moreover, we did observe some intratumoral histologic heterogeneity for microcystic change and/or enlarged intercellular spaces in cases in which larger tumor fragments were available for evaluation. Another contributing factor might be the decreased statistical power of our analyses due to the small sample size.

In our cohort study in children, T2-FLAIR mismatch was observed in some of the *IDH*-mutant astrocytomas but even more frequently in *MYB/MYBL1*–altered tumors, both in angiocentric gliomas and diffuse astrocytomas, *MYB/MYBL1*–altered. Of note, T2-FLAIR mismatch has now also been reported in an H3K27M-mutant (and *IDH* wild-type) diffuse midline glioma in the brainstem of an adult.[14] A diffuse midline glioma is a tumor type that histologically typically does not show prominent microcystic change or an enlarged intercellular space.[4] In contrast, microcysts are frequently present in pilocytic astrocytomas.[15] However, T2-FLAIR mismatch has not been reported in these patients in relevant series,[16] and we did not observe it in our own center either. Again, this challenges the hypothesis that such microcystic changes are an important part of the explanation for the occurrence of the T2-FLAIR mismatch sign.

Finally, a recent study revealed that the inversion time used for the FLAIR sequence and field strength impacts the diagnostic accuracy of T2-FLAIR mismatch for low-grade astrocytoma imaging.[17] In our cases, the assessment of the T2-FLAIR mismatch will not be influenced by the field strength because all imaging was performed on 3T MR imaging systems (Phillips) at our institute, nor by different inversion times because all FLAIR imaging was performed with a 3D FLAIR sequence with nearly the same parameters.

Our study has some limitations. First, the number of cases is relatively limited. Although it seems clear that T2-FLAIR mismatch is clearly present in *MYB/MYBL1*–altered tumors, more evidence is needed to show the diagnostic value of T2-FLAIR mismatch for this type of tumor in the pediatric population. Second, the patient selection was retrospective with the identification of all patients with a *MYB/MYBL1*–altered, angiocentric glioma or *IDH*-mutant astrocytoma. From these data, the false-

positive rate of T2-FLAIR mismatch can, therefore, not be determined. Also, some patients with *MYB/MYBL1*–altered, angiocentric glioma or *IDH*-mutant astrocytoma may have been missed due to less extensive molecular tumor characterization in the past.

CONCLUSIONS

In our study, T2-FLAIR mismatch was found not only in grade 1–4 *IDH*-mutant astrocytomas but also (and even more frequently) in grade 1 *MYB*/*MYBL1*–altered tumors in children. Therefore, the radiologic differential diagnosis should include a grade 1 *MYB*/*MYBL1*–altered tumor when evaluating the MR imaging of pediatric CNS tumors. Furthermore, our study challenges the hypothesis that microcystic changes and/or enlarged intercellular spaces in the tissue of these tumors are essential for causing T2-FLAIR mismatch.

Disclosure forms provided by the authors are available with the full text and PDF of this article at www.ajnr.org.

REFERENCES

1. Louis DN, Perry A, Wesseling P, et al. **The 2021 WHO Classification of Tumors of the Central Nervous System: a summary.** *Neuro Oncol* 2021;23:1231–51 CrossRef Medline
2. Chiang J, Harreld JH, Tinkle CL, et al. **A single-center study of the clinicopathologic correlates of gliomas with a MYB or MYBL1 alteration.** *Acta Neuropathol* 2019;138:1091–92 CrossRef Medline
3. Ellison DW, Hawkins C, Jones DT, et al. **cIMPACT-NOW update 4: diffuse gliomas characterized by MYB, MYBL1, or FGFR1 alterations or BRAF(V600E) mutation.** *Acta Neuropathol* 2019;137:683–87 CrossRef Medline
4. Ramkissoon LA, Horowitz PM, Craig JM, et al. **Genomic analysis of diffuse pediatric low-grade gliomas identifies recurrent oncogenic truncating rearrangements in the transcription factor MYBL1.** *Proc Natl Acad Sci U S A* 2013;110:8188–93 CrossRef Medline
5. Bandopadhayay P, Ramkissoon LA, Jain P, et al. **MYB-QKI rearrangements in angiocentric glioma drive tumorigenicity through a tripartite mechanism.** *Nat Genet* 2016;48:273–82 CrossRef Medline
6. Wefers AK, Stichel D, Schrimpf D, et al. **Isomorphic diffuse glioma is a morphologically and molecularly distinct tumour entity with recurrent gene fusions of MYBL1 or MYB and a benign disease course.** *Acta Neuropathol* 2020;139:193–209 CrossRef Medline
7. Kalelioglu T, Rama B, Cho BB, et al. **Pediatric-type diffuse low-grade glioma with MYB/MYBL1 alteration: report of 2 cases.** *Neuroradiol J* 2022;36:232–35 CrossRef Medline
8. Park SI, Suh CH, Guenette JP, et al. **The T2-FLAIR mismatch sign as a predictor of IDH-mutant, 1p/19q-noncodeleted lower-grade gliomas: a systematic review and diagnostic meta-analysis.** *Eur Radiol* 2021;31:5289–99 CrossRef Medline
9. Yamashita S, Takeshima H, Kadota Y, et al. **T2-fluid-attenuated inversion recovery mismatch sign in lower grade gliomas: correlation with pathological and molecular findings.** *Brain Tumor Pathol* 2022;39:88–98 CrossRef Medline
10. Broen MP, Smits M, Wijnenga MM, et al. **The T2-FLAIR mismatch sign as an imaging marker for non-enhancing IDH-mutant, 1p/19q-intact lower-grade glioma: a validation study.** *Neuro Oncol* 2018; 20:1393–99 CrossRef Medline
11. Patel SH, Poisson LM, Brat DJ, et al. **T2-FLAIR mismatch, an imaging biomarker for IDH and 1p/19q status in lower-grade gliomas: a TCGA/TCIA project.** *Clin Cancer Res* 2017;23:6078–85 CrossRef Medline
12. Brat DJ, Verhaak RG, Aldape KD, et al; Cancer Genome Atlas Research Network. **Comprehensive, integrative genomic analysis of diffuse lower-grade gliomas.** *N Engl J Med* 2015;372:2481–98 CrossRef Medline
13. Ryall S, Tabori U, Hawkins C. **Pediatric low-grade glioma in the era of molecular diagnostics.** *Acta Neuropathol Commun* 2020;8:30 CrossRef Medline
14. Valentino WL, Okada D, Bhanu S. **A curious case of T2-FLAIR mismatch in H3K27M mutant glioma.** *Radiol Case Rep* 2022;17:2930–35 CrossRef Medline
15. Collins VP, Jones DT, Giannini C. **Pilocytic astrocytoma: pathology, molecular mechanisms and markers.** *Acta Neuropathol* 2015;129:775–88 CrossRef Medline
16. Johnson DR, Kaufmann TJ, Patel SH, et al. **There is an exception to every rule-T2-FLAIR mismatch sign in gliomas.** *Neuroradiology* 2019;61:225–27 CrossRef Medline
17. Kinoshita M, Arita H, Takahashi M, et al. **Impact of inversion time for FLAIR acquisition on the T2-FLAIR mismatch detectability for IDH-nutant, non-CODEL astrocytomas.** *Front Oncol* 2020;10:596448 CrossRef Medline

Identification of Multiclass Pediatric Low-Grade Neuroepithelial Tumor Molecular Subtype with ADC MR Imaging and Machine Learning

Matheus D. Soldatelli, Khashayar Namdar, Uri Tabori, Cynthia Hawkins, Kristen Yeom, Farzad Khalvati, Birgit B. Ertl-Wagner, and Matthias W. Wagner

ABSTRACT

BACKGROUND AND PURPOSE: Molecular biomarker identification increasingly influences the treatment planning of pediatric low-grade neuroepithelial tumors (PLGNTs). We aimed to develop and validate a radiomics-based ADC signature predictive of the molecular status of PLGNTs.

MATERIALS AND METHODS: In this retrospective bi-institutional study, we searched the PACS for baseline brain MRIs from children with PLGNTs. Semiautomated tumor segmentation on ADC maps was performed using the semiautomated level tracing effect tool with 3D Slicer. Clinical variables, including age, sex, and tumor location, were collected from chart review. The molecular status of tumors was derived from biopsy. Multiclass random forests were used to predict the molecular status and fine-tuned using a grid search on the validation sets. Models were evaluated using independent and unseen test sets based on the combined data, and the area under the receiver operating characteristic curve (AUC) was calculated for the prediction of 3 classes: *KIAA1549-BRAF* fusion, *BRAF* V600E mutation, and non-*BRAF* cohorts. Experiments were repeated 100 times using different random data splits and model initializations to ensure reproducible results.

RESULTS: Two hundred ninety-nine children from the first institution and 23 children from the second institution were included (53.6% male; mean, age 8.01 years; 51.8% supratentorial; 52.2% with *KIAA1549-BRAF* fusion). For the 3-class prediction using radiomics features only, the average test AUC was 0.74 (95% CI, 0.73–0.75), and using clinical features only, the average test AUC was 0.67 (95% CI, 0.66–0.68). The combination of both radiomics and clinical features improved the AUC to 0.77 (95% CI, 0.75–0.77). The diagnostic performance of the per-class test AUC was higher in identifying *KIAA1549-BRAF* fusion tumors among the other subgroups (AUC = 0.81 for the combined radiomics and clinical features versus 0.75 and 0.74 for *BRAF* V600E mutation and non-*BRAF*, respectively).

CONCLUSIONS: ADC values of tumor segmentations have differentiative signals that can be used for training machine learning classifiers for molecular biomarker identification of PLGNTs. ADC-based pretherapeutic differentiation of the *BRAF* status of PLGNTs has the potential to avoid invasive tumor biopsy and enable earlier initiation of targeted therapy.

ABBREVIATIONS: AUC = area under the receiver operating characteristic curve; *FGFR* = fibroblast growth factors receptor; GG = ganglioglioma; GLMD = gray-level dependence matrix; ML = machine learning; NF1 = neurofibromatosis 1; NPV = negative predictive value; OvR = one versus the rest; PA = pilocytic astrocytoma; pLGG = pediatric low-grade glioma; PLGNT = pediatric low-grade neuroepithelial tumor; RF = random forests; WHO = World Health Organization

Pediatric low-grade neuroepithelial tumors (PLGNTs) are the most common pediatric CNS tumors, representing approximately 40% of all pediatric brain tumors.[1,2] According to the 5th Edition of the World Health Organization (WHO) classification, PLGNTs are grade 1 and 2 neoplasms described in 3 groups: diffuse pediatric low-grade gliomas (pLGGs), circumscribed astrocytic gliomas, and glioneuronal and neuronal tumors.[3] The genetic

Received November 10, 2023; accepted after revision January 16, 2024.

From the Department Diagnostic Imaging (M.D.S., B.B.E.-W., M.W.W.), Division of Neuroradiology, The Arthur and Sonia Labatt Brain Tumour Research Centre (U.T., C.H.), Program in Genetics and Genome Biology (U.T.), and Division of Pathology (C.H.), The Hospital for Sick Children, Toronto, Ontario, Canada; Department of Medical Imaging (M.D.S., K.N., F.K., B.B.E.-W., M.W.W.), Institute of Medical Science (M.D.S., K.N., U.T., F.K., B.B.E.-W.), Department of Laboratory Medicine and Pathobiology (C.H.), and Department of Computer Science (F.K.), University of Toronto, Toronto, Ontario, Canada; Vector Institute (K.N., F.K.), Toronto, Ontario, Canada; Department of Radiology (K.Y.), Lucile Packard Children's Hospital, Stanford University School of Medicine, Stanford, California; and Department of Diagnostic and Interventional Neuroradiology (M.W.W.), University Hospital Augsburg, Augsburg, Germany.

C. Hawkins was supported by the Canadian Cancer Society (grant No. 702296) and the Canadian Institute of Health Research (grant No. 159805).

Please address correspondence to Matheus D. Soldatelli, MD, PhD, EDiNR/EDiPNR, Department of Diagnostic Imaging, Division of Neuroradiology, The Hospital for Sick Children, 170 Elizabeth St, Toronto, ON 02115; e-mail: md.soldatelli@gmail.com; @md_Soldatelli

Indicates article with online supplemental data.

http://dx.doi.org/10.3174/ajnr.A8199

and molecular features have been incorporated in this updated classification and, along with the histologic phenotype, relate to different prognoses and new targeted therapies.[4,5]

Most commonly, PLGNTs present with genetic changes causing upregulation of the Ras/mitogen-activated protein kinase (*RAS/MAPK)* pathway, usually fusions or mutations in the B-Raf proto-oncogene, serine/threonine kinase *(BRAF)* gene. The chromosomal alteration in *BRAF* fusion involves the duplication of the *BRAF* oncogene, followed by its insertion into one of several fusion targets, most often the *K1AA1549* gene (*KIAA1549-BRAF* fusion).[6] *BRAF* V600E point mutations activate *BRAF*, causing deregulation in the mitogen-activated p.V600E protein kinase pathway.[7] Other common mutations include neurofibromatosis 1 (NF1), fibroblast growth factors receptors 1 and 2 (*FGFR* 1/2),[2,8] and *MYB/MYBL1* rearrangements.[9-11] The most common histology for the *KIAA1549-BRAF* fusion and *BRAF* V600E mutation tumors is pilocytic astrocytoma (PA) and ganglioglioma (GG), respectively.[2,12] However, except for molecularly defined tumors, molecular subtypes are often found across various entities.[2,13]

Even though surgery is the preferred treatment for most PLGNTs when possible, more than one-half of PLGNTs cannot be completely resected, requiring subsequent pharmacologic therapy, often leading to high morbidity.[5,14] Genetic differences are essential for therapeutic decision-making, with *BRAF* and *MEK* inhibitors gaining popularity and new trials being developed.[15-17] Notably, *BRAF* inhibitors exhibit efficacy in *BRAF* V600E mutation tumors, while *KIAA1549-BRAF* fusion tumors might exhibit progression due to pathway paradoxic activation when treated with these inhibitors. Instead, *KIAA1549-BRAF* fusion tumors respond positively to *MEK* inhibitors.[15] However, implementing these new therapeutic strategies requires tissue sampling and molecular testing, mostly restricted to academic reference centers. Therefore, neuroimaging surrogates would be valuable tools for prognosis and treatment-planning.[2]

Radiomics has been applied to determine tumor histology, prognostication, and molecular classification (radiogenomics) in pediatric neuro-oncology.[18] Zhang et al[19] developed an MR imaging–based machine learning (ML) decision path that identified the 4 molecular subgroups of medulloblastomas. Wagner et al[17] demonstrated that FLAIR sequences predicted molecular subgroups of pLGG with a high area under the receiver operating characteristic curve (AUC) using a supervised ML approach. In addition, qualitative ADC features have recently been shown to predict *BRAF* V600E mutations among pLGGs.[16]

Despite the increased application of ML in pediatric neuroradiology, to date, there are no studies assessing radiomic features of ADC images in PLGNTs. Given the widespread use of ADC images and their relatively straightforward interpretation in the context of neoplastic cellularity and prognostication,[16] we hypothesized that *KIAA1549-BRAF* fusion, *BRAF* V600E mutation, and other non-*BRAF* PLGNTs can be differentiated quantitatively using the ADC map segmentations and that radiomics can improve diagnostic accuracy. Specifically, we aimed to develop and validate a radiomics ADC signature predictive of the molecular status of PLGNTs in pediatric patients using a bi-institutional cohort.

MATERIALS AND METHODS

Patients

This retrospective study was approved by the institutional review boards or research ethics boards of the 2 participating academic institutions: The Hospital for Sick Children, Toronto, Canada and Lucile Packard Children's Hospital, Stanford, Palo Alto, California. Due to the retrospective nature of the study, informed consent was waived by the local institutional review board/research ethics board. An interinstitutional data-transfer agreement was obtained for data-sharing. Patients were identified from the respective electronic health record database from January 2009 to January 2018. Patient inclusion criteria were the following: 1) 0–18 years of age, 2) availability of molecular information on *BRAF* status in histopathologically confirmed PLGNTs, and 3) availability of pretherapeutic brain MR imaging with non-motion-degraded FLAIR and DWI sequences, including ADC maps. Patients with spinal cord tumors were excluded.

Molecular Analysis

We used a targeted testing protocol. *BRAF* fusion status was determined using an nCounter Metabolic Pathways Panel (NanoString Technologies) or fluorescence in situ hybridization. *BRAF* p.V600E mutation was determined using immunohistochemistry, Droplet Digital (Bio-Rad Laboratories) polymerase chain reaction, as previously described.[14,20] For 233 patients, molecular analysis was performed with formalin-fixed paraffin-embedded tissue obtained during surgery. Nineteen patients had molecular subtyping based on frozen tissue. Fluorescence in situ hybridization was further used to detect *MYB*, *MYBL1,* and *FGFR2* fused transcripts. Droplet Digital polymerase chain reaction was used to detect *FGFR1* alteration, *CDKN2A* deletion, and *IDH1* mutation. DNA sequencing was used for samples negative for our targeted testing protocol.

MR Imaging Acquisition, Data Retrieval, and Image Segmentation

Patients from the first academic institution (The Hospital for Sick Children, Toronto, Ontario, Canada) underwent brain MR imaging at 1.5T or 3T across various vendors (Signa, GE Healthcare; Achieva, Philips Healthcare; Magnetom Skyra, Siemens). Sequences acquired included axial DWI with ADC map calculation ($b = 0$ and 1000 s/mm^2, TR/TE, 6000–11,000/70–110 ms; 3- to 4-mm section thickness, 1 -to 3-mm gap), axial 2D T2 FLAIR, axial or coronal 2D T2-weighted FSE, and axial or sagittal 3D T1-weighted and axial or sagittal gadolinium-based contrast agent–enhanced T1-weighted sequences. Patients from the second academic institution (Lucile Packard Children's Hospital, Palo Alto, California) underwent brain MR imaging at 1.5T or 3T from a single vendor (Signa or Discovery 750; GE Healthcare). MR imaging was performed using the brain tumor protocol of the institution, which included 2D axial T2-weighted FSE, 2D axial or sagittal precontrast T1-weighted spin-echo, 2D axial T2 FLAIR, DWI with ADC calculation ($b = 0$ and 1000 s/mm^2, TR/TE, 7000–10,000/80–110 ms, 3- to 5-mm section thickness, 1- to 3-mm gap), and 2D axial gadolinium-based contrast agent–enhanced T1-weighted spin-echo sequences.

All MR imaging data were extracted from the respective PACS and de-identified for further analysis. Tumor segmentation

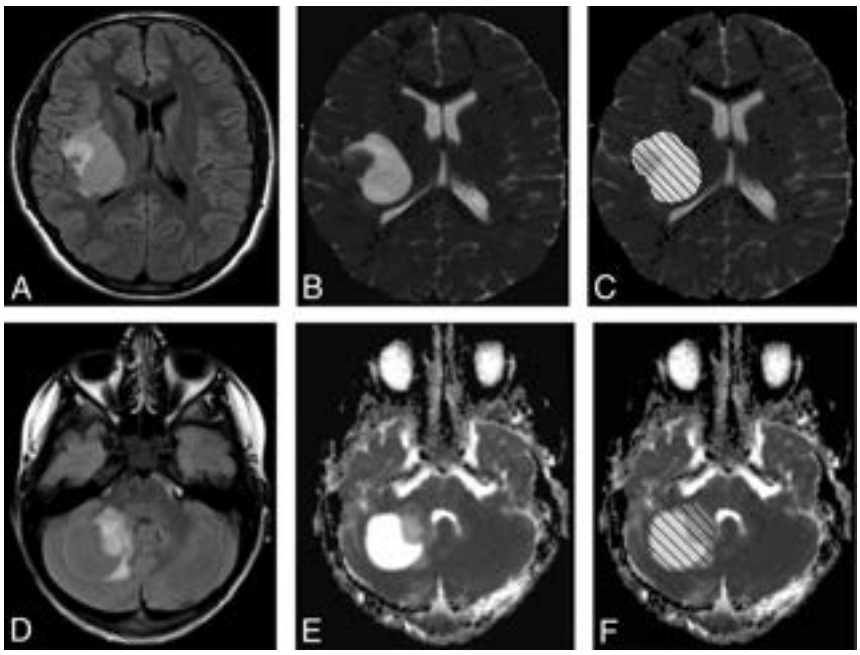

FIG 1. Axial FLAIR (*A* and *D*), ADC maps (*B* and *E*), and manual tumor segmentation using semiautomatic tools in 3D Slicer (*C* and *F*). Upper row: a 15-year-old adolescent boy with a supratentorial *BRAF*-mutated low-grade glioma. Lower row: a 3-year-old boy with a cerebellar *BRAF*-fused low-grade glioma.

was performed by a pediatric neuroradiology fellow with 3 years of neuroradiology research experience using 3D Slicer (Version 5.0.3; http://www.slicer.org).[21] Semiautomated tumor segmentation on ADC images was performed with the level tracing effect tool. Given that the tumors are better demonstrated on FLAIR images, these sequences were used as a guide to achieving the segmentation on the ADC images. The segmentation included both cystic and solid components of the tumor. This semiautomatic approach has been found superior to multiuser manual delineation concerning the reproducibility and robustness of results.[22] The senior author, a board-certified neuroradiologist, confirmed the final and proper placement of VOIs. Figure 1 demonstrates the segmentation process.

Radiomics Feature-Extraction Methodology

We used min-max normalization to scale the ADC images to [0, 1] and used the pyradiomics library with default hyperparameters to extract the radiomics features. A total of 688 radiomic features from the 3D VOIs in the ADC images were extracted for each patient. The radiomics features included shape, histogram, and texture features with and without wavelet-based filters. All features are listed in the Online Supplemental Data. Bias field correction was performed before segmentation to standardize the range of all image features.[23,24] Preprocessing and radiomics feature extraction in 3D Slicer and other software have been described elsewhere.[25-27] Clinical variables, including age, sex, and location, were appended to the data set.

Machine Learning and Statistical Analysis

We used random forests (RF) as the classification algorithm.[28] Previously, Wagner et al[29] demonstrated that RF perform best with limited data sets compared with other ML algorithms, including XGBoost (https://xgboost.readthedocs.io/en/stable/), and neural network architectures. The hyperparameter grid space was defined according to the Online Supplemental Data. We conducted 100 experiments and used an AUC to evaluate the classifiers. We randomly split our data into test (20%, 50 patients) and development (dev, 80%, 202 patients) sets in each iteration in a loop with N repetitions. Subsequently, a filtration algorithm was trained on the dev set and applied to the test set to eliminate highly correlated features (correlation coefficient >0.95). To measure the validation performance, models with the best hyperparameter set were trained and validated 100 times (N_val) on random dev data splits with a 75/25 ratio. Finally, an instance of the model with the best hyperparameters was trained on the entire dev set and evaluated on the test cohort. The whole process was repeated 100 times (N); thus, we have 100 test AUCs. The final evaluation of the model was conducted on the unseen test cohort.

We trained the RF classifiers in the supervised learning framework with 3 different inputs: 1) radiomics alone, 2) clinical variables (age, sex [binary], tumor location [binary]), and 3) radiomics and clinical variables together. A one versus the rest (OvR) multiclass AUC was used as the evaluation metric. Additionally, we monitored average per-class AUCs. We also captured the most meaningful features of the classifiers and selected the top 10 features across the experiments.

"Large p, Small n" is a well-known problem in ML, in which the number of features has a higher order in comparison with the number of examples. Radiomics-based ML is often affected by Large p, Small-n and is prone to overfitting. A crucial step is allocating an unseen cohort of data for test (compared with conventional methods such as standard cross-validation) to tackle the issue. To that end, we had separate train, validation, and test cohorts. In terms of feature selection, we filtered low-variance features (feature variance <0.05) and highly correlated features (correlation coefficient >0.95). Last, we repeated the experiments using different model initializations and data splits to ensure that the test performance was reproducible and overfitting was indeed avoided.

The analysis was conducted using Python 3.9.7 and scikit-learn 1.3.0 (https://scikit-learn.org/stable/index.html). For feature extraction, we used PyRadiomics 3.0.1 (https://pyradiomics.readthedocs.io/en/v3.0.1/changes.html) with SimpleITK 2.1.1.2 (https://simpleitk.org/doxygen/v1_0/html/).

RESULTS

Patients

The data of 422 patients were screened for inclusion. The data sets of 168 patients were excluded due to the absence of DWI-

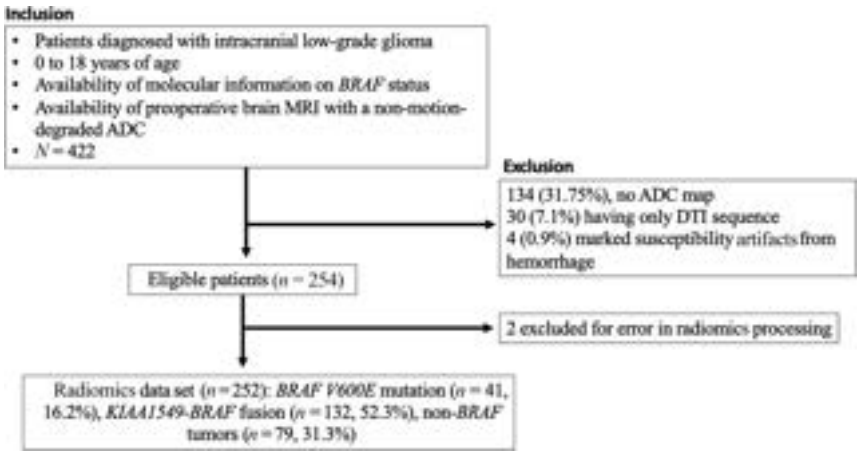

FIG 2. Flow chart of the study.

Table 1: Patient demographics

	Institutional Cohort		
	Toronto	Stanford	Total
No. of patients	229	23	252
Age (mean) (yr)	8.18	6.32	8.01
Male (No.) (%)	124 (54.1%)	11 (47.8%)	135 (53.6%)
Histologic diagnosis (No.)			
PA	112	16	128
GG	24	5	29
LGA	36	0	36
PMA	8	2	10
PXA	4	0	4
DNET	10	0	10
DA	17	0	17
ODG	3	0	3
GNT	5	0	5
ACG	5	0	5
NC	1	0	1
DIG	1	0	1
PLNTY	1	0	1
Mixed tumor components	2	0	2
Molecular subgroup (No.) (%)			
KIAA1549-BRAF fusion	114 (49.7%)	18 (78.3%)	132 (52.2%)
BRAF V600E mutation	36 (15.7%)	5 (21.7%)	41 (16.6%)
Non-BRAF	79 (34.4%)	0	79 (31.2%)
Supratentorial (No.) (%)	125 (54.5%)	5 (21.7%)	130 (51.8%)
Infratentorial (No.) (%)	104 (45.4%)	18 (78.3%)	122 (48.2%)

Note:—ACG indicates angiocentric glioma; DA, diffuse astrocytoma; DIG, desmoplastic infantile ganglioglioma; DNET, dysembryoplastic neuroepithelial tumor; GNT, glioneural tumor; LGA, low-grade astrocytoma; NC, neurocytoma; PMA, pilomyxoid astrocytoma; PXA, pleomorphic xanthoastrocytoma; PLNTY, polymorphous low-grade neuroepithelial tumor of the young; ODG, oligodendroglioma.

derived ADC images (134 for not having ADC maps and 30 for having DTI). Four patients were excluded due to marked susceptibility artifacts from hemorrhage, and 2 were excluded for errors in radiomics processing (Fig 2). After all preprocessing and radiomics extraction steps, 252 patients were included (first institution, $n = 229$, second institution, $n = 23$), comprising 135 boys (53.6%); mean age, 8.01 (SD, 4.88) years. Patient demographics and pathologic information consisting of age, sex, histologic diagnosis, *BRAF* molecular status, and anatomic location of the tumor (supra-versus-infratentorial) are shown in Table 1.

Among the non-*BRAF* tumors ($n = 79$, 31.2%), we identified the following molecular markers: *FGFR1* ($n = 10$, 3.9%), NF1 ($n = 5$, 2%), *MYB* proto-oncogene like 1 (*MYBL1*) ($n = 4$, 1.6%), *MYB* proto-oncogene (*MYB*) ($n = 4$, 1.6%), *FGFR2* ($n = 2$, 0.8%), isocitrate dehydrogenase 1 (*IDH1*) ($n = 2$, 0.8%), *histone H3.3 K27M* ($n = 2$, 0.8%), transforming acidic coiled-coil containing protein 1 (*TACC1*) ($n = 2$, 0.8%), platelet-derived growth factor receptor α (*PDGFRA*) ($n = 2$, 0.8%), *PIK3CA* ($n = 2$, 0.8%), *QKI-RAF1* ($n = 2$, 0.8%), as well as a single case (0.4%) of anaplastic lymphoma kinase (*ALK*), neurotrophic tyrosine receptor kinase (*NTRK*), *MYB-QKI* rearrangement, mitogen-activated protein kinase 1 (*MAPK1*), chloride voltage-gated channel 6 (*CLCN6*), *FYCO-RAF1*, G protein subunit α 11, and *GOPC-ROS1*. In addition, cyclin-dependent kinase inhibitor 2A (*CDKN2A*) gene deletions were identified in 29 tumors (11.5%): 12 *KIAA1549-BRAF* fusions (4.76%), 7 *BRAF* V600E mutations (2.77%), and 10 non-*BRAF tumors* (3.96%).

Radiomics Model Evaluation

Given that one of our cohorts did not have 1 tumor subtype, the bi-institutional cohort was analyzed together, and 252 patients were randomly split into 80% development and 20% test cohorts in each experiment, as illustrated in the radiomics pipeline in Fig 3. We used 3-class classifiers and achieved the following results (OvR, AUC) over 100 experiments (different data splits).

The top discriminative features are shown in Table 2. We encountered the first-order and gray-level dependence matrix (GLMD) classes among our top discriminative features. The mean, kurtosis, and 90th percentile in this class differ among the 3 subgroups. In addition, the dependence variance, large dependence emphasis, and large dependence high gray-level emphasis differed among our subgroups. The most important clinical feature was tumor location (supra- and infratentorial).

Figure 4 shows the average AUC across all groups. By means of only the radiomics features, the average test AUC was 0.74 (95% CI, 0.73–0.75) using the OvR method. When the input was restricted to clinical features, the average test AUC dropped to 0.67 (95% CI, 0.66–0.68). The combination of both radiomics and clinical features improved the predictive performance to an AUC of 0.77 with (95% CI, 0.75–0.77).

The diagnostic performance of the per-class test AUC in identifying *KIAA1549-BRAF* fusion, *BRAF* V600E mutation, and non-*BRAF* tumors among the other subgroups is shown in Table 3. It was higher in identifying *KIAA1549-BRAF* fusion tumors among the other subgroups (AUC = 0.81 for the combined radiomics and clinical features versus 0.75, 0.74 for *BRAF* V600E mutation, and non-*BRAF*, respectively).

DISCUSSION

Using a bi-institutional cohort, we trained and tested radiomics models predictive of *KIAA1549-BRAF* fusion, *BRAF* V600E mutations, and non-*BRAF* alterations in PLGNTs. The optimal

RF model achieved an accuracy AUC of 0.77 when combining radiomics and clinical features. In addition, we showed that the diagnostic performance was higher in differentiating *KIAA1549-BRAF* fusion from *BRAF* V600E mutation and non-*BRAF* tumors, regardless of which features were used (radiomics, clinical, and combined). To our knowledge, this is the first study that investigated ADC-based radiomics features in PLGNTs.

PLGNTs are a heterogeneous group of tumors arising predominantly from the glial cell lineage, including astrocytic, oligodendrocytic, or mixed neuronal and glial lineage.[9] These neoplasms are classified as WHO grades 1 and 2 and are grouped into 3 categories in the fifth WHO classification: circumscribed astrocytic gliomas, glioneural and neuronal tumors, and pediatric-type diffuse low-grade gliomas (those with characteristic ill-defined infiltrative margins).[3] PAs are the most common well-circumscribed PLGNT (up to 85%) and are by far the most common brain tumor type with *KIAA1549-BRAF* fusion. Therefore, the *KIAA1549-BRAF* fusion is a useful putative diagnostic

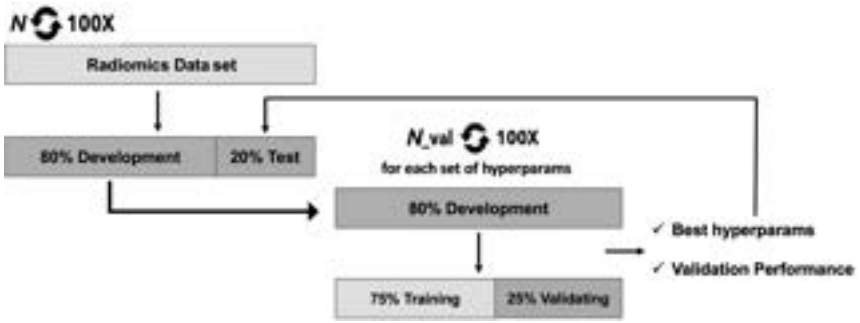

FIG 3. The repetitive classification approach.

Table 2: Top predictive radiomics and clinical features

Type	Source	Feature Category	Feature
Clinical	NA	NA	Tumor location
Radiomics	3D wavelet transform	Gray-level difference matrix	Large dependence high gray-level emphasis
Radiomics	3D wavelet transform	First order	Mean
Radiomics	3D wavelet transform	First order	Kurtosis
Radiomics	Original	Gray-level difference matrix	Dependence variance
Radiomics	Original	Gray-level difference matrix	Large dependence high gray-level emphasis
Radiomics	Logarithm	Gray-level difference matrix	Large dependence high gray-level emphasis
Radiomics	Local binary pattern 3D	Gray-level difference matrix	Large dependence emphasis
Radiomics	Exponential	First order	90th Percentile
Radiomics	3D wavelet transform	First order	Kurtosis

Note:—NA indicates not applicable.

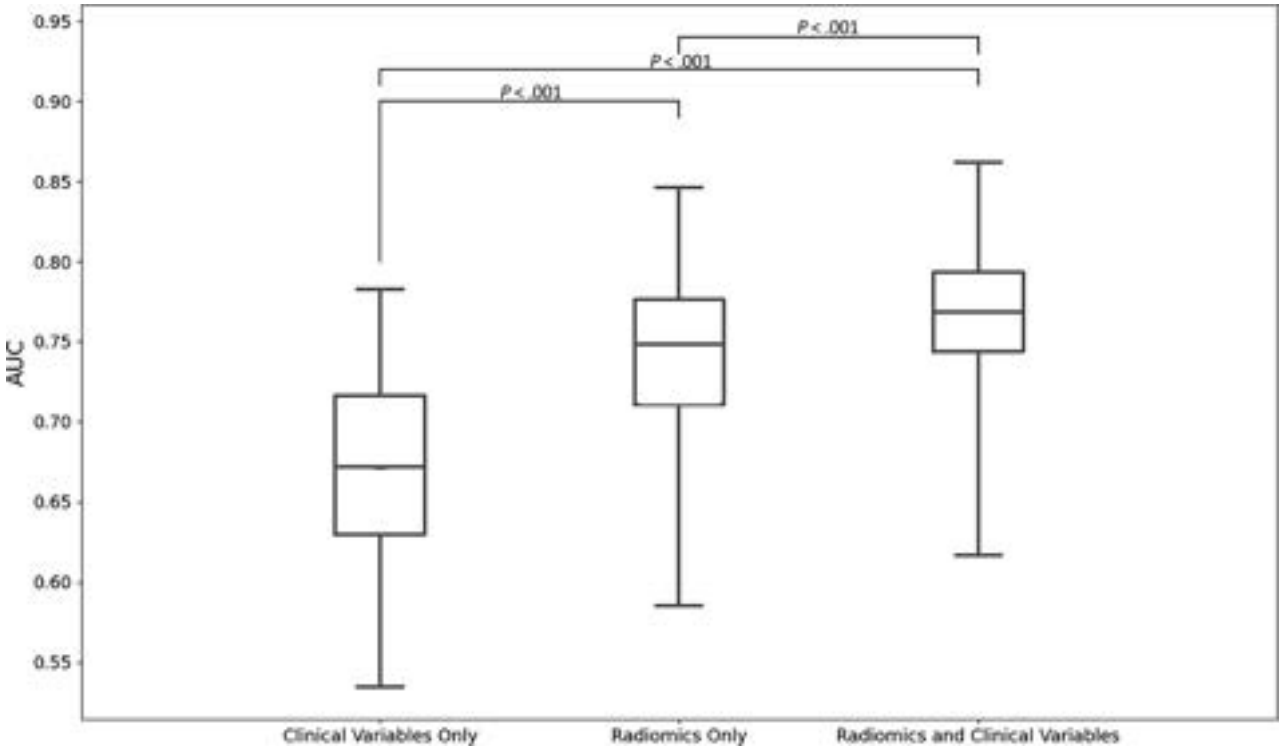

FIG 4. Boxplots of test AUCs. Note that *P* values are calculated on the basis of Student *t* tests.

Table 3: Per-class and overall OvR test of AUC performance of the models

	KIAA1549-BRAF Fusion versus the Rest	*BRAF* V600E Mutation versus the Rest	Non-*BRAF* versus the Rest	Average
Radiomics features only	AUC = 0.80 95% CI, 0.79–0.81	AUC = 0.74 95% CI, 0.73–0.75	AUC = 0.67 95% CI, 0.66–0.68	AUC = 0.74 95% CI, 0.73–0.75
Clinical features only	AUC = 0.75 95% CI, 0.74–0.7	AUC = 0.62 95% CI, 0.61–0.63	AUC = 0.63 95% CI, 0.62–0.6	AUC = 0.67 95% CI, 0.66–0.68
Combined radiomics and clinical features	AUC = 0.81 95% CI, 0.81–0.82	AUC = 0.75 95% CI, 0.73–0.75	AUC = 0.74 95% CI, 0.672–0.74	AUC = 0.76 95% CI, 0.75–0.7)

marker, particularly for PAs, which can show the neuropathologic features of necrosis and microvascular proliferation, also seen in high-grade gliomas.[30] The *BRAF* V600E mutation, on the other hand, is present in a more heterogeneous group of neoplasms with a worse prognosis, such as GG, dysembryoplastic neuroepithelial tumors, pleomorphic xanthoastrocytomas, astroblastomas, and diffuse low-grade gliomas *MAPK* pathway-altered.[31] These 2 *BRAF* tumor subgroups also differ clinically because those with the V600E mutation tend to be supratentorial, while those with *KIAA1549-BRAF* fusion are usually located in the brainstem or cerebellum.[9]

DWI reflects the free movement of water molecules in tissue.[32] Highly cellular tumors often show decreased ADC values.[33] Most studies use ROI analysis to evaluate brain tumors,[34] though it represents only a part of the lesion and is highly subjective. A better alternative is ADC histogram calculation, which analyzes the entire lesion and may show tissue heterogeneity;[35] however, this technique is limited because different tissue components may have overlapping signal intensities.[36] Alternatively, ML classifiers using radiomics features can extract data from larger volumes of images, increasing reproducibility, providing signatures in different CNS neoplasms, and assessing therapeutic interventions.[36-39] ML models are associated with randomness; and especially with small data sets, it is crucial to measure the randomness of the models. Additionally, the reproducibility of radiomics studies is a major concern that demands a systematic evaluation. In this research, we followed the OpenRadiomics (https://arxiv.org/abs/2207.14776)[38,40] protocol to achieve reproducible results.

Ramaglia et al[41] first described the association between *BRAF* V600E and lower relative ADC values. Similar diagnostic performances were predicted by different parameters, such as relative ADC mean (AUC = 0.83, $P < .001$) and relative ADC minimum (AUC = 0.85, $P < .001$).[41] Trasolini et al[16] and Shrot et al[35] also reported the association of *BRAF* V600E and lower ADC values in cohorts of 70 and 40 patients, respectively, suggesting higher tumor aggressiveness and cellularity in this subgroup.[42] With a larger cohort, our results support the use of ADC in subgroup differentiation and add that radiomics features can predict the *BRAF* status. In addition, we exploit the entire set of radiomics features, including but not limited to histogram parameters.[16,35,41] We also expand the use of ADC in subgroup differentiation by adding a third non-*BRAF* cohort to the prediction.

RF is an ensemble learning method that combines decision trees and handles various data types, including missing data.[43] In our study, first-order and GLMD classes were among our top discriminative features. First-order statistics describe the distribution of voxel intensities within the image region through commonly used and basic metrics. The mean, kurtosis, and 90th percentile in this class differ among the 3 subgroups. Larger mean, 90th percentile, and kurtosis have been associated with reduced overall survival in glioblastomas.[44] In addition, the mean, median, and 90th percentiles among pediatric patients were lower in the *BRAF* V600E subgroup.[35] These metrics reflect the microstructure at the cellular level.[45] In particular, the low diffusivity of *BRAF* V600E-mutant pLGG may be explained by the dense, compact architecture with fiber-rich regions.[46] GLMD quantifies gray-level dependencies in an image, defined as the number of connected voxels in a certain distance dependent on a central voxel. The dependence variance, large dependence emphasis, and large dependence high gray-level emphasis in this class differed among our subgroups. These are the main features quantifying tumor heterogeneity, which might be missed through the human eyes on MR imaging.[47] Texture features have been shown to differ among brain tumors[48] and predict *IDH* status in low-grade gliomas.[49] Also, the GLMD was the main feature class among the top discriminative features in *KIAA1549-BRAF* fusion and *BRAF* V600E mutation tumors,[17] reflecting the molecular and histologic differences of these tumors.[50]

In our study, tumor location (supra- versus infratentorial) was the most important clinical discriminative feature across the experiments. Many studies support this finding,[9,16,17,35] because *KIAA1549-BRAF* fusion is more often described in the posterior fossa and *BRAF* V600E mutation in the cerebral hemispheres and diencephalon.[35] Sex and age were not significantly different among groups.[16] Other features have also been reported, such as ill-defined margins[35] and a higher number of cystic components.[41] However, the significance of these findings varies in the literature. Ramaglia et al,[41] for instance, did not find significant differences in tumor margins, the presence of hemorrhage/calcification, and contrast enhancement among *BRAF* subgroups in a cohort of 56 participants. Conversely, Shrot et al[35] showed that *KIAA1549-BRAF* fusion tumors had significantly better-defined margins compared with *BRAF* V600E mutation tumors and that *BRAF* subgroups showed more cystic components than the NF1 subgroup in a cohort of 51 participants.

Wagner et al[17] trained and validated the radiomics features of FLAIR sequences to predict *BRAF* status in 115 patients with pLGGs, achieving an AUC of 0.85 on the external validation data set. Similarly, Xu et al[51] extracted features from FLAIR sequences in a cohort of 113 pediatric patients, building a model with a test set AUC of 0.87. We believe that the lower AUC for the ADC values in our study is because we expanded the cohort to include rare subtypes and compared each group versus the rest 3 times. In addition, FLAIR sequences show better margins and facilitate semiautomatic segmentation with good reproducibility.[18] Finally,

pLGGs are heterogeneous neoplasms, and FLAIR sequences may better depict this heterogeneity, including cystic and solid components, margins, and the range of signal changes.[17]

In this study, we noted that the prediction of the *KIAA1549-BRAF* fusion cohort achieved the highest AUC in the per-class analysis. This may be, in part, explained by the larger number of cases in this cohort. In addition, the heterogeneity of histopathologically defined entities was lower in this cohort compared with the other 2 cohorts. Most cases are PA. While it is conceivable to assume that the driver behind this prediction is histopathologic rather than molecular, we also noted that the predictive performance of our algorithm remained high with the other 2 cohorts in the per-class analysis. In contrast to the *KIAA1549-BRAF* fusion cohort, those cohorts were heterogeneous with respect to histopathology. Therefore, we speculate that radiomics can extract predictive information from ADC maps beyond histopathology.

Our study has limitations that need to be considered when interpreting the results. First, due to the retrospective and bi-institutional nature, there was heterogeneity in the DWI sequence acquisition, including using different imaging parameters, field strengths, and scanner vendors. The incorporation of heterogeneous training and testing data was previously shown to be an important component in the development of a robust and predictive ML model. In fact, training of heterogeneous imaging data might increase the generalizability of our findings.[52] Second, our study segmented only ADC images. Incorporating additional sequences could further increase the model performance. Third, we opted to merge the 2 cohorts rather than keep them separated due to an imbalanced distribution of the third class (non-*BRAF*). Fourth, the larger number of cases of *KIAA1549-BRAF* fusion tumors may partially explain the higher AUC among the "fusion versus the rest" per-class analysis. Last, although our study cohort is one of the largest PLGNT cohorts to date, we did not analyze the predictive performance of radiomics features in the subgroup-specific determination of histopathologically defined tumors across molecular markers. Large international MR imaging data sets are necessary for robust subanalyses.

CONCLUSIONS

We explored the feasibility of radiomics features to predict *BRAF* status in PLGNT using ADC-based MR images in a bi-institutional cohort. The optimal RF model included a combination of clinical and radiomic features and achieved diagnostic accuracy. In particular, the highest accuracy was achieved to identify the *KIAA1549-BRAF* fusion tumor subgroup. Differentiating these molecular subgroups in PLGNT is paramount for newer target therapies.[42] Future investigations with additional imaging sequences, such as T2WI and contrast-enhanced T1WI, may improve prediction accuracy.

Disclosure forms provided by the authors are available with the full text and PDF of this article at www.ajnr.org.

REFERENCES

1. Ostrom QT, Price M, Neff C, et al. **CBTRUS Statistical Report: Primary Brain and Other Central Nervous System Tumors Diagnosed in the United States in 2015-2019.** *Neuro Oncol* 2022;24:v1–95 CrossRef Medline
2. Ryall S, Tabori U, Hawkins C. **Pediatric low-grade glioma in the era of molecular diagnostics.** *Acta Neuropathol Commun* 2020;8:30 CrossRef Medline
3. Bale TA, Rosenblum MK. **The 2021 WHO Classification of Tumors of the Central Nervous System: an update on pediatric low-grade gliomas and glioneuronal tumors**. *Brain Pathol* 2022;32:e13060 CrossRef Medline
4. Plant-Fox AS, O'Halloran K, Goldman S. **Pediatric brain tumors: the era of molecular diagnostics, targeted and immune-based therapeutics, and a focus on long term neurologic sequelae**. *Curr Probl Cancer* 2021;45:100777 CrossRef Medline
5. Armstrong GT, Conklin HM, Huang S, et al. **Survival and long-term health and cognitive outcomes after low-grade glioma.** *Neuro Oncol* 2011;13:223–34 CrossRef Medline
6. AlRayahi J, Zapotocky M, Ramaswamy V, et al. **Pediatric brain tumor genetics: what radiologists need to know.** *RadioGraphics* 2018;38:2102–22 CrossRef Medline
7. Chalil A, Ramaswamy V. **Low-grade gliomas in children.** *J Child Neurol* 2016;31:517–22 CrossRef Medline
8. Engelhardt S, Behling F, Beschorner R, et al. **Frequent FGFR1 hotspot alterations in driver-unknown low-grade glioma and mixed neuronal-glial tumors.** *J Cancer Res Clin Oncol* 2022;148:857–66 CrossRef Medline
9. Bag AK, Chiang J, Patay Z. **Radiohistogenomics of pediatric low-grade neuroepithelial tumors.** *Neuroradiology* 2021;63:1185–213 CrossRef Medline
10. Grob ST, Nobre L, Campbell KR, et al. **Clinical and molecular characterization of a multi-institutional cohort of pediatric spinal cord low-grade gliomas.** *Neurooncol Adv* 2020;2:vdaa103 CrossRef Medline
11. Mhatre R, Sugur HS, Nandeesh BN, et al. **MN1 rearrangement in astroblastoma: study of eight cases and review of literature.** *Brain Tumor Pathol* 2019;36:112–20 CrossRef Medline
12. Moreira DC, Lam CG, Bhakta N, et al. **Tackling pediatric low-grade gliomas: a global perspective.** *JCO Glob Oncol* 2023;9:e2300017 CrossRef Medline
13. Vagvala S, Guenette JP, Jaimes C, et al. **Imaging diagnosis and treatment selection for brain tumors in the era of molecular therapeutics.** *Cancer Imaging* 2022;22:19 CrossRef Medline
14. Ryall S, Zapotocky M, Fukuoka K, et al. **Integrated molecular and clinical analysis of 1,000 pediatric low-grade gliomas.** *Cancer Cell* 2020;37:569–83.e5 CrossRef Medline
15. Nobre L, Zapotocky M, Ramaswamy V, et al. **Outcomes of BRAF V600E pediatric gliomas treated with targeted BRAF inhibition.** *JCO Precis Oncol* 2020;4:561–71 CrossRef Medline
16. Trasolini A, Erker C, Cheng S, et al. **MR imaging of pediatric low-grade gliomas: pretherapeutic differentiation of BRAF V600E mutation, BRAF musion, and wild-type tumors in patients without neurofibromatosis-1.** *AJNR Am J Neuroradiol* 2022;43:1196–201 CrossRef Medline
17. Wagner MW, Hainc N, Khalvati F, et al. **Radiomics of pediatric low-grade gliomas: toward a pretherapeutic differentiation of BRAF-mutated and BRAF-fused tumors.** *AJNR Am J Neuroradiol* 2021;42:759–65 CrossRef Medline
18. Madhogarhia R, Haldar D, Bagheri S, et al. **Radiomics and radiogenomics in pediatric neuro-oncology: a review.** *Neurooncol Adv* 2022;4:vdac083 CrossRef Medline
19. Zhang M, Wong SW, Wright JN, et al. **MRI radiogenomics of pediatric medulloblastoma: a multicenter study.** *Radiology* 2022;304:406–16 CrossRef Medline
20. Guerrini F, Paolicchi M, Ghio F, et al. **The Droplet Digital PCR: a new valid molecular approach for the assessment of B-RAF V600E mutation in hairy cell leukemia.** *Front Pharmacol* 2016;7:363 CrossRef Medline
21. Fedorov A, Beichel R, Kalpathy-Cramer J, et al. **3D slicer as an image computing platform for the quantitative imaging network.** *Magn Reson Imaging* 2012;30:1323–41 CrossRef Medline

22. Parmar C, Velazquez ER, Leijenaar R, et al. **Robust radiomics feature quantification using semiautomatic volumetric segmentation.** *PloS One* 2014;9:e102107 CrossRef Medline
23. Li J, Liu S, Qin Y, et al. **High-order radiomics features based on T2 FLAIR MRI predict multiple glioma immunohistochemical features: a more precise and personalized gliomas management.** *PLoS One* 2020;15:e0227703 CrossRef Medline
24. Tustison NJ, Avants BB, Cook PA, et al. **N4ITK: improved N3 bias correction.** *IEEE Trans Med Imaging* 2010;29:1310–20 CrossRef Medline
25. Aerts HJ, Velazquez ER, Leijenaar RTH, et al. **Decoding tumour phenotype by noninvasive imaging using a quantitative radiomics approach.** *Nat Commun* 2014;5:4006–09 CrossRef Medline
26. Chaddad A, Kucharczyk MJ, Daniel P, et al. **Radiomics in glioblastoma: current status and challenges facing clinical implementation.** *Front Oncol* 2019;9:374 CrossRef Medline
27. Eun Park J, Sung Kim H. **Radiomics as a quantitative imaging biomarker: practical considerations and the current standpoint in neuro-oncologic studies.** *Nucl Med Mol Imaging* 2018;52:99–108 CrossRef Medline
28. Breiman L. **Bagging predictors.** *Mach Learn* 1996;24:123–40 CrossRef
29. Wagner M, Namdar K, Alqabbani A, et al. **Dataset size sensitivity analysis of machine learning classifiers to differentiate molecular markers of pediatric low-grade gliomas based on MRI.** *Research Square* 2021 Sept 17 [Epub ahead of print] CrossRef
30. Faulkner C, Ellis HP, Shaw A, et al. **BRAF fusion analysis in pilocytic astrocytomas: KIAA1549-BRAF 15-9 fusions are more frequent in the midline than within the cerebellum.** *J Neuropathol Exp Neurol* 2015;74:867–72 CrossRef Medline
31. Di Nunno V, Gatto L, Tosoni A, et al. **Implications of BRAF V600E mutation in gliomas: molecular considerations, prognostic value and treatment evolution.** *Front Oncol* 2022;12:1067252 CrossRef Medline
32. Koh DM, Collins DJ. **Diffusion-weighted MRI in the body: applications and challenges in oncology.** *AJR Am J Roentgenol* 2007;188:1622–35 CrossRef Medline
33. Guo AC, Cummings TJ, Dash RC, et al. **Lymphomas and high-grade astrocytomas: comparison of water diffusibility and histologic characteristics.** *Radiology* 2002;224:177–83 CrossRef Medline
34. Doskaliyev A, Yamasaki F, Ohtaki M, et al. **Lymphomas and glioblastomas: Differences in the apparent diffusion coefficient evaluated with high b-value diffusion-weighted magnetic resonance imaging at 3T.** *Eur J Radiol* 2012;81:339–44 CrossRef Medline
35. Shrot S, Kerpel A, Belenky J, et al. **MR imaging characteristics and ADC histogram metrics for differentiating molecular subgroups of pediatric low-grade gliomas.** *AJNR Am J Neuroradiol* 2022;43:1356–62 CrossRef Medline
36. Kolossváry M, Karády J, Kikuchi Y, et al. **Radiomics versus visual and histogram-based assessment to identify atheromatous lesions at coronary CT angiography: an ex vivo study**. *Radiology* 2019;293:89–96 CrossRef Medline
37. Capobianco E, Deng J. **Radiomics at a glance: a few lessons learned from learning approaches.** *Cancers (Basel)* 2020;12:2453 CrossRef Medline
38. Namdar K, Wagner MW, Ertl-Wagner BB, Khalvati F. **Open-radiomics: a collection of standardized datasets and a technical protocol for reproducible radiomics machine learning pipelines.** *arXiv* July 29 [Epub ahead of print]. https://arxiv.org/abs/2207.14776
39. Lam LH, Do DT, Diep DT, et al. **Molecular subtype classification of low-grade gliomas using magnetic resonance imaging-based radiomics and machine learning.** *NMR Biomed* 2022;35:e4792 CrossRef Medline
40. Manoharan N, Liu KX, Mueller S, Haas-Kogan DA, Bandopadhayay P. **Pediatric low-grade glioma: Targeted therapeutics and clinical trials in the molecular era.** *Neoplasia* 2023;36:100857 CrossRef Medline
41. Ramaglia A, Tortora D, Mankad K, et al. **Role of diffusion weighted imaging for differentiating cerebral pilocytic astrocytoma and ganglioglioma BRAF V600E-mutant from wild type.** *Neuroradiology* 2020;62:71–80 CrossRef Medline
42. Kan P, Liu JK, Hedlund G, et al. **The role of diffusion-weighted magnetic resonance imaging in pediatric brain tumors.** *Childs Nerv Syst* 2006;22:1435–39 CrossRef Medline
43. Erickson BJ, Korfiatis P, Akkus Z, et al. **Machine learning for medical imaging.** *Radiographics* 2017;37:505–15 CrossRef Medline
44. Li Y, Kim MM, Wahl DR, et al. **Survival prediction analysis in glioblastoma with diffusion kurtosis imaging.** *Front Oncol* 2021;11:690036 CrossRef Medline
45. Wu CC, Jain R, Radmanesh A, et al. **Predicting genotype and survival in glioma using standard clinical MR imaging apparent diffusion coefficient images: a pilot study from The Cancer Genome Atlas.** *AJNR Am J Neuroradiol* 2018;39:1814–20 CrossRef Medline
46. Ho CY, Mobley BC, Gordish-Dressman H, et al. **A clinicopathologic study of diencephalic pediatric low-grade gliomas with BRAF V600 mutation.** *Acta Neuropatho* 2015;130:575–85 CrossRef Medline
47. Cho HH, Lee SH, Hak Kim J, et al. **Classification of the glioma grading using radiomics analysis.** *PeerJ* 2018;6:e5982 CrossRef Medline
48. Widhiarso W, Yohannes Y, Prakarsah C. **Brain tumor classification using gray level co-occurrence matrix and convolutional neural network.** *Indonesian J Electron Instrum Syst* 2018;8:179–90 CrossRef
49. Chekouo T, Mohammed S, Rao A. **A Bayesian 2D functional linear model for gray-level co-occurrence matrices in texture analysis of lower grade gliomas.** *Neuroimage Clin* 2020;28:102437 CrossRef Medline
50. Zachariah RM, Priya PS, Pendem S. **Classification of low- and high-grade gliomas using radiomic analysis of multiple sequences of MRI brain.** *J Cancer Res Ther* 2023;19:435–46 CrossRef Medline
51. Xu J, Lai M, Li S, et al. **Radiomics features based on MRI predict BRAF V600E mutation in pediatric low-grade gliomas: a non-invasive method for molecular diagnosis.** *Clin Neurol Neurosurg* 2022;222:107478 CrossRef Medline
52. Mårtensson G, Ferreira D, Granberg T, et al. **The reliability of a deep learning model in clinical out-of-distribution MRI data: amulticohort study**. *Med Image Anal* 2020;66:101714 CrossRef Medline

The Clinical Value of Cranial CT Venography for Predicting *Fusobacterium necrophorum* as the Causative Agent in Children with Complicated Acute Mastoiditis

Shelly I. Shiran, Li-tal Pratt, Ari DeRowe, Sophie Matot, Narin Carmel Neiderman, and Oshri Wasserzug

ABSTRACT

BACKGROUND AND PURPOSE: *Fusobacterium necrophorum* (*F necrophorum*) is an anaerobic bacteria that causes invasive head and neck infections in children. Several studies have demonstrated an increasing prevalence of *F necrophorum* as the causative agent in acute mastoiditis in children, with associated high rates of intracranial complications such as epidural abscess and sinus venous thrombosis, to name a few. *F necrophorum* requires a treatment protocol that differs from the empiric treatment that is tailored to more common pathogens (eg, group A streptococci, *Streptococcus* pneumonia), and hence expediting the diagnosis is important. For evaluating complicated acute mastoiditis in children, cranial CT venography remains the imaging study of choice in most medical centers due to its availability in emergency situations. Based on our clinical experience, our hypothesis is that children with *F necrophorum*–associated complicated acute mastoiditis can be differentiated from those with other etiologies using CT venography.

MATERIALS AND METHODS: CT venography studies of 76 children hospitalized and treated for complicated acute mastoiditis were retrospectively reviewed. Retrieved imaging data included intracranial complications (epidural abscess, sinus venous thrombosis), cranial bone-related complications, and extracranial complications (subperiosteal abscess, temporomandibular joint abscess, and soft-tissue inflammation). The cohort was divided into children with *F necrophorum*–related disease (study group) and those with non-*F necrophorum*–related disease (control group).

RESULTS: Thirty-seven children (49%) comprised the study group, and 39 children in whom the causative agents were other bacteria comprised the control group. There were significantly higher rates of complications in the study group: sinus venous thrombosis ($P < .001$), perisigmoid epidural abscess ($P = .036$), and extramastoid osteomyelitis ($P < .001$). Thrombosis in venous sites beyond the sigmoid sinus and jugular foramen (a pattern consistent with an otogenic variant of Lemierre syndrome) and emphysematous osteomyelitis were found only among children in the *F necrophorum*–related study group (32% and 22% accordingly).

CONCLUSIONS: In children with complicated acute mastoiditis, CT venography findings of emphysematous osteomyelitis and/or thrombosis in venous sites beyond the sigmoid sinus and jugular foramen (a pattern consistent with the otogenic variant of Lemierre syndrome) should lead the radiologist to suggest *F necrophorum*–related mastoiditis.

ABBREVIATIONS: AM = acute mastoiditis; CAM = complicated acute mastoiditis; CTV = CT venography; IJV = internal jugular vein; NPV = negative predictive value; PPV = positive predictive value; SVT = sinus venous thrombosis; TMJ = temporomandibular joint

Acute mastoiditis (AM) in children is a serious complication of acute otitis media, with a potential to rapidly deteriorate and cause complications, both extracranial (eg, subperiosteal abscess, temporomandibular joint [TMJ] abscess) and intracranial (eg, perisigmoid epidural empyema, sinus venous thrombosis [SVT]). The clinical diagnosis of AM is based on findings of pus in the middle ear cavity associated with swelling and fluctuation over the mastoid bone, protrusion of the auricle, and fever.[1] Treatment of pediatric AM has shifted from a surgically-treated disease to a mainly medically-treated disease with treatment consisting of hospitalization, middle ear drainage with myringotomy, and IV antibiotic treatment; thus, canal wall up mastoidectomy is reserved for patients with coalescent mastoiditis who do not respond to the initial therapy and/or experience complications.[2-4] The empiric antibiotic treatment initiated before the arrival of the results of microbiologic investigation is used to treat the most common pathogens (eg, Streptococcus pyogenes *Streptococcus* pneumonia)[5], and in our institution, it is IV cefuroxime. In accordance with the as low as reasonably achievable concept and as was recommended by Mansour et al,[6] we do not routinely image the temporal

Received October 22, 2023; accepted after revision February 5, 2024.

From the Department of Radiology (S.I.S., L.-t.P.), Pediatric Otorhinolaryngology Unit, "Dana" Children's Hospital (A.D., O.W.), and Department of Otolaryngology, Head & Neck and Maxillofacial Surgery (S.M., N.C.N.), Tel Aviv Sourasky Medical Center, Faculty of Medicine, Tel Aviv University, Tel Aviv, Israel.

Please address correspondence to Shelly Shiran, MD, Department of Pediatric Radiology, "Dana" Children's Hospital, Tel Aviv Sourasky Medical Center, 6 Weizman St, Tel Aviv, Israel 6423906; e-mail: shellyshi@tlvmc.gov.il

http://dx.doi.org/10.3174/ajnr.A8217

SUMMARY

PREVIOUS LITERATURE: There is a reported trend of increasing prevalence of *Fusobacterium necrophorum (F necrophorum)* as the causative agent in pediatric complicated acute mastoiditis. Infection with this Gram-negative anaerobic bacteria has been shown by several studies to cause higher rates of intracranial complications, with a specifically high rate of sinus venous thrombosis. CT venography remains the study of choice to evaluate children with acute mastoiditis who are clinically suspected of developing extra- or intracranial complications. We hypothesized that children with *F necrophorum*–associated complicated acute mastoiditis can be differentiated from those with other etiologies using CT venography.

KEY FINDINGS: There were significantly higher rates of complications in *F necrophorum*–related complicated acute mastoiditis: sinus venous thrombosis ($P < .001$), perisigmoid epidural abscess ($P = .036$), and extramastoid osteomyelitis ($P < .001$). Extensive thrombophlebitis beyond the sigmoid sinus and jugular foramen (a pattern consistent with the otogenic Lemierre syndrome variant) and emphysematous osteomyelitis were found only among those with *F necrophorum*–related complicated acute mastoiditis.

KNOWLEDGE ADVANCEMENT: In children with complicated acute mastoiditis, CT venography findings of emphysematous osteomyelitis and/or the otogenic Lemierre syndrome variant should lead the radiologist to suggest *F necrophorum*–related mastoiditis, to expedite appropriate medical and surgical management.

bones in children who are hospitalized and treated for AM. Imaging is reserved for children suspected of having complicated acute mastoiditis (CAM) either due to severe illness at diagnosis or nonimprovement within the initial 24–48 hours of IV antibiotocs.[6,7] Imaging remains an important tool to assess the type and extent of complications for presurgical evaluation. In patients with suspected CAM, we perform cranial CT venography (CTV), which remains the imaging study of choice in most medical centers due to its availability in emergency situations.[6]

Several studies have demonstrated an increasing prevalence of *Fusobacterium necrophorum* (*F necrophorum*) as the causative agent in acute mastoiditis in children.[8,9] *F necrophorum* is a nonspore-forming, obligatory anaerobic, Gram-negative rod-shaped bacteria that is responsible for a wide spectrum of infections in the head and neck, such as tonsillitis, peritonsillar abscesses, cervical lymphadenitis, sinusitis, and mastoiditis. It is also known as causative agent of Lemierre syndrome, a disease in which oropharyngeal infection is followed by septic thrombophlebitis of the internal jugular vein (IJV).[10] The increased prevalence of *F necrophorum*–related AM in children was found to be associated with high rates of complications, including subperiosteal and epidural abscess, SVT, osteomyelitis, and the otogenic Lemierre syndrome variant (extensive septic thrombophlebitis from otogenic source of infection).[8-10] Due to its anaerobic nature, *F necrophorum* is difficult to culture and isolate, resulting in the need to use molecular diagnostic methods such as polymerase chain reaction for identification, leading to a delayed diagnosis,[10] which, in our medical center, can be up to 10 days. Early diagnosis of this pathogen is crucial for administering the correct antibiotic regimen, which, in our institution, is IV ceftriaxone and metronidazole. Several studies have suggested clinical criteria for identifying children with CAM in which *F necrophorum* is the causative agent to facilitate early imaging and intervention. Those clinical findings include high C-reactive protein levels, high fever, substantial leukocytosis, a history of prior antibiotic treatment, and suspected subperiosteal abscess on physical examination.[6,11] However, these variables are neither specific nor sensitive.

Based on our clinical experience, our hypothesis is that children with *F necrophorum*–associated CAM can be differentiated from those with other etiologies using CTV. To test our hypothesis, we compared the imaging characteristics of CAM in children with AM caused by *F necrophorum* with the imaging characteristics in children with AM caused by other bacteria.

MATERIALS AND METHODS

Patients

After study approval by the institutional ethics committee, the electronic medical records database of a university-affiliated pediatric medical center was retrospectively searched for children hospitalized and treated for acute mastoiditis from 2010 through 2021. Children who had a contrast-enhanced cranial CTV study were included; children who did not undergo a contrast-enhanced cranial CTV were excluded from the study. From the group of children with a CTV study, further exclusion criteria were the presence of cholesteatoma and an unidentified causative organism. Documented data on sex, age, and microbiologic diagnosis were retrieved from the participants' medical charts. On the basis of the causative organism, the study participants were divided into *F necrophorum*–related disease (study group) and non-*F necrophorum*–related disease (control group).

Imaging

Per our departmental protocol for evaluating children with suspected CAM, we perform a contrast-enhanced CTV study of the skull from the mastoid tip to the vertex without a precontrast scan. Some children are placed under sedation or general anesthesia depending on their clinical status and underlying condition. Scanning is performed in the axial plane parallel to the hard palate, with a 50-second delay after a 2-mL/kg IV injection of iohexol (Omnipaque; GE Healthcare). Contrast injection is given intravenously by a power injector at a rate of 2 mL/s. Scanning parameters are 100 kV(peak), with modulated milliampere-seconds according to the patient's size. Section thickness was 1 mm. Most studies during 2010–2013 were performed on a 64-section CT scanner (Brilliance 64; Philips Healthcare), and from 2013 to

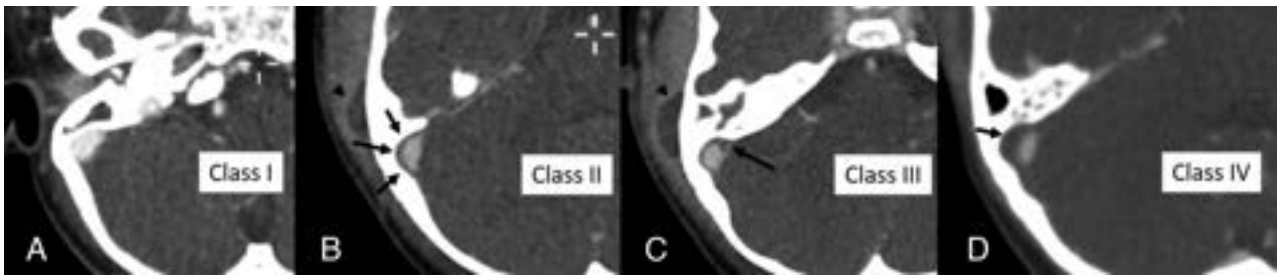

FIG 1. Perisigmoid abscess classification in 4 different cases of complicated mastoiditis: class I (*A*), normal dura with no thickening; class II (*B*), linear smooth halo of thickened dura (*arrows*); class III (*C*), focal nodular dural thickening ≤4 mm thick (*arrow*); class IV (*D*), large nodular halo >4 mm thick (*arrow*). Classes III and IV comprise the patients considered positive for perisigmoid abscess on imaging. Note that there is an extracranial subperiosteal abscess present in *B* and *C* (*arrowhead*).

end of study period, on a 256-section multidetector CT scanner (Brilliance ICT 256). Postprocessing sequences include multiplanar reformats and bone algorithm high-resolution images.

The CTV studies were evaluated by a fellowship-trained senior pediatric neuroradiologist with Head & Neck Imaging training and 18 years of experience who was blinded to the causative agent. We documented the following imaging findings:

Intracranial Complications. The presence of a perisigmoid abscess was evaluated by the perisinus classification as described by Horowitz et al[12] and validated by Saat et al.[13] According to this classification, perisinus dural lesion classes are defined as normal (class I), linear smooth halo (class II), nodular halo ≤4 mm thick (class III), and nodular halo >4 mm thick (class IV). Classes III and IV were considered positive for perisigmoid abscess (Fig 1). Epidural abscess in the middle cranial fossa was described as present or absent, and thickness was measured. Subdural empyema was described as present or absent. SVT evaluation included documentation of the presence and extent of thrombotic changes. For presence, a partial or complete filling defect in a dural venous sinus was considered positive for SVT. For extent, all venous structures affected with thrombotic changes were documented.

Cranial Bone Complications. Mastoid cortical erosion is a typical feature of coalescent mastoiditis and is frequently present in CAM with typical involvement of the sigmoid plate, retro auricular cortex and mastoid tegmen. We defined extramastoid bone osteomyelitis when cortical bone erosion and lytic changes were present beyond the anatomic borders of the mastoid itself. The presence of abnormal gas deposits in nonpneumatized bones, consistent with emphysematous osteomyelitis, was documented. Findings suggestive of chronic ear changes, including decreased pneumatization and increased sclerosis of mastoid bone, were also documented.

Extracranial Complications. The presence of a subperiosteal abscess was documented, and volume was calculated on the basis of anterior-posterior, transverse, and height measurements. The presence of additional phlegmon changes was considered mild when it was retroauricular and/or adjacent to the subperiosteal abscess and extensive when larger and more extensive than the subperiosteal abscess and/or with extensive inflammatory changes to the upper neck and face. TMJ abscess was documented if present. Ipsilateral neck lymphadenopathy, ipsilateral parotid gland hyperemia, contralateral mastoid opacification, and paranasal sinus disease were also documented as present or not.

Statistics

SPSS software (IBM) was used for all statistical analyses. Categoric variables were summarized as frequency and percentage. Distribution of continuous variables was evaluated by histograms. All continuous variables were not normally distributed, and they were reported as median and interquartile range. Two-sided Fisher exact tests were used to compare categoric variables, and 2-sided Mann-Whitney tests were used to compare continuous variables. All reported P values were adjusted by the Benjamini-Hochberg procedure to control for the false discovery rate at the .05 level. The χ^2 automatic interaction detector was applied to identify subgroups of patients with an increased risk for *F necrophorum* infection. Sensitivity, specificity, positive predictive value (PPV), and negative predictive value (NPV) were calculated for findings that reached statistical significance.

RESULTS

A total of 364 children were hospitalized and treated for acute mastoiditis during the study period. Ninety children met our inclusion criteria and had a CTV study due to suspected complications. From this cohort of patients, 14 children were excluded due to lack of microbiologic identification, leaving 76 children in the final combined study and control groups. Of note, 4 patients had their CTV study performed in another hospital and then were transferred to our medical center for treatment. Their CTV studies were of similar quality to our protocol, and we included them in the study. The results are summarized in Table 1. The age of the study participants ranged from 0.5 to 11.3 years (median = 2, interquartile range = 2.25), and the male/female ratio was 1.2. Thirty-seven children (49%) were diagnosed as having *F necrophorum* mastoiditis (the study group), while the causative agents were other bacteria in the remaining 39 children (the control group) (Fig 2). There was no significant group difference in age or sex. There was equal distribution of infection in the right and left ears in both groups.

Intracranial Complications

SVT was identified in 24 children in the study group (64%) and in 4 children in the control group (10%) ($P < .001$). Thrombosis in

Table 1: Results

Finding	*Fusobacterium* (*n* = 37)	Other (*n* = 39)	*P* Value
Male/female ratio	19:18 (1.01)	23:16 (1.4)	.967
Site of ear infection RT:LT ratio	19:18 (1.01)	22:17 (1.3)	.658
Chronic ear changes	6 (16%)	5 (13%)	.674
Intracranial perisigmoid epidural abscess	27 (73%)	16 (41%)	.036
Intracranial middle cranial fossa epidural abscess	10 (27%)	4 (10%)	.199
Subdural empyema	1 (2.7%)	1 (2.6%)	1
SVT	24 (64%)	4 (10%)	< .001
Extramastoid bone changes consistent with osteomyelitis	20 (54%)	4 (10%)	< .001
Emphysematous osteomyelitis	8 (22%)	0	.015
Subperiosteal abscess	30 (81%)	30 (77%)	1
Inflammatory phlegmon (mild and extensive)	34 (92%)	38 (97%)	.961
TMJ abscess	7 (19%)	1 (2.6%)	.099
Ipsilateral neck lymphadenopathy	32 (87%)	33 (85%)	1
Parotid hyperemia	26 (70%)	24 (62%)	.838
Contralateral ear air cell opacification	25 (68%)	28 (72%)	1
Sinonasal air cell opacification (partial and complete)	24 (65%)	31 (79%)	.309

Note:—RT indicates right; LT, left.

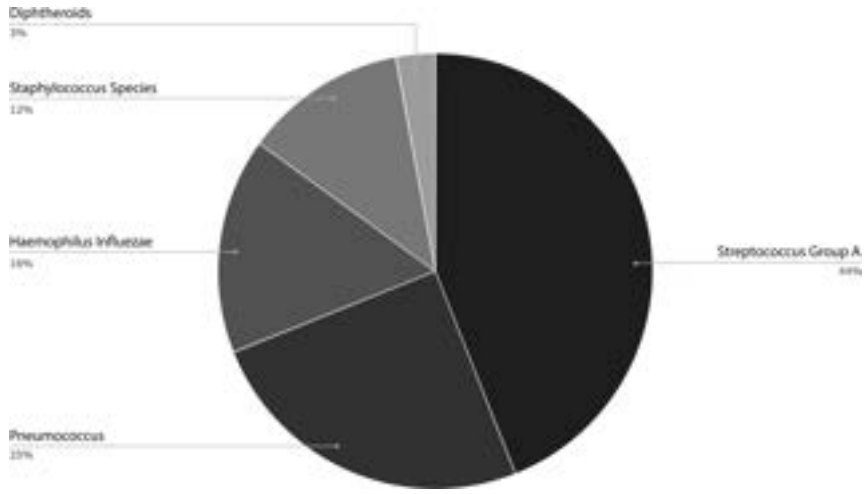

FIG 2. The prevalence of bacteria species in the non-*F necrophorum*–related disease group.

Table 2: Sites of venous thrombosis

Site of Thrombosis	*F necrophorum* (*n* = 37)	Other Bacteria (*n* = 39)
Sigmoid sinus	20 (54%)	4 (10.3%)
Transverse sinus	3 (8%)	0 (0%)
Jugular fossa	13 (35%)	2 (5%)
IJV	8 (22%)	0 (0%)
Cavernous sinus	6 (16%)	0 (0%)
Superior ophthalmic vein	5 (14%)	0 (0%)

venous sites beyond the sigmoid sinus and jugular foramen, including the transverse sinus, IJV, cavernous sinus, and superior ophthalmic vein, was found in 12 of the 37 children (32%) in the study group and among none of the controls (Table 2 and Fig 3). Perisigmoid epidural abscess was present in 27 children in the study group (73%) and in 16 controls (41%) ($P = .036$). Epidural abscess in the middle cranial fossa was present in 10 children (27%) in the study group and in 4 (10%) controls ($P = .199$). Subdural empyema was present in 1 child (2.7%) in the study group and in 1 child (2.6%) in the control group, ($P = 1$).

Cranial Bone-Related Complications

Extramastoid osteomyelitis was identified in 20 of the 37 (54%) children in the study group compared with 4 of the 39 (10%) controls ($P < .001$). Emphysematous osteomyelitis was diagnosed in 8 children in the study group (22%) and was not present in the control group (Fig 4).

Extracranial Complications

A subperiosteal abscess was present in 30 children (81%) in the study group and in 30 (77%) controls, with no significant difference due to its presence ($P = 1$) or volume ($P = .199$). An abscess involving the TMJ was present in 7 children in the study group and in 1 control ($P = .099$) (Fig 5). The following variables showed no significant group differences: extent of inflammatory phlegmon, the presence of cervical lymphadenopathy, ipsilateral parotid gland hyperemia, opacification of the contralateral ear air cells, and sinonasal disease. Table 3 summarizes the sensitivity, specificity, PPV, and NPV for the significant variables.

DISCUSSION

We hypothesized that children with *F necrophorum*–associated CAM can be differentiated from those with other etiologies using CT venography. We tested this hypothesis by comparing the imaging characteristics of CAM in children with acute mastoiditis caused by *F necrophorum* with the imaging characteristics in children with acute mastoiditis caused by other bacteria. Our results revealed that imaging features had very high specificity for the diagnosis of *F necrophorum* as the causative agent in CAM in children.

Almost one-half (49%) of the children who underwent CTV due to suspected complicated mastoiditis were infected with *F necrophorum*. This result supports the reported trend of increasing prevalence of *F necrophorum* as the causative agent in CAM

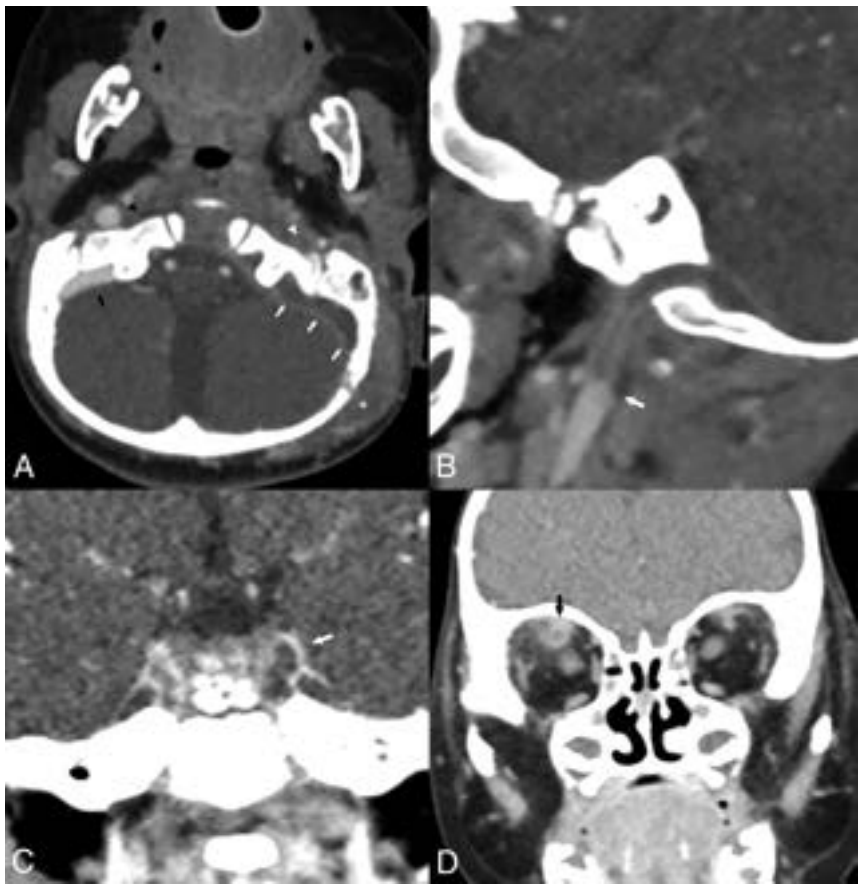

FIG 3. A 9-month-old old boy with *F necrophorum*–related left-sided CAM causing otogenic Lemierre syndrome variant. Axial CTV image (*A*) at the level of the sigmoid sinus demonstrates an obstructing filling defect in the left sigmoid sinus consistent with SVT (*white arrows*), as apposed to normal contrast filling in the right sigmoid sinus (*black arrow*). No contrast is seen in the left IJV (*white arrowhead*) with normal contrast filling in the right IJV (*black arrowhead*). Also note extensive retroauricular soft-tissue phlegmon (*asterisk*). Sagittal-oblique MPR centered on the left jugular bulb (*B*) demonstrates extension of thrombus with complete obstruction of the jugular bulb and proximal IJV, with abrupt transition (*arrow*) where the thrombus ends. Coronal reformat of the sella region (*C*) demonstrates asymmetric contrast enhancement of the cavernous sinuses with a filling defect on the left (*arrow*), consistent with thrombosis. Coronal reformat of the orbits (*D*) demonstrates thrombophlebitis of the right superior ophthalmic vein with enhancement and fat-stranding along the obstructed vein (*arrow*).

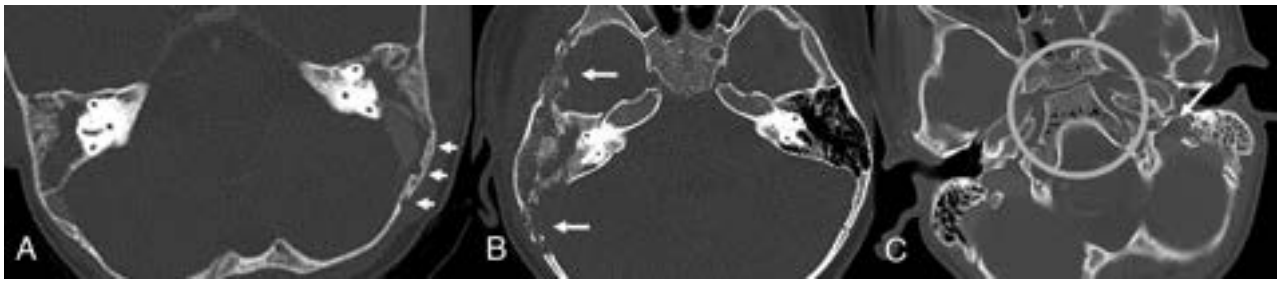

FIG 4. Extramastoid osteomyelitis–related bone changes in 3 different children with *F necrophorum*–related CAM. A 3-year-old girl (*A*) with left mastoid CAM. The mastoid air cells are opacified bilaterally, but only on the left is there demineralization of the mastoid sinus plate as well as extension of focal cortical lytic changes posteriorly along the left sigmoid plate, consistent with subtle extramastoid osteomyelitis (*arrows*). A 2-year-old boy (*B*) with right-sided CAM with more extensive destructive bone changes posterior and anterior to the mastoid (*arrows*). A 4-year-old boy (*C*) with left-sided CAM has abnormal air deposits in the nonpneumatized sphenoid bone, consistent with emphysematous osteomyelitis (*circle*). Note also the presence of SVT in the left jugular bulb (*arrow*).

in Israeli children, ranging from 8%[6] to 32%[14] during the past decade. These findings are not a local phenomenon and are supported by studies from other areas of the world that demonstrated an increased prevalence of *F necrophorum*–related otogenic infections.[15,16] In addition, a national population-based study from Sweden[17] reported increased *F necrophorum*-related head and neck and non-head and neck invasive infections.

Several studies have demonstrated a higher prevalence of intracranial complications with *F necrophorum* infection, with a specifically high rate of SVT.[14,18-20] It was, therefore, not unexpected that

the most significant finding in the current study was the presence of SVT ($P < .001$), with high specificity (0.897) and moderate sensitivity (0.649) for *F necrophorum*–related CAM. SVT development in children with CAM is likely related to infection extending to the dura through infected bone or through emissary veins. The higher rate of SVT development in children with *F necrophorum*–associated AM reflects the invasive nature of *F necrophorum* infections, which cause blood vessel invasion, inflammation, and thrombosis. Virulent factors of this anaerobic bacteria include production of a lipopolysaccharide capsule, leukocidins, lipases, deoxyribonuclease, hemolysins, hemagglutinins, neutrophil-cytotoxic factors, and the ability to aggregate platelets and produce proteolytic enzymes that enhance invasion.[10] In addition, host factors such as prior viral infection or immune system immaturity may also play a role.[8,10] The prevalence of SVT in our study group was 62%, which is much higher than the rates reported in other studies: Gelbart et al[14] reported a prevalence of 21% in 19 children with *F necrophorum* and Ulanovski et al[19] reported a prevalence of 36.6% in 41 patients with *F necrophorum*. It is unclear though if the increased rate of SVT in this study is related to changes in *F necrophorum* virulence or in clinical parameters in the studied population. This question will need to be further addressed in future prospective studies.

Our results showed the importance of documenting the location and extent of thrombosis. SVT involving venous structures beyond the sigmoid sinus and jugular bulb was found to be present in 12 (32%) children in the study group and in none of the controls. These findings differ from those reported by Coudert et al,[16] who did not observe any significant difference in the extent of SVT between FN mastoiditis and mastoiditis related to other bacteria. However, those authors defined the extent of SVT in relation to sigmoid sinus obstruction as being partial, complete, or extended (involving the sigmoid sinus and the jugular vein), and it is unclear whether their report includes a distinction between the jugular bulb and the IJV or if they documented thrombosis in distant venous structures. The pattern of extensive thrombophlebitis that we encountered in this study is consistent with the otogenic Lemierre syndrome variant (Fig 3), which was also described in 4 of 14 pediatric cases of *F necrophorum*–related complicated mastoiditis in a study by Le Monnier et al,[15] and in 7 of 12 cases reviewed by Stergiopoulou and Walsh.[8] Lemierre syndrome is a serious complication of head and neck *F necrophorum* infection characterized by thrombophlebitis of the jugular venous system, bacteremia, and possible septic embolism, leading to necrotizing pneumonia or involvement of multiple organs or joints.[10] The otogenic Lemierre syndrome variant in our study was found to be unique to *F necrophorum* and not encountered in our control group, thus establishing it as an important pattern to be recognized by the radiologist to suggest *F necrophorum* infection.

Another significant finding with clinical importance was the presence of extramastoid bone erosions, reflecting osteomyelitis beyond the coalescent mastoiditis, which was present in 20 study group children (54%) compared with 4 controls (4%) ($P = .00036$). Additionally, a pattern of gas bubbles in a nonpneumatized mastoid and/or extramastoid bone was found in 8 study group children (22%) compared with none of the controls. The finding of extramastoid osteomyelitis was also described in 5 of the 12 cases (42%) reviewed by Stergiopoulou and Walsh,[8] in 4 of the 19 cases (21%) described by Gelbart et al,[14] and in 3 of the 7 cases (43%) described by Yarden-Bilavsky et al.[18] The authors of the latter study described 1 case of extensive osteolysis with "small gas bubbles in the soft tissue surrounding the mastoid cells" depicted in a CT study, but it is unclear from their description if gas bubbles were present in the bone itself. Gas in bone as a manifestation of *F necrophorum* osteomyelitis has been described in skeletal bones as a complication of *F necrophorum* bacteremia.[21] Osteomyelitis related

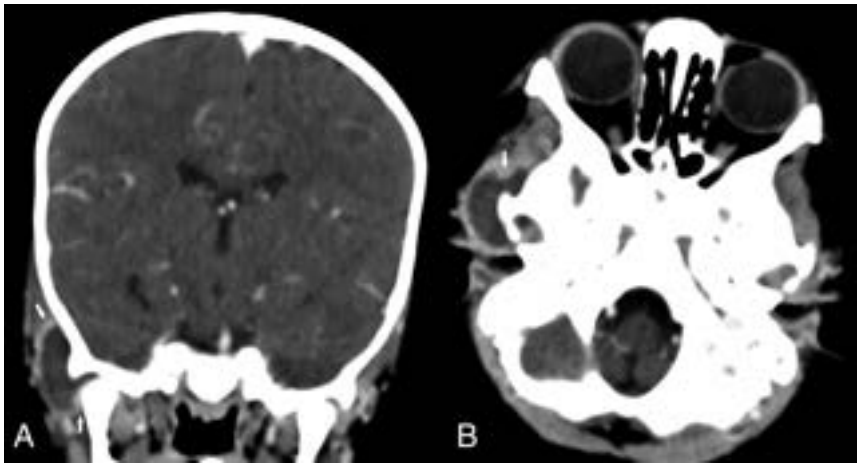

FIG 5. An 11-month-old girl with *F necrophorum*–related right-sided CAM with TMJ abscess. Coronal reformat (*A*) and axial (*B*) CTV images demonstrate a large subperiosteal abscess (*arrows*) extending to the zygomatic arch and into the glenoid fossa of the right TMJ.

Table 3: The sensitivity, specificity, PPV, and NPV for statistically significant variables

Variable	PPV	Sensitivity	Specificity	NPV	*F necrophorum* ($n = 37$)	Other Bacteria ($n = 39$)	*P* Value Adjusted
SVT	0.857	0.649	0.897	0.73	24 (64%)	4 (10%)	.000024
Extramastoid osteomyelitis	0.833	0.541	0.897	0.67	20 (54%)	4 (10%)	.00036
Perisigmoid epidural abscess	0.63	0.73	0.59	0.69	27 (73%)	16 (43%)	.005
SVT and extramastoid bone erosion	1	0.459	1	0.66	17 (46%)	0	.000023
SVT and perisigmoid epidural abscess	0.826	0.514	0.897	0.66	19 (51%)	4 (10%)	.0006
Perisigmoid epidural abscess and extramastoid bone erosion	0.889	0.432	0.949	0.64	16 (43%)	2 (5%)	.00054

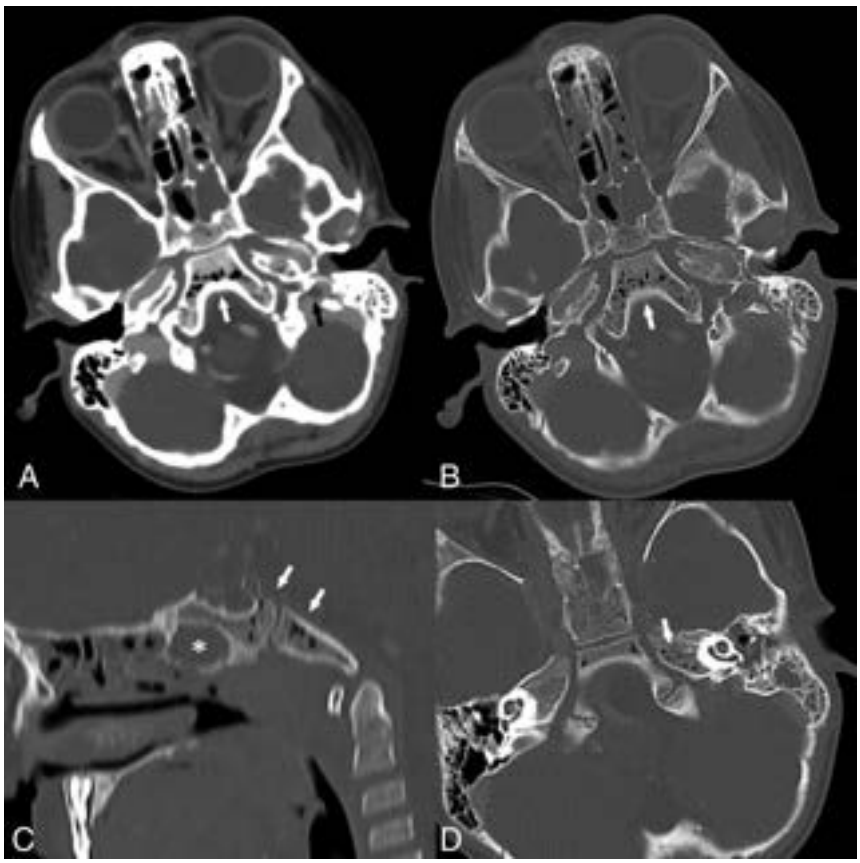

FIG 6. A 4-year-old boy with left-sided *F necrophorum*–related CAM complicated with a pumice bone pattern extramastoid osteomyelitis. The hallmark of this pattern is abnormal air deposits in a nonpneumatized bone without extensive cortical destruction, as seen in this child. Axial CTV image in a soft-tissue window (*A*) and in the bone algorithm (*B*) demonstrates abnormal air deposits in the nonpneumatized clivus (*white arrows*). A sagittal reformat (*C*) shows that both sphenoidal and basilar parts of the clivus are involved (*arrows*), distinguished from the sphenoid sinus that has mucosal thickening (*asterisk*). Similar changes are seen in the left petrous apex (*arrow*) (*D*) compared with the normal bone in the right petrous apex. Note also the presence of SVT in the left jugular bulb (*back arrow*) (*A*).

to gas-forming organisms in an adult population was referred to as emphysematous osteomyelitis, and the unique pattern of gas deposits in the bone, such as the one we encountered in this pediatric study, was termed a "pumice stone" pattern due to its resemblance to the surface appearance of pumice stone.[22] Those authors also noted a lack of cortical destruction in most cases of pumice stone pattern, as had also been seen among the children presenting with this pattern of bone destruction in our study (Fig 6). This pattern is most discernable in nonpneumatized bones (eg, clivus prepneumatization), and it helps to compare the affected bone with the contralateral side for comparison of the pneumatization pattern. The pumice stone pattern of osteomyelitis is considered rare,[22] but our findings suggest that it is an important pathognomonic pattern to recognize in *F necrophorum*–related CAM in the pediatric population.

Abscess involving the TMJ is an important complication of acute mastoiditis, which may lead to ankyloses if untreated.[23,24] We found more cases of TMJ abscess in the study group (7 children) compared with the control group (1 child). Although this difference did not reach a level of significance ($P = .099$), we believe it is of clinical importance, in agreement with Burgess et al,[24] who also reported *F necrophorum* as the most common pathogen in their case series of 9 children with complicated mastoiditis-related TMJ septic arthritis.

The most common complication we encountered was extracranial subperiosteal abscess, which was present in 30 study group children (81%) and 30 controls (77%). However, there was no significant difference in the presence ($P = 1$) or volume ($P = .199$) by which to differentiate *F necrophorum* from other bacteria. Our findings differ from a study by Coudert et al,[16] which reported significantly higher volumes of subperiosteal abscess in *F necrophorum* acute mastoiditis. The second most common finding in our study was intracranial perisigmoid epidural abscess, with a significantly higher prevalence in the *F necrophorum* group ($P = .036$), but with moderate sensitivity and specificity (0.73 and 0.59, respectively).

Our findings suggest that the radiologist plays an essential role in suggesting the likelihood of *F necrophorum*–related infection. This is of clinical importance because the clinical course of *F necrophorum*–related CAM in children differs significantly from that of other pathogens related to CAM. Ulanovski et al[19] reported that children with *F necrophorum*–related mastoiditis had a statistically significantly more complex postoperative course and a significantly longer IV treatment period, which averaged 22 days for *F necrophorum*–related disease versus 7 days for other pathogen-related disease ($P = .0001$). Expediting the diagnosis based on the imaging characteristics will allow an early change of IV antibiotic protocol, guide a more aggressive surgical approach, and facilitate parental counseling in preparation for a more protracted healing process, including the need for extended IV antibiotics treatment, which requires, in many cases, a peripherally inserted central catheter placement.

In this study both otogenic Lemierre syndrome variant–related findings and pumice stone pattern emphysematous osteomyelitis were pathognomonic to *F necrophorum* infection. The presence of SVT (PPV = 0.857) or extramastoid osteomyelitis (PPV = 0.833) or a combination of both (PPV = 1) is highly suggestive of *F necrophorum*. The presence of a perisigmoid epidural abscess is not highly specific for *F necrophorum* (PPV = 0.63), but in combination with SVT (PPV = 0.826) or extramastoid osteomyelitis (PPV = 0.889), the positive predictive value increases. The sensitivity of imaging findings is not as high as the specificity; hence, the NPV is not high enough to allow exclusion of *F necrophorum*–related disease, especially due to the increasing prevalence of *F necrophorum* as the causative agent in pediatric CAM.

Our study has a few limitations. First, its retrospective nature precludes precision verification of the retrieved clinical data and complete standardization of imaging technique, because patients were scanned on >1 CT scanner, including 4 children who were referred to our tertiary medical center with imaging studies performed elsewhere. Of note, all CTV studies were found to be of adequate technique to allow diagnosis. Second, the study design did not include an additional reader, precluding assessment of interobserver variability. Third, statistical evaluation was limited by the small number of subjects with clinically important findings, such as the presence of thrombosis in the superior ophthalmic vein, suggesting that a prospective multicenter study will be warranted to further validate our findings. Fourth, this study did not include an MR imaging correlation, which may enhance our understanding of disease extent in pediatric CAM and will need to be addressed in future studies.

CONCLUSIONS

In children with CAM, CTV findings of emphysematous osteomyelitis and/or thrombosis in venous sites beyond the sigmoid sinus and jugular foramen (a pattern consistent with the otogenic Lemierre syndrome variant) should lead the radiologist to suggest *F necrophorum*–related mastoiditis.

Disclosure forms provided by the authors are available with the full text and PDF of this article at www.ajnr.org.

REFERENCES

1. van den Aardweg MT, Rovers MM, de Ru JA, et al. **A systematic review of diagnostic criteria for acute mastoiditis in children.** *Otol Neurotol* 2008;29:751–57 CrossRef Medline
2. Tamir S, Shwartz Y, Peleg U, et al. **Shifting trends: mastoiditis from a surgical to a medical disease.** *Am J Otolaryngol* 2010;31:467–71 CrossRef Medline
3. Loh R, Phua M, Shaw CL. **Management of paediatric acute mastoiditis: systematic review.** *J Laryngol Otol* 2018;132:96–104 CrossRef Medline
4. Anne S, Schwartz S, Ishman SL, et al. **Medical versus surgical treatment of pediatric acute mastoiditis: a systematic review.** *Laryngoscope* 2019;129:754–60 CrossRef Medline
5. Laulajainen-Hongisto A, Saat R, Lempinen L, et al. **Bacteriology in relation to clinical findings and treatment of acute mastoiditis in children.** *Int J Pediatr Otorhinolaryngol* 2014;78:2072–78 CrossRef Medline
6. Mansour T, Yehudai N, Tobia A, et al. **Acute mastoiditis: 20 years of experience with a uniform management protocol.** *Int J Pediatr Otorhinolaryngol* 2019;125:187–91 CrossRef Medline
7. Marom T, Roth Y, Boaz M, et al. **Acute mastoiditis in children: necessity and timing of imaging.** *Pediatr Infect Dis J* 2016;35:30–34 CrossRef Medline
8. Stergiopoulou T, Walsh TJ. **Fusobacterium necrophorum otitis and mastoiditis in infants and young toddlers.** *Eur J Clin Microbiol Infect Dis* 2016;35:735–40 CrossRef Medline
9. Shamriz O, Engelhard D, Temper V, et al. **Infections caused by Fusobacterium in children: a 14-year single-center experience.** *Infection* 2015;43:663–70 CrossRef Medline
10. Brook I. **Fusobacterial head and neck infections in children.** *Int J Pediatr Otorhinolaryngol* 2015;79:953–58 CrossRef Medline
11. Stern Shavit S, Raveh E, Levi L, et al. **Surgical intervention for acute mastoiditis: 10 years experience in a tertiary children hospital.** *Eur Arch Otorhinolaryngol* 2019;276:3051–56 CrossRef Medline
12. Horowitz G, Fishman G, Brenner A, et al. **A novel radiographic sign and a new classifying system in mastoiditis-related epidural abscess.** *Otol Neurotol* 2015;36:1378–82 CrossRef Medline
13. Saat R, Kurdo G, Brandstack N, et al. **A new classification system is helpful in diagnosing intracranial complications of acute mastoiditis in CT.** *Clin Neuroradiol* 2018;28:523–28 CrossRef Medline
14. Gelbart M, Bilavsky E, Chodick G, et al. **Fusobacterium necrophorum as an emerging pathogen of acute mastoiditis.** *Pediatr Infect Dis J* 2019;38:12–15 CrossRef Medline
15. Le Monnier A, Jamet A, Carbonnelle E, et al. **Fusobacterium necrophorum middle ear infections in children and related complications: report of 25 cases and literature review.** *Pediatr Infect Dis J* 2008;27:613–17 CrossRef Medline
16. Coudert A, Fanchette J, Regnier G, et al. **Fusobacterium necrophorum, a major provider of sinus thrombosis in acute mastoiditis: a retrospective multicentre paediatric study.** *Clin Otolaryngol* 2020;45:182–89 CrossRef Medline
17. Nygren D, Holm K. **Invasive infections with Fusobacterium necrophorum including Lemierre's syndrome: an 8-year Swedish nationwide retrospective study**. *Clin Microbiol Infect* 2020;26:1089.e7-1089–e12 CrossRef Medline
18. Yarden-Bilavsky H, Raveh E, Livni G, et al. **Fusobacterium necrophorum mastoiditis in children - emerging pathogen in an old disease.** *Int J Pediatr Otorhinolaryngol* 2013;77:92–96 CrossRef Medline
19. Ulanovski D, Shavit SS, Scheuerman O, et al. **Medical and surgical characteristics of fusobacterium necrophorum mastoiditis in children.** *Int J Pediatr Otorhinolaryngol* 2020;138:110324 CrossRef Medline
20. Yosefof E, Hilly O, Sokolov M, et al. **Paediatric otogenic sinus venous thrombosis: the role of Fusobacterium necrophorum.** *Acta Otorhinolaryngol Ital* 2022;42:388–94 CrossRef Medline
21. Riordan T. **Human infection with Fusobacterium necrophorum (Necrobacillosis), with a focus on Lemierre's syndrome**. *Clin Microbiol Rev* 2007;20:622–59 CrossRef Medline
22. Small JE, Chea P, Shah N, et al. **Diagnostic features of emphysematous osteomyelitis.** *Curr Probl Diagn Radiol* 2022;51:666–72 CrossRef Medline
23. Luscan R, Belhous K, Simon F, et al. **TMJ arthritis is a frequent complication of otomastoiditis.** *J Craniomaxillofac Surg* 2016;44:1984–87 CrossRef Medline
24. Burgess A, Celerier C, Breton S, et al. **Otogenic temporomandibular arthritis in children.** *JAMA Otolaryngol Head Neck Surg* 2017;143:466–71 CrossRef Medline

Brainstem Chipmunk Sign: A Diagnostic Imaging Clue across All Subtypes of Alexander Disease

Thaís Armangue, Matthew T. Whitehead, Davide Tonduti, Laura Farina, Ali Reza Tavasoli, Arastoo Vossough, Mariko L. Bennett, Ylenia Vaia, Geneviève Bernard, Ettore Salsano, Saadet Mercimek-Andrews, Amy Waldman, and Adeline Vanderver

ABSTRACT

BACKGROUND AND PURPOSE: While classic brain MR imaging features of Alexander disease have been well-documented, lesional patterns can overlap with other leukodystrophies, especially in the early stages of the disease or in milder phenotypes. We aimed to assess the utility of a new neuroimaging sign to help increase the diagnostic specificity of Alexander disease.

MATERIALS AND METHODS: A peculiar bilateral symmetric hyperintense signal on T2-weighted images affecting the medulla oblongata was identified in an index patient with type I Alexander disease. Subsequently, 5 observers performed a systematic MR imaging review for this pattern by examining 55 subjects with Alexander disease and 74 subjects with other leukodystrophies. Interobserver agreement was assessed by the κ index. Sensitivity, specificity, and receiver operating characteristic curves were determined.

RESULTS: The identified pattern was present in 87% of subjects with Alexander disease and 14% of those without Alexander disease leukodystrophy ($P < .001$), 3 with vanishing white matter, 4 with adult polyglucosan body disease, and 3 others. It was found equally in both type I and type II Alexander disease (28/32, 88% versus 18/21, 86%; $P = .851$) and in subjects with unusual disease features (2/2). Sensitivity (87.3%; 95% CI, 76.0%–93.7%), specificity (86.5%; 95% CI, 76.9%–92.5%), and interobserver agreement (κ index = 0.82) were high.

CONCLUSIONS: The identified pattern in the medulla oblongata, called the chipmunk sign due to its resemblance to the face of this rodent, is extremely common in subjects with Alexander disease and represents a diagnostic tool that can aid in early diagnosis, especially in subjects with otherwise atypical MR imaging findings and/or clinical features.

ABBREVIATIONS: APBD = adult polyglucosan body disease; ADLD = adult-onset autosomal dominant leukodystrophy; AxD = Alexander disease; *GFAP* = glial fibrillary acidic protein; ION = inferior olivary nucleus; IQR = interquartile range; VWM = vanishing white matter

Alexander disease (AxD) is a devastating leukodystrophy caused by gain of function de novo or, less commonly, dominant missense pathogenic variants in the glial fibrillary acidic protein (*GFAP*) gene.[1] Brain MR imaging pattern recognition is crucial in guiding molecular tests to confirm the diagnosis in AxD. Before the identification of the causative genetic etiology of AxD, Van der Knaap et al[2] described 5 MR imaging–based criteria for the diagnosis. Several disease classifications are currently in use. The traditional one classifies AxD on the basis of age at disease onset into neonatal (<30 days), infantile (0–2 years), juvenile (2–12 years), and adult (older than 12 years) forms.[3,4] AxD can also be classified on the basis of clinical features at onset and brain MR imaging findings in type I and type II AxD.[5] Type I generally presents at an earlier age with classic imaging features, including extensive supratentorial leukodystrophy with frontal predominance, brainstem and basal ganglia involvement, and parenchymal enhancement. Type II manifests across the life span, showing atypical imaging

Received November 29, 2023; accepted after revision February 1, 2024.

From the Neuroimmunology Program (T.A.), Institut d'Investigacions Biomèdiques August Pi i Sunyer (IDIBAPS)-Hospital Clinic, and Neurology Department (T.A.), Neuroimmunology Unit, Sant Joan de Deu Children's Hospital, University of Barcelona, Barcelona, Spain; Department of Radiology (M.T.W., A. Vossough), and Division of Neurology (M.L.B., Y.V., A.W., A.Vanderver), Children's Hospital of Philadelphia, Philadelphia, Pennsylvania; Perelman School of Medicine (M.T.W., A. Vossough, A.W., A. Vanderver), University of Pennsylvania, Philadelphia, Pennsylvania; Unit of Pediatric Neurology (D.T., Y.V.), Center for diagnosis and treatment of Leukodystrophies, V. Buzzi Children's Hospital, University of Milan, Milan, Italy; Neuroimaging Laboratory (L.F.), IRCCS Fondazione Santa Lucia, Rome, Italy; Department of Neurology (A.R.T.), Children's Medical Center, Tehran University of Medical Sciences, Tehran, Iran; Department of Neurology (A.R.T.), Barrow Neurological Institute, Phoenix Children's Hospital, Phoenix, Arizona; Departments of Neurology and Neurosurgery, Pediatrics, and Human Genetics (G.B.), and Specialized Medicine (G.B.), Division of Medical Genetics, McGill University Health Centre, Montreal, Quebec, Canada; Child Health and Human Development Program (G.B.), Research Institute of the McGill University Health Centre, Montreal, Quebec, Canada; Unit of Rare Neurological Diseases (E.S.), Fondazione IRCCS Istituto Neurologico Carlo Besta, Milan, Italy; Department of Medical Genetics (S.M.-A.), Faculty of Medicine and Dentistry, University of Alberta, Edmonton, Alberta, Canada; and The Hospital for Sick Children (S.M.-A.), Toronto, Ontario, Canada.

T. Armangue and M.T. Whitehead contributed equally to the article.

This study was partially supported by Children's National Medical Center, Department of Neurology (A. Vanderver), Carlos III Spanish Health Institute (CM14/00081, CV15/00021 TA).

Please address correspondence to Adeline Vanderver, MD, Children's Hospital of Philadelphia, 3615 Civic Center Blvd Abramson Research Center 516H, Philadelphia, PA 19104; e-mail: Vandervera@chop.edu

Indicates article with online supplemental data.

http://dx.doi.org/10.3174/ajnr.A8220

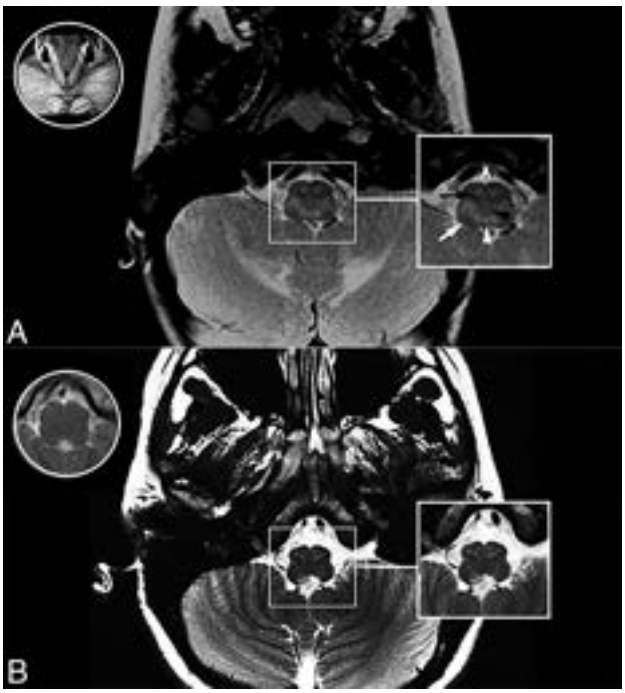

FIGURE Chipmunk MR imaging sign. T2-weighted axial MRI through the medulla oblongata in subjects with AxD type I (*A*) and AxD type II (*B*), an image of a chipmunk face (*A*, *white circle*), and a T2WI axial scan of the medulla oblongata in a healthy subject (*B*, *white circle*). A typical chipmunk sign in AxD type I (*white box* in *A*) and AxD type II (*white box* in *B*). The *black arrow* indicates the inferior olivary nucleus; *black arrowhead*, medial lemniscus; *white arrow*, inferior peduncle; *white arrowhead*, medial longitudinal fasciculus; *double white arrows*, pyramidal tracts.

features with predominant involvement of the brainstem, and, in some cases, additional supratentorial WM involvement.[5] In particular, mild-to-severe atrophy of the medulla oblongata is a common finding with or without signal abnormalities,[6] with involvement of the middle cerebellar peduncles.[7] Additionally, atypical neuroradiologic features have been identified in AxD, including isolated brainstem involvement and focal MR imaging lesions.[8,9]

Yoshida et al[10] have described bilateral abnormal MR signal of the anterior portion of medulla oblongata in 4 subjects with elderly-onset AxD, with the signal abnormality in the pyramids resembling the "eye spot" of the Taenaris butterfly. We identified a characteristic MR imaging pattern on axial T2-weighted images affecting the medulla oblongata, with bilateral symmetric hyperintensity involving the central inferior olivary nucleus (ION), the pyramids, and the cuneate and gracile fascicles with peripheral ION and inferior peduncle sparing in an index AxD individual and called it the chipmunk sign due to its resemblance to the appearance of the face of this rodent. This study aims to describe this neuroradiologic sign in subjects with AxD and assess its sensitivity and specificity in the diagnostic process of AxD compared with other leukodystrophies and genetic leukoencephalopathies.

MATERIALS AND METHODS

Setting and Participants

A new MR imaging pattern affecting the medulla oblongata on axial T2-weighted images at the mid-olivary level, resembling a chipmunk face, was identified in an index subject with type I AxD, and it was defined as the chipmunk sign (Fig 1*A*).

Fifty-five additional subjects with pathogenic variants in *GFAP* for whom at least axial T2-weighted images from brain MR imaging were available in electronic digital format were enrolled in the study. Seventy-four subjects with other leukodystrophies and genetic leukoencephalopathies confirmed by molecular testing, with potential brainstem involvement on MR imaging, were included for comparison (see Online Supplemental Data for details).[11] All participants were recruited from 5 different centers (Children's National Health System, Washington DC, center 1; Children's Hospital of Philadelphia, Philadelphia, center 2; Fondazione IRCCS Istituto Neurologico "Carlo Besta," Milan, Italy, center 3; Hospital for Sick Children Toronto, Ontario, Canada, center 4; Montreal Children's Hospital, Québec, Canada, center 5). Institutional review board approval was obtained at each respective institution. Informed consent for the use of deidentified data for scientific purposes was obtained from all the subjects who participated in clinical investigations.

MR Imaging Evaluation

A single axial T2-weighted image in TIFF for each MR imaging was obtained at the mid-olivary level of the medulla oblongata from the 55 subjects with AxD and 74 with non-AxD leukodystrophy. All images were assigned to a randomized order number (STATA randomization function; StataCorp) and included without additional clinical and/or MR imaging data in a blinded PowerPoint file (Microsoft). All the slides were scored for the presence or absence of the chipmunk sign (T2-hyperintense signal changes of the dorsal medulla, pyramids, and central olives and T2-hypointense signal changes of the peripheral ION and inferior peduncles) by 5 independent examiners (3 pediatric neurologists with expertise in leukodystrophies (A. Vanderver, T.A., D.T. with >10 years' experience in leukodystrophies) and 2 pediatric neuroradiologists (L.F., M.T.W. with >12 years' experience). The images were also scored independently for the presence of T2-hyperintense signal changes of the medial lemniscus and T2-hypointense signal of the medial longitudinal fasciculus. The presence of atrophy and/or lesional mass effect was evaluated as well. The chipmunk sign and the other MR imaging features were considered positive by consensus if ≥3 observers considered it positive. When available, an additional file with a single axial T2-FLAIR image at the same level was assessed by the same procedure and reviewed separately from the T2-weighted images to assess the sensitivity and specificity of the chipmunk sign on T2-FLAIR sequences as well.

Statistical Analysis

Interobserver agreement was assessed by the κ index for multiple observers. Comparative analyses on demographics were performed using the Fisher exact test and the χ^2 test, Student *t* test, or Wilcoxon rank-sum test when appropriate. The confidence interval (95%) of the sensitivity and specificity of the chipmunk sign in the diagnosis of AxD was assessed by the Wilson procedure. Multivariate binary logistic regression was used to evaluate age at the time of MR imaging and type of

AxD as possible predictors of the presence of the chipmunk sign in subjects with AxD.

RESULTS

Fifty-five subjects with AxD were included in this study (32 type I MR imaging patterns, 21 type II MR imaging patterns, and 2 with an atypical MR imaging pattern with predominant supratentorial, bilateral, and symmetric occipital involvement). Among the 32 subjects with the type I AxD MR imaging pattern, 23 developed a clinical picture classical for type I AxD (early infantile onset, macrocephaly, delayed motor skills, and seizures), but 8 had atypical clinical features, such as substantial brainstem–related symptoms and slow progression, clinically resembling type II AxD.

The median age at the time of brain MR imaging was 2.1 years (interquartile range [IQR], 1.6–5.5 years) for AxD type I MR imaging pattern; 39 years of age (IQR, 16.4–54.0 years) for AxD type II MR imaging pattern; 2.0 years of age (IQR, 0.8–3.1 years) for subjects with an atypical MR imaging pattern; and 2.9 years of age (IQR, 0.7–9.3 years; range, 0–81 years) for subjects with other leukodystrophies and genetic leukoencephalopathies.

Interobserver agreement in assessing the presence or absence of the chipmunk sign in subjects with AxD and a comparison group among the 5 reviewers was excellent (κ index = 0.82).

Medullary signal abnormalities resembling the chipmunk sign were found more frequently in subjects with AxD (48/55, 87%) than in the comparison non-AxD leukodystrophy group (10/74, 14%; OR = 43.8; 95% CI, 15.5–123.6; $P < .001$). This sign was found equally in both type I and type II AxD (28/32, 88% versus 18/21, 86%; OR = 1.17, $P = .851$) (Figure and Online Supplemental Data), including the subjects with type I MR imaging but atypical clinical features ($n = 8$) and in the subjects with an atypical MR imaging pattern with predominant supratentorial, bilateral, occipital involvement ($n = 2$). Among the subjects with AxD, a multivariate logistic analysis showed that neither AxD type nor age at the time of MR imaging was a predictor of the presence of the chipmunk sign ($P = .865$ and $P = .303$).

Subjects with AxD with a type II MR imaging pattern showed more frequent T2-hyperintensity in the medial lemniscus and atrophy but less frequent T2-hypointense signal in medial longitudinal fasciculus than subjects with AxD with a type I MR imaging pattern ($P < .05$ in all) (Table). No other differences in the involvement of anatomic structures of the medulla oblongata were found when comparing both subgroups of subjects with AxD. In some subjects with AxD, the chipmunk sign was considered atypical due to the coexistence with additional signal abnormalities (Table).

The small subgroup of subjects with other leukodystrophies and an MR imaging pattern resembling the chipmunk sign were the following: 4/4 with adult polyglucosan body disease (APBD), 3/6 with vanishing white matter (VWM), 3 others (1 with 4H leukodystrophy, 1 with adult-onset autosomal dominant leukodystrophy [ADLD]), and 1 with Pelizaeus-Merzbacher disease. However, these leukodystrophies are easily distinguishable from AxD on the basis of concurrent differing supratentorial brain MR imaging patterns (Online Supplemental Data). Furthermore, the reduced diffusivity of WM structures that is common in VWM and some mitochondrial disorders is not an expected imaging finding in AxD.

Overall, the sensitivity and specificity of the chipmunk sign in the diagnosis of AxD compared with other leukodystrophies were 87.3% (95% CI, 76.0%–93.7%) and 86.5% (95% CI, 76.9%–92.5%), respectively, when only brainstem imaging was reviewed, and the area under the receiver operating characteristic curve was 0.86 (95% CI, 0.80–0.92). Among the 28 subjects (14 with AxD, 14 with non-AxD leukodystrophies) in whom axial T2-FLAIR images were available, detection of a chipmunk sign in this sequence showed lower interobserver agreement (κ index = 0.63) and lower sensitivity (57.1%; 95% CI, 32.6%–78.6%), specificity (78.6%; 95% CI, 52.4%–92.4%), and area under the curve (0.687; 95% CI, 0.51–0.87) compared with T2-weighted images. In addition, in 7/11 (64%) subjects in whom this sign was considered positive on just axial T2-FLAIR images, it was categorized as mild or partial.

DISCUSSION

AxD is known to have characteristic MR imaging features.[2,8,9] Brain involvement in the typical form is characterized by a frontal predominance, periventricular T1 and T2 shortening, deep gray nuclear involvement, brainstem involvement, and contrast enhancement. Before the availability of molecular genetic testing of *GFAP*, when brain biopsy was the mainstay of diagnosis, if 4 of 5 of these criteria were satisfied, neuroimaging was considered diagnostic. However, the neuroimaging phenotype may, in some cases, be variable, and diagnostic criteria may be incompletely fulfilled early in the disease process, especially in mild phenotypes and in atypical variants, particularly in type II AxD.[1–4] Additional features are helpful to establish the diagnosis in these subjects.

We have identified an additional imaging pattern that can be seen in subjects with AxD. Specifically, hyperintense signal on T2-weighted images infiltrating the medullary pyramids, central ION, and the dorsal medulla, often involving the regions of the cuneate and gracile fascicles and sparing the inferior cerebellar peduncles. The medial longitudinal fasciculus is often spared as well. Signal alteration affecting the medulla oblongata resembles the face of a chipmunk. The residual T2 hypointensity of the ION corresponds to the chipmunk's eyes, while spared inferior cerebellar peduncles form the cheeks.

When the chipmunk sign is seen, the remainder of the MR imaging should be analyzed for features consistent with AxD, even in the presence of atypical brain MR imaging features such as occipital involvement or isolated brainstem involvement in adults. In particular, tumorlike brainstem lesions can be found in patients with AxD.[12] In these cases, correct and prompt diagnosis can be challenging because lesion biopsy would be expected to reveal Rosenthal fibers, which are common in various neoplastic CNS conditions, including pilocytic astrocytoma.[13] The coexistence of the chipmunk sign could obviate the need for biopsy in these circumstances.

The only genetic disorders other than AxD that consistently exhibited a similar pattern of medullary signal in our study were APBD and VWM. However, AxD can be easily distinguished from these disorders from both a clinical and neuroimaging perspective. Unlike AxD, VWM manifests restricted diffusion in the involved WM early on and ultimately causes rarefaction of WM

Involvement of different anatomic structures of the medulla oblongata and additional MR imaging features in subjects with AxD and non-AxD leukodystrophy on T2-weighted images[a]

	AxD	Non-AxD	AxD Type I	AxD Type II	VWM	APBD	Other
Total MRIs reviewed	55	74	32	21	6	4	67
Positive chipmunk sign	48	10	28	18	3	4	3
T2-hyperintense dorsal medulla	52	17	29	21	5	4	8
T2-hyperintense pyramids							
No	8	59	7	1	2	0	57
Yes, asymmetric	5	1	2	3	0	0	1
Yes, symmetric	42	13	23	17	4	4	5
T2-hyperintense central ION							
No	8	58	6	2	1	0	57
Yes, asymmetric	5	1	1	4	0	0	1
Yes, symmetric	41	13	24	15	4	4	5
T2-hypointense peripheral ION							
No	6	62	4	2	2	0	60
Yes, asymmetric	1	0	0	1	0	0	0
Yes, symmetric	47	11	27	18	4	4	3
T2-hypointense IP							
No	7	58	4	3	1	0	57
Yes, asymmetric	3	1	1	2	0	0	1
Yes, symmetric	45	14	27	16	5	3	6
T2-hyperintense ML	38	12	19	18	4	4	4
Atrophy	20	7	4	16	1	4	2
Mass effect lesions	5	2	3	2	0	0	2
T2-hypointense MLF	35	8	25	8	3	3	2

Note:—MLF indicates medial longitudinal fasciculus; ML, medial lemniscus; IP, inferior peduncle.
[a] See the Online Supplemental Data for details on patients and the comparison group.

signal that approaches the CSF signal. Clinically, it is often characterized by an evident sensitivity to febrile infections and minor head trauma, which may cause a rapid neurologic deterioration with often marked cerebellar ataxia.[14,15] In APBD, the cerebral WM involvement is more diffuse, lacking evidence of a disease gradient, and subjects usually develop neurogenic bladder, progressive spastic gait, and peripheral neuropathy.[16] Further studies may be useful, however, to further characterize these medullary imaging findings in APBD.

Limitations of this study include the retrospective design and the possibility of observer bias. Against this confound, the sensitivity was only 87.3% on T2-weighted images and 57.1% on T2-FLAIR images. Moreover, due to the rarity of the disease, the sample size is relatively small, which may affect the external validity of the chipmunk sign, though the high prevalence of this sign further supports our analyses. Further prospective blinded studies may be useful to validate our findings.

CONCLUSIONS

We have suggested an imaging finding called the chipmunk sign to be characteristic of AxD in the appropriate clinical and MR imaging context, after excluding a few other metabolic and genetic conditions. Our approach may help physicians consider this disorder earlier in the diagnostic odyssey, particularly in subjects with otherwise atypical MR imaging findings and/or clinical features. Subjects with VWM or APBD can show a similar brainstem involvement, but clinical features as well as additional supratentorial MR imaging features easily help to distinguish them from AxD. Identification of the chipmunk sign should prompt careful assessment for other supportive AxD imaging findings and consideration of genetic studies for the sequencing of *GFAP*.

Disclosure forms provided by the authors are available with the full text and PDF of this article at www.ajnr.org.

REFERENCES

1. Messing A. **Alexander disease.** *Handb Clin Neurol* 2018;148:693–700 CrossRef Medline
2. van der Knaap MS, Naidu S, Breiter SN, et al. **Alexander disease: diagnosis with MR imaging.** *AJNR Am J Neuroradiol* 2001;22:541–52 Medline
3. Russo LS, Aron A, Anderson PJ. **Alexander's disease: a report and reappraisal**. *Neurology* 1976;26:607–14 CrossRef Medline
4. Springer S, Erlewein R, Naegele T, et al. **Alexander disease: classification revisited and isolation of a neonatal form.** *Neuropediatrics* 2000;31:86–92 CrossRef Medline
5. Prust M, Wang J, Morizono H, et al. **GFAP mutations, age at onset, and clinical subtypes in Alexander disease.** *Neurology* 2011;77:1287–94 CrossRef Medline
6. van der Knaap MS, Ramesh V, Schiffmann R, et al. **Alexander disease: ventricular garlands and abnormalities of the medulla and spinal cord.** *Neurology* 2006;66:494–98 CrossRef Medline
7. Resende LL, de Paiva AR, Kok F, et al. **Adult leukodystrophies: a step-by-step diagnostic approach.** *Radiographics* 2019;39:153–68 CrossRef Medline
8. van der Knaap MS, Salomons GS, Li R, et al. **Unusual variants of Alexander's disease**. *Ann Neurol* 2005;57:327–38 CrossRef Medline
9. Barreau P, Prust MJ, Crane J, et al. **Focal central white matter lesions in Alexander disease.** *J Child Neurol* 2011;26:1422–24 CrossRef Medline
10. Yoshida T, Mizuta I, Saito K, et al. **Characteristic abnormal signals in medulla oblongata "eye spot" sign: four cases of elderly-onset Alexander disease**. *Neurol Clin Pract* 2015;5:259–62 CrossRef Medline
11. Vanderver A, Prust M, Tonduti D, et al; GLIA Consortium. **Case definition and classification of leukodystrophies and leukoencephalopathies.** *Mol Genet Metab* 2015;114:494–500 CrossRef Medline
12. Tan AP, Sahil C, Robinson R, et al. **Neuroimaging in juvenile Alexander disease: tumour-like brainstem lesions.** *Ann Acad Med Singap* 2018;47:191–93 CrossRef
13. Van Poppel K, Ellison D, Broniscer A, et al. **Alexander disease: an important mimicker of focal brainstem glioma-response.** *Pediatr Blood Cancer* 2010;54:487 CrossRef Medline
14. van der Knaap MS, Pronk JC, Scheper GC. **Vanishing white matter disease.** *Lancet Neurol* 2006;5:413–23 CrossRef Medline
15. van der Lei HD, Steenweg ME, Bugiani M, et al. **Restricted diffusion in vanishing white matter.** *Arch Neurol* 2012;69:723–27 CrossRef Medline
16. Mochel F, Schiffmann R, Steenweg ME, et al. **Adult polyglucosan body disease: natural history and key magnetic resonance imaging findings.** *Ann Neurol* 2012;72:433–41 CrossRef Medline

DOTATATE PET/MR Imaging Differentiates Secondary-Progressive from de Novo World Health Organization Grade 3 Meningiomas

Joon Tae Kim, Se Jung Chris Chang, Arsalan Haghdel, Rohan R. Ramakrishna, Susan C. Pannullo, Theodore H. Schwartz, Joseph R. Osborne, Rajiv S. Magge, Howard A. Fine, Babacar Cisse, Philip Stieg, Eaton Lin, Michelle Roytman, Joshua D. Palmer, Nicolas A. Karakatsanis, David Pisapia, Benjamin Liechty, Jonathan P.S. Knisely, and Jana Ivanidze

ABSTRACT

BACKGROUND AND PURPOSE: WHO grade 3 meningiomas are rare and poorly understood and have a higher propensity for recurrence, metastasis, and worsened clinical outcomes compared with lower-grade meningiomas. The purpose of our study was to prospectively evaluate the molecular profile, PET characteristics, and outcomes of patients with World Health Organization grade 3 meningiomas who were imaged with gallium 68 (^{68}Ga) DOTATATE PET/MR imaging.

MATERIALS AND METHODS: Patients with World Health Organization grade 3 meningiomas enrolled in our prospective observational cohort evaluating the utility of (^{68}Ga) DOTATATE PET/MR imaging in somatostatin receptor positive brain tumors were included. We stratified patients by de novo–versus–secondary-progressive status and evaluated the differences in the PET standard uptake value, molecular profiles, and clinical outcomes.

RESULTS: Patients met the inclusion criteria (secondary-progressive: 7/14; de novo: 7/14). The secondary-progressive cohort had a significantly higher per-patient number of surgeries (4.1 versus 1.6; $P = .011$) and trended toward a higher number of radiation therapy courses (2.4 versus 1.6; $P = .23$) and cumulative radiation therapy doses (106Gy versus 68.3Gy; $P = .31$). The secondary-progressive cohort had a significantly lower progression-free survival compared with the de novo cohort (4.8 versus 37.7 months; $P = .004$). Secondary-progressive tumors had distinct molecular pathology profiles with higher numbers of mutations (3.5 versus 1.2; $P = .024$). Secondary-progressive tumors demonstrated higher PET standard uptake values (17.1 versus 12.4; $P = .0021$).

CONCLUSIONS: Our study confirms prior work illustrating distinct clinical outcomes in secondary-progressive and de novo World Health Organization grade 3 meningiomas. Furthermore, our findings support (^{68}Ga) DOTATATE PET/MR imaging as a useful management strategy in World Health Organization grade 3 meningiomas and provide insight into meningioma biology, as well as clinical management implications.

ABBREVIATIONS: GTR = gross total resection; PFS = progression-free survival; RANO = Response Assessment in Neuro-Oncology; RT = radiation therapy; SSS = superior sagittal sinus; *SSTR* = *somatostatin-receptor*; SUV = standard uptake value; SUVR = SUV ratio; WHO = World Health Organization

Meningiomas are the most common primary brain tumor, accounting for approximately 40% of all intracranial lesions.[1] The World Health Organization (WHO) classification criteria stratify meningiomas into 3 grades based on the frequency of mitotic figures as evaluated histologically. Most meningiomas are WHO grade 1 and have a favorable prognosis.[1] However, a smaller subset are classified as either WHO grade 2 or 3 meningiomas and are associated with greater morbidity and mortality.[1]

WHO grade 3 meningiomas, which account for <2% of all graded cases, are particularly aggressive with a higher propensity for recurrence, metastases, and worse clinical outcomes compared with lower-grade meningiomas.[1,2] While patients with WHO grade 3 meningiomas are typically treated with maximal surgical resection and radiation therapy (RT), prognosis is poor with 5-year recurrence rates of 50%–90% after surgery and 5-year overall survival rates ranging from 20% to 50%.[1,3] The 2021 WHO classification defines WHO grade 3 meningiomas both histologically and molecularly. Histologic criteria for grade 3 meningiomas include ≥20 mitotic figures per 10 high-power (400x) fields, well-formed papillary or rhabdoid architecture (typically supported by the presence of *PBRM1* and *BAP1* mutations,

Received December 15, 2023; accepted after revision February 2, 2024.

From the Weill Cornell Medical College (J.T.K., S.J.C.C., A.H.), Departments of Neurological Surgery (R.R.R., S.C.P., T.H.S., B.C., P.S.), Radiology (J.R.O., E.L., M.R., N.A.K., J.I.), Neurology (R.S.M., H.A.F.), Pathology and Laboratory Medicine (D.P., B.L.), and Radiation Oncology (J.P.S.K.), Weill Cornell Medicine/NewYork-Presbyterian Hospital, New York, New York; and Department of Neuro-Oncology (J.D.P.), Ohio State University, Columbus, Ohio.

Paper previously presented as an abstract at: Annual Meeting of the Radiological Socity of North America, November 26–30, 2023. Chicago, Illinois.

The study was partially funded by an investigator-initiated clinical trial grant (funder: Novartis Pharmaceuticals *CAAA501A0US05T* to J.I.).

Please address correspondence to Jana Ivanidze, MD, 1305 York Ave, 3rd Floor, New York, NY 10021; e-mail: jai9018@med.cornell.edu; @jana_ivanidze

http://dx.doi.org/10.3174/ajnr.A8219

SUMMARY

PREVIOUS LITERATURE: WHO grade 3 meningiomas are rare, representing only 2% of all meningiomas, and are associated with high morbidity and mortality. MRI has significant limitations in meningioma evaluation, especially in intermediate- and high-risk tumors. [^{68}Ga] DOTATATE PET has demonstrated high utility in meningioma evaluation and treatment planning. There thus exists a marked unmet need for improved targeted imaging strategies in the management of WHO grade 3 meningiomas. In this study, we evaluate the imaging characteristics, molecular profile, and clinical outcomes of patients with WHO grade 3 meningiomas who were imaged with [^{68}Ga] DOTATATE PET/MRI.

KEY FINDINGS: We found patients with secondary-progressive WHO grade 3 meningiomas to have worse progression-free survival (PFS) compared with those with de novo disease, concordant with prior literature. We further found that the secondary progressive cohort demonstrated higher lesion SUV on [^{68}Ga] DOTATATE PET/MRI, as well as increased rate of mutations.

KNOWLEDGE ADVANCEMENT: This work supports [^{68}Ga] DOTATATE PET/MRI as a management strategy in WHO grade 3 meningiomas and raises the possibility of non invasively differentiating secondary-progressive and de novo meningiomas. Additionally, this work raises important questions regarding meningioma biology such as the role of *SSTR2* signaling and mutation rate in higher-grade meningiomas.

respectively), or frank histologic anaplasia with sarcomatoid, melanomatoid, or carcinomatoid architecture, while molecular criteria for grade 3 meningiomas include the presence of a *TERT* promoter mutation or homozygous deletion of *CDKN2A/B*. They can arise de novo or from secondary progression of meningiomas of lower histologic grade, the latter of which are known to have poorer clinical outcomes such as markedly decreased progression-free survival (PFS).[2,4]

While WHO grade has been used widely to guide clinical decision-making and treatment-planning in meningiomas, histopathologic findings alone have proved suboptimal in predicting clinical and biologic behavior and prognosis of meningiomas. For instance, many cases of WHO grade 1 meningioma will progress with unexpectedly early recurrences, while many WHO grade 2 meningiomas will remain indolent and benign for the entirety of their clinical course.[5] WHO grade 3 meningiomas are even less predictable and poorly understood compared with their lower-grade counterparts. Therefore, additional understanding of the diagnosis, management, and prognostic factors surrounding WHO grade 3 meningiomas is needed to optimize treatment-planning and patient outcomes.

The primary neuroimaging approach for the evaluation of meningiomas is contrast-enhanced MR imaging. However, MR imaging has considerable limitations such as in the distinction of recurrent or residual disease from postoperative inflammation and scarring, especially in intermediate- and high-risk meningiomas, further compounded in the context of prior RT.[6] More recently, gallium 68 (^{68}Ga) DOTATATE PET has demonstrated utility in meningioma evaluation, including diagnostic confirmation, surgical planning, delineation of radiation therapy target volumes, and posttreatment surveillance.[7] By targeting a receptor highly expressed on the surface of meningiomas, somatostatin receptor 2 (*SSTR2*), (^{68}Ga) DOTATATE PET has contributed to improved molecular imaging-guided management of meningiomas.[7,8]

The potential role of (^{68}Ga) DOTATATE PET/MR imaging in the characterization of WHO 3 meningiomas has not been previously studied. Here, we evaluate the clinical, pathologic, imaging characteristics, and outcomes of patients with WHO grade 3 meningiomas in our prospective observational cohort of patients with meningiomas undergoing (^{68}Ga) DOTATATE PET/MR imaging and evaluate the differences in PET findings between patients with de novo and those with secondary-progressive WHO grade 3 meningiomas.

MATERIALS AND METHODS

Patient Population

In this institutional review board at Weill Cornell Medicine–approved study, a total of 151 patients with clinically suspected or histologically proved meningiomas underwent (^{68}Ga) DOTATATE PET/MR imaging as part of a prospective observational study (ClinicalTrials.gov Identifier: NCT04081701). Exclusion criteria included contraindications to gadolinium-based contrast agents, a history of an allergic reaction to (^{68}Ga) DOTATATE, and pregnancy. Within this larger cohort, 14 patients were identified as having pathology-proved WHO grade 3 meningiomas and were included in our study. None of the patients met the exclusion criteria.

Clinical Annotation

Clinical chart review was performed to collect clinical and demographic characteristics of the patient population, including age, sex, surgical history, and RT history. PFS was determined from the date of the initial surgery with a diagnosis of malignant meningioma to the date of recurrence or progression by the Response Assessment in Neuro-Oncology (RANO; https://radiopaedia.org/articles/rano-criteria-for-glioma?lang=us) criteria on MR imaging, death, or last radiologic follow-up.[9]

Image Acquisition

PET/MR imaging was performed on a Biograph mMR scanner (Siemens) in all cases except in 1 patient who was scanned on the Signa PET/MR scanner (GE Healthcare). All PET data acquisitions started at a mean of 7 [SD, 3] minutes postinjection of 172.9 [SD, 18.4] MBq of (^{68}Ga) DOTATATE. The PET data were continuously acquired in 3D list-mode for a total of 50 minutes and then histogrammed to a single sinogram of a timeframe of 7–57 [SD, 3] minutes postinjection. The PET data were continuously

acquired in 3D list-mode for a total of 50 minutes and then histogrammed to a single sinogram of a timeframe of 7–57 [SD, 3] minutes postinjection.

All PET images were reconstructed with the default ordered subsets expectation maximization reconstruction algorithms of the manufacturer with point spread function modeling using 3 iterations and 21 (Biograph mMR) or 28 subsets (Signa). The resulting image matrix size was 344 × 344 × 127 (192 × 192 × 89) voxels with a voxel size of 2.086 × 2.086 × 2.031 mm (1.875 × 1.875 × 2.780) mm for Biograph mMR (Signa). During image reconstruction, the PET data were corrected for attenuation, scatter, randoms, normalization, dead time, decay, and frame duration using the default settings. For attenuation and scatter correction, the manufacturer's default method and settings for estimating the MR imaging–based brain tissue attenuation map were used.

MR imaging was performed according to institutional protocol, including pre- and postcontrast sagittal 3D T1 sampling perfection with application-optimized contrasts by using different flip angle evolution (SPACE; Siemens) (TR/TE, 600–700 ms/11–19 ms, 120° flip angle, 1-mm section thickness) and postcontrast 3D T2 FLAIR (TR/TE, 6300–8500 ms/394–446 ms, 120° flip angle, 1-mm section thickness). MR imaging–based attenuation correction was obtained according to the manufacturer's standard-of-care specifications. For patients who underwent PET/CT and MR imaging separately, the CT image set of PET/CT was subsequently registered to the postcontrast T1-weighted MR images using the rigid registration algorithm residing on a syngo.via workstation (Siemens), and the resulting transformation matrix was then applied to the PET image set to register it to the MR images.

Quantitative Image Analysis

All reconstructed PET images were initially displayed in quantitative units of becquerel/milliliter. Then the absolute maximum standard uptake value (SUV) metric was calculated at every image voxel by dividing the respective becquerel/milliliter pixel value by the ratio of the administered dose of the radiotracer in units of becquerel over the subject's body weight (in grams) to remove the confounding effect of radiotracer dose and body weight when quantifying the (^{68}Ga) DOTATATE uptake in every tissue. Regional absolute maximum SUV scores were subsequently extracted from a set of image pixels defining the VOIs in each PET image. Previous studies with (^{68}Ga) DOTATATE PET have demonstrated high sensitivity and specificity in measuring cellular *SSTR2* expression in the target regions with both absolute maximum SUV and SUV ratio (SUVR) normalized to the superior sagittal sinus (SSS).[10] If multiple (^{68}Ga) DOTATATE scans were available, the scan closest to the time of the initial surgery that diagnosed WHO grade 3 meningioma was used for analysis.

To standardize the comparison of lesion SUV across patients, we normalized the VOI-based lesion SUV to the SSS SUV (cranial blood pool). The VOIs were drawn for the target lesions, and maximum SUVs were reported as part of the routine clinical radiology report at our institution. The maximum SUV is referred to as SUV hereafter. The PET/MR imaging and PET/CT images were read by a fellowship-trained neuroradiologist with additional board certification in nuclear medicine. The images were interpreted for the clinical purpose of diagnosing suspected CNS *SSTR2*-positive tumors, and the radiologists had access to the full patient information at the time of study interpretation. The anatomic delineation of the VOIs in the PET images was based on the coregistered sagittal 3D T1-weighted postcontrast MR images with respective axial and coronal reformats, which were drawn to include the entire pituitary gland as visualized on postcontrast T1 imaging, as determined by the interpreting neuroradiologist.

Genomic and Molecular Pathology Characterization

Next-generation targeted sequencing was performed on surgically removed tumors in 11 of 14 patients using the Oncomine Comprehensive Assay. Of the 6 tumors analyzed from the secondary-progressive cohort, 1 sample was WHO grade 1, three samples were WHO grade 2, and 2 samples were WHO grade 3 at the time of genetic analysis. All 5 samples from the de novo cohort were WHO grade 3. The oncologic assay detects mutations in 99 genes, copy number variation in 49 genes, and fusion in 23 genes. *TERT* promoter mutations were not included in this panel. If multiple molecular pathology studies were obtained in an individual patient, only the most recent results were included for analysis.

Statistical Analysis

The Mann-Whitney test was performed to compare SUVs, surgical and radiation therapy history, and mutational burden of meningioma lesions of patients with de novo–versus–secondary-progressive tumor. PFS was analyzed by Kaplan-Meier curves, and comparisons between groups were performed using log-rank tests.

Ethics Approval and Consent to Participate

Institutional review board approval was obtained from the institutional review board committee of Weill Cornell Medicine for this Health Insurance Portability and Accountability Act–compliant study. All experimental protocols were approved by the Weill Cornell Medicine institutional review board committee. Informed consent was obtained from all subjects. All methods were carried out in accordance with relevant guidelines and regulations.

Consent for Publication

Consent to publish any individual data has been obtained as part of the informed consent process.

RESULTS

Patient Characteristics

Fourteen patients met the inclusion criteria. The mean age was 65.6 years (range, 43–81 years), and 7 of 14 were women (50%). The average follow-up time defined by time elapsed from initial surgery diagnosing WHO grade 3 meningioma to the latest neuroradiographic follow-up was 3.6 years (range, 0.3–11.5 years). All patients had surgical resection of their meningioma, 9 of 14 required ≥2 surgeries in total, and 13 of 14 patients (93%) had adjuvant RT. Twelve of 14 patients (86%) had progression or recurrence of disease by the RANO criteria applied on follow-up MR imaging examinations post-initial surgical resection.

Table 1: Comparison of demographics, surgical, and radiation history, PFS, molecular pathology, and SUV on (^{68}Ga) DOTATATE PET between patients with de novo–versus–secondary-progressive WHO grade 3 meningioma[a]

	De Novo WHO Grade 3	Secondary-Progressive WHO Grade 3	
No. of Patients	7	7	
Age (mean) (yr)	69.1 (range, 46–80)	62.6 (range, 43–81)	
Sex	28% female (2/7)	58% female (4/7)	$P = .59$
Median No. of distinct lesions	3	7	$P = .13$
Percentage of patients with extracranial metastasis	13% (1/7)	43% (3/7)	$P = .56$
Average total number of surgeries per patient	1.6	4.1 (2.3)	$P = .011$
Average total rounds of RT per patient	1.6	2.4 (1.1)	$P = .23$
Average total cumulative radiation dose per patient	68.3 Gy	106 Gy	$P = .31$
PFS (median)	37.7 mo	4.8 mo	$P = .004$
Recurrence or progression to date	71% (5/7)	100% (7/7)	$P = .46$
Average No. of genomic alterations per tumor	1.3 (range, 0–3)	3.6 (range, 1–6)	$P = .037$
Average maximum SUV of (^{68}Ga) DOTATATE	12.4 (range, 4.1–58.7)	17.1 (range, 4.7–99.4)	$P = .0021$

[a] For the secondary-progressive WHO grade 3 cohort, the number of surgical and radiation treatments reported reflects patients' entire clinical course, while the number in parentheses reflects treatment that occurred after degeneration into WHO grade 3.

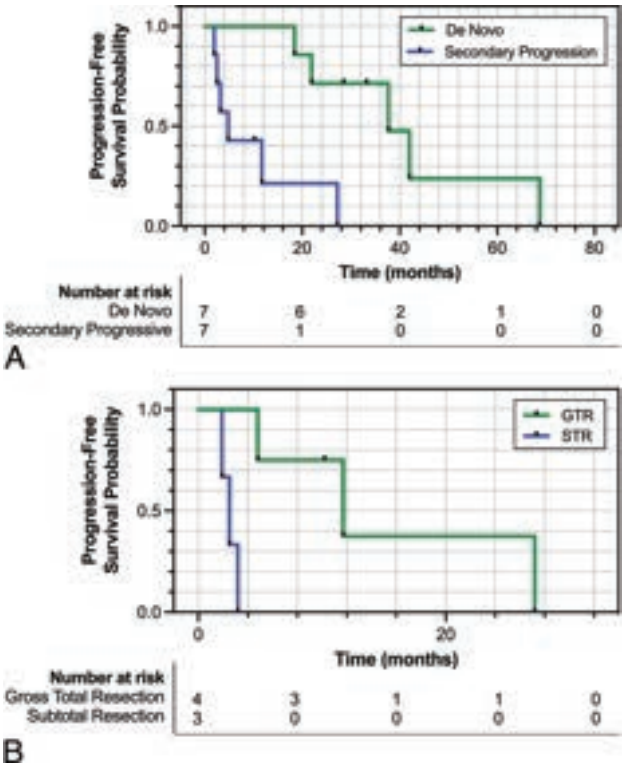

FIG 1. *A*, Kaplan-Meier curve comparing the PFS of patients with de novo (*green*) versus secondary-progressive (*blue*) WHO grade 3 meningioma. *B*, Kaplan-Meier curve comparing the PFS of patients with secondary-progressive WHO grade 3 meningioma who underwent GTR (*green*) versus subtotal resection (STR) (*blue*). PFS was determined using the RANO criteria on follow-up MR imaging post-initial surgery diagnosing WHO grade 3 meningioma.

When we compared de novo–versus–secondary-progressive disease cohorts, 7 patients (50%) were initially diagnosed with de novo WHO grade 3 meningiomas and 7 (50%) were initially diagnosed with either WHO grade 1 or 2 and secondarily progressed to WHO grade 3 meningioma. Within the secondary-progressive cohort, 2 patients had an initial diagnosis of WHO grade 1 meningioma, while 5 patients had an initial diagnosis of WHO grade 2 meningioma. Clinical and demographic characteristics of comparing the 2 cohorts are outlined in Table 1. The secondary-progressive cohort had a significantly higher per-patient number of surgeries (4.1 versus 1.6; $P = .011$) and a trend toward a higher number of RT courses (2.4 versus 1.6; $P = .23$) and a higher cumulative RT dose (106Gy versus 68.3Gy; $P = .31$) during their treatment course. Gross total resection (GTR), assessed by MR imaging following initial surgery diagnosing malignant meningioma, was achieved in 86% of patients in the de novo cohort versus only 57% in the secondary-progressive cohort ($P = .56$). The secondary-progressive cohort had a median of 7 individual lesions per patient compared with a median of 3 individual lesions per patient identified in the de novo cohort ($P = .13$). Extracranial metastasis of meningioma was observed in 3 of 7 patients in the secondary-progressive cohort versus 1 of 7 patients in the de novo cohort ($P = .56$), with metastasis sites most commonly found in the liver but also in the lung and bones. There was no statistically significant difference in age or sex between the 2 groups.

Clinical Outcomes

Patients in the secondary-progressive cohort had significantly lower PFS following a diagnosis of WHO grade 3 meningioma, with a median PFS of 4.8 months compared with 37.7 months observed in the de novo cohort ($P = .004$) (Fig 1*A*). Across the entire cohort, the median PFS was 20.1 months. Within the secondary-progressive cohort, those determined to have achieved GTR on postsurgical MR imaging had a significantly higher median PFS of 11.7 months compared with those with subtotal resection who had a median PFS of only 2.5 months ($P = .01$) (Fig 1*B*).

Genomic Analysis

Molecular pathology profiling was performed using the Oncomine Comprehensive Assay across 5 samples in the de novo cohort as well as 6 samples from the secondary-progressive cohort. Notably, the 6 samples from the secondary-progressive cohort included 1 sample that was WHO grade 1, two samples that were WHO grade 2, and 3 samples that were WHO grade 3 at the time of genetic analysis. Despite undergoing molecular pathology profiling at lower grades, the secondary-progressive tumors exhibited a distinct molecular profile with a statistically significant higher number of mutations overall at 3.5-versus-1.2 mutations identified per tumor

in the de novo cohort ($P = .024$) (Fig 2). The secondary-progressive malignant meningiomas were also found to have significantly higher clinically significant mutations (Table 2). Mutations identified by the Oncomine Comprehensive Assay were stratified into either pathogenic or variants of uncertain significance. When the specific mutations were stratified by clinical significance, the de novo cohort had mutations that were 33% pathogenic and 67% of unknown significance, whereas the secondary-progressive malignant meningiomas exhibited mutations that were 72% pathogenic and 28% of unknown significance (Table 2). Across the cohort, the most common mutations were in *NF2* followed by *CDKN2A* and *TP53*.

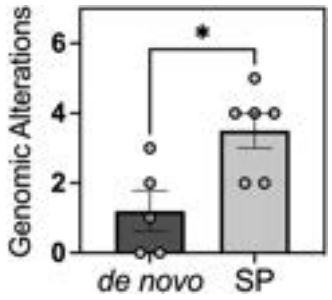

FIG 2. Comparison of the number of genomic alternations per tumor between de novo versus secondary-progressive (SP) WHO grade 3 meningiomas. The Mann-Whitney test was performed to test statistical significance. A *single asterisk* indicates *P* value $< .05$.

Descriptive and Correlative Analysis of SUV

Across all lesions, the mean SUV was 15.8. (^{68}Ga) DOTATATE PET demonstrated significantly higher SUVs in secondary-progressive tumors, with a mean SUV of 17.1 compared with 12.4 in the de novo group ($P = .0021$) (Fig 3). Similarly, the SUV ratio relative to the SSS tended to be higher in the secondary-progressive cohort; however, this difference did not reach statistical significance (SUVR of 14.8 versus 11.5, $P = .31$). Pituitary gland SUVs were not significantly different between the 2 groups (pituitary SUV of 16.3 versus 15.3 in the secondary-progressive and de novo cohorts, respectively; $P = .63$). SUV_SSS were not statistically

Table 2: Summary of molecular pathology profiling through the Oncomine Comprehensive Assay across 5 samples in the de novo cohort as well as 6 samples from secondary-progressive cohort[a]

De Novo (D.N.)/Secondary Progressive (S.P.)	Pathogenic Variants	Variants of Unknown Significance	WHO Grade at Time of Analysis
S.P.	1) *CDKN2A* loss 2) *CDKN2B* loss 3) *FANCG* splice site deletion 4) *MTAP* loss 5) *TP53 V31L*	–	3
S.P.	1) *ARID1* frameshift alteration 2) *FBXW7* frameshift deletion	1) *TSC2* in frame insertion 2) *CDH1* missense	3
S.P.	1) *NF2* nonsense 2) *CDKN2A* deletion	–	3
S.P.	1) MSH2 nonsense 2) *TP53* nonsense 3) *PTEN* frameshift deletion 4) *GNAS* missense	–	2
S.P.	–	1) *PIK3R1* missense 2) *TSC1* missense 3) *NOTCH1* missense 4) *NF2* missense	2
S.P.	1) *NF2* splice site 2) *CDKN2A* deletion	–	1
D.N.	1) *BRCA2* frameshift deletion 2) *NF2* nonsense	1) *BRCA2* missense	3
D.N.	–	1) *CCND1* amplification 2) *RPS6KB1* amplification	3
D.N.	–	1) *ATM* missense	3
D.N.	–	–	3
D.N.	–	–	3

Note:—The en dash indicates no mutations found.

[a] Notably, the 6 samples from the secondary-progressive cohort included 1 sample that was WHO grade 1, two samples that were WHO grade 2, and 3 samples that were WHO grade 3 at the time of genetic analysis. Mutations were stratified by clinical significance and categorized as either pathogenic or variants of unknown significance. *TERT* promoter mutations were not included in this panel.

different between the 2 cohorts, with SUV_SSS of 1.1 and 1.4 in the de novo and secondary-progressive cohorts, respectively ($P = .17$). Representative patient images from each cohort are shown in Fig 4.

DISCUSSION

While meningiomas overall are the most common primary brain tumor, WHO grade 3 meningiomas are rare and thus understudied, with only around 300 cases of WHO grade 3 meningiomas diagnosed annually in the United States, limiting our understanding of the natural history as well as the optimal diagnostic and therapeutic management.[11] While patients with WHO grade 3 meningiomas are typically treated with maximal surgical resection and RT, clinical outcomes are poor, with recurrence rates of 50%–90% by 5 years after surgery and a 5-year overall survival rate of 20%–50%.[1-3] Given their high morbidity and mortality rates, it is critical to optimize the diagnostic and therapeutic management of WHO grade 3 meningiomas.

Whether WHO grade 3 meningiomas arise de novo or from secondary progression has also proved to have important prognostic implications. Approximately one-half of all WHO grade 3 meningiomas are diagnosed de novo, while the other half arise from secondary progression of a previously diagnosed lower histologic grade. In our study, patients with secondary-progressive WHO grade 3 meningiomas had markedly decreased PFS compared with the de novo cohort, consistent with previous findings from other studies.[2,4] The exact mechanism underlying this observation is not yet clearly understood, though 1 explanation may lie in the differences in molecular pathology.

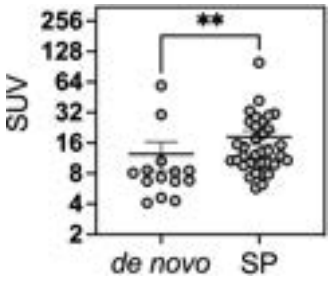

FIG 3. SUV on (^{68}Ga) DOTATATE PET/MR of de novo–versus–secondary-progressive (SP) WHO grade 3 meningioma lesions. The Mann-Whitney test was performed to test the statistical significance. *Double asterisks* indicate *P* value < .01.

Although it is known that higher-grade meningiomas have greater rates of genetic mutations, we found that even within WHO grade 3 meningiomas, those that progressed from lower-grade tumors compared with de novo cases had a distinct molecular profile with higher rates of genetic mutations overall and in specific genes such as *NF2* and *CDKN2A/B*, which have been known to be implicated in more aggressive disease reported in the literature.[12] Our genetic data were collected through the Oncomine Comprehensive Assay, which is a targeted next-generation sequencing assay that tests a panel of genes with known oncologic implications, but it notably did not include *TERT* promoter mutations. For the secondary-progressive cohort, genomic data were available from 6 patients; however, some samples were analyzed before dedifferentiation to WHO grade 3, with 1 sample being WHO grade 1 and 2 samples being WHO grade 2 at the time of molecular testing. Nevertheless, the secondary-progressive cohort still had a greater mutational burden both in number and clinical relevance compared with the de novo cohort. This finding may help to explain the more aggressive clinical course of secondary-progressive WHO grade 3 meningiomas, arguing that de novo–versus–secondary-progressive status may be an important prognostic factor for WHO grade 3 meningiomas, and they may even be considered 2 distinct clinical entities moving forward.

MR imaging, the criterion standard for meningioma surveillance, has significant limitations such as distinguishing recurrent or residual disease from postoperative findings, and there has been a marked unmet need for more targeted imaging strategies, especially in intermediate- and high-risk tumors.[6] More recently, (^{68}Ga) DOTATATE PET has demonstrated high utility in meningioma evaluation, including diagnostic confirmation, surgical planning, delineation of radiation therapy target volumes, and post-treatment surveillance.[7] Although the utility of (^{68}Ga) DOTATATE PET/MR has been shown in meningioma diagnosis and treatment-planning, its role has not previously been systematically investigated in patients with WHO grade 3 meningioma, in part due to limited sample sizes. This is the first study evaluating the clinical characteristics and utility of (^{68}Ga) DOTATATE PET/MR imaging in a cohort of patients with exclusively WHO grade 3 meningioma and comparing secondary-progressive and de novo cohorts. Just as seen previously with WHO grades 1 and 2 meningiomas, (^{68}Ga) DOTATATE PET is very useful in distinguishing recurrent or residual disease from postoperative findings in WHO grade 3 meningioma compared with evaluation on MR imaging alone. For

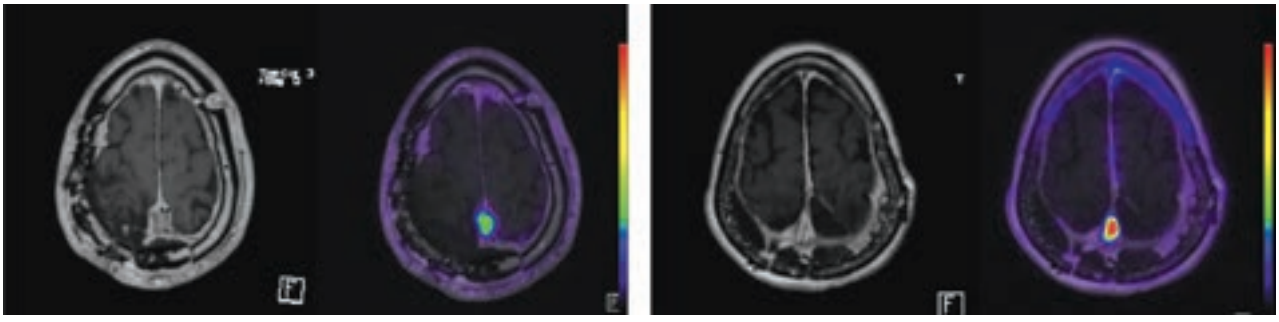

FIG 4. Representative cases of DOTATATE-PET/MR imaging and corresponding T1-weighted postcontrast images of a patient with de novo WHO grade 3 meningioma (*left*) and a patient with secondary-progressive WHO 3 meningioma (*right*).

instance, 1 patient with surgical resection of WHO grade 3 meningioma was thought to have achieved GTR on postsurgical MR imaging with questionable residual disease versus postoperative changes but then later was found to have had definitive residual disease and subtotal resection on (^{68}Ga) DOTATATE PET.

Previously, (^{68}Ga) DOTATATE has been routinely used in the evaluation of gastroenteropancreatic neuroendocrine tumors years before it was used in meningioma management. For gastroenteropancreatic neuroendocrine neoplasms, the sensitivity of (^{68}Ga) DOTATATE decreases with an increased grade of the tumor, possibly due to downregulation of *SSTR2* with increasing tumor grade.[13] A similar mechanism in meningiomas could be hypothesized; however, we found that on the contrary, (^{68}Ga) DOTATATE PET SUV was significantly higher in secondary-progressive WHO grade 3 tumors compared with de novo tumors, despite the secondary-progressive tumors having significantly higher rates of genetic mutations. Our findings suggest that downregulation of *SSTR2* does not occur with an increase in WHO grade in meningiomas, with the possibility that the receptor may be upregulated. Thus, (^{68}Ga) DOTATATE remains a clinically useful approach in meningiomas regardless of WHO grade.

At present, determining meningioma grade is not possible on the basis of neuroimaging alone. Our findings suggest the possibility of noninvasively differentiating secondary-progressive from de novo WHO grade 3 meningiomas using (^{68}Ga) DOTATATE PET/MR imaging, which has high clinical relevance, given the known difference in prognosis between the 2 groups previously shown by other authors and confirmed in our study.

Additionally, this work raises important questions regarding the role of *SSTR2* in meningioma biology. *SSTR2* downstream signaling is implicated in a diverse range of physiologic processes such as the secretion of insulin and glucagon, thyroid-stimulating hormone and growth, and neuronal excitability.[14-16] However, the role of *SSTR2* in meningioma biology and the correlation between *SSTR2* expression and clinical outcomes remain to be determined prospectively. In immunohistochemical studies, no correlation between *SSTR2* expression and tumor grade was found; however, there was a positive correlation with higher microvessel density.[17,18] Clinically, higher *SSTR2* expression was correlated with a higher risk of recurrence after surgical resection.[18,19] Notably, higher *SSTR2* expression was correlated with improved PFS following somatostatin-receptor (*SSTR*)-targeted radionuclide therapy, which may be due to higher binding of the *SSTR*-targeted theragnostic agent and thus higher treatment effectiveness.[18,19]

Taken together, it is still unclear whether *SSTR2* expression is related to tumor grade or prognosis. Our data suggest that secondary-progressive WHO grade 3 meningiomas have an elevated (^{68}Ga) DOTATATE SUV compared with de novo disease, suggesting a link between elevated *SSTR2* expression and worsened clinical outcomes, though formal immunohistochemical studies have yet to be performed. Notably, in a study encompassing all WHO grade meningiomas, a higher DOTATATE PET SUV was associated with a higher tumor growth rate,[20] which is concordant with our WHO grade 3–specific findings, with higher SUVs reflecting worsened PFS. However, in our study, we were unable to directly correlate tumor SUV and PFS due to the small sample size. In another study, there was a strong correlation between tumor vascularity and *SSTR2* expression in WHO grades 2 and 3 but not grade 1 meningiomas, suggesting that *SSTR2* may play a role in tumor vascularity in higher-grade tumors.[21]

SSTR2 expression in meningiomas has also emerged as a potential therapeutic target. *SSTR2*-directed peptide receptor radionuclide therapy with β-emitters 90 yttrium (^{90}Y) and 177 lutetium (^{177}Lu) has shown promise in the treatment of unresectable or refractory meningiomas.[22,23] Other systemic treatment options have emerged such as dacarbazine and adriamycin, hydroxyurea, temozolomide, and irinotecan, but their efficacy has not yet been shown in clinical trials.[24] While rare, *SSTR2*-negative meningioma has been reported in the literature and is an important additional indication of a lack of direct correlation between *SSTR2* expression and WHO grade.[25] *SSTR2*-targeted therapeutic effort may be beneficial in WHO grade 3 meningiomas, possibly more so in the secondary-progressive cohort, which may be expressing higher levels of *SSTR2*.

One significant limitation of this study is the determination of de novo disease, because it is possible that tumors arose from lower-grade meningiomas but were only first diagnosed with pathology once the tumor had already progressed to WHO grade 3 disease. Although this limitation may be an unavoidable confounder in the original categorization of WHO grade 3 meningiomas as either being de novo or secondary-progressive, our data suggest that regardless of de novo–versus–secondary-progressive status, those with a higher SUV, on average, had shortened PFS following surgical resection. This finding suggests that in WHO grade 3 meningiomas, SUV alone could be predictive of worse prognosis and thus guide clinical decision-making. Another limitation to our study is the small sample size; however, due to the low incidence of the disease, this has been the case in all other published studies and remains a bottleneck in our effort to fully understand the natural history and optimal management of WHO grade 3 meningiomas. Nevertheless, our study remains the first to investigate a cohort of WHO grade 3 meningiomas with (^{68}Ga) DOTATATE PET/MR imaging and thus has the potential to increase our understanding of this rare entity, thereby improving clinical outcomes.

CONCLUSIONS

This is the first study evaluating the clinical characteristics and utility of (^{68}Ga) DOTATATE PET/MR imaging in a cohort of patients with WHO grade 3 meningiomas and comparing secondary-progressive and de novo WHO grade 3 tumors. We found that compared with the de novo group, the secondary-progressive cohort demonstrated worsened clinical outcomes, including significantly decreased PFS, in accordance with previous studies. In addition to distinct molecular profiles with higher mutational burden, we also report significantly increased SUVs in secondary-progressive compared with de novo WHO grade 3 meningiomas. This work further supports (^{68}Ga) DOTATATE PET/MR imaging as a useful management strategy in WHO grade 3 meningiomas and raises the possibility of differentiating secondary-progressive and de novo malignant meningiomas with PET/MR imaging in the clinical context. This work raises important questions regarding meningioma biology such as the potential role of *SSTR2* signaling in WHO grade 3 meningiomas, which may represent a potential therapeutic target in future clinical trials.

ACKNOWLEDGMENTS

We thank the patients and their families for their contributions to the study and especially Ms Alexis Watson and Ms Eileen Chang for their help with research coordination and administrative support.

Disclosure forms provided by the authors are available with the full text and PDF of this article at www.ajnr.org.

REFERENCES

1. Ostrom QT, Gittleman H, Liao P, et al. **CBTRUS Statistical Report: primary brain and other central nervous system tumors diagnosed in the United States in 2010-2014.** *Neuro Oncol* 2017;19:v1–88 CrossRef Medline
2. Tian W, Liu J, Zhao K, et al. **Analysis of prognostic factors of World Health Organization grade III meningiomas.** *Front Oncol* 2020; 10:593073 CrossRef Medline
3. Durand A, Labrousse F, Jouvet A, et al. **WHO grade II and III meningiomas: a study of prognostic factors.** *J Neurooncol* 2009;95:367–75 CrossRef Medline
4. Masalha W, Heiland DH, Delev D, et al. **Survival and prognostic predictors of anaplastic meningiomas.** *World Neurosurg* 2019;131: e321–28 CrossRef Medline
5. Harter PN, Braun Y, Plate KH. **Classification of meningiomas-advances and controversies.** *Chin Clin Oncol* 2017;6(Suppl 1):S2 CrossRef Medline
6. Kunz WG, Jungblut LM, Kazmierczak PM, et al. **Improved detection of transosseous meningiomas using 68 Ga-DOTATATE PET/CT compared with contrast-enhanced MRI.** *J Nucl Med* 2017;58:1580–87 CrossRef Medline
7. Ivanidze J, Roytman M, Lin E, et al. **Gallium-68 DOTATATE PET in the evaluation of intracranial meningiomas.** *J Neuroimaging* 2019;29:650–56 CrossRef Medline
8. Mizutani G, Nakanishi Y, Watanabe N, et al. **Expression of somatostatin receptor (SSTR) subtypes (SSTR-1, 2A, 3, 4 and 5) in neuroendocrine tumors using real-time RT-PCR method and immunohistochemistry.** *Acta Histochem Cytochem* 2012;45:167–76 CrossRef Medline
9. Huang RY, Bi WL, Weller M, et al. **Proposed response assessment and endpoints for meningioma clinical trials: report from the Response Assessment in Neuro-Oncology Working Group.** *Neuro Oncol* 2019;21:26–36 CrossRef Medline
10. Kim SH, Roytman M, Madera G, et al. **Evaluating diagnostic accuracy and determining optimal diagnostic thresholds of different approaches to [68Ga]-DOTATATE PET/MRI analysis in patients with meningioma.** *Sci Rep* 2022;12:9256 CrossRef Medline
11. Hoffman S, Propp JM, McCarthy BJ. **Temporal trends in incidence of primary brain tumors in the United States, 1985-1999.** *Neuro Oncol* 2006;8:27–37 CrossRef Medline
12. Okano A, Miyawaki S, Teranishi Y, et al. **Advances in molecular biological and translational studies in World Health Organization grades 2 and 3 meningiomas: a literature review.** *Neurol Med Chir (Tokyo)* 2022;62:347–60 CrossRef
13. Zhang P, Yu J, Li J, et al. **Clinical and prognostic value of PET/CT imaging with combination of 68 Ga-DOTATATE and 18 F-FDG in gastroenteropancreatic neuroendocrine neoplasms.** *Contrast Media Mol Imaging* 2018;2018:2340389 CrossRef Medline
14. Günther T, Tulipano G, Dournaud P, et al. **International union of basic and clinical pharmacology. CV. Somatostatin receptors: structure, function, ligands, and new nomenclature**. *Pharmacol Rev* 2018;70:763–835 CrossRef Medline
15. Vasilaki A, Thermos K. **Somatostatin analogues as therapeutics in retinal disease.** *Pharmacol Ther* 2009;122:324–33 CrossRef Medline
16. Bassant MH, Simon A, Poindessous-Jazat F, et al. **Medial septal GABAergic neurons express the somatostatin sst2A receptor: functional consequences on unit firing and hippocampal theta.** *J Neurosci* 2005;25:2032–41 CrossRef Medline
17. Barresi V, Alafaci C, Salpietro F, et al. **Sstr2A immunohistochemical expression in human meningiomas: is there a correlation with the histological grade, proliferation or microvessel density?** *Oncol Rep* 2008;20:485–92 Medline
18. de Oliveira Silva CB, Ongaratti BR, Trott G, et al. **Expression of somatostatin receptors (SSTR1-SSTR5) in meningiomas and its clinicopathological significance.** *Int J Clin Exp Pathol* 2015;8:13185–92 Medline
19. Seystahl K, Stoecklein V, Schüller U, et al. **Somatostatin receptor-targeted radionuclide therapy for progressive meningioma: benefit linked to 68Ga-DOTATATE/-TOC uptake**. *Neuro Oncol* 2016;18:1538–47 CrossRef Medline
20. Sommerauer M, Burkhardt JK, Frontzek K, et al. **68 Gallium-DOTATATE PET in meningioma: a reliable predictor of tumor growth rate?** *Neuro Oncol* 2016;18:1021–27 CrossRef Medline
21. Roytman M, Kim S, Glynn S, et al. **PET/MR imaging of somatostatin receptor expression and tumor vascularity in meningioma: implications for pathophysiology and tumor outcomes.** *Front Oncol* 2021;11:820287 CrossRef Medline
22. Laudicella R, Albano D, Annunziata S, et al. **Theragnostic use of radiolabelled dota-peptides in meningioma: from clinical demand to future applications.** *Cancers (Basel)* 2019;11:1412 CrossRef Medline
23. Van Essen M, Kenning EP, Kooij PP, et al. **Effects of therapy with [177 Lu-DOTA 0, Tyr 3] octreotate in patients with paraganglioma, meningioma, small cell lung carcinoma, and melanoma.** *J Nucl Med* 2006;47:1599–606 Medline
24. Moazzam AA, Wagle N, Zada G. **Recent developments in chemotherapy for meningiomas: a review.** *Neurosurg Focus* 2013;35:E18 CrossRef Medline
25. Roytman M, Pisapia DJ, Liechty B, et al. **Somatostatin receptor-2 negative meningioma: pathologic correlation and imaging implications.** *Clin Imaging* 2020;66:18–22 CrossRef Medline

Optimization of [^{18}F]-FDOPA Brain PET Acquisition Times for Assessment of Parkinsonism in the Clinical Setting

Graham Keir, Faizullah Mashriqi, Christopher Caravella, Sean A.P. Clouston, Josephine N. Rini, and Ana M. Franceschi

ABSTRACT

BACKGROUND AND PURPOSE: Fluorine 18-fluoro-L-dopa ([^{18}F]-FDOPA) was approved by the FDA in 2019 and reimbursed by the Centers for Medicare & Medicaid Services in 2022 for use with PET to visualize dopaminergic nerve terminals in the striatum for evaluation of parkinsonism. We sought to determine the optimal image acquisition time for [^{18}F]-FDOPA PET by evaluating rater-estimated FDOPA positivity and image quality across 4 time points.

MATERIALS AND METHODS: Brain PET/CT was acquired 90 minutes following injection of 185 megabecquerel (5 mCi) of [^{18}F]-FDOPA. PET was acquired in list mode for 20 minutes, and data were replayed to represent 15-, 10-, and 5-minute acquisitions. By means of MIMneuro, PET/MR imaging or PET/CT was independently graded for FDOPA positivity and image quality by 2 readers, blinded to the clinical report and diagnosis. Expert neuroradiologist clinical reads were used as the criterion standard.

RESULTS: Twenty patients were included, average age 65.6 years, 55% women. Image-quality ratings decreased with shorter acquisition times for both readers (reader 1, $\rho = 0.23$, $P = .044$; reader 2, $\rho = 0.24$, $P = .036$), but there was no association between abnormality confidence scores and acquisition time (reader 1, $\rho = -0.13$, $P = .250$; reader 2, $\rho = -0.19$, $P = .100$). There was a high degree of consistency in intra- and interrater agreement and agreement with the expert reads when using acquisition times of ≥10 minutes (maximal confidence score consistency [$\rho = 0.92$] and interrater agreement [$\kappa = 0.90$] were observed at 15 minutes), while image quality was consistently rated as low and FDOPA positivity ratings were inconsistent when using a 5-minute acquisition time.

CONCLUSIONS: Our study suggests that image-quality ratings were stable after 15 minutes and that between-subject abnormality detection rates were highly consistent between the 2 readers when acquired for at least 10 and up to 20 minutes but were inconsistent at 5 minutes. Shorter [^{18}F]-FDOPA PET acquisition times may help maximize patient comfort while increasing throughput in the clinical setting.

ABBREVIATIONS: AADC = aromatic amino acid decarboxylase; AC = attenuation-corrected; DaT = dopamine transporter; PD = Parksinson disease; PS = parkinsonian syndromes

Parkinsonian syndromes (PS) are a heterogeneous group of disorders that present with motor symptoms that are mostly ascribed to idiopathic Parkinson disease (PD). This group includes PD as well as atypical PS such as multiple system atrophy, progressive supranuclear palsy, dementia with Lewy bodies, and corticobasal degeneration. PS are distinguished from other causes of parkinsonism (essential tremor, drug-induced parkinsonism, and vascular parkinsonism) by the presence of nigrostriatal degeneration. This distinction is crucial to initiate the appropriate therapy and prevent the possible harmful effects of unsupported levodopa therapy when the symptoms mimic PD but are not neurodegenerative. Functional imaging with dopamine ligands can aid with this distinction by targeting either the presynaptic or postsynaptic dopaminergic system.[1]

Several radiotracers are currently used for presynaptic dopaminergic molecular imaging, with the most common being radiopharmaceuticals N-3-fluoropropyl-2-(R)- carboxymethoxy-3-(R)-(4-[iodine 123] iodophenyl) nortropane ([^{123}I FP-CIT, dopamine transporter scan [DaTscan]) and 3,4-dihydroxy-6-[fluorine 18

Received November 7, 2023; accepted after revision January 25, 2024.

From the Neuroradiology Division (G.K., F.M., A.M.F.), Department of Radiology, Donald and Barbara Zucker School of Medicine at Hofstra/Northwell, Lenox Hill Hospital, New York, New York; Nuclear Medicine Division (C.C., J.N.R.), Department of Radiology, Donald and Barbara Zucker School of Medicine at Hofstra/Northwell, Manhasset, New York; and Department of Family, Population and Preventive Medicine (S.A.P.C.), Renaissance School of Medicine at Stony Brook University, Stony Brook, New York.

Please address correspondence to Ana M. Franceschi, MD, PhD, Department of Radiology, Lenox Hill Hospital, 100 East 77th St, 3rd Floor, New York, NY, 10075; e-mail: afranceschi@northwell.edu; @AFrances_MDPhD

Indicates article with online supplemental data.

http://dx.doi.org/10.3174/ajnr.A8207

Table 1: [^{18}F]-FDOPA brain PET/CT protocol[a]

CT Parameters		PET Parameters	
Kilovolt (peak)	120	Acquisition (1-bed)	20-Min static acquired in list mode
Max mA (auto mA off)	95	Reconstruction	VUE Point FX[b]
Noise index	NA	Matrix	192 × 192
CT section thickness (mm)	3.75	Iterations	2
Rotation (sec)	0.8	Subsets	32
Pitch (mm/rot)	1.375	Z-axis filter	Heavy
FOV (cm)	50	Postfilter (mm, FWHM)	4
		FOV (cm)	30

Note:—Max indicates maximum; FWHM, full width at half maximum; rot, rotation; NA, not applicable; mA, milliamperê.
[a] Discovery 710HD scanner.
[b] GE Healthcare.

fluoro-L-dopa ([^{18}F]-FDOPA).[2] [^{18}F]-FDOPA is a radiolabeled analog of L-DOPA used to image metabolic abnormalities of presynaptic DaTs and L-type amino acid transporters and may be used for the assessment of PS.[3] Tracer accumulation in the striatum corresponds to the level of radiotracer uptake into the presynaptic nerve terminal, dopa-decarboxylase (aromatic amino acid decarboxylase [AADC]) activity, and vesicular storage in the presynaptic dopaminergic neurons.[4,5] Studies have demonstrated that the uptake of [^{18}F]-FDOPA in the basal ganglia is reduced in PD,[6] thereby facilitating the differentiation between PS and nonneurodegenerative causes of parkinsonism. Characteristic findings in patients with PD include asymmetric reduction of [^{18}F]-FDOPA uptake in the striatum, with greater reductions typically noted contralateral to the clinically more-affected side.[7,8] In addition, radiopharmaceutical binding is lowest in the posterior putamen compared with the anterior putamen and caudate nucleus, which is referred to as the rostrocaudal gradient of FDOPA uptake.[9,10] Reductions in [^{18}F]-FDOPA uptake have consistently been shown to best correlate with disease severity and clinical bradykinesia scores, while the correlation with tremor, rigidity, and postural disturbance is less significant.[11-15]

[^{18}F]-FDOPA has been FDA-approved to visualize dopaminergic nerve terminals in the striatum for the evaluation of adult patients with suspected PS since 2019 and received Centers for Medicare & Medicaid Services payment approval in late 2022.[16,17] Our current institutional protocol for [^{18}F]-FDOPA brain PET is in accordance with the FDA prescribing guidelines[18] and includes list mode acquisition for 20 minutes, though acquisition times for PET vary depending on scanner sensitivity and administered dose. Notably, the highest uptake of the radiotracer in the striatum is approximately 90 minutes postinjection of [^{18}F]-FDOPA.[19,20] Using dynamic acquisitions, we noted anecdotally that the clarity of the images might imply that a shorter acquisition time could be sufficient for the assessment of nigrostriatal dysfunction in the clinical setting. There are several potential benefits to a shorter acquisition time. First, patients with parkinsonism often have trouble lying still in the scanner for long periods owing to tremors or other movement disorders or cognitive impairments, so a shorter PET scan duration may improve patient comfort and reduce motion artifacts. Additionally, shorter acquisition times could allow increased throughput of patients, enabling greater access and allowing more patients the opportunity to be evaluated by this emerging technique. Therefore, we sought to determine the optimal image acquisition time for [^{18}F]-FDOPA brain PET by evaluating reader confidence and image quality across 4 acquisition periods.

MATERIALS AND METHODS

We started our clinical FDOPA PET imaging service in November 2022, and the first 20 patients imaged at our institution were selected for this study. Patients were instructed to withhold PD medications, if applicable, for 12 hours before the PET scan, and followed a low-protein diet beginning in the evening before the examination, with nothing by mouth except for water for 4 hours before the examination. All subjects were pretreated with carbidopa, 150 mg, approximately 1 hour before IV injection of 185-megabecquerel [5-mCi] [^{18}F]-FDOPA. Brain PET/CT was acquired on a Discovery 710HD scanner (GE Healthcare) 90 minutes following injection in list mode for 20 minutes and reconstructed according to the standard institutional protocol (Table 1). Following each 20-minute acquisition, data were reconstructed to represent 15-, 10-, and 5-minute acquisition times.

Following Northwell institutional review board approval, the attenuation-corrected (AC) PET data across 4 time points were anonymized, and all indicators of acquisition time were removed, as were the CT and separately acquired brain MR imaging studies for each subject. These anonymized studies were then analyzed by 2 readers, blinded to the clinical report and final diagnosis. These 2 readers were the same for every patient and consisted of senior residents in diagnostic radiology with clinical experience reading DaTscans. Both readers participated in multiple training sessions for FDOPA PET interpretation using MIMNeuro software (Version 7.3.2; MIM Software) before study commencement. By means of MIMneuro, findings of [^{18}F]-FDOPA PET/MR imaging or PET/CT (if MR imaging was unavailable) were independently graded for reader confidence on the likely FDOPA positivity of an image using a 5-point scale (0 = definitely normal, 1 = probably normal, 2 = equivocal, 3 = probably abnormal, 4 = definitely abnormal). For analyses of inter- and intrarater agreement and when comparing scores with the expert rater, confidence scores were dichotomized to indicate the presence/absence of abnormal findings using a cutoff of ≥3 (probably abnormal). Image quality was graded on a 3-point scale (1 = poor quality, 2 = acceptable, 3 = excellent); poor-quality images were those rated as 1 in this scale.

Expert clinical reads by a board-certified fellowship-trained neuroradiologist with an MD/PhD and 10 years of brain PET/MR imaging clinical and research experience were used as the criterion standard.

Statistical Analysis

Sample characteristics were described using means (SDs) or percentages if appropriate and stratified by neuroradiology expert reads (Tables 2 and 3). Nonparametric trend tests were used to determine whether demographic characteristics, image quality,

and abnormality confidence scores varied by FDOPA abnormality. Next, intraindividual consistency was measured using the Spearman rank-order correlation within individuals to determine the extent to which FDOPA images were rated consistently in terms of confidence of abnormal findings and image quality across scanning parameters. Because the Spearman ρ may be biased in cases in which rankings remain stable though average scores differ, the Cohen κ was also used to examine the presence/absence of abnormal imaging findings for all rater times and when comparing raters and the neuroradiologist's expert reads. To visually differentiate these measures, we used a different cell color (red, green, and blue) to differentiate the test type; then darker hues of each color were used to indicate stronger associations (Table 4). Two-tailed t tests were used to examine the statistical significance of the Spearman ρ and Cohen κ in all tests. Because of the large number of comparisons and the small sample size made up of relatively unique patients, statistical significance in the final analyses was reported in 2 ways. Bold italicized typeface was used to report statistically significant results that passed the false discovery rate (0.05). Supplemental analyses were completed to examine image-quality ratings using χ^2 tests to estimate the impact of acquisition time on the raters' ratings of image quality. However, while we did attempt to account for image-quality rankings when considering positivity scores, due to the small sample size, these efforts were unsuccessful in most cases and these analyses are not presented. Analyses were completed by using STATA 17/MP (StataCorp).

Table 2: Demographic characteristics for subjects ($n = 20$) stratified by neuroradiologist expert read results at the standard 20-minute acquisition time

Characteristic	Whole Sample ($n = 20$)	Expert Rated Scan Findings as Abnormal ($n = 10$)	Expert Rated Scan Findings as Normal ($n = 10$)	*P* Value
Age (yr)	65.6 (14.9)	62.8 (17.4)	68.4 (12.3)	.402
Female (%)	55.0	40.0	70.0	.189
Clinical history				
Tremor in hand/leg (%)	60.0	70.0	50.0	.361
PD (%)	15.0	30.0	0.0	.060
Right unilateral (%)	10.0	10.0	10.0	1.000
Left unilateral (%)	20.0	30.0	10.0	.264
Bilateral (%)	20.0	20.0	20.0	1.000
Bradykinesia (%)	25.0	50.0	0.0	.010

Table 3: Reader confidence and image quality scores stratified by neuroradiologist expert read results at the standard 20-minute acquisition time[a]

	Whole Sample ($n = 20$)	Expert Rated Scan Findings as Abnormal ($n = 10$)	Expert Rated as Scan Findings as Normal ($n = 10$)	*P* Value
Confidence score (mins)				
20	1.6 (1.4)	2.9 (0.8)	0.4 (0.5)	<.001
15	1.8 (1.4)	3 (0.7)	0.6 (0.5)	<.001
10	2 (1.5)	3.3 (0.7)	0.7 (0.9)	<.001
5	2.2 (1.3)	3 (0.9)	1.4 (1)	.001
Image quality (mins)				
20	2.2 (0.7)	1.8 (0.7)	2.6 (0.6)	.003
15	2.2 (0.8)	1.8 (0.7)	2.6 (0.6)	.004
10	2 (0.9)	1.6 (0.7)	2.5 (0.8)	.006
5	1.7 (0.8)	1.3 (0.5)	2.2 (0.9)	.009

[a] No differences between scans with abnormal and normal findings were statistically significant as determined using nonparametric trend tests.

Table 4: Measures of image-rating agreement and consistency across the 2 raters and the expert neuroradiologist read using different acquisition times[a]

		First Rater				Second Rater			
Rater	Minutes	20	15	10	5	20	15	10	5
First rater	20	0.79	0.79	0.89	0.79	0.56	0.89	0.61	0.22
	15	0.89	0.99	0.90	1.00	0.79	0.90	0.80	0.41
	10	0.93	0.93	0.80	0.90	0.68	0.79	0.71	0.31
	5	0.84	0.85	0.84	0.90	0.79	0.90	0.80	0.41
Second rater	20	0.84	0.80	0.83	0.88	0.70	0.68	0.61	0.22
	15	0.87	0.92	0.87	0.83	0.84	0.80	0.71	0.31
	10	0.81	0.87	0.83	0.77	0.82	0.83	0.90	0.39
	5	0.55	0.44	0.55	0.53	0.54	0.45	0.64	0.50

[a] Rank order agreement is shown in blue; intra-/interrater agreement across image ratings is shown in green. The correspondence of confidence scores to the expert neuroradiologist read completed at a standard 20-minute acquisition time is shown in shades of red across the diagonal. The strength of the association is reported by color gradations. Statistically significant associations evident after adjusting for the false discovery rate are shown in bold italicized typeface. The optimal cutoff for rater 1 compared with the expert rating included scans rated as equivocal, while the optimal cutoff for rater 2 compared with expert raters included only those with a probable abnormal finding and above.

RESULTS

Demographic and clinical characteristics for $n = 20$ subjects included in the study are depicted in Tables 2 and 3. The patients had an average age of 65.6 years, and 55% were women. No differences were evident in demographic characteristics between groups, but the confidence and quality scores differed between groups across all ratings. In general, the scans rated by the neuroradiologist's expert read as having abnormal findings had higher confidence scores and lower image-quality ratings than those rated as having normal findings.

Per the neuroradiologist's expert read, 10 studies (50%) had abnormal findings as evaluated at the standard 20-minute acquisition time (Fig 1). There was no association between reader confidence and acquisition time (reader 1, $\rho = -0.13$, $P = .250$; reader 2, $\rho = -0.19$, $P = .100$). However, image-quality ratings were lower among images with shorter acquisition times for both reviewers (reader 1, $\rho = 0.23$, $P = .044$; reader 2, $\rho = 0.24$, $P = .036$) (Figs 2 and 3).

Analysis of interrater reliability (Table 4) revealed that an abnormal finding on an image was rated similarly between readers at 20-, 15-, and 10-minute acquisition times. However, the interrater confidence scores were inconsistent across raters and between the raters and the expert neuroradiologist read at 5 minutes. In contrast, ratings were relatively consistent both in terms of rank order and abnormality agreement when using image-acquisition times of 10–15 minutes. Of interest, the maximal association in confidence scores between raters occurred at 15 minutes (ρ = 0.92), while the maximal κ when comparing raters also occurred at 15 minutes ($\kappa = 0.90$).

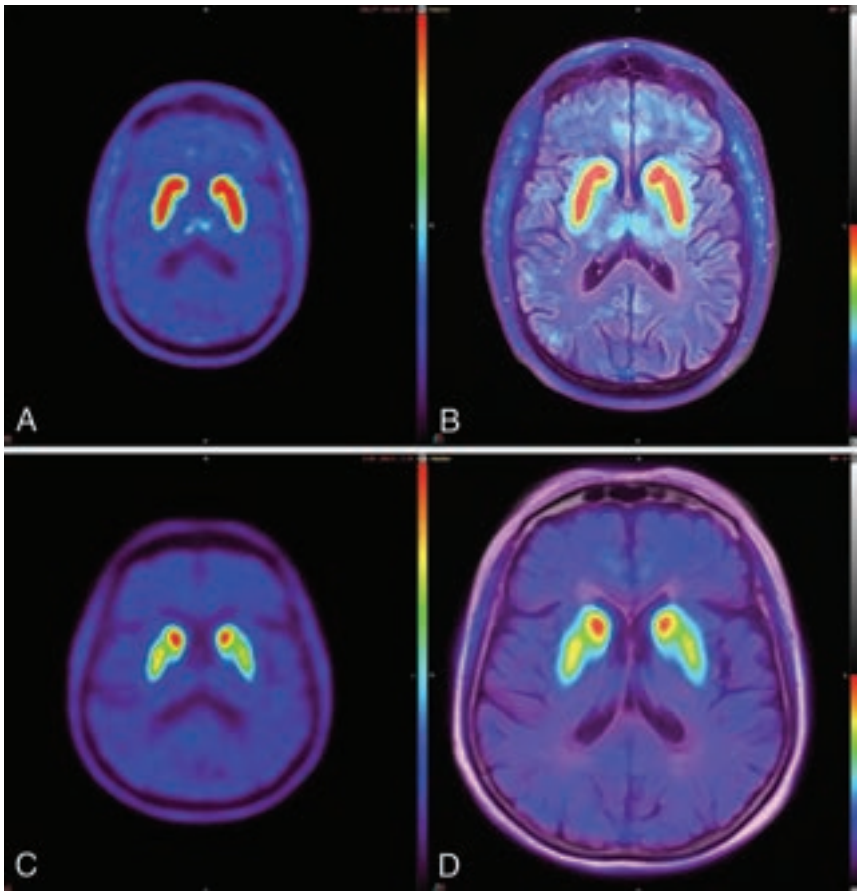

FIG 1. [^{18}F]-FDOPA brain PET and fused [^{18}F]-FDOPA brain PET/MR imaging at a standard 20-minute acquisition time. The healthy subject (*A* and *B*) demonstrates the characteristic "comma sign" uptake in the striatum. The subject with abnormal findings (*C* and *D*) demonstrates marked loss of uptake in the bilateral striatum, particularly involving the bilateral putamina and left > right caudate nuclei, corresponding to more extensive right-sided clinical deficits.

Not shown as main results are examinations of image-quality ratings made by the 2 readers (Online Supplemental Data), which showed relatively less consistent results. For example, the raters consistently scored image quality lower when acquisition times were 5 minutes (ρ = 0.68, P = .001), compared with 10-minute (ρ = 0.36, P = .124), 15-minute (ρ = 0.43, P = .058), or 20-minute (ρ = 0.29, P = .209) acquisition times. Raters agreed that image quality was poor in most scans when using a 5-minute acquisition time (Online Supplemental Data).

DISCUSSION

Functional imaging with dopamine ligands targets the dopaminergic system and is currently used to aid with the distinction of PD from other conditions that mimic the disease. Following the FDA approval of [^{18}F]-FDOPA PET in 2019, which was obtained on the basis of a clinical trial of 56 patients with suspected PS,[16,21] we introduced [^{18}F]-FDOPA PET into practice and incorporated this study into our routine clinical

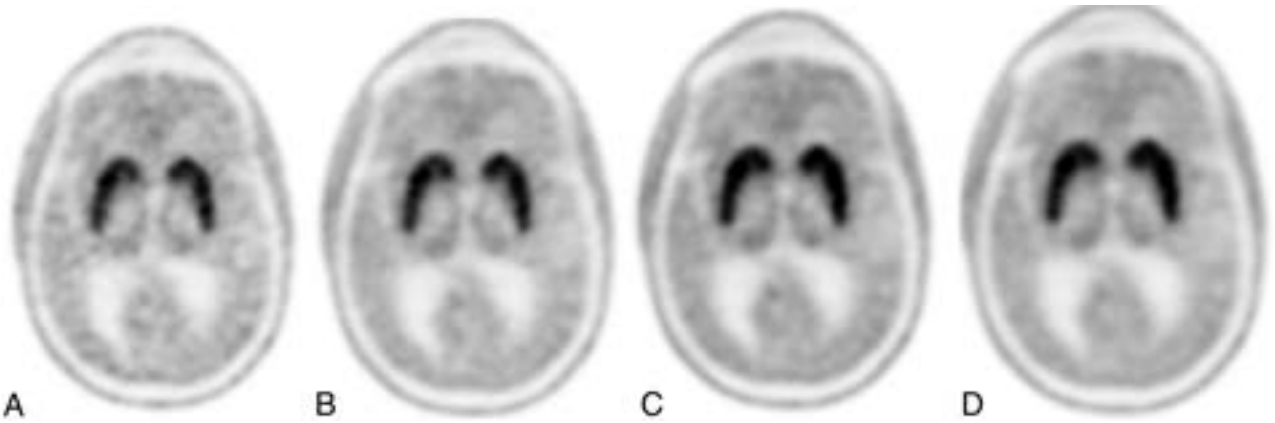

FIG 2. Normal findings on [^{18}F]-FDOPA AC PET at 5-minute (*A*), 10-minute (*B*), 15-minute (*C*), and 20-minute (*D*) acquisition times. Note that image-quality ratings were stable following 15 minutes, and between-subject abnormality detection rates were highly consistent between the 2 readers when using 10-, 15-, or 20-minute acquisition times but were inconsistent at 5 minutes.

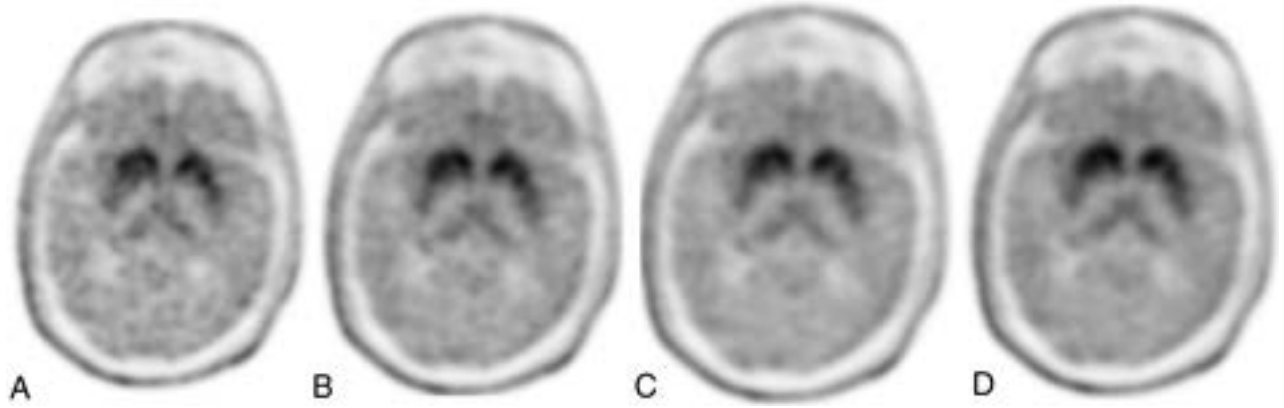

FIG 3. Abnormal findings on [^{18}F]-FDOPA AC PET at 5-minute (*A*), 10-minute (*B*), 15-minute (*C*), and 20-minute (*D*) acquisition times. Note that image-quality ratings were stable following 15 minutes, and between-subject abnormality detection rates were highly consistent between the 2 readers when using 10-, 15-, or 20-minute acquisition times but were inconsistent at 5 minutes.

workflow for PD assessment, because it is currently reimbursed by the Centers for Medicare & Medicaid Services in the United States.[17] The present study sought to examine the influence of imaging-parameter selection and quality on abnormality ratings and found that the optimal acquisition times for [^{18}F]-FDOPA PET for clinical purposes was approximately 10–15 minutes.

The European Association of Nuclear Medicine and the Society of Nuclear Medicine and Molecular Imaging have developed joint clinical practice guidelines that address clinical and technical aspects of dopaminergic imaging for patients with PS, to assist radiologists in recommending, performing, interpreting, and reporting the results of dopaminergic imaging in patients with PS.[22] Per these guidelines, the diagnostic importance of presynaptic dopaminergic imaging (ie, [^{18}F]-FDOPA PET; DaT SPECT) is the following: 1) to support the differential diagnosis between essential tremor and neurodegenerative PS;[23-26] 2) to help distinguish dementia with Lewy bodies and other dementias (in particular, Alzheimer disease);[27-29] 3) to support the differential diagnosis between PS due to presynaptic degenerative dopamine deficiency and other forms of PS (eg, drug-induced, psychogenic, or vascular parkinsonism);[30-32] and 4) to detect early presynaptic PS.[33,34]

The goal of [^{18}F]-FDOPA PET visual assessment is to qualitatively analyze uptake in the striatum (putamen and caudate nucleus) by setting the maximum color scale value to the maximal tracer value in the striatum. Moreover, [^{18}F]-FDOPA not only allows qualitative interpretation, but there are established quantitative parameters that can be calculated to objectively quantify the degree of striatal neuronal loss.[35-38] Semiquantitative analysis may be performed in the clinical setting, typically by calculating the striato-occipital ratio, which has been shown to correlate with clinical disability ratings.[35] Quantitative analysis of dynamic time-activity curves may also be used to determine multiple aspects of [^{18}F]-FDOPA influx constants (Ki maps).[36] For example, Dhawan et al[38] demonstrated a graphic approach to compare the striatal-to-occipital ratio and influx constant in [^{18}F]-FDOPA PET studies, highlighting a similar accuracy using a short 10-minute scan at 95 minutes post-radiopharmaceutical injection. Similarly, in our study, visual image-quality ratings were stable following 15 minutes, and between-subject abnormality detection rates were highly consistent between 2 readers when using 10-, 15-, or 20-minute acquisition times but were inconsistent at 5 minutes. While acquisition times for PET vary depending on the scanner sensitivity and the administered dose, these results suggest that neuroradiologists may consistently and reliably interpret [^{18}F]-FDOPA PET at acquisition times shorter than the traditionally used 20 minutes.

Several studies have found that [^{18}F]-FDOPA PET and the DaTscan are highly accurate and diagnose PD with similar levels of sensitivity and specificity.[2,19,39] There are several major advantages that favor the use of [^{18}F]-FDOPA PET over DaT SPECT.[2,39-42] These include improved image resolution (~5mm for PET versus ~13-14 mm for SPECT), shorter imaging sessions, lower radiation burden, similar-to-reduced cost, and no risk of potential iodine-induced thyroid-related side effects and therefore no need for the administration of the Lugol solution before the examination to fully saturate the thyroid to protect it from radiation exposure.[41] Furthermore, the ability to fuse [^{18}F]-FDOPA PET with either CT or MR structural imaging and the introduction of simultaneous PET/MR imaging scanners for the assessment of movement disorders provides the ability to correlate with concurrent anatomic abnormalities (eg, lacunar infarcts in the striatum; enlarged perivascular spaces), which may provide added value and help confirm or exclude the existence of concomitant pathologies.[43]

There are several limitations to [^{18}F]-FDOPA PET dopaminergic imaging. For example, Wallert et al[40] suggested that [^{18}F]-FDOPA PET may be less sensitive than DaTscans in patients with clinically uncertain PS in the clinical setting. This suggestion may relate to the challenges of interpretation in routine practice outside the research setting. A meta-analysis has also suggested that the decrease in activity in the striatum of patients with PD is consistently smaller in studies assessing [^{18}F]-FDOPA PET compared with DaT SPECT.[10] Furthermore, in early disease, there is a relative increase in [^{18}F]-FDOPA uptake compared with vesicle monoamine transporter 2 imaging, with the radiotracer carbon 11 [^{11}C] dihydrotetrabenazine likely corresponding to compensatory upregulation of AADC activity in early-stage PD.[5] Finally, limitations specific to our study include its relatively small sample size, lack of quantitative analyses (we focused on visual interpretation

only in an attempt to closely mimic routine clinical practice), and absence of long-term follow-up of study subjects for clinical monitoring of disease progression.

CONCLUSIONS

[^{18}F]-FDOPA PET is a promising emerging technique for the assessment of parkinsonism. Despite several minor limitations, our study suggests that image-quality ratings were stable at 10–15 minutes, and that between-subject abnormality detection rates were highly consistent between 2 readers when using 10-, 15-, or 20-minute acquisition times but were inconsistent at 5 minutes. As this novel dopaminergic imaging technique translates into clinical practice, shorter PET acquisition times may help maximize patient comfort while increasing throughput in the clinical setting.

Disclosure forms provided by the authors are available with the full text and PDF of this article at www.ajnr.org.

REFERENCES

1. Ponisio MR, Iranpour P, Benzinger T. **FDOPA in Movement Disorders and Neuro-Oncology**. In: Franceschi AM, Franceschi D. eds. *Hybrid PET/MR Neuroimaging: A Comprehensive Approach*. Springer-Verlag; 2022:121–35
2. Eshuis SA, Jager PL, Maguire RP, et al. **Direct comparison of FP-CIT SPECT and F-DOPA PET in patients with Parkinson's disease and healthy controls**. *Eur J Nucl Med Mol Imaging* 2009;36:454–62 CrossRef Medline
3. Chondrogiannis S, Marzola MC, Al-Nahhas A, et al. **Normal biodistribution pattern and physiologic variants of 18F-DOPA PET imaging.** *Nucl Med Commun* 2013;34:1141–49 CrossRef Medline
4. Buu NT. **Vesicular accumulation of dopamine following L-DOPA administration.** *Biochem Pharmacol* 1989;38:1787–92 CrossRef Medline
5. Lee CS, Samii A, Sossi V, et al. **In vivo positron emission tomographic evidence for compensatory changes in presynaptic dopaminergic nerve terminals in Parkinson's disease**. *Ann Neurol* 2000;47:493–503 CrossRef Medline
6. Morrish PK, Sawle GV, Brooks DJ. **An [18F]dopa-PET and clinical study of the rate of progression in Parkinson's disease**. *Brain* 1996;119(Pt 2):585–91 CrossRef Medline
7. Leenders KL, Salmon EP, Tyrrell P, et al. **The nigrostriatal dopaminergic system assessed in vivo by positron emission tomography in healthy volunteer subjects and patients with Parkinson's disease**. *Arch Neurol* 1990;47:1290–98 CrossRef Medline
8. Bruck A, Aalto S, Rauhala E, et al. **A follow-up study on 6-[18F]fluoro-L-dopa uptake in early Parkinson's disease shows nonlinear progression in the putamen**. *Mov Disord* 2009;24:1009–15 CrossRef Medline
9. Calabria FF, Calabria E, Gangemi V, et al. **Current status and future challenges of brain imaging with (18)F-DOPA PET for movement disorders.** *Hell J Nucl Med* 2016;19:33–41 CrossRef Medline
10. Kaasinen V, Vahlberg T. **Striatal dopamine in Parkinson disease: a meta-analysis of imaging studies.** *Ann Neurol* 2017;82:873–82 CrossRef Medline
11. Ghaemi M, Raethjen J, Hilker R, et al. **Monosymptomatic resting tremor and Parkinson's disease: a multitracer positron emission tomographic study**. *Mov Disord* 2002;17:782–88 CrossRef Medline
12. Broussolle E, Dentresangle C, Landais P, et al. **The relation of putamen and caudate nucleus 18F-Dopa uptake to motor and cognitive performances in Parkinson's disease**. *J Neurol Sci* 1999;166:141–51 CrossRef Medline
13. Eidelberg D, Moeller JR, Dhawan V, et al. **The metabolic anatomy of Parkinson's disease: complementary [18F]fluorodeoxyglucose and [18F]fluorodopa positron emission tomographic studies**. *Mov Disord* 1990;5:203–13 CrossRef Medline
14. Vingerhoets FJ, Schulzer M, Calne DB, et al. **Which clinical sign of Parkinson's disease best reflects the nigrostriatal lesion?** *Ann Neurol* 1997;41:58–64 CrossRef Medline
15. Otsuka M, Ichiya Y, Kuwabara Y, et al. **Differences in the reduced 18F-Dopa uptakes of the caudate and the putamen in Parkinson's disease: correlations with the three main symptoms**. *J Neurol Sci* 1996;136:169–73 CrossRef Medline
16. Food and Drug Administration. **Drug Trials Snapshots: Fluorodopa F 18.** https://www.fda.gov/drugs/drug-trials-snapshots-fluorodopa-f-18. Accessed: July 7, 2023
17. Centers for Medicare and Medicaid Services. **Billing and Coding: Positron Emission Tomography Scans Coverage.** https://www.cms.gov/medicare-coverage-database/view/article.aspx?articleid=54666. Accessed July 7, 2023
18. Food and Drug Administration. **Highlights of Prescribing Information.** October 22, 2019. https://www.accessdata.fda.gov/drugsatfda_docs/label/2019/200655s000lbl.pdf. Accessed: July 7, 2023
19. Ishikawa T, Dhawan V, Kazumata K, et al. **Comparative nigrostriatal dopaminergic imaging with iodine-123-beta CIT-FP/SPECT and fluorine-18-FDOPA/PET.** *J Nucl Med* 1996;37:1760–65 Medline
20. Dhawan V, Ishikawa T, Patlak C, et al. **Combined FDOPA and 3OMFD PET studies in Parkinson's disease**. *J Nucl Med* 1996;37:209–16 Medline
21. Food and Drug Administration. https://www.fda.gov/drugs/drug-approvals-and-databases/drug-trials-snapshots-fluorodopa-f-18. Accessed: March 21, 2024
22. Morbelli S, Esposito G, Arbizu J, et al. **EANM practice guideline/SNMMI procedure standard for dopaminergic imaging in Parkinsonian syndromes 1.0.** *Eur J Nucl Med Mol Imaging* 2020;47:1885–912 CrossRef Medline
23. Benamer TS, Patterson J, Grosset DG, et al. **Accurate differentiation of parkinsonism and essential tremor using visual assessment of [123I]-FP-CIT SPECT imaging: the [123I]-FP-CIT study group.** *Mov Disord* 2000;15:503–10 CrossRef
24. Booij J, Hemelaar TG, Speelman JD, et al. **One-day protocol for imaging of the nigrostriatal dopaminergic pathway in Parkinson's disease by [123I]FPCIT SPECT**. *J Nucl Med* 1999;40:753–61 Medline
25. Scherfler C, Schwarz J, Antonini A, et al. **Role of DAT-SPECT in the diagnostic work up of parkinsonism.** *Mov Disord* 2007;22:1229–38 CrossRef Medline
26. Nicastro N, Garibotto V, Burkhard PR. **123I-FP-CIT SPECT accurately distinguishes parkinsonian from cerebellar variant of multiple system atrophy.** *Clin Nucl Med* 2018;43:e33–36 CrossRef Medline
27. McKeith I, O'Brien J, Walker Z, et al; DLB Study Group. **Sensitivity and specificity of dopamine transporter imaging with 123I-FP-CIT SPECT in dementia with Lewy bodies: a Phase III, multicentre study**. *Lancet Neurol* 2007;6:305–13 CrossRef Medline
28. Thomas AJ, Attems J, Colloby SJ, et al. **Autopsy validation of 123I-FP-CIT dopaminergic neuroimaging for the diagnosis of DLB.** *Neurology* 2017;88:276–83 CrossRef Medline
29. McKeith IG, Boeve BF, Dickson DW, et al. **Diagnosis and management of dementia with Lewy bodies: fourth consensus report of the DLB Consortium.** *Neurology* 2017;89:88–100 CrossRef Medline
30. Lorberboym M, Treves TA, Melamed E, et al. **[123I]-FP/CIT SPECT imaging for distinguishing drug-induced parkinsonism from Parkinson's disease**. *Mov Disord* 2006;21:510–14 CrossRef Medline
31. Felicio AC, Godeiro-Junior C, Moriyama TS, et al. **Degenerative parkinsonism in patients with psychogenic parkinsonism: a dopamine transporter imaging study.** *Clin Neurol Neurosurg* 2010;112:282–85 CrossRef Medline
32. Brigo F, Matinella A, Erro R, et al. **[123I]FP-CIT SPECT (DaTSCAN) may be a useful tool to differentiate between Parkinson's disease and vascular or drug-induced parkinsonisms: a meta-analysis**. *Eur J Neurol* 2014;21:1369–90 CrossRef Medline
33. Baucknehtt M, Chincarini A, De Carli F, et al. **Presynaptic dopaminergic neuroimaging in REM sleep behavior disorder: a systematic review and meta-analysis.** *Sleep Med Rev* 2018;41:266–74 CrossRef Medline

34. Berg D, Postuma RB, Adler CH, et al. **MDS research criteria for prodromal Parkinson's disease**. *Mov Disord* 2015;30:1600–11 CrossRef Medline
35. Takikawa S, Dhawan V, Chaly T, et al. **Input functions for 6-[fluorine-18]fluorodopa quantitation in parkinsonism: comparative studies and clinical correlations.** *J Nucl Med* 1994;35:955–63 Medline
36. Sossi VD, La Fuente-Fernandez R, Holden JE, et al. **Increase in dopamine turnover occurs early in Parkinson's disease: evidence from a new modeling approach to PET 18 F-fluorodopa data**. *J Cereb Blood Flow Metab* 2002;22:232–39 CrossRef Medline
37. Hazut Krauthammer S, Cohen D, Even-Sapir E, et al. **Beyond visual assessment of basal ganglia uptake: can automated method and pineal body uptake assessment improve identification of nigrostriatal dysfunction on 18F-DOPA PET/CT?** *Int J Mol Sci* 2023;24:5683 CrossRef Medline
38. Dhawan V, Ma Y, Pillai V, et al. **Comparative analysis of striatal FDOPA uptake in Parkinson's disease: ratio method versus graphical approach**. *J Nucl Med* 2002;43:1324–30 Medline
39. Huang WS, Chiang YH, Lin JC, et al. **Crossover study of (99m)Tc-TRODAT-1 SPECT and (18)F-FDOPA PET in Parkinson's disease patients**. *J Nucl Med* 2003;44:999–1005 Medline
40. Wallert E, Letort E, van der Zant F, et al. **Comparison of [18F]-FDOPA PET and [123I]-FP-CIT SPECT acquired in clinical practice for assessing nigrostriatal degeneration in patients with a clinically uncertain parkinsonian syndrome.** *EJNMMI Res* 2022;12:68 CrossRef Medline
41. Dhawan V, Niethammer MH, Lesser ML, et al. **Prospective F-18 FDOPA PET imaging study in human PD.** *Nucl Med Mol Imaging* 2022;56:147–57 CrossRef Medline
42. Khamis K, Giladi N, Levine C, et al. **The added value of 18F-FDOPA PET/CT in the work-up of patients with movement disorders.** *Neurographics* 2019;9:344–48 CrossRef
43. Struck AF, Hall LT, Kusmirek JE, et al. **(18)F-DOPA PET with and without MRI fusion, a receiver operator characteristics comparison.** *Am J Nucl Med Mol Imaging* 2012;2:475–82 Medline

Callosal Interhemispheric Communication in Mild Traumatic Brain Injury: A Mediation Analysis on WM Microstructure Effects

Sohae Chung, Tamar Bacon, Joseph F. Rath, Alaleh Alivar, Santiago Coelho, Prin Amorapanth, Els Fieremans, Dmitry S. Novikov, Steven R. Flanagan, Joshua H. Bacon, and Yvonne W. Lui

ABSTRACT

BACKGROUND AND PURPOSE: Because the corpus callosum connects the left and right hemispheres and a variety of WM bundles across the brain in complex ways, damage to the neighboring WM microstructure may specifically disrupt interhemispheric communication through the corpus callosum following mild traumatic brain injury. Here we use a mediation framework to investigate how callosal interhemispheric communication is affected by WM microstructure in mild traumatic brain injury.

MATERIALS AND METHODS: Multishell diffusion MR imaging was performed on 23 patients with mild traumatic brain injury within 1 month of injury and 17 healthy controls, deriving 11 diffusion metrics, including DTI, diffusional kurtosis imaging, and compartment-specific standard model parameters. Interhemispheric processing speed was assessed using the interhemispheric speed of processing task (IHSPT) by measuring the latency between word presentation to the 2 hemivisual fields and oral word articulation. Mediation analysis was performed to assess the indirect effect of neighboring WM microstructures on the relationship between the corpus callosum and IHSPT performance. In addition, we conducted a univariate correlation analysis to investigate the direct association between callosal microstructures and IHSPT performance as well as a multivariate regression analysis to jointly evaluate both callosal and neighboring WM microstructures in association with IHSPT scores for each group.

RESULTS: Several significant mediators in the relationships between callosal microstructure and IHSPT performance were found in healthy controls. However, patients with mild traumatic brain injury appeared to lose such normal associations when microstructural changes occurred compared with healthy controls.

CONCLUSIONS: This study investigates the effects of neighboring WM microstructure on callosal interhemispheric communication in healthy controls and patients with mild traumatic brain injury, highlighting that neighboring noncallosal WM microstructures are involved in callosal interhemispheric communication and information transfer. Further longitudinal studies may provide insight into the temporal dynamics of interhemispheric recovery following mild traumatic brain injury.

ABBREVIATIONS: aCR/sCR/pCR = anterior/superior/posterior corona radiata; aIC/pIC/rIC = anterior/posterior/retrolenticular limb of the internal capsule; CC = corpus callosum; Cg = cingulum (cingulate gyrus); Ch = cingulum (hippocampus); D_a = intra-axonal diffusivity; $D_e^{\parallel}$ = extra-axonal axial diffusivity; $D_e^{\perp}$ = extra-axonal radial diffusivity; DKI = diffusional kurtosis imaging; f = axonal water fraction; FA = fractional anisotropy; gCC/bCC/sCC = genu/body/splenium of corpus callosum; IHSPT = interhemispheric speed of processing task; L = left; LVF = left visual field; MD/AD/RD = mean/axial/radial diffusivities; MK/AK/RK = mean/axial/radial kurtosis; MTBI = mild traumatic brain injury; R = right; RT = reaction time; RVF = right visual field; SFOF = superior fronto-occipital fasciculus; SLF = superior longitudinal fasciculus; SM = standard model; TBSS = Tract-Based Spatial Statistics

Mild traumatic brain injury (MTBI), commonly known as concussion, is a major public health problem with potentially serious clinical sequelae for weeks to months after injury or even longer.[1,2] It is known that stretch and torsion injury to the WM can occur after head injury and that the corpus callosum (CC) is particularly at risk.[3,4] Several MTBI studies using diffusion MR imaging to study human brain microstructure corroborate findings from biomechanical modeling reflective of this finding.[5-8]

The CC forms a critical central pathway for interhemispheric communication and information transfer. Damage to the CC is likely to impact normal interhemispheric communication[9,10] and could contribute to the complex and subtle symptoms central to MTBI.[11,12] Indeed, some prior studies have shown that callosal degradation may influence the information transfer and integration

Received May 26, 2023; accepted after revision January 27, 2024.

From the Department of Radiology (S. Chung, A.A., S. Coelho, E.F., D.S.N., Y.W.L.), Center for Advanced Imaging Innovation and Research, Department of Radiology (S. Chung, A.A., S. Coehlo, E.F., D.S.N., Y.W.L.), Bernard and Irene Schwartz Center for Biomedical Imaging, and Departments of Neurology (T.B., J.H.B.), and Rehabilitation Medicine (J.F.R., P.A., S.R.F.), New York University Grossman School of Medicine, New York, New York.

This work was supported by the National Institutes of Health R01 NS119767-01A1, R01 NS039135-11, R56 NS119767, P41 EB017183, and the Department of Defense PT190013.

Please address correspondence to Sohae Chung, PhD, 660 1st Ave, 4th floor, New York, NY 10016; e-mail: sohae.chung@nyulangone.org

Indicates article with online supplemental data.

http://dx.doi.org/10.3174/ajnr.A8213

between the hemispheres in patients with CC degradation as well as in normal aging.[13] Also, an association between posterior callosal atrophy and slowed cross-hemisphere processing of visual information has been shown in patients with MS.[14] However, impairments relating to callosal injury are not easily identified. Further complicating the situation, the CC does not function alone but instead connects adjacent WM bundles across the brain in an intricate way[15] that could mediate the callosal interhemispheric communication.

Because MTBI comprises a heterogeneous group of injuries and manifests as a heterogeneous group of symptoms, there is a great need for focused studies of region-specific injury and its impact on specific functional domains. Therefore, the purpose of this work is to study how callosal interhemispheric communication is affected by WM microstructure in patients with MTBI compared with healthy controls. Callosal and neighboring WM microstructures are studied in both healthy controls and patients with MTBI using advanced diffusion MR imaging methods including DTI,[16] diffusional kurtosis imaging (DKI),[17] and the standard model (SM) of diffusion in WM[18,19] to tap tissue microstructure noninvasively. While DTI and DKI parameters are, by design, not specific to tissue components,[20] the SM can estimate biophysically more meaningful and compartment-specific parameters of tissue microstructure,[21,22] including axonal water fraction (f), intra-axonal diffusivity (D_a), and extra-axonal axial and radial diffusivities ($D_e^{\parallel}$ and $D_e^{\perp}$, respectively). Several studies including animal validation[21,23] and in vivo human studies[6,24-27] suggest that these parameters are more informative than empirical diffusion measures.

A visual stimulus-response test, the interhemispheric speed of processing task (IHSPT),[14] has been used in this work to assess interhemispheric processing speed. The IHSPT measures latency in articulating a word presented to the left hemi-visual field, requiring information to travel across hemispheres (Fig 1). It has been shown that performance on this task is facilitated through the CC, a critical pathway for interhemispheric communication.[14,28] Here, we hypothesize that there are measurable changes in neighboring WM microstructures in patients with MTBI that may disrupt the callosal interhemispheric communication. A mediation framework is used to investigate how a neighboring WM microstructure (ie, mediator) indirectly affects the association between callosal microstructure and interhemispheric processing in MTBI (Fig 2*B*). In addition, a univariate correlation analysis is performed to investigate the direct association between callosal microstructures and IHSPT performance, and a multivariate regression analysis is performed to jointly evaluate both callosal and neighboring WM microstructures simultaneously in association with IHSPT performance for each group.

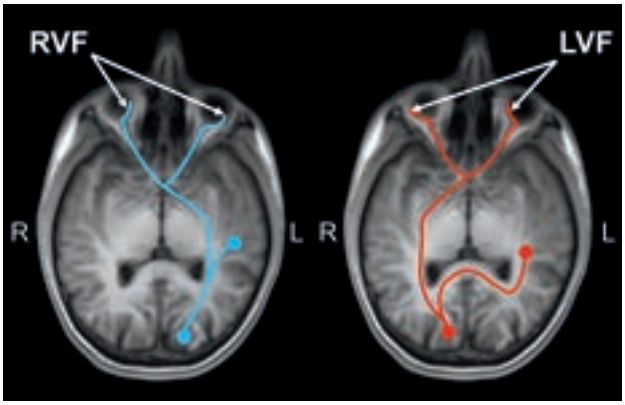

FIG 1. A schematic illustration of the IHSPT probes of hemispheric and callosal WM integrity by measuring processing speed and latency in the articulation of words presented to the LVF and RVF in individuals with left-hemisphere language dominance and vice versa for right-hemisphere-dominant individuals. For individuals with left-language dominance (most), visual information presented to the RVF projects to the left primary visual cortex with access to primary language centers in the same hemisphere (blue), whereas visual information from the subject's LVF projects to the contralateral (right) primary visual cortex and must then cross the midline to access core language centers in the left brain (red). A difference in latency between presentation and oral articulation of the word can be measured to tap interhemispheric processing speed.

MATERIALS AND METHODS

Study Population

This study has been approved by our Institutional Review Board, and all experiments were performed under relevant guidelines and regulations. All subjects were prospectively recruited from the Institutional Concussion Center or Emergency Department and provided written informed consent before the procedure. Inclusion criteria were the following: 1) age range of 18–65 years, 2) diagnostic MTBI criteria defined by the American Congress of Rehabilitation Medicine[29] including loss of consciousness of <30 minutes, and 3) brain injury within 1 month. We excluded patients with the following: 1) a reported history of head trauma, neurologic illness, or psychiatric disorders; 2) a history of participation in organized contact sports; 3) any contraindication to MR imaging; and 4) non-right-handed individuals to avoid the confounding effects of handedness in IHSPT test performance. We studied 23 patients with MTBI (mean age, 36 [SD, 14] years; 9 men) and 17 healthy controls (mean age, 34 [SD, 1] years; 8 men). Postconcussion symptoms were assessed by using the Rivermead Postconcussion Symptoms Questionnaire.[30] The mean total scores of this questionnaire for patients with

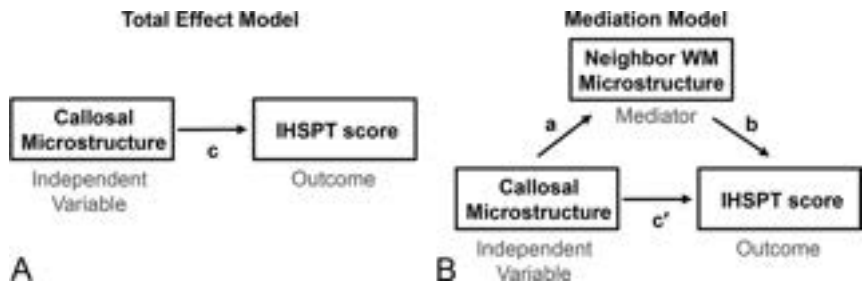

FIG 2. Path diagrams illustrate the total (or entire) effect model (*A*) and the mediation model (*B*).[19] The mediation model decomposes the total effect, c, into the direct effect, c', and the indirect effect, ab = c–c', where a is the independent-mediator effect and b is the mediator-outcome effect. The paths a, b, c, and c represent the regression coefficients.

Characteristics of the patients and healthy controls

	Patients with MTBI ($n = 23$)	Healthy Controls ($n = 17$)
Male/female	9:14	8:9
Age (mean) (yr)	36 (SD, 14)	34 (SD, 11)
Education (mean) (yr)	16 (SD, 2)	17 (SD, 2)
Time since injury (mean) (days)	18 (SD, 8)	–
Injury mechanism (No.)		
Hit by object	8	
Fall	8	
Car collision	4	
Assault	1	
Other	2	
RPQ total score (mean)	23 (SD, 16)	6 (SD, 8)
IHSPT score (mean) (range) (%)	5.8 (SD, 5.7) (0.1–25.6)	5.2 (SD, 3.1) (0.3–10.8)

Note:—RPQ indicates Rivermead Postconcussion Symptoms Questionnaire; IHSPT; Interhemispheric Processing Speed Test.

MTBI were 23 (SD, 16). The characteristics of the study population are summarized in the Table. For all subjects, brain MR imaging and an IHSPT test were acquired within 1 week of each other.

MR Imaging Acquisition

MR imaging was performed on 3T MR imaging scanners (Magnetom Skyra or Magnetom Prisma, Siemens), with 23 subjects using Magnetom Skyra and 17 using Magnetom Prisma. Multishell diffusion imaging was performed with 5 b-values (250, 1000, 1500, 2000, 2500 s/mm^2) along with 5 diffusion-encoding direction schemes (6, 20, 20, 30, 60, respectively) using multiband (factor of 2)[31] EPI for accelerated acquisitions with an anterior-posterior phase-encoding direction. Other parameters included the following: FOV = 220 × 220 mm, matrix = 88 × 88, number of slices = 56, 2.5-mm isotropic resolution, a partial Fourier factor = 6/8, TR/TE = 4900/95 ms, bandwidth = 2104 Hz/pixel, a generalized autocalibrating partially parallel acquisition factor of 2. Three nonweighted diffusion images ($b = 0$ s/mm^2) were also acquired. An additional image with b=0 s/mm^2 with a reversed phase-encoding direction was acquired for geometric artifact correction.[32]

IHSPT

The IHSPT test was used to evaluate the interhemispheric speed of processing by measuring latency between words presented to the left visual field (LVF) and right visual field (RVF) and the subject's oral articulation of these words.[14] This test links visual perception and expressive language, specifically testing interhemispheric communication between primary visual and language pathways. For left-language-dominant individuals, words presented to the RVF project to the left hemisphere, and the average reaction time (RT) between presentation and articulation (Fig 1, blue) is slightly faster than for words presented to the LVF, which project to the right hemisphere and then are required to cross the midline to access core language centers in the left hemisphere (Fig 1, red). This process is reversed for right-language-dominant individuals. The test was performed using E-Prime 2.0 software (Psychology Software Tools) to control the precision of visual stimulus presentation and data collection. Each trial consisted of a simple 3-letter word randomly presented for 150 ms to either the LVF or RVF. Subjects were instructed to speak the word as quickly as possible, and the RT between presentation and articulation was recorded automatically. Eighty random trials were conducted from a set of 110 three-letter words. Trials were excluded if the RT was 2 SDs above or below the subject's own mean (considered distraction or a possible unrelated vocal trigger). The IHSPT test score (percentage) was calculated using the absolute difference of the median RTs for LVF and RVF word presentations, divided by the average RT between them, and then multiplied by 100 to obtain a percentage score. Note that to account for individual variabilities of language dominance, the absolute difference of the RTs was used.

Image Analyses

Diffusion Image Processing. Denoising for the DWIs was performed using the Marchenko-Pastur principal component analysis method.[33] By means of the Diffusion parameter EStImation with Gibbs NoisE removal (DESIGNER) pipeline (https://github.com/NYU-DiffusionMRI/DESIGNER-v2),[34] denoised diffusion images were corrected for Gibbs ringing artifacts[35] and then were rigidly aligned and corrected for eddy current distortions and subject motion simultaneously.[36] EPI-included distortions were also corrected using a b=0 image with reverse phase-encoding.[32] For DTI parameters, a b-value of 1000 was used. In total, 11 diffusion metrics including DTI (fractional anisotropy [FA], mean/axial/radial diffusivities [MD/AD/RD]), DKI (mean/axial/radial kurtosis [MK/AK/RK]), and SM metrics (f, D_a, $D_e^{\parallel}$, $D_e^{\perp}$) were calculated using in-house software (SMI toolbox; https://www.smisupplychain.com/tools/smi-toolbox/).[19,37] To minimize scanner variability, we used ComBat (https://github.com/Jfortin1/ComBatHarmonization)[38,39] for harmonization of diffusion parametric maps, preserving biologic variabilities such as age, sex, and disease group.

Tract-Based Spatial Statistics. Voxelwise group comparisons of diffusion metrics were performed using Track-Based Spatial Statistics (TBSS)[36] with age as a covariate. Briefly, all subjects' FA maps were projected to the FA skeleton template (Montreal Neurological Institute 152 space), which was thresholded at an FA of 0.3 to restrict the analysis to WM regions with highly aligned fiber bundles. Other diffusion maps underwent unified processes by projecting them to the FA skeleton. Voxelwise analysis was then performed on the skeleton for each diffusion parameter.

ROI. Twenty-seven ROIs were explored on the basis of being major cerebral WM tracts, including the genu, body, splenium of the CC (gCC, bCC, sCC), right and left anterior, posterior, retrolenticular limb of the internal capsule (aIC, pIC, rIC), anterior, superior, posterior corona radiata (aCR, sCR, pCR), posterior thalamic radiation, external capsule, cingulum (cingulate gyrus) (Cg), cingulum (hippocampus) (Ch), superior longitudinal fasciculus (SLF), and superior fronto-occipital fasciculus (SFOF), respectively. ROIs were generated on the basis of the John Hopkins

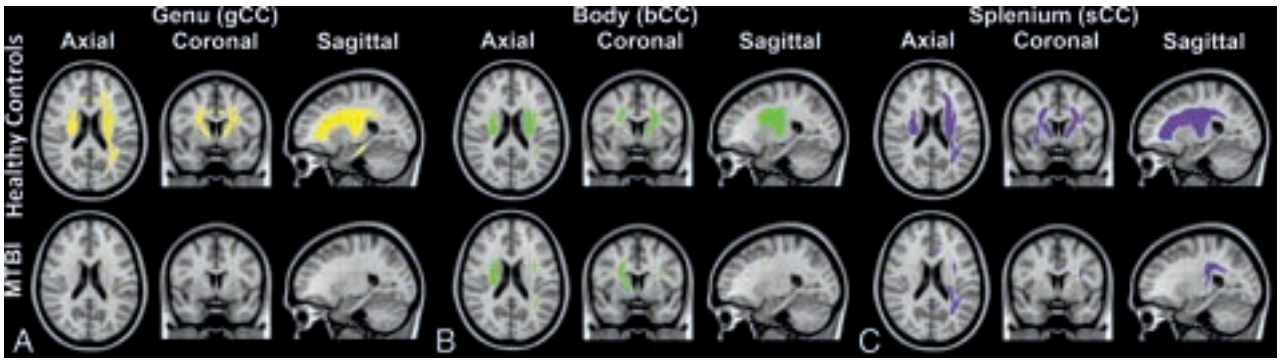

FIG 3. Mediation analysis demonstrates significant indirect mediators (neighbor WM ROIs) in the relationships (*A*) between the genu of the CC and IHSPT performance including areas (yellow) of aIC, pIC, rIC, aCR_L, sCR, pCR_L, Cg, Ch_L, SLF_L, and SFOF in healthy controls (*upper row*) and no area in patients with MTBI (*lower row*); (*B*) between the body of the CC and IHSPT performance including areas (green) of aIC_L, pIC, rIC_R, sCR, SLF_L, and $SFOF_L$ in healthy controls (*upper row*) and aIC_R, sCR_R, SLF_L, and $SFOF_R$ in patients with MTBI (*lower row*); and (*C*) between the splenium of the CC and IHSPT performance including areas (purple) of aIC, pIC, rIC_R, aCR_L, sCR, pCR_L, EC_R, Ch_R, SLF_L, and $SFOF_L$ in healthy controls (*upper row*) and rIC_L, pCR_L, Cg_L, and SLF_L in patients with MTBI (*lower row*). Details are in the Online Supplemental Data.

University ICBM-DTI-81 WM Atlas labels[40] by nonlinearly registering each subject's FA map to the FA template using FSL (http://www.fmrib.ox.ac.uk/fsl).[36] A reversed warping procedure was performed to assign the atlas labels to each subject's space. All ROIs were manually reviewed and edited as needed. For each ROI, the mean value of each diffusion metric was obtained only in voxels with FA $\geq$ 0.3 to restrict the analysis to WM regions.

Statistical Analyses

Groups were compared in terms of sex using a Fisher exact test and in terms of age using an exact Mann-Whitney *U* test. Group differences on the IHSPT scores were assessed with 1-way ANCOVA with age as a covariate.

Mediation analysis was performed to decompose the total effect of the CC microstructure on IHSPT (c in Fig 2*A*) into a direct effect (c' in Fig 2*B*) and an indirect, mediated effect (ab in Fig 2*B*) through 1 mediator (ie, neighbor WM microstructure), where the paths a, b, c', and c represented the regression coefficients in Fig 2. The mediation model used in this work included 1 mediator as shown in Fig 2*B*. Mediation analysis was conducted using PROCESS[41] in the SPSS (SPSS) framework with 5000 bootstrap resamples adjusted for age. A significant mediated effect was determined if the 95% CI did not contain zero.

In addition, we conducted a univariate correlation analysis with age as a covariate to investigate the association between callosal microstructures and IHSPT performance as well as a multivariate regression analysis to jointly evaluate both callosal and neighboring WM microstructures in association with IHSPT scores for each group. We used SPSS, Version 28.

For TBSS, statistical analysis was conducted with 5000 random permutations to identify statistically significant voxels, corrected for multiple comparisons with threshold-free cluster enhancement. For ROI analysis, MANCOVA, was performed by adjusting for age. The level of significance was set at $P < .05$.

RESULTS

Groups were not significantly different in terms of sex ($P = .75$, Fisher exact test), age ($P = .98$, Mann-Whitney *U* test), and IHSPT scores ($P = .65$, ANCOVA).

Mediation analysis found several significant mediators in the healthy control group, located mostly in an array of areas: 1) between gCC and IHSPT: aIC, pIC, rIC, aCR_L, sCR, pCR_L, Cg_R, Ch_L, SLF_L, SFOF; 2) between bCC and IHSP: aIC_L, pIC, rIC_R, sCR, $SFOF_L$; and 3) between sCC and IHSPT: aIC, pIC, rIC_R, sCR_L, EC_R, Ch_R, $SFOF_L$ (Fig 3, *upper row*). Patients with MTBI appeared to lose some of the normal associations (Fig 3, *lower row*). More details are summarized in the Online Supplemental Data.

Significant univariate correlations and a trend toward significance between the CC and IHSPT scores were observed in the healthy control group: gCC (D_a, $r = 0.51$, $P = .046$; $D_e^{\parallel}$, $r = -0.49$, $P = .052$) and sCC (D_a, $r = 0.46$, $P = .071$; $D_e^{\parallel}$, $r = -0.58$, $P = .019$), but these relationships were not seen in the MTBI group. Multivariate regression analysis also found significant associations of several WM regions with IHSPT scores mainly including gCC, sCC, aIC_L, pIC_R, rIC_R, sCR_L, $SFOF_L$ in the healthy control group, but fewer WM regions in the MTBI group (Online Supplemental Data), showing consistent results with the results of mediation analysis.

Group differences were revealed using TBSS analysis in several diffusion maps (Fig 4). There were significantly different areas demonstrating lower FA, MK, AK, RK in the MTBI group compared with the healthy control group as well as areas demonstrating higher MD, AD, RD, D_a, and $D_e^{\perp}$ in MTBI, mainly in left-sided WM regions including bCC, aIC_L, aICl, aCR_L, sCR_L, pCR_L, EC_L, Cg_L, SLF_L and $SFOF_L$. The results of ROI analyses were consistent with TBSS results (Online Supplemental Data).

DISCUSSION

In this study, univariate analysis has found significant correlations between callosal microstructures and IHSPT performance in the healthy control group because we know that the callosum serves as a link between 2 cerebral hemispheres, allowing them to communicate. However, these relationships have not been seen in the MTBI group. Moreover, we have found several significant mediators in the healthy control group, involving mainly bilateral WM regions including capsular WM, the corona radiata, cingulum,

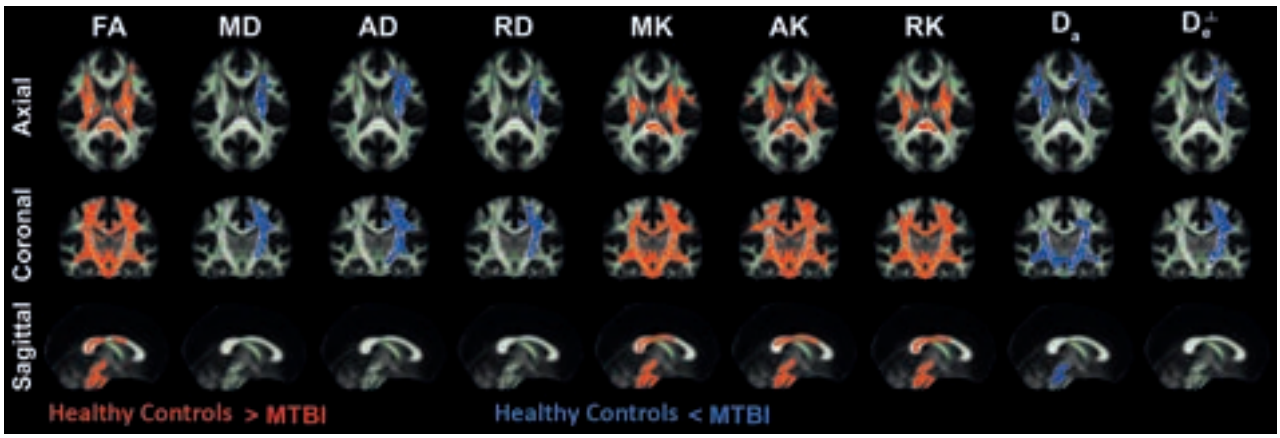

FIG 4. TBSS results comparing diffusion measures between MTBI and healthy control groups. Clusters of voxels (red) demonstrating significantly lower FA, MK, AK, and RK in the MTBI group compared with the healthy control group ($P < .05$, family-wise error–corrected) are present diffusely across the entire WM. Increased MD, AD, RD, D_a, and $D_e^{\perp}$ are seen in mainly left-sided, WM regions including bCC, aIC_L, pIC_L, aCR_L, sCR_L, pCR_L, EC_L, Cg_L, SLF_L, and $SFOF_L$ in the MTBI group. A heat map showing differences between groups is overlaid on the mean FA template and WM skeleton (green).

SLF, and SFOF (Fig 3, *upper row*). These results support the idea that callosal interhemispheric communication is also mediated by neighboring WM microstructures. This mediation is plausible because we know that the CC is not an isolated structure. However, in patients with MTBI, we found a loss of normal mediators, suggesting the anticipated disruption of normal relationships possibly due to increased IHSPT scores (ie, slowing of interhemispheric communication) that may be related to microstructural changes after injury (Fig 3, *lower row*). Our finding is supported by the TBSS results showing microstructural alterations in patients with MTBI compared with healthy controls (Fig 4), in keeping with prior diffusion findings indicative of extra-axonal changes such as vasogenic edema in the acute and subacute periods of injury considered reversible.[42] In particular, extra-axonal diffusion markers, $D_e^{\parallel}$ and $D_e^{\perp}$, have been suggested as potential markers of oligodendrocytes, extracellular inflammation, gliosis, and vasogenic edema.[43-45] Thus, significant increases in extra-axonal diffusion have been previously reported in patients with mild cognitive impairment, Alzheimer disease, as well as MTBI, particularly in callosal regions.[6,45] The results of multivariate regression analysis, which assesses the impact of the relationships between multiple WM regions and IHSPT scores simultaneously, are consistent with the mediation analysis results showing significant associations of several callosal and noncallosal WM microstructures with IHSPT scores in the healthy control group but fewer regions in the MTBI group (Online Supplemental Data).

There are several limitations to this study. First, it includes a relatively small number of total subjects. The variability between patients in the early phases (<1 month postinjury) of MTBI results in a heterogeneous sample, which may dilute the generalizability of the results. The use of this method to inform the degree of injury in the context of clinical presentation and symptoms on an individual level would require larger cohorts. Second, the mediation model used in this study includes a single mediator, and there is a potential for multiple mediators that warrants further studies. Third, analyses were performed on MR images obtained from 2 scanners. We did reduce interscanner variability by using an established data-harmonization method, ComBat,[38] which was performed on a larger-scale data set of 125 subjects, including diffusion images from other MTBI studies using the same diffusion sequence. Biologic variabilities such as age, sex, and disease group were preserved while removing interscanner variability. Fourth, although groups were not significantly different in terms of sex ($P = .75$, Fisher exact test), there may still be possible limitations in our analysis due to potential differences in terms of different interhemispheric connectivity between men and women.[46] This issue warrants further study with larger cohorts. Finally, a small percentage of individuals does have hemispheric codominance for language, making it difficult to accurately capture interhemispheric speed of processing using this tool. In most individuals, the left hemisphere is dominant for language; however, there is variability across the population. To reduce the confounding effects of handedness in IHSPT test performance, we excluded non-right-handed individuals.

CONCLUSIONS

This study reveals significant WM mediators that affect the relationships between callosal microstructure and interhemispheric processing in healthy controls, supporting the idea that callosal interhemispheric communication is also influenced by neighboring WM microstructures. In MTBI, a loss of normal relationships is observed. This disruption may contribute to the subtle symptoms central to MTBI, especially those involving complex tasks. Future longitudinal studies with a larger cohort would provide insight into the temporal dynamics of interhemispheric recovery after MTBI.

ACKNOWLEDGMENTS

This work was also performed under the rubric of the Center for Advanced Imaging Innovation and Research (CAI2R), a National Institute of Biomedical Imaging and Bioengineering Biomedical Technology Resource Center (National Institutes of Health, P41 EB017183).

Disclosure forms provided by the authors are available with the full text and PDF of this article at www.ajnr.org.

REFERENCES

1. Hiploylee C, Dufort PA, Davis HS, et al. **Longitudinal study of post-concussion syndrome: not everyone recovers.** *J Neurotrauma* 2017; 34:1511–23 CrossRef Medline
2. Levin HS, Diaz-Arrastia RR. **Diagnosis, prognosis, and clinical management of mild traumatic brain injury.** *Lancet Neurol* 2015; 14:506–17 CrossRef Medline
3. McAllister TW, Ford JC, Ji S, et al. **Maximum principal strain and strain rate associated with concussion diagnosis correlates with changes in corpus callosum white matter indices.** *Ann Biomed Eng* 2012;40:127–40 CrossRef Medline
4. Patton DA, McIntosh AS, Kleiven S. **The biomechanical determinants of concussion: finite element simulations to investigate tissue-level predictors of injury during sporting impacts to the unprotected head.** *J Appl Biomech* 2015;31:264–68 CrossRef Medline
5. Chung S, Fieremans E, Wang X, et al. **White matter tract integrity: an indicator of axonal pathology after mild traumatic brain injury.** *J Neurotrauma* 2018;35:1015–20 CrossRef Medline
6. Chung S, Chen J, Li T, et al. **Investigating brain white matter in football players with and without concussion using a biophysical model from multishell diffusion MRI.** *AJNR Am J Neuroradiol* 2022;43:823–CrossRef Medline
7. Rutgers DR, Fillard P, Paradot G, et al. **Diffusion tensor imaging characteristics of the corpus callosum in mild, moderate, and severe traumatic brain injury.** *AJNR Am J Neuroradiol* 2008; 29:1730–35 CrossRef Medline
8. Aoki Y, Inokuchi R, Gunshin M, et al. **Diffusion tensor imaging studies of mild traumatic brain injury: a meta-analysis.** *J Neurol Neurosurg Psychiatry* 2012;83:870–76 CrossRef Medline
9. Huynh-Le MP, Tibbs MD, Karunamuni R, et al. **Microstructural injury to corpus callosum and intrahemispheric white matter tracts correlate with attention and processing speed decline after brain radiation.** *Int J Radiat Oncol Biol Phys* 2021;110:337–47 CrossRef Medline
10. Quigley M, Cordes D, Turski P, et al. **Role of the corpus callosum in functional connectivity.** *AJNR Am J Neuroradiol* 2003;24:208–12 Medline
11. Marquez de la Plata CD, Garces J, Shokri Kojori E, et al. **Deficits in functional connectivity of hippocampal and frontal lobe circuits after traumatic axonal injury.** *Arch Neurol* 2011;68:74–84 CrossRef Medline
12. Bai L, Bai G, Wang S, et al. **Strategic white matter injury associated with long-term information processing speed deficits in mild traumatic brain injury.** *Hum Brain Mapp* 2020;41:4431–41 CrossRef Medline
13. Schulte T, Muller-Oehring EM. **Contribution of callosal connections to the interhemispheric integration of visuomotor and cognitive processes.** *Neuropsychol Rev* 2010;20:174–90 CrossRef Medline
14. Bacon JH, Bacon T, Kister I, et al. **Posterior corpus callosum atrophy is correlated with worse performance on inter-hemispheric speed of processing task in unimpaired MS patients.** In: *Proceedings of the Annual Meeting of the American Academy of Neurology*, April 18–25, 2015. Washington, DC: No. 148
15. Bloom JS, Hynd GW. **The role of the corpus callosum in interhemispheric transfer of information: excitation or inhibition?** *Neuropsychol Rev* 2005;15:59–71 CrossRef Medline
16. Basser PJ, Mattiello J, LeBihan D. **Estimation of the effective self-diffusion tensor from the NMR spin echo.** *J Magn Reson B* 1994; 103:247–54 CrossRef Medline
17. Jensen JH, Helpern JA, Ramani A, et al. **Diffusional kurtosis imaging: the quantification of non-gaussian water diffusion by means of magnetic resonance imaging.** *Magn Reson Med* 2005;53:1432–40 CrossRef Medline
18. Novikov DS, Fieremans E, Jespersen SN, et al. **Quantifying brain microstructure with diffusion MRI: theory and parameter estimation.** *NMR Biomed* 2019;32:e3998 CrossRef Medline
19. Coelho S, Baete SH, Lemberskiy G, et al. **Reproducibility of the standard model of diffusion in white matter on clinical MRI systems.** *Neuroimage* 2022;257:119290 CrossRef Medline
20. Jelescu IO, Fieremans E. **Chapter 2 - Sensitivity and specificity of diffusion MRI to neuroinflammatory processes**. In: Cornelia Laule, John D. Port, ed. *Advances in Magnetic Resonance Technology and Applications*. Academic Press; 2023;9: 31–50
21. Coronado-Leija R, Abdollahzadeh A, Lee HH, et al.] **Volume electron microscopy in injured rat brain validates white matter microstructure metrics from diffusion MRI.** *ArXiv* [Preprint]. 2024 Jan 9: arXiv:2310.04608v2 Medline
22. Liao Y, Coelho S, Chen J, et al. **Mapping brain microstructure in vivo in health and disease using diffusion MRI.** *ArXiv* 2023. https://arxiv.org/abs/2307.16386. Accessed January 31, 2024
23. Jelescu IO, Zurek M, Winters KV, et al. **In vivo quantification of demyelination and recovery using compartment-specific diffusion MRI metrics validated by electron microscopy.** *Neuroimage* 2016;132:104–14 CrossRef Medline
24. Jelescu IO, Veraart J, Adisetiyo V, et al. **One diffusion acquisition and different white matter models: how does microstructure change in human early development based on WMTI and NODDI?** *Neuroimage* 2015;107:242–56 CrossRef Medline
25. Hui ES, Fieremans E, Jensen JH, et al. **Stroke assessment with diffusional kurtosis imaging.** *Stroke* 2012;43:2968–73 CrossRef Medline
26. de Kouchkovsky I, Fieremans E, Fleysher L, et al. **Quantification of normal-appearing white matter tract integrity in multiple sclerosis: a diffusion kurtosis imaging study.** *J Neurol* 2016;263:1146–55 CrossRef Medline
27. Chung S, Wang X, Fieremans E, et al. **Altered relationship between working memory and brain microstructure after mild traumatic brain injury.** *AJNR Am J Neuroradiol* 2019;40:1438–44 CrossRef Medline
28. Kim A, Bacon J, Bacon T, et al. **Correlation of quantitative MR metrics of morphology and lesion load with performance on a novel inter-hemispheric speed of processing task in multiple sclerosis patients.** In: *Proceedings of the Annual Meeting of the American Society of Neuroradiology*. April 25–30, 2015. Chicago, Illinois
29. Kay T, Harrington DE, Adams R, et al. **Definition of mild traumatic brain injury.** *J Head Trauma Rehabil* 1993;8:86–87
30. Potter S, Leigh E, Wade D, et al. **The Rivermead Post Concussion Symptoms Questionnaire: a confirmatory factor analysis.** *J Neurol* 2006;253:1603–14 CrossRef Medline
31. Setsompop K, Gagoski BA, Polimeni JR, et al. **Blipped-controlled aliasing in parallel imaging for simultaneous multislice echo planar imaging with reduced g-factor penalty.** *Magn Reson Med* 2012; 67:1210–24 CrossRef Medline
32. Andersson JL, Skare S, Ashburner J. **How to correct susceptibility distortions in spin-echo echo-planar images: application to diffusion tensor imaging.** *Neuroimage* 2003;20:870–88 CrossRef Medline
33. Veraart J, Novikov DS, Christiaens D, et al. **Denoising of diffusion MRI using random matrix theory.** *Neuroimage* 2016;142:394–406 CrossRef Medline
34. Ades-Aron B, Veraart J, Kochunov P, et al. **Evaluation of the accuracy and precision of the diffusion parameter EStImation with Gibbs and NoisE removal pipeline.** *Neuroimage* 2018;183:532–43 CrossRef Medline
35. Lee HH, Novikov DS, Fieremans E. **Removal of partial Fourier-induced Gibbs (RPG) ringing artifacts in MRI.** *Magn Reson Med* 2021;86:2733–50 CrossRef Medline
36. Smith SM, Jenkinson M, Woolrich MW, et al. **Advances in functional and structural MR image analysis and implementation as FSL.** *Neuroimage* 2004;23(Suppl 1):S208–19 CrossRef Medline
37. **Standard Model Imaging (SMI) toolbox.** https://github.com/NYU-DiffusionMRI/SMI. Accessed January 31, 2024
38. Fortin JP, Parker D, Tunc B, et al. **Harmonization of multi-site diffusion tensor imaging data.** *Neuroimage* 2017;161:149–70 CrossRef Medline

39. Johnson WE, Li C, Rabinovic A. **Adjusting batch effects in microarray expression data using empirical Bayes methods.** *Biostatistics* 2007;8:118–27 CrossRef Medline
40. Mori S, Oishi K, Jiang H, et al. **Stereotaxic white matter atlas based on diffusion tensor imaging in an ICBM template.** *Neuroimage* 2008;40:570–82 CrossRef Medline
41. Preacher KJ, Hayes AF. **SPSS and SAS procedures for estimating indirect effects in simple mediation models.** *Behav Res Methods Instrum Comput* 2004;36:717–31 CrossRef Medline
42. Shenton ME, Hamoda HM, Schneiderman JS, et al. **A review of magnetic resonance imaging and diffusion tensor imaging findings in mild traumatic brain injury.** *Brain Imaging Behav* 2012;6:137–92 CrossRef Medline
43. Taquet M, Jankovski A, Rensonnet G, et al. **Extra-axonal restricted diffusion as an in-vivo marker of reactive microglia.** *Sci Rep* 2019;9:13874 CrossRef Medline
44. Grossman EJ, Kirov II, Gonen O, et al. **N-acetyl-aspartate levels correlate with intra-axonal compartment parameters from diffusion MRI.** *Neuroimage* 2015;118:334–43 CrossRef Medline
45. Fieremans E, Benitez A, Jensen JH, et al. **Novel white matter tract integrity metrics sensitive to Alzheimer disease progression.** *AJNR Am J Neuroradiol* 2013;34:2105–12 CrossRef Medline
46. Ingalhalikar M, Smith A, Parker D, et al. **Sex differences in the structural connectome of the human brain.** *Proc Natl Acad Sci U S A* 2014;111:823–28 CrossRef Medline

Functional Connectivity Changes on Resting-State fMRI after Mild Traumatic Brain Injury: A Systematic Review

Siddhant Dogra, Soroush Arabshahi, Jason Wei, Lucia Saidenberg, Stella K. Kang, Sohae Chung, Andrew Laine, and Yvonne W. Lui

ABSTRACT

BACKGROUND: Mild traumatic brain injury is theorized to cause widespread functional changes to the brain. Resting-state fMRI may be able to measure functional connectivity changes after traumatic brain injury, but resting-state fMRI studies are heterogeneous, using numerous techniques to study ROIs across various resting-state networks.

PURPOSE: We systematically reviewed the literature to ascertain whether adult patients who have experienced mild traumatic brain injury show consistent functional connectivity changes on resting-state -fMRI, compared with healthy patients.

DATA SOURCES: We used 5 databases (PubMed, EMBASE, Cochrane Central, Scopus, Web of Science).

STUDY SELECTION: Five databases (PubMed, EMBASE, Cochrane Central, Scopus, and Web of Science) were searched for research published since 2010. Search strategies used keywords of "functional MR imaging" and "mild traumatic brain injury" as well as related terms. All results were screened at the abstract and title levels by 4 reviewers according to predefined inclusion and exclusion criteria. For full-text inclusion, each study was evaluated independently by 2 reviewers, with discordant screening settled by consensus.

DATA ANALYSIS: Data regarding article characteristics, cohort demographics, fMRI scan parameters, data analysis processing software, atlas used, data characteristics, and statistical analysis information were extracted.

DATA SYNTHESIS: Across 66 studies, 80 areas were analyzed 239 times for at least 1 time point, most commonly using independent component analysis. The most analyzed areas and networks were the whole brain, the default mode network, and the salience network. Reported functional connectivity changes varied, though there may be a slight trend toward decreased whole-brain functional connectivity within 1 month of traumatic brain injury and there may be differences based on the time since injury.

LIMITATIONS: Studies of military, sports-related traumatic brain injury, and pediatric patients were excluded. Due to the high number of relevant studies and data heterogeneity, we could not be as granular in the analysis as we would have liked.

CONCLUSIONS: Reported functional connectivity changes varied, even within the same region and network, at least partially reflecting differences in technical parameters, preprocessing software, and analysis methods as well as probable differences in individual injury. There is a need for novel rs-fMRI techniques that better capture subject-specific functional connectivity changes.

ABBREVIATIONS: DMN = default mode network; FC = functional connectivity; ICA = independent component analysis; IQR = interquartile range; mTBI = mild traumatic brain injury; rs-fMRI = resting-state fMRI; SN = salience network; TBI = traumatic brain injury

Mild traumatic brain injury (mTBI) is a common injury that, nevertheless, can pose difficult diagnostic and therapeutic challenges.[1] Conventional neuroimaging including CT and structural MR imaging plays a key role in mTBI assessment and management, such as the identification of intracranial hemorrhage, but it has limited sensitivity for the detection of underlying abnormalities that have no clear macrostructural correlate.[2] Advanced neuroimaging has been used during the past decade in an attempt to characterize more subtle post-mTBI neurobiological changes.

After mTBI, it is believed that disruptions occur in the organization of large-scale brain activity.[2] Blood oxygen level–dependent functional MR imaging has, thus, been used to study changes

Received October 30, 2023; accepted after revision January 22, 2024.

From the Departments of Radiology (S.D., J.W., S.K.K., S.C., Y.L.) and Neurology (L.S.), New York University Grossman School of Medicine, New York, New York; and Department of Biomedical Engineering (S.A., A.L.), Department of Radiology, Columbia University, New York, New York.

Please address correspondence to Yvonne W. Lui, MD, FACR, Department of Radiology, New York University Grossman School of Medicine, 660 First Ave, New York, NY 10016; e-mail: Yvonne.Lui@nyulangone.org; @SidDograMD

Indicates article with online supplemental data.

http://dx.doi.org/10.3174/ajnr.A8204

in intrinsic brain connectivity. In particular, functional connectivity (FC) as reflected in low-frequency blood oxygen level–dependent fluctuations of resting-state fMRI (rs-fMRI),[3] and its organization into various resting-state networks[1,4] has been used in an attempt to understand the injury.

Approximately a decade ago, a comprehensive review of fMRI in mTBI by McDonald et al[1] included a mere 2 studies of resting-state changes following mTBI. Since then, there has been an explosion of literature in this area. Part of the challenge in interpreting these results is the diversity of brain regions and networks studied and the great variety of methods that can be used to analyze FC in rs-fMRI. Common approaches include correlational methods (relying on selections of ROIs and/or seeds and correlating the corresponding rs-fMRI signal time-series with time-series of all other voxels [ROI/seed-to-voxel] or other ROIs/seeds [ROI/seed-to-ROI/seed] to map connectivity[5]) as well as independent component analysis (ICA; decomposition of brain-wide rs-fMRI into independent spatiotemporal components that can be correlated to determine connectivity[6]), both of which may be performed in a static fashion using the entire time-series or in a dynamic fashion using a sliding-window approach. Graph theory can also be used to study FC at either local or global levels.[7] Finally, regional homogeneity is commonly used to measure synchronization of low-frequency fluctuations of a particular voxel with its nearest neighbors,[8] while fractional amplitude of low-frequency fluctuations quantifies low-frequency oscillations as a reflection of local spontaneous activity.[9]

In this systematic review, we explore the current literature on FC in mTBI regarding whether adult patients who have mTBI show consistent FC changes on rs-fMRI, compared with healthy patients. We summarize thematic findings in terms of FC changes following injury and comment on discordances that are observed.

MATERIALS AND METHODS

Database Search

This study was registered with the International Prospective Register of Systematic Reviews (PROSPERO; ID CRD42022360114) and performed as per Preferred Reporting Items for Systematic Reviews and Meta-Analyses of Diagnostic Test Accuracy (PRISMA) guidelines.

In November 2022, five databases ("PubMed," "EMBASE," "Cochrane Central," "Scopus," "Web of Science") were searched for research published since 2010. The search strategy used the keywords "functional MR imaging" and "mild traumatic brain injury" as well as related terms. Search terms can be found in the Online Supplemental Data.

Inclusion criteria were the following: peer-reviewed human research 1) performed in adults older than 18 year of age; 2) written in English; 3) involving the use of rs-fMRI; 4) including a measure of FC; 5) published in or after 2010; and 6) comparing patients with mTBI with healthy controls. Blast/military traumatic brain injury (TBI) was excluded because military-related blast injury has a unique mechanism relating to propagating pressure waves. Sport- and athletic-related injury was also excluded because many such studies occur either in pediatric subjects and/or specifically feature individuals exposed to repetitive head impacts and repeat TBI. Of course, many studies may have included a number of these types of etiologies without distinguishing their results from those of other etiologies. Consequently, we were able to exclude only studies whose entire cohort had one of these mechanisms. Specifically, exclusion criteria were the following: 1) preclinical animal studies; 2) inclusion of pediatric patients younger than 18 years of age; 3) reviews, meta-analyses, books, case reports, or case series; 4) moderate or severe TBI; 5) cohorts of only sports- or athletic-related TBI; 6) cohorts of only blast-related TBI; 7) cohorts of only military TBI; 8) cohorts of only repetitive TBI; and 9) only task-mediated fMRI studies.

All results were screened at the abstract and title levels by 4 reviewers (S.D., S.A., J.W., L.S.) according to predefined inclusion and exclusion criteria. Each study was evaluated independently by 2 reviewers, with discordant screening settled by consensus. Two reviewers (S.D., S.A.) performed full-text data screening and extraction, with disagreements settled by consensus.

Data Extraction and Synthesis

We excluded the following categories: article characteristics (title, author, journal, year), cohort demographics (time since injury, age, sex), fMRI scan parameters (ie, TE, TR, scan duration, scanner model, and magnet strength), data analysis processing software, atlas used, data characteristics (including analysis method applied, studied ROI or network, connectivity measures), and statistical analysis information (method, multiple-comparison correction).

FC changes were graded on an ordinal scale from −2 to +2: −2 and +2 denoting studies reporting only decreases or increases in FC, respectively; −1 and +1 denoting studies reporting mixed results with most areas showing decreased or increased FC, respectively; and 0 if no changes were reported. If there were an equal number of areas with increased and decreased changes, we assigned an ordinal score of 0 but noted that there was equal change in each direction.

For all studies, time since mTBI was binned into either <1 month, 1–6 months, or >6 months, with some studies having multiple evaluations at different time points. For these studies, results were examined separately for each of these time periods.

Of note, in some cases, the whole brain was evaluated by ICA, and several resting-state networks were subsequently identified as independent components. In most such cases, the identified components were specific named resting-state networks; for these studies, we report the individual networks and their changes, as well as the whole brain and its change as a conglomeration of the network changes.

Risk of bias and applicability were assessed by 3 reviewers (S.D., S.A., J.W.). Each study was evaluated by 2 reviewers with disagreements settled by consensus. The case-control version of Newcastle-Ottawa Scale was used for this assessment.[10]

RESULTS

Our initial search found 10,946 results, 2405 of which were duplicates and were removed before screening. The remaining 8541 underwent title and abstract screening from which 107 results were considered for full-text review. Four of these could not be

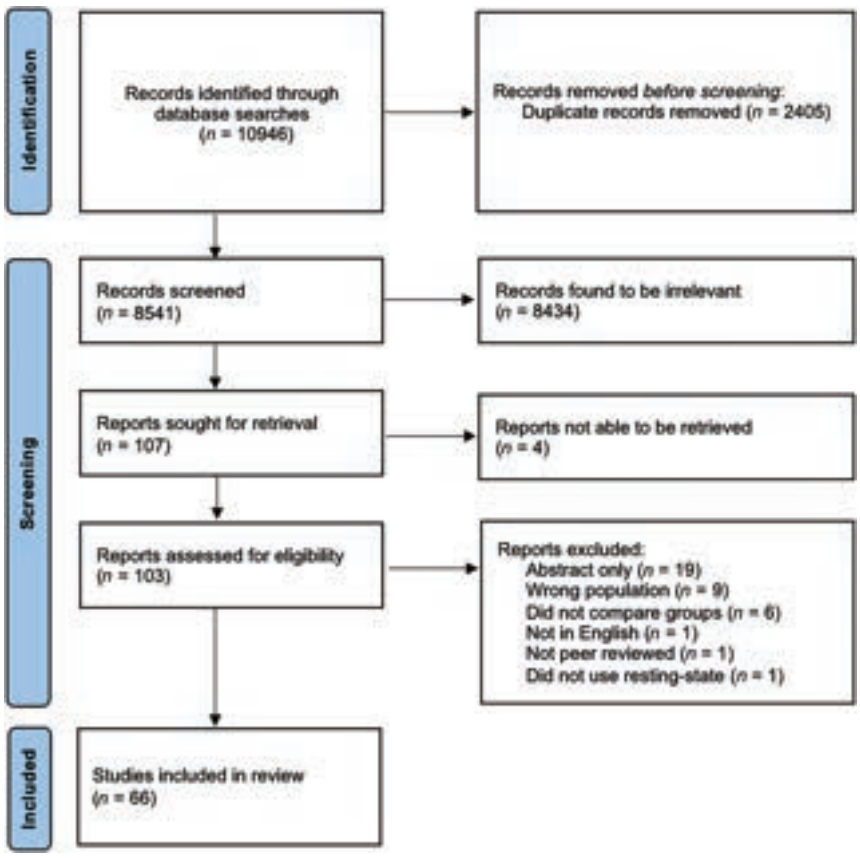

FIG 1. PRISMA flow diagram detailing study identification, screening, and inclusion.

found online and may have been abstracts or conference papers. Among the 103 remaining results, 19 were only abstracts and 18 did not meet the criteria for inclusion (9 studied the wrong population, 6 did not compare with a healthy control group, 1 was not in English, 1 was not peer-reviewed, and 1 was not an rs-fMRI study). Full-text data extraction was ultimately performed for 66 studies (Fig 1).[2,4,8,11-73] A summary of these articles can be found in the Online Supplemental Data.

Risk of Bias

The case-control version of the Newcastle-Ottawa Scale was used for assessment of the risk of bias. Representativeness of cases for Shumskaya et al[70] was thought to have unclear applicability because only fronto-occipital injuries were included. Otherwise, there was appropriate selection, comparability, and exposure for all studies, because subjects with and without mTBI were clearly distinguishable and verified through interview.

Cohort Characteristics and Technical Parameters

These studies included a median of 31 healthy controls (interquartile range [IQR], 20–42). Depending on the time since mTBI was evaluated in the study, studies with subjects scanned within 1 month of mTBI included a median of 48 (IQR, 28.5–56.5) subjects, studies with subjects scanned between 1 and 6 months of mTBI included a median of 25 (IQR, 23–42) subjects, and studies with subjects scanned >6 months from mTBI included a median of 28 (IQR, 20.5–50) subjects. Thirty-eight of 66 (57.6%) studies did not specify the mechanisms of mTBI. Among the 28 that did, traffic/motor vehicle collisions were by far the most common etiology (18/28, 64.3%).

On average, the healthy control cohort consisted of a mean of 47.6% women (SD, 12.6%) with a mean age of 36.6 (SD, 6.7) years, and the mTBI cohort consisted of 43.6% women (SD, 14.3%) with a mean age of 36.6 (SD, 7.0) years.

Regarding the MR imaging scanner, 60 studies (90.9%) used a 3T magnet, 5 studies (7.6%) used a 1.5T magnet, and one (1.5%) did not specify the magnet strength. The mean TE and TR were 29.1 (SD, 4.4) ms and 2082.1 (SD, 308) ms. The mean rs-fMRI duration was 7.4 (SD, 2.5) minutes.

Processing software used across all the studies varied from statistical parametric mapping (SPM, Versions 5, 6, 8, 12; http://www.fil.ion.ucl.ac.uk/spm/software/spm12), FMRIB Software Library (FSL; http://www.fmrib.ox.ac.uk/fsl), Group ICA of fMRI Toolbox Software (GIFT; http://mialab.mrn.org/software/gift/), Analysis of Functional NeuroImages (AFNI; http://afni.nimh.nih.gov/), medInria (https://med.inria.fr/), Data Processing & Analysis of Brain Imaging (DPABI; http://rfmri.org/DPABI), FreeSurfer (https://surfer.nmr.mgh.harvard.edu/fswiki/DownloadAndInstall), the graph theoretical network analysis (GRETNA; https://www.nitrc.org/projects/gretna/) toolbox, to the Resting-State fMRI Data Analysis Toolkit (REST; http://rfmri.org/REST).

Connectivity Changes

Across 66 studies, 80 distinct areas were collectively analyzed 239 times at least at 1 time point (Online Supplemental Data). Sixteen analyses included multiple time points (<1 month between mTBI and the scan, 1–6 months, and >6 months) (Online Supplemental Data). The most common analysis approaches used were ICA ($n = 106$), ROI/seed-to-ROI/seed ($n = 62$), and ROI/seed-to-voxel ($n = 32$), followed distantly by graph theory methods ($n = 17$, Online Supplemental Data), ICA-based dynamic FC ($n = 14$), regional homogeneity ($n = 4$), and fractional amplitude of low-frequency fluctuations ($n = 4$).

The most-commonly analyzed areas and networks were the whole brain (45 analyses across 37 studies), the default mode network (DMN) (32 analyses across 25 studies), and the salience network (SN, 13 analyses across 10 studies). Studies that separately analyzed patients with and without postconcussive symptoms are explicitly labeled in Supplementary Table 2 (Online Supplementary Data).

Figure 2 shows panels of histograms of FC changes in the whole brain, the DMN, and the SN, with respect to scans performed <1 month since mTBI, 1–6 months since mTBI, and

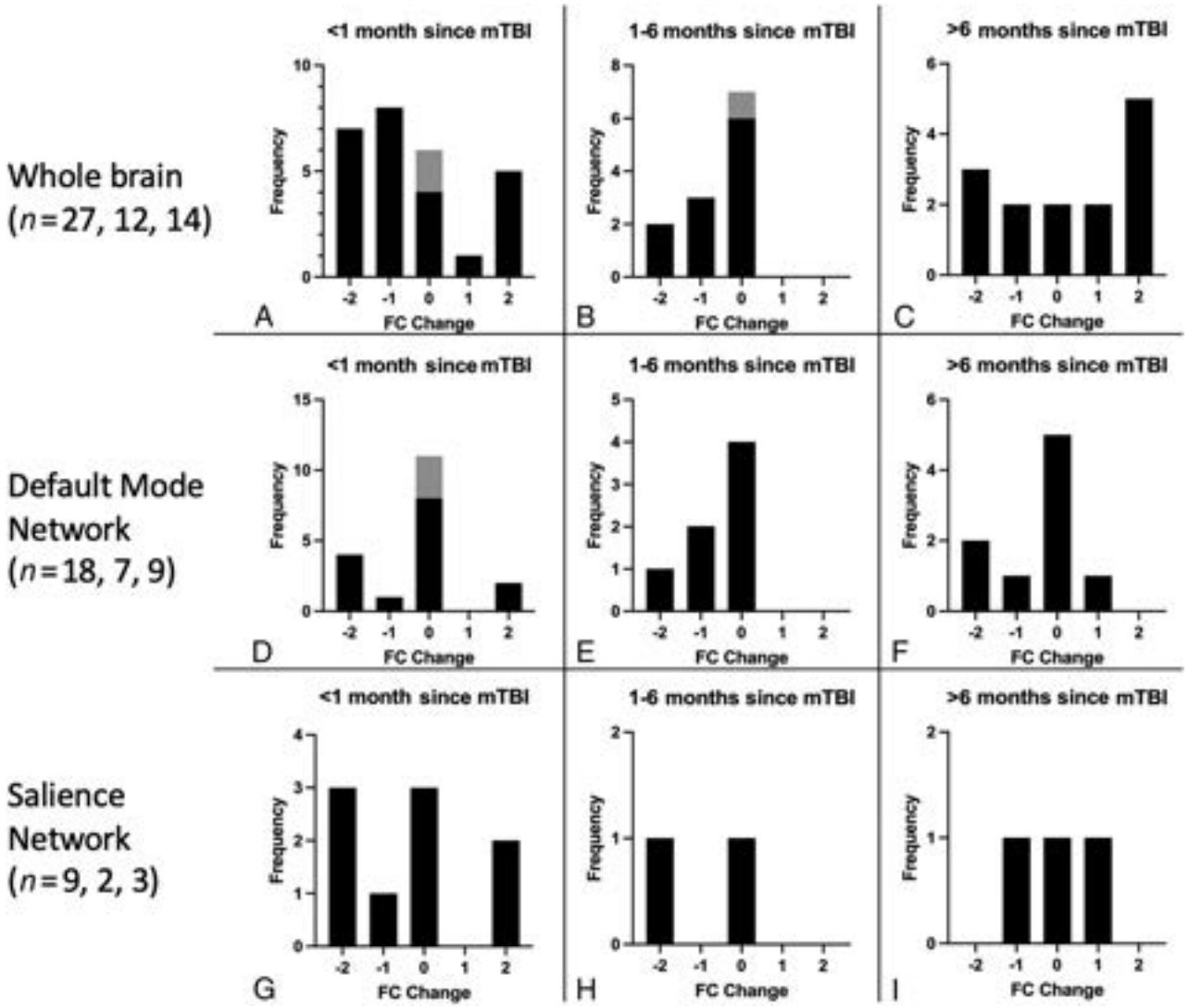

FIG 2. FC changes, categorized on an ordinal scale and separated by the time since injury. −2 = only decreased FC changes, −1 = more areas of decreased FC change than areas of increased FC change, 0 = no FC changes (*black*) or the same number of areas of decreased and increased FC (*gray*), 1 = more areas of increased FC change, 2 = only areas of increased FC changes (changes all relative to results in healthy controls). *Gray bars* are separate from *black bars*, ie, 3 studies found an equal number of areas of increased and decreased FC in the DMN at <1 month. Eight found no changes, so a total of 11 studies were classified as a 0.

>6 months since mTBI. By comparing the left half of each plot (frequencies of −2 and −1) with the right half (frequencies of 1 and 2), we can get a sense of the relative frequency of decreased-versus-increased FC. For example, <1 month after mTBI, there were 9 more analyses that found decreased FC across the whole brain compared with increased FC (7, −2 studies; 8, −1 study; 1, +1 study; and 5, +2 studies), possibly suggesting a trend toward decreased whole-brain FC acutely after mTBI. These changes may persist 1–6 months post-mTBI in the whole brain, whereas there are 5 studies that found decreased FC versus none with increased FC. At >6 months in the whole brain, as well as all time points with the DMN and SN, the differences are not as robust.

DISCUSSION

In the past decade, many more approaches to studying mTBI using rs-fMRI have been developed and applied. The 2012 review of McDonald et al[1] found only 2 studies evaluating the effect of mTBI on resting-state FC, one of which looked at the thalamus with ROI-to-voxel and ICA approaches and another that looked at the DMN and the task-related network with an ROI-to-ROI approach.[4,72] In comparison, this present review includes 66 studies using any of 9 analysis methods to study a total of 61 distinct areas, demonstrating how much the literature has grown in the interim.

In part, because of this growth, the data we reviewed show immense heterogeneity with respect to FC changes, even among studies that evaluate the same networks or ROIs using the same techniques in the same timeframe since injury. Most reassuring, control and mTBI groups, on average, were similar in both age and sex distribution, and nearly all studies were performed on 3T magnets. Besides variability in methods as noted above, probably one of the most challenging aspects of studying mTBI arises from the heterogeneity of the injury itself and the manifestations of

injury. This issue continues to plague the field because injured individuals are inherently difficult to categorize. In addition, another source of variability among studies likely arises from technical sources such as scan parameters, preprocessing methods, brain atlas selected, and so forth.

When analyzing FC changes, we focused on 3 main regions: the whole brain, DMN, and SN, because these were the most widely studied. There was a slight predilection toward decreased whole-brain FC early after mTBI (<1 month of injury), though the heterogeneity of the results precludes drawing any strong conclusion. Also, there was no definite trend across time, though more studies showed decreased FC within 1 month of injury compared with 1–6 months or >6 months after injury, suggesting that perhaps functional hypoconnectivity is the dominant response immediately following mTBI and is followed by recovery with time.

The underlying neurophysiologic changes following mTBI are not yet fully characterized, so it is difficult to confidently identify a biological basis for acute hypoconnectivity. Increasing evidence points to cerebrovascular injury as a key hallmark of mTBI, characterized by disrupted cerebrovascular reactivity and neurovascular coupling.[74] Studies using arterial spin-labeling to quantify CBF after mTBI report inconsistent findings, with suggested reduced CBF acutely after injury and varied responses in the subacute phase, similar to our findings regarding FC after mTBI.[75] Because cerebrovascular disease is known to influence network connectivity, there may be a link between FC changes and CBF changes.[76] In any case, it is clearly possible that there is a temporal evolution of connectivity changes across time after injury, and this is reflected in the literature.

Limitations include exclusion of studies consisting entirely of military, sports-related mTBI, and pediatric patients. Moreover, some studies included a small number of participants with sports-related mTBI; we were unable to exclude FC changes from only these specific subjects, so they do contribute to our results. Second, due to the high data heterogeneity, we could not be as granular as we would have liked. For example, we were forced to bin FC changes into arbitrary temporal categories, which likely limit our view of temporal changes after injury. It is certainly possible that there are more nuanced temporal changes within or across these bins that were not feasible to capture; and, in fact, the current results suggest that this possibility may be true. Similarly, for the sake of practicality, we present FC changes on an ordinal scale based on the number of regions within each study found to show FC changes; however, this particular metric may not well-capture FC changes in mTBI. We also were not able to report the location of FC changes due to the amount of data analyzed. Finally, we did not perform subgroup analyses on patients with persistent symptoms, though the Online Supplementary Data do include information on studies that looked at ROIs/networks in asymptomatic-versus-symptomatic patients. We hope that our conglomerated data summary makes it easier for future investigations to identify and analyze subsets of these studies to answer more focused questions.

CONCLUSIONS

rs-fMRI is a noninvasive method to study FC of the brain that has been increasingly applied over the past decade to understand underlying functional brain alterations after mTBI. Due to a variegated landscape of rs-fMRI analysis methods and the still relatively naive understanding we have of mTBI, we find immense heterogeneity in the literature. We see a slight tendency toward decreased whole-brain FC within 1 month of mTBI, though group-based fMRI analysis at the present time does not easily reveal clear concordance among published studies. This issue may relate to a combination of underlying heterogeneity in the mTBI population as well as current limitations of rs-fMRI group-wise analysis methods. As a result, the present study is also limited in its ability to parse temporal differences and nuanced changes in connectivity across studies. There is a need for an improved description of subjects with mTBI as well as new rs-fMRI approaches that better capture subject-specific alterations of brain connectivity.

Disclosure forms provided by the authors are available with the full text and PDF of this article at www.ajnr.org.

REFERENCES

1. McDonald BC, Saykin AJ, McAllister TW. **Functional MRI of mild traumatic brain injury (mTBI): progress and perspectives from the first decade of studies.** *Brain Imaging Behav* 2012;6:193–207 CrossRef Medline
2. Stevens MC, Lovejoy D, Kim J, et al. **Multiple resting state network functional connectivity abnormalities in mild traumatic brain injury.** *Brain Imaging Behav* 2012;6:293–318 CrossRef Medline
3. Biswal B, Yetkin FZ, Haughton VM, et al. **Functional connectivity in the motor cortex of resting human brain using echo-planar MRI.** *Magn Reson Med* 1995;34:537–41 CrossRef Medline
4. Mayer AR, Mannell MV, Ling J, et al. **Functional connectivity in mild traumatic brain injury.** *Hum Brain Mapp* 2011;32:1825–35 CrossRef Medline
5. Seewoo BJ, Joos AC, Feindel KW. **An analytical workflow for seed-based correlation and independent component analysis in interventional resting-state fMRI studies.** *Neurosci Res* 2021;165:26–37 CrossRef Medline
6. Kelly RE, Wang Z, Alexopoulos GS, et al. **Hybrid ICA-seed-based methods for fMRI functional connectivity assessment: a feasibility study.** *Int J Biomed Imaging* 2010;2010:868976 CrossRef Medline
7. Farahani FV, Karwowski W, Lighthall NR. **Application of graph theory for identifying connectivity patterns in human brain networks: a systematic review.** *Front Neurosci* 2019;13:585 CrossRef Medline
8. Vedaei F, Newberg AB, Alizadeh M, et al. **Resting-state functional MRI metrics in patients with chronic mild traumatic brain injury and their association with clinical cognitive performance.** *Front Hum Neurosci* 2021;15:768485 CrossRef Medline
9. Zou QH, Zhu CZ, Yang Y, et al. **An improved approach to detection of Amplitude of Low-Frequency Fluctuations (ALFF) for resting-state fMRI: fractional ALFF.** *J Neurosci Methods* 2008;172:137–41 CrossRef Medline
10. Wells GA, Shea B, O'Connell D, et al. **The Newcastle-Ottawa Scale (NOS) for assessing the quality of nonrandomised studies in meta-analyses**. The Ottowa Hospital Research Institute, 2021. https://www.ohri.ca/programs/clinical_epidemiology/oxford.asp. Accessed October 29, 2023
11. Bittencourt M, van der Horn HJ, Balart-Sanchez SA, et al. **Effects of mild traumatic brain injury on resting state brain network connectivity in older adults.** *Brain Imaging Behav* 2022;16:1863–72 CrossRef Medline
12. Kim E, Seo HG, Seong MY, et al. **An exploratory study on functional connectivity after mild traumatic brain injury: preserved global but altered local organization.** *Brain Behav* 2022;12:e2735 CrossRef Medline

13. Li F, Liu Y, Lu L, et al. **Rich-club reorganization of functional brain networks in acute mild traumatic brain injury with cognitive impairment.** *Quant Imaging Med Surg* 2022;12:3932–46 CrossRef Medline
14. Li W, Ding S, Zhao G. **Static and dynamic topological organization of brain functional connectome in acute mild traumatic brain injury.** *Acta Radiol* 2022;64:1175–83 CrossRef Medline
15. Lu L, Zhang J, Li F, et al. **Aberrant static and dynamic functional network connectivity in acute mild traumatic brain injury with cognitive impairment.** *Clin Neuroradiol* 2022;32:205–14 CrossRef Medline
16. Amir J, Nair JK, Del Carpio-O'Donovan R, et al. **Atypical resting state functional connectivity in mild traumatic brain injury**. *Brain Behav* 2021;11:e2261 CrossRef Medline
17. Bajaj S, Raikes AC, Razi A, et al. **Blue-light therapy strengthens resting-state effective connectivity within default-mode network after mild TBI.** *J Cent Nerv Syst Dis* 2021;13:11795735211015076 CrossRef Medline
18. Bittencourt-Villalpando M, van der Horn HJ, Maurits NM, et al. **Disentangling the effects of age and mild traumatic brain injury on brain network connectivity: a resting state fMRI study.** *Neuroimage Clin* 2021;29:102534 CrossRef Medline
19. Jia X, Chang X, Bai L, et al. **A longitudinal study of white matter functional network in mild traumatic brain injury.** *J Neurotrauma* 2021;38:2686–97 CrossRef Medline
20. Shi J, Teng J, Du X, et al. **Multi-modal analysis of resting-state fMRI data in mTBI patients and association with neuropsychological outcomes.** *Front Neurol* 2021;12:639760 CrossRef Medline
21. Sun Y, Wang S, Gan S, et al. **Serum neuron-specific enolase levels associated with connectivity alterations in anterior default mode network after mild traumatic brain injury.** *J Neurotrauma* 2021;38:1495–505 CrossRef Medline
22. Wang T, Hu Y, Wang D, et al. **Arcuate fasciculus subsegment impairments distinctly associated with memory and language deficits in acute mild traumatic brain injury patients.** *J Neurotrauma* 2021;38:3279–87 CrossRef Medline
23. Wang Z, Zhang M, Sun C, et al. **Single mild traumatic brain injury deteriorates progressive interhemispheric functional and structural connectivity.** *J Neurotrauma* 2021;38:464–73 CrossRef Medline
24. Zhang D, Zhu P, Yin B, et al. **Frontal white matter hyperintensities effect on default mode network connectivity in acute mild traumatic brain injury.** *Front Aging Neurosci* 2021;13:793491 CrossRef Medline
25. D'Souza MM, Kumar M, Choudhary A, et al. **Alterations of connectivity patterns in functional brain networks in patients with mild traumatic brain injury: a longitudinal resting-state functional magnetic resonance imaging study**. *Neuroradiol J* 2020;33:186–97 CrossRef Medline
26. Li F, Lu L, Chen H, et al. **Neuroanatomical and functional alterations of insula in mild traumatic brain injury patients at the acute stage.** *Brain Imaging Behav* 2020;14:907–16 CrossRef Medline
27. Li F, Lu L, Shang S, et al. **Disrupted functional network connectivity predicts cognitive impairment after acute mild traumatic brain injury.** *CNS Neurosci Ther* 2020;26:1083–91 CrossRef Medline
28. Liu Y, Wu W, Chen X, et al. **Aberrant correlation between the default mode and salience networks in mild traumatic brain injury.** *Front Comput Neurosci* 2020;14:68 CrossRef Medline
29. Lu L, Li F, Chen H, et al. **Functional connectivity dysfunction of insular subdivisions in cognitive impairment after acute mild traumatic brain injury.** *Brain Imaging Behav* 2020;14:941–48 CrossRef Medline
30. Lu L, Li F, Wang P, et al. **Altered hypothalamic functional connectivity in post-traumatic headache after mild traumatic brain injury.** *J Headache Pain* 2020;21:93 CrossRef Medline
31. Shafi R, Crawley AP, Tartaglia MC, et al. **Sex-specific differences in resting-state functional connectivity of large-scale networks in postconcussion syndrome.** *Sci Rep* 2020;10:21982 CrossRef Medline
32. Chong CD, Wang L, Wang K, et al. **Homotopic region connectivity during concussion recovery: a longitudinal fMRI study.** *PLoS One* 2019;14:e0221892 CrossRef Medline
33. Hou W, Sours Rhodes C, Jiang L, et al. **Dynamic functional network analysis in mild traumatic brain injury.** *Brain Connect* 2019;9:475–87 CrossRef Medline
34. Kuceyeski AF, Jamison KW, Owen JP, et al. **Longitudinal increases in structural connectome segregation and functional connectome integration are associated with better recovery after mild TBI.** *Hum Brain Mapp* 2019;40:4441–56 CrossRef Medline
35. Li F, Lu L, Chen H, et al. **Disrupted brain functional hub and causal connectivity in acute mild traumatic brain injury.** *Aging (Albany NY)* 2019;11:10684–96 CrossRef Medline
36. Lu L, Li F, Ma Y, et al. **Functional connectivity disruption of the substantia nigra associated with cognitive impairment in acute mild traumatic brain injury.** *Eur J Radiol* 2019;114:69–75 CrossRef Medline
37. Niu X, Bai L, Sun Y, et al. **Disruption of periaqueductal grey-default mode network functional connectivity predicts persistent post-traumatic headache in mild traumatic brain injury.** *J Neurol Neurosurg Psychiatry* 2019;90:326–32 CrossRef Medline
38. Dailey NS, Smith R, Vanuk JR, et al. **Resting-state functional connectivity as a biomarker of aggression in mild traumatic brain injury.** *Neuroreport* 2018;29:1413–17 CrossRef Medline
39. Wang S, Hu L, Cao J, et al. **Sex differences in abnormal intrinsic functional connectivity after acute mild traumatic brain injury.** *Front Neural Circuits* 2018;12:107 CrossRef Medline
40. Xu H, Wang X, Chen Z, et al. **Longitudinal changes of caudate-based resting state functional connectivity in mild traumatic brain injury.** *Front Neurol* 2018;9:467 CrossRef Medline
41. Dall'Acqua P, Johannes S, Mica L, et al. **Functional and structural network recovery after mild traumatic brain injury: a 1-year longitudinal study**. *Front Hum Neurosci* 2017;11:280 CrossRef Medline
42. Palacios EM, Yuh EL, Chang YS, et al. **Resting-state functional connectivity alterations associated with six-month outcomes in mild traumatic brain injury.** *J Neurotrauma* 2017;34:1546–57 CrossRef Medline
43. Rajesh A, Cooke GE, Monti JM, et al. **Differences in brain architecture in remote mild traumatic brain injury.** *J Neurotrauma* 2017;34:3280–87 CrossRef Medline
44. van der Horn HJ, Liemburg EJ, Scheenen ME, et al. **Graph analysis of functional brain networks in patients with mild traumatic brain injury.** *PLoS One* 2017;12:e0171031 CrossRef Medline
45. van der Horn HJ, Scheenen ME, de Koning ME, et al. **The default mode network as a biomarker of persistent complaints after mild traumatic brain injury: a longitudinal functional magnetic resonance imaging study.** *J Neurotrauma* 2017;34:3262–69 CrossRef Medline
46. Vergara VM, Mayer AR, Kiehl KA, et al. **Dynamic functional network connectivity discriminates mild traumatic brain injury through machine learning.** *Neuroimage Clin* 2018;19:30–37 CrossRef Medline
47. Vergara VM, Mayer AR, Damaraju E, et al. **Detection of mild traumatic brain injury by machine learning classification using resting state functional network connectivity and fractional anisotropy.** *J Neurotrauma* 2017;34:1045–53 CrossRef Medline
48. Yan H, Sun C, Wang X, et al. **Deteriorating neural connectivity of the hippocampal episodic memory network in mTBI patients: a cohort study**. In: *Proceedings of the International Joint Conference on Neural Networks*, May 14–19; 2017:2979–86. Anchorage, Alaska
49. Yan Y, Song J, Xu G, et al. **Correlation between standardized assessment of concussion scores and small-world brain network in mild traumatic brain injury.** *J Clin Neurosci* 2017;44:114–21 CrossRef Medline
50. Zhou Y. **Abnormal structural and functional hypothalamic connectivity in mild traumatic brain injury.** *J Magn Reson Imaging* 2017;45:1105–12 CrossRef Medline

51. Astafiev SV, Zinn KL, Shulman GL, et al. **Exploring the physiological correlates of chronic mild traumatic brain injury symptoms.** *Neuroimage Clin* 2016;11:10–19 CrossRef Medline
52. Banks SD, Coronado RA, Clemons LR, et al. **Thalamic functional connectivity in mild traumatic brain injury: longitudinal associations with patient-reported outcomes and neuropsychological tests.** *Arch Phys Med Rehabil* 2016;97:1254–61 CrossRef Medline
53. Iraji A, Chen H, Wiseman N, et al. **Compensation through functional hyperconnectivity: A longitudinal connectome assessment of mild traumatic brain injury.** *Neural Plast* 2016;2016:4072402 CrossRef Medline
54. Nordin LE, Moller MC, Julin P, et al. **Post mTBI fatigue is associated with abnormal brain functional connectivity.** *Sci Rep* 2016;6:21183 CrossRef Medline
55. van der Horn HJ, Liemburg EJ, Scheenen ME, et al. **Brain network dysregulation, emotion, and complaints after mild traumatic brain injury.** *Hum Brain Mapp* 2016;37:1645–54 CrossRef Medline
56. Xiong KL, Zhang JN, Zhang YL, et al. **Brain functional connectivity and cognition in mild traumatic brain injury.** *Neuroradiology* 2016;58:733–39 CrossRef Medline
57. Yan H, Feng Y, Wang Q. **Altered effective connectivity of hippocampus-dependent episodic memory network in mTBI survivors.** *Neural Plast* 2016;2016:6353845 CrossRef Medline
58. Bharath RD, Munivenkatappa A, Gohel S, et al. **Recovery of resting brain connectivity ensuing mild traumatic brain injury.** *Front Hum Neurosci* 2015;9:513 CrossRef Medline
59. Iraji A, Benson RR, Welch RD, et al. **Resting state functional connectivity in mild traumatic brain injury at the acute stage: independent component and seed-based analyses.** *J Neurotrauma* 2015;32:1031–45 CrossRef Medline
60. Mayer AR, Ling JM, Allen EA, et al. **Static and dynamic intrinsic connectivity following mild traumatic brain injury.** *J Neurotrauma* 2015;32:1046–55 CrossRef Medline
61. Sours C, Chen H, Roys S, et al. **Investigation of multiple frequency ranges using discrete wavelet decomposition of resting-state functional connectivity in mild traumatic brain injury patients.** *Brain Connect* 2015;5:442–50 CrossRef Medline
62. Sours C, George E, Zhuo JC, et al. **Hyper-connectivity of the thalamus during early stages following mild traumatic brain injury.** *Brain Imaging Behav* 2015;9:550–63 CrossRef Medline
63. Sours C, Rosenberg J, Kane R, et al. **Associations between interhemispheric functional connectivity and the Automated Neuropsychological Assessment Metrics (ANAM) in civilian mild TBI.** *Brain Imaging Behav* 2015;9:190–203 CrossRef Medline
64. Sours C, Zhuo J, Roys S, et al. **Disruptions in resting state functional connectivity and cerebral blood flow in mild traumatic brain injury patients.** *PLoS One* 2015;10:e0134019 CrossRef Medline
65. Vergara VM, Damaraju E, Mayer AB, et al. **The impact of data preprocessing in traumatic brain injury detection using functional magnetic resonance imaging.** In: *Proceedings of the Annual International Conference of the IEEE Engineering in Medicine and Biology Society*, August 25–29, 2015:5432–35 Milan, Italy
66. Zhan J, Gao L, Zhou F, et al. **Decreased regional homogeneity in patients with acute mild traumatic brain injury: a resting-state fMRI study.** *J Nerv Ment Dis* 2015;203:786–91 CrossRef Medline
67. Zhou Y, Lui YW, Zuo XN, et al. **Characterization of thalamo-cortical association using amplitude and connectivity of functional MRI in mild traumatic brain injury.** *J Magn Reson Imaging* 2014;39:1558–68 CrossRef Medline
68. Messe A, Caplain S, Pelegrini-Issac M, et al. **Specific and evolving resting-state network alterations in post-concussion syndrome following mild traumatic brain injury.** *PLoS One* 2013;8:e65470 CrossRef Medline
69. Sours C, Zhuo J, Janowich J, et al. **Default mode network interference in mild traumatic brain injury: a pilot resting state study.** *Brain Res* 2013;1537:201–15 CrossRef Medline
70. Shumskaya E, Andriessen T, Norris DG, et al. **Abnormal whole-brain functional networks in homogeneous acute mild traumatic brain injury.** *Neurology* 2012;79:175–82 CrossRef Medline
71. Zhou Y, Milham MP, Lui YW, et al. **Default-mode network disruption in mild traumatic brain injury.** *Radiology* 2012;265:882–92 CrossRef Medline
72. Tang L, Ge Y, Sodickson DK, et al. **Thalamic resting-state functional networks: disruption in patients with mild traumatic brain injury.** *Radiology* 2011;260:831–40 CrossRef Medline
73. Wang S, Gan S, Yang X, et al. **Decoupling of structural and functional connectivity in hubs and cognitive impairment after mild traumatic brain injury.** *Brain Connect* 2021;11:745–58 CrossRef Medline
74. Sullivan DR. **A cerebrovascular hypothesis of neurodegeneration in mTBI.** *J Head Trauma Rehabil* 2019;34:E18–27 CrossRef Medline
75. Baker TL, Agoston DV, Brady RD, et al. **Targeting the cerebrovascular system: next-generation biomarkers and treatment for mild traumatic brain injury.** *Neuroscientist* 2021;28:594–612 CrossRef Medline
76. Chong JS, Liu S, Loke YM, et al. **Influence of cerebrovascular disease on brain networks in prodromal and clinical Alzheimer's disease**. *Brain* 2017;140:3012–22 CrossRef Medline

Structural Brain MR Imaging Alterations in Patients with Systemic Lupus Erythematosus with and without Neuropsychiatric Events

Sebastiano Vacca, Michele Porcu, Matteo Piga, Lorenzo Mannelli, Elisabetta Chessa, Jasjit S. Suri, Antonella Balestrieri, Alberto Cauli, and Luca Saba

ABSTRACT

BACKGROUND AND PURPOSE: Systemic lupus erythematosus is a complex autoimmune disease known for its diverse clinical manifestations, including neuropsychiatric systemic lupus erythematosus, which impacts a patient's quality of life. Our aim was to explore the relationships among brain MR imaging morphometric findings, neuropsychiatric events, and laboratory values in patients with systemic lupus erythematosus, shedding light on potential volumetric biomarkers and diagnostic indicators for neuropsychiatric systemic lupus erythematosus.

MATERIALS AND METHODS: Twenty-seven patients with systemic lupus erythematosus (14 with neuropsychiatric systemic lupus erythematosus, 13 with systemic lupus erythematosus), 24 women and 3 men (average age, 43 years, ranging from 21 to 62 years) were included in this cross-sectional study, along with 10 neuropsychiatric patients as controls. An MR imaging morphometric analysis, with the VolBrain online platform, to quantitatively assess brain structural features and their differences between patients with neuropsychiatric systemic lupus erythematosus and systemic lupus erythematosus, was performed. Correlations and differences between MR imaging morphometric findings and laboratory values, including disease activity scores, such as the Systemic Lupus Erythematosus Disease Activity Index and the Systemic Lupus International Collaborating Clinics Damage Index, were explored. An ordinary least squares regression analysis further explored the Systemic Lupus Erythematosus Disease Activity Index and Systemic Lupus International Collaborating Clinics Damage Index relationship with MR imaging features.

RESULTS: For neuropsychiatric systemic lupus erythematosus and non-neuropsychiatric systemic lupus erythematosus, the brain regions with the largest difference in volumetric measurements were the insular central operculum volume (P value = .003) and the occipital cortex thickness (P = .003), which were lower in neuropsychiatric systemic lupus erythematosus. The partial correlation analysis showed that the most correlated morphometric features with neuropsychiatric systemic lupus erythematosus were subcallosal area thickness asymmetry (P < .001) and temporal pole thickness asymmetry (P = .011). The ordinary least squares regression analysis yielded an R^2 of 0.725 for the Systemic Lupus Erythematosus Disease Activity Index score, with calcarine cortex volume as a significant predictor, and an R^2 of 0.715 for the Systemic Lupus International Collaborating Clinics Damage Index score, with medial postcentral gyrus volume as a significant predictor.

CONCLUSIONS: The MR imaging volumetric analysis, along with the correlation study and the ordinary least squares regression analysis, revealed significant differences in brain regions and their characteristics between patients with neuropsychiatric systemic lupus erythematosus and those with systemic lupus erythematosus, as well as between patients with different Systemic Lupus Erythematosus Disease Activity Index and Systemic Lupus International Collaborating Clinics Damage Index scores.

ABBREVIATIONS: Ang = angular gyrus; APS = antiphospholipid syndrome; C3 = complement component 3; C4 = complement component 4; Calc = calcarine cortex; norm = normalized; NP = neuropsychiatric; NPSLE = neuropsychiatric systemic lupus erythematosus; OCP = occipital cortex; OLS = ordinary least squares; PGA = Physician Global Assessment; SCA = subcallosal area; SLE = systemic lupus erythematosus; SLEDAI = Systemic Lupus Erythematosus Disease Activity Index; SLICC-DI = The Systemic Lupus Erythematosus International Collaborating Clinic Damage Index/American College of Rheumatology Damage Index; TMP = temporal pole; WMH = white matter hyperintensities

Systemic lupus erythematosus (SLE) is a complex autoimmune disease, characterized by a dysregulated immune system that leads to chronic inflammation and the potential for multiorgan involvement,[1] affecting 5.14 (range, 1.4–15.13) per 100,000 person-years and 0.40 million annually, respectively.[2,3] SLE more

Received November 9, 2023; accepted after revision January 18, 2024.

From the School of Medicine and Surgery (S.V.) and Department of Medical Science and Public Health (M. Piga, A.B., A.C.), University of Cagliari, Cagliari, Italy; Department of Radiology (M. Porcu, A.B., L.S.) and Rheumatology Unit (M. Piga, E.C., A.C.), Azienda Ospedaliero-Universitaria, Cagliari, Italy; Institute for Hospitalization and Healthcare (L.M.), SYNLAB istituto di Diagnostica Nucleare, Napoli, Italy; and Stroke Monitoring and Diagnostic Division (J.S.S.), AtheroPoint, Roseville, California.

Please address correspondence to Luca Saba, MD, Department of Radiology, Azienda Ospedaliero-Universitaria, di Cagliari—Polo di Monserrato, Cagliari, Italy; e-mail: lucasaba@tiscali.it

Indicates article with online supplemental data.

http://dx.doi.org/10.3174/ajnr.A8200

frequently affects the musculoskeletal system and skin, but it can also manifest as neuropsychiatric events,[4] causing significant mortality and morbidity, accounting for up to 19% of deaths in patients with SLE,[5] while impairing patients' quality of life. The etiology of neuropsychiatric SLE (NPSLE) remains poorly understood, and the identification of reliable biomarkers would be crucial for early diagnosis, prognosis, and therapeutic intervention.[6]

Advances in medical imaging techniques, particularly MR imaging of the brain, have provided valuable insights into the structural and functional alterations associated with NPSLE.[7-11] MR imaging allows noninvasive visualization of brain structures and facilitates the detection of abnormalities that may contribute to the development of neuropsychiatric symptoms in patients with lupus. Despite imaging advancements, there is still little consensus on the association of MR imaging measurements and the clinical side of NPSLE.

The diversity of neuropsychiatric manifestations in lupus presents significant diagnostic challenges. These manifestations can range from mild cognitive dysfunction to severe disorders, including psychosis, mood disorders, seizures, and cerebrovascular events.[12-14] Moreover, these symptoms may be unrelated to SLE and represent primary psychiatric conditions in the overlap with SLE, making accurate diagnosis, the attribution process, and appropriate management essential.[13] Laboratory investigations, including autoantibody profiles and serologic markers, play a crucial role in the diagnosis and monitoring of lupus.

The association between structural MR imaging alterations and SLE has been investigated by few studies, such those included in the meta-analysis by Cox et al,[15] in which they confirmed that hippocampus, corpus callosum, and total gray matter volume measures in patients with SLE were considerably lower than those in age- and sex-matched controls. However, their association with brain MR imaging findings and neuropsychiatric events remains insufficiently explored.

The aim of the study was to explore the correlations among brain morphometric MR imaging findings, neuropsychiatric events, and laboratory values in NPSLE.

MATERIALS AND METHODS

The study was designed as exploratory and cross-sectional. Patients with SLE were recruited from those referred to the Lupus Clinic, rheumatology department of our university hospital (Rheumatology Unit, Azienda Ospedaliero-Universitaria, Cagliari, Italy) between April 2019 and February 2020, on the basis of the following inclusion criteria: 1) fulfillment of the 2019 criteria of the American College of Radiology/European Alliance of Associations for Rheumatology; 2) 18 years of age or older; and 3) the ability to provide informed consent. The local Independent Ethics Committee examined and approved the study protocol (protocol No. PG/2019/4522). All participants provided written informed consent.

Clinical and Immunologic Data

Demographics, classic atherogenic risk variables (such as hypertension, hyperlipidemia, and smoking), and basic laboratory data were evaluated for patients and controls. Patients were classified regarding SLE duration, activity, damage, conventional serology, autoantibodies, and therapy. Disease activity by the Physician Global Assessment (PGA) was evaluated on a 0–3 visual scale.[16] The SLE Disease Activity Index (SLEDAI)[17] was used to evaluate the state of the disease in 9 organ systems, including the CNS, vascular, renal, musculoskeletal, serosal, cutaneous, immunologic, constitutional, and hematologic systems. An SLEDAI of $\geq$6 is consistent with active disease. To evaluate accumulated damage in multiple organs, we used the Systemic Lupus International Collaborative Clinics/American College of Rheumatology Damage Index.[18]

Complement component 3 and 4 (C3 and C4) levels, anti-double stranded DNA, anti-Ro/SSA, anti-La/SSB, anti-Sm, anti-RNP, and antiphospholipid antibodies (lupus anticoagulant, anticardiolipin and anti-β2 glycoprotein I) were recorded. Also, brain-reactive antibodies, such as antineuronal antibodies, anti-Ribosomal P, and anti-DWEYS were included in the immunologic data.[19]

Furthermore, therapeutic information was acquired, including whether the patients were under any anticoagulant and antiplatelet agent and the milligrams/day equivalent of their prednisone dosage, hydroxychloroquine, immunosuppressants, and any biologic drug.

The presence of NPSLE was assessed according to the 1999 American College of Radiology nomenclature[20] through the confirmation of the attribution of a neurologic event to SLE according to expert opinion.

The control group with 10 patients who were diagnosed with a neuropsychiatric (NP) event derives from the article by Babayan et al:[21] 6 patients were diagnosed with a major depressive episode, 1 with anorexia nervosa, 1 with alcohol use disorder, 1 with bipolar disorder, and 1 with obsessive-compulsive disorder.

Neuroradiologic Data

MR imaging examinations were conducted within 1 month of enrollment. The Vantage Titan 3T scanner (Canon Medical Systems), equipped with a 32-channel head coil, was used for brain MR imaging. Patients with contraindications for MR imaging, such as claustrophobia or the presence of incompatible MR imaging devices, were excluded from the study.

The MR imaging protocol included a structural 3D T1-weighted fast-field echo (3D MPRAGE) sequence for morphometric analysis. The 3D MPRAGE was acquired in the axial plane from the cranial vertex to the occipital foramen, with the following parameters: section thickness = 1 mm; matrix = 1024; FOV = 256 × 256; TE = 2.8 ms; TI = 950 ms; TR = 6.3 ms; flip angle = 9°. Patients with brain MR imaging scans positive for incidental clinically significant pathologic findings, such as brain tumors, were excluded from the study.

For the NP control group, MR imaging was performed on a 3T scanner (Magnetom Verio; Siemens) equipped with a 32-channel head coil. The MP2RAGE sequence was acquired for assessment of brain structures with a voxel resolution of 1 mm (isotropic). Most important, these T1-weighted images differ from MPRAGE T1-weighted images because they are uniform and free of other imaging properties (ie, proton density, T2*) that can affect morphometric measurements. The total acquisition time for MP2RAGE was 8 minutes 22 seconds.[21]

Volumetric Analysis

The morphometric analysis was performed on anonymized structural 3D MPRAGE scans using the automated Vol2Brain online

tool (https://www.volbrain.net).[22] This Internet-based system was used for the automated analysis of volumetric brain data, quantifying the global brain volume (intracranial cavity, GM, WM, CSF) as well as the volume and mean cortical thickness of 135 brain structures.

Statistical Analysis

To compare continuous and categoric variables between groups, respectively, we used the Student *t* test or Mann-Whitney *U* test (for normally or non-normally distributed data, respectively) and the Fisher exact test. ANCOVA was used to correct for variables. Correlation analysis, using either the Pearson coefficient or Spearman coefficient (for normally or non-normally distributed data, respectively) was performed on every variable. The most correlated MR imaging features with every clinical and immunologic variable were partially correlated with the neurologic events, accounting for the prednisone dose, SLEDAI, the presence of NPSLE, and age and sex as partial correlations. Moreover, the neurologic events were correlated with MR imaging variables, accounting for prednisone dose, SLEDAI, age, and sex.

Ordinary least squares (OLS) regression analysis was performed on every clinical and immunologic continuous feature, considered as the target variable, using the most correlated MR imaging features as the predictor variables. A *P* value of $<.05$ was considered statistically significant. All statistical analyses were conducted on Python, Version 3.9.

RESULTS

Patient Characteristics

Twenty-seven patients with a diagnosis of SLE were included in the study, of which 24 were women and 3 were men. The average age was 43 years, with a mean disease duration of 7.8 (SD, 11.9) years (Online Supplemental Data). On average, their SLEDAI-2K score was 8.29, while The Systemic Lupus Erythematosus International Collaborating Clinic Damage Index (SLICC-DI) and PGA were 0.96 and 1.04, respectively. The 14 patients who had ≥1 NP event (6 mood abnormalities, 4 seizures, 3 cerebrovascular accidents, 2 cases of psychosis, 1 movement disorder, 1 acute confusional state) had, on average, a SLEDAI-2K of 10.5, while those who did not experience an NP event of 5.9. Likewise, the patients with NPSLE had a higher PGA and SLICC-DI, as well as, on average, a higher double stranded DNA titer (Online Supplemental Data). Every patient except one was on a steroid regimen (96%), prednisone, while 8 were taking an anticoagulant (29%); 19, hydroxychloroquine (70%); 23, an immunosuppressive agent (85%); and 9, a biologic drug (33%). Other patient characteristics are in the Online Supplemental Data.

Volumetric Analysis

Volumetric differences between various groups were tested. Differences in MR imaging scans of patients with SLE were analyzed by grouping them on the basis of different clinical and immunologic data. Regarding patients with NPSLE and non-NPSLE, many brain regions and their characteristics were found to be different, and the 5 most statistically significant that were lower in the NPSLE group were the following: central operculum of insula total volume percentage (*P* value = .003), occipital cortex (OCP) total thickness norm ($P = .003$), OCP left thickness norm ($P = .004$), angular gyrus (Ang) right thickness in millimeters ($P = .004$), OCP total thickness in millimeters ($P = .005$) (Fig 1). When comparing NP events with NPSLE and SLE, with the Wilcoxon test and ANOVA, the brain regions differing the most between the groups were the GRe (gyrus rectus), SGT, and IGt ($P < .001$).

Regarding the SLEDAI-2K, after the Wilcoxon test, the main differences in MR imaging features between the 2 groups, one with a score of <4 and the other above it, based on studies such as Yee et al,[23] were the following: parahippocampal gyrus total thickness greater in higher SLEDAI ($P = .006$), as well as both its right and left thickness taken separately were greater the higher the SLEDAI ($P < .02$), and calcarine cortex (Calc) right volume percentage, greater with higher SLEDAI scores. (Fig 2).

The SLICC-DI analysis, in which the patients were divided on the basis of the presence of organ damage or not (SLICC-DI of at least 1 and 0), revealed how the opercular part of the inferior frontal gyrus total and right volume percentage differed the most between groups ($P = .003$ and .007), with the damaged group having the smaller volume; another region was the right medial precentral gyrus volume percentage ($P = .008$), volume in cubic centimeters (*P* value = .015). (Fig 3).

Four patients were diagnosed with antiphospholipid syndrome and were shown to have diminished thickness in the following areas: Anterior insula left thickness in millimeters ($P = .001$), anterior cingulate gyrus right thickness in millimeters ($P = .001$), middle temporal gyrus total volume percentage (*P* value = .001), as well as more abnormal-appearing white matter volume in cubic centimeters ($P = .006$).

Correlation Analysis

Regarding the partial correlation analysis (Fig 2), the most correlated MR imaging features with NPSLE were the following: subcallosal area (SCA) thickness asymmetry ($r = 0.45$, $P = .003$), amygdala right volume percentage ($r = 0.43$, $P = .042$), temporal thickness asymmetry ($r = 0.47$, $P = .025$), and temporal pole (TMP) thickness asymmetry ($r = 0.52$, $P = .011$). Both SCA and TMP thickness asymmetry were positively correlated with the presence of a CVA event after partial correlation ($r = 0.71$, $P < .001$ and $r = 0.69$, $P < .001$, respectively) (Online Supplemental Data).

On the other hand, the partial correlation analysis of the neurocognitive events revealed a strong positive partial correlation (correlation: 0.662, $P < .001$) between depression and medial precentral gyrus volume asymmetry, with a negative one for the volume percentage of the cerebellar vermal lobules VIII–X (correlation: −0.5784, $P = .004$). Similarly, a strong positive partial correlation between seizures and angular gyrus thickness asymmetry (correlation: 0.671, $P < .001$) was found, as well as a negative one with medial orbital gyrus left thickness norm (correlation: −0.548, $P = .006$). Our analysis demonstrated a strong negative partial correlation between psychosis and insular right volume percentage (correlation: −0.688, $P < .001$), in addition to a positive correlation with pallidum total volume in cubic centimeters (correlation: 0.644, $P < .001$). Furthermore, the correlation with cerebrovascular accidents yielded significant results, such as its relationship with SCA thickness asymmetry (correlation:

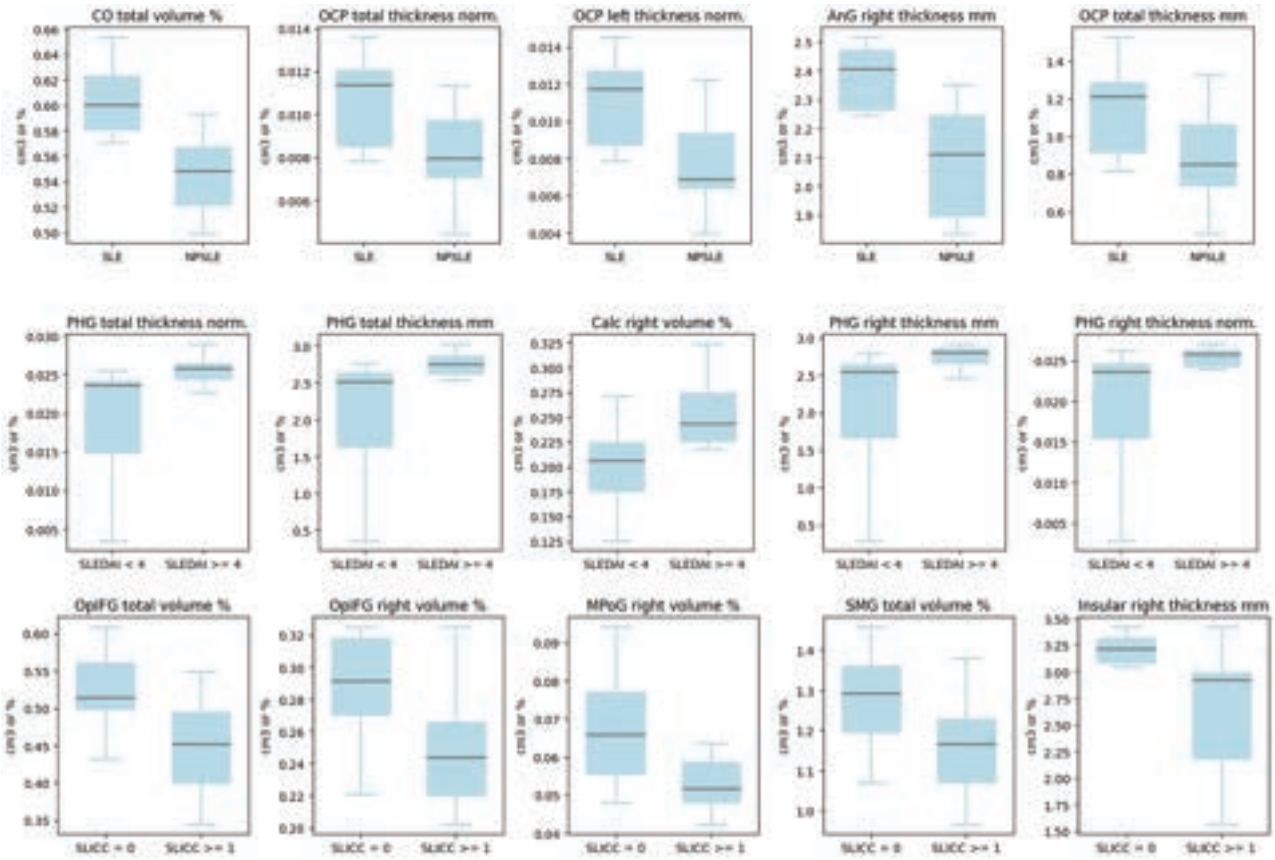

FIG 1. Wilcoxon rank-sum test results combining multimodal MR brain imaging and machine learning to unravel neurocognitive function in non-NPSLE for volumetric differences between patients with SLE and NPSLE, SLEDAI-2K higher or lower than 4, and SLICC-DI higher or lower than 1. PHG indicates parahippocampal gyrus; OpiFG, opercular part of the inferior frontal gyrus; MPoG, medial precentral gyrus; CO, central operculum of the insula; SMG, supramarginal gyrus.

0.710, $P < .001$) and gyrus rectus right thickness in millimeters (correlation: −0.693, $P < .001$).

OLS Regression

The OLS regression analysis conducted on the continuous variables as the target ones, yielded an R^2 of 0.725 and an adjusted R^2 of 0.553 for the SLEDAI score, and a R^2 of 0.715 and an adjusted R^2 of 0.537 for the SLICC-DI score. For SLEDAI, the overall significance of the model, as measured by the F-statistic ($F = 4.226$, $P = .005$; $F = 4.012$, $P = .006$), indicates that at least one of the predictor variables has a statistically significant effect on SLEDAI-2k and SLICC-DI, respectively.

DISCUSSION

The purpose of this study was to explore the relationship between laboratory values, specifically antibodies, and brain MR imaging findings in patients with SLE. Additionally, it examined the incidence of NP events in connection with brain MR imaging results.

Among our patient cohort, the most prevalent NP manifestations included mood abnormalities, particularly depression, in addition to seizures, psychosis, and cerebrovascular disease. The prevalence of NP events in our population aligns with a meta-analysis by Unterman et al,[24] in which the most common neurologic syndromes encompassed headache, mood abnormalities (especially depression), cognitive dysfunction, seizures, and cerebrovascular disease.

Few studies have explored brain MR imaging lesion loads in patients with NPSLE, especially in contrast to controls or patients without NPSLE. Roldan et al[25] conducted a retrospective study involving 76 patients with SLE and 26 controls, revealing significantly higher whole-brain and hemisphere lesion loads in patients (all, $P < .020$). Moreover, a robust association emerged between neurocognitive z scores across all categories and whole-brain and hemisphere lesion loads. Notably, these associations became more pronounced when factoring in glucocorticoid medication and the SLEDAI.

When investigating GM atrophy and its correlation with NPSLE and SLE, an article by Cagnoli et al,[26] in which 20 patients with NPSLE, 18 with SLE, and 18 controls, were included, highlighted how GM atrophy was seen in both groups in the temporal and parietal lobes and was most pronounced in the posterior thalamus bilaterally ($P < .05$); moreover, both groups showed a significant increase in regional GM volume in the posterior parahippocampal gyrus.

A retrospective study by Sârbu et al[27] exploring 108 patients with NPSLE elucidated the relationship between WM alterations and NPSLE cognitive and immunologic features. In 59.3% of cases, brain abnormalities were detected. Cerebrovascular syndrome and microbleeds correlated with large-vessel disease,

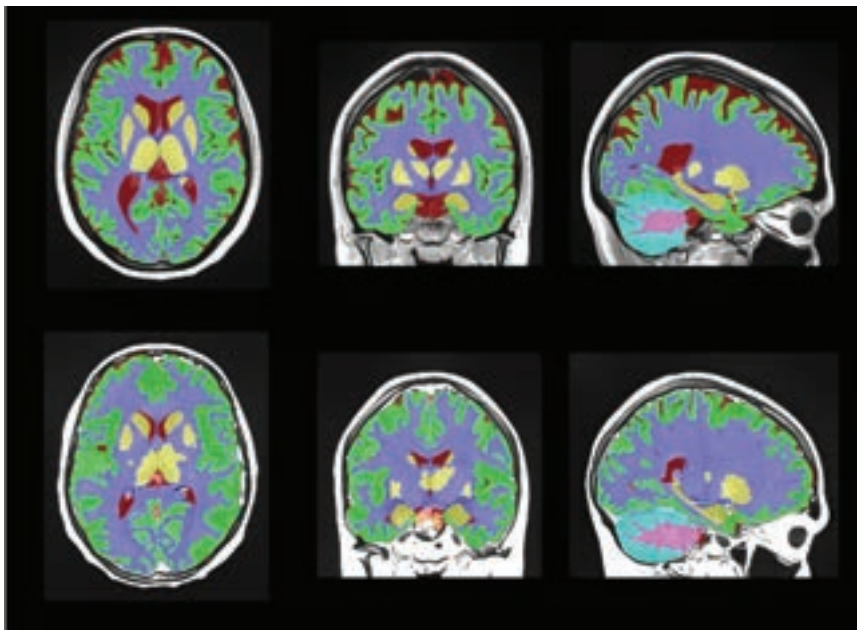

FIG 2. Tissue segmentation of a patient with NPSLE and one with SLE, respectively, first and second row. Each color represents a different brain structure, such as gray and white matter and CSF.

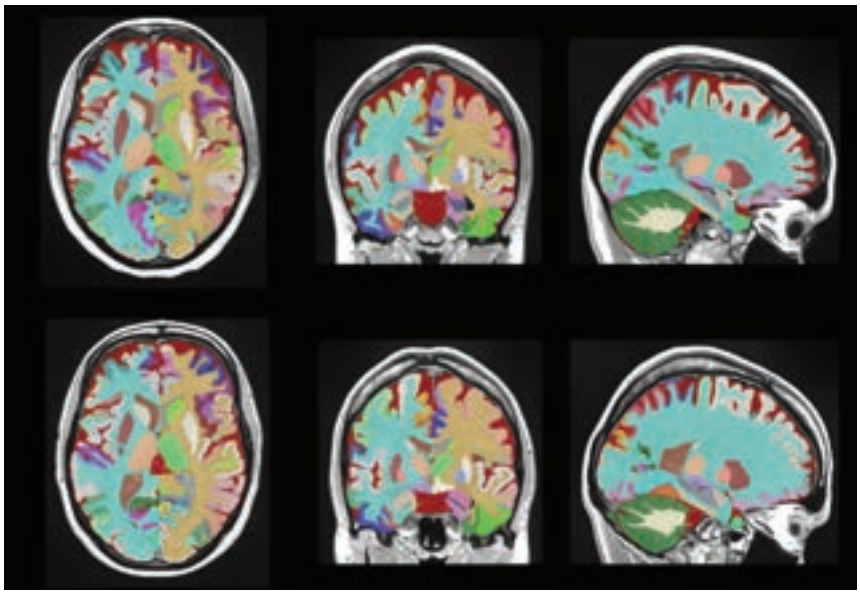

FIG 3. Structure segmentation of a patient with NPSLE and one with SLE, respectively, first and second row. Each color represents a different brain region.

cognitive impairment linked to white matter hyperintensities (WMH), and myelopathy associated with inflammatory-like lesions. Low C4 and CH50 levels were related to inflammatory-like lesions, while lupus anticoagulant levels were related to WMH, microbleeds, and atrophy ($P < .010$).

In our investigation, the comparison between patients with NPSLE and those without NPSLE revealed the OCP, particularly its total thickness and the left-hemispheric portion, as a potential biomarker distinguishing these 2 groups. Specifically, the total thickness of the OCP and the angular gyrus, along with the total volume percentage of the central operculum of the insula, appeared smaller in the NPSLE group than in the non-NPSLE group. Notably, a statistically significant positive connection emerged between the NPSLE diagnosis and SCA thickness asymmetry, indicating that individuals with NPSLE exhibit greater asymmetry. After adjusting for confounders, every other MR imaging feature retained statistical significance, reinforcing the relationship. Subsequently, these same regions were scrutinized concerning NP events. Both the TMP and SCA thickness asymmetry were associated with cerebrovascular events ($P < .050$).

The volume of cerebellar vermal lobules VIII–X differed significantly. These findings corroborate those of Mártensson et al,[28] who observed lower cerebellar GM density in patients with SLE, especially within cerebellar vermal lobules VIII and VII.

To explore this issue further, we assessed the correlation and partial correlation of cerebellar vermal lobules VIII–X with and in the presence of specific NP events. While the correlation was significant ($r = -0.55$, $P < .001$), the adjusted P value slightly exceeded significance ($r = -0.40$, $P = .057$). Concerning NP events, the partial correlation with a depressive disorder was notable ($r = -0.44$, $P < .001$). These findings align with previous research highlighting the weak correlation between SLE and delayed psychomotor speed,[29] a common feature of major depressive disorder, as proved by several studies[29,30] including a systematic review by Bennabi et al,[31] who pointed out how it might be correlated with the disease severity.

Anti-double stranded DNA antibodies, a pertinent marker in SLE,[32,33] were associated with depressive episodes and notably reduced insular, hippocampal, and brainstem volumes. The activation of the complement system, reflected in reduced C3 levels, correlated with diminished precuneus left and total thickness. Intriguingly, Calc right and total volume showed inverse correlations with C3 levels and a direct association with seizures ($P < .05$).

The impact of antiphospholipid syndrome (APS) on the CNS has been well-documented.[34,35] Kaichi et al[35] demonstrated a higher prevalence of abnormal MR imaging findings in patients with APS and SLE, including large territorial infarcts, lacunar infarcts, and those with cortical localization ($P = .010$), compared with the CNS in patients with SLE without APS. Our findings

confirm a moderate association between APS and the presence of WM abnormalities ($r = 0.47$, $P < .001$). WMH have been shown to correlate with neurocognitive disfunction in patients with NPSLE, as shown by Monahan et al,[36] because they reported that lower total brain volume and GM volume are associated with lower cognitive functioning in all domains ($P < .01$). In our study, we observed significant positive correlations between CVA events and white matter abnormalities ($r = 0.44$, $P = .041$), as well as depressive episodes, suggesting that their pathogenesis could be vascular or inflammatory, as discussed by Huang et al,[37] along with a recent review by Leal Reato et al,[38] highlighting its multifaceted pathophysiology. Notably, we also discovered relationships between these events and GM features, including SCA thickness asymmetry, TMP thickness asymmetry, and right frontal operculum of the insula thickness.

Regarding the other NP events, one of the few studies that investigated their association with WMH or GM hyperintensities has been conducted by Arinuma et al,[39] in which 53 patients with NPSLE underwent brain MR imaging, and the frequency of brain lesions, present in 25 of them, for different NP events was assessed. Most of the events were associated with WMH and GM atrophy, with marked severity in almost one-half of them. Events such as psychosis and mood disorders were rarely associated with MR imaging abnormalities in this article, while we found that depressive episodes were positively correlated with features like medial precentral gyrus volume asymmetry ($P < .001$), and negative correlations were observed with features related to the OCP thickness ($P = .002$); instead, insular ($P < .001$) and frontal volumes ($P = .001$) were negatively correlated with psychotic events, and superior temporal gyrus ($P = .004$) and cuneus ($P = .010$) thickness asymmetry was directly correlated with movement disorders, contrary to FO right volume ($P = .014$), which was lower in such patients.

Furthermore, to better assess the impact of NP events on their own on brain volumes, we tested whether the NP group significantly differed from the NPSLE and SLE groups. Indeed, our volumetric analysis revealed that different brain regions differed between the NP and the other groups, such as GRe, SGT and IGT ($P < .001$), instead of those that stood out when comparing NPSLE and SLE, suggesting that there is a difference between patients with NPSLE and those with NP disorders.

To conclude our analysis, we used an OLS regression model to further assess MR imaging and clinical variable association (Online Supplemental Data). Notably, Calc right volume percentage has a positive coefficient of 63.0838 with a significant P value of .035, suggesting that an increase in Calc right volume percentage is associated with higher SLEDAI-2k scores. Inferior occipital gyrus volume asymmetry and SCA left thickness in millimeters both have coefficients with P values slightly above the typical significance threshold of .05 ($P = .061$ and .151, respectively). Medial precentral gyrus right volume percentage ($P = .01$) was negatively associated (−68.4273) with SLICC-DI, indicating a decrease in its volume for higher scores.

This last step adds to the increasing literature on machine learning applications in NPSLE, with MR imaging data, as shown by recent articles such as the one by Tay et al,[40] in which a multimodal model, constructed using machine learning and incorporating microstructural, perfusion, and permeability parameters, effectively predicted the neurocognitive performance of individuals with SLE.

A limitation of this study is the difference in imaging acquisition between the 2 data sets, because it can affect morphometric measurements.

CONCLUSIONS

These findings confirm the interplay between brain structural attributes and NP events, suggesting that quantitative MR imaging–based biomarkers could be helpful in stratifying this condition. However, further research is warranted to validate and extend these preliminary observations.

Disclosure forms provided by the authors are available with the full text and PDF of this article at www.ajnr.org.

REFERENCES

1. Fanouriakis A, Tziolos N, Bertsias G, et al. **Update on the diagnosis and management of systemic lupus erythematosus.** *Ann Rheum Dis* 2020;80:14–25 CrossRef Medline
2. Tian J, Zhang D, Yao X, et al. **Global epidemiology of systemic lupus erythematosus: a comprehensive systematic analysis and modelling study.** *Ann Rheum Dis* 2022;82:351–56 CrossRef Medline
3. Jeltsch-David H, Muller S. **Neuropsychiatric systemic lupus erythematosus: pathogenesis and biomarkers.** *Nat Rev Neurol* 2014;10:579–96 CrossRef Medline
4. Popescu A, H. Kao A. **Neuropsychiatric systemic lupus erythematosus.** *Curr Neuropharmacol* 2011;9:449–57 CrossRef Medline
5. Sarwar S, Mohamed AS, Rogers S, et al. **Neuropsychiatric systemic lupus erythematosus: a 2021 update on diagnosis, management, and current challenges.** *Cureus* 2021;13:e17969 CrossRef Medline
6. Chessa E, Piga M, Perra A, et al. **The effect of anti-P ribosomal and anti-NR2 antibodies on depression and cognitive processes in SLE: an integrated clinical and functional MRI study.** *Lupus Sci Med* 2023;10:e001005 CrossRef Medline
7. Piga M, Peltz MT, Montaldo C, et al. **Twenty-year brain magnetic resonance imaging follow-up study in systemic lupus erythematosus: factors associated with accrual of damage and central nervous system involvement.** *Autoimmun Rev* 2015;14:510–16 CrossRef Medline
8. Postal M, Lapa AT, Reis F, et al. **Magnetic resonance imaging in neuropsychiatric systemic lupus erythematosus: current state of the art and novel approaches.** *Lupus* 2017;26:517–21 CrossRef Medline
9. Zhang Z, Wang Y, Shen Z, et al. **The neurochemical and microstructural changes in the brain of systemic lupus erythematosus patients: a multimodal MRI study.** *Sci Rep* 2016;6:19026 CrossRef Medline
10. Appenzeller S, Amorim BJ, Ramos CD, et al. **Voxel-based morphometry of brain SPECT can detect the presence of active central nervous system involvement in systemic lupus erythematosus.** *Rheumatology (Oxford)* 2007;46:467–72 CrossRef Medline
11. Ota Y, Srinivasan A, Capizzano AA, et al. **Central nervous system systemic lupus erythematosus: pathophysiologic, clinical, and imaging features.** *Radiographics* 2022;42:212–32 CrossRef Medline
12. Magro-Checa C, Beaart-van de Voorde LJ, Middelkoop HA, et al. **Outcomes of neuropsychiatric events in systemic lupus erythematosus based on clinical phenotypes; prospective data from the Leiden NP SLE cohort.** *Lupus* 2017;26:543–51 CrossRef Medline
13. Mak A, Ho RC, Tng HY, et al. **Early cerebral volume reductions and their associations with reduced lupus disease activity in patients with newly-diagnosed systemic lupus erythematosus.** *Sci Rep* 2016;6:22231 CrossRef Medline

14. Sarbu N, Toledano P, Calvo A, et al. **Advanced MRI techniques: biomarkers in neuropsychiatric lupus.** *Lupus* 2017;26:510–16 CrossRef Medline
15. Cox JG, de Groot M, Cole JH, et al. **A meta-analysis of structural MRI Physician Global Assessment studies of the brain in systemic lupus erythematosus (SLE).** *Clin Rheumatol* 2022;42:319–26 CrossRef Medline
16. Chessa E, Piga M, Floris A, et al. **Use of Physicians Global Assessment in systemic lupus erythematosus: a systematic review of its psychometric properties.** *Rheumatology (Oxford)* 2020;59:3622–32 CrossRef Medline
17. Gladman DD, Ibañez D, Urowitz MB. **Systemic lupus erythematosus disease activity index 2000**. *J Rheumatol* 2002;29:288–91
18. Gladman DD, Goldsmith CH, Urowitz MB, et al. **The Systemic Lupus International Collaborating Clinics/American College of Rheumatology (SLICC/ACR) Damage Index for systemic lupus erythematosus international comparison.** *J Rheumatol* 2000;27:373–76 Medline
19. Cocco C, Manca E, Corda G, et al. **Brain-reactive autoantibodies in neuropsychiatric systemic lupus erythematosus.** *Front Immunol* 2023;14:1157149 CrossRef Medline
20. **The American College of Rheumatology nomenclature and case definitions for neuropsychiatric lupus syndromes.** *Arthritis Rheum* 1999;42:599–608 CrossRef Medline
21. Babayan A, Erbey M, Kumral D, et al. **A mind-brain-body dataset of MRI, EEG, cognition, emotion, and peripheral physiology in young and old adults.** *Sci Data* 2019;6:180308 CrossRef Medline
22. Manjón JV, Romero JE, Vivo-Hernando R, et al. **vol2Brain: a new online pipeline for whole brain MRI analysis**. *Front Neuroinform* 2022;16:862805 CrossRef Medline
23. Yee CS, Farewell VT, Isenberg DA, et al. **The use of Systemic Lupus Erythematosus Disease Activity Index-2000 to define active disease and minimal clinically meaningful change based on data from a large cohort of systemic lupus erythematosus patients.** *Rheumatology (Oxford)* 2011;50:982–88 CrossRef Medline
24. Unterman A, Nolte JES, Boaz M, et al. **Neuropsychiatric syndromes in systemic lupus erythematosus: a meta-analysis.** *Semin Arthritis Rheum* 2011;41:1–11 CrossRef Medline
25. Roldan P, Jung RE, Sibbitt WL, et al. **Correlation of neurocognitive function and brain lesion load on magnetic resonance imaging in systemic lupus erythematosus.** *Rheumatol Int* 2018;38:1539–46 CrossRef Medline
26. Cagnoli P, Sundgren PC, Kairys A, et al. **Changes in regional brain morphology in neuropsychiatric systemic lupus erythematosus.** *J Rheumatol* 2012;39:959–67 CrossRef Medline
27. Sârbu N, Alobeidi F, Toledano P, et al. **Brain abnormalities in newly diagnosed neuropsychiatric lupus: Systematic MRI approach and correlation with clinical and laboratory data in a large multicenter cohort**. *Autoimmun Rev* 2015;14:153–59 CrossRef Medline
28. Mårtensson J, Rumetshofer T, Nystedt J, et al. **Structural changes on MRI demonstrate specific cerebellar involvement in SLE patients: a VBM study**. *Brain Sciences* 2021;11:510 CrossRef
29. Buyukdura JS, McClintock SM, Croarkin PE. **Psychomotor retardation in depression: biological underpinnings, measurement, and treatment.** *Prog Neuropsychopharmacol Biol Psychiatry* 2011;35:395–409 CrossRef Medline
30. Blackburn IM. **Mental and psychomotor speed in depression and mania.** *Br J Psychiatry* 1975;126:329–35 CrossRef Medline
31. Bennabi D, Vandel P, Papaxanthis C, et al. **Psychomotor retardation in depression: a systematic review of diagnostic, pathophysiologic, and therapeutic implications.** *BioMed Res Int* 2013;2013:158746 CrossRef Medline
32. Conti F, Ceccarelli F, Perricone C, et al. **Systemic lupus erythematosus with and without Anti-dsDNA antibodies: analysis from a large monocentric cohort.** *Mediators of Inflammation* 2015;2015:328078 CrossRef Medline
33. Ter Borg EJ, Horst G, Hummel EJ, et al. **Measurement of increases in anti-double-stranded dna antibody levels as a predictor of disease exacerbation in systemic lupus erythematosus.** *Arthritis Rheum* 1990;33:634–43 CrossRef Medline
34. Rodrigues CEM, Carvalho JF, Shoenfeld Y. **Neurological manifestations of antiphospholipid syndrome.** *Eur J Clin Invest* 2010;40:350–59 CrossRef Medline
35. Kaichi Y, Kakeda S, Moriya J, et al. **Brain MR findings in patients with systemic lupus erythematosus with and without antiphospholipid antibody syndrome.** *AJNR Am J Neuroradiol* 2013;35:100–05 CrossRef Medline
36. Monahan RC, Inglese F, Middelkoop H, et al. **White matter hyperintensities associate with cognitive slowing in patients with systemic lupus erythematosus and neuropsychiatric symptoms.** *RMD Open* 2021;7:e001650 CrossRef Medline
37. Huang CJ, Zhou X, Yuan X, et al. **Contribution of inflammation and hypoperfusion to white matter hyperintensities-related cognitive impairment.** *Front Neurol* 2021;12:786840 CrossRef Medline
38. Leal Rato M, Bandeira M, Romão VC, et al. **Neurologic manifestations of the antiphospholipid syndrome: an update**. *Curr Neurol Neurosci Rep* 2021;21:41 CrossRef Medline
39. Arinuma Y, Kikuchi H, Wada T, et al. **Brain MRI in patients with diffuse psychiatric/neuropsychological syndromes in systemic lupus erythematosus.** *Lupus Sci Med* 2014;1:e000050 CrossRef Medline
40. Tay SH, Stephenson MC, Allameen NA, et al. **Combining multimodal magnetic resonance brain imaging and machine learning to unravel neurocognitive function in non-neuropsychiatric systemic lupus erythematosus.** *Rheumatology (Oxford)* 2024;63:414–22 CrossRef Medline

Investigating Sea-Level Brain Predictors for Acute Mountain Sickness: A Multimodal MRI Study before and after High-Altitude Exposure

Wei Zhang, Jie Feng, Wenjia Liu, Shiyu Zhang, Xiao Yu, Jie Liu, Baoci Shan, and Lin Ma

ABSTRACT

BACKGROUND AND PURPOSE: Acute mountain sickness is a series of brain-centered symptoms that occur when rapidly ascending to high altitude. Predicting acute mountain sickness before high-altitude exposure is crucial for protecting susceptible individuals. The present study aimed to evaluate the feasibility of predicting acute mountain sickness after high-altitude exposure by using multimodal brain MR imaging features measured at sea level.

MATERIALS AND METHODS: We recruited 45 healthy sea-level residents who flew to the Qinghai-Tibet Plateau (3650 m). We conducted T1-weighted structural MR imaging, resting-state fMRI, and arterial spin-labeling perfusion MR imaging both at sea level and high altitude. Acute mountain sickness was diagnosed for 5 days using Lake Louise Scoring. Logistic regression with Least Absolute Shrinkage and Selection Operator logistic regression was performed for predicting acute mountain sickness using sea-level MR imaging features. We also validated the predictors by using MR images obtained at high altitude.

RESULTS: The incidence rate of acute mountain sickness was 80.0%. The model achieved an area under the receiver operating characteristic curve of 86.4% (sensitivity = 77.8%, specificity = 100.0%, and $P < .001$) in predicting acute mountain sickness At sea level, valid predictors included fractional amplitude of low-frequency fluctuations (fALFF) and degree centrality from resting-state fMRI, mainly distributed in the somatomotor network. We further learned that the acute mountain sickness group had lower levels of fALFF in the somatomotor network at high altitude, associated with smaller changes in CSF volume and higher Lake Louise Scoring, specifically relating to fatigue and clinical function.

CONCLUSIONS: Our study found that the somatomotor network function detected by sea-level resting-state fMRI was a crucial predictor for acute mountain sickness and further validated its pathophysiologic impact at high altitude. These findings show promise for pre-exposure prediction, particularly for individuals in need of rapid ascent, and they offer insight into the potential mechanism of acute mountain sickness.

ABBREVIATIONS: AMS = acute mountain sickness; ASL = arterial spin-labeling; AUC = area under the curve; DC = degree centrality; fALFF = fractional amplitude of low-frequency fluctuations; LASSO-LR = Least Absolute Shrinkage and Selection Operator logistic regression; LLS = Lake Louise Score; rs-fMRI = resting-state fMRI; ROC = receiver operating characteristic; SMN = somatomotor network; SpO_2 = saturation of pulse oxygen

Approximately 25%–90% of sea-level residents who travel to high altitude will have acute mountain sickness (AMS), depending on the altitude, the speed of ascent, and individual susceptibility.[1] AMS is a series of symptoms including headache, dizziness, and malaise. It can even lead to incapacitation or life-threatening conditions such as high-altitude cerebral edema and pulmonary edema.[2]

It was recommended that high-altitude travelers have medical consulting regarding AMS before exposure.[3] Predicting AMS

Received November 20, 2023; accepted after revision January 23, 2024.

From the Beijing Engineering Research Center of Radiographic Techniques and Equipment (W.Z., B.S.), Institute of High Energy Physics, Chinese Academy of Sciences, Beijing, China; School of Nuclear Science and Technology (W.Z., B.S.), University of Chinese Academy of Sciences, Beijing, China; The Graduate School (J.F., X.Y., L.M.), Medical School of Chinese People's Liberation Army, Beijing, China; Department of Radiology (J.F., W.L., S.Z., X.Y., L.M.), The First Medical Center of Chinese People's Liberation Army General Hospital, Beijing, China; Department of Radiology (S.Z.), Capital Medical University Affiliated Beijing Friendship Hospital, Beijing, China; Department of Radiology (X.Y.), Beijing Jingmei Group General Hospital, Beijing, China; Department of Radiology (J.L.), General Hospital of Tibet Military Region, Tibet, China; and Cognitive Neuroimaging Centre (W.Z.) and Lee Kong Chian School of Medicine (W.Z.), Nanyang Technological University, Singapore.

W. Zhang and J. Feng contributed equally to this work.

This work was supported by National Natural Science Foundation of China, grant No. 81741115, 81771923, 11975249, and 12175268, Chinese Military Creative Project, grant No. 16CXZ014, Chinese Military Healthcare, grant No. 16BJZ11.

Please address correspondence to Lin Ma, MD, Department of Radiology, The First Medical Center of Chinese People's Liberation Army General Hospital, 28 Fuxing Road, Beijing 100853, China; e-mail: cjr.malin@vip.163.com

Indicates article with online supplemental data.

http://dx.doi.org/10.3174/ajnr.A8206

before exposure is also essential for protecting individuals from greater health risks. Because rapid ascent is a risk factor of AMS,[1] individuals requiring rapid ascent to high-altitude areas might particularly need the prediction, such as those undertaking urgent high-altitude missions like disaster relief, medical rescue, and some scientific investigations. Currently, 2 main factors show promise in predicting AMS: the history of AMS and migraine[4] and the adaptation performance in moderate hypoxia, such as the cardiopulmonary function in artificial hypoxic environments[4-7] and adaptation extents at moderate altitudes.[8-12] However, the prediction performance was inconsistent and debated, because studies have reported conflicting results using the same predictors.[13-16] Furthermore, most individuals have limited high-altitude experience, making prediction based on history less feasible. The artificial hypoxic environments, often requiring specialized labs, are also debated for not adequately replicating the hypobaric conditions of real high altitude.[17]

The inconsistent performance in predicting AMS may be due to an incomplete understanding of the mechanisms.[18] Among the hypotheses, the brain plays a key role in both human and animal research.[19,20] The physiologic adaptation after high-altitude exposure is brain-centered and crucial for the onset of AMS, which is hypothesized to involve multiple neural processes such as the perception and processing of the sensory information from a high-altitude environment[21,22] and the activation of the autonomic neural system.[23,24] The swelling of gray and white matter, the morphologic changes of the cortex, the restricted outflow of CSF, and the increased CBF can increase intracranial pressure and thus cause AMS,[25,26] while the contributions of different components toward AMS are still debated.[27] Those hypotheses involve multiple aspects of the brain, including function, structure, and perfusion. However currently, multimodal MR imaging studies for AMS scanned at both sea level and high altitude are still rare and have not involved integrated pre-exposure prediction.[28,29] The feasibility of using multimodal MR imaging to investigate and predict AMS requires further verification.

In this study, we arranged for 45 participants to fly from sea level to the Qinghai-Tibet Plateau. They underwent 3 modalities of MR imaging twice (before and after high-altitude exposure) and were diagnosed as having AMS or non-AMS. On the basis of the previous studies, we hypothesized that the AMS group would have distinct cerebral features at sea level, detectable by multimodal MR imaging, and that we could further investigate its pathophysiologic impact using MR imaging after exposure.

MATERIALS AND METHODS

Study Design

This study was conducted in both sites of the Chinese People's Liberation Army General Hospital (Beijing, at sea level) and The General Hospital of Tibet Military Region (Lhasa, 3650 m above sea level). In Beijing as a baseline, participants were scanned by 3 modalities: T1-weighted imaging, resting-state fMRI (rs-fMRI), and arterial spin-labeling (ASL) perfusion MR imaging. Then, participants traveled to Lhasa via commercial flights within 2 days. In Lhasa, participants underwent the same MR imaging protocol at 22 hours and were diagnosed as either having AMS or not having AMS during the first 5 days at the following time points: 9, 22, 46, 70, and 94 hours. The flow chart of the study design is shown in Fig 1*A*. Demographic and physiologic features were recorded at baseline for prediction.

Participants

A total of 49 participants were recruited through community advertising. Four participants were excluded due to strong head-motion artifacts on MR imaging at baseline, identified after post hoc checking. Two rs-fMRIs from the 45 participants at high altitude were excluded due to poor image quality, but sea-level data from these 2 participants were still valid and included for prediction.

The recruitment criteria were as follows: 1) 20–40 years of age; 2) no history of severe head trauma, chronic headache, chronic sleep disorders, other neuropathy, or psychosis; 3) nonsmokers and not abusing alcohol; 4) not taking any prescription or nonprescription medications at the time of the study; 5) no chronic heart or lung disease, diabetes, hypertension, or other basic diseases; 6) right-handed; 7) originally from and currently residing at sea level and not having traveled to an altitude above 1500 m in the past year; and 8) no carotid or intracranial vascular lesions detected by MRA.

AMS Diagnosis

The AMS diagnosis is based on the latest Lake Louise scoring.[30] Participants with a headache score of $\geq$1 and a Lake Louise Score (LLS) of $\geq$ 3 were diagnosed with AMS on a daily basis. Participants diagnosed with AMS at least once during the 5 days at high altitude were grouped as having AMS. The LLS is composed of 4 main different subscores: 1) headache, 2) gastrointestinal symptoms, 3) fatigue and/or weakness, and 4) dizziness/light-headedness. The extra subscore, the clinical-functional score, was used to evaluate the overall impact on patients with AMS but is not included in the total score.

Multimodal MR Imaging Acquisitions and Preprocessing

MR imaging was performed using a 3T Discovery MR 750 scanner (GE Healthcare) both at sea level and high altitude to minimize variance caused by scanner differences.

T1-weighted structural MR imaging was acquired using the 3D fast-spoiled gradient recalled protocol with the following parameters: TR = 6.9 ms, TE = 3.0 ms, TI = 450 ms, flip angle = 12°, FOV = 25.6 cm, 188 slices with section thickness = 1 mm, matrix = 256 × 256, voxel resolution = 1 mm, and number of excitations = 1.

rs-fMRI was acquired measuring blood oxygenation level–dependent signals with an EPI sequence: TR = 2000 ms, TE = 30 ms, flip angle = 90°, FOV = 24.0 cm, 41 slices with section thickness = 3 mm, matrix = 64 × 64, voxel resolution = 3.75 mm, and time-series length = 240.

For pseudocontinuous ASL perfusion images, the labeling duration = 1.5 seconds, postlabel delay = 2.0 seconds, TR = 4844 ms, TE = 10.5 ms, TI = 2025 ms, flip angle = 111°, bandwidth = 62.5 kHz, FOV = 24 cm, 36 slices with section thickness = 4 mm, acquisition matrix = 128 × 128, resolution = 1.875 mm, and number of excitations = 3. The proton density–weighted images

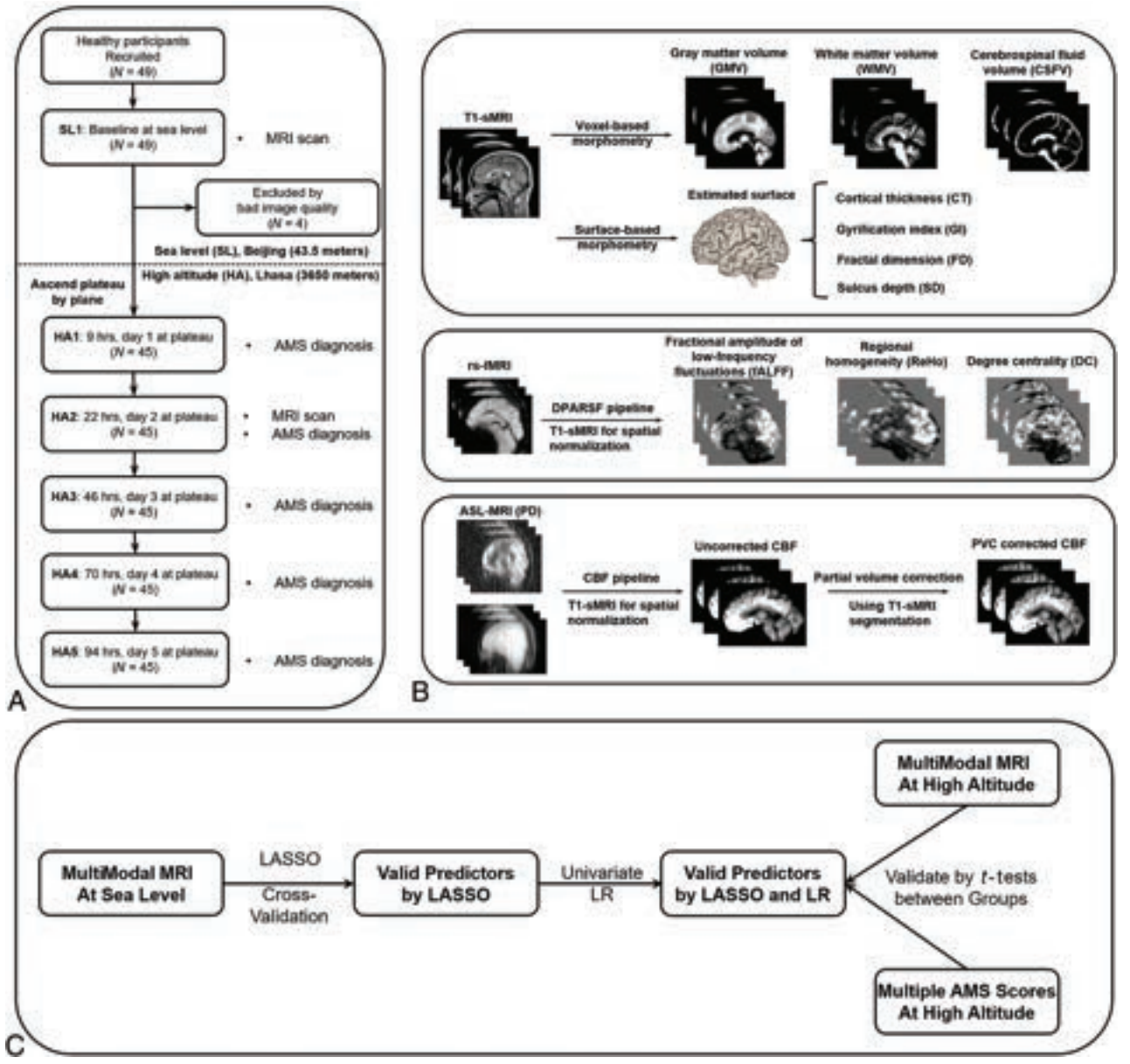

FIG 1. The study design and the analysis pipelines for multimodal MR images. *A*, The study design. Participants were recruited and underwent MR imaging at sea level, ascended to the high altitude by plane, were scanned by MR imaging at 22 hours, and evaluated for AMS 5 times at high altitude. *B*, Multimodal MR imaging preprocessing. Different preprocessing pipelines produced 11 features from 3 modalities of MR imaging, and these features were further summarized by the mean value in ROIs. *C*, Feature selection. The sea-level MR imaging features for prediction of AMS were selected by LASSO-LR and re-verified by univariate logistic regression. Sea-level predictors were subsequently verified using high-altitude MR imaging and AMS scores (LLS) collected at high altitude. DPARSF indicates Data Processing Assistant for Resting-State fMRI; LR, logistic regression; PD, proton density–weighted images; PVC, partial volume correction.

were obtained with a saturation recovery acquisition with identical parameters.

A summary of the multimodal MR imaging preprocessing pipeline is shown in Fig 1*B*. We have summarized the preprocessing steps and features extracted for each technique in Table 1. For detailed preprocessing steps, refer to the Online Supplemental Data.

Prediction Input and Methods

The sea-level MR imaging features were summarized by the mean values in ROIs from the Automated Anatomical Labeling atlas[31] (https://www.sciencedirect.com/science/article/pii/S1053811919307803) or the surface atlas[32] and were used as prediction input. Sea-level demographic and physiologic features were also entered as potential confounding covariates.

For the prediction methods, we used the Least Absolute Shrinkage and Selection Operator[33] logistic regression (LASSO-LR) due to its capability for feature selection (detailed implementation is in the Online Supplemental Data). We applied the leave-one-out framework for cross-validation.

We primarily evaluated the final prediction performance using the area under the curve (AUC) of the receiver operating

Table 1: Preprocessing and features of multimodal MR imaging

Technique	Preprocessing Pipeline	Main Preprocessing Steps	Features after Preprocessing	ROI No.
T1-sMRI (volume)	Voxel-based morphometry	Denoising, bias cleaning, affine registration, segmentation, spatial normalization, volume modulation, smoothing	GM volume	166
			WM volume	166
			CSF volume	166
T1-sMRI (surface)	Surface-based morphometry	Surface reconstruction, cortical parcellation, spatial normalization, smoothing	Cortical thickness	68
			Gyrification index	68
			Fractal dimension	68
			Sulcus depth	68
Rs-fMRI	DPARSF standard preprocessing pipeline	Time point removal, section timing, realignment, affine registration, nuisance regression, head motion correction, spatial normalization, metric calculation, smoothing	fALFF	166
			Regional homogeneity	166
			DC	166
ASL	CBF quantification pipeline	Coregistration, CBF calculation, partial volume correction, spatial normalization, whole-brain normalization, smoothing	CBF	166

Note:—DPARSF indicates Data Processing Assistant for Resting-State fMRI (Matlab); sMRI, structural MR imaging.

Table 2: Demographic and physiologic features for the AMS and non-AMS groups at sea-level baseline[a]

	Non-AMS ($n = 9$)	AMS ($n = 36$)	*P* Value
Age (yr)	27.3 (SD, 3.8)	29.4 (SD, 4.6)	.1497
Sex (M/F)	5/4	17/19	.1779
Height (cm)	168.9 (SD, 6.5)	168.4 (SD, 8.5)	.8776
Weight (kg)	61.1 (SD, 8.0)	64.7 (SD, 13.3)	.4462
BMI (kg/m^2)	21.4 (SD, 2.3)	22.6 (SD, 3.2)	.2848
SBP (min^{-1})	111.3 (SD, 12.1)	111.9 (SD, 12.4)	.9094
DBP (min^{-1})	75.1 (SD, 8.1)	75.6 (SD, 8.7)	.8703
MAP (min^{-1})	87.2 (SD, 9.2)	87.7 (SD, 9.6)	.8823
HR (min^{-1})	74.3 (SD, 7.2)	74.1 (SD, 8.1)	.9402
SpO_2 (%)	97.8 (SD, 0.8)	97.6 (SD, 0.7)	.4137

Note:—BMI indicates body mass index; DBP, diastolic blood pressure; HR, heart rate; MAP, mean arterial pressure; SBP, systolic blood pressure.
[a] Data are means unless otherwise indicated.

characteristic (ROC) because of the unbalanced labels (36 AMS of 45 participants). The ROC is suitable for measuring the classification performance on unbalanced labels[34-36] because it is generated across a range of decision thresholds and is less sensitive to unbalanced label distribution. Sensitivity and specificity were also calculated at the cut-point of the best Youden index. All prediction methods were implemented using the scikit-learn toolbox, Version 1.0.2 (https://scikit-learn.org/stable/index.html).

Statistical Analyses

For investigating the valid predictors, we performed the feature-selection pipeline shown in Fig 1*C*. Specifically, we accepted valid predictors that passed both multivariate LASSO-LR and univariate logistic regressions.

T tests were performed to compare image features between groups. Because the predictors are regionally averaged, we further reverified them by detecting group differences between AMS and non-AMS at both voxelwise and network-wise scales, using MR imaging data from both sea level and high altitude.

All features were converted to a standard normal *z* score before prediction and statistical analyses.

The voxelwise analysis of MR images was performed on the basis of Statistical Parametric Mapping (SPM 12;http://www.fil.ion.ucl.ac.uk/spm/software/spm12). The network-wise *t* tests between groups used the predefined brain network atlas (https://surfer.nmr.mgh.harvard.edu/fswiki/CorticalParcellation_Yeo2011).[37] This atlas was used to re-verify the regional predictors and to detect potential networks involved. A partial Pearson correlation was used to assess the relationship between MR imaging predictors and other brain features they might influence. Before the statistical tests mentioned above, the values were regressed by the covariates of age and sex to exclude their potential effects. The statistical analyses were performed using related in-house scripts in Matlab (MathWorks).

RESULTS

Incidence Rate of AMS

The demographic and physiologic information at sea-level baseline is provided in Table 2, and no significant difference between AMS and non-AMS groups was detected using *t* tests and χ^2 tests.

The overall incidence rate of AMS during 5 days was 80.0% (36 of 45 participants; 95% CI , 66.7%–1.1%). The daily incidence rates of AMS were as follows: 66.7% at 9 hours after exposure (95% CI, 51.1%–80.0%), 48.9% at 22 hours (95% CI, 33.3%–64.4%), 46.7% at 46 hours (95% CI, 31.2%–62.2%), 31.1% at 70 hours (95% CI, 17.8%–46.7%), and 17.8% at 94 hours (95% CI, 6.7%–28.9%). Individual AMS diagnoses are provided in the Online Supplemental Data.

Prediction of AMS Using Multimodal Sea-Level MR Imaging

We used each type of feature in ROIs from sea-level multimodal MR imaging to predict AMS at high altitude (Fig 2, and with Youden cutoff in the Online Supplemental Data). Two fMRI metrics showed significant predictive performance: for fALFF as input, AUC = 78.1%, sensitivity = 80.5%, and specificity = 77.8% ($P = .0098$) and for degree centrality (DC) as input, AUC = 86.4%, sensitivity = 77.8%, and specificity = 100.0%

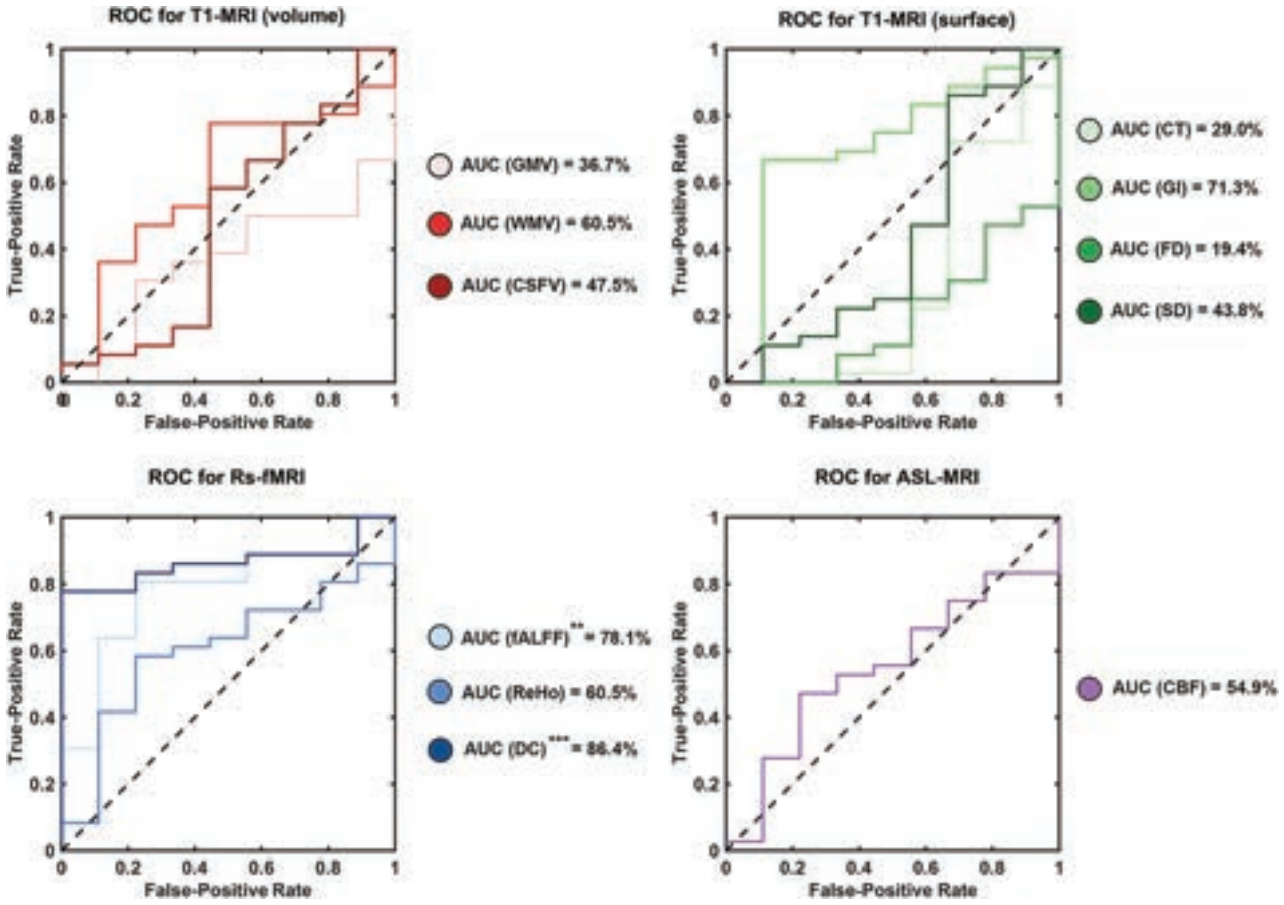

FIG 2. ROC curve analysis of MR imaging features. The prediction performance using different features of multimodal MR imaging as input, measured by the AUC of the ROC curves. fALFF and DC from fMRI were detected as valid predictors, yielding significant AUC values. CT indicates cortical thickness; FD, fractal dimension; GI, gyrification index; GMV, gray matter volume; ReHo, regional homogeneity; SD, sulcus depth; WMV, white matter volume, CSFV, CSF volume. ** $P < .01$, *** $P < .001$.

($P = .0008$). Other input features had no significant predictive performance, including combined features (such as all fMRI features or all multimodal MR imaging features). The full performance list of all types of input is provided in the Online Supplemental Data.

Identification and Verification of Sea-Level MR Imaging Predictors

Following the predictions, sea-level predictors were identified from the multivariate LASSO-LR. Then, these potential predictors were re-verified by univariate logistic regression, and only those that passed both regressions were regarded as valid predictors. Valid predictors were fALFF and DC values in the regions listed in Table 3.

Among the valid predictors, risk factors with ORs > 1 were mainly located in the orbitofrontal cortex and the right supramarginal gyrus. Protective factors with odds ratios < 1 were mainly located in the paracentral lobule, supplementary motor area, and Rolandic operculum, all of which belonged to the somatomotor network (SMN). The left superior and middle temporal gyri were also included as protective factors, which were near the Rolandic operculum. These predictors selected by the LASSO-LR models remained robust during the leave-one-out cross-validation (Online Supplemental Data).

Predictors of AMS Present in the SMN Both at Sea Level and High Altitude

To further verify the region-wise predictors, we performed voxel-wise *t* tests between groups on the fMRI metrics (fALFF and DC) maps. Both at sea level and at high altitude, the AMS group showed weaker functional metrics mainly in the motor and sensorimotor areas (Fig 3*A*, -*C*) than the non-AMS group (under $P < .05$, corrected by Gaussian random field).

We further verified the region-wise predictors by detecting network-wise group difference on the *z*-scored fMRI metric (fALFF and DC) maps using a predefined atlas.[37] At sea level (Fig 3*B*), the significant functional group difference in the predefined SMN between the AMS and non-AMS groups was detected by *t* tests: For fALFF, the AMS group showed significantly ($P = .0082$) lower values than the non-AMS group in the SMN (mean AMS) = −0.2095 (SD, 0.1613), mean (non-AMS) = 0.8381 (SD, 0.2140), group difference = 1.0476 (95% CI, 0.3590–1.7362). Similarly, for DC, the AMS group had significantly ($P = .0424$) lower values than the non-AMS group in the SMN (mean AMS) = −0.1706 (SD, 0.1632), mean (non-AMS) = 0.6824 (SD, 0.2693), group difference = 0.8529 (95% CI, 0.1394−1.5665). At high altitude (Fig 3*D*), for fALFF, the AMS group showed significantly ($P = .0320$) lower values than the non-AMS group in the SMN (mean AMS) = −0.1486 (SD, 0.1685), mean (non-AMS) = 0.5615 (SD, 0.3019), group

Table 3: ORs of significant predictors for AMS, selected by both the LASSO-LR and univariate logistic regression

Input Features/Input Regions	B	OR (95% CI)	*P* Value
fALFF			
Left Rolandic operculum	−1.324	0.266 (0.091–0.778)	.0157
Left supplementary motor area	−1.931	0.145 (0.025–0.857)	.0331
Right superior frontal gyrus, medial orbital	1.272	3.567 (1.207–10.543)	.0214
Right anterior orbital gyrus	0.852	2.344 (1.049–5.236)	.0379
Right supramarginal gyrus	1.288	3.624 (1.296–10.139)	.0141
Left paracentral lobule	−2.727	0.065 (0.009–0.488)	.0078
Left superior temporal gyrus	−1.040	0.354 (0.150–0.836)	.0179
Left middle temporal gyrus	−1.367	0.255 (0.081–0.803)	.0196
Right pulvinar inferior thalamus	0.894	2.445 (1.014–5.895)	.0466
DC			
Right superior frontal gyrus, dorsolateral	1.363	3.907 (1.169–13.058)	.0268
Right superior frontal gyrus, medial orbital	1.230	3.422 (1.213–9.649)	.0200
Right gyrus rectus	1.432	4.186 (1.280–13.693)	.0179
Right medial orbital gyrus	1.157	3.179 (1.076–9.396)	.0365
Right supramarginal gyrus	0.879	2.409 (1.053–5.513)	.0374
Left paracentral lobule	−1.463	0.232 (0.079–0.677)	.0075
Right paracentral lobule	−1.587	0.205 (0.066–0.633)	.0059

Note:—B indicates β coefficient.

difference = 0.7101 (95% CI, −0.0227−1.4429). No significant group differences were observed in networks other than the SMN under the threshold of $P = .05$.

AMS Features Associated with the SMN at High Altitude

Using the multimodal MR imaging scanned at high altitude, we further identified the influence of fMRI predictors (fALFF and DC in SMN) by performing the partial Pearson correlation between fMRI predictors and other modalities of brain MR imaging at high altitude (including the whole-brain GM, WM, CSF, and CBF). At 22 hours after exposure, the fALFF in the SMN was significantly correlated with the percentage changes of CSF volume ($r = 0.3277$ and $P = .0365$, shown in Fig 4*A*). Other brain components except CSF were also examined but showed no significance; these are listed in the Online Supplemental Data.

Moreover, we examined the relationship between fMRI predictors in the SMN and 5 different LLS subscores, which were all measured immediately before MR imaging and at 22 hours at high altitude. In Fig 4*B*, by performing the *t* tests, we found that the group that showed significantly ($P = .0460$) positive fatigue symptoms had lower fALFF in the SMN (mean positive LLS) = −0.2578 (SD, 0.1523), (mean negative LLS) = 0.4186 (SD, 0.3341), group difference = 0.6764 (95% CI,−0.0136−1.3664), and the group whose clinical function was affected had significantly ($P = .0024$) lower fALFF (mean positive LLS) = −0.5836 (SD, 0.1265), (mean negative LLS) = 0.3525 (SD, 0.3214), group difference = 0.9361 (95% CI, 0.3403−1.5320), and significantly ($P = .0112$) lower DC, (mean positive LLS) = −0.5452 (SD, 0.1612), (mean negative LLS) = 0.2380 (SD, 0.2799), group difference = 0.7832 (95% CI, 0.0856−1.4808) in the SMN.

DISCUSSION

Although a previous MR imaging study for AMS[28,29] had detected several brain abnormalities in the diffusion MR imaging after exposure, to the best of our knowledge, our study was the first to perform multimodal MR imaging at sea level and at high altitude for both integrated predicting and mechanistic investigating of AMS. The major findings lie in 2 parts: First, we discovered that sea-level SMN function can predict AMS with a high performance of AUC = 86.4%, which offered a method to predict the AMS risk for individuals requiring rapid ascent to high-altitude areas, such as those undertaking urgent high-altitude missions. Second, we further verified that the predictors also showed significant group difference between AMS and non-AMS at high altitude. The predictors were also associated with the changes in CSF volume and the extent of fatigue and clinical function.

These findings suggest that a cerebral functional basis for AMS can be detected early at sea level and shows promise as a noninvasive and accurate prediction tool and can offer insight into the neural basis of the susceptibility and development of AMS.

Methodologic Considerations for the Reliability of Prediction

We used LASSO-LR for its capability for feature selection (Online Supplemental Data). The selected features remained robust in cross-validation and different coefficient thresholds (Online Supplemental Data). We did not correct multiple comparisons among predictors because we used a data-driven LASSO-LR but did not screen all features. The multiple-comparisons correction might unnecessarily increase the risk of type II errors (false-negatives), thereby hindering the exploring of meaningful predictors. Despite including ASL MR imaging and structural MR imaging at both sites, our exploratory analyses rarely identified significant predictors from these modalities. We observed several ROC curves significantly below the diagonal line. This finding suggests that while these modalities may hold some useful information, they fail to provide robust and reliable predictions, indicating their limited applicability in this context.[34,38] The combined features like all fMRI or all MR imaging features showed insignificant performance (Online Supplemental Data), which indicates that simply combining all features into the prediction model will lead to overfitting and that each type of feature should be tested independently.

AMS Predictors as the Functional Features in the SMN

We found that functional features of fALFF and DC in the SMN were significant predictors for AMS (Table 3). We used both voxelwise and network-wise *t* tests to re-verify these predictors, as shown in Fig 3. The SMN in the predefined brain network atlas[37] broadly includes the primary motor and somatosensory cortices as well as part of the superior temporal gyrus, and these regions match the protective predictors well (Table 3).

For the fALFF and DC as predictors, higher DC in the SMN indicates that the SMN plays a more critical role in facilitating communication and information flow among other brain regions,

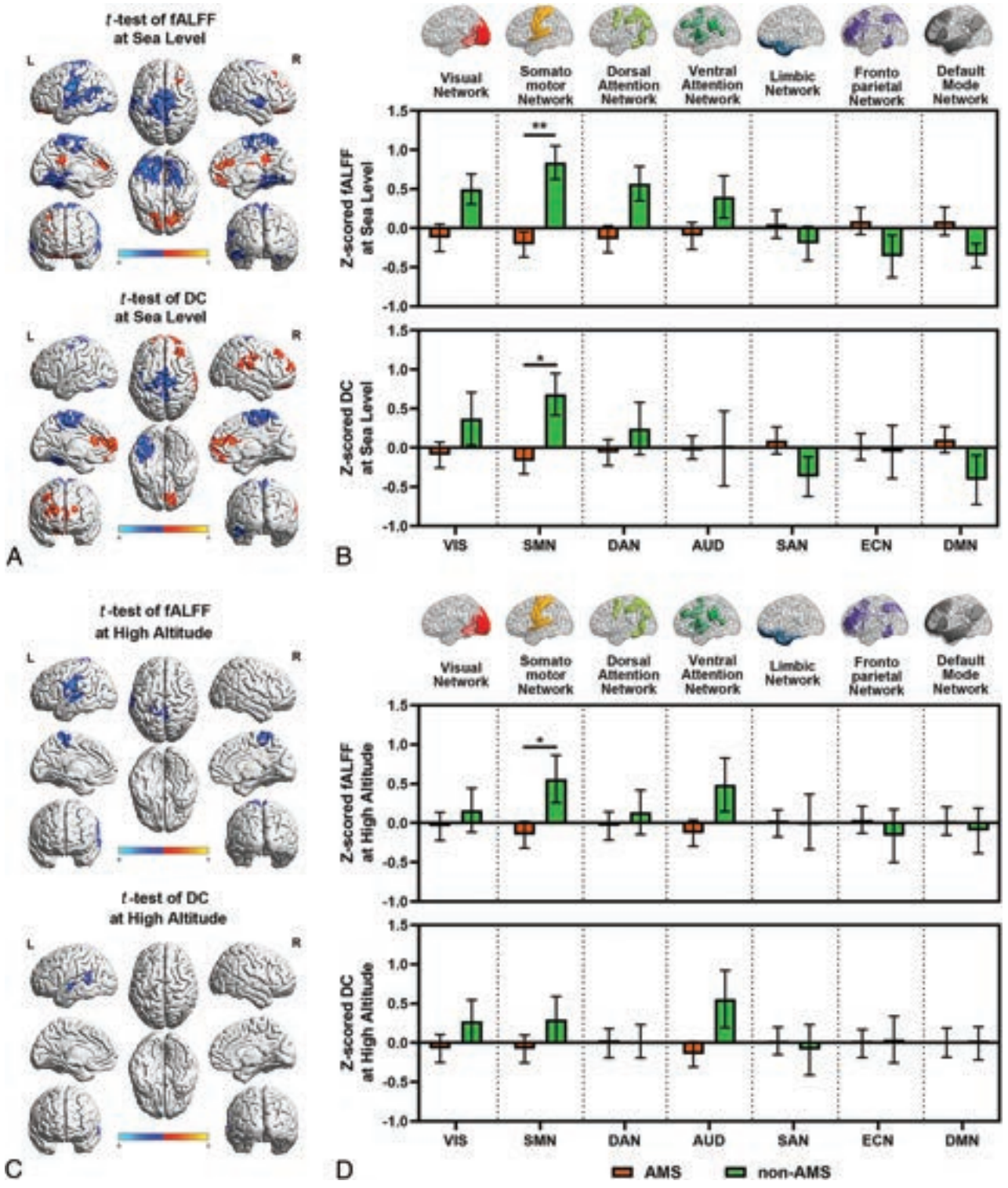

FIG 3. Comparison of functional metrics between AMS and non-AMS groups. *A*, Sea-level voxelwise differences. Differences between AMS and non-AMS groups are identified using *t* tests, corrected with the Gaussian random field at $P < .05$. For both fALFF and DC, AMS showed increased functional metrics in the medial prefrontal cortex, supramarginal gyrus, posterior cingulate cortex, and superior frontal gyrus and decreased functional metrics in the supplementary motor area, postcentral gyrus, paracentral lobule, Rolandic operculum, middle cingulate cortex, and superior temporal gyrus. *B*, Sea-level network-wise differences. Among 7 typical functional networks at sea level, we detected significant lower fALFF and DC in the SMN in the AMS group (*: $P < .05$; **: $P < .01$). The *error bars* present the standard error of the mean (SEM). *C*, High-altitude voxelwise differences. At high altitudes, for both fALFF and DC, AMS showed decreased functional metrics in the postcentral gyrus, Rolandic operculum, and superior temporal gyrus. *D*, High-altitude network-wise differences. Among 7 typical functional networks at high altitude, we detected significant lower fALFF in SMN in the AMS group (*: $P < .05$). The *error bars* present SEM. L indicates left; R, right.

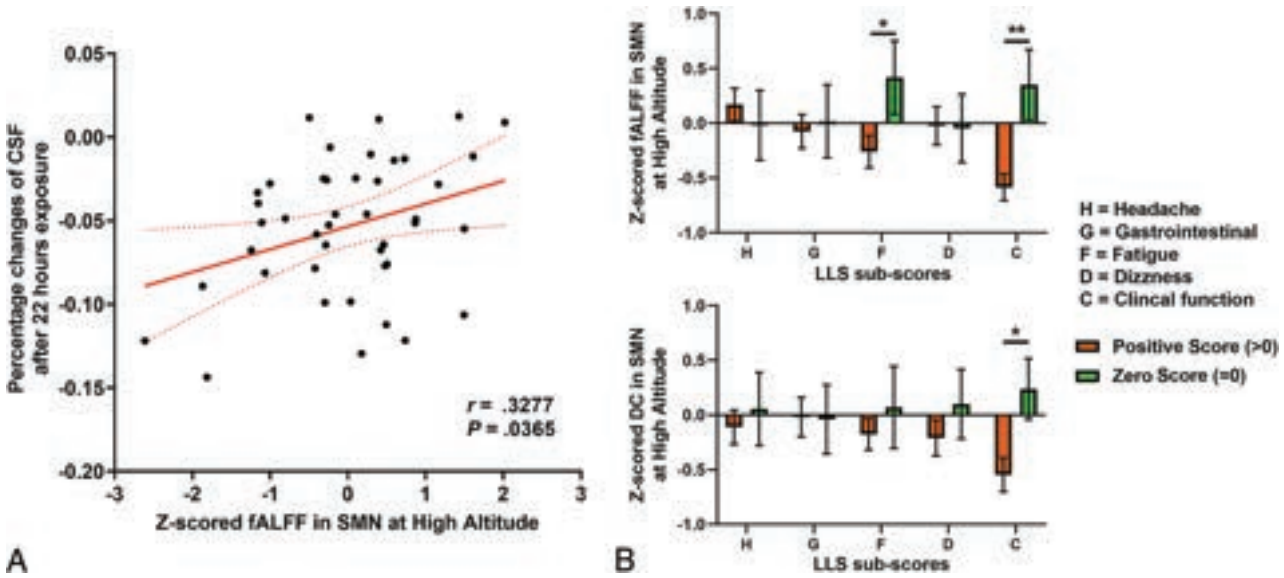

FIG 4. The pathophysiologic impact of sea-level functional predictors on AMS, measured at 22 hours after high-altitude exposure. *A*, Correlation between the fALFF in the SMN and the percentage change in CSF volume. The partial Pearson correlation coefficient is $r = 0.3277$ and $P = .0365$, considering the effects age and sex. *B*, *T* test comparisons show significant differences in fALFF and DC in the SMN between participants having positive LLS subscores and those with zero subscores. The *error bars* present standard error of the mean. The LLS subscores associated with SMN function were fatigue and clinical function scores. * $P < .05$; ** $P < .01$.

while higher fALFF in the SMN means stronger spontaneous neural activity.[39,40] Insignificant regional homogeneity results suggested that AMS might be less related to local synchrony within brain regions. Because weaker SMN function leads to higher AMS probability in this study, resting-state sea-level SMN could potentially indicate the capability for subsequent high-altitude adaptation, showing promise for clinical use. The stronger SMN activity for better adaptation aligns with previous studies, which regard the SMN as regions responsible for integrating sensory signals from the environment, especially for the sensation of hypoxia,[41-43] while hypoxia is a commonly-recognized trigger of AMS.[1] Moreover, the SMN is found to be specifically affected by the brain hypoxia–ischemia injury in the former reports on neonatal rats and humans;[44-46] this finding can also be related to the important role of SMN during the high-altitude hypoxia and the onset of AMS. In summary, we speculated that a functionally more active SMN could imply a more efficient processing and integration of sensory input, indicating protective and adaptive compensatory mechanisms in response to exposure.

The risk factors of AMS in Table 3 and Fig 3*A* were mainly distributed in the orbitofrontal cortex and right supramarginal gyrus, aligning with the sensory processing function that was previously proposed.[47,48] However, these group differences did not remain significant at high altitude (Fig 3*C*). Therefore, this study focused more on the SMN as the most promising protective predictor of AMS.

Identifying the Pathophysiologic Impact of AMS Predictors at High Altitude

At high altitude, a weaker SMN function showed a significant association with less change of CSF volume after exposure (Fig 4*A*). Other modalities of GM, WM, and CBF showed no correlation with SMN function (Online Supplemental Data). Changes in CSF and the saturation of pulse oxygen (SpO_2) are shown in the Online Supplemental Data. This result provides evidence for the differential effects of various brain components at the onset of high-altitude symptoms.[25,27] On the basis of the high-altitude MR imaging, our results propose that among the volume effect of different brain components,[19] CSF is directly related to brain functional activity during AMS, a relationship also observed in a previous study,[49] and we propose a potential mechanism of AMS susceptibility: SMN-based functional predictors might be dynamically associated with AMS by reflecting changes in CSF flow after exposure.

Then, we detected the differences of SMN function between LLS-positive and -negative groups (Fig 4*B*). Although headache is widely believed to be the key factor of AMS,[2] our *t* test analyses suggest that the SMN function might lead to the development of AMS by influencing the levels of fatigue and the clinical function. In detail, the clinical function measures the overall influence extent of the symptoms on the individual's activity. The relationships between weaker SMN function and fatigue or clinical function was formerly confirmed in studies without high-altitude exposure[50,51] and was in line with our results. However, our results further suggest that this mechanism can underlie the onset of AMS.

Overall, we suggest that the functional features of the SMN within the brain serve as early indicators and pathologic features of AMS, which suggests focusing on the functional aspects of the brain in future AMS research.

Potential Clues for Future Treatment and Prevention of AMS

Our SMN-based hypothesis on AMS susceptibility could potentially explain why lower-altitude or hypoxic training before exposure is effective in preventing AMS,[52] as interpreted by the augmentation of SMN functionality during training, because this augmentation

was also observed in training patients with incomplete spinal cord injury.[53] Additionally, the relationship between SMN activity and CSF dynamics or LLS subscores might suggest a potential treatment target. Treatments that modulate CSF volume and flow in response to changes in clinical function or fatigue state could be explored during the development of AMS.

Limitations

Our study had limitations. First, we defined AMS as any diagnosis during the 5 time points at the plateau to achieve a generic prediction for wider populations, but future studies can consider the different onset, duration, and extent of AMS as separate subgroups. Second, all participants are sea-level residents with ages relatively limited to 20–40 years (mean, 28.7 [SD, 4.4] years). Therefore, the generalizability to other age ranges and to residents at high altitude is relatively weaker. However, we selected this age range to minimize the potential confounding effects of age-related brain changes.

CONCLUSIONS

Our multimodal MR imaging study revealed that the SMN function, as detected by sea-level rs-fMRI, emerged as a crucial predictor for AMS among multimodal MR imaging features. Furthermore, we validated its pathophysiologic impact at high altitudes. Although this study is derived from a relatively small sample size of 45 and should be considered as a preliminary feasibility study that requires validation in larger and more diverse populations, these significant findings offer a potential direction for developing a screening tool to predict AMS, particularly for individuals requiring rapid ascent to high-altitude areas, such as those undertaking urgent high-altitude missions, and also offer insight into the underlying mechanisms of AMS at high altitudes.

Disclosure forms provided by the authors are available with the full text and PDF of this article at www.ajnr.org.

REFERENCES

1. Luks AM, Swenson ER, Bärtsch P. **Acute high-altitude sickness**. *Eur Respir Rev* 2017;26:160096 CrossRef Medline
2. Bärtsch P, Swenson ER. **Acute high-altitude illnesses**. *N Engl J Med* 2013;368:2294–302 CrossRef Medline
3. Luks AM, Hackett PH. **Medical conditions and high-altitude travel.** *N Engl J Med* 2022;386:364–73 CrossRef Medline
4. Canoui-Poitrine F, Veerabudun K, Larmignat P, et al. **Risk prediction score for severe high altitude illness: a cohort study.** *PLos One* 2014;9:e100642 CrossRef Medline
5. Burtscher M, Flatz M, Faulhaber M. **Prediction of susceptibility to acute mountain sickness by Sa(O2) values during short-term exposure to hypoxia.** *High Alt Med Biol* 2004;5:335–40 CrossRef Medline
6. Cochand NJ, Wild M, Brugniaux JV, et al. **Sea-level assessment of dynamic cerebral autoregulation predicts susceptibility to acute mountain sickness at high altitude.** *Stroke* 2011;42:3628–30 CrossRef Medline
7. Faulhaber M, Wille M, Gatterer H, et al. **Resting arterial oxygen saturation and breathing frequency as predictors for acute mountain sickness development: a prospective cohort study.** *Sleep Breath* 2014;18:669–74 CrossRef Medline
8. Karinen HM, Peltonen JE, Kahonen M, et al. **Prediction of acute mountain sickness by monitoring arterial oxygen saturation during ascent.** *High Alt Med Biol* 2010;11:325–32 CrossRef Medline
9. Karinen HM, Uusitalo A, Vaha-Ypya H, et al. **Heart rate variability changes at 2400 m altitude predicts acute mountain sickness on further ascent at 3000-4300 m altitudes.** *Front Physiol* 2012;3:336 CrossRef Medline
10. Mandolesi G, Avancini G, Bartesaghi M, et al. **Long-term monitoring of oxygen saturation at altitude can be useful in predicting the subsequent development of moderate-to-severe acute mountain sickness.** *Wilderness Environ Med* 2014;25:384–91 CrossRef Medline
11. Modesti PA, Rapi S, Paniccia R, et al. **Index measured at an intermediate altitude to predict impending acute mountain sickness.** *Med Sci Sports Exerc* 2011;43:1811–18 CrossRef Medline
12. Shen Y, Yang YQ, Liu C, et al. **Association between physiological responses after exercise at low altitude and acute mountain sickness upon ascent is sex-dependent.** *Mil Med Res* 2020;7:53 CrossRef Medline
13. MacInnis MJ, Lohse KR, Strong JK, et al. **Is previous history a reliable predictor for acute mountain sickness susceptibility? A meta-analysis of diagnostic accuracy.** *Br J Sports Med* 2015;49:69–75 CrossRef Medline
14. Chen HC, Lin WL, Wu JY, et al. **Change in oxygen saturation does not predict acute mountain sickness on Jade Mountain.** *Wilderness Environ Med* 2012;23:122–27 CrossRef Medline
15. Small E, Juul N, Pomeranz D, et al. **Predictive capacity of pulmonary function tests for acute mountain sickness.** *High Alt Med Biol* 2021;22:193–200 CrossRef Medline
16. Wagner DR, Knott JR, Fry JP. **Oximetry fails to predict acute mountain sickness or summit success during a rapid ascent to 5640 meters.** *Wilderness Environ Med* 2012;23:114–21 CrossRef Medline
17. Millet GP, Faiss R, Pialoux V. **Point: hypobaric hypoxia induces different physiological responses from normobaric hypoxia.** *J Appl Physiol (1985)* 2012;112:1783–84 CrossRef Medline
18. Meier D, Collet TH, Locatelli I, et al. **Does this patient have acute mountain sickness?: the rational clinical examination systematic review.** *JAMA* 2017;318:1810–19 CrossRef Medline
19. Lawley JS, Alperin N, Bagci AM, et al. **Normobaric hypoxia and symptoms of acute mountain sickness: elevated brain volume and intracranial hypertension.** *Ann Neurol* 2014;75:890–98 CrossRef Medline
20. Zhou Y, Huang X, Zhao T, et al. **Hypoxia augments LPS-induced inflammation and triggers high altitude cerebral edema in mice.** *Brain Behav Immun* 2017;64:266–75 CrossRef Medline
21. Storz JF, Scott GR. **Life ascending: mechanism and process in physiological adaptation to high-altitude hypoxia.** *Annu Rev Ecol Evol Syst* 2019;50:503–26 CrossRef Medline
22. Zhang X, Zhang J. **The human brain in a high-altitude natural environment: a review.** *Front Hum Neurosci* 2022;16:915995 CrossRef Medline
23. Dhar P, Sharma VK, Das SK, et al. **Differential responses of autonomic function in sea level residents, acclimatized lowlanders at >3500 m and Himalayan high altitude natives at >3500 m: a cross-sectional study**. *Respir Physiol Neurobiol* 2018;254:40–48 CrossRef Medline
24. Sander M. **Does the sympathetic nervous system adapt to chronic altitude exposure?** *Adv Exp Med Biol* 2016;903:375–93 CrossRef Medline
25. Wilson MH. **Monro-Kellie 2.0: The dynamic vascular and venous pathophysiological components of intracranial pressure.** *J Cereb Blood Flow Metab* 2016;36:1338–50 CrossRef Medline
26. Wei W, Wang X, Gong Q, et al. **Cortical thickness of Native Tibetans in the Qinghai-Tibetan Plateau.** *AJNR Am J Neuroradiol* 2017;38:553–60 CrossRef Medline
27. Benson JC, Madhavan AA, Cutsforth-Gregory JK, et al. **The Monro-Kellie Doctrine: a review and call for revision.** *AJNR Am J Neuroradiol* 2023;44:2–6 CrossRef Medline
28. Fan C, Zhao Y, Yu Q, et al. **Reversible brain abnormalities in people without signs of mountain sickness during high-altitude exposure.** *Sci Rep* 2016;6:33596 CrossRef Medline

29. Hunt JS, Theilmann RJ, Smith ZM, et al. **Cerebral diffusion and T-2: MRI predictors of acute mountain sickness during sustained high-altitude hypoxia.** *J Cereb Blood Flow Metab* 2013;33:372–80 CrossRef Medline
30. Roach RC, Hackett PH, Oelz O, et al; Lake Louise AMS Score Consensus Committee. **The 2018 Lake Louise Acute Mountain Sickness Score.** *High Alt Med Biol* 2018;19:4–6 CrossRef Medline
31. Rolls ET, Huang CC, Lin CP, et al. **Automated anatomical labelling atlas 3.** *Neuroimage* 2020;206:116189 CrossRef Medline
32. Desikan RS, Segonne F, Fischl B, et al. **An automated labeling system for subdividing the human cerebral cortex on MRI scans into gyral based regions of interest.** *Neuroimage* 2006;31:968–80 CrossRef Medline
33. Tibshirani R. **Regression shrinkage and selection via the Lasso.** *Journal of the Royal Statistical Society: Series B (Methodological)* 1996;58:267–88 CrossRef
34. Fawcett T. **An introduction to ROC analysis.** *Pattern Recognition Letters* 2006;27:861–74. Accessed December 26, 2023 CrossRef
35. Jeni LA, Cohn JF, De La Torre F. **Facing imbalanced data recommendations for the use of performance metrics.** *Int Conf Affect Comput Intell Interact Workshops* 2013;2013:245–51 CrossRef Medline
36. Wang L, Han M, Li X, et al. **Review of classification methods on unbalanced data sets.** *IEEE Access* 2021;9:64606–28. Accessed December 25, 2023 CrossRef
37. Thomas Yeo BT, Krienen FM, Sepulcre J, et al. **The organization of the human cerebral cortex estimated by intrinsic functional connectivity.** *J Neurophysiol* 2011;106:1125–65 CrossRef Medline
38. Flach PA, Wu S. **Repairing concavities in ROC curves.** Internattional Joint Conference on Artificial Intelligence 2005:702–07. https://www.academia.edu/download/35346892/2000402.pdf. Accessed December 26, 2023
39. Zou QH, Zhu CZ, Yang Y, et al. **An improved approach to detection of amplitude of low-frequency fluctuation (ALFF) for resting-state fMRI: Fractional ALFF.** *J Neurosci Methods* 2008;172:137–41 CrossRef Medline
40. Zuo XN, Ehmke R, Mennes M, et al. **Network centrality in the human functional connectome.** *Cereb Cortex* 2012;22:1862–75 CrossRef Medline
41. Legros A, Marshall HR, Beuter A, et al. **Effects of acute hypoxia on postural and kinetic tremor.** *Eur J Appl Physiol [Physiol* 2010; 110:109–19 CrossRef Medline
42. Kline DD. **Chronic intermittent hypoxia affects integration of sensory input by neurons in the nucleus tractus solitarii.** *Respir Physiol Neurobiol* 2010;174:29–36 CrossRef Medline
43. LaManna JC, Vendel LM, Farrell RM. **Brain adaptation to chronic hypobaric hypoxia in rats.** *J Appl Physiol (1985)* 1992;72:2238–43 CrossRef Medline
44. Quairiaux C, Sizonenko SV, Mégevand P, et al. **Functional deficit and recovery of developing sensorimotor networks following neonatal hypoxic–ischemic injury in the rat**. *Cereb Cortex* 2010; 20:2080–91 CrossRef Medline
45. Wang Y, Wang Y, Hua G, et al. **Changes of functional brain network in neonates with different degrees of hypoxic-ischemic encephalopathy.** *Brain Connect* 2023;13:427–35 CrossRef Medline
46. Jiang L, El-Metwally D, Sours Rhodes C, et al. **Alterations in motor functional connectivity in neonatal hypoxic ischemic encephalopathy.** *Brain Inj* 2022;36:287–94 CrossRef Medline
47. Peng W, Jia Z, Huang X, et al. **Brain structural abnormalities in emotional regulation and sensory processing regions associated with anxious depression.** *Prog Neuropsychopharmacol Biol Psychiatry* 2019;94:109676 CrossRef Medline
48. Kessner SS, Schlemm E, Gerloff C, et al. **Grey and white matter network disruption is associated with sensory deficits after stroke.** *Neuroimage Clin* 2021;31:102698 CrossRef Medline
49. Williams SD, Setzer B, Fultz NE, et al. **Neural activity induced by sensory stimulation can drive large-scale cerebrospinal fluid flow during wakefulness in humans.** *PLoS Biol* 2023;21:e300203 CrossRef Medline
50. Gay CW, Robinson ME, Lai S, et al. **Abnormal resting-state functional connectivity in patients with chronic fatigue syndrome: results of seed and data-driven analyses.** *Brain Connect* 2016;6:48–56 CrossRef Medline
51. Betzel RF, Satterthwaite TD, Gold JI, et al. **Positive affect, surprise, and fatigue are correlates of network flexibility.** *Sci Rep* 2017;7:520 CrossRef Medline
52. Schommer K, Wiesegart N, Menold E, et al. **Training in normobaric hypoxia and its effects on acute mountain sickness after rapid ascent to 4559 m.** *High Alt Med Biol* 2010;11:19–25 CrossRef Medline
53. Trumbower RD, Jayaraman A, Mitchell GS, et al. **Exposure to acute intermittent hypoxia augments somatic motor function in humans with incomplete spinal cord injury.** *Neurorehabil Neural Repair* 2012;26:163–72 CrossRef Medline

Imaging Outcomes of Emergency MR Imaging in Dizziness and Vertigo: A Retrospective Cohort Study

Tatu Happonen, Mikko Nyman, Pauli Ylikotila, Kimmo Mattila, and Jussi Hirvonen

ABSTRACT

BACKGROUND AND PURPOSE: Patients exhibiting acute dizziness or vertigo often represent a diagnostic challenge, and many undergo neuroimaging for stroke detection. We aimed to demonstrate the imaging outcomes of first-line emergency MR imaging among patients with acute dizziness or vertigo and to determine the clinical risk factors for stroke and other acute pathology.

MATERIALS AND METHODS: This retrospective study included consecutive patients with acute dizziness or vertigo referred for emergency MR imaging in a tertiary hospital during 5 years. We recorded and analyzed patient characteristics, relevant clinical information, and imaging outcomes. Risk score models were derived to predict which patients were more likely to present with positive MR imaging findings.

RESULTS: A total of 1169 patients were included. Acute stroke was found in 17%; other clinically significant pathology, in 8% of patients. In 75% of the patients, emergency MR imaging showed no significant abnormalities. Risk factors for acute stroke included older age, male sex, and a prevalence of cardiovascular risk factors and neurologic signs. Isolated dizziness had no discriminative power on imaging outcomes, and 14% of these patients showed acute stroke. Risk scores had only moderate performance in predicting acute ischemic stroke (receiver operating characteristic area under curve = 0.75) or any significant pathology (receiver operating characteristic area under curve = 0.70).

CONCLUSIONS: Acute dizziness and vertigo remain challenging even when emergency MR imaging is readily available. One in 4 patients had acute pathology on MR imaging. Predictors for acute pathology (older age, male sex, cardiovascular risk factors, and neurologic signs) may aid in patient selection for MR imaging, optimizing the yield and clinical impact of emergency neuroimaging. Low diagnostic yields of CT and internal acoustic canal MR imaging may offer an opportunity to reduce health care expenditures in the future.

ABBREVIATIONS: AIS = acute ischemic stroke; AUC = area under the curve; HINTS = head impulse, nystagmus, and test of skew; IQR = interquartile range; NPV = negative predictive value; NS = nonsignificant findings; PPV = positive predictive value; ROC = receiver operating characteristic; S = significant-but-nonischemic pathology; STANDING = SponTAneous Nystagmus, Direction, head Impulse test, standiNG

Dizziness (including vertigo) is a rather common symptom among the general population, affecting 15%–35% at some point in their lives.[1] According to the International Classification of Vestibular Disorders, dizziness is defined as a sensation of disturbed or impaired spatial orientation without a false or distorted sense of motion, whereas vertigo is described as a sensation of self-motion when no self-motion is occurring or the sensation of distorted self-motion during an otherwise normal head movement.[2] Patients and physicians often use these terms interchangeably, which may lead to imprecision and inconsistency in patient care and research.[3,4] In this article, vertigo denotes a vestibular symptom encompassing false spinning sensations, though the exact definition varies among studies.

Patients exhibiting acute dizziness or vertigo often represent a diagnostic challenge. Despite many patients being diagnosed with a benign peripheral vestibular disorder, some patients may need neuroimaging to rule out central causes of dizziness. Stroke, particularly vertebrobasilar acute ischemic stroke, is the primary differential diagnosis among central causes and is diagnosed in approximately 3%–5% of all emergency visits for dizziness and vertigo.[5,6] Several bedside examination patterns, such as head impulse, nystagmus, and test of skew (HINTS) and SponTAneous

Received November 27, 2023; accepted after revision January 19, 2024.

From the Department of Radiology (T.H., M.N., K.M., J.H.) and Neurocenter (P.Y.), Turku University Hospital and University of Turku, Turku, Finland; and Department of Radiology (J.H.), Tampere University Hospital and Tampere University, Tampere, Finland.

Please address correspondence to Jussi Hirvonen, MD, PhD, Department of Radiology, University of Turku, Kiinamyllynkatu 4-8, FIN-20520, Turku, Finland; e-mail: jussi.hirvonen@utu.fi; @jussihirvonen

Indicates open access to non-subscribers at www.ajnr.org

Indicates article with online supplemental data.

http://dx.doi.org/10.3174/ajnr.A8202

Nystagmus, Direction, head Impulse test, standiNG (STANDING), and clinical risk scores (such as TriAGe+ and ABCD^2) have been developed for early stroke detection.[7-10] Despite these attempts to focus on high-risk patients, generally 30% to 50% of acutely dizzy emergency patients undergo neuroimaging.[6,8,11] According to the American College of Radiology guidelines on dizziness (American College of Radiology Appropriateness Criteria), MR imaging is usually an appropriate imaging method when dizziness is accompanied by neurologic deficits, or the HINTS examination findings are consistent with central vertigo.[12]

Imaging options include CT/CTA and MR imaging. CT is the most used method to exclude stroke due to widespread availability and fast scan times, but it has a low sensitivity for stroke of around 30% among patients with acute dizziness and vertigo.[13] CT is especially challenging in the posterior fossa, where vertebrobasilar acute ischemic strokes occur. Although less commonly used, conventional MR imaging has a higher sensitivity of 80%.[13] If one included thin-section DWI with a 3-mm section thickness, an even higher sensitivity of 95% for posterior circulation stroke may be reached.[14] Recently, MR imaging was shown to demonstrate a higher rate of critical findings[15] and improved cost-effectiveness[16] compared with CTA in emergency patients with dizziness.

In the United States, recent annual spending for neuroimaging dizziness is as high as US $88 million, of which MR imaging accounted for 70%, though a head CT scan was the most used test across settings.[17] In total, neuroimaging was applied >376,000 times per year within 6 months of the first presentation with dizziness to an emergency department or an outpatient clinic.

Only a few studies have been published on the yield of emergency MR imaging in dizziness and vertigo. In a study among 188 emergency patients with dizziness or vertigo who underwent MR imaging, around a 20% acute stroke rate and a 17% rate in other significant abnormalities were reported.[18] In this study, risk factors for acute stroke were age older than 50 years, a high number of cardiovascular risk factors, a short duration of symptoms, and at least 1 neurologic sign.[18] A higher proportion of stroke (33%) has been prospectively recorded among selected emergency patients with acute-onset vertigo who did not have a previous diagnosis of peripheral vertigo.[19]

The primary aim of this study was to assess the imaging outcomes of emergency MR imaging among patients with acute dizziness or vertigo and to characterize these patients in terms of demographics, history, and specific signs and symptoms. We also aimed to demonstrate factors related to significant imaging outcomes to aid clinical decision-making and improve the effective use of emergency neuroimaging.

MATERIALS AND METHODS

This retrospective cohort study was conducted at Turku University Hospital, an academic tertiary care referral center with an approximate patient catchment area of 480,000. During the study period, the emergency radiology department had an Ingenia 3T system (Philips Healthcare) dedicated to emergency imaging only.[20,21]

Permission for this study was obtained from the hospital district board, and patient consent was waived due to the retrospective nature of the study. Consecutive emergency MR imaging scans obtained between April 2014 and January 2019 were retrospectively identified from the PACS and radiologic information systems using standard MR imaging codes. The MR imaging protocols varied, but most included routine sequences such as T1WI and T2WI, FLAIR, DWI (axial), SWI, 3D TOF arterial angiography, high-resolution T2-weighted sequences of the internal acoustic canal and inner ear (selected patients), and contrast-enhanced T1WI (selected patients). Imaging data were cross-referenced with those from the electronic medical records.

To identify cases with dizziness and vertigo, we queried the referrals with the keywords "dizziness" and "vertigo." The retrospective study design did not allow us to reliably separate central and peripheral vertigo. Postoperative patients, patients with a ventriculoperitoneal shunt, and patients with a recent head injury were excluded because they almost always undergo neuroimaging if presenting with dizziness and may have specific complications that are not well-generalizable. Patients of all age groups, whether emergency admissions or inpatients, were included as long as the aforementioned keywords were featured in the clinical indication for the emergency MR imaging request. All patients had emergency MR imaging as a part of their routine care, and the decision to refer the patient was made by the attending physician on clinical grounds.

From the referrals, we recorded the patients' demographic characteristics, cardiovascular risk factors, neurologic signs, and other clinical symptoms. Missing information was then retrieved from the electronic medical records. Imaging findings were recorded from the MR imaging reports. On the basis of the emergency MR imaging findings, the patients were allocated to one of the 3 groups: those with acute ischemic stroke (AIS), those with other significant-but-nonischemic pathology (S), and those with nonsignificant findings (NS). Nonischemic MR imaging findings deemed likely to be causative and clinically significant incidental findings were included in the S category. A finding was considered clinically significant if it led to a change in management or to further examinations. Scans showing incidental findings, anatomic variations, lack of novel findings, or notable progression in chronic brain diseases were considered nonsignificant because they would be unlikely to account for the acute dizziness. The MR imaging reports were evaluated and then classified by 2 fellowship-trained neuroradiologists (J.H. and M.N.), first separately and then together to achieve consensus. We did not record interobserver agreement. A clinical neurologist was consulted when necessary. For the patients in the AIS category, results of the preceding CT studies were noted if available.

Results are typically expressed as percentages, medians, interquartile ranges (IQRs), and ORs with 95% CIs. The normality assumptions were evaluated both visually and using the Shapiro Wilk test. At the univariate level, we used the χ^2 test to compare nominal data and the Mann–Whitney U and the Kruskal–Wallis H tests as nonparametric tests to compare continuous variables that were not normally distributed. Optimal cutoff points for continuous variables were determined using the Youden J statistic. All variables were also entered into binary (2 outcome classes) and multinomial (3 outcome classes) logistic regression models. Variables that were statistically significant predictors at the multivariate level were then included in the risk scores for predicting

Table 1: Significant-but-nonischemic emergency MR imaging findings[a]

Findings	No. (%)
Tumor/metastases	44 (45)
Demyelination	12 (12)
Infection, inflammation	19 (19)
Other	9 (9)
Vascular diseases	
Intracranial hemorrhage	6 (6)
Other	7 (7)
Total	97 (100)

[a] Data are numbers (percentages).

Table 2: Nonsignificant emergency MR imaging findings[a]

Findings	No. (%)
Unremarkable	368 (42)
White matter hyperintensities	256 (29)
Benign incidental/variants	143 (16)
Known existing pathology	
Old infarcts/bleeds	105 (12)
Other	3 (0)
Total	875 (100)

[a] Data are numbers (percentages).

significant imaging outcomes. Risk score points were derived by rounding the OR (or 1/OR) of the included variables to the nearest integer. The points were summed to form a risk score for each patient. A sample calculation is available in the Online Supplemental Data. Receiver operating characteristic (ROC) and area under the curve (AUC) with sensitivity, specificity, positive predictive value (PPV), and negative predictive value (NPV) were used to evaluate the diagnostic ability of our model. The ROC AUC provides an overall estimate of the model classification accuracy (proportion of correctly classified patients). The optimal cutoff points for the risk scores to maximize sensitivity and specificity were determined by the Youden J statistic.

The data were analyzed using JMP for Mac (Version 16.1 Pro; SAS Institute, 1989–2019). *P* values $< .05$ were considered statistically significant.

RESULTS

From 8772 unique emergency MR imaging scans, the initial search identified 1419 patients, of whom a total of 1169 patients met the inclusion criteria. The median age was 61 (IQR, 45–71) years, ranging from 6 to 90 years. A narrow majority were female ($n = 646$, 55%). Most patients had undergone their MR imaging study <24 hours after the referral (82%), and the rest had a median delay of 1 day (IQR = 1–2 days).

AIS was present in 197 (17%) of the MR imaging studies (Online Supplemental Data). Ninety-seven patients (8%) had other significant pathology (S), and for the rest of the patients ($n = 875$, 75%), the MR imaging scans remained NS. Of the 197 patients with AIS, 171 (87%) underwent a head CT scan before MR imaging, usually on the same or the previous day. Acute pathology was suggested in only 62 (36%) of these CT studies. The cerebellum was the most common infarct location among patients with AIS, involved in 39% of the patients. Other infarcts were found in the cerebrum (23%), pons (10%), medulla oblongata (5%), thalamus (5%), basal ganglia (2%), mesencephalon (2%), and for 15% of patients in multiple aforementioned locations. Nonischemic significant findings included tumors and infections, among other rare findings, such as neurosarcoidosis or central pontine myelinolysis (Table 1). The most common incidental findings among the NS group were white matter hyperintensities (Table 2).

In the overall univariate analyses among the 3 findings groups (AIS/S/NS), numerous statistically significant associations were identified (Online Supplemental Data). Patients in the AIS group were more likely older, and men, and had a higher prevalence of cardiovascular risk factors and neurologic signs. A cutoff point for older age was 55 years. Patients in the S group had a high prevalence of headache and a long duration of symptoms. Patients with vertigo were less likely to present with any acute findings on MR imaging. Pair-wise group comparisons further elaborate these differences (Fig 1). Among the 126 patients with isolated dizziness, 14% had AIS, 10% had other significant findings, and 76% had nonsignificant findings, in similar proportions to patients with additional signs and symptoms (17% AIS, 8% S, 75% NS; $P = .49$).

In a multivariate analysis, statistically significant predictors of clinically significant acute pathology (AIS/S) were aphasia/dysarthria, ataxia, old cerebral infarction, auditory symptoms, inpatient hospitalization status, diplopia, nausea/vomiting, age older than 55 years, male sex, and absence of vertigo (Fig 2). The risk score points for each variable are presented in the Online Supplemental Data. The ROC AUC for the risk score was 0.70. With a single cutoff of 6 points, the model had a sensitivity of 66% and a specificity of 64%. PPV was 38%, and NPV was 85%. The mean risk score was 7.6 points in the AIS/S group and 5.7 points in the NS group (Fig 3).

We also calculated a similar risk score for acute infarcts only (AIS versus S/NS) and found improved performance, with an ROC AUC of 0.75 (Fig 2). With a single cutoff of 8 points, sensitivity was 51%, specificity was 84%, PPV was 40%, and NPV was 90%. The mean risk score was 8.8 points in the AIS group and 5.6 points in the S/NS group (Fig 3).

To ensure that early MR imaging did not miss infarcts (false-negative), we determined whether patients with negative findings on DWI <48 hours after symptom onset had follow-up neuroimaging the following week. Among the 470 patients fulfilling these criteria, only 4 (0.9%) underwent follow-up CT or MR imaging. Only one (0.2%) of these patients, scanned because of new neurologic symptoms after vertigo had dissipated, had a small new cortical infarction on CT. All patients in the catchment area with a clinically meaningful suspicion of stroke are referred to our tertiary hospital. Therefore, it is likely that acute MR imaging did not miss any clinically meaningful infarcts in these patients to the extent that such infarcts would warrant repeat neuroimaging.

A total of 145 patients underwent dedicated internal acoustic canal and inner ear imaging with heavily T2-weighted images (3D driven equilibrium radiofrequency reset pulse [DRIVE]). None of these images revealed any acute findings. One patient was diagnosed with acute labyrinthitis, but this was evident only on postcontrast T1-weighted images and not on T2-weighted images.

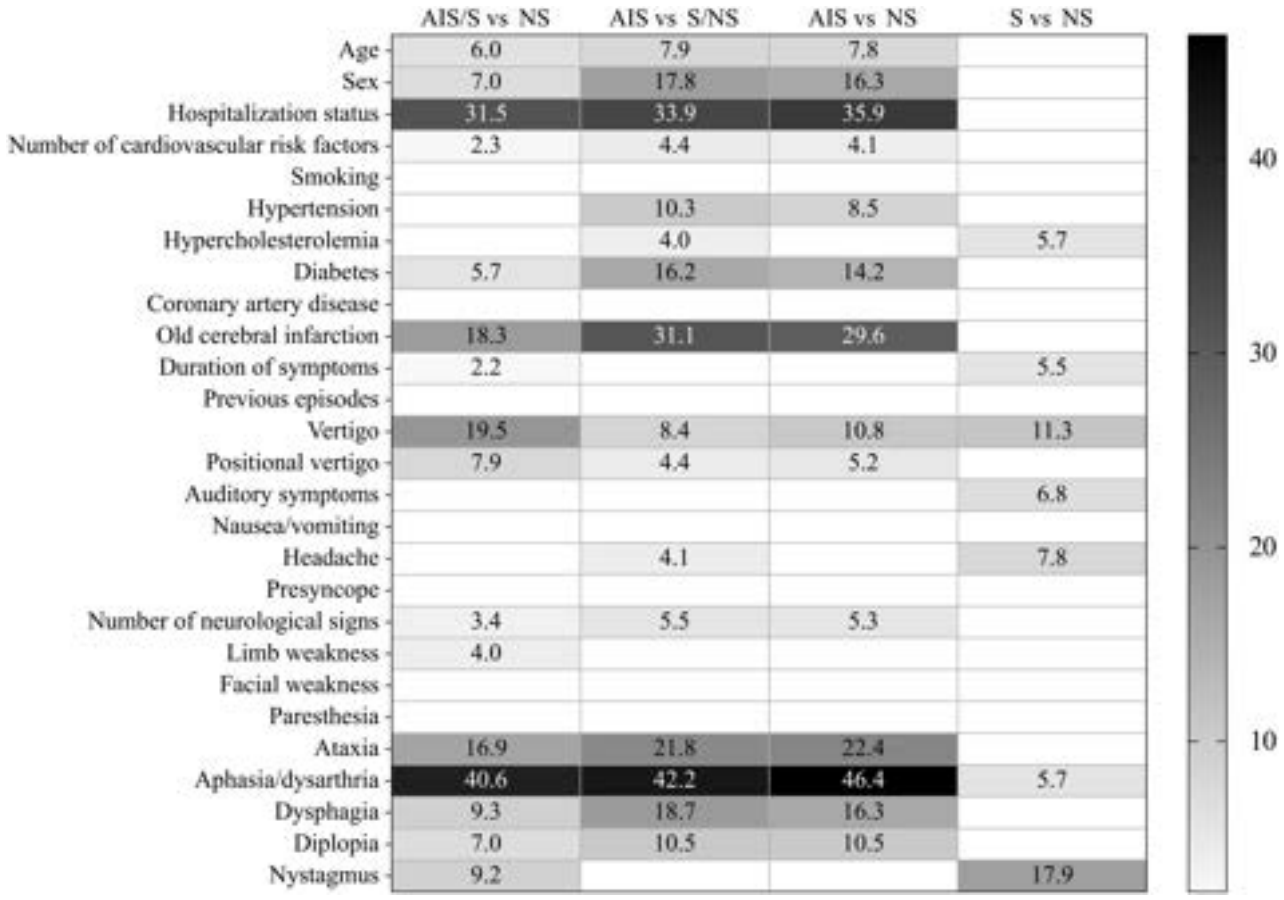

FIG 1. Statistical test values between dichotomic imaging outcome groups. Only values with statistical significance ($P < .05$) are shown. The χ^2 test was used for categoric variables, and the Mann-Whitney *U* test, for continuous variables.

DISCUSSION

In this large-scale emergency MR imaging study, we found a prevalence of acute ischemic strokes in roughly 1 in 6 patients imaged for dizziness or vertigo. Nearly 1 in 10 patients had other clinically significant findings, whereas in 3 of 4 patients, MR imaging was unremarkable for acute pathology. Risk scores had only moderate performance in predicting any significant pathology or acute ischemic stroke. Isolated dizziness had no discriminative power concerning imaging outcomes. Dedicated internal acoustic canal and inner ear imaging had no role in the acute setting. CT had a low diagnostic yield among patients who had a stroke on MR imaging. Acute dizziness and vertigo remain challenging even when emergency MR imaging is readily available.

Overall, patients who had acute ischemic stroke were characterized by older age (generally older than 55 years of age), male sex, and high prevalences of cardiovascular risk factors and neurologic signs; patients with nonischemic significant pathology, by a high prevalence of headache and longer symptom duration; and patients with no significant pathology, by a high prevalence of vertigo. History-taking and proper clinical examination still play an important role when referring patients for MR imaging, because the aforementioned factors have a considerable impact on imaging outcomes.

We found several statistically significant associations between clinical variables and imaging outcomes that are consistent with those from the existing literature. Kabra et al[18] reported an acute pathology rate of around 38% on early MR imaging and several stroke predictors (age older than 50 years, a high number of cardiovascular risk factors, a short duration of symptoms, and at least 1 neurologic sign). Machner et al[22] reported a 24% acute pathology rate (varying between 0% and 50% among clinically defined subgroups) among emergency patients with dizziness who underwent adequate neuroimaging (early CT or delayed MR imaging). They documented hypertension, high ABCD^2 scores, and any central oculomotor sign or focal abnormality that increased the risk of acute lesions. Similar to our analysis, they noted that among patients with vertigo (spinning sensations), acute lesions were less likely. Our findings further corroborate the use of MR imaging among patients with older age, cardiovascular risk factors, or neurologic signs.

Our risk scores reached moderate performances. The predictive model for acute strokes had an ROC AUC of 0.75 with an NPV of 90%, while the model for all significant pathology was slightly less accurate. We found no previously published risk scores for emergency MR imaging. In a study with 188 patients, Kabra et al[18] demonstrated similar individual predictors of stroke (age, symptom duration, neurologic signs, and cardiovascular risk factors), each having NPVs of around 88%–90%.

The most common infarct location was the cerebellum. Notably, 25% of infarcts were located elsewhere than in the

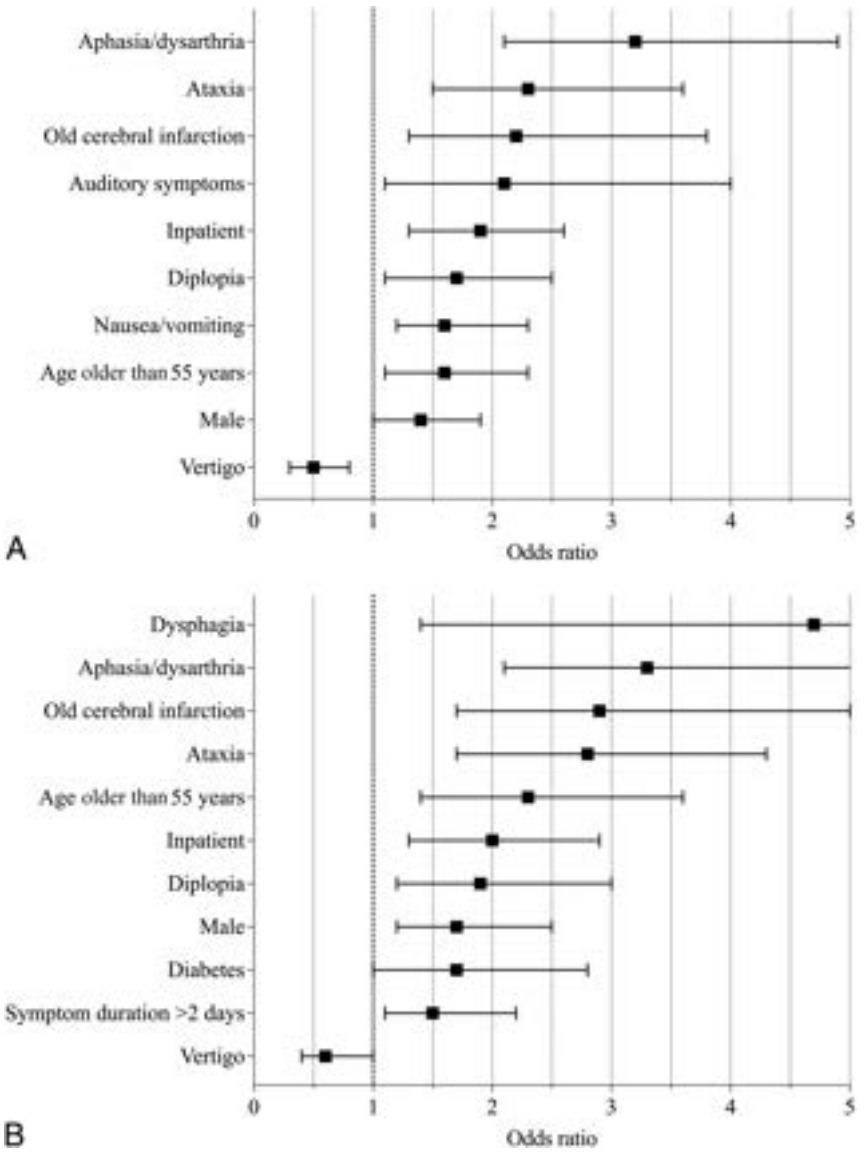

FIG 2. *A*, Variables predicting significant acute pathology (AIS/S versus NS) in emergency MR imaging with statistical significance ($P < .05$) in a multivariate analysis. *B*, Variables predicting acute ischemic stroke (AIS versus S/NS) in emergency MR imaging with statistical significance ($P < .05$) in a multivariate analysis.

cerebellum or the brainstem. According to a recent connectivity-based analysis, supratentorial brain regions involved in the brain vertigo network include the bilateral insula, somatosensory cortex, higher-level visual areas, cingulate sulcus, and thalamus.[23] Only 36% of prior CTs were positive for AIS, corroborating the role of acute MR imaging in detecting AIS in patients with vertigo. Missing an acute stroke may have serious adverse effects, such as predisposing the patient to a high risk of future, potentially more severe infarcts that could otherwise have been prevented, or, potentially, fatal secondary complications of the current stroke, such as brainstem compression and obstructive hydrocephalus.[18,24]

While its accuracy is considered superior to CT, even MR imaging does not have perfect sensitivity in the early detection of an AIS.[25] In fact, DWI has been previously reported to be falsely negative within the first 48 hours in up to 50% of small ischemic strokes in the posterior fossa.[26] In our follow-up analysis of patients with NS, we concluded that acute MR imaging likely did not miss any clinically meaningful infarcts in our cohort. Modern MR imaging technology likely has a substantial sensitivity in detecting small infarcts in the posterior fossa and elsewhere in the brain, as was shown in the current study.

This study has 2 major strengths. First, we had a large sample size due to the routine use of emergency MR imaging in the emergency radiology department.[21] A large sample size affords adequate statistical power to discern clinically meaningful effect sizes. Second, we used a data-driven approach by querying the referrals for specific symptoms instead of relying on diagnosis codes. This approach mitigates sampling bias because all patients with vertigo will be included irrespective of the final diagnosis. This imaging phenotypical approach is likely more proximal to the underlying biology than diagnosis codes. The present study represents a true clinical situation and offers a real-world overview of emergency patients with dizziness and vertigo. The fact that isolated dizziness (no other symptoms) had no significant discriminatory power suggests that the liberal inclusion of patients with various other symptoms did not significantly bias our results.

Yet, this study is limited by its retrospective and single-center design. Some referrals may have been incomplete or imprecise; therefore, the true prevalence of risk factors may have been underestimated. In addition to specific symptoms, relevant comorbidities and medical history may have been missing. The quality of the clinical note-keeping for each patient (reflecting real-world practice) determined the quality of the clinical data included in the present study. Classifying findings into NS and S groups was based on expert opinion and may, therefore, have been biased. In the classification, we used a consensus method among neuroradiologists and did not record interobserver agreement. The lack of relevant data may have contributed to the performance of the risk scores. In addition, the risk scores require prospective validation before claims of clinical utility can be made. The inclusion of patients with symptoms highly indicative of stroke (aphasia, ataxia, dysphagia) may have contributed to the higher diagnostic yield because these patients may be more likely to undergo neuroimaging

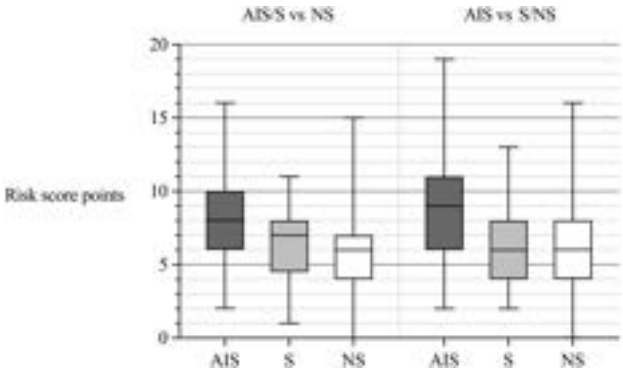

FIG 3. Risk score point distributions for both scores within imaging outcome groups.

regardless of having dizziness. We did not use the combination of axial and coronal DWI, which has been shown to have improved diagnostic accuracy for brainstem infarcts.[27] Regarding generalizability, the present study is limited because we did not include acutely dizzy patients not scheduled for emergency MR imaging. Therefore, we do not know the factors that contributed to the need for emergency MR imaging perceived by the referring physician. We are not able to estimate the proportion of these patients undergoing first-line MR imaging. Most important, emergency MR imaging is not routinely available in all institutions, limiting the generalizability of our findings.

These results provide novel information on the diagnostic yield in this patient group when emergency MR imaging is readily available and commonly used in the emergency radiology department. Regarding the clinical value of emergency MR imaging findings, MR imaging likely altered the clinical management of patients with newly discovered neurologic disorders such as cerebrovascular (including acute infarction), demyelinating, and infectious diseases. Although the rate of nonsignificant pathology may seem too high (75%), ruling out infarctions with high sensitivity in these patients is likely valuable for them and their physicians. Most important, isolated dizziness lacked discriminative power on imaging outcomes because 14% of these patients had AIS on MR imaging.

CONCLUSIONS

Predictive modeling for including or excluding acutely dizzy patients for emergency MR imaging remains challenging. Because we were unable to reliably exclude patients who would not benefit from MR imaging, a relatively low threshold for ordering imaging to avoid misdiagnosis may be warranted. One in 4 patients had acute pathology on MR imaging. Predictors of acute pathology (older age, male sex, cardiovascular risk factors, and neurologic signs) may help to apply emergency neuroimaging more effectively among these patients, thus optimizing both the yield and clinical impact of emergency neuroimaging. Low diagnostic yields of CT and internal acoustic canal MR imaging sequences may offer an opportunity to reduce health care expenditures in the future.

Disclosure forms provided by the authors are available with the full text and PDF of this article at www.ajnr.org.

REFERENCES

1. Neuhauser HK. **The epidemiology of dizziness and vertigo.** *Handb Clin Neurol* 2016;137:67–82 CrossRef Medline
2. Bisdorff A, Von Brevern M, Lempert T, et al. **Classification of vestibular symptoms: towards an international classification of vestibular disorders.** *J Vestib Res* 2009;19:1–13 CrossRef Medline
3. Newman-Toker DE, Cannon LM, Stofferahn ME, et al. **Imprecision in patient reports of dizziness symptom quality: a cross-sectional study conducted in an acute care setting.** *Mayo Clin Proc* 2007;82:1329–40 CrossRef Medline
4. Stanton VA, Hsieh Y-H, Camargo CA, et al. **Overreliance on symptom quality in diagnosing dizziness: results of a multicenter survey of emergency physicians.** *Mayo Clin Proc* 2007;82:1319–28 CrossRef Medline
5. Kerber KA, Brown DL, Lisabeth LD, et al. **Stroke among patients with dizziness, vertigo, and imbalance in the emergency department: a population-based study.** *Stroke* 2006;37:2484–87 CrossRef Medline
6. Saber Tehrani AS, Kattah JC, Kerber KA, et al. **Diagnosing stroke in acute dizziness and vertigo: pitfalls and pearls.** *Stroke* 2018;49:788–95 CrossRef Medline
7. Shah VP, Oliveira JE, Silva L, et al. **Diagnostic accuracy of the physical examination in emergency department patients with acute vertigo or dizziness: a systematic review and meta-analysis for GRACE -3**. *Acad Emerg Med* 2023;30:552–78 CrossRef Medline
8. Quimby AE, Kwok ES, Lelli D, et al. **Usage of the HINTS exam and neuroimaging in the assessment of peripheral vertigo in the emergency department.** *J Otolaryngol Head Neck Surg* 2018;47:54 CrossRef Medline
9. Kuroda R, Nakada T, Ojima T, et al. **The TriAGe+ score for vertigo or dizziness: a diagnostic model for stroke in the emergency department**. *J Stroke Cerebrovasc Dis* 2017;26:1144–53 CrossRef Medline
10. Gerlier C, Hoarau M, Fels A, et al. **Differentiating central from peripheral causes of acute vertigo in an emergency setting with the HINTS, STANDING, and ABCD2 tests: a diagnostic cohort study.** *Acad Emerg Med* 2021;28:1368–78 CrossRef Medline
11. Kim AS, Sidney S, Klingman JG, et al. **Practice variation in neuroimaging to evaluate dizziness in the ED.** *Am J Emerg Med* 2012;30:665–72 CrossRef Medline
12. Wang LL, Thompson TA, Shih RY, et al. **ACR Appropriateness Criteria® Dizziness and Ataxia**. https://acsearch.acr.org/docs/69477/Narrative. American College of Radiology. Accessed January 11, 2024
13. Shah VP, Oliveira JE, Silva L, et al. **Diagnostic accuracy of neuroimaging in emergency department patients with acute vertigo or dizziness: a systematic review and meta-analysis for the guidelines for reasonable and appropriate care in the emergency department**. *Acad Emerg Med* 2023;30:517–30 CrossRef Medline
14. Entwisle T, Perchyonok Y, Fitt G. **Thin section magnetic resonance diffusion-weighted imaging in the detection of acute infratentorial stroke.** *J Med Imaging Radiat Oncol* 2016;60:616–23 CrossRef Medline
15. Tu LH, Navaratnam D, Melnick ER, et al. **CT with CTA versus MRI in patients presenting to the emergency department with dizziness: analysis using propensity score matching.** *AJR Am J Roentgenol* 2023;221:836–45 CrossRef Medline
16. Tu LH, Melnick E, Venkatesh AK, et al. **Cost-effectiveness of CT, CTA, MRI, and specialized MRI for evaluation of patients presenting to the emergency department with dizziness.** *Am J Roentgenol* 2024;222:e2330060 CrossRef Medline
17. Adams ME, Karaca-Mandic P, Marmor S. **Use of neuroimaging for patients with dizziness who present to outpatient clinics vs emergency departments in the US.** *JAMA Otolaryngol Head Neck Surg* 2022;148:465–73 CrossRef Medline
18. Kabra R, Robbie H, Connor SE. **Diagnostic yield and impact of MRI for acute ischaemic stroke in patients presenting with dizziness and vertigo.** *Clin Radiol* 2015;70:736–42 CrossRef Medline
19. Arfa Samreen R, Bhattacharjee S, Shetty SS, et al. **MRI outcomes in patients with acute-onset vertigo in the emergency department: a**

prospective study. *Clin Neurol Neurosurg* 2021;209:106916 CrossRef Medline
20. Heikkinen J, Nurminen J, Velhonoja J, et al. **Clinical and prognostic significance of emergency MRI findings in neck infections.** *Eur Radiol* 2022;32:1078–86 CrossRef Medline
21. Happonen T, Nyman M, Ylikotila P, et al. **Diagnostic yield of emergency MRI in non-traumatic headache.** *Neuroradiology* 2023;65:89–96 CrossRef Medline
22. Machner B, Choi JH, Trillenberg P, et al. **Risk of acute brain lesions in dizzy patients presenting to the emergency room: who needs imaging and who does not?** *J Neurol* 2020;267:126–35 CrossRef Medline
23. Li Y, Qi L, Schaper FL, et al. **A vertigo network derived from human brain lesions and brain stimulation.** *Brain Commun* 2023;5:fcad071 CrossRef Medline
24. Edlow JA, Newman-Toker DE, Savitz SI. **Diagnosis and initial management of cerebellar infarction.** *Lancet Neurol* 2008;7:951–64 CrossRef Medline
25. Chalela JA, Kidwell CS, Nentwich LM, et al. **Magnetic resonance imaging and computed tomography in emergency assessment of patients with suspected acute stroke: a prospective comparison.** *Lancet* 2007;369:293–98 CrossRef Medline
26. Saber Tehrani AS, Kattah JC, Mantokoudis G, et al. **Small strokes causing severe vertigo: Frequency of false-negative MRIs and nonlacunar mechanisms.** *Neurology* 2014;83:169–73 CrossRef Medline
27. Steffen P, Beyer LS, McDonough R, et al. **Improved detectability of brain stem ischemia by combining axial and coronal diffusion-weighted imaging.** *Stroke* 2021;52:1843–46 CrossRef Medline

Evaluating Biases and Quality Issues in Intermodality Image Translation Studies for Neuroradiology: A Systematic Review

Shannon L. Walston, Hiroyuki Tatekawa, Hirotaka Takita, Yukio Miki, and Daiju Ueda

ABSTRACT

BACKGROUND: Intermodality image-to-image translation is an artificial intelligence technique for generating one technique from another.

PURPOSE: This review was designed to systematically identify and quantify biases and quality issues preventing validation and clinical application of artificial intelligence models for intermodality image-to-image translation of brain imaging.

DATA SOURCES: PubMed, Scopus, and IEEE Xplore were searched through August 2, 2023, for artificial intelligence–based image translation models of radiologic brain images.

STUDY SELECTION: This review collected 102 works published between April 2017 and August 2023.

DATA ANALYSIS: Eligible studies were evaluated for quality using the Checklist for Artificial Intelligence in Medical Imaging (CLAIM) and for bias using the Prediction model Risk Of Bias ASsessment Tool (PROBAST). Medically-focused article adherence was compared with that of engineering-focused articles overall with the Mann-Whitney *U* test and for each criterion using the Fisher exact test.

DATA SYNTHESIS: Median adherence to the relevant CLAIM criteria was 69% and 38% for PROBAST questions. CLAIM adherence was lower for engineering-focused articles compared with medically-focused articles (65% versus 73%, $P < .001$). Engineering-focused studies had higher adherence for model description criteria, and medically-focused studies had higher adherence for data set and evaluation descriptions.

LIMITATIONS: Our review is limited by the study design and model heterogeneity.

CONCLUSIONS: Nearly all studies revealed critical issues preventing clinical application, with engineering-focused studies showing higher adherence for the technical model description but significantly lower overall adherence than medically-focused studies. The pursuit of clinical application requires collaboration from both fields to improve reporting.

ABBREVIATION: AI = artificial intelligence

Artificial intelligence (AI)-based image translation converts an image into a similar-but-different image.[1,2] This feature may mean changing a landscape from a summer to a winter scene, or a CT into an MR image. The accuracy and capacity to do what humans physically cannot has always been the promise of AI in medicine.[3] In neuroradiology specifically, using an AI model to convert among radiologic image modalities such as PET, MR imaging, and CT has several advantages, including increased accessibility and decreased time and radiation exposure. In the case of MR imaging, for example, patients with metal implants or contrast allergies cannot undergo the examination, though they may be able to undergo a CT.[4] An AI model produces the image almost immediately, while scheduling the examination can take days; this issue is known to affect prognosis.[5] For radiography, CT, and PET, patients are exposed to ionizing radiation, and the repeat examinations required for radiation therapy can cause cumulative damage. Thus, image translation models have been in development to harness these advantages for MR imaging-only radiation therapy planning[6] and ischemic stroke lesion segmentation since 2017.[7-10]

Despite these potential advantages and a 6-year history of published research, intermodality image translation models are

Received November 21, 2023; accepted after revision January 27, 2024.

From the Department of Diagnostic and Interventional Radiology (S.L.W., H.Tatekawa, H.Takita, Y.M., D.U.), Graduate School of Medicine, and Smart Life Science Lab (D.U.), Center for Health Science Innovation, Osaka Metropolitan University, Osaka, Japan.

Please address correspondence to Daiju Ueda, MD, PhD, Department of Diagnostic and Interventional Radiology, Osaka Metropolitan University Graduate School of Medicine, 1-4-3 Asahi-machi, Abeno-ku, Osaka 545-8585, Japan; e-mail: ai.labo.ocu@gmail.com

Indicates article with online supplemental data.

http://dx.doi.org/10.3174/ajnr.A8211

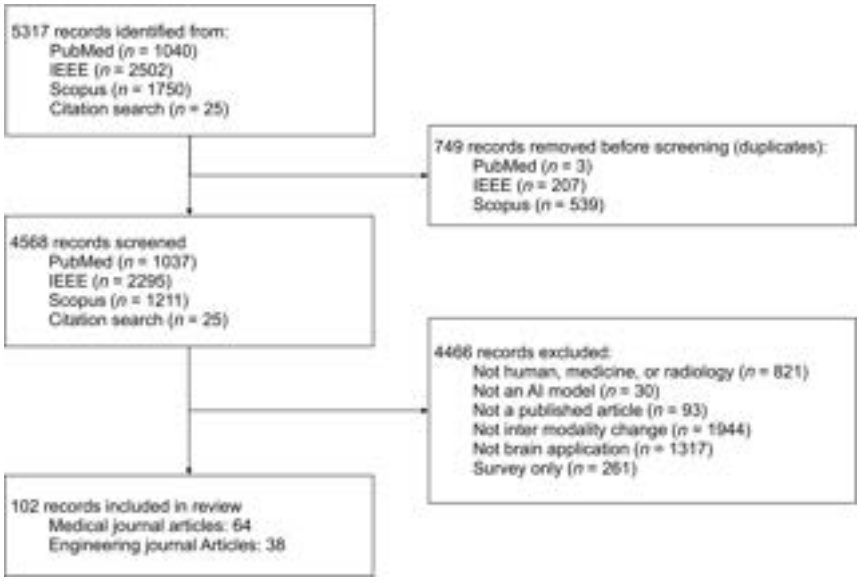

FIG 1. PRISMA flow chart.

still in the initial development stage. It has been suggested that fewer than one-quarter of AI studies could be reproduced from these methods,[11] reproduction being a necessary validation step before clinical application. Previous reviews described some study-design trends that might be related to the lack of progress toward clinical application.[4,6,12,13] There are also trends in the results for medically-focused journals and engineering-focused journals.[13,14] Various checklists have been designed to support authors in this task, but few are applicable to AI, and even fewer, to imaging-based studies. The Checklist for Artificial Intelligence in Medical Imaging (CLAIM)[15] is a prominent checklist for AI models built to classify, generate, or otherwise use medical images. This checklist includes 42 items that authors should include to ensure that readers can thoroughly assess and reproduce the work. Additionally, the Prediction model Risk Of Bias ASsessment Tool (PROBAST)[16] is designed for assessing bias in diagnostic or prognostic prediction models. This bias assessment is an integral part of any systematic review of health care models because it allows readers to visualize which studies have shortcomings that may lead to distorted results. Although many questions are not applicable to AI models, some PROBAST items can be used to evaluate biases specific to image-to-image translation studies. Using multiple checklists may provide more comprehensive coverage of all the salient points of each work.[17]

As this field grows, researchers must be aware of and consider the quality of and biases in their methods so that they can be transparently and consistently reported and, eventually, systematically mitigated.[18] In this review we used 2 common checklists to quantify the quality and extent of biases in intermodality image translation studies for brain imaging. We found no study applying CLAIM or PROBAST to evaluate image-to-image translation articles in the field of brain imaging.

MATERIALS AND METHODS

This review was registered on PROSPERO (CRD42022368642; https://www.crd.york.ac.uk/PROSPERO/) and was conducted in accordance with the Prisma statement (https://www.prisma.io/).[19] Approval from the ethics board was not necessary because this review used published data.

Searching Strategy

PubMed, Scopus, and IEEE Xplore were searched from inception through August 2, 2023, using variations of the terms artificial intelligence, MR, CT, image-to-image translation, image synthesis, Pix2Pix, and GAN. The full search text is available in the Online Supplemental Data. After a preliminary search, keywords related to the brain or specific brain diseases were considered too limiting, so we excluded these terms to reduce sampling bias. The references of similar reviews and the included studies were also screened for inclusion. Duplicate results were removed, and the remaining published articles were independently screened for inclusion by 2 authors. Inclusion criteria were studies developing or evaluating an AI model capable of converting images of the brain from one image technique to another, from human participants. Only the relevant experiments were considered from studies with multiple experiments (Fig 1).

Data

The data required to identify each study were collected into a predesigned spreadsheet. This spreadsheet includes relevant article information, data set information, the overall model purpose and design, the translation pair for all relevant experiments, and results for all relevant CLAIM and PROBAST criteria.[15,16] To reveal any differences specific to articles published in medically-focused or engineering-focused journals, we grouped journals on the basis of their aims and scope as in Kim et al.[12] Medically-focused journals were defined as those that included terms related to clinical medicine in their scope, and engineering-focused journals were those with an engineering, physics, or computer science scope. Unclear journals were classified in consensus between 2 authors. Extractable data were collected by one author and confirmed by 3 authors.

Quality Evaluation

Adherence to the CLAIM checklist was evaluated by 1 author using the full text and supplements of each study. Values were considered absent if they were missing or unclear. Questions not relevant to the study were marked as not applicable and did not negatively affect the CLAIM adherence estimation. For example, not all studies were classification or diagnosis tasks, so CLAIM question 36 was not applicable to these studies (Online Supplemental Data).

Bias Evaluation

PROBAST-based bias was evaluated by 1 author using questions 1.1, 1.2, 4.1, and 4.8 from PROBAST.[16] We used a generous definition of "external data set" for question 4.8, which includes

Table 1: Included studies

	Number of Studies	Average CLAIM Adherence	Average PROBAST Score
Image-generation direction			
MR imaging-CT	63	71%	38%
MR imaging-PET	13	74%	49%
CT-MR imaging	12	63%	41%
PET-CT	3	67%	33%
PET-MR	2	74%	56%
MR imaging-x-ray	1	64%	31%
US-MR imaging	1	67%	31%
Bidirectional	7	65%	33%
Total	102	70%	39%

Note:—US indicates ultrasound.

temporally separate data as well as data from different facilities, as in Kim et al.[12] Following Kuo et al[20] and Nagendran, et al,[21] we considered the patients included in the test set for domain 1 and excluded the other questions as not relevant to AI models, which perform image-to-image translation. This includes all of domain 2, which is not relevant to AI studies, and all of domain 3, because the outcome is not relevant for image translation studies (Online Supplemental Data).

For paired-image studies, which developed diagnostic, prognostic, or segmentation models, a large gap between the imaging of the 2 ground truth modalities may affect the resultant model classification or segmentation performance. The appropriate timing depends on the specific disease and may vary for individuals within a data set, so this information was collected but not evaluated.

Analysis

For CLAIM, the number of items evaluated as "yes" or "not applicable" was summed and divided by the total items in the checklist to estimate adherence at the study level as in Sivanesan et al.[14] PROBAST adherence is given as "high," "unclear," or "low" risk of bias designations for each study. Data normality was assessed using the Shapiro-Wilk test. Means were compared using the 2-sample *t* test; medians were compared using the Mann-Whitney *U* test between articles in medically-focused publications and those from engineering-focused publications. Item-level evaluation was performed for both CLAIM and PROBAST to show trends in image-to-image translation research. The Fisher exact test was used for each criterion to compare the medically-focused studies with the engineering-focused studies. Significance was defined as $P < .05$. Analysis was performed using R (Version 4.1.3; http://www.r-project.org/).

RESULTS

Study Demographics

There were 102 studies collected for this review. Medically-focused publications made up 64 studies, and 38 were from engineering-focused journals. The source images included MR imaging, CT, PET, and radiography (Table 1). Most studies evaluated MR imaging translation to either CT (63/102) or PET (13/102), citing the better soft-tissue contrast and lack of radiation exposure of MR imaging. Most MR imaging-to-CT studies targeted MR imaging–based radiation therapy planning (48/63). Dosimetry evaluations were included in 17 of these studies. Other targets included attenuation correction (10/63), more accurate registration (3/63), segmentation (1/63), and research data set generation for future AI studies (1/63). The MR imaging-to-PET studies primarily focused on the diagnosis of Alzheimer disease (4/13) or MS (1/13), glioma management and prognosis (2/13), attenuation correction (1/13,) and amyloid-burden estimation (2/13).

CT-to-MR imaging translation (12/102) was the next most common, with the rationale being that CT data are useful for dose calculations of radiation therapy and can be collected quickly, at lower cost, and at more facilities than MR imaging. Most of these studies targeted anomaly segmentation such as ischemic stroke localization (6/12) or CT-based radiation therapy planning (3/12). There were 7 studies that evaluated bidirectional translations; 6 of which comprised the MR imaging-to-CT and CT-to-MR imaging translation pair and 1 study that evaluated the PET-to-CT and CT-to-PET translation as well. One of these studies was designed for segmentation of follow-up images of patients with ischemic stroke; 2 others were designed to assist with radiation therapy planning.

Other translation pairs included MR imaging-to-radiograph for interventional imaging, PET-to-CT for attenuation correction, PET-to-MR imaging for amyloid-burden estimation, and ultrasound-to-MR imaging for easier communication between technicians and obstetricians (Online Supplemental Data).

The specific clinical purpose or application for the model in addition to image generation was described in 95 studies. We determined the remaining studies using the common clinical purposes for the translation pair. These include diagnosis, prognosis, registration, segmentation, and treatment (Online Supplemental Data). There was a significant difference in the CLAIM scores between the medically-focused and engineering-focused groups for both diagnosis and treatment purposes (Online Supplemental Data). The other purpose groups did not have enough data for the Mann-Whitney *U* test.

CLAIM Evaluation

Each study followed between 44% and 88% of applicable CLAIM criteria, with a 70% average overall (Fig 2). There was a significant difference in the adherence between medically-focused journal studies (73% average adherence) and those from engineering-focused journals (65% average adherence) ($P < .001$) (Fig 2 and Table 2). There was no significant difference between the performance of studies published before or after the CLAIM criteria were published. ($P = .841$).

There were 5 criteria with an average adherence of ≤10%. Of note, 1% of studies described the intended sample size (CLAIM 19), 3% of studies described the flow of including participants (CLAIM 33), and 8% of studies used an external testing data set (CLAIM 32).

Engineering-focused studies reported data for the questions related to describing the model in adequate detail (CLAIM 22, 24, 25, 26) in the article, while medically-focused studies more often moved this information to the supplement. On the other hand, medically-focused studies significantly outperformed

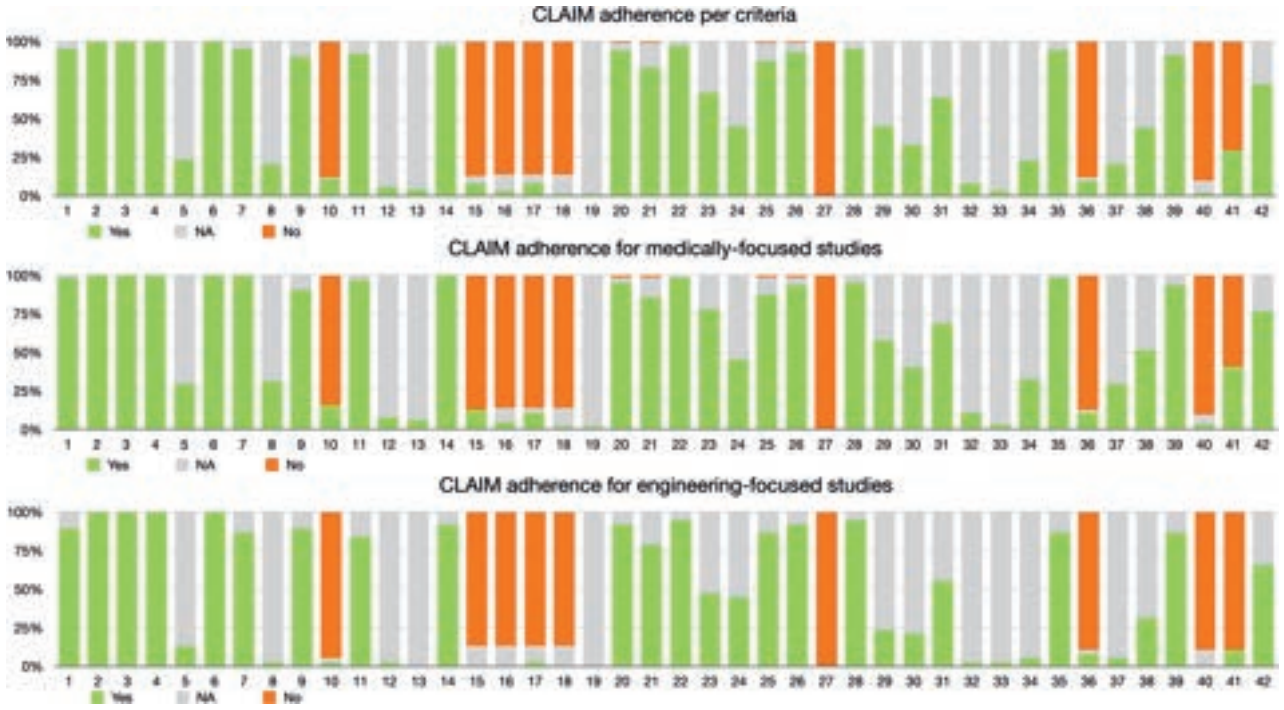

FIG 2. CLAIM evaluation. Each *vertical bar* shows the adherence for all studies for one of the CLAIM criteria. Within each bar, green represents the percentage of studies appropriately adhering to the CLAIM criteria, gray represents studies for which that question was not applicable, and orange represents studies that did not adhere to that CLAIM criteria. *A*, Overall adherence for 102 studies. *B*, Adherence for medically-focused studies ($n = 64$). *C*, Adherence for engineering-focused studies ($n = 38$). NA indicates not applicable.

Table 2: CLAIM adherence results

	Medically-Focused	Engineering-Focused	*P* Value
Title/abstract	99%	95%	.0652
Introduction	100%	100%	1
Methods	72%	63%	<.001
Results	53%	39%	.0046
Discussion	73%	59%	.0629
Other	90%	85%	.2023
Total	73%	65%	<.001

engineering-focused studies in 21% (9/42) of the CLAIM criteria. These criteria related to describing the data sets (CLAIM 7, 8, 11, 14, 15, 34), the software used for model development (CLAIM 23), statistical significance levels (CLAIM 29), and any failures (CLAIM 37).

Publication styles differ for engineering studies, and this feature significantly affected the resultant CLAIM adherence. Specifically, 27 of the 39 engineering-focused works were presented at engineering conferences and published as proceedings. These are given a DOI and widely regarded as citable publications,[22] though the peer review and writing of these submissions may still be of lower quality.[23,24] Thus, conference publications represent 72% of engineering-focused studies but <5% of medically-focused studies. Although they are considered published, we found that works written for engineering-focused conferences had significantly lower resultant CLAIM adherence than engineering-focused works for journals ($P = .01$) (Online Supplemental Data). Without these conference publications, medically-focused studies significantly outperform the engineering-focused studies for only 3 criteria related to describing the data sets (CLAIM 5, 8, 34).

The adherence for medically-focused and engineering-focused studies varied by study purpose (Online Supplemental Data). Medically-focused studies had significantly higher adherence for MR imaging-only radiation therapy planning, with an 11% improvement over the average for engineering-focused studies. Only medically-focused studies attempted dose calculations as part of a radiation therapy planning study, and excluding these did not affect the significance of the difference between the CLAIM score of these and the engineering-focused studies. Although there were not enough studies to confidently establish significance, attenuation correction and stroke lesion localization also had 10% and 18% higher CLAIM adherence than similar engineering-focused studies, respectively.

PROBAST Evaluation

Overall bias via PROBAST was low for 4 studies,[8,25-27] unclear for 4 studies, and high for 94 studies (Fig 3 and Table 3). Medically-focused studies used population-based data in significantly more studies. ($P = .006$) There was no significant difference in the PROBAST adherence for the other 3 questions between studies from medically-focused and engineering-focused journals (Fig 3) (Online Supplemental Data). There was no significant difference between the performance of studies published before or after the PROBAST criteria were published. ($P = 1$).

More than 71% (73/102) of studies used internally collected data for the test data set. These were presumed to be consecutive samples and marked as probably having a low risk of bias for question 1.1 unless stated otherwise. The remaining 29 studies used publicly available data. Although the use of curated public data sets is generally considered appropriate for AI model

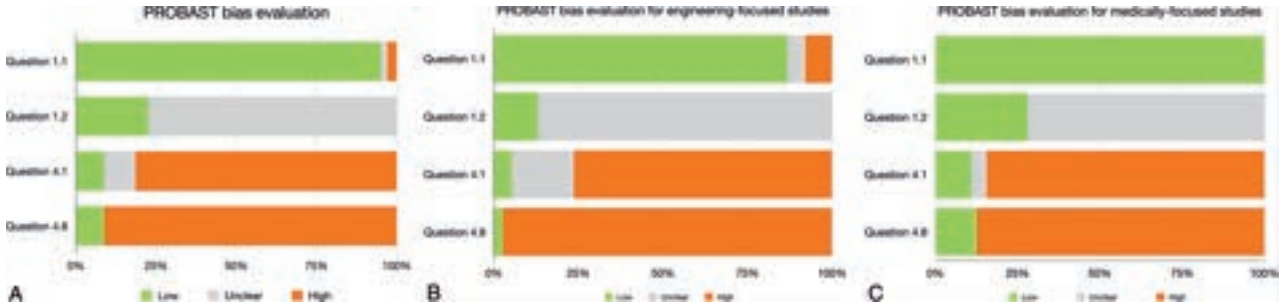

FIG 3. Bias evaluation. Each *horizontal bar* shows the risk of bias for all studies for one of the PROBAST criteria. Within each bar, green represents the percentage of studies with a low risk of bias and gray represents studies for which there was an unclear risk of bias, and orange represents studies with a high risk of bias for the question. Question 1.1 asks if the data source matched the target population. Question 1.2 asks if the inclusion and exclusion criteria were appropriate. Question 4.1 asks if the test data set was appropriately sized. Question 4.8 asks if the model was tested on an external data set to account for overfitting or optimism in the model. *A*, Overall adherence per question for all 102 studies. *B*, Adherence for engineering-focused studies ($n = 38$). *C*, Adherence for medically-focused studies ($n = 64$).

Table 3: Bias risk results

	Low	Unclear	High
All studies			
Question 1.1	97 (95%)	2 (2%)	3 (3%)
Question 1.2	23 (23%)	79 (77%)	0 (0%)
Question 4.1	9 (9%)	10 (10%)	83 (81%)
Question 4.8	9 (9%)	0 (0%)	93 (91%)
Overall bias	4 (4%)	4 (4%)	94 (92%)
Medically-focused adherence			
Question 1.1	64 (100%)	0 (0%)	0 (0%)
Question 1.2	18 (28%)	46 (72%)	0 (0%)
Question 4.1	7 (11%)	3 (5%)	54 (84%)
Question 4.8	8 (13%)	0 (0%)	56 (88%)
Overall bias	3 (5%)	4 (6%)	55 (86%)
Engineering-focused adherence			
Question 1.1	33 (87%)	2 (5%)	3 (8%)
Question 1.2	5 (13%)	33 (87%)	0 (0%)
Question 4.1	2 (5%)	7 (18%)	29 (77%)
Question 4.8	1 (3%)	0 (0%)	37 (97%)
Overall bias	1 (3%)	0 (0%)	37 (97%)

development, PROBAST standards require the model to be tested on data representative of the target population. Studies using public data sets that were not collected or adjusted to match the sampling frequencies of a real population were marked as having a high risk of bias for question 1.1.

Exclusion criteria were described in 17 studies, 13 of which were from medically-focused journals. An additional 6 studies (5 of which were from medically-focused journals) included language that implied that there were some exclusion criteria, though they were not described in detail. These were marked as probably having a low risk of bias for question 1.2. Because it is unclear if exclusions were maliciously hidden or if the authors had included all available images, the remaining 79 studies were marked as having an unclear risk of bias.

There were 6 studies with >100 individuals in the test data set, as recommended by PROBAST. Five of these were published in a medically-focused journal. The remaining studies either had test sets of <100 individuals or were not clear about the number of images of individuals in their test data set (this point is further addressed in CLAIM 21).

External data sets (PROBAST 4.8 and CLAIM 32) were used in 9% (9/102) of studies. Eight of these were published in medically-focused journals. The size of the external test set varied with a median of 17.5 and interquartile range of 126.25. It is difficult to accurately calculate significant changes across time with only 9 studies.

The timing between the index and reference test was reported in 30 of 89 studies that used paired data, and 3 of 13 studies that used unpaired data. We observed a slightly higher reporting rate in medically-focused studies (38% [24/64]) compared with engineering-focused studies (24% [9/38]) ($P = .191$).

DISCUSSION

This systematic review evaluated the quality issues and biases present in intermodality image translation studies relevant to brain imaging published before August 2023 using PROBAST and CLAIM criteria. We found 102 studies using brain images for intermodality image translation using an AI model. The principal findings of this review are that nearly all of the 102 published works had quality issues and critical biases hindering the clinical integration progress, with engineering-focused studies showing significantly lower checklist adherence than medically-focused studies. Studies at a high risk of bias largely lacked an external testing data set and were unclear about the data used, particularly the collection dates, data-source location, any exclusion criteria, the number of individuals included, and how the data were processed to make them fit for the AI model. Replication of results is of great importance in medicine—reflected in the numerous, detailed checklists available to researchers—and replication in the age of AI requires closer collaboration with our computer engineering colleagues.

To our knowledge, this is the first study to evaluate study quality and biases in intermodality image-to-image translation models for brain imaging. CLAIM and PROBAST were used to evaluate whether the methods or data sets used in these studies showed quality issues or risks of bias.[15,16] PROBAST is not only familiar to many readers, but it covers 4 of the signs of bias raised in other reviews and guidelines for applying AI to medical imaging translation.[12,13,28] We additionally chose the CLAIM checklist because it is designed to show the "rigor, quality, and generalizability of the work," by encouraging transparent and thorough reporting specifically of medical AI studies. This

checklist not only addresses all 4 included PROBAST criteria but also exposes bias risks from inadequate reporting of the included data sets and model development methods. The use of these measures together gives us a more granular view of the strengths and weaknesses of these studies.[17]

Because AI-based neurologic image translation represents an intersection of the medical and engineering fields, researchers on both sides must work together to make sure their work is clearly represented in published articles to improve repeatability.[11] Engineering studies in journals effectively described 4 CLAIM questions about the AI model (CLAIM 22, 24–26) more often than medically-focused studies, though this difference was not statistically significant. Similarly, medically-focused studies more often included data set details such as the number of patients and their demographics, included statistical measures such as confidence intervals, and listed some known limitations of their work (CLAIM 5, 8, 29, 34, 38). For these models to continue toward clinical integration, they must prove good performance while following both medical and AI engineering standards. Medically-focused tools such as PROBAST and CLAIM may be improved by requiring more of the model details provided by AI engineers to ensure accurate replication of these ever more complex AI models.[29] Additionally, authors can introduce checklists such as CLAIM for imaging studies, STARD (https://www.equator-network.org/reporting-guidelines/stard/)[30] for diagnostic accuracy studies, and TRIPOD (https://www.tripod-statement.org/about/)[31] for diagnostic or prognostic prediction studies to their collaborators who may be unfamiliar with them as a guide for writing their sections. Open collaboration between medical and AI engineering researchers is key to moving these models past the initial development stage.

Our findings of extensive risks of bias do not imply that a validated AI model would be insufficient as a clinician's support tool. Current tools and procedures have weaknesses for which AI may be able to compensate.[32] For example, there are scenarios such as radiation therapy planning that benefit from having both the better soft-tissue contrast of MR imaging and the electron density estimates of CT.[33] Because it is not always practical or possible to perform both examinations, an image translation model could generate this image. Furthermore, the CT scans and MR images must be registered for tasks like atlas-based methods or ischemic stroke lesion localization, which can lead to artifacts from misalignment.[4,6,34] By negating these weaknesses, image-generation AI models can lead to speedier, safer, more cost-efficient workflows, benefitting both the patient and the facility.

Limitations

This review had several limitations. There was heterogeneity in study designs of the collected studies, limiting our ability to compare the models and data sets directly. Our inclusion criteria may have excluded relevant studies, though we attempted to correct this possibility by scanning the references of both the collected works and previous reviews on the topic. We did not compare the publication requirements for the included journals, so it is unclear whether requirements, such as word-count limits, supplementary-material limits, or requirements on the use of standardized checklists, impacted quality and bias estimates. This study used only 2 checklists to estimate study design failures and risk of bias. While PROBAST is a common tool for bias evaluation of medical studies, it is difficult to apply to AI and even more so for image translation models. New guidelines specific to medical AI applications are in development that may address this difficulty.[29,35,36] Perhaps future AI works will modify their methods accordingly to minimize bias.

CONCLUSIONS

Image-to-image translation AI models represent a promising tool for reducing radiation exposure, examination costs, and time delay. However, currently published models have quality issues and are at high risk of bias, attributable to weak adherence to established reporting guidelines such as CLAIM and PROBAST. From a clinical applicability point of view, studies published in engineering-focused journals have significantly more quality issues and higher risk of bias than those published in medically-focused journals. However, medically-focused studies often lack necessary model development details found in engineering-focused studies. Our analysis shows that closer cooperation between medical and engineering researchers could improve overall guideline adherence, so these models can be validated and developed into valuable clinical tools.

Disclosure forms provided by the authors are available with the full text and PDF of this article at www.ajnr.org.

REFERENCES

1. Wolterink JM, Mukhopadhyay A, Leiner T, et al. **Generative adversarial networks: a primer for radiologists.** *Radiographics* 2021;41:840–57 CrossRef Medline
2. Ueda D, Shimazaki A, Miki Y. **Technical and clinical overview of deep learning in radiology.** *Jpn J Radiol* 2019;37:15–33 CrossRef Medline
3. Matheny ME, Whicher D, Thadaney Israni S. **Artificial Intelligence in Health Care: A Report From the National Academy of Medicine.** *JAMA* 2020;323:509–10 CrossRef Medline
4. Laino ME, Cancian P, Politi LS, et al. **Generative adversarial networks in brain imaging: a narrative review.** *J Imaging* 2022;8:83 CrossRef Medline
5. Seymour ZA, Fogh SE, Westcott SK, et al. **Interval from imaging to treatment delivery in the radiation surgery age: how long is too long?** *Int J Radiat Oncol Biol Phys* 2015;93:126–32 CrossRef Medline
6. Sorin V, Barash Y, Konen E, et al. **Creating artificial images for radiology applications using generative adversarial networks (GANs): a systematic review.** *Acad Radiol* 2020;27:1175–85 CrossRef Medline
7. Feng E, Qin P, Chai R, et al. **MRI generated from CT for acute ischemic stroke combining radiomics and generative adversarial networks.** *IEEE J Biomed Health Inform* 2022;26:6047–57 CrossRef Medline
8. Garzon G, Gomez S, Mantilla D, et al. **A deep CT to MRI unpaired translation that preserve ischemic stroke lesions.** *Conf Proc IEEE Eng Med Biol Soc* 2022;2022:2708–11 CrossRef Medline
9. Gutierrez A, Tuladhar A, Wilms M, et al. **Lesion-preserving unpaired image-to-image translation between MRI and CT from ischemic stroke patients.** *Int J Comput Assist Radiol Surg* 2023;18:827–36 CrossRef Medline
10. Rubin J, Abulnaga SM. **CT-to-MR conditional generative adversarial networks for ischemic stroke lesion segmentation.** In: *2019 IEEE International Conference on Healthcare Informatics (ICHI)*, June 10–13, 2019. Xi'an, China CrossRef
11. Bontempi D, Nuernberg L, Krishnaswamy D, et al. **Transparent and Reproducible AI-based Medical Imaging Pipelines Using the**

Cloud. *Research Square*. https://doi.org/10.21203/rs.3.rs-3142996/v1. Accessed October 1, 2023
12. Kim DW, Jang HY, Kim KW, et al. **Design characteristics of studies reporting the performance of artificial intelligence algorithms for diagnostic analysis of medical images: results from recently published papers.** *Korean J Radiol* 2019;20:405–10 CrossRef Medline
13. England JR, Cheng PM. **Artificial intelligence for medical image analysis: a guide for authors and reviewers.** *AJR Am J Roentgenol* 2019;212:513–19 CrossRef Medline
14. Sivanesan U, Wu K, McInnes MD, et al. **Checklist for artificial intelligence in medical imaging reporting adherence in peer-reviewed and preprint manuscripts with the highest altmetric attention scores: a meta-research study.** *Can Assoc Radiol J* 2023;74:334–42 CrossRef Medline
15. Mongan J, Moy L, Kahn CE Jr. **Checklist for artificial intelligence in medical imaging (CLAIM): a guide for authors and reviewers.** *Radiol Artif Intell* 2020;2:e200029 CrossRef Medline
16. Wolff RF, Moons KG, Riley RD, et al; PROBAST Group. **PROBAST: a tool to assess the risk of bias and applicability of prediction model studies.** *Ann Intern Med* 2019;170:51–58 CrossRef Medline
17. Klontzas ME, Gatti AA, Tejani AS, et al. **AI reporting guidelines: how to select the best one for your research.** *RadiolArtif Intell* 2023;5:e230055 CrossRef Medline
18. Ueda D, Kakinuma T, Fujita S, et al. **Fairness of artificial intelligence in healthcare: review and recommendations.** *Jpn J Radiol* 2024;42:3–15 CrossRef Medline
19. Page MJ, Moher D, Bossuyt PM, et al. **PRISMA 2020 explanation and elaboration: updated guidance and exemplars for reporting systematic reviews.** *BMJ* 2021;372:n160 CrossRef Medline
20. Kuo RY, Harrison C, Curran T-A, et al. **Artificial intelligence in fracture detection: a systematic review and meta-analysis.** *Radiology* 2022;304:50–62 CrossRef Medline
21. Nagendran M, Chen Y, Lovejoy CA, et al. **Artificial intelligence versus clinicians: systematic review of design, reporting standards, and claims of deep learning studies.** *BMJ* 2020;368:m689 CrossRef Medline
22. Patterson D, Snyder L, Ullman J. **Evaluating computer scientists and engineers for promotion and tenure.** *Computer Research Association* 1999 Aug 1. [Epub ahead of print]
23. Vardi MY. **Conferences vs. journals in computing research.** *Communications of ACM* 2009;52:5 CrossRef
24. Fortnow L. **Viewpoint: Time for computer science to grow up.** *Communications of ACM* 2009;52:33–35 CrossRef
25. Choi H, Lee DS, Alzheimer's Disease Neuroimaging Initiative. **Generation of structural MR images from amyloid PET: application to MR-less quantification**. *J Nucl Med* 2018;59:1111–17 CrossRef Medline
26. Pan Y, Liu M, Lian C, et al. **Synthesizing missing PET from MRI with cycle-consistent generative adversarial networks for Alzheimer's disease diagnosis**. *Med Image Comput Comput Assist Interv* 2018; 11072:455–63 CrossRef Medline
27. Takita H, Matsumoto T, Tatekawa H, et al. **AI-based virtual synthesis of methionine PET from contrast-enhanced MRI: development and external validation study.** *Radiology* 2023;308:e223016 CrossRef Medline
28. Park SH, Han K. **Methodologic guide for evaluating clinical performance and effect of artificial intelligence technology for medical diagnosis and prediction.** *Radiology* 2018;286:800–09 CrossRef Medline
29. Collins GS, Dhiman P, Andaur Navarro CL, et al. **Protocol for development of a reporting guideline (TRIPOD-AI) and risk of bias tool (PROBAST-AI) for diagnostic and prognostic prediction model studies based on artificial intelligence.** *BMJ Open* 2021;11: e048008 CrossRef Medline
30. Bossuyt PM, Reitsma JB, Bruns DE, et al; STARD Group. **STARD 2015: an updated list of essential items for reporting diagnostic accuracy studies.** *BMJ* 2015;351:h5527 CrossRef Medline
31. Moons KG, Altman DG, Reitsma JB, et al; Transparent Reporting of a Multivariate Prediction Model for Individual Prognosis or Development Initiative. **New guideline for the reporting of studies developing, validating, or updating a multivariable clinical prediction model: the tripod statement.** *Adv Anat Pathol* 2015;22:303–05 CrossRef Medline
32. Willemink MJ, Koszek WA, Hardell C, et al. **Preparing medical imaging data for machine learning.** *Radiology* 2020;295:4–15 CrossRef Medline
33. Wang T, Lei Y, Fu Y, et al. **A review on medical imaging synthesis using deep learning and its clinical applications.** *J Appl Clin Med Phys* 2021;22:11–36 CrossRef Medline
34. Yonezawa H, Ueda D, Yamamoto A, et al. **Maskless 2-dimensional digital subtraction angiography generation model for abdominal vasculature using deep learning.** *J Vasc Interv Radiol* 2022;33:845–51.e8 CrossRef Medline
35. Tejani AS, Klontzas ME, Gatti AA, et al. **Updating the Checklist for Artificial Intelligence in Medical Imaging (CLAIM) for reporting AI research.** *Nat Mach Intell* 2023;5:950–51 CrossRef
36. Sounderajah V, Ashrafian H, Golub RM, et al; STARD-AI Steering Committee. **Developing a reporting guideline for artificial intelligence-centred diagnostic test accuracy studies: the STARD-AI protocol.** *BMJ Open* 2021;11:e047709 CrossRef Medline

Jacob Valk, MD, PhD

This memorial aims to honor Professor Jaap Valk, who passed away on April 13, 2024, at 94 years of age, for his many clinical, educational, and scientific accomplishments.

Jaap was born in Rotterdam, the Netherlands, on July 23, 1929. He obtained his medical degree at Leiden University, followed by a residency in neurology and psychiatry. He practiced neurology and psychiatry for several years but decided to become a neuroradiologist and did his training with the famous Professor Bernard George Ziedses des Plantes, who invented planigraphy and radiographic subtraction. Jaap completed his thesis on brain atrophy in schizophrenia in 1971, with Ziedses des Plantes as supervisor. After his training in radiology and neuroradiology, Jaap became Head of the Department of Neuroradiology of VU University Medical Center as well as the Valerius Clinic, a psychiatric hospital in Amsterdam. In 1979, he was appointed full Professor of Neuroradiology at VU University. In 1981 he became the Head of Radiology of VU University Medical Center. He retired from his academic job in 1999 but continued to work in private practice.

Jaap loved to be at the forefront of new developments. He excelled in pneumoencephalography, myelography, angiography, intervention, and CT. His landmark articles on lateral cervical puncture, described in 1977 and re-evaluated in 1982 with more than 1000 cases, were required reading for radiology trainees. When the amazing, novel technique MR imaging entered medicine, he dived into it and wrote a book on the basic principles of MR imaging, together with Professor Cor MacLean and Dr Paul Algra (Elsevier, 1985). He got his first MR imaging machine in 1985, a 0.6 Technicare (Ridderkerk, The Netherlands). He had a keen interest in pediatric neuroradiology, and many children from the Netherlands came to Amsterdam for MR imaging, providing Jaap with a wealth of cases for studies, papers, courses, and international lectures.

Jaap had a true scientific mind. He taught his residents and PhD students that when coming to a conclusion, they always needed to be open to doubt and alternative interpretations. Nothing was set in stone for him. He was very interested in fields outside radiology and neurology, including physics, biochemistry, toxicology, embryology, pathology, immunology, molecular biology, and statistics. A review of his myriad publications confirmed his interest in these fields and his ability to encourage trainees in their academic pursuits. He supervised trainees not just in neurology and neuroradiology, but also in pathology, otolaryngology, orthopedics, and cardiology, inspiring them to explore new techniques, such as MR arteriography and blood flow to organ systems outside the brain and spine. He was highly regarded by both clinicians and basic scientists, always curious about the latest technical developments, suggesting improvements for more meaningful applications in patient populations.

Jaap was extremely productive. He favored writing books and authored and co-authored many, among which were *Computed Tomography of Cerebral Infarctions* (1981), *Basic Principles of Nuclear Magnetic Resonance Imaging* (1985), *Magnetic Resonance of Head, Neck and Spine* (1987), *Magnetic Resonance of Myelination and Myelin Disorders* (1989, 1995, and 2005), and *Magnetic Resonance of Dementia* (2002). He also co-authored many articles, more than 300 on PubMed. He gave numerous invited lectures at international meetings, which were impressive and overwhelming. He received many awards, including the Wertheim Salomonson Medal of the Dutch Society of Radiology (1996), the Gold Medal of the International Society of Magnetic Resonance in Medicine (1999), the Cornelia de Lange award of the Dutch Society of Child Neurology (2007), and the Gold Medal of the American Society of Pediatric Neuroradiology (2011). He became an honorary member of numerous international medical societies, including the Radiological Society of North America (2003) and the European Society of Neuroradiology (2018).

Jaap Valk was an inspiration to many. His relentless energy, his curiosity, his analytic thinking, and his unwavering interest to explore, study, and understand the fascinating complexity of the

Professor Jaap Valk was a wonderful clinical radiologist and physician who was able to connect to children with ease, instantaneously gaining their trust and sympathy.

human brain were unparalleled. One of his favorite phrases was "no matter, no mind," referencing the many inborn errors of metabolism and neurodegenerative disorders he studied during his long and illustrious career. During his entire life, he was a visionary. Jaap Valk recognized technologies early in his career and knew how to use them to advance science. He was one of the first to use CT and later MR imaging to study the CNS. The concept of pattern recognition of white matter disorders propelled the correct classification, recognition, and discovery of many neurodegenerative disorders. Together with Marjo van der Knaap, a child neurologist, he published the landmark article titled "Pattern Recognition in MR Imaging of White Matter Disorders in Children and Young Adults" in 1991.[1] It mentions the following: "The pattern recognition program was written so that when fed data about MR imaging abnormalities observed in a new case, the computer produces a differential diagnosis with probabilities and 95% confidence intervals for each differential diagnosis. The database is open-ended. It is hoped that the addition of new cases will result in more complete insight into the variability of patterns observed in disease categories and subcategories, and it will make the computer diagnosis more specific and reliable."

These conclusions were visionary and groundbreaking 33 years ago and could even today be the key message of any scientific article on artificial intelligence, machine learning, and deep learning, which is even more impressive. Jaap Valk was always far ahead of his time. MR imaging pattern recognition for white matter disorders turned out to be a magnificent diagnostic tool, which is still central for white matter disorders today. At its introduction, approximately two-thirds of the patients with a suspected genetic white matter disorder, a so-called leukodystrophy, did not receive a specific diagnosis. MR imaging pattern recognition of these unsolved cases led to the identification and definition of a series of novel leukodystrophies. The subsequent identification of related gene mutations proved that these novel disorders were real disease entities. One could say that MR imaging pattern recognition revolutionized the field of leukodystrophies. Throughout his life, Jaap kept a keen interest in leukodystrophies and supported the research when he could. Other subjects Jaap worked on included MR imaging of developmental anomalies of the spinal cord, multiple sclerosis, and dementia.

Jaap Valk was, of course, more than "just" a physician, educator, mentor, and scientist. He was a true renaissance man who enjoyed the company of people, traveled around the world, and made friends on at least 6 of the 7 continents. Knowing Jaap Valk, it may very well be that he also visited Antarctica, the seventh continent. Jaap Valk was generous, warm, welcoming, and interested in all aspects of culture and art. He showed a true interest in every person he met and made one feel special. He truly enjoyed being questioned by trainees at conferences and had the delightful habit of showing up at their presentations to be an encouraging presence. Jaap welcomed visits to his reading room by those same trainees, proud to highlight the accomplishments of his team. He loved to mentor people; he shared his wisdom, gave advice, and shaped and supported the careers of many of us.

Jaap Valk was a gifted pianist. During scientific meetings, whenever he could find a piano, he would sit down and play a happy tune for everybody to enjoy. He also wrote several plays. One of his recommendations was to try to write at least 1 book per year. Another piece of advice was that if you do not know anything about the subject, it helps to write a book about it.

A giant in medicine, a superb scientist, a great mentor, a world traveler, and a friend to so many has left us, but his legacy will endure and we are grateful for all he gave us.

REFERENCE

1. Van der Knaap MS, Valk J, de Neeling N, et al. **Pattern recognition in magnetic resonance imaging of white matter disorders in children and young adults.** *Neuroradiology* 1991;33:478–93 CrossRef Medline

Marjo S. van der Knaap
Susan Blaser
Peter van Zijl
Thierry A.G.M. Huisman

http://dx.doi.org/10.3174/ajnr.A8318

A Public Health Perspective on Radiologists' Interpretation Volumes

In the recent *AJNR* study by Ivanovic et al,[1] interpretation volume is associated with diagnostic error at the time of interpretation, presumably in the form of a missed diagnosis or misdiagnosis. The actual error rates may be even higher since RADPEER likely biases reviewers to save time and protect colleagues by minimizing discrepancy. While we support the goal to limit volumes, we note that suddenly limiting ourselves to 32 or 40 neuroradiology examinations per shift would rapidly lead to large queues of unread examinations and would inevitably delay many diagnoses. A delay in diagnosis is also a diagnostic error as defined by the National Academies. In England, delays in reporting have contributed to one-third of examined radiology systems failures.[2]

Also, we cannot estimate how volume limits would reduce error without knowing the degree to which the study model explains error. In our experience, regression models in radiology quality studies often explain only 10%–15% of the studied effect. We, thus, advocate for including the R^2 value to help elucidate the potential impact of interventions on the studied outcome.

Furthermore, as illustrated by the cited airline and anesthesiology experiences, risk mitigation entails addressing many factors that contribute both directly and indirectly to error. For example, examination types are associated with radiologists' recommendation rates,[3] due to diagnostic uncertainty, and there is likely a similar association with error. The Ivanovic et a1[1] study did not address whether the small fraction of studied shifts with <26 examinations included a high proportion of high-certainty/low-error examination types. Additional unstudied factors that potentially contribute to or confound the error association are noninterpretative responsibilities,[4] case complexity, and shift time of day.

Radiologists largely agree that higher interpretation volumes are psychologically unacceptable and unsustainable. Nevertheless, imaging volumes continue increasing, and our work is most valuable to patients and referring providers when performed promptly. Increasing the number of radiologists is virtually impossible in the short term given the 10-year American training pipeline and the barriers to hiring foreign-trained radiologists.[5] Meanwhile, strategies to limit radiologists' workloads and mitigate error should include the following: clinical trial–validated technologies, including artificial intelligence tools, to reduce ancillary and repetitive tasks and interruptions; reduction of clinically unnecessary imaging; examination scheduling triage based on urgency; and evidence-based guidelines that rank and reward quality and safety to counterbalance the incentive for workflows that maximize revenues and profits.

Disclosure forms provided by the authors are available with the full text and PDF of this article at www.ajnr.org.

REFERENCES

1. Ivanovic V, Broadhead K, Chang YM, et al. **Shift volume directly impacts neuroradiology error rate at a large academic medical center: the case for volume limits.** *AJNR Am J Neuroradiol* 2024 Jan 18. [Epub ahead of print] CrossRef Medline
2. Parliamentary and Health Service Ombudsman. **Unlocking Solutions in Imaging: working together to learn from failings in the NHS.** July 2021. https://www.ombudsman.org.uk/publications/unlocking-solutions-imaging-working-together-learn-failings-nhs. Accessed January 23, 2024
3. Guenette JP, Lynch E, Abbasi N, et al. **Actionability of recommendations for additional imaging in head and neck radiology.** *J Am Coll Radiol* 2024 Jan 12. [Epub ahead of print] CrossRef Medline
4. Glover M, Almeida RR, Schaefer PW, et al. **Quantifying the impact of noninterpretive tasks on radiology report turn-around times.** *J Am Coll Radiol* 2017;14:1498–503 CrossRef Medline
5. Khoshpouri P, Khalili N, Khalili N, et al. **Visa opportunities for international medical graduates applying for U.S. academic radiology department faculty positions: A national survey.** *AJR Am J Roentgenol* 2024;222:e2330008 CrossRef Medline

Jeffrey P. Guenette
Division of Neuroradiology
Brigham and Women's Hospital
Boston, Massachusetts

Center for Evidence-Based Imaging
Brigham and Women's Hospital
Boston, Massachusetts

Geoffrey S. Young
Division of Neuroradiology
Brigham and Women's Hospital
Boston, Massachusetts

http://dx.doi.org/10.3174/ajnr.A8240

Rajiv Gupta
Javier M. Romero
Division of Neuroradiology
Massachusetts General Hospital
Boston, Massachusetts

Raymond Y. Huang
Division of Neuroradiology
Brigham and Women's Hospital
Boston, Massachusetts

Peer Learning in Neuroradiology: Easier Than It Sounds

As multispecialty members of the Peer Learning Committee of the American College of Radiology (ACR), we read "Peer Learning in Neuroradiology: Not as Easy as It Sounds" with great interest. While it has been a long and ongoing process to create a paradigm shift away from traditional score-based peer review (RADPEER; https://www.acr.org/Clinical-Resources/RADPEER) to true peer learning (PL) and many challenges remain, we would like to emphasize that PL is, in fact, being widely embraced by the radiology community,[1] enabling neuroradiologists to improve patient care, radiologist satisfaction, and team engagement.

RADPEER has failed to demonstrate accuracy in determining radiologists' "competence," or improve learning or radiologists' engagement. By contrast, PL champions heed the call of the Institute of Medicine by viewing errors as avenues for system improvement that foster collaboration and growth within teams. The operative question, then, is "who wouldn't want to be a PL champion?" PL creates rewarding opportunities for neuroradiology leaders to positively contribute to their specialty by aligning stakeholders, promoting education, and inspiring collaboration across disciplines to improve care.[1] PL programs provide a platform to enact system improvements, including protocol optimization, workflow efficiency, sharing evidence-based clinical guidelines, and incorporating artificial intelligence into clinical practice. In doing so, neuroradiology leaders are following established paths endorsed by the ACR, American Board of Radiology (ABR), and more than one-half of all radiologists in the United States who already engage in PL[1] and have already demonstrated that it is a very "possible lift."

Effective health care leaders recognize value and eliminate barriers that may prevent success. Implementing any program without local leadership support, including time, is burdensome, so practice leaders should seek to transfer current resources from scored peer review into PL programs.

Practices that have already embraced PL use existing tools, Health Insurance Portability and Accountability Act–compliant forms and case-identification mechanisms, to gather learning opportunities while ensuring patient confidentiality. In fact, some authors of this article have recently documented their implementation details.[2] Continued clarification of needs and vendor advocacy is underway to create an off-the-shelf solution to reduce the "lift" of PL implementation.

Contrary to misconceptions, regulatory oversight agencies like The Joint Commission (TJC), Centers for Medicare & Medicaid Service, ABR, and ACR do not prohibit the transition to PL. The Ongoing Professional Practice Evaluation guidelines of TJC offer flexibility in data collection and metric establishment, without mandating score-based peer review. Recent shifts in TJC requirements reflect this flexibility, relieving health systems of rigid adherence to specific radiology peer review structures.[3]

The evidence supporting the effectiveness of PL is growing,[1] indicating its potential to engage radiologists, decrease burnout, and improve diagnostic accuracy. While further scientific research is needed to directly link PL to improved patient outcomes, we will not get there without the combined effort of thought-leaders in all radiology subspecialties. Rather than persisting with models that do not work, current effort should be directed at nurturing PL and studying which methods best allow sustained measurable learning and improved patient care. Recently published strategies for overcoming potential challenges and the wealth of resources available on the ACR Peer Learning Resources website (https://www.acr.org/Practice-Management-Quality-Informatics/Peer-Learning-Resources) will further support these efforts.

Disclosure forms provided by the authors are available with the full text and PDF of this article at www.ajnr.org.

REFERENCES

1. Sharpe RE, Tarrant MJ, Brook OR Jr, et al. **Current state of peer learning in radiology: a survey of ACR members.** *J Am Coll Radiol* 2023;20:699–711 CrossRef Medline
2. Kadom N, Reddy KM, Khanna G, et al. **Peer learning program metrics: a pediatric neuroradiology example.** *AJNR Am J Neuroradiol* 2022;43:1680–84 CrossRef Medline
3. Donnelly LF, Podberesky DJ, Towbin AJ, et al. **The Joint Commission's Ongoing Professional Practice Evaluation (OPPE): costly, ineffective, and potentially harmful to safety culture**. *J Am Coll Radio* 2023; 21:61–69 CrossRef

Mara M. Kunst
Department of Radiology
Lahey Hospital and Medical Center
Burlington, Massachusetts

Richard E. Sharpe
Department of Radiology
Mayo Clinic Arizona
Phoenix, Arizona

http://dx.doi.org/10.3174/ajnr.A8263

Jay K. Pahade
Department of Radiology
Yale New Haven Health
New Haven, Connecticut

Lane F. Donnelly
Department of Radiology
University of North Carolina
Chapel Hill, North Caroline

Jennifer Broder
Department of Radiology
Lahey Hospital and Medical Center
Burlington, Massachusetts

Reliability of CTA Alone and in Combination with CTP in the Detection of Cerebral Vasospasm: Methodologic Issues on Reliability to Avoid Misinterpretation

I was interested in the article by Heitkamp et al[1] published in the March 2024 issue of the *American Journal of Neuroradiology*. The authors investigated the reliability of CTA alone and in combination with CTP in the detection of cerebral vasospasm and the decision to initiate endovascular treatment. Three neuroradiologists were asked to grade 15 intracranial artery segments in 71 cases using a tripartite scale (no, mild <50%, or severe >50% vasospasm). They reported that the interrater reliability for per-segment analysis of vessels was highly variable ($\kappa = 0.16–0.61$). When one focused on senior raters, the addition of CTP images resulted in higher interrater reliability for severe vasospasm ($\kappa = 0.28$ versus $\kappa = 0.46$) and subsequently higher concordance ($\kappa = 0.23$ versus $\kappa = 0.73$) for the decision to start endovascular treatment.

Although the article provides insight into the decision about using CTA in combination with CTP to increase the reliability of endovascular treatment, its conclusion is limited in 2 important methodologic and statistical ways. First, the value of κ depends on the prevalence in each category. It is possible to have the prevalence of concordance cells equal to 90% and discordance cells equal to 10% and, however, obtain different κ values (0.44 as moderate versus 0.81 as very good, respectively).[2-4] Second, the Fleiss κ is a statistical measure for assessing the reliability of agreement among a fixed number of raters when assigning categoric ratings to a number of items. This use contrasts with other applications of κ such as the simple Cohen κ, which works only when assessing the agreement between not more than 2 raters or the intrarater reliability.

The authors concluded that CTA alone offers only low interrater reliability in the graduation of cerebral vasospasm. However, using CTA in combination with CTP might help, especially senior neuroradiologists, to increase the interrater reliability to identify severe vasospasm following aneurysmal SAH and to increase the reliability regarding endovascular treatment decisions. Considering the above-mentioned methodologic and statistical issues, such conclusions can easily be a misleading message.[2-4] Briefly, the prevalence-adjusted and bias-adjusted Fleiss κ should be applied to correctly assess the reliability of CTA alone and in combination with CTP in the detection of cerebral vasospasm and the decision to initiate endovascular treatment.

Disclosure forms provided by the authors are available with the full text and PDF of this article at www.ajnr.org.

REFERENCES

1. Heitkamp C, Geest V, Tokareva B, et al. **CTA supplemented by CTP increases interrater reliability and endovascular treatment use in patients with aneurysmal SAH.** *AJNR Am J Neuroradiol* 2024;45:284–90 CrossRef Medline
2. Sabour S. **Methodologic concerns in reliability of noncalcified coronary artery plaque burden quantification.** *AJR Am J Roentgenol* 2014;203:W343 CrossRef Medline
3. Sabour S, Rutten A, van der Schouw YT, et al. **Inter-scan reproducibility of coronary calcium measurement using multi detector-row computed tomography (MDCT).** *Eur J Epidemiol* 2007;22:235–43 CrossRef Medline
4. Sabour S. **Reliability of the ASA physical status scale in clinical practice: methodological issues.** *Br J Anaesth* 2015;114:162–63 CrossRef Medline

Siamak Sabour
Safety Promotion and Injury Prevention Research Center
Shahid Beheshti University of Medical Sciences
Tehran, I.R. Iran

Department of Clinical Epidemiology
School of Public Health and Safety
Shahid Beheshti University of Medical Sciences
Tehran, I.R. Iran

http://dx.doi.org/10.3174/ajnr.A8241

REPLY:

We appreciate the interest of Mr Sabour in our study and his knowledgeable comments regarding our article recently published in the *American Journal of Neuroradiology*.[1] We are grateful for the opportunity to address his concerns.

As correctly pointed out by Mr Sabour, we used the Cohen κ to assess interrater reliability between 2 raters with categoric ratings (treatment yes/no), while the Fleiss κ was used to calculate the agreement for all 3 raters (refer to Supplementary Figure 2). The dependence of κ coefficients on prevalence has been frequently criticized and discussed;[2] however, the relevance remains controversial.[3,4] In the selection of methodologic and statistical test procedures, we referred to previous studies on interrater reliability in patients with vasospasm to ensure sound comparability and coherence.[5,6] For the sake of clarity, we concur that a prevalence-adjusted and bias-adjusted interrater analysis may provide additional value. Please see below the prevalence-adjusted and bias-adjusted κ coefficients regarding the detection of severe vasospasm in any arterial segment (>50% narrowing), endovascular treatment decision, and the presence of a perfusion deficit (Table). The results before and after adjustment for prevalence and bias were very similar, leaving the clinical implications of our study unchanged. These findings are also in line with the standards applied in most clinics.

REFERENCES

1. Heitkamp C, Geest V, Tokareva B, et al. **CTA supplemented by CTP increases interrater reliability and endovascular treatment use in patients with aneurysmal SAH.** *AJNR Am J Neuroradiol* 2024;45:284–90 CrossRef Medline
2. Hallgren KA. **Computing inter-rater reliability for observational data: an overview and tutorial.** *Tutor Quant Methods Psychol* 2012;8:23–34 CrossRef Medline
3. Kottner J, Audigé L, Brorson S, et al. **Guidelines for Reporting Reliability and Agreement Studies (GRRAS) were proposed**. *J Clin Epidemiol* 2011;64:96–106 CrossRef Medline
4. Vach W. **The dependence of Cohen's kappa on the prevalence does not matter**. *J Clin Epidemiol* 2005;58:655–61 CrossRef Medline
5. Darsaut TE, Derksen C, Farzin B, et al. **Reliability of the diagnosis of cerebral vasospasm using catheter cerebral angiography: a systematic review and inter- and intraobserver study.** *AJNR Am J Neuroradiol* 2021;42:501–07 CrossRef Medline
6. Letourneau-Guillon L, Farzin B, Darsaut TE, et al. **Reliability of CT angiography in cerebral vasospasm: a systematic review of the literature and an inter- and intraobserver study.** *AJNR Am J Neuroradiol* 2020;41:612–18 CrossRef Medline

Christian Heitkamp
Christian Thaler
Department of Neuroradiology
University Medical Center Hamburg-Eppendorf
Hamburg, Germany

Interrater reliability regarding graduation and treatment decisions of vasospasm on CT

	Interrater Reliability (95% CI)	
	All Raters (n = 3)	Senior (n = 2)
First rating (CTA)		
Detection of severe vasospasm in any arterial segment (>50% narrowing)	0.27 (0.11–0.42)	0.28 (0.10–0.46)
	0.27 (0.11–0.43)[a]	0.21 (−0.02–0.44)[a]
Endovascular treatment?	0.23 (0.06–0.39)	0.23 (−0.01–0.46)
	0.23 (0.07–0.39)[a]	0.23 (−0.01–0.46)[a]
Second rating (CTA + CTP)		
Detection of severe vasospasm in any arterial segment (>50% narrowing)	0.31 (0.15–0.46)	0.46 (0.26–0.66)
	0.31 (0.15–0.46)[a]	0.46 (0.25–0.68)[a]
Endovascular treatment?	0.47 (0.30–0.64)	0.73 (0.55–0.91)
	0.50 (0.35–0.66)[a]	0.77 (0.62–0.93)[a]
Perfusion deficit?	0.77 (0.63–0.91)	0.82 (0.66–0.97)
	0.83 (0.73–0.94)[a]	0.86 (0.74–0.98)[a]

[a] Prevalence-adjusted and bias-adjusted κ coefficients. Note that the values were highly comparable with the results presented in the published article.

http://dx.doi.org/10.3174/ajnr.A8310

On Behalf of Serial Imaging in Preterm Infants

We read with great interest the article by Roychaudhuri et al.[1] Having gathered a cohort of 30 preterm infants born at <33 weeks' gestational age, the authors found a strong correlation between the white matter injury (WMI) severity, as scored on brain MR imaging, at 2 time points: early (30–34 weeks' postmenstrual age) and term-equivalent age (TEA). Specifically, approximately 80% of infants remained in the same WMI category from early to TEA assessments. Building on these results, the authors suggest performing early-brain MR imaging within 2 weeks after preterm birth. Despite acknowledging the potential prognostic value of an early-brain MR imaging, we are concerned about its applicability and propose a perhaps better-suited approach for less-resourced imaging centers.

TEA-brain MR imaging is reliable at predicting motor outcome in infants with hypoxic-ischemic encephalopathy. The call for an early-brain MR imaging in premature infants is based on 2 premises: 1) We are not good at predicting nonmotor outcomes, and 2) MR imaging is superior to cranial ultrasound (CUS) at depicting noncystic WMI, notably diffuse periventricular leukomalacia (PVL) and punctate white matter lesions (PWMLs), which may be inconspicuous on TEA-brain MR imaging, yet still suspected to impair cognition.

PWMLs have been reported to be the most frequent lesion type (41%) in premature infants, most of whom had other brain abnormalities.[2] We speculate that some of these additional lesions would be highly specific for abnormal cognitive outcomes (eg, hemorrhagic parenchymal infarction, cerebellar hemorrhage >5 mm^2) and are easily outlined on CUS.

Given the presumable ischemic pathophysiology of diffuse PVL, we were intrigued by the low prevalence (<7%) of diffusion-restricted lesions on the initial MR imaging, even though a sizable portion of infants (10 of 30) had a moderate/severe WMI on the later MR imaging; this issue seems to disclose the limited added value, grounded on a brief DWI abnormality and fast ADC pseudonormalization, of performing a complex grading system on a somewhat arbitrarily defined–and dependent on the preterm infant's clinical stability–early-brain MR imaging compared with sequential CUSs.

Most interesting, early confluent DWI hyperintensities–but not focal ones–have been shown to precede cystic degeneration.[3] We believe that optimizing diffusion sequences for portable MR imaging systems[4] may be a "game changer" by enabling serial monitoring for confluent diffusion-restricted lesions, efficiently forecasting cystic WMI in at-risk premature infants.

Disclosure forms provided by the authors are available with the full text and PDF of this article at www.ajnr.org.

REFERENCES

1. Roychaudhuri S, Côté-Corriveau G, Erdei C, et al. **White matter injury on early versus-term-equivalent age brain MRI in infants born preterm**. *AJNR Am J Neuroradiol* 2024;45:224–28 CrossRef Medline
2. Arulkumaran S, Tusor N, Chew A, et al. **MRI findings at term-corrected age and neurodevelopmental outcomes in a large cohort of very preterm infants.** *AJNR Am J Neuroradiol* 2020;41:1509–16 CrossRef Medline
3. Martinez-Biarge M, Groenendaal F, Kersbergen KJ, et al. **MRI based preterm white matter injury classification: the importance of sequential imaging in determining severity of injury.** *PLoS One* 2016;11: e0156245 CrossRef Medline
4. Cawley P, Padormo F, Cromb D, et al; UNITY Consortium. **Development of neonatal-specific sequences for portable ultralow field magnetic resonance brain imaging: a prospective, single-centre, cohort study.** *EClinicalMedicine* 2023;65:102253 CrossRef Medline

J. Saraiva
J.P. Soares-Fernandes
Hospital de Braga
Braga, Portugal

http://dx.doi.org/10.3174/ajnr.A8223

REPLY:

We are grateful to the authors for their reflections on our study supporting the value of serial neuroimaging. The early MR imaging in our study was, on average, 4 weeks after birth for infants with a gestational age of 28 weeks. Thus, early diffusion-weighted imaging was often too late to detect acute white matter injury in most of our infants. We support the premise from the authors that early (first 14 days of life) diffusion imaging may improve early detection of moderate-severe white matter injury. In addition, the presence of other hemorrhagic brain injuries in any preterm infant should highlight the risk that ischemic brain injury occurred and thus elevate the concern for other forms of brain injury such as nonhemorrhagic white matter injury. Unfortunately, many neonatal clinicians still minimize the use of cranial ultrasound, including the number of scans and bone windows used, while many do not undertake any MR imaging. Access to a reliable definition of the nature and severity of brain injury in the high-risk preterm infant, as early as possible, can assist in targeting rehabilitative therapeutic services to those who may benefit most.

Terrie Inder
Center for Neonatal Research
Childrens Hospital of Orange County
Orange, California

University of California Irvine
Irvine, California

http://dx.doi.org/10.3174/ajnr.A8316